9-27-2018

New derivatives of 1,2,4-benzothiadiazines and their coordination chemistry

Konstantina Pringouri
University of Windsor

Recommended Citation

Pringouri, Konstantina, "New derivatives of 1,2,4-benzothiadiazines and their coordination chemistry" (2018). *Electronic Theses and Dissertations*. 7560.
https://scholar.uwindsor.ca/etd/7560

NEW DERIVATIVES OF 1,2,4-BENZOTHIADIAZINES AND THEIR COORDINATION CHEMISTRY

By

Konstantina Pringouri

A Dissertation
Submitted to the Faculty of Graduate Studies
through the Department of Chemistry and Biochemistry
in Partial Fulfillment of the Requirements for
the Degree of Doctor of Philosophy
at the University of Windsor

Windsor, Ontario, Canada

2018

New derivatives of 1,2,4-benzothiadiazines and their coordination chemistry

by

Konstantina Pringouri

APPROVED BY:

J. Brusso, External Examiner
University of Ottawa

D. Northwood
Department of Mechanical, Automotive and Materials Engineering

C. Macdonald
Department of Chemistry and Biochemistry

S. Loeb
Department of Chemistry and Biochemistry

J. Rawson, Advisor
Department of Chemistry and Biochemistry

September 18th, 2018

DECLARATION OF CO-AUTHORSHIP AND PREVIOUS PUBLICATION

I. Co-Authorship

I hereby declare that this thesis incorporates some material that is the result of joint research, as follows: Kinetic studies on the preparation of benzothiadiazines presented in Chapter 2 were undertaken by undergraduate student Mr. Nathan Doupnik under my guidance. I gratefully acknowledge the generosity of Dr. M. Pilkington (Brock University) for access to the single crystal X-ray diffractometer at the University of Brock for the collection of selected sets of single crystal X-ray diffraction data presented in this thesis. Dr. Rawson assisted with the processing and refinement of a number of particularly problematic crystallographic data sets. I would like to thank Ms. Nadia Stephaniuk for collecting the X-ray powder diffraction patterns presented in Chapter 4. Assistance with the simulation of anisotropic EPR spectra throughout this thesis was provided by Dr. Rawson. I acknowledge assistance with ligand development presented in Chapters 4 and 5 from two PDFs in the Rawson group, Dr. Elodie Heyer and Dr. M. Usman Anwar respectively. Dr. Heyer, along with Dr. Yassine Beldjoudi, also provided assistance with the electrochemical studies presented in Chapter 5. Magnetic data presented in this thesis were collected by Dr. Emma Gavey (University of Brock) or Dr. Javier Campo (University of Zaragoza) and analyzed by Dr. Rawson.

I am aware of the University of Windsor Senate Policy on Authorship and I certify that I have properly acknowledged the contribution of other researchers to my thesis, and have obtained written permission from each of the co-author(s) to include the above material(s) in my thesis. I certify that, with the above qualification, this thesis, and the research to which it refers, is the product of my own work.

II. Previous Publication

At the time of submission of this thesis, some of the work originating from the studies described in this thesis has already been published or has been submitted for publication as follows:

1. "Synthesis and characterization of green-to-yellow emissive Ir(III) complexes of pyridylbenzothiadiazine ligand"
   Amlan K. Pal, David B. Cordes, **Konstantina Pringouri**, Muhammad U. Anwar, Alexandra M. Z. Slawin, Jeremy M. Rawson, and Eli Zysman-Colman,
   Journal of Coordination Chemistry, 2016, **11-13**, 1924-1937

The ligand synthesis was undertaken by myself in conjunction with Dr. Anwar, while the iridium coordination chemistry was undertaken by A.K. Pal and D.B. Cordes within the Zysman-Colman group at the University of St. Andrews. The crystallographic studies were undertaken by Dr. Slawin and all authors contributed to preparation of the manuscript.

2. **Konstantina Pringouri**, Muhammad U. Anwar, Bryce J. Leontowicz, and Jeremy M. Rawson,
   "Zinc complexes of 3-pyrimidinyl-benzo-1,2,4-thiadiazine"
   Polyhedron, 2018, **150**, 110-117

The initial ligand synthesis was undertaken by RA, Mr. Bryce Leontowicz, in conjunction with Dr. Anwar. All other studies were undertaken by myself and all authors contributed to manuscript preparation.

3. **Konstantina Pringouri**, Muhammad U. Anwar, Liz Mansour, Nathan Doupnik, Yassine Beldjoudi, Emma L. Gavey, Melanie Pilkington, and Jeremy M. Rawson,
   "A novel bis-1,2,4-benzothiadiazine pincer ligand: Synthesis, characterization and first row transition metal complexes"
   Dalton Trans., Under revision

I acknowledge assistance in the synthesis of the ligand and metal complexes from Dr. Anwar and Ms. Liz Mansour. Electrochemistry studies were undertaken from Dr. Beldjoudi. Magnetic data were collected by Dr. Gavey (University of Brock) and analyzed by Dr. Rawson. All other studies were undertaken by myself and all authors contributed to manuscript preparation.

I certify that I have obtained a written permission from the copyright owners to include the above published materials in my thesis. I certify that the above material describes work completed during my registration as a graduate student at the University of Windsor.

III. General

I certify that, to the best of my knowledge, my thesis does not infringe upon anyone's copyright nor violate any proprietary rights and that any ideas, techniques, quotations, or any other material from the work of other people included in my thesis, published or otherwise, are fully acknowledged in accordance with the standard referencing practices. Furthermore, to the extent that I have included copyrighted material that surpasses the bounds of fair dealing within the meaning of the Canada Copyright Act, I certify that I have obtained a written permission from the copyright owner(s) to include such material(s) in my thesis and have included copies of such copyright clearances to my appendix.

I declare that this is a true copy of my thesis, including any final revisions, as approved by my thesis committee and the Graduate Studies office, and that this thesis has not been submitted for a higher degree to any other University or Institution.

ABSTRACT

Chapter 1 provides an introduction to coordination chemistry and polydentate N-donor ligands along with a synopsis of heterocycles with N and S/N donor atoms. An overview of the chemistry and applications of 1,2,4-benzothiadiazines as well as their previously reported coordination chemistry follows.

Chapter 2 describes the synthesis of the ligand 3-(2′-pyridyl)benzothiadiazine (pybtdaH). Computational studies on the ligand determining the most stable conformation and tautomer, as well as the energy barrier of the pyridyl ring rotation. The coordination chemistry of pybtdaH with more basic counterions (hfac$^-$ and OAc$^-$) or Lewis acidic metal (Fe^{III}) results to oxidation of pybtdaH forming either pybtdaH$_{ox}$ or pybtda$_{ox}^-$. The ligand acts as terminal in the mononuclear complexes with formulas $FeCl_3$(pybtdaH$_{ox}$)(CH_3OH), M(hfac)$_2$(pybtdaH$_{ox}$) (M = Mn, Co, Ni) and Co(pybtda$_{ox}$)$_3$. The pybtda$_{ox}^-$ offers a *N*,*N*′-pocket and an additional *O*-donor *via* the S=O group leading to polynuclear metal complexes with formulas $Fe_4Cl_4(OCH_3)_6$(pybtda$_{ox}$)$_2$, $Cu_2(OAc)_2$(pybtda$_{ox}$)$_2$(H_2O)$_2$, $Zn_2(OAc)_2$(pybtda$_{ox}$)$_2$, and the polymer [Cu(hfac)(pybtda$_{ox}$)]$_n$. The addition of base (Et_3N) in the reaction schemes favoured aggregation resulting to the polynuclear complexes Ni_3(hfac)(pybtda$_{ox}$)$_5$(H_2O), $Cu_4(OH)_4$(pybtda$_{ox}$)$_4$ and $Cu_{14}(OH)_{12}(CO_3)_2$(pybtda$_{ox}$)$_{12}$(H_2O)$_2$.

The synthesis of the novel redox active ligand 3-(2',6'-pyrimidine)-benzo-1,2,4-thiadiazine (pmbtdaH) is reported in Chapter 3. The radical pmbtda$^\bullet$ can be prepared by *in situ* 1*e*$^-$ oxidation and its radical character confirmed by EPR spectroscopy and DFT calculations. Reaction of pmbtdaH with $MCl_2\cdot 2H_2O$ (M = Mn, Fe, Co, Ni) affords a series of mononuclear complexes with formula MCl_2(pmbtdaH)$_2$ and the dinuclear complex Zn_2Cl_4(pmbtdaH)$_2$ in which the ligand coordinates in a simple *N*,*N*′-chelate fashion. The reactions of pmbtdaH with M(hfac)$_2$ (M = Mn, Co, Ni, Cu, Zn) rapidly afforded the mononuclear complexes M(hfac)$_2$(pmbtdaH). The hfac$^-$ ligand appears sufficiently basic to promote slow aerial oxidation of the pmbtdaH ligand and a series of complexes were isolated on extended storage incorporating either pmbtdaH$_{ox}$ or pmbtda$_{ox}^-$. These include the mononuclear complexes M(hfac)$_2$(pmbtdaH$_{ox}$) (M = Co, Ni) and the dimer

$Mn_2(hfac)_2(tfa)_2(pmbtdaH_{ox})_2$. The deprotonated and oxidized form of the ligand bridges three metal centres *via* two *N*,*N′*-chelate coordination pockets and the S-O group resulting in the tetranuclear complexes $Cu_4(hfac)_4(tfa)_2(pmbtda_{ox})_2$ and $Zn_4(hfac)_6(pmbtda_{ox})_2$. The complexes were characterized by X-ray diffraction, elemental analysis, IR and UV-Vis spectroscopies, as well as ^1H NMR spectroscopy for the diamagnetic complex $Zn(hfac)_2(pmbtdaH)$.

Chapter 4 describes the *S*-functionalization of the pybtdaH ligand to afford the 1-methyl-3-(2′-pyridinyl)benzothiadiazine (pybtdaSMe). The reaction of the ligand with $MCl_2{\cdot}2H_2O$ (M = Mn, Ni, Zn) gives two mononuclear complexes with general formula $MCl_2(pybtdaSMe)_2$ and the 1:1 adduct $ZnCl_2(pybtdaSMe)$. The reaction of $CuCl_2$ with pybtdaSMe is sensitive to the solvent resulting in two polymorphs, $Cu_2Cl_4(pybtdaSMe)_2$ and $Cu_2Cl_4(pybtdaSMe)_2{\cdot}2CuCl_2(pybtdaSMe)$. Preliminary results examining the reactivity of this ligand with $M(hfac)_2$ (M = Co, Ni) afforded the corresponding mononuclear complexes $M(hfac)_2(pybtdaSMe)$ (M = Co, Ni).

In Chapter 5, the synthesis and characterization of the novel terpy-like ligand 3,3'-pyridine-2,6-diylbis(benzothiadiazine) ($bisbtdaH_2$) is reported. Electrochemical studies on the free ligand $bisbtdaH_2$ reveal a single well-defined $2e^-$ oxidation process and EPR studies of the *in situ* chemical oxidation on $bisbtdaH_2$. The coordination chemistry of the ligand with a range of divalent transition metal salts MX_2 (M = Mn, Fe, Zn, X = CF_3SO_3; Fe, X = BF_4; Co, Ni, X = Cl) afforded mononuclear complexes of general formula $[M(bisbtdaH_2)_2][X]_2$, whereas reaction of $Cu(NO_3)_2$ with $bisbtdaH_2$ afforded the 1:1 complex $Cu(bisbtdaH_2)(NO_3)_2$. In all cases the $bisbtdaH_2$ ligand binds in a tridentate *N*,*N′*,*N″*-chelate fashion *via* both N_{BTDA} and N_{py} atoms. The low-spin Fe^{II} complexes were implemented for NMR and UV-Vis solution studies of ligand reactivity, as well as cyclic voltammetry which reveals the oxidation process occurs *via* two single e^- oxidation waves. The metal complexes reveal a range of 6-coordinate geometries between octahedral and trigonal prismatic with the greatest deviation from octahedral symmetry apparent for ions with no crystal field stabilization energy.

Chapter 6 provides a brief overview of the results presented in this dissertation, the insight provided within this research area and the potential for future exploitation.

To my parents, Γεωργία and Βασίλη, and my brother, Γιάννη

To my grandparents, Κωνσταντίνα and Παναγιώτη

ACKNOWLEDGMENTS

The journey of the last four years has been one of the greatest experiences of my life. As in any journey, the most exciting part is the people you meet along the way in addition to the ones you always carry inside you.

First of all, I would like to thank Dr. Jeremy M. Rawson for the opportunity he gave me to join his group, as the start of the whole journey. I am extremely grateful for the guidance, encouragement and unwavering support during the last four years. Thank you for your belief and trust throughout the journey, but especially towards the end of it. Thank you for all your patience on my repetitive questions and always making everything so simple and understandable. I am very blessed and grateful for having a “Rawsome” supervisor.

I would like to thank my committee members, Dr. Stephen Loeb, Dr. Charles Macdonald and Dr. Derek Northwood for their constructive feedback and guidance over the course of my degree which helped me improve my existing knowledge. I would like to thank Dr. Jaclyn Brusso for accepting the role of the external examiner. I thank you all for taking the time to read this dissertation, but also to travel and be present in my defence.

Ontario welcomed me with the best possible way with the Ontario Trillium Scholarship to fund my studies, so “Thank you”!

The best welcome in the lab by Dr. M. Usman Anwar was a great start for me. Although we shared a coordination “mixing” background, he made the introduction to organic synthesis and the world of benzothiadiazines a very smooth and comfort procedure for me. Thank you for being patient on my first steps, encouraging me with your calm and positive attitude and reassuring me that the flask will not explode just like that!

Dr. Elodie Heyer gave me the boost I really needed, in my second year, both mentally and physically. She took the organic synthesis to the next level, by turning it to a world of columns and TLCs, which almost made me love organic chemistry (although I will betray my crystals). Thank you for teaching me the way to look properly for the answers and understanding whatever I observe. You were there to help me with every little thing I could think or not! Thank you for communicating without having to talk (even though sometimes it was extremely confusing for the boss!). There are so many memories coming out of their box at this moment, and the least I can do is to thank you for every single one.

The Rawson group has been essential for the completeness of this work. Starting from the current group members Aisha Alsaleh, Dominique Leckie, Mitchell Nascimento, Nadia Stephaniuk, and Lara Watanabe and going back to the former group members Zeinab Ahmed, Natalia Mroz and Dr. Yassine Beldjoudi, I am thankful to all of you for all of your encouragement and support throughout my studies. Thank you for helping with measurements, offering great partnership when I had to share the lab, providing great and valuable conference memories and supplies with lemons, soups and hugs through my first rough winters in Canada.

I would like to thank Nathan Doupnik for all his help on various projects and the supplies of starting material. Through him, I clearly realized that supervising is not teaching but mostly learning and I am grateful for this. I would also like to thank Dr. John Hayward for the mechanistic organic discussions, interpretation of NMR spectra and of course my “Great Job” sticker for the reproducible Cu_{14}!

Many thank you to: Ghazale Gholami, the first person I met in UWindsor and helped me from my first day, Stephanie Kosnik, for the opportunity to act a student representative during my last year, Giorgio Baggi, for his help with the titration drama I had to experience, and Pablo Martinez-Bulit, Justin Binder, Stanislav Veinberg, Manar Shoshani, Alex Stirk, and Thanasis Katsenis for helping with X-ray, as well as valuble presentation and lab tips throughout the years.

A special thanks is owed to the members of the graduate office for their continued support; Elizabeth Kickham for the endless work orders to have an efficient fume hood to work and all the GA arrangements and travel reimbursements. Catherine Wilson for her help introducing me in the administrative world of academia while I was the student representative. Marlene Bezaire for being the greatest Ph.D. coordinator and keeping me in the deadlines. It meant the world to me!!

Thanks to Dr. Janeen Auld for introducing me to the “elemental” world and all her help with accommodating the measurements to match my schedule. Dr. Matt Revington for always being around to answer my questions on NMR and keeping the magnets running properly. Joe Lichaa could not be forgotten (especially the one on the third floor!); saving me from hardware and software crises and all his work on the X-ray machine to have it running smoothly, even at very low temperatures to avoid fixing all the disorder on my structures! I will try to remember all the life advices and stop being a W^2. A big thank you goes to Nedhal Al-Nidawy for the motherly advices and encouragement all those years as well as her understanding with my load of work. Thank you for your GA Excellence Award nominations; it was great to feel acknowledged. Special thanks are to be given to Una Lee for her rides to school and Ronan San Juan for the relaxing talks and chocolate supplies.

Besides chemistry, this Ph.D. helped realize that friends and family, are among the greatest values in life. I was grateful to have many “families” around the world on this journey and I would like to thank all of them.

My Windsor family: Spiro and Endelia, my Greek landlords for welcoming me in “Spiroville” and their home these past four years, helping me on every aspect of my everyday life, but especially for making sure I am staying alive. Pauline and Petro, my Greek neighbours for finding a great aunt and uncle, always with nice treats and sweet smelling lilac to brighten my day. Christopher and Susan, my yogi neighbours who helped me get through the last four months, the writing season, to maintain a healthy mind in a healthy body.

My Chicago family: my home away from home. My theio Jimmy and theia Georgia for being there for me from the very first day, August 18th 2014, when we entered Canada and always welcomed me when I needed a break. My cousin Angela, her husband Larry, and their little princesses Isabel, Gabrielle and Danielle, for not letting me forget how life is outside of school and truly believe in me. A special thank you goes to my goddaughter, Isabel, encouraging me all this time: a vivid picture of her on one of the numerous facetimes telling me: “You can do it Nouna!!”.

My family: My mother, my dad and my brother. I would not have been the person I am today without you. My uncle, Παναγιώτη, my aunt Μαρία and my cousin, Γιώργο. Thank you for reassuring me that you will be there for my parents and brother while I am far away. Always being the one leaving from home, I cannot imagine how hard was for you to stand by my side. Thank you for not giving up on me, for your patience and constant support, especially during my hardest moments of this journey.

Thank you all for being there for me in million ways and never getting tired of pushing me forward. Words simply cannot express how grateful and blessed I feel.

As much as I really want to express my gratitude, I feel the same need to apologize to my family and friends.

I am sorry for my absence from your lives all those years.

I am sorry I was not there to share your joy, not to stand by you at the hard times.

I am sorry for the all the weddings, christenings, birthdays, school plays and graduations I missed.

I am sorry for not celebrating Christmas and Easter holidays with you.

Nothing can turn back time, but I hope that all of you can share my happiness at the end of this chapter of my life.

Let the journey continue..

Konstantina Pringouri

August 15th, 2018

TABLE OF CONTENTS

DECLARATION OF CO-AUTHORSHIP AND PREVIOUS PUBLICATION iii

ABSTRACT vi

DEDICATION viii

ACKNOWLEDGMENTS ix

LIST OF FIGURES xxii

LIST OF SCHEMES xxxi

LIST OF TABLES xxxiii

LIST OF COMPOUNDS xxxv

LIST OF ABBREVIATIONS xxxix

CHAPTER 1. 2

Introduction to Benzothiadiazines and Coordination Chemistry 2

1.1. Introduction 3

- 1.1.1 Overview of coordination chemistry 3
- 1.1.2 Polydentate *N*-donor ligands 4
- 1.1.3 Heterocycles containing N and S/N atoms 6

1.2. Overview of 1,2,4-benzothiadiazines 9

- 1.2.1 The family of 1,2,4-benzothiadiazines 9
- 1.2.2 Previous synthetic studies of 1,2,4-benzothiadiazines 11
- 1.2.3 Coordination chemistry of 1,2,4-benzothiadiazines 12

1.3. Coordination Chemistry 14

- 1.3.1 Theory of coordination chemistry 14
  - 1.3.1.a Classification of ligands 14

1.3.1.b Coordination number and geometries 16
1.3.1.c Isomerism in coordination compounds 17
1.3.1.d Crystal Field Theory (CFT) 18
1.3.1.e Spin Crossover 21
1.3.2 Synthetic methodology of coordination chemistry 24
1.3.3 Coordination modes of acetate (OAc^-) and hexafluoroacetylacetate ($hfac^-$) groups 26
1.4. Dissertation Objectives 29
1.5. References 32
CHAPTER 2. 39
Synthesis and characterization of pybtdaH and its coordination chemistry 39
2.1. Introduction 40
2.2. Results and Discussion 43
2.2.1 Synthesis, characterization and computational studies on the ligand pybtdaH 43
2.2.1.a Synthesis and characterization of the ligand pybtdaH 43
2.2.1.b Mechanistic studies on the formation of the ligand pybtdaH 46
2.2.1.c Computational studies on ligand pybtdaH 48
2.2.2 Reactivity of pybtdaH with $FeCl_3$ 50
2.2.2.a Synthesis and crystal structure of $[FeCl_3(pybtdaH_{ox})(CH_3OH)]\cdot CH_3OH$ (2.3a) 50
2.2.2.b Synthesis and crystal structure of $Fe_4Cl_4(OCH_3)_6(pybtda_{ox})_2$ (2.3b) 52
2.2.3 Reactivity of pybtdaH with $M(OAc)_2$ (M = Co, Cu and Zn) 54
2.2.3.a Synthesis and crystal structure of $Co(pybtda_{ox})_3$ (2.4) 54
2.2.3.b Synthesis and crystal structure of $[Cu_2(OAc)_2(pybtda_{ox})_2(H_2O)_2]\cdot 2H_2O$ (2.5) 56

2.2.3.c Synthesis and crystal structure of $Zn_2(OAc)_2(pybtda_{ox})_2$ (2.6) 59

2.2.4 Reactivity of pybtdaH with $M(hfac)_2$ (M = Mn, Co, Ni, Cu, Zn) 62

2.2.4.a Syntheses and crystal structures of $M(hfac)_2(pybtdaH_{ox})$ (M = Mn (2.7), Co (2.8), Zn (2.9)) 62

2.2.4.b Synthesis and crystal structure of $Ni(hfac)_2(pybtdaH)$ (2.10) 65

2.2.4.c Synthesis and crystal structure of $Ni_3(hfac)(pybtda_{ox})_5(H_2O)$ (2.11) 66

2.2.4.d Synthesis and crystal structure of $[Cu(hfac)(pybtda_{ox})]_n$ (2.12) 68

2.2.4.e Synthesis and crystal structure of $[Cu_4(OH)_4(pybtda_{ox})_4]\cdot H_2O$ (2.13) 69

2.2.4.f Synthesis and crystal structure of $[Cu_{14}(OH)_{12}(CO_3)_2(pybtda_{ox})_{12}(H_2O)_2]\cdot 14[H_2O]\cdot[CH_3OH]$ (2.14) 72

2.2.5 Spectroscopic studies of the metal complexes 2.3a, 2.4 – 2.10, 2.12 – 2.14 77

2.2.6 Reactivity trends in coordination chemistry of pybtdaH 78

2.3. Conclusions 81

2.4. Experimental 82

2.4.1 General considerations and physical measurements 82

2.4.2 Ligand Synthesis 82

2.4.2.a 2-(propylthio)aniline (2.1) 83

2.4.2.b N′-(2-propylthiophenyl)-picolinamidine (2.2) 84

2.4.2.c 3-(pyridin-2-yl)-4H-benzo-1,2,4-thiadiazine (pybtdaH) 85

2.4.3 Complex Syntheses with MCl_3 (M = Fe) 86

2.4.3.a $[FeCl_3(pybtdaH_{ox})(CH_3OH)]\cdot CH_3OH$ (2.3a) 86

2.4.3.b $Fe_4Cl_4(OCH_3)_6(pybtda_{ox})_2$ (2.3b) 86

2.4.4 Complex Syntheses with $M(OAc)_2$ (M = Co (2.4), Cu(2.5), Zn (2.6)) 87

2.4.4.a $Co(pmbtda_{ox})_3$ (2.4) 87

2.4.4.b $[Cu_2(OAc)_2(pybtda_{ox})_2(H_2O)_2]\cdot 2H_2O$ (2.5) 87

2.4.4.c $Zn_2(OAc)_2(pybtda_{ox})_2$ (2.6) 88

2.4.5 Complex Syntheses with $M(hfac)_2$ (M = Mn, Co, Ni, Cu, Zn) 88

2.4.5.a $Mn(hfac)_2(pybtdaH_{ox})$ (2.7) 88

2.4.5.b $Co(hfac)_2(pybtdaH_{ox})$ (2.8) 89

2.4.5.c $Zn(hfac)_2(pybtdaH_{ox})$ (2.9) 89

2.4.5.d $Ni(hfac)_2(pybtdaH)$ (2.10) 90

2.4.5.e $[Ni_3(hfac)(pybtda_{ox})_5(H_2O)$ (2.11) 90

2.4.5.f $[Cu(hfac)(pybtda_{ox})]_n$ (2.12) 90

2.4.5.g $[Cu_4(OH)_4(pybtda_{ox})_4]\cdot H_2O$ (2.13) 91

2.4.5.h $[Cu_{14}(OH)_{12}(CO_3)_2(pybtda_{ox})_{12}(H_2O)_2]\cdot 14[H_2O]\cdot[CH_3OH]$ (2.14) 91

2.4.6 Single-crystal X-ray crystallography 92

2.5. References 94

CHAPTER 3. 96

Synthesis and characterization of pmbtdaH and its coordination chemistry 96

3.1. Introduction 97

3.2. Results and Discussion 99

3.2.1 Synthesis and characterization of the ligand pmbtdaH 99

3.2.1.a Synthesis of pmbtdaH 99

3.2.1.b Electrochemical studies on pmbtdaH 101

3.2.1.c *In situ* $1e^-$ oxidation of pmbtdaH: DFT and EPR studies 102

3.2.2 Coordination chemistry of pmbtdaH with MCl_2 (M = Mn, Fe, Co, Ni, Zn) 103

3.2.2.a Syntheses and crystal structures of $[MCl_2(pmbtdaH)_2]\cdot 2CH_3OH$ (M = Mn (3.2), Fe (3.3), Co (3.4), Ni (3.5)) 103

3.2.2.b Synthesis and crystal structure of $Zn_2Cl_4(pmbtdaH)_2$ (3.6) 107

3.2.3 Coordination chemistry of pmbtdaH with $M(hfac)_2$ (M = Mn, Co, Ni, Cu, Zn) 109

3.2.3.a Syntheses and crystal structures of M(hfac)$_2$(pmbtdaH) (M = Mn (3.7a), Co (3.8a), Ni (3.9a), Cu (3.10a) and Zn (3.11a)) 109
3.2.3.b Synthesis and crystal structure of [Mn$_2$(hfac)$_2$(tfa)$_2$(pmbtdaH$_{ox}$)$_2$]·2CH$_2$Cl$_2$ (3.7b) 113
3.2.3.c Syntheses and crystal structures of M(hfac)$_2$(pmbtdaH$_{ox}$) (M= Co (3.8a), Ni (3.9a)) 115
3.2.3.d Synthesis and crystal structure of Cu$_4$(hfac)$_4$(tfa)$_2$(pmbtda$_{ox}$)$_2$ (3.10b) 118
3.2.3.e Synthesis and crystal structure of Zn$_4$(hfac)$_6$(pmbtda$_{ox}$)$_2$ (3.11b) 120
3.2.4 Spectroscopic studies of the metal complexes 122
3.2.5 Reactivity trends in the coordination chemistry of pmbtdaH 127
3.3. Conclusions 130
3.4. Experimental 132
3.4.1 General considerations and physical measurements 132
3.4.2 Ligand Synthesis 133
3.4.2.a N’-(2-propylthiophenyl)-picolinamidine (3.1) 133
3.4.2.b 3-(2',6'-pyrimidine)-benzo-1,2,4-thiadiazine (pmbtdaH) 134
3.4.3 Reactivity of pmbtdaH with MCl$_2$ (M = Mn, Fe, Co, Ni, Zn) 135
3.4.3.a [MnCl$_2$(pmbtdaH)$_2$]·2CH$_3$OH (3.2) 135
3.4.3.b [FeCl$_2$(pmbtdaH)$_2$]·2CH$_3$OH (3.3) 136
3.4.3.c [CoCl$_2$(pmbtdaH)$_2$]·2CH$_3$OH (3.4) 136
3.4.3.d [NiCl$_2$(pmbtdaH)$_2$]·2CH$_3$OH (3.5) 137
3.4.3.e Zn$_2$Cl$_4$(pmbtdaH)$_2$ (3.6) 137
3.4.4 Reactivity of pmbtdaH with M(hfac)$_2$ (M = Mn, Co, Ni, Cu, Zn) 138
3.4.4.a Mn(hfac)$_2$(pmbtdaH) (3.7a) 138
3.4.4.b [Mn$_2$(hfac)$_2$(tfa)$_2$(pmbtdaH$_{ox}$)$_2$]·2CH$_2$Cl$_2$ (3.7b) 139
3.4.4.c Co(hfac)$_2$(pmbtdaH) (3.8a) 139

3.4.4.d Co(hfac)$_2$(pmbtdaH$_{ox}$) (3.8b) 140
3.4.4.e Ni(hfac)$_2$(pmbtdaH) (3.9a) 140
3.4.4.f [Ni(hfac)$_2$(pmbtdaH$_{ox}$)]·2CH$_2$Cl$_2$ (3.9b) 140
3.4.4.g Cu(hfac)$_2$(pmbtdaH) (3.10a) 141
3.4.4.h Cu$_4$(hfac)$_4$(tfa)$_2$(pmbtda$_{ox}$)$_2$ (3.10b) 141
3.4.4.i Zn(hfac)$_2$(pmbtdaH) (3.11a) 142
3.4.4.j Zn$_4$(hfac)$_6$(pmbtda$_{ox}$)$_2$ (3.11b) 142

3.4.5 Single-crystal X-ray crystallography 143

3.5. References 145

CHAPTER 4. 147

Synthesis and characterization of pybtdaSMe and its coordination chemistry 147

4.1. Introduction 148

4.2. Results and Discussion 150

4.2.1 Synthesis and characterization of the ligand pybtdaSMe 150
4.2.2 Reactivity of pybtdaSMe with MCl$_2$ (M = Mn, Ni, Cu, Zn) 154

4.2.2.a Syntheses and crystal structures of MCl$_2$(pybtdaSMe)$_2$ (M = Mn (4.1), Ni (4.2)) 154
4.2.2.b Synthesis and crystal structures of polymorphs Cu$_2$Cl$_4$(pybtdaSMe)$_2$ (4.3a) and Cu$_2$Cl$_4$(pybtdaSMe)$_2$·2(CuCl$_2$pybtdaSMe) (4.3b) 157
4.2.2.c Synthesis and crystal structure of ZnCl$_2$(pybtdaSMe) (4.4) 161

4.2.3 Reaction of pybtdaSMe with M(hfac)$_2$ (M = Co, Ni) 163

4.2.3.a Syntheses and crystal structures of M(hfac)$_2$(pybtdaSMe) (M = Co (4.5), Ni (4.6)) 163

4.2.4 Spectroscopic studies of metal complexes 4.3a, 4.3b, 4.4 and 4.5 166
4.2.5 Reactivity trends in the coordination chemistry of pybtdaSMe 167

4.3. Conclusions 169

4.4. Experimental 170

4.4.1 General considerations and physical measurements 170

4.4.2 Ligand Synthesis 170

4.4.2.a 1-methyl-3-(pyridin-2-yl)-1λ^4,2,4-benzothiadiazine (pybtdaSMe) 170

4.4.3 Complex Syntheses with MCl_2 (M = Mn, Ni, Cu, Zn) 172

4.4.3.a $MnCl_2(pybtdaSMe)_2$ (4.1) 172

4.4.3.b $NiCl_2(pybtdaSMe)_2$ (4.2) 172

4.4.3.c $Cu_2Cl_4(pybtdaSMe)_2$ (4.3a) 173

4.4.3.d $Cu_2Cl_4(pybtdaSMe)_2\cdot 2CuCl_2(pybtdaSMe)$ (4.3b) 173

4.4.3.e $ZnCl_2(pybtdaSMe)$ (4.4) 174

4.4.4 Complex Syntheses with $M(hfac)_2$ (M = Co, Ni) 174

4.4.4.a $Co(hfac)_2(pybtdaSMe)$ (4.5) 174

4.4.4.b $Ni(hfac)_2(pybtdaSMe)$ (4.6) 175

4.4.5 Single-crystal X-ray crystallography 175

4.5. References 177

CHAPTER 5. 179

Synthesis and characterization of $bisbtdaH_2$ and its coordination chemistry 179

5.1. Introduction 180

5.2. Results and Discussion 182

5.2.1 Synthesis and structural characterization of the ligand $bisbtdaH_2$ 182

5.2.2 Redox studies on $bisbtdaH_2$ 186

5.2.3 Syntheses and characterization of metal complexes of $bisbtdaH_2$ 189

5.2.3.a Syntheses and description of $[M(bisbtdaH_2)_2][X]_2$ (M = Mn, X = CF_3SO_3 (5.3); Fe, X = CF_3SO_3 (5.4); Fe, X = BF_4 (5.5); Co, X = Cl (5.6); Ni, X = Cl (5.7); Zn, X = CF_3SO_3 (5.8)) 189

5.2.3.b Synthesis and characterization of complex [Cu(bisbtdaH_2)(NO_3)$_2$]·DMF (5.9) 196

5.2.4 Spectroscopic studies of the metal complexes 197

5.2.4.a UV-Vis spectroscopy of complexes 5.3 − 5.8 197
5.2.4.b Electronic structure of complexes [Fe(bisbtdaH_2)$_2$]$^{2+}$ (5.4 and 5.5) 198
5.2.4.c Electrochemical studies on complex [Fe(bisbtdaH_2)$_2$]$^{2+}$ (5.4) 200
5.2.4.d Magnetic properties of complex [Co(bisbtdaH_2)$_2$][Cl]$_2$ (5.6) 201

5.2.5 Reactivity trends in coordination chemistry of bisbtdaH_2 202

5.3. Conclusions 204

5.4. Experimental 205

5.4.1 General considerations and physical measurements 205
5.4.2 Ligand Synthesis 206

5.4.2.a (2Z,6Z)-*N'*^{2},*N'*^{6}-bis(2-(propylthio)phenyl)pyridine-2,6-bis(carboximidamide) (5.1) 206
5.4.2.b 3,3'-pyridine-2,6-diylbis(4H-1,2,4-benzothiadiazine) (bisbtdaH_2) 207
5.4.2.c 3-[6-(1,3-benzothiazol-2-yl)pyridin-2-yl]-4H-1,2,4-benzothiadiazine (5.2) 208

5.4.3 Complex Syntheses with MX_2 (M = Mn, Fe, Co, Ni, Cu, Zn, X = Cl, CF_3SO_3, NO_3) 209

5.4.3.a [Mn(bisbtdaH_2)$_2$][CF_3SO_3]$_2$ (5.3) 209
5.4.3.b [Fe(bisbtdaH_2)$_2$][CF_3SO_3]$_2$·2CH_3CN (5.4) 209
5.4.3.c [Fe(bisbtdaH_2)$_2$][BF_4]$_2$·CH_3CN (5.5) 210
5.4.3.d [Co(bisbtdaH_2)$_2$][Cl]$_2$ (5.6) 210
5.4.3.e [Ni(bisbtdaH_2)$_2$][Cl]$_2$·4CH_3OH (5.7) 211
5.4.3.f [Zn(bisbtdaH_2)$_2$][CF_3SO_3]$_2$·CH_3OH (5.8) 211
5.4.3.g [Cu(bisbtdaH_2)(NO_3)$_2$]·DMF (5.9) 212

5.4.4 Single-crystal X-ray crystallography 212

5.5. References 215

CHAPTER 6. 220

Conclusions and Future Work 220

6.1. Conclusions 221

6.2. Future Work 229

6.3. References 234

APPENDIX 1: Crystal Data and Structure Refinement for Compounds of Chapter 2 236

APPENDIX 2: Crystal Data and Structure Refinement for Compounds of Chapter 3 252

APPENDIX 3: Crystal Data and Structure Refinement for Compounds of Chapter 4 270

APPENDIX 4: Crystal Data and Structure Refinement for Compounds of Chapter 5 279

VITA AUCTORIS 289

LIST OF FIGURES

Figure 1.1 Coordination modes of pybtdaH and pybtda$_{ox}^{-}$ reported to date. 14

Figure 1.2 The shapes of the five *d*-orbitals. 19

Figure 1.3 Splitting of the *d*-orbitals in an octahedral crystal field. 19

Figure 1.4 High-spin (weak field) and low-spin (strong field) configuration of Mn^{2+} (d^5). 20

Figure 1.5 High- and low-spin configurations of Fe^{2+} (d^6) ion. 22

Figure 1.6 Spin transition curves of high-spin molar fraction *vs* temperature; (a) abrupt, (b) gradual, (c) incomplete, (d) hysteresis. 23

Figure 2.1 Coordination modes of neutral or anionic S^{II} (left) and the S^{IV} (right) benzothiadiazine ligand. 42

Figure 2.2 Molecular structure of N′-(2-propylthiophenyl)-picolinamidine (**2.2**). 44

Figure 2.3 Molecular structure of pybtdaH. 45

Figure 2.4 ^{1}H NMR screening of the pybtdaH formation upon addition of NCS in **2.2** at 35 ^oC highlighting the conversion of the pseudo-triplet into two doublets (aromatic region) (500 MHz, $CDCl_3$). 47

Figure 2.5 ^{1}H NMR screening of the pybtdaH formation upon addition of NCS in **2.2** at 35 ^oC focusing in the aliphatic region showing the formation of the by-product, 1-chloropropane after 28 hours (500 MHz, $CDCl_3$, (3.48 (Cl-CH_2), 1.77 (Cl-CH_2CH_2), 0.99 (CH_3), 2.69 (succinimide) ppm). 47

Figure 2.6 Rotation of pyridyl group of pybtdaH for the DFT studies. 49

Figure 2.7 DFT calculations (B3LYP/6-311G^{*+}) of pybtdaH with the folding angle of pyridyl group varied between 0° and 360°. 50

Figure 2.8 Molecular structure of $FeCl_3$(pybtdaH$_{ox}$)(CH_3OH) (**2.3a**) (solvent molecule omitted for clarity). 51

Figure 2.9 Crystal packing of **2.3a** highlighting the centrosymmetric π-π interactions (red) and the N-H···O=S hydrogen bonding (green). 52

Figure 2.10 Molecular structure of $Fe_4Cl_4(OCH_3)_6(pybtda_{ox})_2$ (**2.3b**) (H on CH_3 groups omitted for clarity)... 53

Figure 2.11 Molecular structure of $Co(pybtda_{ox})_3$ (**2.4**) (the three ligands are illustrated with different colors for a better perspective of the structure)............ 55

Figure 2.12 Crystal packing of **2.4** highlighting the π-π interactions (red) and the C-H···O hydrogen bonding between the C-H groups and the O atom of the sulfoxide (green). .. 56

Figure 2.13 Molecular structure of $Cu_2(OAc)_2(pybtda_{ox})_2(H_2O)_2$ (**2.5**) (solvent molecules omitted for clarity)... 57

Figure 2.14 (top) Crystal packing of **2.5** highlighting the π-π interactions (red) and the O-H···N hydrogen bonding between the water molecule and the N atom of the ligand (green); (bottom) One dimensional chain of dinuclear complexes along *c* axis. 58

Figure 2.15 Crystal packing of **2.5** revealing the three dimensional nature of the supramolecular arrangement of molecules generated through hydrogen bonds and π-π interactions. 59

Figure 2.16 Molecular structure of one complete molecule in the asymmetric unit $Zn_2(OAc)_2(pybtda_{ox})_2$ (**2.6**).. 60

Figure 2.17 (left) Crystal packing of **2.6** highlighting the intramolecular π-π interactions (red) on Zn dimers, and the intermolecular interactions between Zn(1) (blue) and Zn(2) (green) dimers along *a* axis; (right) top-view of the π-π interactions down the crystallographic *a* axis.. 62

Figure 2.18 (left) Molecular structure of $Co(hfac)_2(pybtdaH_{ox})$ (**2.8**); (right) Crystal packing of **2.8** highlighting the π-π interactions (red) and the N-H···O hydrogen bonding between the amino group and the O atoms of the neighbouring sulfoxide (green). 63

Figure 2.19 (left) Molecular structure of Ni(hfac)$_2$(pybtdaH) (**2.10**); (right) Crystal packing of **2.10** highlighting the π-π interactions (red) and the N-H···O hydrogen bonding between the amino group and the O atoms of the neighbouring hfac$^-$ group (green)... 66

Figure 2.20 Molecular structure of Ni$_3$(hfac)(pybtda$_{ox}$)$_5$(H$_2$O) (**2.11**). 67

Figure 2.21 (top) Asymmetric unit of polymer [Cu(hfac)(pybtda$_{ox}$)]$_n$ (**2.12**); (bottom) One dimensional polymer of complex **2.12** along *b* axis.. 69

Figure 2.22 Molecular structure of Cu$_4$(OH)$_4$(pybtda$_{ox}$)$_4$ (**2.13**) (solvent molecule omitted for clarity)... 70

Figure 2.23 The [Cu$_4$(μ_2-OH)$_2$(μ_3-OH)$_2$]$^{4+}$ core of complex **2.13** illustrating the ladder-type conformation. 71

Figure 2.24 Crystal packing of **2.13** highlighting the π-π interactions (red) between neighbouring molecules and the centroids shown in yellow are not participating in π-π interactions. 72

Figure 2.25 Molecular structure of Cu$_{14}$(OH)$_{12}$(CO$_3$)$_2$(pybtda$_{ox}$)$_{12}$(H$_2$O)$_2$ (**2.14**) (solvent molecules omitted for clarity). 73

Figure 2.26 The [Cu$_{14}$] core of complex **2.14** (green dashed lines indicate missing edges of the "cubane"). 76

Figure 2.27 Solid state EPR of complex **2.12** at room temperature (experimental-black, simulation-red); $g_x = 2.030$, $g_y = 2.137$, $g_z = 2.220$ ($<g>= 2.129$), $a_x = 20$ G, $a_y = 34$ G, $a_z = 47$ G. 77

Figure 2.28 Coordination modes of pybtdaH, pybtdaH$_{ox}$ and pybtda$_{ox}^-$ observed in the metal complexes of Chapter 2. 81

Figure 3.1 Coordination modes of neutral or anionic S^{II} (left) and the S^{IV} (right) benzothiadiazine ligand. 98

Figure 3.2 Molecular structure of 2-(propylthiophenyl)-picolinamidine (**3.1**). 99

Figure 3.3 Molecular structure of pmbtdaH. 100

Figure 3.4 Crystal packing of pmbtdaH highlighting N-H···N hydrogen bonding along *c* axis. 101

Figure 3.5 Cyclic voltammogram of ligand pmbtdaH ($C_0 = 8.72 \times 10^{-3}$ mol·L^{-1}) in a solution of ^{n}Bu$_4$N(PF$_6$) in dichloromethane (0.1 M) (Pt working- and counter-electrodes and an Ag$^+$/AgCl/KCl reference electrode which was referenced to the ferrocene/ferrocenium redox couple ($E_{½}$(Fc$^+$/Fc) = 502 mV *vs* SCE)) 102

Figure 3.6 (left) Solution EPR spectrum and simulation of the radical pmbtda$^•$; (right) computed spin density distribution (UB3LYP/6-311G*) with red indicating regions of positive spin density and blue reflecting regions of negative spin density. 103

Figure 3.7 Molecular structure of CoCl$_2$(pmbtdaH)$_2$ (**3.4**, solvent molecules omitted for clarity). 104

Figure 3.8 Molecular structure of **3.4** highlighting hydrogen bonding between the heterocyclic N-H and the O atoms of the solvent CH$_3$OH molecules, the O-H of the CH$_3$OH and the Cl of the complex (green); (bottom) π-π interactions between the benzo rings of the neighbouring molecules (red). 106

Figure 3.9 Molecular structure of Zn$_2$Cl$_4$(pmbtdaH)$_2$ (**3.6**). 107

Figure 3.10 Crystal packing of **3.6** highlighting the π-π interactions (red) and the N-H···Cl hydrogen bonding between the heterocyclic N-H and the Cl atoms of the neighbouring molecule (green). 108

Figure 3.11 (left) Molecular structure of Zn(hfac)$_2$(pmbtdaH) (**3.11a**); (right) Crystal packing of **3.11a** highlighting the π-π interactions (red) and the N-H···O hydrogen bonding between the amino group and the O atoms of the neighbouring hfac$^-$ group (green). 110

Figure 3.12 Molecular structure of complex **3.10a**, highlighting the two racemic forms the complex can adopt (lighter colour carbon in front of the plane, darker colour carbons behind the plane). 112

Figure 3.13 Molecular structure of $Mn_2(hfac)_2(tfa)_2(pmbtdaH_{ox})_2$ (**3.7b**, solvent molecules omitted for clarity). 114

Figure 3.14 Crystal packing of **3.7b** highlighting the π-π (red) interactions and the N-H···O hydrogen bonding between the amino group and the O atoms of the neighbouring sulfoxide group (green) (solvent molecules omitted for clarity). 115

Figure 3.15 (left) Molecular structure of $Ni(hfac)_2(pmbtdaH_{ox})$ (**3.9b**); (right) Crystal packing of **3.9b** highlighting the π-π interactions (red) and the N-H···O hydrogen bonding between the amino group and the O atoms of the neighbouring sulfoxide (green) (solvent molecules have been omitted for clarity). 117

Figure 3.16 Molecular structure of $Cu_4(hfac)_4(tfa)_2(pmbtda_{ox})_2$ (**3.10b**). 119

Figure 3.17 Molecular structure of $Zn_4(hfac)_6(pmbtda_{ox})_2$ (**3.11b**). 121

Figure 3.18 Solution UV-Vis spectra of complexes **3.2** − **3.5** with formula $MCl_2(pmbtdaH)_2$, complex $Zn_2Cl_4(pmbtdaH)_2$ (**3.6**) and the ligand pmbtdaH. Inset: expansion of the visible region highlighting the similar λ_{max} for complexes **3.2** − **3.6** and ligand pmbtdaH (CH_3OH or CH_3CN, rt, $C_{pmbtdaH} \approx 10^{-4}$ M; $C_{complexes} \approx 10^{-5}$ M). 123

Figure 3.19 Solution UV-Vis spectra of $M(hfac)_2(pmbtdaH)$ (**3.7a** − **3.11a**) and the ligand pmbtdaH. Inset: expansion of the visible region highlighting the similar λ_{max} for complexes **3.7a** − **3.11a** and ligand pmbtdaH (Solvent: CH_2Cl_2, CH_3OH or CH_3CN, rt, $C_{pmbtdaH} \approx 10^{-4}$ M; $C_{complexes} \approx 10^{-5}$ M). 124

Figure 3.20 Solution UV-Vis spectra of complexes **3.11a**, **3.11b** and the ligand pmbtdaH. Inset: expansion of the visible region highlighting the similar λ_{max} for complexes **3.11a**, **3.11b** and ligand pmbtdaH (CH_3CN or CH_3OH, rt, $C_{pmbtdaH} \approx 10^{-4}$ M; $C_{complexes} \approx 10^{-5}$ M).125

Figure 3.21 ^1H NMR of complex **3.11a** (red), pmbtdaH (blue) and $Zn(hfac)_2$ (green) (500 MHz, CD_3CN). 126

Figure 3.22 Solid state EPR of complex **3.10a** at room temperature (experimental-black, simulation-red); $g_x = 2.27$, $g_y = 2.25$, $g_z = 2.07$ ($\langle g \rangle = 2.197$), $a_x = a_y = 110$ G, $a_z = 0$ G. ... 127

Figure 3.23 Coordination modes of the ligand pmbtdaH observed in the metal complexes of Chapter 3. 131

Figure 4.1 Coordination modes of ligand pybtdaSMe. 149

Figure 4.2 Molecular structure of pybtdaSMe. 151

Figure 4.3 Comparison of the heterocycle bond lengths of pybtdaH and pybtdaSMe. . 152

Figure 4.4 Crystal packing of pybtdaSMe highlighting π-π interactions along *bc* plane. 153

Figure 4.5 Crystal packing of pybtdaSMe illustrating the two dimensional network (left); three dimensional nature along *b* axis (right). 154

Figure 4.6 Molecular structure of $NiCl_2(pybtdaSMe)_2$ (**4.2**). 155

Figure 4.7 (top) Crystal packing of **4.2** highlighting the π-π interaction the aromatic rings of neighbouring ligand molecules; (bottom) in the *ab* plane revealing the three dimensional nature originated from the π-π interactions and hydrogen bonding. 156

Figure 4.8 Molecular structure of $Cu_2Cl_4(pybtdaSMe)_2$ (**4.3a**). 158

Figure 4.9 Molecular structure of $Cu_2Cl_4(pybtdaSMe)_2 \cdot 2CuCl_2(pybtdaSMe)$ (**4.3b**). 159

Figure 4.10 Structure overlay of complex **4.3b** at T = 170 K (red) and 280 K (blue); highlighting the bridging Cu-Cl bonds (green). 160

Figure 4.11 Powder X-ray diffraction patterns of the simulated data of the collection of complex **4.3b** at 170 K (blue) and 280 K (orange) and the experimental data for **4.3b** recorded at room temperature (green). 161

Figure 4.12 Molecular structure of $ZnCl_2(pybtdaSMe)$ (**4.4**). 162

Figure 4.13 Crystal packing of **4.4** highlighting the π-π (red), the S···N (cyan) and the Cl···S interactions (green). 163

Figure 4.14 (left) Molecular structure of $Co(hfac)_2(pybtdaSMe)$ (**4.5**); (right) Crystal packing of **4.5** highlighting the π-π and the C-H···centroid interactions highlighted in red. 164

Figure 4.15 Crystal packing of **4.5** revealing the three dimensional nature originated from hydrogen bonding and π-π interactions highlighting the repeating unit (blue lines). 165

Figure 4.16 Solution UV-Vis spectra of complexes **4.3a** and **4.3b**, and the ligand pybtdaSMe (CH_2Cl_2, rt, $C \approx 10^{-5}$). 166

Figure 4.17 Solution UV-Vis spectra of complexes **4.5** and **4.6**, and the ligand pybtdaSMe (CH_2Cl_2 or CH_3CN, rt, $C \approx 10^{-5}$). 167

Figure 4.18 Potential bridging mode for ligand pmbtdaSMe. 169

Figure 5.1 Molecular structure of bisbtdaH_2 in one of the two crystallographically independent molecules. 183

Figure 5.2 Crystal packing of bisbtdaH_2 highlighting π-π stacking along *b* axis (top) and the packing revealing the three dimensional nature of the hydrogen-bonded motif with a view down *b* axis (bottom). 184

Figure 5.3 Molecular structure of the side product **5.2**. 185

Figure 5.4 ^1H NMR of side product **5.2** (red) and bisbtdaH_2 (blue) for comparison (500 MHz, $CDCl_3$). 186

Figure 5.5 Cyclic voltammograms of ligand bisbtdaH_2 (C_0 = 5.96 mmol·L^{-1}) in a solution of $^nBu_4N(PF_6)$ in dichloromethane (0.047 mol·L^{-1}). a) Cyclic voltammograms of the ligand bisbtdaH_2 obtained at different scan rates (from 0.12V/s to 0.5V/s); b) Normalized cyclic voltammograms of ligand; c) The intensity of the anodic current peaks as a function of the square root of the scan rate. 187

Figure 5.6 Solution EPR spectra of mono and di-radicals formed from oxidation of bisbtdaH_2; (left) Second derivative and simulation of the monoradical bisbtda$H^{\bullet}$; (right) First derivative of diradical, bisbtda$^{\bullet\bullet}$ (stars indicating the additional features, right). 188

Figure 5.7 Spin density distribution (UB3LYP/6-311G^{*+}: (left) monoradical bisbtda$H^{\bullet}$ and (right) the diradical triplet of bisbtda$^{\bullet\bullet}$. 189

Figure 5.8 Molecular structure of **5.4** as representative of the series of complexes **5.3** – **5.8** (solvent molecules and counter-ions omitted for clarity). 191

Figure 5.9 Side-view of complexes of Mn (**5.3**), Fe (**5.4**) and Zn (**5.8**) illustrating the different conformations the ligand adopts in each compound, along with the angle between the two planes of the ligand. 193

Figure 5.10 Crystal packing of **5.4** highlighting the π-π (green) and C-H···π (yellow) interactions (left) and the N-H···O hydrogen bonding between the amino group and the triflate counter ions (red lines, right)... 195

Figure 5.11 Crystal packing of **5.8** highlighting the π-π interactions between the benzo groups in one of the two complete cations in the crystal structure. 196

Figure 5.12 Crystal structure of $[Cu(bisbtdaH_2)(NO_3)_2]$ (**5.9**) (Jahn-Teller axis is shown in green, methanol solvent omitted for clarity). 196

Figure 5.13 Solution UV-Vis spectra of complexes **5.3** – **5.8** as well as ligand $bisbtdaH_2$ to emphasize the ligand-based nature of the spectroscopic properties (Solvent: CH_3OH or CH_3CN, rt, $C_{bisbtdaH2} \approx 10^{-5}$ M; $C_{complexes} \approx 10^{-6}$ M).. 198

Figure 5.14 ^1H NMR of complex **5.5** (red) and $bisbtdaH_2$ (blue) (500 MHz, CD_3CN)...... 199

Figure 5.15 Titration profile at 570 nm. Changes in absorption spectra of Fe^{II} triflate (10^{-4} M) with an increasing amount of $bisbtdaH_2$ in CH_3CN (inset). Red line corresponds to the fit to formation of $[Fe(bisbtdaH_2)]^{2+}$ ($K_1 = 0.1 \times 10^6$) whereas the green line is the fit to formation of $[Fe(bisbtdaH_2)_2]^{2+}$ ($\beta = 4.6 \times 10^6$)... 200

Figure 5.16 Cyclic voltammogram of **5.4** (black) and $bisbtdaH_2$ (red) in dichloromethane (0.047 $mol \cdot L^{-1}$) with $^nBu_4N(PF_6)$ supporting electrolyte at a scan rate of 0.2 V/s........... 201

Figure 5.17 Temperature dependence of $1/\chi$ for complex **5.6** with a fit to Curie-Weiss behaviour ($C = 2.465$ $emu \cdot K \cdot mol^{-1}$, $\theta = -0.48$ K). 202

Figure 6.1 Coordination modes of the ligands pybtdaH, pmbtdaH, pybtdaSMe and $bisbtdaH_2$ under neutral conditions.. 227

Figure 6.2 Coordination modes of the ligands pybtdaH, pmbtdaH and pybtdaSMe under basic conditions. 228

Figure 6.3 Crystal structure of the S-oxide of the pyridyl derivative of benzothiadiazines (pybtdaH$_{ox}$)... 229

Figure 6.4 Crystal structure of the *S,S*-dioxide of the pyridyl derivative of benzothiadiazines (pybtdaH$_{diox}$). 231

Figure 6.5 The methylated derivative of pyrimidine analogue of 1,2,4-benzothiadiazine (pmbtdaSMe) and its potential chelation modes. 231

Figure 6.6 Molecular structure of Fe(NCS)$_2$(pmbtdaH$_{ox}$)$_2$. 232

LIST OF SCHEMES

Scheme 1.1 Polydentate *N*-donor ligands. 5

Scheme 1.2 Nitrogen and sulphur/nitrogen-centered heterocyclic radicals. 7

Scheme 1.3 Derivatives of phenyl and pyridyl derivatives of thiadiazines (TTA). 8

Scheme 1.4 Benzothiadiazines containing S^{II}, S^{IV}, and S^{VI} centres.................................... 9

Scheme 1.5 Molecular structure of hydrochlorothiazide... 9

Scheme 1.6 Derivatives of S^{II} systems with materials' applications. 10

Scheme 1.7 Synthetic methodologies for the preparation of 1,2,4-benzothiadiazines. *Route 1: (i) morpholine sulphide, (ii) disulphide, (iii) methane- and ethanesulfenyl chloride. 11

Scheme 1.8 Catalytic cycle for the preparation of benzothiadiazines *S*-oxides. 13

Scheme 1.9 Selected crystallographically reported coordination modes of the OAc^- (left) and $hfac^-$ (right) ligands, and the μ/η and Harris notations which describe these modes. 27

Scheme 1.10 Derivatives of 1,2,4-benzothiadiazines presented in the dissertation. 29

Scheme 1.11 Logarithimic dissociation constants of HCl, AcOH and Hhfac. 30

Scheme 2.1 (top) Formal S^{II}, S^{IV} and S^{VI} oxidation states of the benzothiadiazine framework; (bottom) S^{II}, S^{IV} and S^{VI} variants of the 2-pyridyl benzothiadiazine heterocycle. 40

Scheme 2.2 Synthetic route to ligand pybtdaH. 43

Scheme 2.3 Mechanism of oxidative cyclization of pybtdaH proposed by Kaszynski.[18] .. 46

Scheme 2.4 Proposed mechanism of the oxidative cyclization of pybtdaH.................... 48

Scheme 3.1 (top) Formal S^{II}, S^{IV} and S^{VI} oxidation states of the benzothiadiazine framework; (bottom) S^{II} and S^{IV} variants of the 2-pyridyl and 2-pyrimidinyl benzothiadiazine heterocycles. 97

Scheme 3.2 Synthetic route to ligand pmbtdaH. 99

Scheme 4.1 Molecular structures of pybtdaH, pybtdaH$_{ox}$ and pybtdaSMe. 148

Scheme 4.2 Synthesis of *S*-alkyl-3,5-bis-(2-pyridyl)-1,2,4,6-thiatriazines (Scheme reproduced from publication[4]). 150

Scheme 4.3 Synthetic route to ligand pybtdaSMe. 151

Scheme 5.1 Molecular structures of terpy, bisbtdaH$_2$, pybtdaH and pmbtdaH. 180

Scheme 5.2 Synthetic route to ligand bisbtdaH$_2$. 182

Scheme 6.1 Synthetic routes of coordination chemistry of py$_2$TTAH. 224

Scheme 6.2 Molecular structure 2-pyrimidyl-dithiadiazolyl (pymDTDA). 224

Scheme 6.3 Molecular structure of *S*-alkylated 3,5-bis(2-pyridyl)-1,2,4,6-thiatriazines. 226

Scheme 6.4 Molecular structure of tdapO$_2$ and the potassium salt of its radical anion demonstrating the chelating ability of the ligand. 230

LIST OF TABLES

Table 1.1 Coordination numbers and their common coordination geometries. 16

Table 2.1 DFT calculations (B3LYP-D3/6-311G^{*+}) of the tautomers of different orientation of the pyridyl group of pybtdaH. 49

Table 2.2 Selected bond lengths and angles for complexes **2.7** – **2.9**. 64

Table 2.3 Coordination geometry and geometry index values of Cu centres in complex **2.14**. 74

Table 2.4 Selected bond lengths and angles of complex **2.14**. 75

Table 3.1 Selected bond lengths and angles for complexes **3.2** – **3.5**. 105

Table 3.2 Selected bond lengths and angles for complexes **3.7a** – **3.11a**. 111

Table 3.3 Selected bond lengths and angles for complexes **3.8b** and **3.9b**. 118

Table 4.1 Selected bond lengths and angles for complexes **4.1** and **4.2**. 155

Table 4.2 Unit cell parameters for complexes **4.3a** and **4.3b** in T = 170 K and 280 K. .. 160

Table 4.3 Selected bond lengths and angles for complexes **4.3a** and **4.3b** in T = 170 K and 280 K. 160

Table 4.4 Selected bond lengths and angles for complexes **4.5** and **4.6**. 164

Table 5.1 Density functional theory (DFT) calculations of the conformers of bisbtdaH$_2$ using the dispersion-corrected B3LYP-D3 functional and 6-311G^{*+}. 185

Table 5.2 Selected bond lengths and angles for complexes **5.3** − **5.9**. 191

Table 5.3 Angles between planes for complexes **5.3** – **5.8** and the RMS deviation for each complex from idealised octahedral, trigonal prismatic or pentagonal bipyramid (with equatorial vacancy). For each complex the smallest deviation is underlined. 192

Table 5.4 Density functional theory (DFT) single point energy calculations of the conformation of the ligand found in the metal complexes using the dispersion-corrected B3LYP-D3 functional and 6-311G**. 194

LIST OF COMPOUNDS

CHAPTER 2

Ligands

2.1	2-(propylthio)aniline	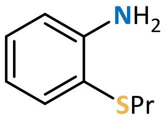
2.2	N'-(2-propylthiophenyl)-picolinamidine	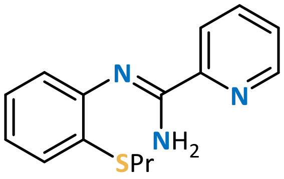
pybtdaH	3-(pyridin-2-yl)-4H-benzo-1,2,4-thiadiazine	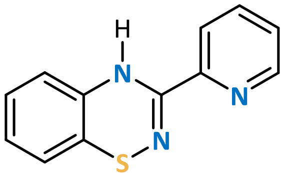

Metal Complexes

2.3a	$[FeCl_3(pybtdaH_{ox})(CH_3OH)]\cdot CH_3OH$
2.3b	$Fe_4Cl_4(OCH_3)_6(pybtda_{ox})_2$
2.4	$Co(pybtda_{ox})_3$
2.5	$[Cu_2(OAc)_2(pybtda_{ox})_2(H_2O)_2]\cdot 2H_2O$
2.6	$Zn_2(OAc)_2(pybtda_{ox})_2$
2.7	$Mn(hfac)_2(pybtdaH_{ox})$
2.8	$Co(hfac)_2(pybtdaH_{ox})$
2.9	$Zn(hfac)_2(pybtdaH_{ox})$
2.10	$Ni(hfac)_2(pybtdaH)$
2.11	$Ni_3(hfac)(pybtda_{ox})_5(H_2O)$
2.12	$[Cu(hfac)(pybtda_{ox})]_n$
2.13	$[Cu_4(OH)_4(pybtda_{ox})_4]\cdot H_2O$
2.14	$[Cu_{14}(OH)_{12}(CO_3)_2(pybtda_{ox})_{12}(H_2O)_2]\cdot 14[H_2O]\cdot[CH_3OH]$

CHAPTER 3

Ligands

3.1	N'-(2-propylthiophenyl)-picolinamidine	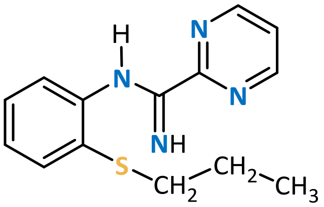
pmbtdaH	(3-(2',6'-pyrimidine)-benzo-1,2,4-thiadiazine)	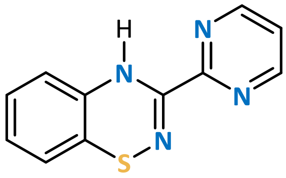

Metal Complexes

3.2	$[MnCl_2(pmbtdaH)_2]\cdot 2CH_3OH$		
3.3	$[FeCl_2(pmbtdaH)_2]\cdot 2CH_3OH$		
3.4	$[CoCl_2(pmbtdaH)_2]\cdot 2CH_3OH$		
3.5	$[NiCl_2(pmbtdaH)_2]\cdot 2CH_3OH$		
3.6	$Zn_2Cl_4(pmbtdaH)_2$		
3.7a	$Mn(hfac)_2(pmbtdaH)$	**3.7b**	$[Mn_2(hfac)_2(tfa)_2(pmbtdaH_{ox})_2]\cdot 2CH_2Cl_2$
3.8a	$Co(hfac)_2(pmbtdaH)$	**3.8b**	$Co(hfac)_2(pmbtdaH_{ox})$
3.9a	$Ni(hfac)_2(pmbtdaH)$	**3.9b**	$[Ni(hfac)_2(pmbtdaH_{ox})]\cdot 2CH_2Cl_2$
3.10a	$Cu(hfac)_2(pmbtdaH)$	**3.10b**	$Cu_4(hfac)_4(tfa)_2(pmbtda_{ox})_2$
3.11a	$Zn(hfac)_2(pmbtdaH)$	**3.11b**	$Zn_4(hfac)_6(pmbtda_{ox})_2$

CHAPTER 4

Ligands

pybtdaSMe	1-methyl-3-(pyridin-2-yl)-1λ^4,2,4-benzothiadiazine	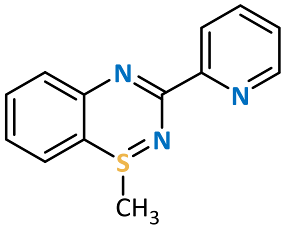

Metal Complexes

4.1	$MnCl_2(pybtdaSMe)_2$
4.2	$NiCl_2(pybtdaSMe)_2$
4.3a	$Cu_2Cl_4(pybtdaSMe)_2$
4.3b	$Cu_2Cl_4(pybtdaSMe)_2 \cdot 2CuCl_2(pybtdaSMe)$
4.4	$ZnCl_2(pybtdaSMe)$
4.5	$Co(hfac)_2(pybtdaSMe)$
4.6	$Ni(hfac)_2(pybtdaSMe)$

CHAPTER 5

Ligands

5.1	(2Z,6Z)-N'^{2},N'^{6}-bis(2-(propylthio)phenyl)pyridine-2,6-bis(carboximidamide)	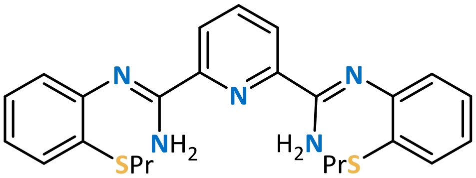
5.2	3-[6-(1,3-benzothiazol-2-yl)pyridin-2-yl]-4H-1,2,4-benzothiadiazine	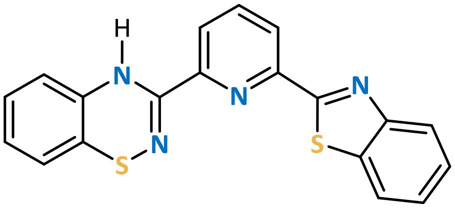
bisbtdaH$_2$	3,3'-pyridine-2,6-diylbis(4H-1,2,4-benzothiadiazine)	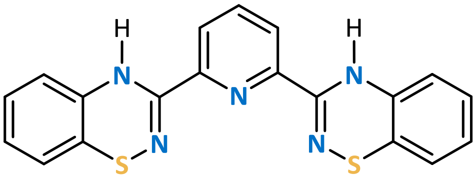

Metal Complexes

5.3	$[Mn(bisbtdaH_2)_2][CF_3SO_3]_2$
5.4	$[Fe(bisbtdaH_2)_2][CF_3SO_3]_2\cdot 2CH_3CN$
5.5	$[Fe(bisbtdaH_2)_2][BF_4]_2\cdot CH_3CN$
5.6	$[Co(bisbtdaH_2)_2][Cl]_2$
5.7	$[Ni(bisbtdaH_2)_2][Cl]_2\cdot 4CH_3OH$
5.8	$[Zn(bisbtdaH_2)_2][CF_3SO_3]_2\cdot CH_3OH$
5.9	$[Cu(bisbtdaH_2)(NO_3)_2]\cdot DMF$

LIST OF ABBREVIATIONS

°	degree
°C	degree Celsius
$6\text{-}311G^{*+}$	split-valence triple-zeta basis set with polarization and diffuse Gaussian functions
Å	Angström
AcOH	acetic acid
Ar	aryl
a_X	hyperfine coupling constant to nucleus X
br	broad (IR and NMR)
bpm	2,2′-bipyrimidine
bpp	2,6-bis(pyrazol-3-yl)pyridine
bpy	2,2′-bipyridine
BTA	benzotriazinyl
btda	benzothiadiazine
Bu	butyl
ca	circa (approximately)
cf	confer (compare)
$CF_3SO_3^-$	trifluromethanesulfonic (triflate) anion
CFSE	Crystal Field Stabilization Energy
CFT	Crystal Field Theory
CSD	Cambridge Structural Database
d	doublet (NMR) or bond length (crystal structures)
dd	doublet of doublets (NMR spectra)
DFT	Density Functional Theory
DMF	dimethylformamide
e^-	electron
e.g.	exempli gratia (for example)
EPR	Electron Paramagnetic Resonance
et al.	et alia (and others)

etc	et cetera (and so on)
Et_2O	diethyl ether
EtOH	ethanol
eV	electron Volt
g	gram or g value (EPR)
h	hour(s)
hfac	hexafluoroacetylacetonate
HRMS	high-resolution mass spectrometry
HS	high-spin
Hz/MHz	Hertz/Megahertz
i.e.	id est (it is)
iPr	isopropyl
IR	infrared
IUPAC	International Union of Pure and Applied Chemistry
J	NMR coupling constant
K	Kelvin
kJ	kilojoule
LiHMDS	lithium bis(trimethylsilyl)amide
LS	low-spin
m	multiplet (NMR) or medium (IR)
Me	methyl
mg	milligram
min	minute
mL	milliliter
mmol	millimole
MOF	metal organic frameworks
NCS	*N*-chlorosuccinimide, isothiocyanate
NMR	Nuclear Magnetic Resonance
OAc	acetate
OTf	trifluromethanesulfonic (triflate) anion
PB	Prussian Blue

P_E	pairing energy
ph	phenyl
phen	1,10-phenanthroline
pm	pyrimidyl
PXRD	Powder X-Ray Diffraction
py	pyridyl
pyTTAH	3,5-dipyrid-2-yl-1,2,4,6-thiatriazinyl
q	quartet (NMR)
R	organic substituent
R_{int}	reliability factors (crystallography)
R_1, wR_2	residual factors (crystallography)
$RCOO^-$	carboxylate
RO^-	alkoxide
RT	room temperature
s	singlet (NMR) or strong (IR)
SCO	Spin Crossover
σ_m, σ_p	Hammett parameters (meta and para substituted benzene rings)
T	temperature
t	triplet (NMR)
terpy	terpyridine
THF	tetrahydrofuran
TLC	Thin Layer Chromatography
TTA	thiatriazinyl
V	volt
VD	verdazyl
vdW	van der Waal's
w	weak (IR)
X	halogen
Δ_{oct}	Octahedral Field Splitting
δ	chemical shift (NMR) or atomic partial charge (DFT calculation)
ΔG	Gibb's free energy

ΔH	enthalpy
ΔS	entropy
θ	angle
υ_{max} (cm^{-1})	IR absorption frequency

Ithaca gave you the marvelous journey.

Without her you would not have set out.

She has nothing left to give you now.

And if you find her poor, Ithaca won't have fooled you.

Wise as you will have become, so full of experience,

you will have understood by then what these Ithacas mean.

-Ithaca, 1911

C.P. Cavafy

Η Ιθάκη σ' έδωσε τ' ωραίο ταξίδι.

Χωρίς αυτήν δε θα `βγαινες στον δρόμο.

Αλλά δεν έχει να σε δώσει πια.

Κι αν πτωχική την βρεις, η Ιθάκη δε σε γέλασε.

έτσι σοφός που έγινες, με τόση πείρα,

ήδη θα το κατάλαβες η Ιθάκες τι σημαίνουν.

-Ιθάκη, 1911

Κ.Π. Καβάφης

CHAPTER 1.

Introduction to Benzothiadiazines and Coordination Chemistry

1.1. Introduction

1.1.1 Overview of coordination chemistry

Naturally occurring pigments have had applications as colorants since prehistoric times. Archaeologists have evidence that humans used paint for aesthetic purposes such as art and decorative uses. The range of colours available was very limited. Most of the pigments originated from earth minerals, such as ochres and iron oxides, or derived from pigments of biological origin. Some colours from unusual sources such as botanical materials or insects were harvested and traded over long distances increasing the cost of the pigment. For example, all shades of blue were associated with royalty because of their rarity. Prussian Blue (PB) was one of the first synthetic pigments and has the formula $Fe_4[Fe(CN)_6]_3 \cdot xH_2O$. It is believed to have been synthesized initially by the paint maker Diesbach in Berlin around 1706 and used extensively. The oldest known use of PB was in the 'Entombment of Christ' (1709) by van der Werff.[1] The first published synthesis of PB was reported by Stahl in 1731.[2] Although first used as a pigment, PB has found many other applications through the years. In the pharmaceutical industry, PB is used as an antidote to treat thallium or radioactive cesium poisoning. It is also in the list of the most important medications needed for a basic health system, the World Health Organization's List of Essential Medicines.[3] Pathologists use PB as a histopathology stain to detect the presence of iron in biopsy specimens, such as in bone marrow samples. In analytical chemistry, PB is used for the determination of total phenols or polyphenols. Last, Engineer's blue (PB in an oily base) is used by toolmakers for spotting metal surfaces, such as surface plates and bearings for hand scraping. PB is just one example of coordination compounds and highlights the many varied applications they can exhibit.

In the 19th century, a number of theories were proposed for a better understanding of their formation and properties, as more complexes were discovered. The most successful and widely accepted of these theories was introduced by Alfred Werner (1866-1919; Nobel Prize in Chemistry in 1913). His work was based on the physical and chemical behaviour of a large number of coordination compounds which he studied by simple experimentation. Werner’s observations led him to propose that metal ions have two different kinds of valence: (1) a primary valence that corresponds to the positive charge of the metal ion, known as oxidation state and (2) a secondary valence that is the total number of ligands bound to the metal ion, known as coordination number. A plethora of coordination compounds can be formed given the numerous combinations of metal ions and ligands. The applications of the metal complexes can be modified through ligand design relying on the complementarity of ligand-based functional groups coupled with the conformational preference(s) of metal ions. The field of coordination chemistry is steadily increasing with applications in various fields from bioinorganic chemistry,[4–6] medicine,[7,8] catalysis[9,10] and magnetism.[11,12]

1.1.2 Polydentate *N*-donor ligands

Coordination compounds are defined as ‘an assembly consisting of a central atom (usually metallic) to which is attached a surrounding array of other groups of atoms (ligands).[13] Metal complexes can be mononuclear in which the metals are surrounded by terminal ligands or polynuclear in which two or more metals are typically linked together through organic ligands that can adopt bridging modes. Although there are many classes of organic ligands, the focus of this dissertation will be polydentate *N*-donor ligands. Polydentate *N*-donor ligands have exhibited predictable coordination reactivity and ease of functionalization. The coordination chemistry of poly-pyridine ligands such as 2,2′-bipyridine (bpy),[14,15] 2,2′-bipyrimidine (bpm),[16–19] phenanthroline (phen),[20] and the terpyridine pincer (terpy)[21–25] as well as larger macrocyclic ligands such as porphyrins[26,27] has been extensively studied[28–30] (Scheme 1.1). These ligands have found to act as ‘non-innocent’ ligands which can potentially be involved in redox reactions.[31–34]

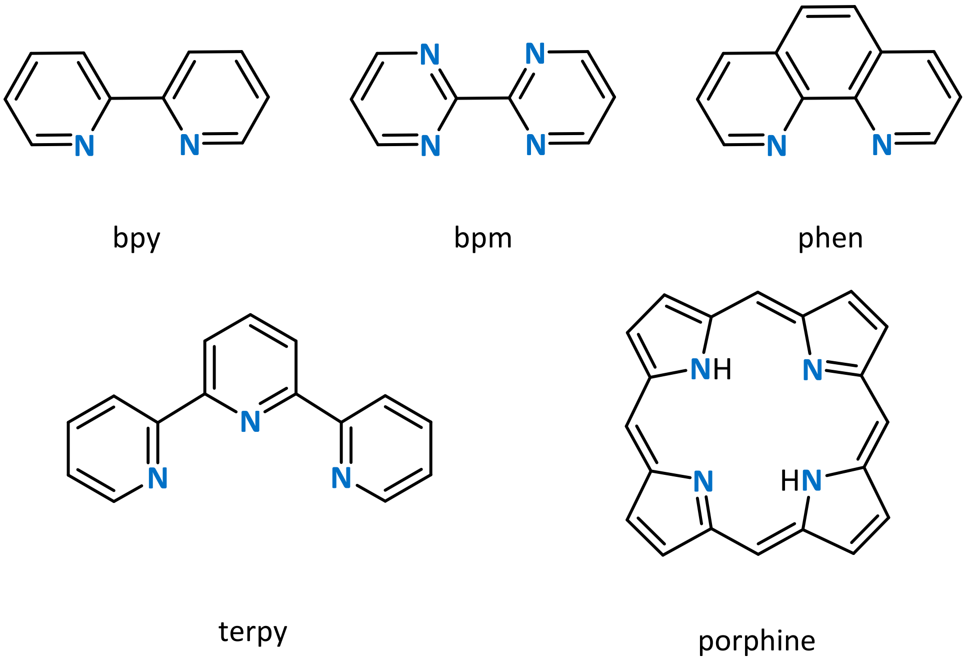

Scheme 1.1 Polydentate *N*-donor ligands.

Such polydentate *N*-donor ligands are found extensively in biological systems such as haems and chlorophyll[35,36] and materials applications include light-harvesting and light emitting properties of the heavier transition metal complexes of 2,2′-bipyridine and its derivatives, such as $[Ru(bpy)_3]^{2+}$.[37] These ligands have also found applications in molecular magnetism since they offer a medium strength ligand field for first row transition metal complexes.

Spin crossover (SCO) behaviour for these systems occurs when the crystal field splitting (Δ) is comparable with the magnitude of the inter-electron repulsion term (P_E) making the two possible electronic states (high- and low-spin) for octahedral metal complexes near equi-energetic.[38–41] The ability to tune the crystal field by manipulating the coordination sphere of the metal permits the value of Δ to be tailored to compliment the pairing energy, P_E. The cobalt(II) complex, $Co(terpy)_2$ complex ion was one of the first compounds to be shown to exhibit thermal spin crossover.[42–45] Some SCO transitions occur slowly whereas other transitions are abrupt and others exhibit thermal hysteresis, i.e. the temperature of the high-spin (HS) to low-spin (LS) transition does not occur at the same temperature as the LS to HS transition (See section 1.3.1.e). There are many subtle factors determining the characteristics of the HS/LS transition including (i) the nature of the counter-ion (cationic complexes) and (ii) the existence of intermolecular interactions between the SCO complexes, and (iii) the presence/absence of solvates in the lattice.[46,47] Spin-transitions have been associated with the loss or gain of solvated molecules such as in $[Fe(bpp)_2]X_2$ complex salts (bpp = 2,6-bis(pyrazol-3-yl)pyridine; X = anion).[48,49] In these cases, the imine N atoms coordinate to the Fe^{2+} cation, whereas the amino groups form strong hydrogen bonds with solvent molecules and/or anions present in the crystal structure.[50] Therefore, the development of polydentate *N*-donor ligands with tunable coordination chemistry is highly desirable for the construction of new functional materials.

1.1.3 Heterocycles containing N and S/N atoms

New classes of magnetic materials include the formation of organic-inorganic composite materials in which a coordinated bridging radical ligand achieves efficient magnetic communication between paramagnetic transition metal ions. The ‘metal-radical approach’ was first proposed by Gatteschi[51] and a number of open-shell ligands such as semi-quinones,[52,53] nitroxides,[54] thiazyl radicals,[55–57] and verdazyls[58–62] have been extensively studied. The two most common strategies for the preparation of radical complexes are: (i) the synthesis of the radical ligand followed by coordination to the paramagnetic metal ion and (ii) coordination of the radical precursor to the desired transition metal center and subsequent chemical/electrochemical oxidation or reduction to afford the desired radical complex. The latter approach provides insight into the preferred coordination modes of the radical precursor and its likely crystal field strength.

The thermodynamic stability of carbon-based radicals can be improved by the replacement of one or more ring carbons by more electronegative atoms such as nitrogen and sulphur. The incorporation of these electronegative elements lower the energies of the orbitals adding electronic stabilization. In addition π-delocalization leads to the distribution of the unpaired electron density over multiple atoms, reducing its chemical reactivity (with respect to free radical H atom abstraction, halogen atom abstraction or reaction with O_2).[63,64] Below, we illustrate the cyclic 6-membered hydrazyl and thiazyl radicals: verdazyls (VD), 1,2,4-benzotriazinyls (BTA), 1,2,4,6-thiatriazinyls (TTA) and benzothiadiazines (BTDA) (Scheme 1.2).

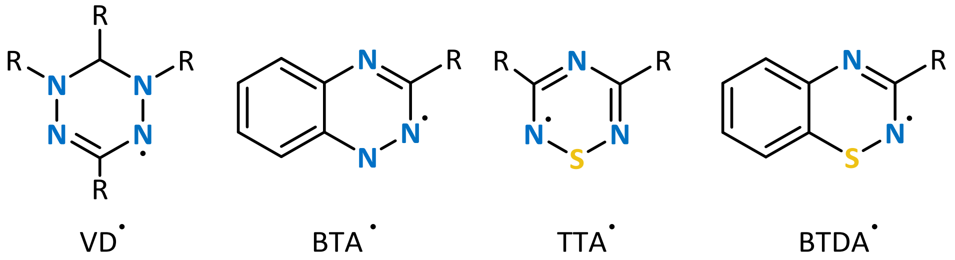

Scheme 1.2 Nitrogen and sulphur/nitrogen-centered heterocyclic radicals.

Verdazyls (VD) were first reported in 1963, and their radicals are extensively resonance delocalized and thermodynamically stable with exceptional air and moisture stability.[65] Pioneering work by Hicks and subsequently others on verdazyls has explored them as ligands for coordination to first, second and third row transition metals, as well as lanthanides.[66,67] The 1,2,4-benzotriazinyl (BTA) radicals were first reported in 1968 and are air, moisture, and thermally stable species which possess fully reversible redox behavior.[68] Although the majority of benzotriazinyls retain their monomeric character in the solid state,[69–71] there are two examples of strong association and spin-pairing reported.[72,73] Recently, the coordination chemistry of 1-phenyl-3-pyrid-2-yl-1,2,4-benzotriazinyl to first-row metal ions has been explored.[74,75] Thiazyls are electron-rich radicals containing S and N atoms. In many cases thiazyl radicals are thermally robust but the inherently polar nature of the S-N bond makes them susceptible to hydrolysis. The first report of a thiatriazinyl (TTA) radical was described by Markovskii in 1983 using electron paramagnetic resonance spectroscopy[76] and in 1985 Oakley isolated and structurally characterized the phenyl derivative (ph_2TTAH, Scheme 1.3).[77] The coordination chemistry of 3,5-dipyrid-2-yl-1,2,4,6-thiatriazinyl (py_2TTAH) has been explored and shown to act as a pincer-type ligand forming mononuclear Fe complexes[78,79] and a dysprosium dimer.[80] The ligand has been oxidised *in situ* upon reaction to FeF_3

forming an one dimensional polymer with fluorine bridges but no coordination of the S=O.[79] In contrast, the ligand is bridging two dysprosium metal ions upon *S*-oxidation of the ligand with the ligand bridging the metal centres.[80] The Dy_2 complex displays single-molecule magnet behaviour where the origin has been attributed to the single-ion anisotropy of the metal ion. The oxides of the phenyl (ph_2TTA_{ox})[81] and pyridyl (py_2TTA_{ox})[56] TTAs have been previously synthesised but no coordination chemistry has been reported (Scheme 1.3).

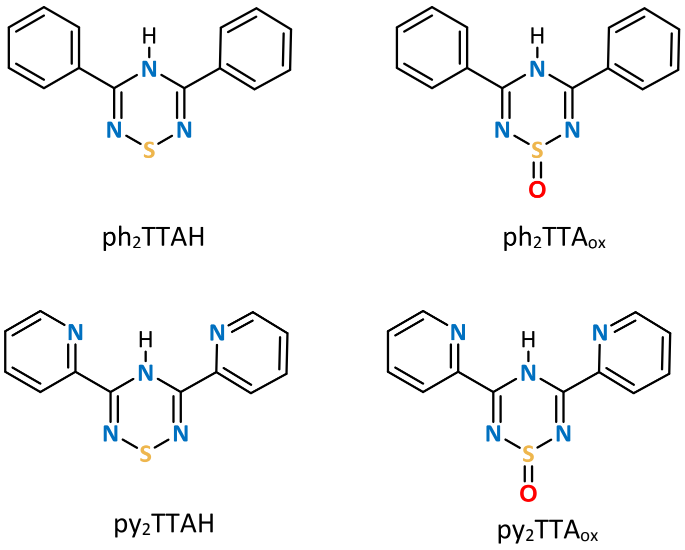

Scheme 1.3 Derivatives of phenyl and pyridyl derivatives of thiadiazines (TTA).

The family of 1,2,4-benzothiadiazines (btda) will be discussed in more detail in the following section.

1.2. Overview of 1,2,4-benzothiadiazines

1.2.1 The family of 1,2,4-benzothiadiazines

The family of 1,2,4-benzothiadiazines in various oxidation states have attracted attention for both materials and pharmaceuticals applications. The benzothiadiazine heterocycle is known in the S^{II}, S^{IV} and S^{VI} oxidation states (Scheme 1.4).

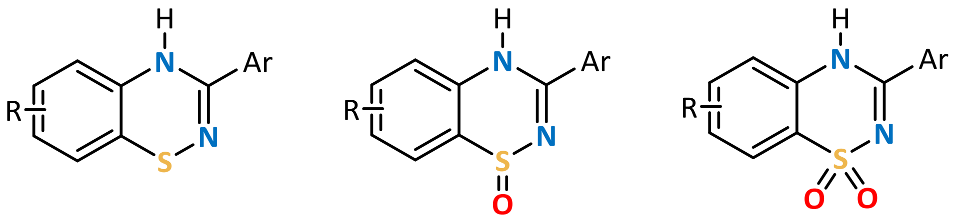

thiadiazine (S^{II}) thiadiazine *S*-oxide (S^{IV}) thiadiazine *S,S*-dioxide

Scheme 1.4 Benzothiadiazines containing S^{II}, S^{IV}, and S^{VI} centres.

The benzothiadiazine ring system in the S^{VI} oxidation state is particularly well-established where it is an important constituent in a family of commercial thiazide diuretics (Scheme 1.5) and was initially developed by Merck-Sharpe-Dohme[82,83] for treating hypertension. More recently it has proved successful in the treatment of hyperglycemia and osteoporosis.[3–6] Thiazides proved to decrease mineral bone loss by directly stimulating bone mineral formation as well as promoting calcium retention in the kidney.[88] In addition, derivatives of 1,2,4-benzothiadiazine-dioxides have been used in patents for various applications, such as inhibitors of hepatitis C virus replication,[89] diabetes,[90] arthritis[91] and many others.

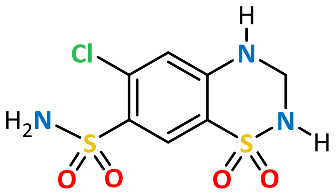

Scheme 1.5 Molecular structure of hydrochlorothiazide.

The S^{II} benzothiadiazines have found various applications in materials. The π-conjugated S^{II} system was first reported in the 1980's to be redox active and undergoes $1e^-$ chemical oxidation to form persistent (long-lived) radicals.[92] Stable (isolable) radicals have been isolated by Kaszynski when the benzo-fused ring is protected with chloro- or fluoro-substituents, and long-chain alkyl ether-functionalised derivatives of phenyl-benzothiadiazines have been found to exhibit liquid crystalline properties (Scheme 1.6, A,B).[93,94] Resonance-stabilized bis(thiadiazines) (R = H, Ph, thienyl) and related species have also attracted attention as conducting materials (Scheme 1.6, C).[95–97]

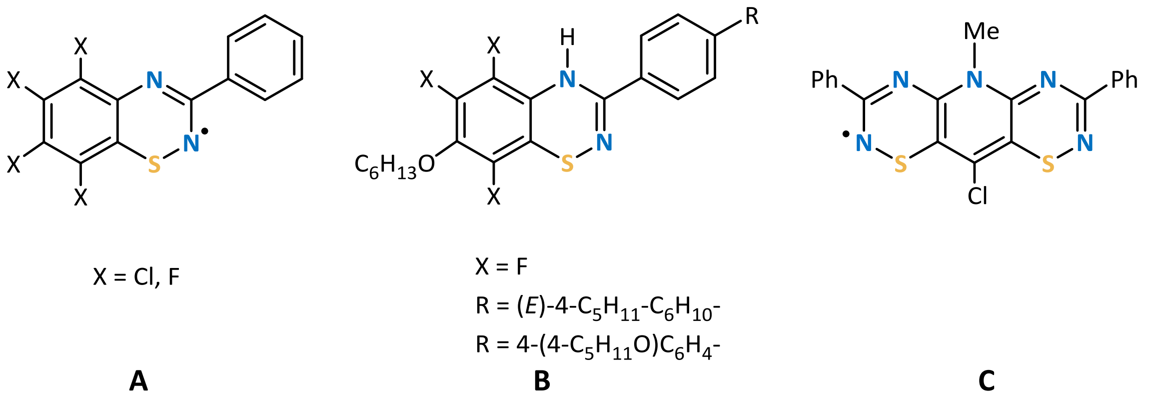

X = Cl, F

X = F
R = (*E*)-4-C_5H_{11}-C_6H_{10}-
R = 4-(4-$C_5H_{11}O$)C_6H_4-

Scheme 1.6 Derivatives of S^{II} systems with materials' applications.

Conversely, the S^{IV} system had been barely investigated with the interconversion from sulfide to sulfoxide to sulfone relying on careful control of the oxidizing agent and its stoichiometric quantities.[98–101] Recently, the metal-catalysed aerial oxidation of S^{II} to S^{IV} under mild conditions was reported by Rawson.[102] The S^{II} system undergoes aerial oxidation to the S^{IV} system in the presence of a Lewis acidic metal of stoichiometric (S^{II}:Cu^{2+} = 2:1) and sub-stoichiometric (S^{II}:Cu^{2+} = 20:1) quantities of Cu^{II} to form the corresponding *S*-oxide. The Cu ions are taking part in a catalytic cycle in which initial *N*-coordination of the btda ring activates the benzothiadiazine ring to *N*-deprotonation and subsequent *S*-oxidation and the regeneration of Cu^{2+} results after liberation of the deprotonated benzothiadiazine *S*-oxide. The first structurally characterized benzothiadiazine *S*-oxides with non-coordinating phenyl or 2'-thienyl rings in C(3) revealed that the *S*-oxide acts as a strong hydrogen-bond acceptor and unambiguously determine the site of N-H protonation (at the 4-position of the heterocyclic ring).

1.2.2 Previous synthetic studies of 1,2,4-benzothiadiazines

There are a number of synthetic methodologies to access various derivatives of 1,2,4-benzothiadiazines depending on the fused substituents and the group attached to C(3) as shown in Scheme 1.7. Different synthetic routes are required depending on the heteroatoms and ring substituents which affect the charge delocalisation and energy of molecular orbitals. The most commonly used synthetic method is Route 1 in which the benzothiadiazine is formed by the reaction of benzamidines with morpholine sulphide, disulphide, or methane- and ethanesulfenyl chloride to give the ylide followed by a ring closing reaction comprising NCS and heat.[103–105] The relatively high temperatures required in this synthetic route can lead to ring contraction and formation of

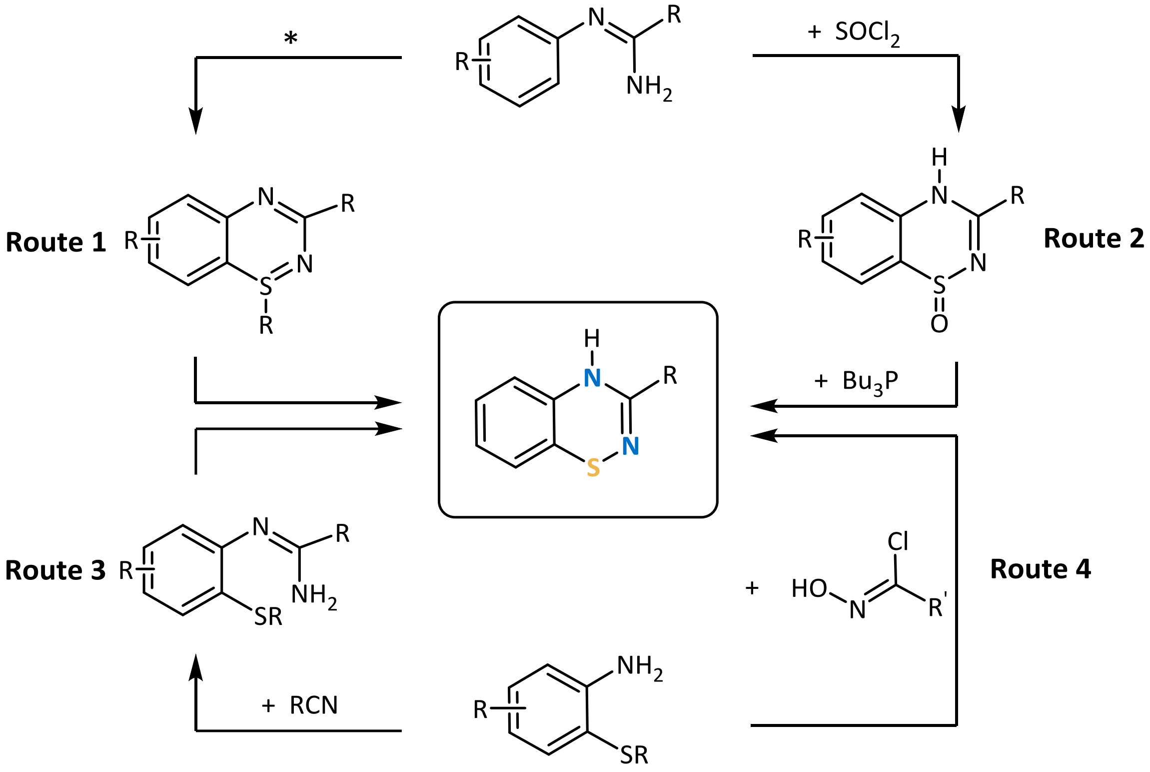

Scheme 1.7 Synthetic methodologies for the preparation of 1,2,4-benzothiadiazines. *Route 1: (i) morpholine sulphide, (ii) disulphide, (iii) methane- and ethanesulfenyl chloride.

benzothiazole as side-products.[103,106] Route 2 involves the ring closure of the benzamidine with $SOCl_2$ to give the *S*-oxide which is then reduced with thionyl chloride or Bu_3P to give the final product. Although this method gives yields over 70% there are side products involved in the synthesis.[107,108] For example, reduction with Bu_3P can also result in ring contraction to the benzothiazole and the use of $SOCl_2$ results in chlorination of the benzo-ring. The synthetic methodology of Route 3 provides an alternative strategy for the formation of *S*-alkyl sulfilimines by the condensation of the amine and carbonitrile. Oxidative cyclization of amidine by *N*-chlorosuccinimide gave the sulfilimine followed by thermolysis to afford the benzothiadiazine.[109,110] The only direct method to give the desired benzothiadiazine is Route 4 and involves the condensation reaction of *ortho*-aminophenols with hydroxamyl.[111,112]

1.2.3 Coordination chemistry of 1,2,4-benzothiadiazines

The first examples of coordination compounds with 1,2,4-benzothiadiazines were recently reported by Rawson.[113] The 3-(2'-pyridyl)-functionalized benzothiadiazine (pybtdaH) has been shown to form a series of mononuclear complexes to first row transition metal complexes of formula $MCl_x(pybtdaH)_y$.[113] The reaction of pybtdaH with the transition metal chloride salts $MCl_2{\cdot}xH_2O$ (M^{II} = Mn, Fe, Co, Cu, Zn) in a 2:1 mole ratio afforded the $MCl_2(pybtdaH)_2$ complexes in which pybtdaH binds in a chelate fashion *via* the heterocyclic N and the pyridyl N atoms. In the case of $CuCl_2$ the 1:1 four-coordinate complex $MCl_2(pybtdaH)$ was also isolated which adopts a polymeric structure with pseudo-square planar molecules linked via long Cu⋯S contacts ($d_{Cu\cdots S}$ = 2.938(1) Å) in the apical position. Reaction of pybtdaH with VCl_3 in a 2:1 mole ratio afforded the vanadyl complex [V(=O)Cl(pybtdaH)$_2$][Cl]. In $FeCl_2(pybtdaH)_2$ the metal was found to adopt a high-spin configuration, but reaction of pybtdaH with $Fe(CF_3SO_3)_2$ in a 3:1 ratio afforded the low-spin complex $[Fe(pybtdaH)_3][CF_3SO_3]_2$, consistent with the stronger field ligand imposed by pybtdaH relative to Cl.

The reaction of $CuCl_2$ with pybtdaH affords a stable red solution of $CuCl_2(pybtdaH)_2$ but addition of Et_3N led to the isolation of the green dimetallic complex $[Cu(pybtda_{ox})_2]_2$ complex.[102] The ligand has been both oxidised and deprotonated and adopts two different coordination modes. The first adopts a simple *N*,*N′*-chelate mode to a single metal centre in which the pyridyl N and the heterocyclic N atoms are involved in metal binding, as described above. The second $pybtda_{ox}^-$ anion takes up a bridging mode between two Cu^{II} centres. For this second ligand, the N atom at the 4-position of the heterocyclic ring and the pyridyl N atom chelate one metal centre and the *S*-oxide bridges to the second metal ion (Figure 1.1). In this process, it seems likely that initial *N*-coordination activates the benzothiadiazine ring to *S*-oxidation and *N*-deprotonation, proceeding *via* a $pybtda_{ox}^-$ anion which has been isolated in the form of $[Cu(pybtda_{ox})_2]_2$ (Scheme 1.8).

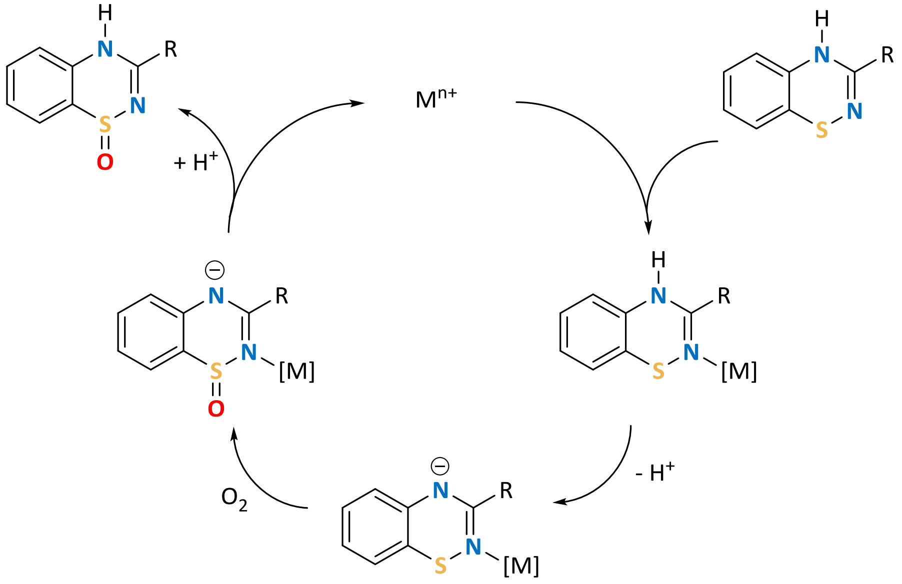

Scheme 1.8 Catalytic cycle for the preparation of benzothiadiazines *S*-oxides.

In 2016, Zysman-Colman reported two new Ir^{III} complexes bearing the pybtdaH, $[Ir(ppy)_2(pybtdaH)]^+$ and $Ir(ppy)_2(pybtda_{ox})$ (ppyH = 2-phenylpyridine).[114] The ligand underwent oxidation to the *S*-oxide analogue under basic conditions (K_2CO_3) with the ligand adopting a simple *N*,*N′*-chelate mode. Both complexes exhibit mixed ligand-centered and charge-transfer transitions at energies lower than 300 nm, with the absorption in $[\text{Ir(ppy)}_2\text{(pybtdaH)}]^+$ trailing further into the visible region. Both complexes were poorly emissive with the emission of cationic complex blue-shifted compared to the neutral complex. The coordination modes of pybtdaH and $\text{pybtda}_{\text{ox}}^-$ reported to date are shown in Figure 1.1.

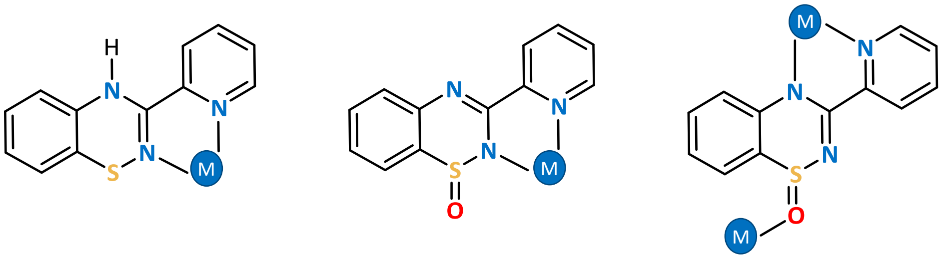

pybtdaH

$\text{pybtda}_{\text{ox}}^-$

$\text{pybtda}_{\text{ox}}^-$

Figure 1.1 Coordination modes of pybtdaH and $\text{pybtda}_{\text{ox}}^-$ reported to date.

1.3. Coordination Chemistry

1.3.1 Theory of coordination chemistry

In a classical coordination complex, a central metal atom or ion is coordinated by one or more molecules or ions (ligands), which act as Lewis bases forming coordination bonds with the central atom or ion which acts as a Lewis acid. The atoms of the ligands that are directly bonded to the central atom or ion are called donor atoms. A coordinate bond (also called a dative covalent bond) is a covalent bond (a shared pair of electrons) in which both electrons come from the same atom. In simple diagrams, a coordinate bond is usually shown by an arrow pointing from the atom donating (ligand) the lone pair to the atom accepting it (metal).

1.3.1.a Classification of ligands

The ligands can be classified in terms of the charge and the number of coordination sites it occupies. Ligands can be neutral (e.g. H_2O, NH_3, CH_3OH) or anionic (e.g. HO^-, Cl^-, CO_3^{2-}). The ligands are also defined by their denticity (Latin, *dentis*, meaning ‘tooth’) which refers to the number of donor pairs in a single ligand that bind to a central atom in a coordination complex. Ligands coordinating to a metal ion through a single pair of electrons are described as monodentate or unidentate. Ligands which interact with a metal ion through two or more donor pairs are called polydentate or multidentate ligands. For example a bidentate ligand interacts with metals through two pairs of electrons, a tridentate through three, and so on.

If two or more of the donor atoms are interacting with the same metal center and it forms a 4-, 5- or 6-membered ring, the ligands are described as chelating (Greek *χηλή*, meaning 'claw'). It is generally found that there is an extra thermodynamic stability associated with complexes which contain chelating ligands and this is the so-called chelate effect. The chelate effect is the result of both enthalpic and entropic contributions. The value of ΔG^{o} gives a measure of the effect and the relative signs and magnitudes of the contributing ΔH^{o} and $T\Delta S^{o}$ terms play a crucial role (Equation 1.1).

$$\Delta G^{o} = \Delta H^{o} - T\Delta S^{o}$$

Equation 1.1

The enthalpic contribution is due to the reduction of the electrostatic repulsion between the δ^{-} donor atoms on going from two monodentate to one bidentate. The entropic effect deriving from chelation arises largely from the number of ligands displaced during the chemical reaction when comparing chelating and the corresponding monodentate ligands. For example, comparison of the binding of ethylenediamine (en) with ammonia (NH_3); in equation 1.2, monodentate ligands are involved on both sides of the equation with no change in the total number of molecules. In contrast, in equation 1.3, monodentate NH_3 ligands are being substituted by bidentate en ligands leading to an increase in the total number of molecules in the system and thus an increase in entropy ($\Delta S > O$).

$$\underbrace{[Ni(OH_2)_6]^{2+} + 6\ NH_3}_{\text{7 complex ions/molecules}} \rightleftharpoons \underbrace{[Ni(NH_3)_6]^{2+} + 6\ H_2O}_{\text{7 complex ions/molecules}}$$

Equation 1.2

$$\underbrace{[Ni(NH_3)_6]^{2+} + 3\ en}_{\text{4 complex ions/molecules}} \rightleftharpoons \underbrace{[Ni(en)_3]^{2+} + 6\ NH_3}_{\text{7 complex ions/molecules}}$$

Equation 1.3

In some cases, a donor atom or a ligand offer a pair of electrons to two different central metal ions each and these ligands are called bridging ligands and are preceded by the Greek letter 'mu', μ. In all the other cases, the ligand is described as being terminal.

1.3.1.b Coordination number and geometries

The coordination number of a metal ion is the total number of bonds which it forms to the surrounding ligands. The most common coordination numbers are 4 and 6 for transition metal ions but they can range between 2 and 12. For each coordination number there may be certain arrangements that the donor atoms can adopt around the metal center resulting in several geometries as shown in Table 1.1. Both steric and electronic factors are involved in dictating the coordination geometry around the metal ion.

Table 1.1 Coordination numbers and their common coordination geometries.

Coordination Number	Coordination geometry
2	linear
3	trigonal planar, trigonal pyramidal
4	tetrahedral, square planar
5	trigonal bipyramidal, square pyramidal
6	octahedral, trigonal prismatic, ‘nido’ pentagonal bipyramid.
7	pentagonal bipyramidal, monocapped trigonal prismatic, monocapped octahedral
8	Dodecahedral, square antiprismatic, hexagonal bipyramidal, cube, bicapped trigonal prismatic
9	Tricapped trigonal prismatic

The most common geometry for 6-coordinate metal centres is the octahedral, for 5-coordinate trigonal bipyramidal and square pyramidal, and for 4-coordinate tetrahedral and square planar. In some structures the final geometry adopted may be intermediate between two or more of these idealized geometries and a series of parameters are provided to establish the degree of distortion between different geometries for each coordination number, e.g. τ_4 would be used to measure the distortion between the four-coordinate tetrahedral and square planar geometries.[115] The τ parameter ranges between 0 and 1 with 0 and 1 corresponding to one of two idealized structures. The τ parameters for 4, 5 and 6 coordinate geometries will be utilized in more detail later in this thesis. An alternative approach to assess distortions from idealized geometries is to compute a set of root mean square (RMS) deviations from the idealized geometries and the geometry which has the smallest RMS deviation from ideality can be considered the best descriptor of the coordination environment.[116] The RMS deviation approach is discussed in Chapter 5.

1.3.1.c Isomerism in coordination compounds

Isomers are compounds with the same formula but different properties that result from different structures. There are two broad classes of isomers: structural isomers and stereoisomers. Structural (or constitutional) isomers have the same molecular formula but different molecular structures (different connectivities or different numbers of chemical bonds). There are many types of structural isomers in transition metal complexes. Some of the main types are the following:

(i) Ionization isomers: Interchange of anionic ligands between the first coordination sphere with the outside, e.g. $[Co(H_2O)_5F]^+Cl^-$ and $[Co(H_2O)_5Cl]^+F^-$.

(ii) Linkage isomers: one or more ligands can coordinate to the metal ion in more than one way (ambidentate ligands), e.g. $[CO(NH_3)_5(NO_2)]^{2+}$ and $[Co(NH_3)_5(ONO)]^{2+}$.

(iii) Coordination isomers: these exhibit the same ligands bound to the metal centre but arranged in chemically distinct ways. Common examples are square planar complexes where the ligands can be bound either *cis* (adjacent) or *trans* (opposite) to each other, e.g. *cis*- and *trans*- isomers of platin, $PtCl_2(NH_3)_2$.

Optical isomers have the same chemical formulae and atom connectivities but are non-superimposable mirror images. Metal complexes in which the ligand bears three chelate ligands such as $M(en)_3^{2+}$ can exhibit optical isomers and examples in this thesis will be discussed in Chapter 3. Such complexes are typically described as being of *R* or *S* handedness for tetrahedral complexes in an analogous fashion to organic chiral centres. For octahedral complexes bearing three chelate ligands, the labels Λ and Δ are used depending on whether their absolute configuration is left or right handed respectively. The interconversion of Δ and Λ forms can occur through twist mechanisms including the Bailar and the Ray-Dutt twist.[117] These mechanisms include a transition through trigonal prismatic geometry and the two mechanisms differ only in which pair of opposing triangular faces is twisting. Some crystals of optical isomers may be of a single optical isomer e.g. pure Λ or pure Δ and crystallise in non-centrosymmetric space groups. However, optical isomers crystallising in centrosymmetric space groups will have a 50:50 mixture of both Λ and Δ forms. A racemic (50:50) mix of optical isomers may also be generated by having two molecules in the asymmetric unit; one Λ and one Δ isomer.

1.3.1.d Crystal Field Theory (CFT)

Crystal field theory is one of the three approaches to the bonding in complexes of the *d*-block metals, along with ligand field (LF) theory and molecular orbital (MO) theory. The most used approach in coordination chemistry is CFT which is a simple electrostatic model which defines the ligands as negative point charges. Therefore, there is an electrostatic attraction between the metal ion and the ligands, as well as repulsion between the electrons in *d*-orbitals and the ligand point charges. In crystal field theory, the presence of ligands leads to a splitting of the *d*-orbital degeneracy. The splitting depends on the coordination geometry of the crystal field and the type of ligands which determine the magnitude of the splitting. The shape of the *d*-orbitals is shown in Figure 1.2.

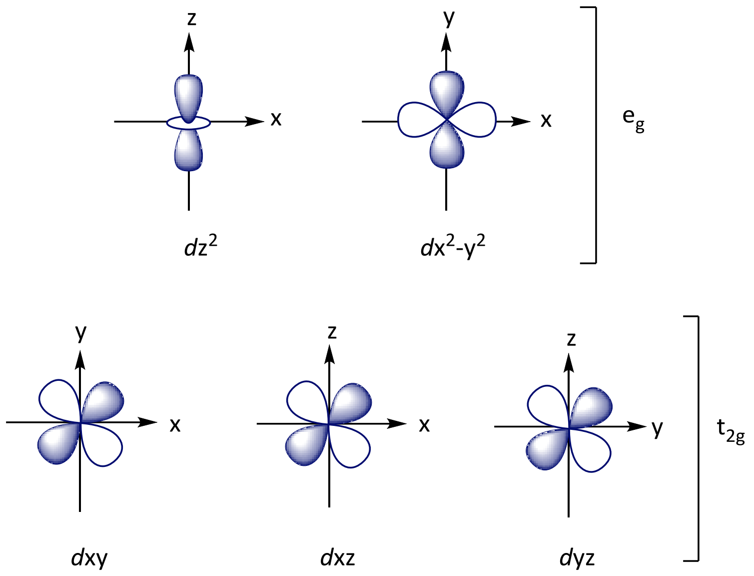

Figure 1.2 The shapes of the five *d*-orbitals.

In an octahedral field, the *d*-orbitals which interact directly with the ligand are the e_g set of orbitals consisting of the d_{z^2} and $d_{x^2-y^2}$ and these feel the most repulsion. These orbitals are higher in energy than the remaining three *d*-orbitals, the t_{2g} set. The energy difference between these sets of orbitals is the octahedral field splitting parameter Δ_{oct}, in which the t_{2g} orbitals are stabilized by $-\frac{2}{5}\Delta_{oct}$ and the e_g orbitals are destabilized by $+\frac{3}{5}\Delta_{oct}$. Because the electronic occupancy of the t_{2g} and e_g sets need not be equal then certain configurations gain additional stabilization known as crystal field stabilization energy (CFSE). This is calculated based on the number of electrons in the e_g and t_{2g} orbitals as well as the pairing energy (Figure 1.3).

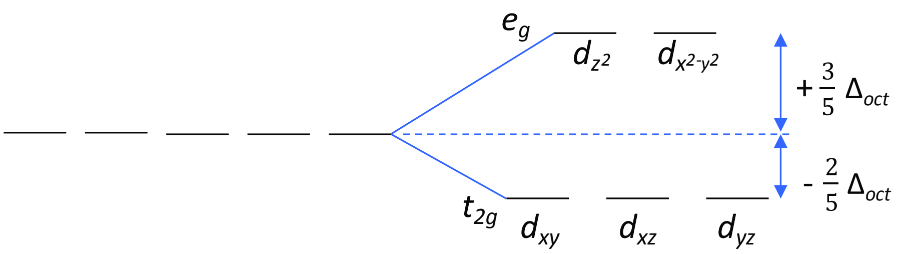

Figure 1.3 Splitting of the *d*-orbitals in an octahedral crystal field.

The placement of the electrons in the *d*-orbitals can lead to two possible configurations for d^4 to d^7 systems under octahedral geometry; a low-spin or high-spin state. Ultimately, this depends on whether the pairing energy *P* (destabilization that occurs from pairing two electrons) is greater or less than the energy required to promote an electron from the t_{2g} to the e_g orbitals. So, if $P >> \Delta_{oct}$ then the electrons will be high-spin and if $P << \Delta_{oct}$, then it will prefer to pair electrons and be low-spin (Figure 1.4).

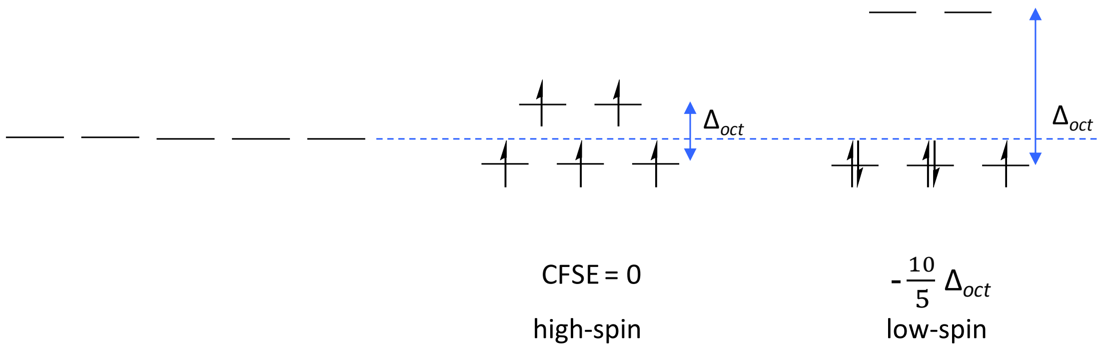

Figure 1.4 High-spin (weak field) and low-spin (strong field) configuration of Mn^{2+} (d^5).

The magnitude of the octahedral field splitting parameter (Δ_{oct}) is affected by three factors:

(i) The oxidation state of the metal: Metals with higher oxidation states have higher values of Δ_{oct} because the ligands are attracted closer to the metal centre. These types of complexes prefer the low-spin orientation.

(ii) 3*d vs* 4*d vs* 5*d* metals: On descending a triad of transition metal ions, Δ_{oct} increases. [In addition the expansion of the d-orbitals leads to a decrease in inter-electron repulsion (*P* is reduced)]. Therefore, the heavier transition metals are mostly low-spin.

(iii) Nature of the ligand: ligands can be classified as being strong field or weak field ligands and are organized in the Spectrochemical series based on their empirical (experimentally determined) ability to split the *d*-orbitals. I^- is regarded as a weak field ligand and tends to result in high-spin complexes whereas CO produces a large crystal field splitting.

$I^- < Br^- < S^{2-} < SCN^- < Cl^- < NO_3^- < F^- < OH^- < H_2O < NCS^- < CH_3CN < NH_3 < en < bpy$

$< phen < NO_2^- < PPh_3 < CN^- < CO$

Small Δ	Large Δ
Weak-field ligand	Strong-field ligands
Usually high-spin	Usually low-spin

It is also noteworthy that the size of the high-spin M^{II} centres show an initial decrease (M = Mn to Co) associated with increasing effective nuclear charge on traversing the first transition metal series and subsequent increase (Cu and Zn) associated with the addition of extra electrons into the e_g orbitals since electrons in the e_g set lead to greater electron-electron repulsion with the ligand orbitals. [More complex arguments can be made through MO theory where the e_g set is found to be antibonding but ultimately generates the same conclusion].

1.3.1.e Spin Crossover

Spin crossover (SCO) or thermal spin transition is a change in the spin state of a metal complex due to perturbation such as temperature, pressure or irradiation.[40] If the magnitude of the crystal field (Δ_{oct}) is energetically similar to the pairing energy (P_E) then the relative energies of the high- and low- spin complexes are similar. Under these conditions then a perturbation such as temperature can result in a crossover event, where the transition metal ion switches from being high-spin to being low-spin or *vice versa*.

The first row transition metals are the best candidates for SCO due to high inter-electron repulsion (P) than second or third row transition metals which are predominantly low-spin. Whilst many first row transition metals are high-spin, careful tailoring of the crystal field by tuning the ligand coordination environment can lead to low-spin configurations for these first row metals. Numerous methods exist to measure or detect spin crossover including Mössbauer spectra, magnetic measurements, vibrational spectra, EPR and X-ray diffraction. Changes in both the magnetism and structure accompanying a spin-transition will be described here.

One of the most characteristic changes associated with spin transitions is the change in the magnetic response. For example, for Fe^{II}, the high-spin state has 4 unpaired electrons ($S = 2$) whereas the low-spin state has no unpaired electrons ($S = 0$) (Figure 1.5). As a consequence, the magnetic moment, $\mu_{eff} = g[S(S+1)]^{1/2}$ (or $\chi T = Ng^2\beta^2/3k\, S(S+1)$) can be used to detect a spin crossover event.

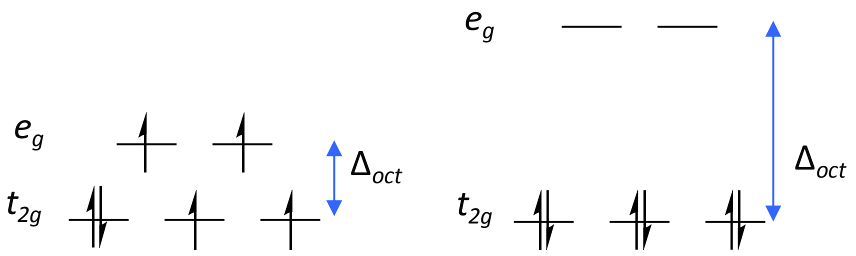

High-spin ($S = 2$) Low-spin ($S = 0$)

Figure 1.5 High- and low-spin configurations of Fe^{2+} (d^6) ion.

The abruptness of the transition (from high-spin to low-spin) is related to the cooperativity of the process which relates to the ability to drive the spin change throughout the whole lattice.[39] In many cases, the spin-crossover phenomenon is associated with an abrupt phase transition from 100 % low-spin (low temperature) to 100 % high-spin (high temperature), leading to a discontinuity in magnetic response which results from the presence of strong cooperativity (Figure 1.6a). Such behaviour has potential for exploitation in 'spin-switching' devices where the magnetic response is turned 'on/off' with small changes in temperature or pressure. In other cases, the spin transition can be more gradual (Figure 1.6b), occurring over a wider temperature range (due to low cooperativity). When equilibrium exists between 'high-spin' (HS) and 'low-spin' (LS) configurations, the conversion from HS to LS may be incomplete (Figure 1.6c). Thermal hysteresis may occur for systems in which cooperativity is high but there is a significant energy barrier to interconversion from LS to HS. Thus at some finite temperature *T* the HS state may be more stable than the LS configuration but the phase transition only occurs once the thermal energy $kT > E_a$. On cooling the HS state is maintained until the LS state becomes more thermodynamically stable (Figure 1.6d), i.e. the LS state may exist as a metastable state until there is sufficient thermal energy to overcome the energy barrier for structural reorganization. This indicates bistability of the system allowing the complex to transition from one electronic state to the other upon the influence of some external perturbation. Such behaviour would allow such complexes to be used in storage, memory and for lighting devices.[39] The described scenarios are shown in the spin transition curves (Figure 1.6, a-d) where $T_{1/2}$ is the spin transition temperature (at which the ratios of HS to LS are 1:1) and γ_{HS} is the molar fraction of the high-spin state.

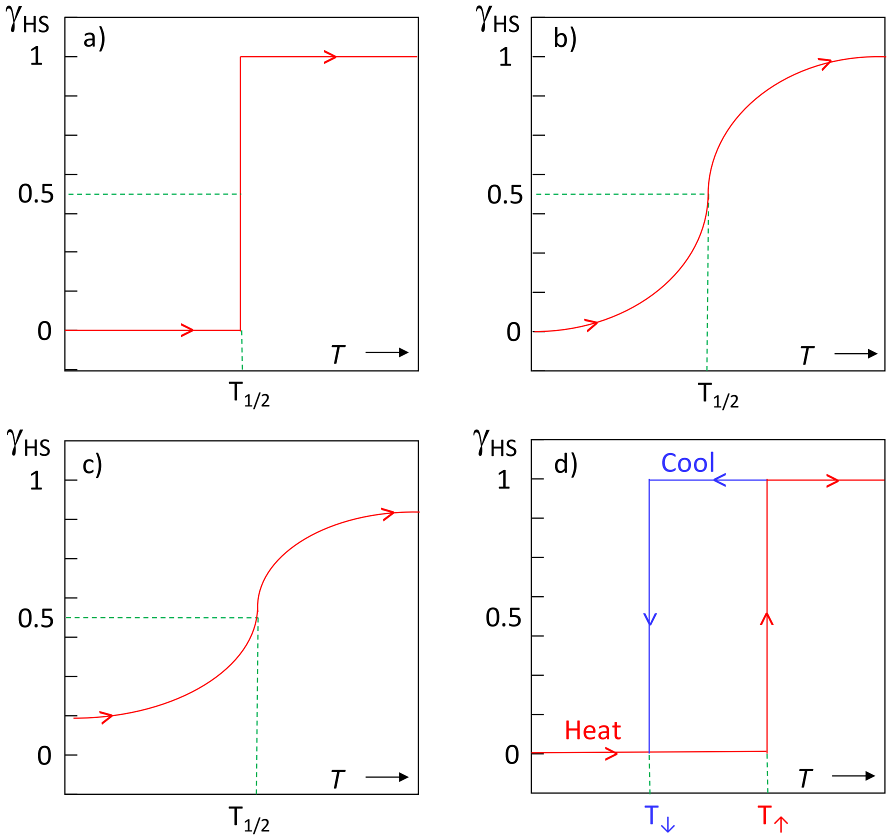

Figure 1.6 Spin transition curves of high-spin molar fraction *vs* temperature; (a) abrupt, (b) gradual, (c) incomplete, (d) hysteresis.

Another characteristic change associated with SCO transitions is the change in metal-ligand bond distance observed in the crystal structure when the spin state goes from high- to low-spin. The high-spin state has some of its electrons in the antibonding e_g orbitals however, demotion of these electrons to the low-spin state places all of them in the nonbonding t_{2g} orbitals (for example Fe^{II}, d^6, Figure 1.5). Therefore, the metal-ligand bond is strengthened (shortened) which can be observed in X-ray. The difference in metal-ligand bond length for Fe^{II} HS *vs* LS is large, and amounts to approximately 0.2 Å.[118] The difference is smaller in Fe^{III} and even in Co^{II} because only one electron is being transferred from e_g to t_{2g} orbitals.[43]

Octahedral complexes of d^9 and high-spin d^4 usually exhibit a Jahn-Teller distortion. The Jahn-Teller theorem states that any non-linear system in a degenerate electronic state will be unstable and will undergo distortion to form a system of lower symmetry and lower energy by removing the degeneracy. As a result, the axial metal-ligand bonds have different bond lengths than the equatorial bonds. The distortion can be either an elongation or compression of the axial bonds and numerous Cu^{2+} complexes described in this thesis show a preferred axial elongation.

1.3.2 Synthetic methodology of coordination chemistry

A key question currently central to the field of coordination chemistry is: 'What are the synthetic strategies for isolating polynuclear metal clusters?'. Two possible synthetic strategies are reported in the literature.

The first approach is to use well-defined structural building units (SBUs) with well-defined topologies coupled with ligands which offer a specific structure-directing metal-ligand interaction. This approach underpins many of the recent developments in areas such as the formation of metal organic frameworks (MOFs). Ligands which offer well-defined chelating or bridging topologies such as polydentate *N*-donors are often implemented in these approaches. This can result in the creation of aesthetically 'beautiful' molecules through the synthesis of complex substitutes that have controlled modes of coordination.[119]

Secondly, 'serendipitous assembly', in which a series of competing reactions are present and a number of system variables (pH, temperature, concentration, ligand:metal ratio, etc) by following some logical principles in order to influence the original product rather than dictate it by using a dominant structure-directing group. A major disadvantage of this approach is the limited synthetic control, while a significant advantage is the possible isolation of a large number of clusters from a particular reaction system, and also new synthetic methods of controlling the structure are discovered.[120] The use of ligands which offer a versatile or flexible set of metal binding sites are well-suited to serendipitous approaches due to the potential for the metal centers to adopt several coordination geometries. Small variations in the chemical identity of the ligands can potentially lead to new products and often involve choice of differing carboxylate ligands ($RCOO^-$) or alkoxides (RO^-) in which the carboxylate has an established versatility in the bonding mode available (section 1.3.3) and the alkoxide can be terminal, or bridging (μ_2 or μ_3). Tuning the R group can change both the steric and electronic demands of these groups and hence change the outcome of their chemical reactivity patterns. Initial observations should lead to new, more 'designed' experiments and logical synthetic thoughts, exhausting all synthetic parameters at each time (ratio of reactants, pH, solvent, counter-ions, and temperature). In this serendipitous self-assembly process, we typically aim to predict certain likely outcomes of the reaction e.g. preferred coordination modes for different ligands but cannot predict *a priori* how these interactions will manifest themselves in the presence of different metals or ligands.

The general synthetic scheme for isolating polynuclear transition metal complexes of the first row transition metals followed in our research is the following:

$$a\ MX_y\ +\ b\ LH \xrightarrow[\text{base}]{\text{solvent}} ?$$

a : b = ratio of metal to ligand

M = first row transition metal ions,

X = counter-ions of the metal salts which may act as a terminal ligand (monodentate, chelate) or as a bridging (bidentate, tridentate, etc.) substituent or can be non-coordinating ligands;

LH = organic molecules which have the ability to act as chelate substituents and after deprotonation can adopt bridging modes.

The metal salts employed during our experiments are the following: MCl_x (x = 2, 3), $M(OAc)_2$ and $M(hfac)_2$. When using MCl_x the reaction mixture is slightly acidic since the Cl^- anion is pH neutral (conjugate base of a strong acid) and the M^{x+} cation is Lewis acidic. Conversely the use of $M(OAc)_2$ and $M(hfac)_2$ offer more basic conditions due to the presence of OAc^- and $hfac^-$ anions which are the conjugate bases of weak acids (HOAc and Hhfac respectively). The pH can be further manipulated by addition of base (Et_3N) to create an even more basic environment and enhance ligand deprotonation.

The ratio of the metal to organic ligand is altered to explore the effect of the reaction outcome. Several solvents and crystallization techniques are employed to adjust to the solubility of the product and isolate single crystals for X-ray crystallography.

The simultaneous presence of a terminal ligand to terminating potential polymerization and a bridging ligand (preferably the organic ligand) that can act as a bridging or simultaneously bridging and chelating substituent is expected to favour the formation of polynuclear complexes.

1.3.3 Coordination modes of acetate (OAc^-) and hexafluoroacetylacetate ($hfac^-$) groups

The employment of acetate (OAc^-) and hexafluoroacetylacetate ($hfac^-$) groups in our reaction scheme is due to two reasons: (i) the weakly basic environment they offer as anions in solution and (ii) the variety of ways in which they can complex metal ions.

Simple carboxylate ions can act as monodentate, *O*-donor ligands, as 1,3-chelate ligands and/or as bridging substituents using μ_2-oxygen atoms. Conversely the $hfac^-$

groups mostly adopt a chelate mode but some examples of bridging hfac groups have been reported. The unsolvated form of first row transition metals, M(hfac)$_3$ (M = Mn, Co, Ni) exhibits the chelating-bridging mode,[121] as well as complexes incorporating Ag, Cd, Hg and In metal ions.[122,123]

The crystallographically established ways of complexing AcO$^-$ and hfac$^-$ with various metal ions are shown in Scheme 1.9 and clearly highlight the diversity of potential coordination modes possible.

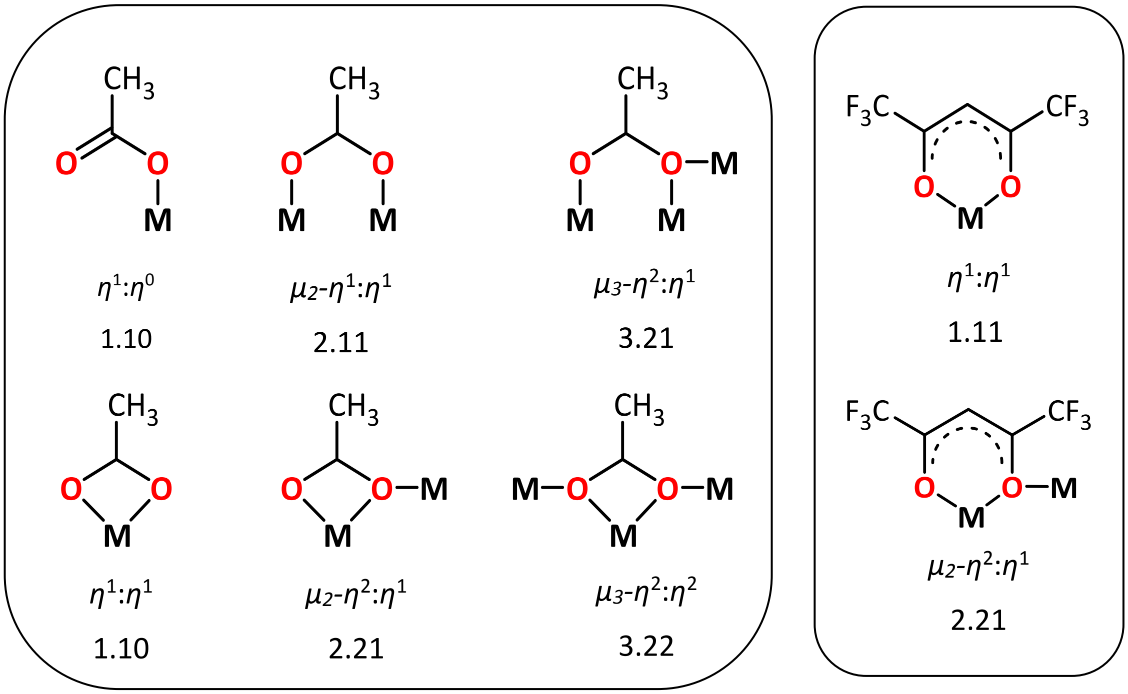

Scheme 1.9 Selected crystallographically reported coordination modes of the OAc$^-$ (left) and hfac$^-$ (right) ligands, and the μ/η and Harris notations which describe these modes.

There are two ways to describe the coordination mode of a ligand to a metal centre. The μ/η and the Harris notation. Denticity is the coordination of a ligand to a metal center through multiple atoms and is described with the Greek letter η ('eta'). In the case of a bridging ligand the letter μ ('mu') is used to indicate the total number of metals bridged. The Harris notation was proposed in 2000 where the binding mode is referred to as [$X.Y_1Y_2Y_3…Y_n$], where X is the overall number of metals bound by the whole ligand, and each value of Y refers to the number of metal atoms attached to the different donor atoms.[124] The ordering of Y is listed by the Cahn-Ingold-Prelog priority rules (i.e. S before O before N). The proposed notation was to distinguish the coordination of different type of atoms of a ligand such as a ligand coordinating through N and O atoms.

1.4. Dissertation Objectives

The coordination chemistry of 1,2,4-benzothiadiazines known to date is limited to a series of mononuclear first row metal complexes of 3-(2’-pyridyl)-functionalized benzothiadiazine (pybtdaH)[113], a dimer with formula $[\mathrm{Cu(pybtda_{ox})_2}]_2$[102], and two iridium complexes, $[\mathrm{Ir(ppy)_2(pybtdaH)}]^+$ and $\mathrm{Ir(ppy)_2(pybtda_{ox})}$[114], as discussed previously. The $\mathrm{S^{II}}$ system undergoes oxidation to the $\mathrm{S^{IV}}$ system in the presence of a base such as $\mathrm{Et_3N}$ or $\mathrm{K_2CO_3}$.[102,114] The *S*-oxide on the dimer offers an additional donor atom leading to a bridging mode of the ligand in addition to the *N*,*N’*-chelate pocket. This ability of the ligand gives rise to a new perspective on the coordination chemistry of 1,2,4-benzothiadiazines since it translates the strictly chelating nature of the pybtdaH ligand to a more versatile bridging ligand with *N,N’* and *O* donor pockets favouring a more serendipitous approach to coordination chemistry. In the following chapters, we will present the synthesis and characterization of a series of 1,2,4-benzothiadiazines in which their structures are tailored to enhance their coordination abilities (Scheme 1.10).

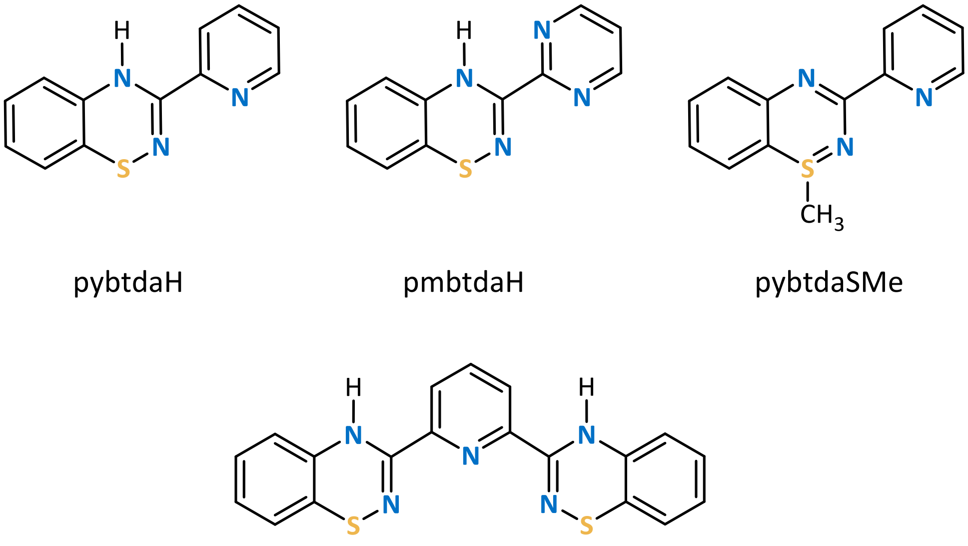

pybtdaH

pmbtdaH

pybtdaSMe

$\mathrm{bisbtdaH_2}$

Scheme 1.10 Derivatives of 1,2,4-benzothiadiazines presented in the dissertation.

In Chapter 2, a new synthetic route of the synthesis of pybtdaH will be discussed as well as kinetics studies on the formation of the final product. Computational studies of the ligand to probe the energetics of the heterocycle upon rotation of the pyridyl ring will be presented. The pybtdaH ligand undergoes oxidation to form the *S*-oxide and deprotonation to form the $\text{pybtda}_{\text{ox}}^{-}$ anion under basic conditions, as discussed above. Previous work investigated only MCl_2 where the chloride has no effect on pH since chloride is the conjugate base of a strong acid (pK_a (HCl) = -6.1 [125]) and has minimal base character. Conversely, the OAc^- and $hfac^-$ anions are the conjugate bases of weak acids (pK_a (AcOH) = 4.76 [126], pK_a (Hhfac) = 4.71 [127]) and generation of the anions in solution could promote the oxidation of the pybtdaH ligand instead of a base, such as Et_3N or K_2CO_3 used previously (Scheme 1.11).[102,114] In addition, the acetate groups (OAc^-) offer a variety of coordination modes and can potentially bridge up to four metal centers favouring the formation of polynuclear complexes (Scheme 1.9).

$$\text{HCl} \longrightarrow \text{H}^{+} + \text{Cl}^{-} \qquad pK_a = -6.1 \qquad \textbf{pH neutral}$$

$$\text{HOAc} \rightleftharpoons \text{H}^{+} + \textbf{OAc}^{-} \qquad pK_a = 4.76 \qquad \textbf{mild base}$$

$$\text{Hhfac} \rightleftharpoons \text{H}^{+} + \textbf{hfac}^{-} \qquad pK_a = 4.71 \qquad \textbf{mild base}$$

Scheme 1.11 Logarithimic dissociation constants of HCl, AcOH and Hhfac.

The employment of first row transition metal salts containing the basic counterions OAc^- and $hfac^-$ with the ligand pybtdaH will be presented. The effect of additional base (Et_3N) in the reaction scheme has been explored and will be discussed.

In Chapter 3, the synthesis and characterization of the novel redox active ligand 3-(2',6'-pyrimidine)-benzo-1,2,4-thiadiazine (pmbtdaH) is reported (Scheme 1.10). The pmbtdaH ligand employs a pyrimidyl ring on position 3 of the heterocycle increasing the donor atoms offered for coordination. The neutral pmbtdaH ligand acts as a simple *N*,*N'*-chelate to transition metal ions whereas the $\text{pmbtda}_{\text{ox}}^{-}$ anion is more versatile offering two *N*,*N′* binding sites for bridging two metal centres as well as a pendant *O*-donor which offers an additional binding site favouring formation of polynuclear metal complexes. The coordination chemistry of the ligand with various first row transition metals salts is presented as well as the effect on the reactivity pathways of pmbtdaH with metal ions with weakly basic anions (hfac$^-$) favouring the deprotonation/oxidation process.

The synthesis and characterization of the 1-methyl-3-(pyridinyl)-1,2,4-benzothiadiazine (pybtdaSMe, Scheme 1.10) is presented in Chapter 4. Although in pybtdaH$_{ox}$ the oxygen acts as an additional donor atom, the oxidation of the ligand in reaction schemes involve basic conditions is inevitable in open-air conditions. Alkylation at sulphur could prevent such behaviour and the effect of the electronics of the heterocycle to the reactivity of the ligand can be explored. The ligand pybtdaSMe offers one coordination pocket to a metal centre through *N*,*N′*-chelation by coordination of either the heterocyclic N atoms at either 2 or 4 positions. In addition, the ligand is not protonated leaving both nitrogen atoms of the heterocycle equally available as donor atoms. Its coordination chemistry to selected first row transition metal complexes with MCl_2 and $M(hfac)_2$ is presented.

In Chapter 5, the novel S/N based terpyridine type ligand bisbtdaH$_2$ has been synthesized and its coordination chemistry with first row transition metal complexes has been investigated (Scheme 1.10). The ligand is designed to offer a tridentate *mer*-binding coordination geometry and its coordination chemistry with selected first row transition metal ions is described.

1.5. References

1 J. Bartoll, in *9th International Conference on NDT of Art, Jerusalem Israel*, 2008.

2 G. E. Stahl, *Exp. Obs. Animadversiones CCC Numer. Chymicae Phys.*, 1731, 281.

3 World Health Organization, *WHO Model List Essential Medicines*, 2013.

4 W. Ruttinger and G. C. Dismukes, *Chem. Rev.*, 1997, **97**, 1.

5 V. K. Yachandra, K. Sauer and M. P. Klein, *Chem. Rev.*, 1996, **96**, 2927.

6 A. K. Poulsen, A. Rompel and C. J. McKenzie, *Angew. Chemie - Int. Ed.*, 2005, **44**, 6916.

7 S. Dasari and P. B. Tchounwou, *Eur. J. Pharmacol.*, 2015, **5**, 364.

8 J. Paken, C. D. Govender, M. Pillay and V. Sewram, *J. Toxicol.*, 2016.

9 G. W. Parshall and S. D. Ittel, *Adv. Chem.*, 1992, 42.

10 D. Morales-Morales, *Rev. la Soc. Química México*, 2004, **48**, 338.

11 O. Kahn, *Molecular Magnetism*, Wiley-VCH, New York, 1993.

12 D. Gatteschi, L. Bogani, A. Cornia, M. Mannini, L. Sorace and R. Sessoli, *Solid State Sci.*, 2008, **10**, 1701.

13 *IUPAC. Compendium of Chemical Terminology, 2nd ed. Compiled by A. D. McNaught and A. Wilkinson.*, Blackwell Scientific Publications, Oxford, 1997.

14 C. Kaes, A. Katz and M. W. Hosseini, *Chem. Rev.*, 2000, **100**, 3553.

15 B. H. Ye, M. L. Tong and X. M. Chen, *Coord. Chem. Rev.*, 2005, **249**, 545.

16 P. Alborés and E. Rentschler, *Dalton Trans.*, 2013, **42**, 9621.

17 P. O. Adelani, N. D. Cook and P. C. Burns, *Cryst. Growth Des.*, 2014, **14**, 5692.

18 I. F. Díaz-Ortega, J. M. Herrera, D. Aravena, E. Ruiz, T. Gupta, G. Rajaraman, H. Nojiri and E. Colacio, *Inorg. Chem.*, 2018, **57**, 6362.

19 P. Alborés and E. Rentschler, *Inorg. Chem.*, 2010, **49**, 8953.

20 P. G. Sammes and G. Yahioglu, *Chem. Soc. Rev.*, 1994, 327.

21 K. Takada, R. Sakamoto, S. T. Yi, S. Katagiri, T. Kambe and H. Nishihara, *J. Am. Chem. Soc.*, 2015, **137**, 4681.

22 H. Hofmeier and U. S. Schubert, *Chem. Soc. Rev.*, 2004, **33**, 373.

23 U. S. Schubert, H. Hofmeier and G. R. Newkome, *Modern Terpyridine Chemistry*, Wiley-VCH, 2006.

24 E. C. Constable, *Chem. Soc. Rev.*, 2007, **36**, 246.

25 A. M. W. Cargill Thompson, *Coord. Chem. Rev.*, 1997, **160**, 1.

26 C. G. Claessens, U. Hahn and T. Torres, *Chem. Rec.*, 2008, **8**, 75.

27 K. Kadish, R. Guilard and K. M. Smith, *The Porphyrin Handbook*, Academic Press, 2003.

28 J. A. G. Williams, *Chem. Soc. Rev.*, 2009, **38**, 1783.

29 M. A. Halcrow, *Coord. Chem. Rev.*, 2005, **249**, 2880.

30 C. Bazzicalupi, A. Bencini, A. Bianchi, A. Danesi, E. Faggi, C. Giorgi, S. Santarelli and B. Valtancoli, *Coord. Chem. Rev.*, 2008, **252**, 1052.

31 G. Accorsi, A. Listorti, K. Yoosaf and N. Armaroli, *Chem. Soc. Rev.*, 2009, **38**, 1690.

32 P. J. Chirik and K. Wieghardt, *Science*, 2010, **327**, 794.

33 A. B. Sorokin, *Chem. Rev.*, 2013, **113**, 8152.

34 T. Zell, P. Milko, K. L. Fillman, Y. Diskin-Posner, T. Bendikov, M. A. Iron, G. Leitus, Y. Ben-David, M. L. Neidiq and D. Milstein, *Chem. – Eur. J.*, 2014, 4403.

35 M. Paoli, J. Marles-Wright and A. Smith, *DNA Cell Biol.*, 2002, **21**, 271.

36 J. K. Hoober, L. L. Eggink and M. Chen, *Photosynth. Res.*, 2007, **94**, 387.

37 E. A. Medlycott and G. S. Hanan, *Chem. Soc. Rev.*, 2005, **34**, 133.

38 M. del C. Gimenez Lopez, M. Clemente Leon and C. Gimenez-Saiz, *Dalton Trans.*, 2018, **47**, 10453.

39 P. Gutlich and H. A. Goodwin, *Spin Crossover in Transition Metal Compounds I–III*, Springer, Top. Curr. Chem., 2004.

40 M. A. Halcrow, *Chem. Soc. Rev.*, 2011, **40**, 4119.

41 A. G. Craig, O. Roubeau and G. Aromí, *Coord. Chem. Rev.*, 2014, **269**, 13.

42 C. A. Kilner and M. A. Halcrow, *Dalton Trans.*, 2010, **39**, 9008.

43 I. Krivokapic, M. Zerara, M. L. Daku, A. Vargas, C. Enachescu, C. Ambrus, P. Tregenna-Piggott, N. Amstutz, E. Krausz and A. Hauser, *Coord. Chem. Rev.*, 2007, **251**, 364.

44 S. Hayami, Y. Komatsu, T. Shimizu, H. Kamihata and Y. H. Lee, *Coord. Chem. Rev.*, 2011, **255**, 1981.

45 S. Hayami, M. R. Karim and Y. H. Lee, *Eur. J. Inorg. Chem.*, 2013, 683.

46 G. Dupouy, M. Marchivie, S. Triki, J. Sala-Pala, J. Y. Salaün, C. J. Gómez-García and P. Guionneau, *Inorg. Chem.*, 2008, **47**, 8921.

47 J. A. Thomas, *Dalton Trans.*, 2011, **40**, 12005.

48 G. A. Craig, J. S. Costa, O. Roubeau, S. J. Teat and G. Aromí, *Chem. - A Eur. J.*, 2012, **18**, 11703.

49 E. Coronado, M. Giménez López, C. Gimenez-Saiz, J. M. Martinez-Agudo and F. M. Romero, *Polyhedron*, 2003, **22**, 2375.

50 K. H. Sugiyarto and H. A. Goodwin, *Aust. J. Chem.*, 1988, **41**, 1645.

51 A. Caneschi, D. Gatteschi, R. Sessoli and P. Rey, *Acc. Chem. Res.*, 1989, **22**, 392.

52 R. M. Buchanan, B. J. Fitzgerald and C. G. Pierpont, *Inorg. Chem.*, 1979, **18**, 3439.

53 H. H. Downs, R. M. Buchanan and C. G. Pierpont, *Inorg. Chem.*, 1979, **18**, 1736.

54 A. Caneschi, D. Gatteschi, R. Sessoli and P. Rey, *Inorg. Chem.*, 1988, **27**, 1756–1761.

55 D. J. Sullivan, R. Clérac, M. Jennings, A. J. Lough and K. E. Preuss, *Chem. Commun.*, 2012, **48**, 10963.

56 K. E. Preuss, *Coord. Chem. Rev.*, 2015, **289**–**290**, 49.

57 J. Wu, D. J. MacDonald, R. Clérac, I. R. Jeon, M. Jennings, A. J. Lough, J. Britten, C. Robertson, P. A. Dube and K. E. Preuss, *Inorg. Chem.*, 2012, **51**, 3827.

58 D. J. R. Brook, S. Fornell, J. E. Stevens, B. Noll, T. H. Koch and W. Eisfeld, *Inorg. Chem.*, 2000, **39**, 562.

59 D. J. R. Brook, *Comments Inorg. Chem.*, 2015, **35**, 1.

60 V. Polo, A. Alberola, J. Andres, J. Anthony and M. Pilkington, *Phys. Chem. Chem. Phys.*, 2008, **10**, 857.

61 M. Chahma, K. Macnamara, A. Van der Est, A. Alberola, V. Polo and M. Pilkington, *New J. Chem.*, 2007, **31**, 1973.

62 R. G. Hicks, M. T. Lemaire, L. K. Thompson and T. M. Barclay, *J. Am. Chem. Soc.*, 2000, **122**, 8077.

63 J. M. Rawson, A. Alberola and A. Whalley, *J. Mater. Chem.*, 2006, **16**, 2560.

64 D. C. Nonhebel, J. M. Tedder and J. C. Walton, *Radicals*, Cambridge University Press, 1979.

65 R. Kuhn and H. Trischmann, *Angew. Chem. Int. Ed.*, 1963, **2**, 155.

66 G. N. Lipunova, T. G. Fedorchenko and O. N. Chupakhin, *Russ. Chem. Rev.*, 2013, **82**, 701.

67 C. Train, L. Norel and M. Baumgarten, *Coord. Chem. Rev.*, 2009, 2342.

68 H. M. Blatter and H. Lukaszewski, *Tetrahedron Lett.*, 1968, **9**, 2701.

69 Y. Takahashi, Y. Miura and N. Yoshioka, *New J. Chem.*, 2015, **39**, 4783.

70 Y. Miura and N. Yoshioka, *Chem. Phys. Lett.*, 2015, **626**, 11.

71 Y. Takahashi, Y. Miura and N. Yoshioka, *Chem. Lett.*, 2014, **43**, 1236.

72 C. P. Constantinides, A. A. Berezin, G. A. Zissimou, M. Manoli, G. M. Leitus, M. Bendikov, M. R. Probert, J. M. Rawson and P. A. Koutentis, *J. Am. Chem. Soc.*, 2014, **136**, 11906.

73 C. P. Constantinides, P. A. Koutentis and G. Loizou, *Org. Biomol. Chem.*, 2011, **9**, 3122.

74 I. S. Morgan, A. Peuronen, M. M. Hänninen, R. W. Reed, R. Clérac and H. M. Tuononen, *Inorg. Chem.*, 2014, **53**, 33.

75 I. S. Morgan, A. Mansikkamäki, G. A. Zissimou, P. A. Koutentis, M. Rouzières, R. Clérac and H. M. Tuononen, *Chem. - A Eur. J.*, 2015, **21**, 15843.

76 O. M. Markovskii, L. N.; Kornuta, P. P.; Kachkovskaya, L. S.; Polumbrik, *Sulfur Lett.*, 1983, 143.

77 P. J. Hayes, R. T. Oakley, A. W. Cordes and W. T. Pennington, *J. Am. Chem. Soc.*, 1985, **107**, 1346.

78 K. L. M. Harriman, A. A. Leitch, S. A. Stoian, F. Habib, J. L. Kneebone, S. I. Gorelsky, I. Korobkov, S. Desgreniers, M. L. Neidig, S. Hill, M. Murugesu and J. L. Brusso, *Dalton Trans.*, 2015, **44**, 10516.

79 K. L. M. Harriman, I. A. Kühne, A. A. Leitch, I. Korobkov, R. Clérac, M. Murugesu and J. L. Brusso, *Inorg. Chem.*, 2016, **55**, 5375.

80 N. Yutronkie, I. Kuehne, I. Korobkov, J. L. Brusso and M. Murugesu, *Chem. Commun.*, 2015, 677.

81 A. W. Cordes and R. T. Oakley, *Acta Cryst.*, 1987, **2**, 1645.

82 P. G. Welling, *Biopharm. Drug Dispos.*, 1986, **7**, 501.

83 A. Fretheim, *BMC Fam. Pr.*, 2003, **4**, 19.

84 R. M. Taylor and M. M. Winbury, *Nature*, 1960, **187**, 603.

85 J. M. Sprague and F. C. Novello, *J. Am. Chem. Soc.*, 1957, 2028.

86 S. S. Fajans, J. C. Floyd Jr., R. F. Knopf, J. Rull, E. M. Guntsche and J. W. Conn, *J. Clin. Invest.*, 1966, 481.

87 A. Fretheim, *BMC Fam. Pr.*, 2003, **4**, 19.

88 M. M. Dvorak, C. De Joussineau, D. H. Carter, T. Pisitkun, M. A. Knepper, G. Gamba, P. J. Kemp and D. Riccardi, *J. Am. Soc. Nephrol.*, 2007, **18**, 2509.

89 L. Beigelman, G. Wang, B. Buckman and A. D. Stoycheva, *Preparation of benzothiadiazine dioxides as inhibitors of hepatitis C virus replication*, InterMune, Inc., USA, 2009.

90 M. S. Congreve, B. G. Christopher, John Andrew Tehan, S. S. Klair and S. J. Aves, *Preparation of 1,2,4-benzothiadiazin-3(4H)-one 1, 1-dioxides as orexin receptor antagonists*, Heptares Therapeutics Limited, UK, 2014.

91 J. Busch-Petersen, W. Fu, J. K. Kerns, M. R. Palovich, K. L. Widdowson and U. Assignee: SmithKline Beecham Corporation, *IL-8 receptor antagonists of substiuted 3-phenylamino-4H-1,2,4-benzothiadiazin-5-ol 1,1-dioxides*, SmithKline Beecham Corporation, USA 2005, 2005.

92 L. N. Markovskii, V. S. Talanov, O. M. Polumbrik and Y. G. Shermolovich, *J. Org. Chem.*, 1981, **17**, 2338.

93 J. Zienkiewicz, P. Kaszynski and V. G. Young Jr, *J. Org. Chem.*, 2004, **69**, 7525.

94 J. Zienkiewicz, A. Fryszkowska, K. Zienkiewicz, F. Guo, P. Kaszynski, A. Januszko and D. Jones, *J. Org. Chem.*, 2007, **72**, 3510.

95 L. Beer, R. C. Haddon, M. E. Itkis, A. A. Leitch, R. T. Oakley, R. W. Reed, J. F. Richardson and D. G. VanderVeer, *Chem. Commun.*, 2005, 1218.

96 S. M. Winter, A. R. Balo, R. J. Roberts, K. Lekin, A. Assoud, P. A. Dubeand and R. T. Oakley, *Chem. Commun.*, 2013, **49**, 1603.

97 A. A. Leitch, R. T. Oakley, R. W. Reed and L. K. Thompson, *Inorg. Chem.*, 2007, **46**, 6261.

98 D. D. Ross and D. Lednicer, *Zh. Org. Khim.*, 1984, **20**, 196.

99 G. Kresze, C. Seyfried and A. Trede, *Tetrahedron Lett.*, 1965, **6**, 3933.

100 N. Finch, S. J. Ricca, L. H. Werner and R. Rodebaugh, *J. Org. Chem.*, 1980, 3416.

101 K. Kaczorowska, Z. Kolarska, K. Mitka and P. Kowalski, *Tetrahedron*, 2005, **61**, 8315–8327.

102 E. R. Clark, J. J. Hayward, B. J. Leontowicz, M. U. Anwar, M. Pilkington and J. M. Rawson, *Dalton Trans.*, 2014, **44**, 2071.

103 T. L. Gilchrist, C. W. Rees and D. Vaughan, *J. Chem. Soc., Perkin Trans*, 1983, 55.

104 T. L. Gilchrist, C. W. Rees and D. Vaughan, *J. Chem. Soc., Chem. Commun.,* 1978, 1049.

105 T. L. Gilchrist, C. W. Rees and D. Vaughan, *J. Chem. Soc., Perkin Trans*, 1983, 49.

106 V. W. Bohnisch, T. L. Gilchrist and C. W. Rees, *J. Chem. Soc., Perkin Trans*, 1979, 2851.

107 N. Finch, S. Ricca, L. H. Werner and R. Rodebaughs, *J. Org. Chem.*, 1980, **45**, 3416.

108 G. Kresze, C. Seyfried and A. Trede, *Liebigs Ann. Chem.*, 1968, **715**, 223.

109 P. Kaszynski and V. G. Young, *J. Org. Chem.*, 2004, **69**, 2551.

110 E. R. Clark, J. J. Hayward, B. J. Leontowicz, D. J. Eislera and J. M. Rawson, *CrystEngComm*, 2014, **16**, 1755.

111 A. A. Leitch, I. Korobkov, A. Assoud and J. L. Brusso, *Chem. Commun.*, 2014, **50**, 4934.

112 A. O. Abdelhamid, A. M. Negm and T. M. S. Abdeen, *Arch. Pharm. (Weinheim Ger.)*, 1988, **321**, 913.

113 E. R. Clark, M. U. Anwar, B. J. Leontowicz, Y. Beldjoudi, J. J. Hayward, W. T. K. Chan, E. L. Gavey, M. Pilkington, E. Zysman-Colman and J. M. Rawson, *Dalton Trans.*, 2014, **43**, 12996.

114 A. K. Pal, D. B. Cordes, K. Pringouri, M. U. Anwar, A. M. Z. Slawin, J. M. Rawson and E. Zysman-Colman, *J. Coord. Chem.*, 2016, **69**, 1924.

115 L. Yang, D. R. Powell and R. P. Houser, *Dalton Trans.*, 2007, 955.

116 C. Andreini, G. Cavallaro and S. Lorenzini, *Bioinformatics*, 2012, **28**, 1658.

117 H. S. Rzepa and M. E. Cass, *Inorg. Chem.*, 2007, **46**, 8024.

118 H. Zheng, K. M. Langner, G. P. Shields, J. Hou, M. Kowiel, F. H. Allen, G. Murshudov and W. Minor, *Acta Crystallogr. Sect. D Struct. Biol.*, 2017, **73**, 316.

119 M. Fujita, K. Umemoto, M. Yoshizawa, N. Fujita, T. Kusukawa and K. Biradha, *Chem. Commun.*, 2001, 509.

120 R. E. P. Winpenny, *J. Chem. Soc. Dalton Trans.*, 2002, **6**, 1.

121 H. Zhang, B. Li, J. Sun, R. Clérac and E. V. Dikarev, *Inorg. Chem.*, 2008, **47**, 10046.

122 H. Zhang, B. Li and E. V. Dikarev, *J. Clust. Sci.*, 2008, **19**, 311.

123 J.-L. Jin, Y.-L. Shen, Y.-P. Xie and X. Lu, *CrystEngComm*, 2018, **20**, 2036.

124 R. A. Coxall, S. G. Harris, D. K. Henderson, S. Parsons, P. A. Tasker and R. E. P. Winpenny, *J. Chem. Soc. Dalton Trans.*, 2000, 2349.

125 A. Trummal, L. Lipping, I. Kaljurand, I. A. Koppel and I. Leito, *J. Phys. Chem. A*, 2016, **120**, 3663.

126 N. J. Tro, *Chemistry: A molecular approach*, Pearson, New Jersey, 2nd Ed., 2011.

127 M. Ellinger, H. Duschner and K. Starke, *J. Inorg. Nucl. Chem.*, 1978, **40**, 1063.

CHAPTER 2.

Synthesis and characterization of pybtdaH and its coordination chemistry

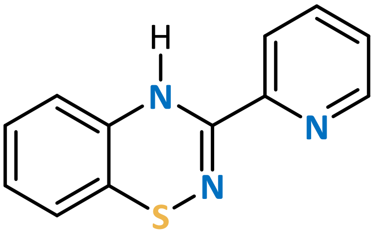

2.1. Introduction

The 3-(2′-pyridyl)-functionalized benzothiadiazine (pybtdaH) has been shown to form a series of chelate complexes to first row transition metal complexes of formula MCl$_x$(pybtdaH)$_y$.[1] More recently we have shown that the S^{II} system undergoes aerial oxidation to the S^{IV} system (Scheme 2.1) in the presence of a Lewis acidic metal and a base, such as Et$_3$N or K$_2$CO$_3$.[2] In this process, it seems likely that initial *N*-coordination activates the benzothiadiazine ring to *S*-oxidation and *N*-deprotonation, proceeding *via* a pybtda$_{ox}^{-}$ anion which has been isolated in the form of [Cu(pybtda$_{ox}$)$_2$]$_2$[2] and Ir(ppy)$_2$(pybtda$_{ox}$).[3] In the former case the ligand adopts a bridging mode in which the ligand is *N*,*N*′-chelating to one metal and binds to a second metal *via* the *S*-oxide O atom. In the iridium complex the ligand adopts a terminal *N*,*N*′-chelate mode. *S*-oxidation of some other thiazyl heterocycles at metal centres has also been described recently.[4,5]

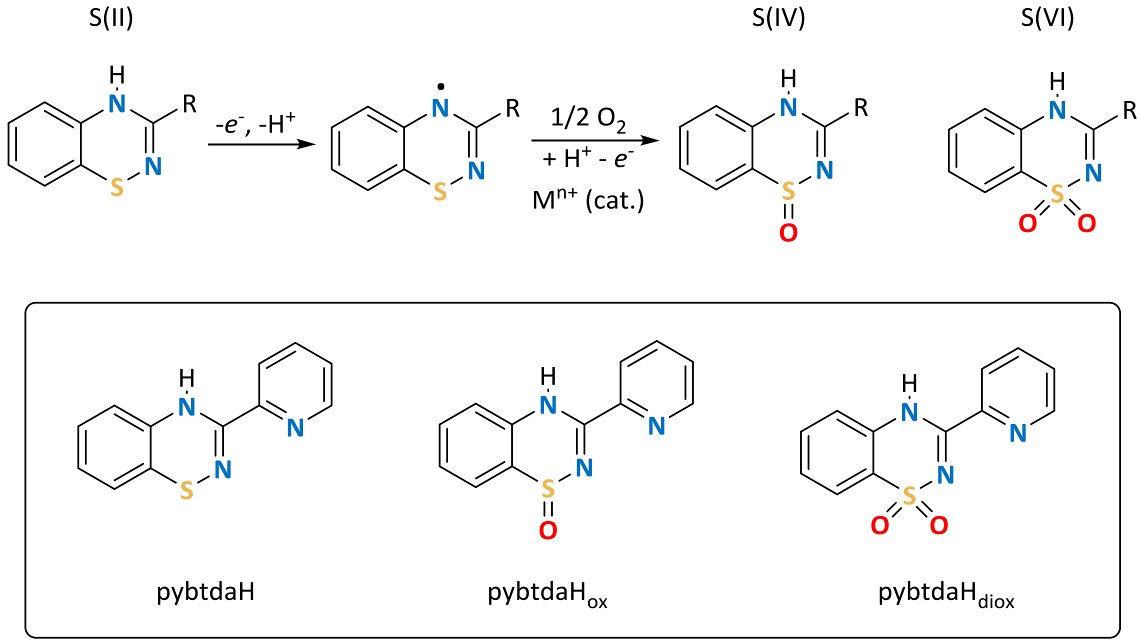

Scheme 2.1 (top) Formal S^{II}, S^{IV} and S^{VI} oxidation states of the benzothiadiazine framework; (bottom) S^{II}, S^{IV} and S^{VI} variants of the 2-pyridyl benzothiadiazine heterocycle.

These initial studies indicated that *S*-oxidation of pybtdaH and other benzothiadiazines only occurred in the presence of a metal and Et_3N.[2] We speculated that the use of metal complexes bearing more basic anions might favour such ligand oxidation processes without the addition of a formal base. Previous studies investigated the reactivity of MCl_2 in which the chloride anion is pH neutral since Cl^- is the conjugate base of a strong acid (pK_a (HCl) = -6.1 [6]). In contrast, anions such as OAc^- and $hfac^-$ are the conjugate bases of weak acids (pK_a (AcOH) = 4.76 [7], pK_a (Hhfac) = 4.71 [8]) and generation of OAc^- and $hfac^-$ in solution could promote the *in situ* oxidation of the pybtdaH ligand. In addition, the acetate groups (OAc^-) offer a variety of coordination modes (Section 1.3.3) and can potentially bridge up to four metal centers,[9,10] while the resultant $pybtda_{ox}^-$ ligand can bind at least two metal ions. The combination of these ligands should favour formation of polynuclear complexes. While $hfac^-$ has been reported to adopt *O*,*O*′-bridging modes,[11–13] it normally adopts a chelate mode and is likely to lead to monomeric complexes, $M(hfac)_2(pybtdaH_{ox})$.

The synthesis of the ligand 3-pyridyl-benzothiadiazine (pybtdaH, Scheme 2.1) has been described previously[14] but several improvements to the ligand synthesis are described in this Chapter as well as an examination of its coordination chemistry to selected first row transition metal complexes, $M(OAc)_2$ and $M(hfac)_2$. The potential versatility of coordination modes of the benzothiadiazine ligand to metal centres is shown in Figure 2.1. The pybtdaH ligand offers one coordination pocket to a metal centre through *N*,*N*′-chelation in its neutral and anionic ($pybtda^-$) or radical form ($pybtda^\bullet$) (Figure 2.1, left). Upon *S*-oxidation, the ligand can offer a more versatile hard *O*-donor centre in addition to the favourable, softer, *N*,*N*′-chelate, leading to enhanced aggregation of up to two metal ions for the $pybtda_{ox}^-$ ligand (Figure 2.1, right) or even up to three metal centers if the oxygen of the *S*-oxide adopts a bridging mode.

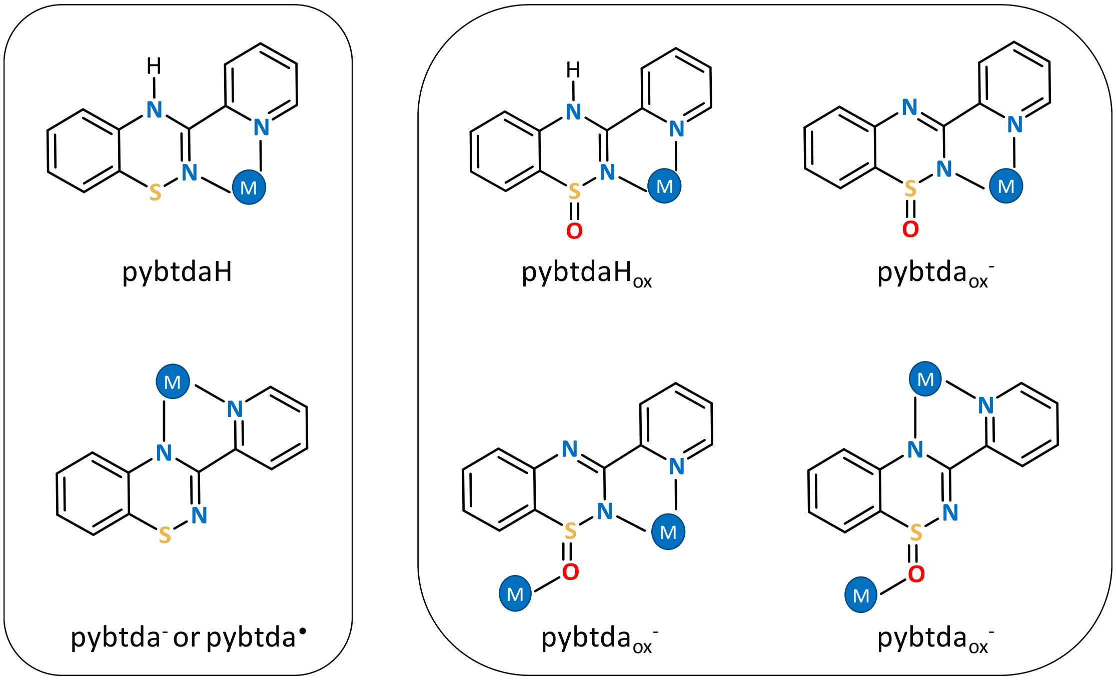

Figure 2.1 Coordination modes of neutral or anionic S^{II} (left) and the S^{IV} (right) benzothiadiazine ligand.

2.2. Results and Discussion

2.2.1 Synthesis, characterization and computational studies on the ligand pybtdaH

2.2.1.a Synthesis and characterization of the ligand pybtdaH

The ligand pybtdaH has been prepared previously.[14] In the current studies several improvements to the original methodology were employed. The new synthetic route is shown in Scheme 2.2.

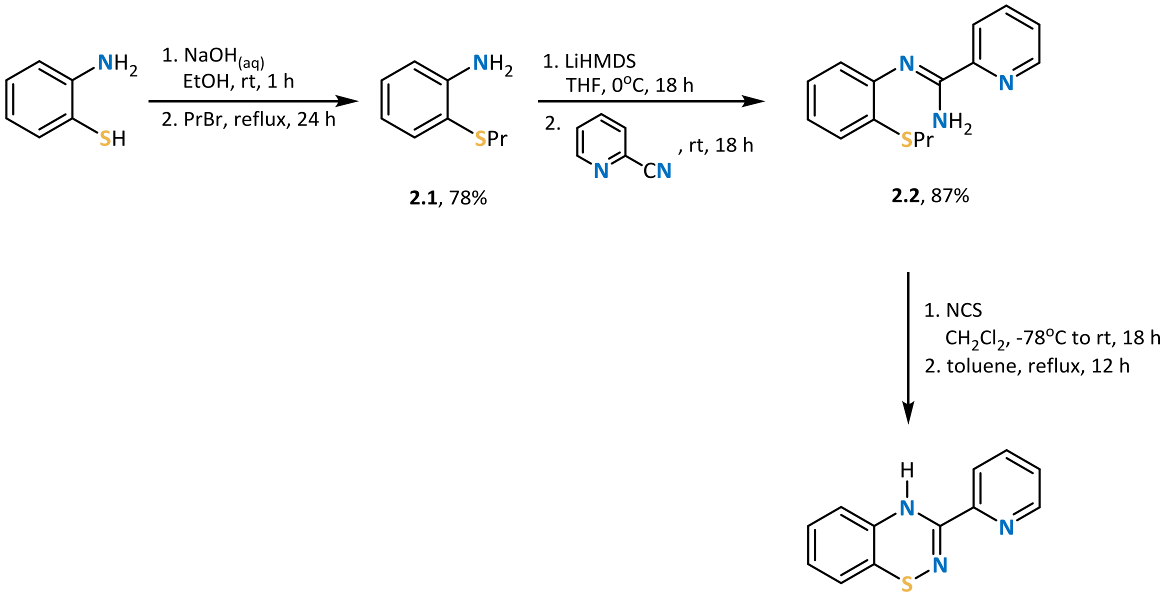

2.1, 78%

2.2, 87%

pybtdaH, 72%

Scheme 2.2 Synthetic route to ligand pybtdaH.

Originally intermediate **2.1** was prepared in a two step reaction.[14] The first step is the reaction of *N*-propylthiolate and the 2-nitrochlorobenzene to form 2-nitrophenyl(propyl)sulfane followed by reduction to the amine using powder iron. Both steps were prepared using microwave synthesis and permitted high yield preparation (95% for both steps) without the need of distillation or column chromatography. Despite the high yields and the purity of the products, the microwave synthesis does not allow for large scale reactions resulting to formation of ≈ 2 g of product for each repetition. In addition, the preparation of *N*-propylthiolate and various startimg materials is required for the synthesis. Instead, reaction of 2-aminothiophenol with *N*-propylbromide afforded

2-(propylthio)aniline (**2.1**) over one step in 78% yield. Although the yield is lower than the reported one, the reaction can be scaled up to 10 g and there is no need for preparation of other reagents. The purification of the product by Kugelrohr distillation does not require the use of solvents making it overall a greener synthesis.

Deprotonation of 2-(propylthio)phenylamine (**2.1**) with LiHMDS, under anaerobic, dry conditions followed by treatment with one equivalent of 2-cyanopyridine and work-up resulted in a brown oil. The oil was washed with hexanes to yield the pure intermediate (**2.2**) in 87% yield as a yellow crystalline powder. The preparation of the amidine follows the reported method with the exception of the purification of the product (washes with hexanes) resulting to the crystalline material and thus more moderate yields. Single-crystal X-ray diffraction revealed the product shown in Figure 2.2 crystallizing in the monoclinic space group *C*2/*c* with one molecule in the asymmetric unit. The ^{1}H NMR spectrum of **2.2** exhibits the expected proton environments in the aromatic and the aliphatic region (propyl group).

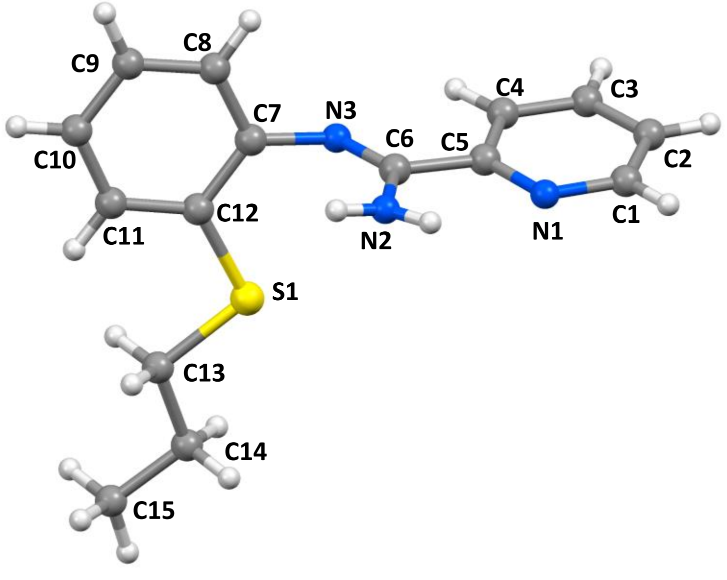

Figure 2.2 Molecular structure of N'-(2-propylthiophenyl)-picolinamidine (**2.2**).

The subsequent oxidative cyclization and pericyclic elimination of **2.2** in the presence of *N*-chlorosuccinimide (NCS) afforded the ligand pybtdaH, which was isolated in 72% yield. The ligand pybtdaH could not be purified by recrystallization using a heated mixture of hexanes and dichloromethane (80:20) as reported,[14] therefore column chromatography was used with dichloromethane as eluent. Single crystals of pybtdaH were grown by slow evaporation from dichloromethane. The ^{1}H NMR spectrum of ligand pybtdaH exhibits the expected proton environments in the aromatic region. The N-H vibration was observed at 3308 cm^{-1} and the imine C=N stretching vibration was observed at 1627 cm^{-1}, as expected.[15] The molecular structure has previously been confirmed by single crystal X-ray studies (Figure 2.3).[14]

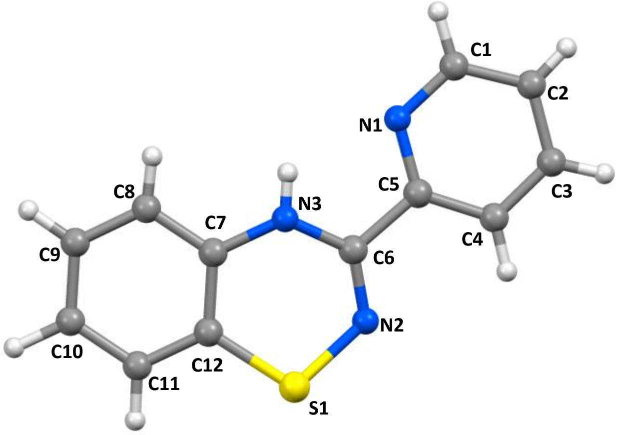

Figure 2.3 Molecular structure of pybtdaH.

The compound crystallizes in the monoclinic space group $P\overline{1}$ with two molecules in the asymmetric unit. The C(6)-N(2) distance is 1.286(2) Å, consistent with predominant double bond character (*cf* imine C=N at 1.279 Å)[16]. The bond length between C(6)-N(3) at 1.375(2) Å is more consistent with a conjugated C-N single bond (*cf* Ph-NH$_2$ at 1.355 Å).[16] The S-N bond length (1.708(1) Å) is comparable with other S-N single bonds (1.62 – 1.74 Å for isomers of $S_{8-x}(NH)_x$)[17] and 1.69 – 1.72 Å for other benzothiadiazine derivatives).[14]

Another feature in the benzothiadiazine ring is the folding (θ) of the molecule about the trans-annular vector S(1)···N(3). The values for the majority of previously reported benzothiadiazines fall in the range 21° < θ < 42° [14] whereas θ is 27.27° in pybtdaH. The folding of the ring is consistent with the formally 8π anti-aromatic nature of the thiadiazine framework.

2.2.1.b Mechanistic studies on the formation of the ligand pybtdaH

The proposed mechanism of the formation of the pybtdaH upon addition of NCS in compound **2.2** by Kaszynski is show in Scheme 2.3. Oxidative cyclization of the amidines (**2.2**) with NCS give the corresponding unstable sulfinimines followed by thermolysis in boiling toluene result in the benzothiadiazine and eliminate propene as by-product.[18]

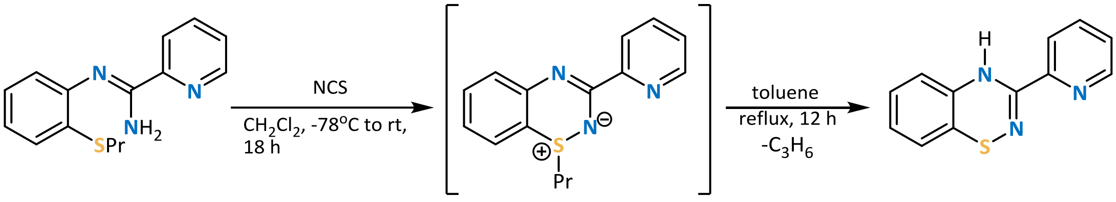

2.2

pybtdaH

Scheme 2.3 Mechanism of oxidative cyclization of pybtdaH proposed by Kaszynski.[18]

During our reactions, unexpected formation of pybtdaH appeared to occur at ambient temperature based on ^{1}H NMR studies and TLC (bright orange spot) with the characteristic ^{1}H NMR peaks of the product appeared in the aromatic region of NMR within 24 h after the reaction of **2.2** with NCS in CH_2Cl_2. Kinetic studies were performed in conjunction with undergraduate Mr. N. Doupnik using ^{1}H NMR to follow the progress of the reaction over the range 20 – 55 °C. Figure 2.4 and Figure 2.5 show the aromatic and aliphatic regions of the ^{1}H NMR spectrum after addition of NCS to amidine **2.2** at 35 °C. It is apparent that after addition of NCS the spectrum changes drastically. The starting material has been converted to the intermediate and all the NCS has been consumed to produce succinimide[19] as observed at 2.69 ppm (Figure 2.5). The intermediate is observed within 28 h along in the aromatic region, e.g. in the region 6.6 – 7.0 ppm. The pseudo-triplet of the intermediate at 6.8 ppm slowly splits into the two doublets, characteristic peaks of the product within three days. The diagnostic peaks of the propyl chain of **2.2** in the aliphatic region have been shifted after 28 h, e.g. the triplet at 2.9 ppm moves downfield to 3.5 ppm. The by-product was readily identified as 1-chloropropane based on the ^{1}H NMR data[20] and the final product was easily purified under high vacuum given the low boiling point of this by-product (46.7 °C). The proposed mechanism of the reaction is shown in Scheme 2.4.

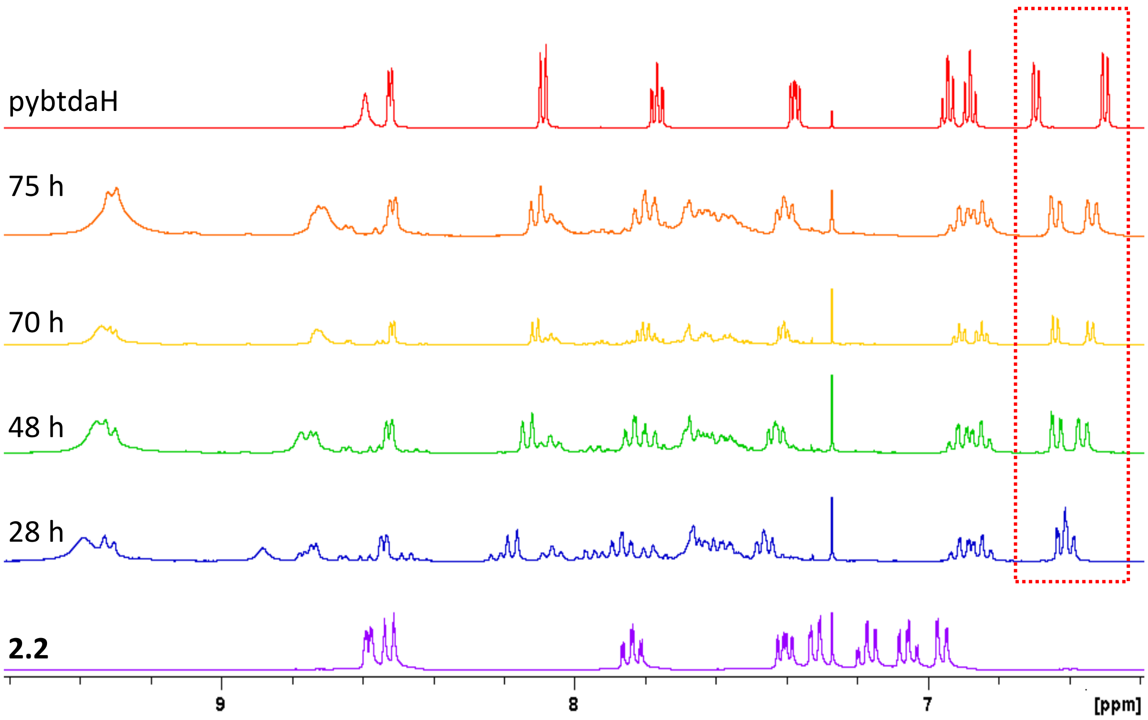

Figure 2.4 ^{1}H NMR screening of the pybtdaH formation upon addition of NCS in **2.2** at 35 °C highlighting the conversion of the pseudo-triplet into two doublets (aromatic region) (500 MHz, $CDCl_3$).

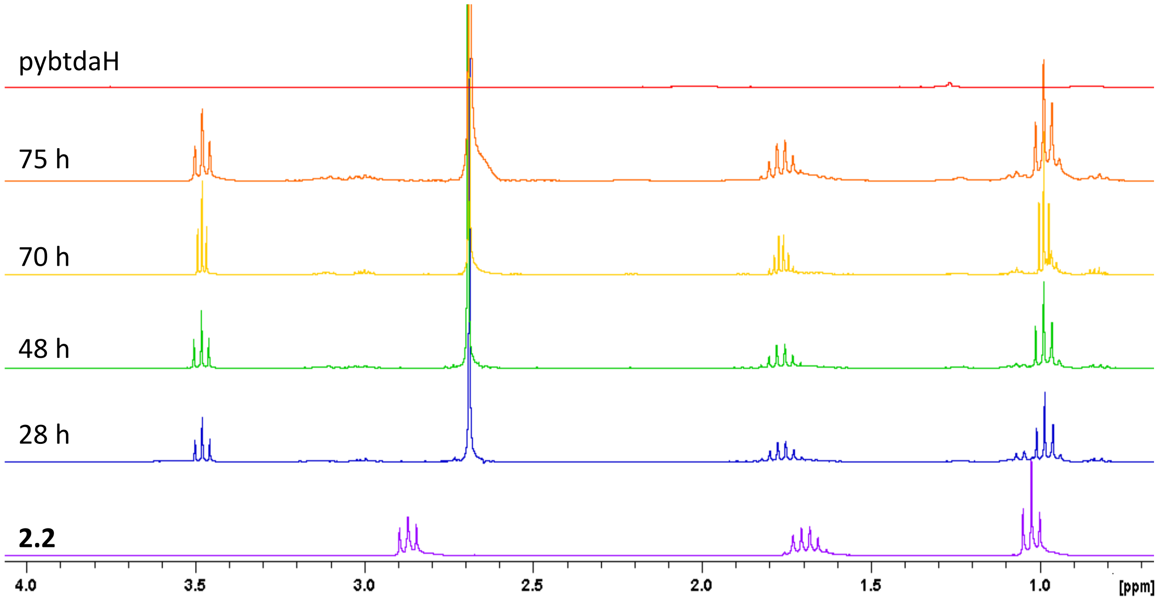

Figure 2.5 ^{1}H NMR screening of the pybtdaH formation upon addition of NCS in **2.2** at 35 °C focusing in the aliphatic region showing the formation of the by-product, 1-chloropropane after 28 hours (500 MHz, $CDCl_3$, (3.48 (Cl-CH_2), 1.77 (Cl-CH$_2$CH_2), 0.99 (CH_3), 2.69 (succinimide) ppm).

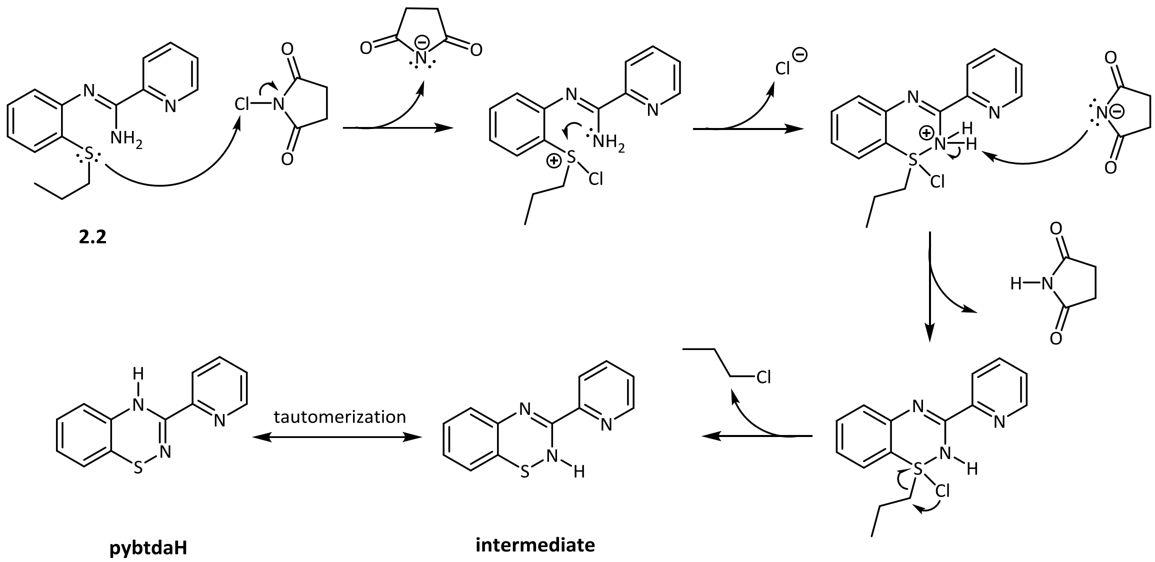

Scheme 2.4 Proposed mechanism of the oxidative cyclization of pybtdaH.

2.2.1.c Computational studies on ligand pybtdaH

Two possible tautomers exist for each orientation of the pyridyl ring of the ligand, depending on whether the N(2) or N(3) atom is protonated, as shown in Table 2.1.

Structural studies located the H atom position at N(3) and this assignment was further supported by shorter imine-like C(6)-N(3) and longer C(6)-N(2) bonds as discussed above. The preference for the crystallographically-determined tautomer (structure 1) was confirmed by DFT calculations (B3LYP-D3/6-311G^{*+}) on structures **1** - **4**. The studies revealed that structure **1** was more stable by 60 kJ/mol, when compared to the least stable structure **4** (Table 2.1). Notably reorientation of the ligand conformation from **1** to **2** in order to adopt an *N*,*N*′-chelate conformation also has a significant energetic cost (44 kJ/mol).

Table 2.1 DFT calculations (B3LYP-D3/6-311G^{*+}) of the tautomers of different orientation of the pyridyl group of pybtdaH.

	1	2	3	4
Structure	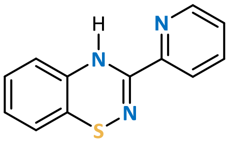	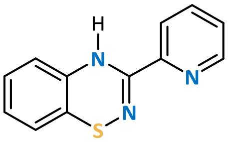	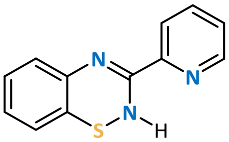	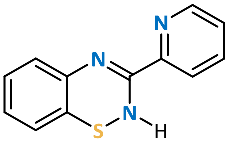
Relative energy (kJ/mol)	0	44	29	60

Geometry optimized B3LYP/6-311G^{*+} DFT studies on pybtdaH were undertaken to probe the energetics of the ring system, varying the rotation angle of the pyridyl ring [torsion N(3)C(6)C(5)N(1)] between 0° and 360° whilst permitting the rest of the molecule to optimize (Figure 2.6).

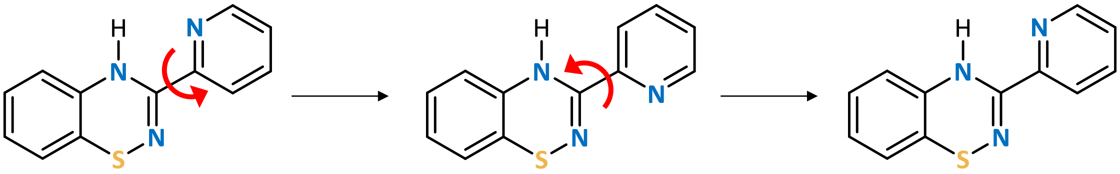

Figure 2.6 Rotation of pyridyl group of pybtdaH for the DFT studies.

These calculations reveal an energy maximum at θ = 180°, as expected due to the repulsion of N(2) of the heterocycle and N(1) of the pyridyl group (Figure 2.7). Two lower energy points are observed at 135° and 225°, which are ±45° from the energy maximum of 180° orientation. This can be attributed to less repulsion of the N atoms in that conformation as the orbitals are not in the same plane.

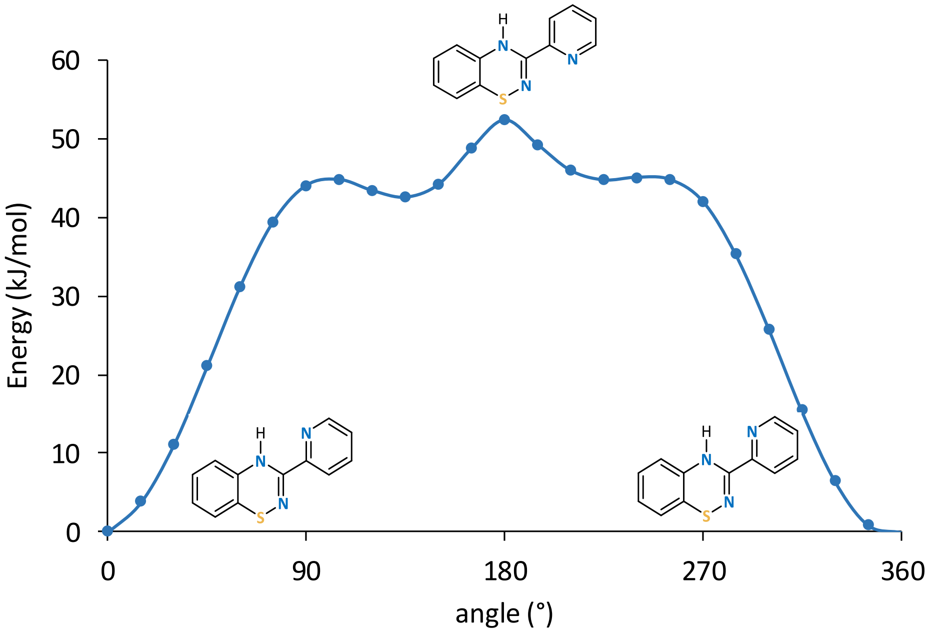

Figure 2.7 DFT calculations (B3LYP/6-311G*⁺) of pybtdaH with the folding angle of pyridyl group varied between 0° and 360°.

2.2.2 Reactivity of pybtdaH with $FeCl_3$

2.2.2.a Synthesis and crystal structure of $[FeCl_3(pybtdaH_{ox})(CH_3OH)]\cdot CH_3OH$ (2.3a)

Reaction of pybtdaH with $FeCl_3\cdot 6H_2O$ in CH_3OH in a 1:1 molar ratio at ambient temperature afforded the complex $FeCl_3(pybtdaH_{ox})(CH_3OH)$ (**2.3a**) in which the pybtaH ligand is oxidized to the *S*-oxide. Crystals suitable for X-ray diffraction were grown by layering with a mixture of diethyl ether/hexanes (1:1) over two weeks. The structure of **2.3a** was determined by X-ray diffraction (Figure 2.8) and crystallizes in the triclinic space group $P\bar{1}$ with two molecules and two methanol solvent molecules in the asymmetric unit. The formation of complex **2.3a** is summarized in Equation 2.1.

$$FeCl_3 + \text{pybtdaH} + CH_3OH + \tfrac{1}{2}O_2 \longrightarrow FeCl_3(\text{pybtdaH}_{ox})(CH_3OH)$$

Equation 2.1

The metal centre is in oxidation state 3+ and adopts a pseudo-octahedral geometry with the three chloride ligands counter-balancing the charge. The Fe-Cl distances are in the range 1.9949(15) – 2.5679(19) Å, as expected for Fe^{III}. The ligand adopts a simple *N*,*N*′-chelate mode to a single metal centre in which the pyridyl N(1) and the heterocyclic N(2) atoms are involved in metal binding. The Fe-N bond distances are in the range 2.157(4) – 2.494(5) Å and the chelate ligand $pybtdaH_{ox}$ exhibits internal N_{py}-Fe-N_{BTDA} angles in the range 62.77(15) – 72.2(2)° and a neutral methanol molecule completes the coordination sphere.

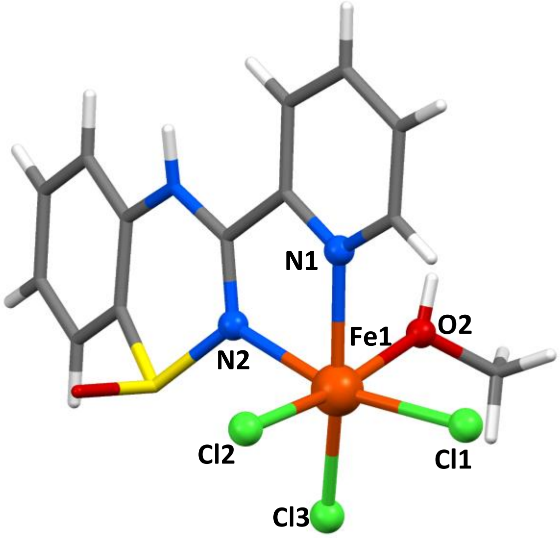

Figure 2.8 Molecular structure of $FeCl_3(pybtdaH_{ox})(CH_3OH)$ (**2.3a**) (solvent molecule omitted for clarity).

Two molecules form a centrosymmetric dimer *via* a pair of N-H···O hydrogen bonding interaction ($d_{N\text{-}H\cdots O}$ = 2.328 Å, $\theta_{N\text{-}H\cdots O}$ = 151.79°) between the N-H group of the benzothiadiazine ring and the oxygen of the sulfoxide (Figure 2.9, green lines). This packing additionally places the benzo and pyridyl rings of neighbouring molecules in close proximity with centroid···centroid distances of 4.148 Å with the closest C···C distance at 3.700 Å (*cf* interlayer separation in graphite at 3.354 Å[21]) (Figure 2.9, red lines). In addition, the molecules are linked *via* O-H···Cl hydrogen bonding from the solvent CH_3OH oxygen atoms and the chlorides on the metal complex ($d_{O\text{-}H\cdots Cl}$ = 2.870 Å, $\theta_{O\text{-}H\cdots Cl}$ = 130.91°).

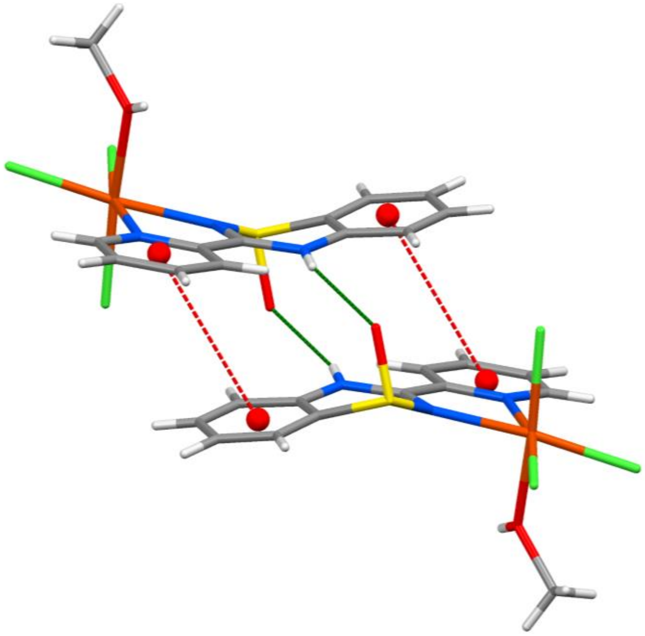

Figure 2.9 Crystal packing of **2.3a** highlighting the centrosymmetric π-π interactions (red) and the N-H···O=S hydrogen bonding (green).

2.2.2.b Synthesis and crystal structure of $Fe_4Cl_4(OCH_3)_6(pybtda_{ox})_2$ (2.3b)

Reaction of pybtdaH with $FeCl_3{\cdot}6H_2O$ in CH_3OH in a 1:1 molar ratio at ambient temperature initially afforded the complex $FeCl_3(pybtdaH_{ox})(CH_3OH)$ (**2.3a**) described above. When the reaction was repeated in more dilute conditions (twice the volume of the solvent) the outcome of the reaction was different. Crystals suitable for X-ray diffraction were grown by layering with a mixture of diethyl ether/hexanes (1:1) over five weeks. The structure was determined by X-ray diffraction to reveal the tetranuclear complex $Fe_4Cl_4(OCH_3)_6(pybtda_{ox})_2$ (**2.3b**) (Figure 2.10) which crystallizes in the triclinic space group $P\overline{1}$ with half a molecule in the asymmetric unit. The formation of complex **2.3b** is summarized in Equation 2.2.

$$4\ FeCl_3 + 2\ \text{pybtdaH} + 6\ CH_3OH + O_2 \longrightarrow Fe_4Cl_4(OCH_3)_6(\text{pybtda}_{ox})_2 + 2\ \text{pybtdaH}_{ox} + 8\ HCl$$

Equation 2.2

Formation of the tetranuclear complex could result from slow condensation of the initially formed mononuclear complex **2.3a** (Equation 2.3). This would be favoured under the more dilute conditions employed which require more time for crystallization:

$$4\ FeCl_3(pybtdaH_{ox})(CH_3OH)\ +\ 2\ CH_3OH \longrightarrow Fe_4Cl_4(OCH_3)_6(pybtda_{ox})_2\ +\ 2\ pybtdaH_{ox}\ +\ 8\ HCl$$

Equation 2.3

Complex **2.3b** consists of four Fe^{III} centres, four terminal Cl ligands, two pybtda$_{ox}^{-}$ and 6 CH_3O^{-} groups, comprising four μ_2-OCH_3 and two μ_3-OCH_3 bridges. The Fe^{III} ions adopt pseudo-octahedral geometry; Fe(1) has a ClO_5 donor set comprising one Cl ligand, one oxygen (S=O), two oxygen atoms from μ_2-OCH_3 and two oxygen atoms from μ_3-OCH_3 whereas Fe(2) has an N_2ClO_3 donor set with one Cl ligand, two nitrogen atoms from pybtda$_{ox}^{-}$, two oxygen atoms from μ_2-OCH_3 and one oxygen atom from μ_3-OCH_3.

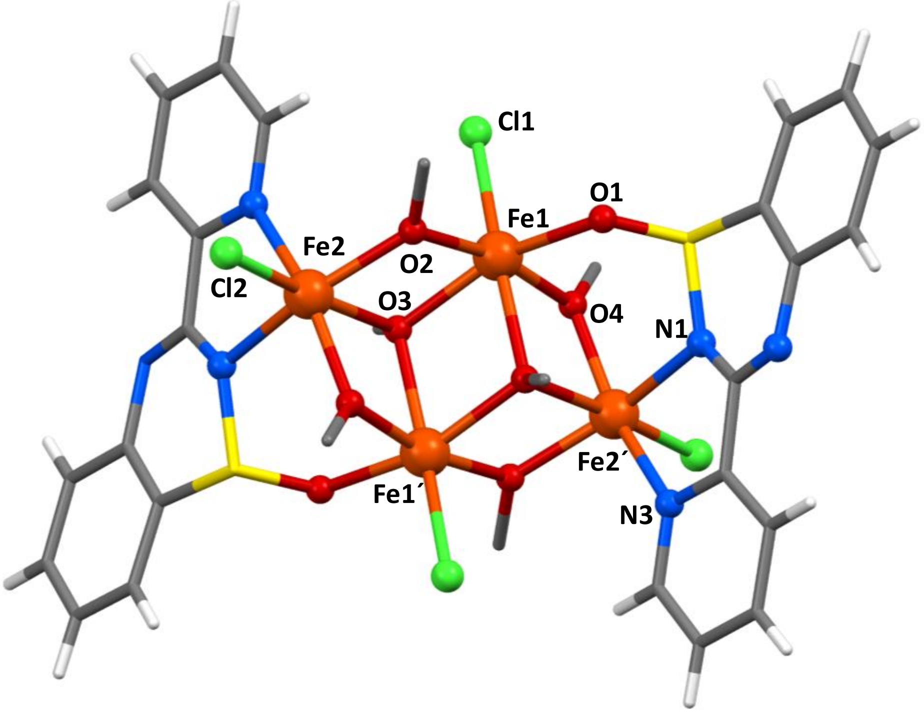

Figure 2.10 Molecular structure of $Fe_4Cl_4(OCH_3)_6(pybtda_{ox})_2$ (**2.3b**) (H on CH_3 groups omitted for clarity).

The Fe(1)-Cl(1) distance is 2.2750(17) Å and the Fe(2)-Cl(2) is 2.2589(14) Å. The oxidised ligand $\text{pybtda}_{\text{ox}}^{-}$ adopts a *N,N′*-chelate mode to Fe(2) in which the pyridyl N(3) and the heterocyclic N(1) atoms are involved in metal binding (Fe-N bond distances are 2.120(4) and 2.137(4) Å and N_{py}-Fe-N_{BTDA} = 75.49(15)°). In addition, the oxygen of the $\text{pybtda}_{\text{ox}}^{-}$ acts as a donor atom to Fe(1) resulting in the ligand adopting a bridging mode. The Fe(1)-O(1) distance is 2.043(3) Å which are intermediate when compared to the range of Fe-O distances in this complex (1.968(3) – 2.166(4) Å).

The packing of **2.3b** places the benzo rings of neighbouring molecules in close proximity having centroid···centroid distances of 3.852 Å with the closest C···C distance at 3.644(7) Å (*cf* interlayer separation in graphite at 3.354 Å).[21]

Insufficient sample of complex **2.3b** was obtained for further characterization within the timeframe of this project. Additional experiments are currently underway to obtain more product.

2.2.3 Reactivity of pybtdaH with $M(OAc)_2$ (M = Co, Cu and Zn)

2.2.3.a Synthesis and crystal structure of $\text{Co(pybtda}_{\text{ox}})_3$ (2.4)

Reaction of pybtdaH with $Co(OAc)_2{\cdot}4H_2O$ in CH_3OH in a 1:1 molar ratio at ambient temperature afforded the mononuclear complex $\text{Co(pybtda}_{\text{ox}})_3$ (**2.4**). Crystals suitable for X-ray diffraction were grown by layering with a mixture of diethyl ether/hexanes (1:1) over two weeks. The structure of **2.4** was determined by X-ray diffraction (Figure 2.11) and crystallizes in the monoclinic space group $P2_1/n$ with one molecule in the asymmetric unit. The formation of complex **2.4** is summarized in Equation 2.4.

$$4\ \text{Co(OAc)}_2 + 12\ \text{pybtdaH} + 7\ \text{O}_2 \longrightarrow 4\ \text{Co(pybtda}_{\text{ox}})_3 + 8\ \text{HOAc} + 2\ \text{H}_2\text{O}$$

Equation 2.4

During the reaction both the metal centre and the ligand have been oxidised. The Co^{III} adopts a pseudo-octahedral geometry with the three $pybtda_{ox}^{-}$ ligands completing the coordination sphere. The oxidised ligand $pybtda_{ox}^{-}$ adopts an *N*,*N'*-chelate mode to Co in which the pyridyl N(1) and the heterocyclic N(2) atoms are involved in metal binding. The oxygen of the $pybtda_{ox}^{-}$ is not participating in the coordination. The Co-N bond distances are in the range 1.9192(19) – 1.964(2) Å. The chelate ligand $pybtda_{ox}^{-}$ exhibits internal N_{py}-M-N_{BTDA} angles in the range 82.26(8) – 83.20(8)°.

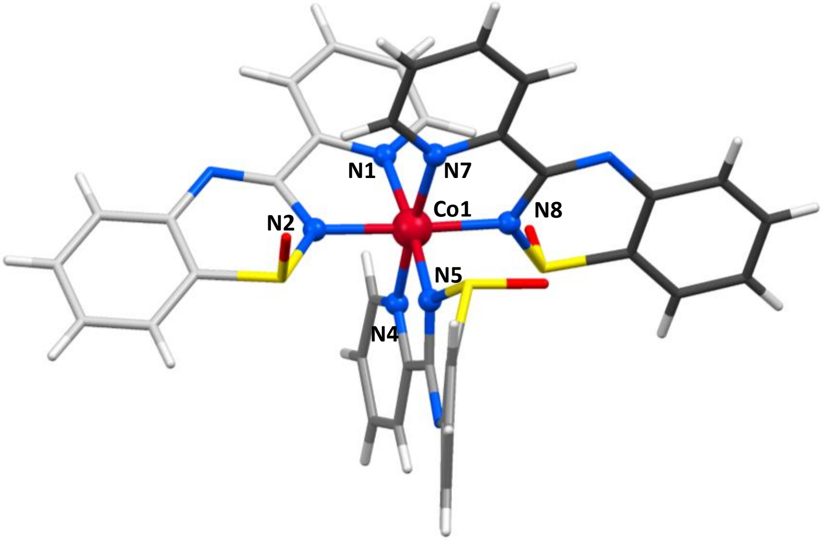

Figure 2.11 Molecular structure of $Co(pybtda_{ox})_3$ (**2.4**) (the three ligands are illustrated with different colors for a better perspective of the structure).

Two of the three oxygen atoms of the sulfoxides make hydrogen bonds with C-H groups with neighbouring complexes as shown in Figure 2.12 (green lines). The C-H···O hydrogen bonds are at 2.503 Å ($\theta_{C\text{-}H\cdots O}$ = 116.66°) and 2.548 Å ($\theta_{C\text{-}H\cdots O}$ = 166.32°). The benzo rings are also in close proximity having centroid···centroid distances of 3.863 Å with the closest C···C distance at 3.606(4) Å (*cf* interlayer separation in graphite at 3.354 Å[21]) (Figure 2.12, red line).

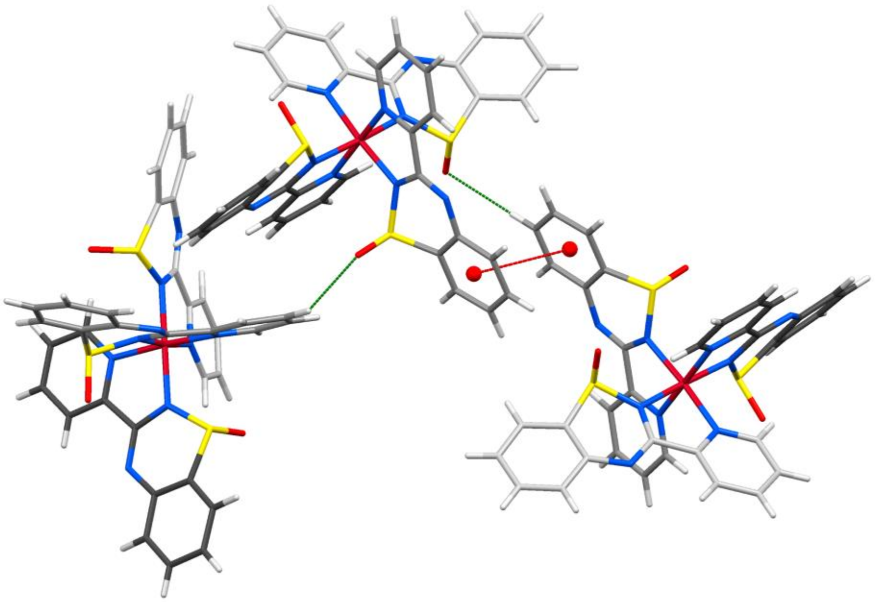

Figure 2.12 Crystal packing of **2.4** highlighting the π-π interactions (red) and the C-H···O hydrogen bonding between the C-H groups and the O atom of the sulfoxide (green).

2.2.3.b Synthesis and crystal structure of $[Cu_2(OAc)_2(pybtda_{ox})_2(H_2O)_2]\cdot 2H_2O$ (2.5)

Reaction of pybtdaH with $[Cu_2(OAc)_4]\cdot 2H_2O$ in CH_3OH in a 1:1 molar ratio at ambient temperature afforded the dinuclear complex $Cu_2(OAc)_2(pybtda_{ox})_2(H_2O)_2$ (**2.5**). Crystals suitable for X-ray diffraction were grown by layering with a mixture of diethyl ether/hexanes (1:1) over two days. The structure crystallizes in the monoclinic space group *C*2/*c* with half a molecule and a water solvent molecule in the asymmetric unit. The formation of complex **2.5** is summarized in Equation 2.5.

$$[Cu_2(OAc)_4]\cdot 2H_2O + 2\ \text{pybtdaH} + O_2 \longrightarrow [Cu_2(OAc)_2(\text{pybtda}_{ox})_2(H_2O)_2] + 2\ \text{AcOH}$$

Equation 2.5

The crystal structure of complex **2.5** is shown in Figure 2.13. The structure is similar to the starting material $[Cu_2(OAc)_4]\cdot 2H_2O$ in which two of the bridging acetate groups of the $Cu_2(OAc)_4$ paddlewheel have been substituted by two chelate $pybtda_{ox}^-$ ligands. The

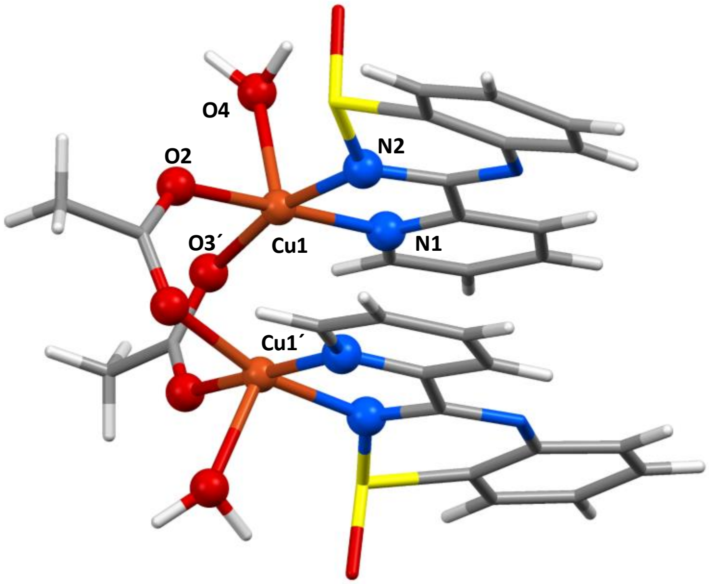

Figure 2.13 Molecular structure of $Cu_2(OAc)_2(pybtda_{ox})_2(H_2O)_2$ (**2.5**) (solvent molecules omitted for clarity).

two Cu^{II} centres within **2.5** are related *via* a 2-fold rotation with each copper ion adopting a 5-coordinate geometry with a N_2O_3 donor set. The Addison τ_5 value[22] (0.17) is consistent with an essentially square pyramidal geometry (trigonal bipyramidal (τ = 1) and square pyramidal (τ = 0)). Approximating the geometry to square pyramidal, the O(4) defines the axial ligand, with the remaining angles in the equatorial plane in the range 81.41(10) – 176.20(10)°. The heterocyclic ligand provides an *N*,*N*′-chelate pocket analogous to complex **2.4** through N(1) and N(2) atoms with Cu-N distances 1.972(3) and 1.982(3) Å, and N_{py}-M-N_{BTDA} angle 81.41(10)°. The acetate groups are bridging the two equivalent Cu ions with Cu-O distances in the range of 1.955(2) – 2.205(3) Å. The coordination sphere is completed by one water molecule.

The structure of **2.5** places the benzo rings in close proximity with the pyridine rings of the neighbouring molecule having centroid···centroid distances of 3.818 Å with the closest C···C distance at 3.454(5) Å (*cf* interlayer separation in graphite at 3.354 Å[21]) (Figure 2.14, top). In addition, the molecules are linked *via* O-H···N hydrogen bonding between the water molecules and the nitrogen atom of the heterocycle ($d_{O\text{-}H\cdots N}$ = 1.975 Å, $\theta_{O\text{-}H\cdots N}$ = 166.64°, Figure 2.14, top). Π - π interactions between adjacent dimers have centroid···centroid distances of 3.958 Å with the closest C···C distance at 3.415(6) Å, forming an one-dimensional chain along *c* axis shown in Figure 2.14 (bottom).

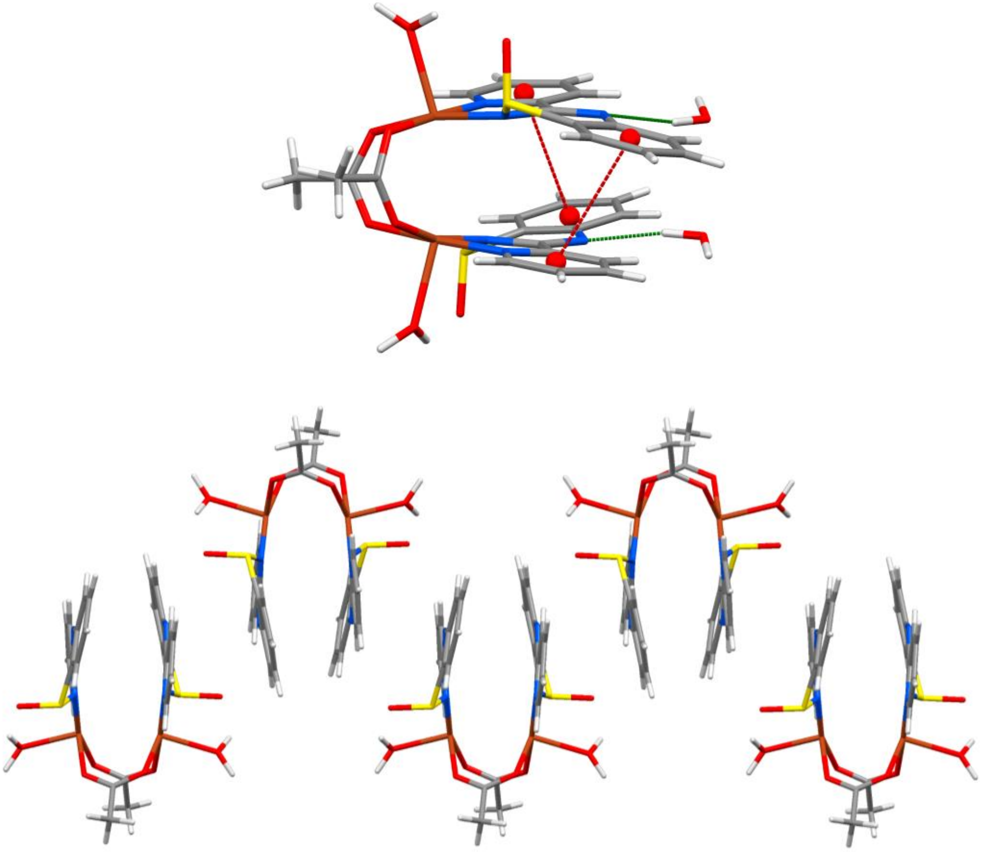

Figure 2.14 (top) Crystal packing of **2.5** highlighting the π-π interactions (red) and the O-H···N hydrogen bonding between the water molecule and the N atom of the ligand (green); (bottom) One dimensional chain of dinuclear complexes along *c* axis.

The packing of the dinuclear complex creates a three dimensional network through the π-π interactions and hydrogen bonding shown in Figure 2.15.

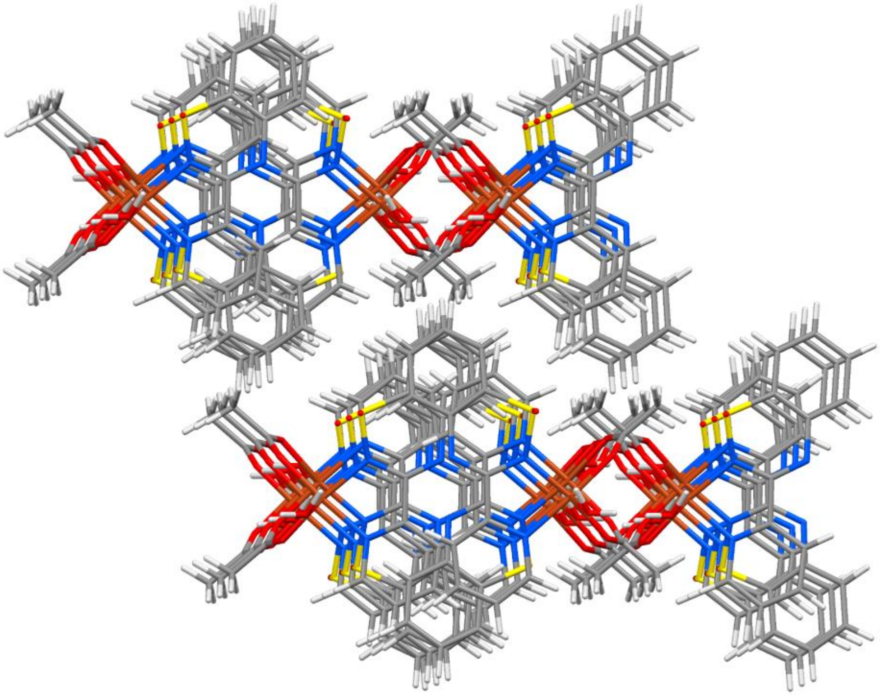

Figure 2.15 Crystal packing of **2.5** revealing the three dimensional nature of the supramolecular arrangement of molecules generated through hydrogen bonds and π-π interactions.

2.2.3.c Synthesis and crystal structure of $Zn_2(OAc)_2(pybtda_{ox})_2$ (2.6)

Reaction of pybtdaH with $[Zn(OAc)_2]\cdot 2H_2O$ in CH_3OH in a 1:1 molar ratio at ambient temperature afforded the dinuclear complex $Zn_2(OAc)_2(pybtda_{ox})_2$ (**2.6**). Crystals suitable for X-ray diffraction were grown by layering with a mixture of diethyl ether/hexanes (1:1) over two days. The structure crystallizes in the triclinic space group $P\overline{1}$ with two half molecules in the asymmetric unit. The formation of complex **2.6** is summarized in Equation 2.6.

$$2[Zn(OAc)_2]\cdot 2H_2O + 2\text{pybtdaH} + O_2 \longrightarrow Zn_2(OAc)_2(\text{pybtda}_{ox})_2 + 2\text{AcOH}$$

Equation 2.6

While the formula of **2.6** ($Zn_2(OAc)_2(pybtda_{ox})_2$) is comparable with the copper complex **2.5** ($(Cu_2(OAc)_2(pybtda_{ox})_2(H_2O)_2)$), their coordination geometries are very different. The crystal structure of complex **2.6** is shown in Figure 2.16. The two Zn^{II} centres within **2.6** adopt a 5-coordinate geometry with a N_2O_3 donor set. The Addison τ_5 values[22] (0.22 for Zn(1) and 0.25 for Zn(2)) are consistent with a distorted square pyramidal geometry ($\tau = 1$ for trigonal bipyramidal and $\tau = 0$ square pyramidal). Approximating the geometry to square pyramidal, the O(1) (for Zn(1)) and O(4) (for Zn(2)) define the axial ligands, with the remaining angles in the equatorial plane in the range 57.38(6) – 144.38(6)° for Zn(1) and 61.35(6) – 152.07(6)° for Zn(2). As with complex **2.5**, the heterocyclic ligand provides an *N*,*N*′-chelate pocket through N(1) and N(2) atoms with Cu-N distances in the range 2.035(3) – 2.054(3) Å and N_{py}-M-N_{BTDA} angles of 80.410(12)° and 81.34(12)°. However in **2.6** the *N*,*N*′-chelate comprises the pyridyl-N and the nitrogen at the 4-position of the $pybtda_{ox}^-$ heterocyclic ring rather than the N atom at the 2-position,

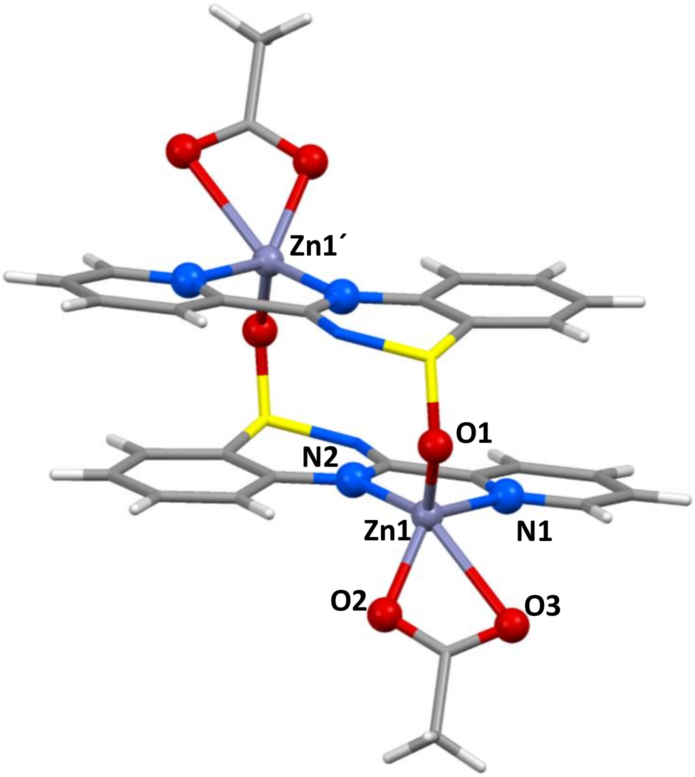

Figure 2.16 Molecular structure of one complete molecule in the asymmetric unit $Zn_2(OAc)_2(pybtda_{ox})_2$ (**2.6**).

common to benzothiadiazines, pybtdaH. Notably, coordination through this N atom has also been seen in another benzothiadiazine *S*-oxide complex,[2] suggesting a possible reversal of *N*-donor ability upon *S*-oxidation and deprotonation. The coordination sphere of each Zn centre is completed by a chelating rather than bridging acetate group with Zn-O distances in the range of 1.982(3) – 2.507(3) Å.

The structure of **2.6** places the benzothiadiazine ligands within the dimers in close proximity resulting in centroid···centroid distances of 3.636 Å (closest C···C distance at 3.468 Å) and 3.643 Å (closest C···C distance at 3.476 Å) for Zn(1) and Zn(2), respectively (*cf* interlayer separation in graphite at 3.354 Å[21]) (Figure 2.17, left, red lines). One-dimensional chains are also formed along *a* axis with π-π interactions between adjacent dimers having centroid···centroid distances of 3.798 Å for Zn(2) dimers (Figure 2.17, left, green lines). The centroid···centroid distances for Zn(1) are at 4.467 Å (Figure 2.17, left, blue lines), much longer than anticipated for π-π interactions and a better visualization of the parallel displacement of the ligand is shown in Figure 2.17 (right).

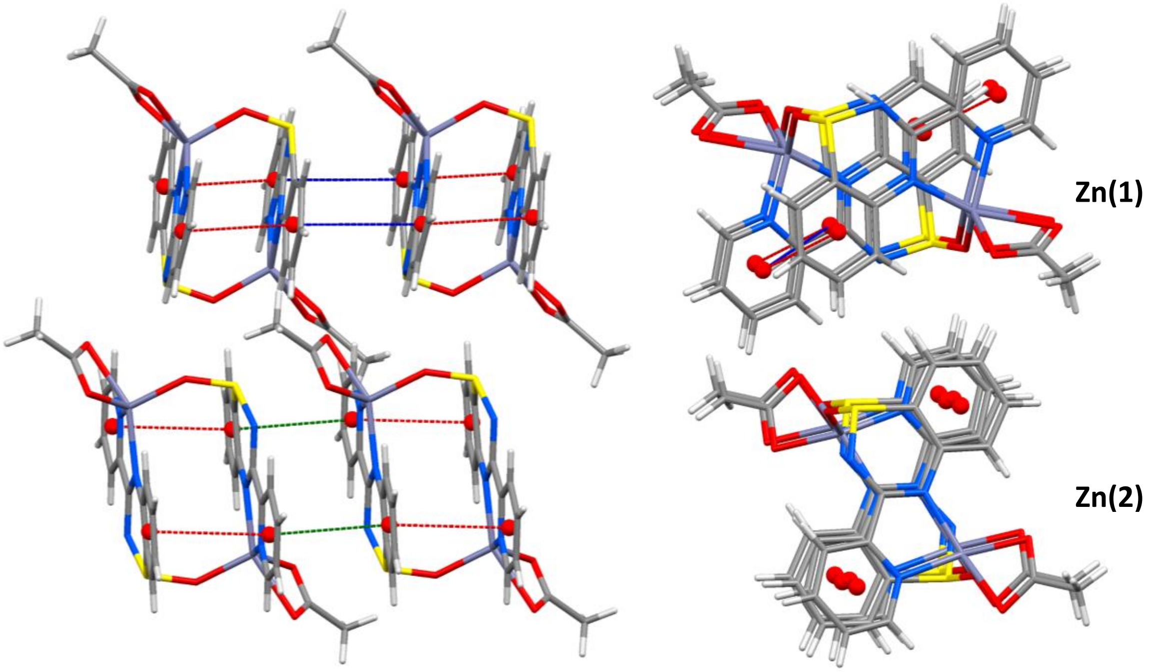

Figure 2.17 (left) Crystal packing of **2.6** highlighting the intramolecular π-π interactions (red) on Zn dimers, and the intermolecular interactions between Zn(1) (blue) and Zn(2) (green) dimers along *a* axis; (right) top-view of the π-π interactions down the crystallographic *a* axis.

2.2.4 Reactivity of pybtdaH with M(hfac)$_2$ (M = Mn, Co, Ni, Cu, Zn)

2.2.4.a Syntheses and crystal structures of M(hfac)$_2$(pybtdaH$_{ox}$) (M = Mn (2.7), Co (2.8), Zn (2.9))

The reaction of [M(hfac)$_2$]·xH$_2$O, (M = Mn, Co, Ni) with the ligand pybtdaH in CH_2Cl_2 or $CHCl_3$ in a 1:1 molar ratio at ambient temperature afforded the complexes M(hfac)$_2$(pybtdaH$_{ox}$) (M = Mn, (**2.7**), Co (**2.8**), Ni (**2.9**)). Red-brown crystals suitable for X-ray diffraction were grown by slow evaporation over a period of one day to five weeks. The formation of complexes **2.7** − **2.9** is summarized in Equation 2.7.

$$\mathrm{M(hfac)_2} + \mathrm{pybtdaH} + \tfrac{1}{2}\,\mathrm{O_2} \longrightarrow \mathrm{M(hfac)_2(pybtdaH_{ox})} \qquad \text{Equation 2.7}$$

Complexes **2.7** and **2.8** crystallize in the triclinic space group $P\overline{1}$ with one molecule in the asymmetric unit whereas complex **2.9** crystallizes in the triclinic space group $P\overline{1}$ with two molecules in the asymmetric unit. All three complexes adopt similar structures and the structure of complex **2.8** is shown in Figure 2.18 (left), as representative of complexes **2.7** − **2.9** and selected bond lengths and angles are shown in Table 2.2. The metal centres have a distorted octahedral geometry with an N_2O_4 donor set. The heterocyclic ligand provides an *N*,*N*′-chelate pocket analogous to complex **2.3a** through N(1) and N(2) atoms with M-N distances in the range 2.102(6) – 2.292(5) Å and N_{py}-M-N_{BTDA} angles in the range 71.78(17) – 77.3(3)°. The two hfac$^-$ groups also chelate the metal centre leading to an octahedral complex with M-O distances in the range of 2.043(5) – 2.153(4) Å. The molecules are linked *via* a N-H···O hydrogen bonding interaction ($d_{N\text{-}H\cdots O}$ = 1.969 – 2.007 Å, $\theta_{N\text{-}H\cdots O}$ = 150.00 – 156.32°) from the heterocyclic N-H to oxygen of the S=O at the neighbouring pybtdaH$_{ox}$. Additional π-π stacking forms a centrosymmetric supramolecular dimer (centroid···centroid distance = 3.816 – 3.914 Å) (Figure 2.18, right).

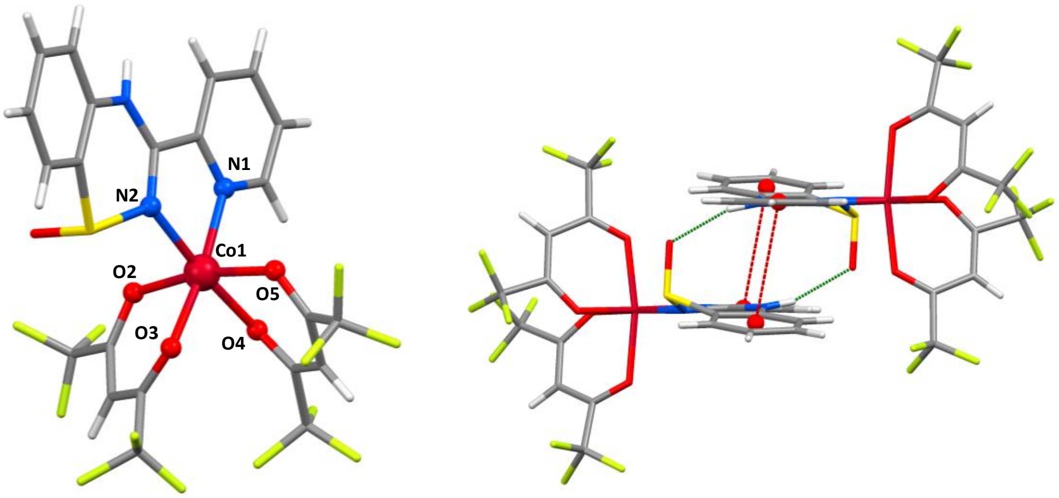

Figure 2.18 (left) Molecular structure of Co(hfac)$_2$(pybtdaH$_{ox}$) (**2.8**); (right) Crystal packing of **2.8** highlighting the π-π interactions (red) and the N-H···O hydrogen bonding between the amino group and the O atoms of the neighbouring sulfoxide (green).

Table 2.2 Selected bond lengths and angles for complexes **2.7** – **2.9**.

	M-N$_{py}$/Å	M-N$_{BTDA}$/Å	M-O/Å	N$_{py}$-M-N$_{BTDA}$/°
Mn (**2.7**)	2.242(5)	2.292(5)	2.131(4)	71.78(17)
			2.145(5)	
			2.150(4)	
			2.153(4)	
Co (**2.8**)	2.102(6)	2.102(6)	2.043(5)	77.2(2)
			2.046(4)	
			2.057(5)	
			2.067(5)	
Zn (**2.9**)	2.120(8)	2.125(8)	2.071 (6)	77.3(3)
	2.131(8)	2.130(7)	2.079(6)	77.3(3)
			2.079(7)	
			2.085(6)	
			2.089(6)	
			2.092(7)	
			2.104(6)	
			2.108(6)	
	N-H···O/Å	N-H···O/°	C···C/Å[a]	centroid-centroid/Å
Mn (**2.7**)	2.000	156.32	3.617	3.914
Co (**2.8**)	1.969	150.96	3.654	3.816
Zn (**2.9**)	2.005	150.00	3.592	3.904
	2.007	150.18	3.609	3.914

[a] Closest C···C distance

Crystals of complex **2.8** were persistently twinned and revealed a high R_{int} value (14.5%) and attempts to improve the refined structure have so far been unsuccessful. Nevertheless, the connectivity of the atoms can be clearly identified. Insufficient samples of complexes **2.8** and **2.9** were obtained for further characterization within the timeframe of this project and additional experiments are currently underway to obtain more product.

2.2.4.b Synthesis and crystal structure of Ni(hfac)$_2$(pybtdaH) (2.10)

The metal salt [Ni(hfac)$_2$]·xH$_2$O was reacted with the ligand pybtdaH in CH_2Cl_2 in a 1:1 molar ratio at ambient temperature and the solution was layered with hexanes. Unlike the Mn, Fe, Co complexes described in section 2.2.4.a, red single crystals of the complex with formula Ni(hfac)$_2$(pybtdaH) (**2.10**), suitable for X-ray diffraction were isolated within 24 h. Complex **2.10** crystallizes in the triclinic space group $P\overline{1}$ with one molecule in the asymmetric unit. The formation of complex **2.10** is summarized in Equation 2.8.

$$\mathrm{Ni(hfac)_2 + pybtdaH \longrightarrow Ni(hfac)_2(pybtdaH)} \qquad \text{Equation 2.8}$$

The Ni^{II} ion has a distorted octahedral geometry with an N_2O_4 donor set. The heterocyclic ligand provides an *N*,*N′*-chelate pocket analogous to complex **2.3a** through N(1) and N(2) atoms (Figure 2.19) with M-N distances 2.044(2) − 2.049(2) Å and N_{py}-M-N_{BTDA} angle at 78.39(9)°. The two hfac$^-$ groups also chelate the metal centre leading to an octahedral complex with M-O distances in the range of 2.016(2) − 2.074(2) Å. The molecules on complex **2.10** are linked *via* an N-H···O hydrogen bonding interaction ($d_{N\text{-}H\cdots O}$ = 2.382 Å, $\theta_{N\text{-}H\cdots O}$ = 145.33°) from the heterocyclic N-H to one of the hfac$^-$ O atoms. Additional π-π stacking forms a centrosymmetric supramolecular dimer (centroid···centroid distance = 3.870 Å) (*cf* interlayer separation in graphite at 3.354 Å[21]) (Figure 2.19, right).

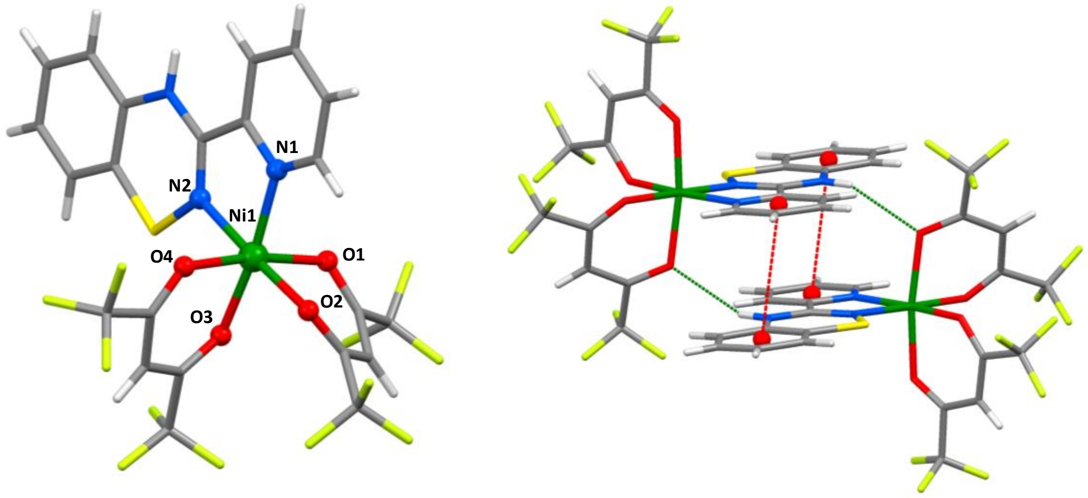

Figure 2.19 (left) Molecular structure of $Ni(hfac)_2(pybtdaH)$ (**2.10**); (right) Crystal packing of **2.10** highlighting the π-π interactions (red) and the N-H···O hydrogen bonding between the amino group and the O atoms of the neighbouring $hfac^-$ group (green).

2.2.4.c Synthesis and crystal structure of $Ni_3(hfac)(pybtda_{ox})_5(H_2O)$ (2.11)

The metal salt $[Ni(hfac)_2]\cdot xH_2O$ was reacted with the ligand pybtdaH in CH_2Cl_2 in a 1:1 molar ratio in the presence of 4 equivalents of Et_3N at ambient temperature and the solution was layered with hexanes. Red single crystals of $Ni(hfac)_2(pybtdaH)$ (**2.10**) formed within two days (see above) but green crystals formed after a more prolonged period. Single X-ray diffraction revealed these to be the trimetallic complex $Ni_3(hfac)(pybtda_{ox})_5(H_2O)$ (**2.11**). Complex **2.11** crystallizes in the monoclinic space group *P*2₁*/c* with one molecule in the asymmetric unit. The formation of complex **2.11** is summarized in Equation 2.9.

$$3\ Ni(hfac)_2 + 5\ pybtdaH + H_2O + \frac{5}{2}O_2 \longrightarrow Ni_3(hfac)(pybtda_{ox})_5(H_2O) + 5\ hfacH$$

Equation 2.9

The structure of complex **2.11** is shown in Figure 2.20. The Ni^{II} ions all have distorted octahedral geometries but each metal center has a different donor set. The Ni(1) ion has an N_2O_4 donor set; two nitrogen atoms from $pybtda_{ox}^-$, two oxygen atoms from an $hfac^-$

ligand, one oxygen atom from the S=O and one terminal water molecule. The Ni(2) ion has also N_2O_4 donor set; two nitrogen atoms from pybtda$_{ox}^-$ and four oxygen atoms from S=O. The coordination sphere of Ni(3) is completed by six nitrogen atoms from three pybtda$_{ox}^-$ ligands.

The heterocyclic ligand takes up a bridging mode between two metal centres, analogous to complex **2.3b**. The *N*,*N′*-chelate pocket, through the pyridyl nitrogen atom and the heterocyclic nitrogen atom next to S, chelates one metal ion and the *S*-oxide bridges to the second metal centre. The M-N distances are in the range of 1.989(15) − 2.118(4) Å and N_{py}-M-N_{BTDA} angles are in the range of 78.02(15) − 81.3(9)°. The M-O distances of the S=O groups are in the range of 2.051(3) – 2.093(3) Å. The hfac$^-$ group chelates to Ni(1) with M-O distances at 2.033(3) Å and 2.042(3) Å.

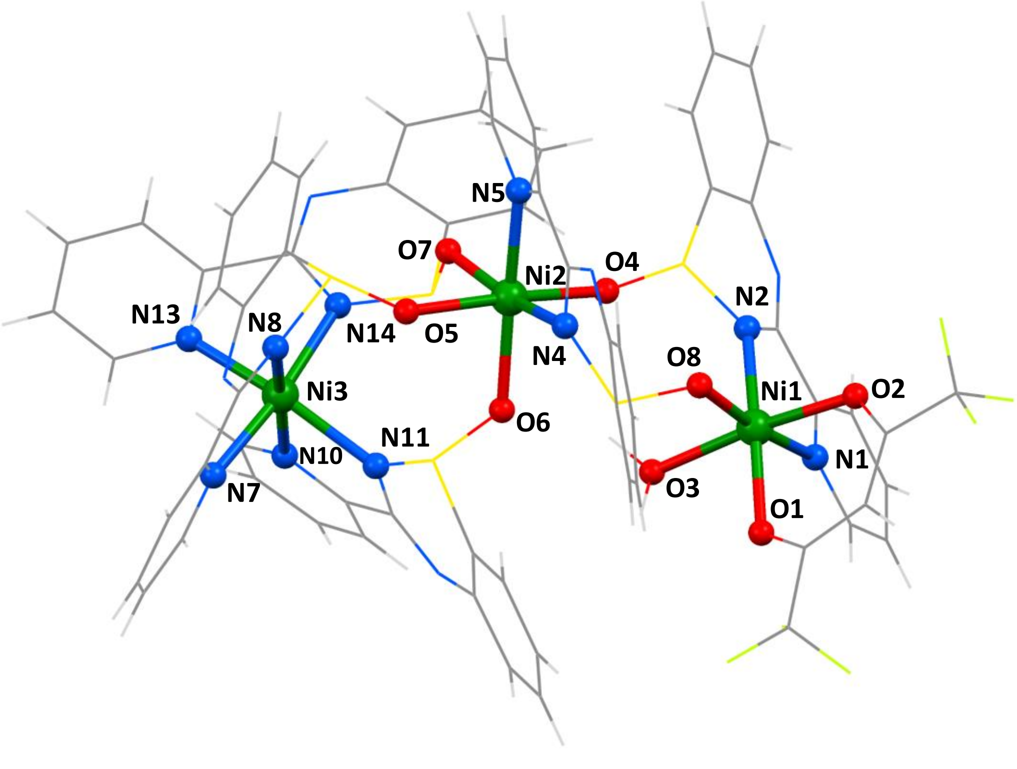

Figure 2.20 Molecular structure of $Ni_3(hfac)(pybtda_{ox})_5(H_2O)$ (**2.11**).

Complex **2.11** crystallized alongside the mononuclear complex $Ni(hfac)_2(pybtdaH)$ (**2.10**), thus making the characterization of complex **2.11** not possible. Attempts to reproduce complex **2.11** and isolate it selectively were unsuccessful.

2.2.4.d Synthesis and crystal structure of [Cu(hfac)(pybtda$_{ox}$)]$_n$ (2.12)

The reaction of [Cu(hfac)$_2$]·xH$_2$O with the ligand pybtdaH in CH$_3$OH in a 1:1 molar ratio at ambient temperature afforded the polymeric complex of [Cu(hfac)(pybtda$_{ox}$)]$_n$ (**2.12**) as green crystals over a week. Complex **2.12** crystallizes in the monoclinic space group $P2_1$ with two crystallographically independent Cu centres in the asymmetric unit. The formation of complex **2.12** is summarized in Equation 2.10.

$$n\ \mathrm{Cu(hfac)_2} + n\ \mathrm{pybtdaH} + \frac{n}{2}\mathrm{O_2} \longrightarrow [\mathrm{Cu(hfac)(pybtda_{ox})}]_n + n\ \mathrm{hfacH}$$

Equation 2.10

The asymmetric unit of complex **2.12** is shown in Figure 2.21 (top) and the one-dimensional polymer along *b* axis (bottom). The two crystallographically inequivalent metal centres are 5-coordinate with a N$_2$O$_3$ donor set. The Addison τ_5 value[22] for Cu(1) is 0.53 and suggests an intermediate geometry between trigonal bipyramidal and square pyramidal geometry (τ = 1 for trigonal bipyramidal and τ = 0 square pyramidal). Approximating the geometry to trigonal bipyramidal, the O(4)-Cu(1)-N(2) defines the axial orientation at 172.0(2)°, with the remaining angles in the equatorial plane in the range 82.75(17) − 140.29(18)°. The Addison τ_5 value[22] for Cu(2) is 0.26 suggesting a distorted square pyramidal geometry with O(1′) defining the axial ligand and the remaining angles in the equatorial plane in the range 81.7(2) − 172.9(2)°.

The heterocyclic ligand takes up a bridging mode between two Cu^{II} centres, analogous to complex **2.3b**. The *N*,*N′*-chelate pocket, through the pyridyl nitrogen atoms (N(1) and N(4)) and the heterocyclic nitrogen atoms next to S (N(2) and N(5)), chelates one Cu ion and the *S*-oxide (O(1) and O(2)) bridges to the second metal centre. The M-N distances are in the range of 1.940(5) − 2.012(5) Å and the N$_{py}$-M-N$_{BTDA}$ angles are at 82.0(2) and 82.0(2)°. The M-O(S=O) bonds are at 2.134(4) Å and 2.184(4) Å. The hfac$^-$ groups also chelate the metal centre with M-O distances in the range of 1.922(4) − 2.096(4) Å.

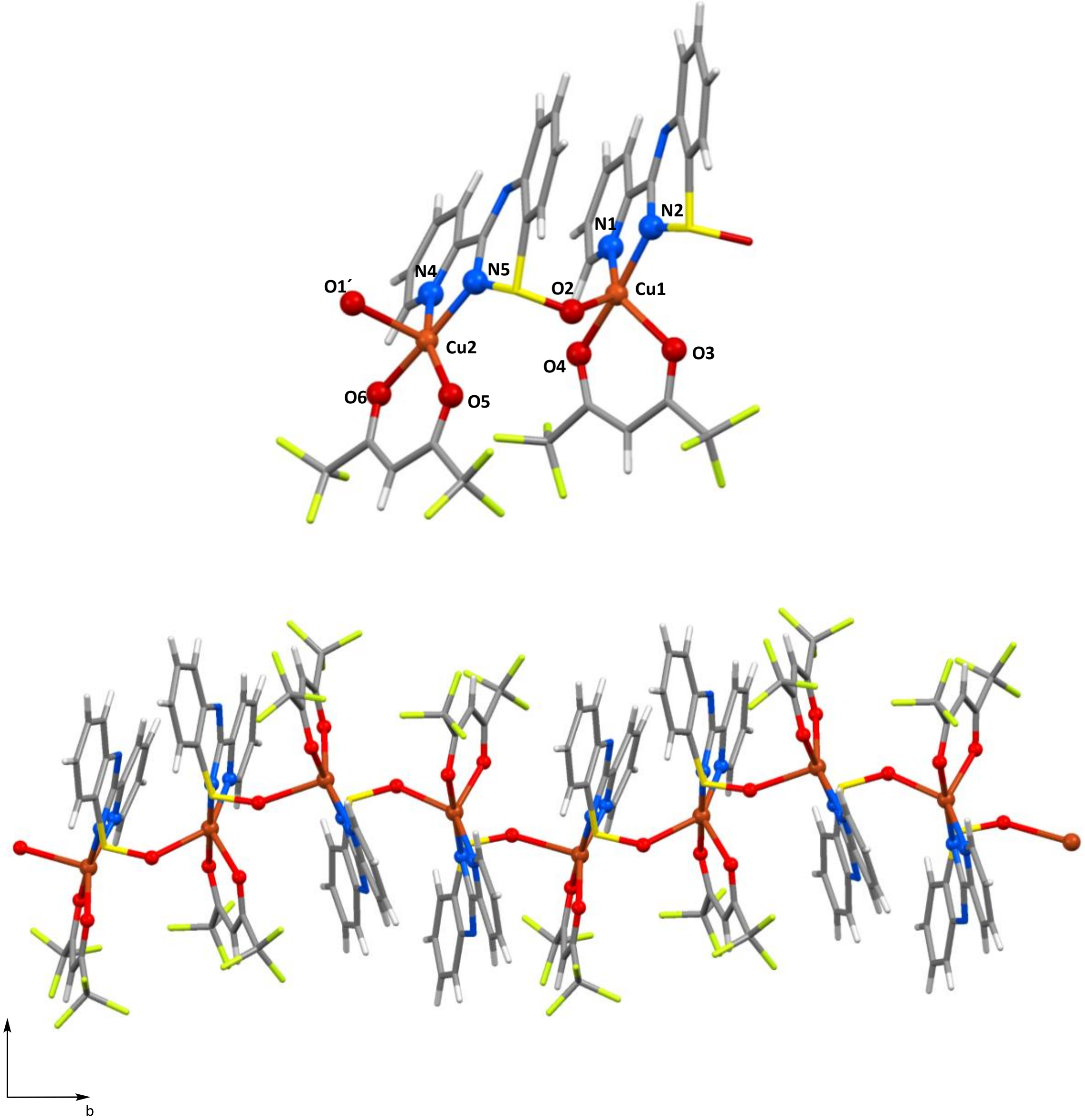

Figure 2.21 (top) Asymmetric unit of polymer [Cu(hfac)(pybtda$_{ox}$)]$_n$ (**2.12**); (bottom) One dimensional polymer of complex **2.12** along *b* axis.

2.2.4.e Synthesis and crystal structure of [Cu$_4$(OH)$_4$(pybtda$_{ox}$)$_4$]·H$_2$O (2.13)

The reaction of [Cu(hfac)$_2$]·xH$_2$O with pybtdaH in 1:1 molar ratio afforded the polymer [Cu(hfac)(pybtda$_{ox}$)]$_n$ (**2.12**), as discussed in section 2.2.4.d. The addition of 4 equivalents of Et$_3$N to this reaction scheme led to a different product revealing a tetranuclear complex with formula $Cu_4(OH)_4(pybtda_{ox})_4$ (**2.13**). The structure of complex **2.13** is shown in Figure 2.22.

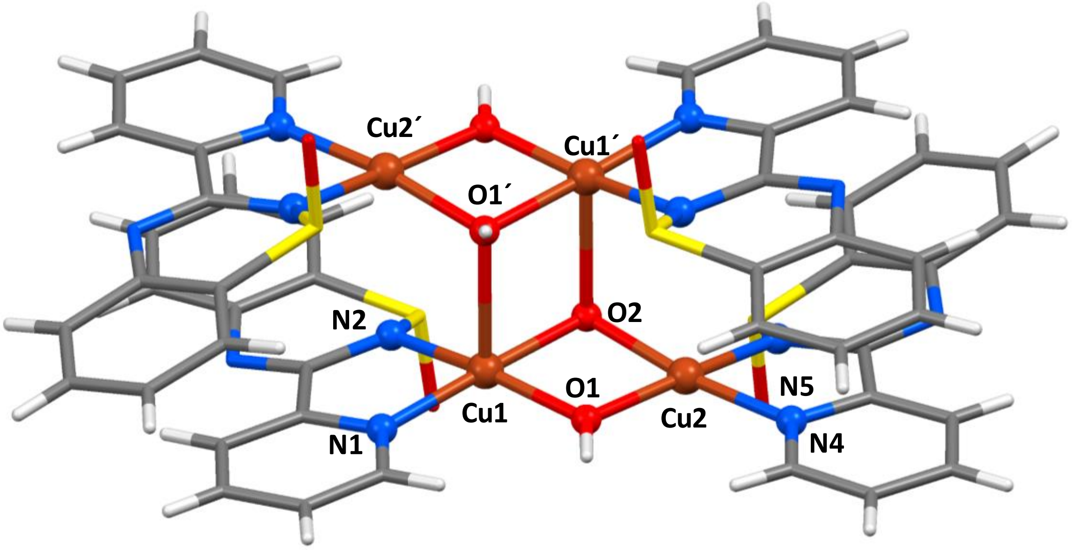

Figure 2.22 Molecular structure of $Cu_4(OH)_4(pybtda_{ox})_4$ (**2.13**) (solvent molecule omitted for clarity).

Complex **2.13** crystallizes in the triclinic space group $P\overline{1}$ with half a molecule in the asymmetric unit. In complex **2.13** the ligand has been deprotonated and oxidized at S to form an *S*-oxide and adopts a simple *N*,*N*′-chelate pocket for metal binding through N(1),N(2) and N(4),N(5). The S-O bonds at 1.494(7) and 1.504(6) Å, are comparable with other literature reported sulfoxide bonds (1.500(4) Å[23]). The two crystallographically independent metal centres are in oxidation state 2+ and Cu(1) adopts 5-coordinate geometries with and N_2O_3 donor set whereas Cu(2) adopts 4-coordinate geometry with a N_2O_2 donor set. The Addison τ_5 value[22] for Cu(1) of 0.16 is consistent with a square pyramidal geometry ($\tau = 1$ for trigonal bipyramidal and 0 for square pyramidal) with Cu(1)-O(2′) defining the axial ligand with the remaining angles in the equatorial plane in the range 78.34(18) − 177.1(2)°. The geometry index for Cu(2) is $\tau_4 = 0.11$ consistent with a square planar geometry ($\tau = 1$ for tetrahedral geometry and $\tau = 0$ for square planar geometry).[24] The two largest angles in the plane are 171.2(2)° and 172.7(2)°. The crystal structure has also four hydroxo groups completing the coordination sphere of the metal centres. Two hydroxo groups are bridging two Cu ions whereas two are bridging three metals with Cu-O bonds in the range 1.905(5) − 2.396(5) Å. The $[Cu_4(\mu_2\text{-}OH)_2(\mu_3\text{-}OH)_2]^{4+}$ core of the complex can be described as ladder type as shown in Figure 2.23.

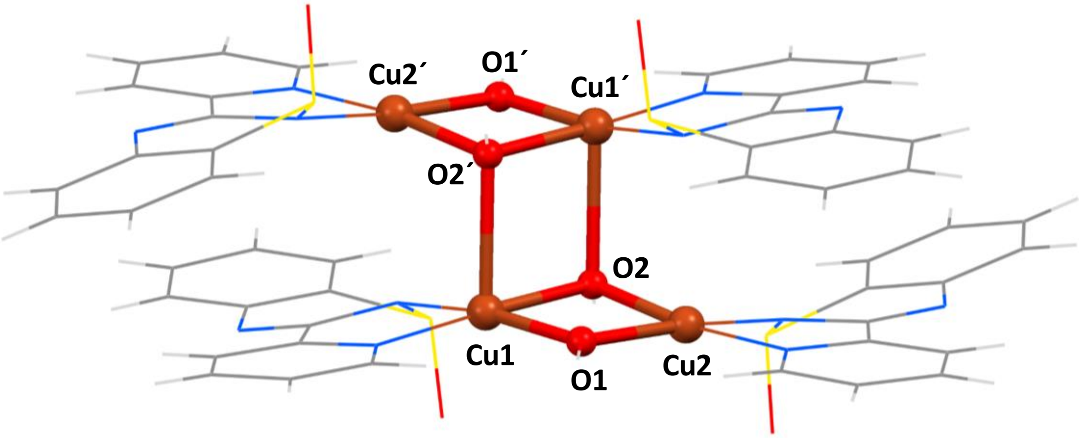

Figure 2.23 The $[Cu_4(\mu_2\text{-}OH)_2(\mu_3\text{-}OH)_2]^{4+}$ core of complex **2.13** illustrating the ladder-type conformation.

The ligand provides a simple *N*,*N*′-chelate pocket through the pyridyl and heterocyclic nitrogen atoms. The chelate ligand $pybtda_{ox}^{-}$ exhibits N_{py}-Cu-N_{BTDA} angles of 82.3(2)° and 82.4(3)° and Cu-N bond lengths are in the range 1.951(6) − 1.982(6) Å. The formation of complex **2.13** is summarized in Equation 2.11.

$$4Cu(hfac)_2 + 4pybtdaH + 4H_2O + 2O_2 \longrightarrow Cu_4(OH)_4(pybtda_{ox})_4 + 8\ hfacH$$

Equation 2.11

The structure of **2.13** exhibits intramolecular π-π interaction with centroid···centroid distances 3.591 Å and 3.932 Å (*cf* interlayer separation in graphite at 3.354 Å[21]). The structure exhibits intermolecular π-π stacking on six of the eight aromatic rings of the ligands with centroid···centroid distances 3.570 Å and 4.113 Å. The π-π interactions are shown in Figure 2.24 as red lines between the red centroids. One of the aromatic rings does not participate in π-π stacking but instead has a short interaction with a Cu ion with centroid-Cu distance of 3.466 Å. The rings not exhibiting π-π interactions are shown with a yellow centroid in Figure 2.24.

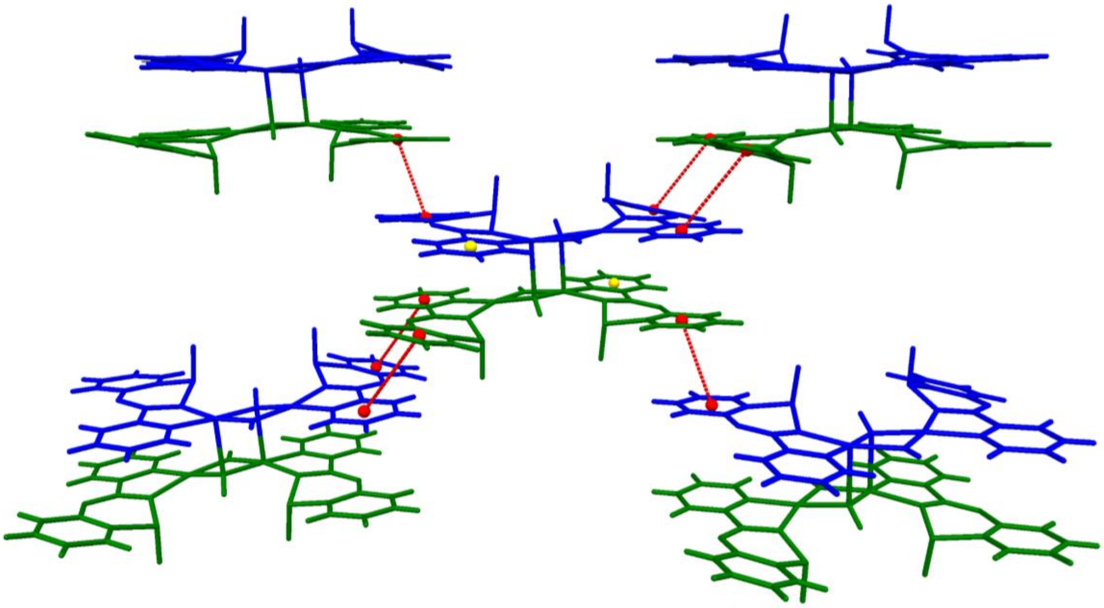

Figure 2.24 Crystal packing of **2.13** highlighting the π-π interactions (red) between neighbouring molecules and the centroids shown in yellow are not participating in π-π interactions.

2.2.4.f Synthesis and crystal structure of [$Cu_{14}(OH)_{12}(CO_3)_2(pybtda_{ox})_{12}(H_2O)_2$]·14[$H_2O$]·[$CH_3OH$] (2.14)

Attempts to reproduce complex **2.13** using the correct stoichiometric ratio (Equation 2.11) led to the reaction of pybtdaH with $Cu(hfac)_2 \cdot xH_2O$ and H_2O in CH_3OH in a 1:1:1 molar ratio under basic conditions. The solution was left for slow evaporation and green needles suitable for X-ray diffraction formed after three days. The crystal structure revealed the complex to unexpectedly be $Cu_{14}(OH)_{12}(CO_3)_2(pybtda_{ox})_{12}(H_2O)_2$ (**2.14**) shown in Figure 2.25. Complex **2.14** crystallizes in the monoclinic space group *P*2$_1$/*n* with one [Cu^{II}_{14}] molecule in the asymmetric unit, one methanol and fourteen water molecules.

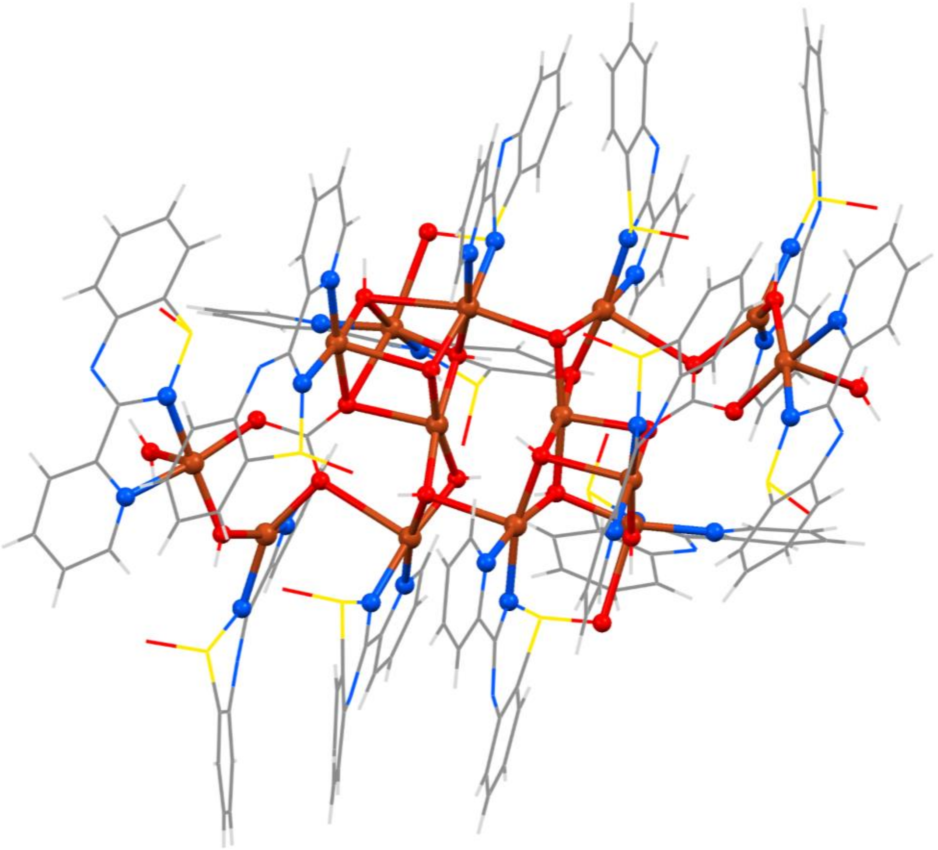

Figure 2.25 Molecular structure of $Cu_{14}(OH)_{12}(CO_3)_2(pybtda_{ox})_{12}(H_2O)_2$ (**2.14**) (solvent molecules omitted for clarity).

The crystal structure contains a total of 14 Cu^{II} centres; two copper ions are 6-coordinate with a N_2O_4 donor set and two metal ions are 4-coordinate with a N_2O_2 donor set. The remaining ten copper ions are 5-coordinate with eight of them having a N_2O_3 donor set and two coordinated to five oxygen atoms. The two 6-coordinate metal centres (Cu(1) and Cu(3)) exhibit Jahn-Teller elongation with bond distances in the range of 2.380(7) – 2.795 (8) Å. The Addison τ_5 values[22] of the 5-coordinate metal centres range between 0.002 and 0.175 consistent with square pyramidal geometry ($\tau = 1$ for trigonal bipyramidal and 0 for square pyramidal). The geometry index for the 4-coordinate metal centres suggests distorted square planar geometry with values of 0.32 and 0.33 ($\tau = 1$ for tetrahedral geometry and $\tau = 0$ for square planar geometry).[24] The geometry values are shown in Table 2.3.

Table 2.3 Coordination geometry and geometry index values of Cu centres in complex **2.14**.

	Cu		
	2 × 4-coordinate	10 × 5-coordinate	2 × 6-coordinate
Geometry index	0.32 (Cu13) 0.33 (Cu11)	0.002 (Cu14) 0.015 (Cu7) 0.017 (Cu4) 0.017 (Cu9) 0.017 (Cu10) 0.061 (Cu2) 0.085 (Cu5) 0.097 (Cu6) 0.103 (Cu8) 0.175 (Cu12)	(Cu1) (Cu3)

The formula of complex **2.14** contains twelve pybtda$_{ox}^{-}$ ligands located in the periphery of the structure. The heterocyclic ligand adopts two coordination modes; ten of the ligands in the structure offer a simple *N*,*N'*-chelate pocket through the pyridyl and heterocyclic nitrogen atoms whereas two of them adopt a bridging mode between two Cu^{II} centres, analogous to complex **2.3b**. The Cu-O (O=S) distances are 2.471(9) and 2.473(9) Å, the M-N distances are in the range of 1.938(12) − 2.010(10) Å and the N$_{py}$-M-N$_{BTDA}$ angles in the range of 81.1(4) − 82.8(4)° (Table 2.4).

Table 2.4 Selected bond lengths and angles of complex **2.14**.

M-N_{py}/Å	M-N_{BTDA}/Å	N_{py}-M-N_{BTDA}/°	M-O/Å (CO_3^{2-})	M-O/Å (μ_2-OH)	M-O/Å (μ_3-OH)
1.938(12)	1.945(9)	81.1(4)	1.924(7)	1.882(8)	1.904(7)
1.964(11)	1.951(9)	81.1(4)	1.945(7)	1.892(9)	1.916(7)
1.982(10)	1.968(9)	81.3(5)	1.949(8)	1.907(8)	1.935(7)
1.982(10)	1.969(10)	81.4(4)	1.957(7)	1.914(8)	1.938(7)
1.987(10)	1.978(9)	81.4(4)	1.964(7)	1.916(7)	1.942(7)
1.994(9)	1.979(9)	81.5(4)	1.979(7)	1.920(7)	1.946(7)
1.995(9)	1.979(9)	81.5(4)	2.225(7)	1.936(7)	1.955(7)
1.995(9)	1.980(9)	81.6(4)	2.231(7)	1.939(7)	1.992(7)
2.002(10)	1.980(10)	81.7(4)	2.609(6)	1.940(7)	1.999(7)
2.008(9)	1.986(9)	82.0(4)	2.637(6)	1.942(7)	2.000(7)
2.020(9)	1.992(10)	82.5(4)	2.795(8)		2.002(7)
2.010(10)	2.002(9)	82.8(4)			2.007(7)
					2.010(7)
					2.334(7)
					2.337(7)
					2.380(7)
					2.386(7)
					2.710(6)

The crystal structure has two carbonate groups completing the coordination sphere of the metals by bridging five and six metal ions respectively. Although there was no direct introduction of any source of carbonate in the initial reaction scheme, carbonates are present in H_2O from the dissolution of atmospheric CO_2. Twelve hydroxo groups are also present; five of them act as μ_2-hydroxo groups bridging two Cu ions, whereas seven are μ_3-hydroxo ligands bridging three metals. Two water molecules occupy the apical position of two 5-coordinate Cu ions (Cu(5) and Cu(7)). The Cu-O bond distances lie in the range of 1.882(8) − 2.710(6) Å (Table 2.4). The formation of complex **2.14** is summarized in Equation 2.12.

$$\begin{aligned} &14\ Cu(hfac)_2 + 12\ pybtdaH + 16\ H_2O \longrightarrow Cu_{14}(OH)_{12}(CO_3)_2(pybtda_{ox})_{12}(H_2O)_2 \\ &+ 6\ O_2 + 2\ CO_2 \qquad\qquad + 28\ hfacH \end{aligned}$$

Equation 2.12

The [Cu_{14}] core is shown in Figure 2.26. It consists of two [Cu_7O_8] sub-cores linked by two μ_2-OH (O(3), O(6)) and two μ_3-OH (O(8), O(12)) groups. Each sub-core can be described as a zig-zag chain of [Cu_3O_2] ending to a [Cu_4O_4] cubane connected by the two μ_3-OH (O(8), O(12)). The zig-zag chains have the three metal centres (Cu(7), C(13), Cu(6) and Cu(5), Cu(11), Cu(10)) linked by one μ_2-OH (O(7), O(4), respectively) and one μ_3-O atom of the CO_3^{2-} groups (O(302), O(203), respectively). The first [Cu_4O_4] cubane (Cu(1), Cu(2), Cu(3) and Cu(4)) is bridged by three μ_3-OH groups (O(5), O(10), O(13)) and μ_3-O atom from the CO_3^{2-} group (O(204)). The second "cubane" comprised by Cu(8), Cu(9), Cu(12) and Cu(14) is missing two edges, shown in Figure 2.26 as dashed green lines. The four metal centers are linked by one μ_2-OH group (O(2), two μ_3-OH groups (O(9), O(14)) and one μ_3-O atom from the CO_3^{2-} group (O(303)). The missing edges correspond to elongated Jahn-Teller axes with the Cu(2)-O(2) distance at 2.801(6) Å and the Cu(12)-O(303) at 2.863(8) Å. The three metal centres Cu(6), Cu(9) and Cu(14) are forming a rod-like chain linked by one μ_2-OH group (O(3) and three μ_3-OH groups (O(9), O(12), O(14) in the centre of the [Cu_{14}] core. The Cu(3), Cu(4) and Cu(10) metal ions are forming a similar rod-like chain connected by one μ_2-OH group and three μ_3-OH groups (O(8), O(10), O(13)).

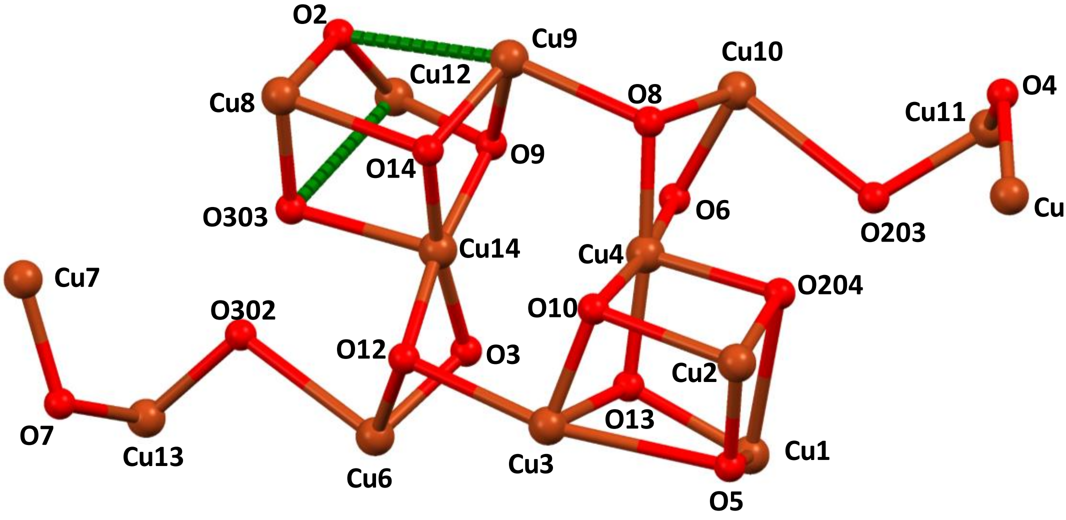

Figure 2.26 The [Cu_{14}] core of complex **2.14** (green dashed lines indicate missing edges of the "cubane").

The structure has intramolecular hydrogen bonds between the oxygen atoms of the sulphoxides and the hydrogen atoms of the OH groups. The distances are in the range of 1.903 – 2.290 Å and the angles at 106.0 − 161.8°. In addition, the presence of a shell of water solvent molecules around the Cu_{14} complex forms an extended hydrogen bond network.

2.2.5 Spectroscopic studies of the metal complexes 2.3a, 2.4 – 2.10, 2.12 – 2.14

The IR spectra exhibit a stretch in the range 1673 − 1574 cm^{-1} characteristic of the C=N imine bond for the complexes.[15] The N-H stretch is present in complexes **2.3a** and **2.7** – **2.10** in the range of 3258 − 3200 cm^{-1}, but is notably absent in all other complexes as expected for the deprotonated state of the pybtda$_{ox}^{-}$ ligand. Conversely, sulfoxides typically exhibit a strong $\nu_{S=O}$in the IR (1070 – 1030 cm^{-1})[25] and the *S*-oxide of all complexes (except Ni(hfac)$_2$(pybtdaH) **2.10**) exhibit a vibration in the range of 1134 − 984 cm^{-1}. This vibration is consistent with the previously reported metal coordinated pybtda$_{ox}^{-}$ anion (985 cm^{-1}) and free *S*-oxide benzothiadiazines (*ca*. 1000 cm^{-1}).[2]

The solid state EPR of complex **2.12** reveals a rhombic spectrum with g_x = 2.030, g_y = 2.137, g_z = 2.220 (<g>= 2.129) consistent with a metal-based electron (Figure 2.27).

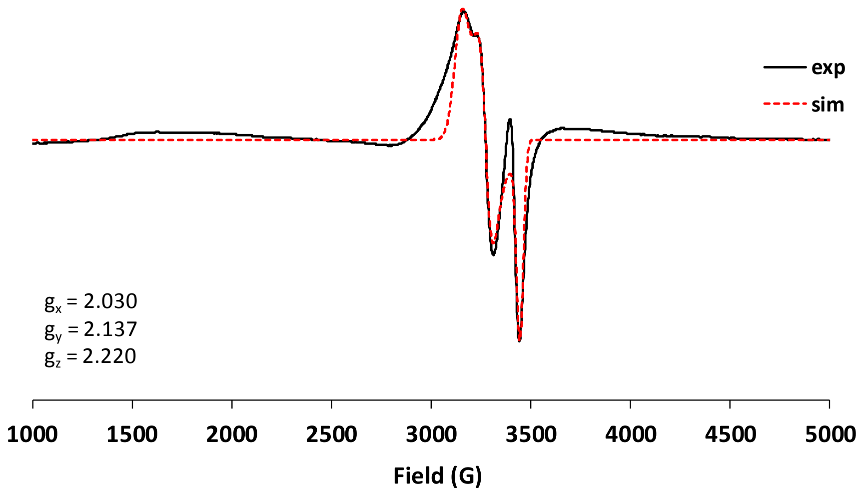

Figure 2.27 Solid state EPR of complex **2.12** at room temperature (experimental-black, simulation-red); g_x = 2.030, g_y = 2.137, g_z = 2.220 (<g>= 2.129), a_x = 20 G, a_y = 34 G, a_z = 47 G.

2.2.6 Reactivity trends in coordination chemistry of pybtdaH

The coordination chemistry of the ligand 3-(2'pyridyl)benzothiadiazine (pybtdaH) has been previously explored with MCl_2 forming a range of *N*,*N'*-chelate complexes with first row transition metals including $FeCl_2$(pybtdaH) and $CuCl_2$(pybtdaH)$_2$.[1] Previous studies indicated that *S*-oxidation of pybtdaH or related benzothiadiazines only occurred in the presence of a metal ***and*** Et_3N. For example, reaction of $CuCl_2$ with pybtdaH affords a stable red solution of $CuCl_2$(pybtdaH)$_2$ but which led to the isolation of the green dimetallic complex [Cu(pybtda$_{ox}$)$_2$]$_2$ complex upon addition of Et_3N.[2] In this chapter, we investigated the effect of Lewis acidic metal ions, more basic counter ions (hfac$^-$ and OAc$^-$) and the introduction of base in the reaction scheme in the oxidation of the ligand pybtdaH to pybtda$_{ox}^-$.

The reaction of pybtdaH and $FeCl_3{\cdot}6H_2O$ afforded the mononuclear complex $FeCl_3$(pybtdaH$_{ox}$)(CH_3OH) (**2.3a**) and the tetranuclear complex $Fe_4Cl_4(OCH_3)_6$(pybtda$_{ox}$)$_2$ (**2.3b**) depending on the concentration of the solution. In these complexes, the ligand pybtdaH has been oxidized to either pybtdaH$_{ox}$ or pybtda$_{ox}^-$ even without the presence of base (such as Et_3N) in the reaction mixture. Previous results with $FeCl_2$ and the ligand pybtdaH resulted in the mononuclear complex $FeCl_2$(pybtdaH)[1] leading to the conclusion that the Lewis acidic nature of Fe^{III} is promoting the oxidation of the ligand in this system.

The next reaction scheme investigated was the ligand pybtdaH with metal salts containing OAc$^-$ as counterions. The mononuclear complex Co(pybtda$_{ox}$)$_3$ (**2.4**) was isolated which does not contain acetate groups. The reaction of pybtdaH and $M(OAc)_2$ (M = Cu, Zn) afforded the dinuclear complexes $Cu_2(OAc)_2$(pybtda$_{ox}$)$_2$(H_2O)$_2$ (**2.5**) and $Zn_2(OAc)_2$(pybtda$_{ox}$)$_2$ (**2.6**) with the acetate groups adopting bridging and chelate coordination modes, respectively. In all three complexes the ligand has been oxidised and deprotonated only by the presence of a more basic counter ion (pK_a (AcOH) = 4.76)[7] and without introduction of base such as Et_3N. In complexes **2.4** and **2.5**, the ligand pybtda$_{ox}^-$ is chelating one metal centre whereas in complex **2.6** the ligand is bridging two Zn ions**.**

The isolation of the mononuclear complexes **2.7** − **2.9** with general formula M(hfac)$_2$(pybtdaH$_{ox}$)$_2$ (M = Mn (**2.7**), Co (**2.8**), Zn (**2.9**)) on addition of pybtdaH to M(hfac)$_2$

in which the ligand has been oxidised was therefore unsurprising, given the similar pK_a values of OAc^- and $hfac^-$. The ligand $pybtdaH_{ox}$ acts as a simple *N*,*N*′-chelate to transition metal ions in a similar fashion to the pybtdaH ligand.[1] In contrast, Ni appears more resilient to promoting ligand oxidation with the reaction of pybtdaH and $Ni(hfac)_2 \cdot xH_2O$ affording the mononuclear complex with formula $Ni(hfac)_2(pybtdaH)$ (**2.10**), in which the ligand has not been oxidised or deprotonated and the basic nature of the hfac group has no effect on the outcome of the reaction, suggesting that this is not merely due to the acidity of the metal ion (Ni^{2+} is intermediate between Mn and Co which both undergo ligand oxidation under the same conditions). Addition of base (Et_3N) in the reaction scheme resulted to the trimetallic complex $Ni_3(hfac)(pybtda_{ox})_5(H_2O)$ (**2.11**) where the ligand has been oxidised to form the deprotonated $pybtda_{ox}^-$.

The outcome of the reaction between the ligand pybtdaH and $Cu(hfac)_2$ proved dependent on: (i) ratio of Cu:pybtdaH, (ii) basic conditions and (iii) the presence of H_2O. The reaction of pybtdaH and $Cu(hfac)_2$ in 1:1 molar ratio afforded the polymer $[Cu(hfac)(pybtda_{ox})]_n$ (**2.12**). The product isolated from the reaction in 1:2 molar ratio was the previously reported dimer $[Cu(pybtda_{ox})_2]_2$ which was isolated by the reaction of $CuCl_2$ with pybtdaH in the presence of base.[2] The addition of base in the 1:1 molar ratio resulted in formation of the tetranuclear complex $Cu_4(OH)_4(pybtda_{ox})_4$ (**2.13**). The stoichiometric reaction for formation of tetranuclear complex **2.13** including 1:1 molar ratio of Cu:pybtdaH in the presence of Et_3N and H_2O unexpectedly afforded the polymetallic complex $Cu_{14}(OH)_{12}(CO_3)_2(pybtda_{ox})_{12}(H_2O)_2$ (**2.14**), permitting us to conclude that increasing the basic environment resulted in complexes free of $hfac^-$ groups and also of higher nuclearity**.**

In initial studies with MCl_2 displacement of chloride has no effect on pH since chloride is the conjugate base of a strong acid (pK_a (HCl) = -6.1)[6] and effectively has minimal base character. The reaction with more acidic metal ion such as $FeCl_3$ promoted the oxidation of the ligand in this system. Conversely the OAc^- and $hfac^-$ anions are the conjugate bases of weak acids (pK_a (AcOH) = 4.76 [7], pK_a (Hhfac) = 4.71 [8]) and generation of OAc^- and $hfac^-$ in solution appeared sufficient to promote the oxidation of the coordinated pybtdaH ligand and reflected in the decolourization of the initial red solution associated with S^{II} pybtdaH. The resultant $pybtda_{ox}^{-}$ ligand offers a more versatile hard *O*-donor centre in addition to the favourable, softer, *N*,*N*′-chelate, leading to enhanced aggregation and polynuclear complexes.

A comparison of the ligand coordination geometry with respect to the free ligand indicates, as expected, that the major changes in geometry of the coordinated ligand are associated with the N-bound heteroatom of the thiadiazine ring. The free ligand $pybtdaH_{ox}$ has been isolated and a better comparison can be made with the complexes. When comparing pybtdaH with $pybtdaH_{ox}$, a marked shortening of the S-N bond by approximately 0.04 Å (from *ca.* 1.71 to *ca.* 1.67 Å) is observed.

The *N*-coordination to the metal ions leads to somewhat variable results. The N-S bond lengths of the $pybtdaH_{ox}$ are in the range 1.684 – 1.700 Å indicating a slight lengthening of the bond upon coordination (*cf* $pybtdaH_{ox}$ ligand at 1.6656(18) Å). The N-S bonds in the species in which the ligand is in its $pybtda_{ox}^{-}$ form is affected by the coordination of the oxygen of the S=O. The distances are in the range 1.635 – 1.680 Å for complexes with non-coordinating O, whereas for the complexes with coordinating oxygen the bonds in the range of 1.635 – 1.657 Å indicating a shortening of the bond. The C–N bond lengths of the metal complexes containing $pybtdaH_{ox}$ are in the range 1.289 – 1.322 Å showing no significant deviation from the free ligand (*cf* $pybtdaH_{ox}$ ligand at 1.306(3) Å). In the complexes where the ligand adopts the anionic form, $pybtda_{ox}^{-}$, the electronics of the heterocycle are altered, resulting to a lengthening of the bonds indicative of single bond character ranging from 1.332 – 1.378 Å. The S–O bonds in the terminal $pybtdaH_{ox}$ are in the range of 1.488 – 1.499 Å and are comparable with the free ligand (*cf* 1.4969(16) Å) as well as other literature reported sulfoxide bonds (average 1.50 Å).[2,26]

2.3. Conclusions

The synthesis of the ligand 3-(2’pyridyl)benzothiadiazine (pybtdaH) is reported using a new synthetic route. Computational studies have been performed on the ligand determining the most stable conformation and tautomer as well as the energy minimum of the pyridyl ring rotation. A new mechanism has been proposed for the formation of the benzothiadiazine based on NMR studies.

The coordination chemistry of the ligand 3-(2’pyridyl)benzothiadiazine (pybtdaH) with $FeCl_3$, $M(OAc)_2$ (M = Co, Cu, Zn) and $M(hfac)_2$ (M = Mn, Co, Ni, Cu, Zn) is reported. A series of mononuclear complexes have been isolated as well as polymetallic with the nuclearities of 2 (**2.5**, **2.6**), 3 (**2.11**), 4 (**2.3b**, **2.13**) and 14 (**2.14**). The reactivity pathway is dependent on the basic environment of the reaction mixture; by the use of (i) basic ligands (OAc^-, $hfac^-$) and/or (ii) basic conditions (Et_3N) promoting ligand oxidation and deprotonation to form pybtdaH$_{ox}$ or the pybtda$_{ox}^{-}$ anion. The neutral pybtdaH and pybtdaH$_{ox}$ ligands act as a simple *N*,*N*′-chelate to transition metal ions, whereas the pybtda$_{ox}^{-}$ anion is more versatile offering one *N*,*N*′ binding site as well as a pendant *O*-donor which offers an additional binding site favouring formation of polynuclear metal complexes (Figure 2.28).

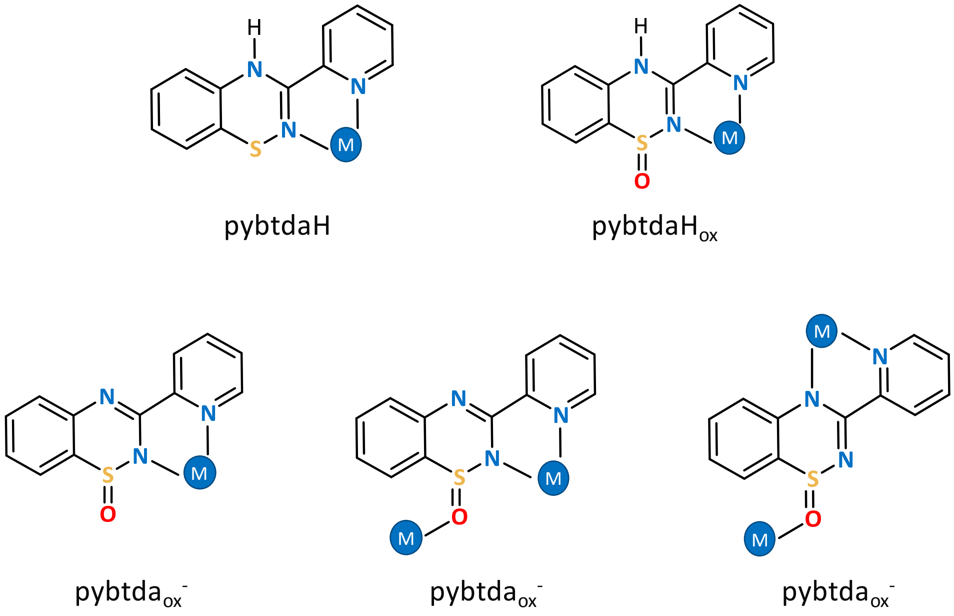

pybtdaH

pybtdaH$_{ox}$

pybtda$_{ox}^{-}$

pybtda$_{ox}^{-}$

pybtda$_{ox}^{-}$

Figure 2.28 Coordination modes of pybtdaH, pybtdaH$_{ox}$ and pybtda$_{ox}^{-}$ observed in the metal complexes of Chapter 2.

2.4. Experimental

2.4.1 General considerations and physical measurements

Solvents, starting materials and metal salts were obtained from commercial suppliers and used without further purification. Manipulation of air-sensitive materials was carried out under an atmosphere of dry nitrogen using standard Schlenk techniques and a dry-nitrogen glove box (MBraun Labmaster). Melting points were determined using a Stanford Research Systems MPA120 EZ-Melt automated melting point apparatus. Elemental compositions were determined on a Perkin Elmer 2400 Series II CHNS/O Analyzer. IR spectra were obtained using a Bruker Alpha FT-IR spectrometer equipped with a Platinum single reflection diamond ATR module. NMR spectra were recorded on a Bruker 500 MHz spectrometer with a Broadband AX Probe using $CDCl_3$ (^1H $\delta = 7.26$ ppm, s; ^{13}C $\delta = 77.16$ ppm) or CD_2Cl_2 (^1H $\delta = 5.32$ ppm, t; ^{13}C $\delta = 53.84$ ppm) as an internal reference point relative to Me_4Si ($\delta = 0$ ppm). Mass spectra were recorded on a Waters XEVO G2-XS specifically using the atmospheric solids analysis probe in positive resolution mode. EPR spectrum of complex **2.12** was measured on a Bruker EMXplus X-band EPR spectrometer at room temperature. Simulation of the anisotropic EPR spectrum of complex **2.12** was made using the PIP4Win software.[27] Density functional theory (DFT) calculations of pybtdaH were undertaken using the B3LYP and dispersion-corrected B3LYP-D3 functional and 6-311G^{*+} basis set[28–30] functional within Jaguar[31].

2.4.2 Ligand Synthesis

Ligand pybtdaH was prepared according to a modification of the literature procedure for pybtdaH[14]:

2.4.2.a 2-(propylthio)aniline (2.1)

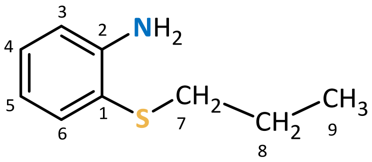

Sodium hydroxide (1.6 g, 40 mmol) was dissolved in H_2O (3 mL) and added dropwise to a solution of 2-aminothiophenol (5.0 g, 40 mmol) in ethanol (50 mL). The reaction mixture was heated at reflux for 1 h. A solution of 1-bromopropane (4.92 g, 40 mmol) in EtOH (25 mL) was added to the reaction mixture and it was stirred at reflux for 18 h. The solvent was removed *in vacuo* and the residue was dissolved in CH_2Cl_2 (20 mL). The organic phase was washed with H_2O (3 × 10 mL) and brine (1 × 10 mL), dried over Na_2SO_4 and the solvent was removed *in vacuo* to yield a dark green viscous oil. The product was purified by Kugelrohr distillation (140 °C, 0.5 – 2.0 Torr) to yield a honey-coloured oil. Yield: 5.22 g, 78%.

Elemental Analysis calc. for $C_9H_{13}NS$: C, 64.62; H, 7.83; N, 8.37, Found: C, 64.68; H, 7.73; N. 8.41%.

IR (oil, cm^{-1}) $\tilde{\nu}_{max}$ = 3458 (w), 3351 (w), 3065 (w), 3017 (w), 2960 (m), 2929 (w), 2870 (w), 1603 (m), 1477 (m), 1447 (m), 1301 (m), 1237 (w), 1157 (w), 1025 (w), 744 (s).

^{1}H NMR (500 MHz, ppm, CD_2Cl_2) δ_H = 7.35 (1H, dd, *J* = 7.7, 1.5 Hz, C^6H), 7.09 (1H, td, *J* = 7.6, 1.5 Hz, C^4H), 6.72 (1H, dd, *J* = 8.0, 1.2 Hz, C^3H), 6.67 (1H, td, *J* = 7.5, 1.2 Hz, C^5H), 4.37 (2H, bs, NH_2), 2.72 (2H, t, *J* = 7.3 Hz, S C^7H_2), 1.57 (2H, sextet, *J* = 7.3 Hz, $SCH_2C^8H_2$), 0.98 (3H, t, *J* = 7.3 Hz, C^9H_3).

^{13}C NMR (125 MHz, ppm, CD_2Cl_2) δ_C = 148.76 (C^2), 135.88 (C^6), 129.70 (C^4), 118.51 (C^5), 118.46 (C^1), 114.99 (C^3), 37.16 (C^7), 23.36 (C^8), 13.46 (C^9).

HRMS (ASAP) *m/z* $[M+H]^+$ calc. for $C_9H_{14}NS$: 168.0847, found 168.0840.

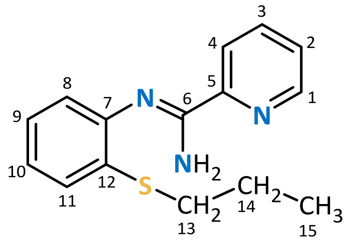

2.4.2.b N’-(2-propylthiophenyl)-picolinamidine (2.2)

Compound **2.1** (5 g, 30 mmol) was dissolved in dry THF (10 mL) and added dropwise to a stirred solution of lithium *bis*(trimethylsilyl)amide (6.02 g, 36 mmol) in THF (25 mL) at 0 °C under a nitrogen atmosphere. The dark reaction mixture was allowed to warm to room temperature and stirred for 18 h. 2-Cyanopyridine (3.12 g, 30 mmol) was dissolved in THF (10 mL) then added dropwise to the reaction mixture and stirred for a further 18 h. The volume of solvent was reduced to approximately 10 mL and the reaction mixture treated with 50 mL of $NaHCO_{3(aq.)}$ on ice, then extracted with CH_2Cl_2 (50 mL). The organic phase was washed with $NaHCO_{3(aq.)}$ (1 x 50 mL) and brine (1 x 20 mL), dried over Na_2SO_4 and the solvent was removed *in vacuo*. The resulting brown oil was washed with hexanes (3 x 10 mL) to yield the product as a white crystalline powder. Yield 7.08 g, 87%.

Melting point 58.3 °C.

Elemental Analysis calc. for $C_{15}H_{17}N_3S$: C, 66.39; H, 6.31; N, 15.48. Found: C, 66.08; H, 6.46; N, 15.09%.

IR (solid, cm^{-1}) $\tilde{\upsilon}_{max}$ = 3490 (w), 3371 (w), 3054 (w), 2960 (m), 2929 (w), 2870 (w), 1637 (s), 1560 (s), 1469 (m), 1434 (m), 1370 (m), 1265 (m), 1056 (m), 1039 (m), 828 (m), 800 (m), 743 (m), 623 (w).

^{1}H NMR (500 MHz, ppm, $CDCl_3$) δ_H = 8.58 (1H, dq, *J* = 4.8, 0.8 Hz, C^1H), 8.52 (1H, d, *J* = 7.9 Hz, C^4H), 7.83 (1H, td, *J* = 11.6, 1.8 Hz, C^3H), 7.40 (1H, ddd, *J* = 7.5, 4.8 , 1.2 Hz, C^2H), 7.31 (1H, dd, *J* = 7.9, 1.2 Hz, C^8H), 7.16 (1H, td, *J* = 11.3, 1.3 Hz, $C^{10}H$), 7.05 (1H, td, *J* = 11.4, 1.4 Hz, C^9H), 6.98 (1H, d, *J* = 7.1 Hz, $C^{11}H$), 2.87 (2H, t, *J* = 7.4 Hz, $SC^{13}H_2$), 1.69 (2H, sextet, *J* = 7.4 Hz, $SCH_2C^{14}H_2$), 1.02 (3H, t, *J* = 7.3 Hz, $C^{15}H_3$).

^{13}C NMR (125 MHz, ppm, $CDCl_3$) δ_C = 152.24 (C^6), 151.31 (C^5), 147.99 (C^1), 147.73 (C^7), 136.97 (C^3), 129.94 (C^{12}), 127.67 (C^8), 126.16 (C^{10}), 125.34 (C^2), 123.74 (C^9), 122.02 (C^4), 121.02 (C^{11}), 33.88 (C^{13}), 22.43 (C^{14}), 13.82 (C^{15}).

HRMS (ASAP+) *m/z* $[M+H]^+$ calc. for $C_{15}H_{18}N_3S$: 272.1221, found 272.1225.

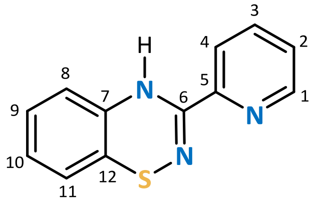

2.4.2.c 3-(pyridin-2-yl)-4H-benzo-1,2,4-thiadiazine (pybtdaH)

A solution of *N*-chlorosuccinimide (2.88 g, 22 mmol) in CH_2Cl_2 (40 mL) was added dropwise to a solution of **2.2** (5.0 g, 18 mmol) in CH_2Cl_2 (40 mL) at -78 °C and the reaction mixture was allowed to warm to room temperature and stirred for 18 h. The reaction mixture was then washed with water (2 × 40 mL), brine (1 × 40 mL) and then dried over Na_2SO_4. The solvent was removed *in vacuo* and the oily residue re-dissolved in toluene (40 mL) and brought to reflux for 12 h. The solvent was again removed *in vacuo* to yield a brown solid. The product was purified by column chromatography in CH_2Cl_2/hexane 1:1 ratio to yield orange powder. Yield 2.94 g, 72%.

Melting point 117.5 °C.

Elemental Analysis calc. for $C_{12}H_9N_3S$: C, 63.41; H, 3.99; N, 18.49. Found: C, 63.59; H, 4.09; N, 18.22%.

IR (solid, cm^{-1}) $\tilde{\upsilon}_{max}$ = 3308 (m, NH), 3054 (w), 1627 (m), 1586 (m), 1564 (m), 1488(m), 1461 (s), 1438 (m), 1417 (m), 1294 (m), 1101 (m), 1040 (w), 994 (m), 792 (m), 739 (s), 619 (m), 468 (w), 455 (w).

^{1}H NMR (500 MHz, ppm, $CDCl_3$) δ_H = 8.59 (1H, b, N*H*), 8.52 (1H, d, *J* = 4.8 Hz, C^1*H*), 8.09 (1H, d, *J* = 8.0 Hz, C^4*H*), 7.76 (1H, td, *J* = 7.7, 1.7 Hz, C^3*H*), 7.37 (1H, ddd, *J* = 7.5, 4.8, 1.1 Hz, C^2*H*), 6.94 (1H, td, *J* = 7.6, 1.4 Hz, C^9*H*), 6.88 (1H, td, *J* = 7.6, 1.3 Hz, C^{10}*H*), 6.69 (1H, d, *J* = 7.5 Hz, C^{11}*H*), 6.50 (1H, dd, *J* = 7.7, 1.0 Hz, C^8*H*).

^{13}C NMR (125 MHz, ppm, CDCl$_3$) δ_C = 154.34 (C^6), 148.04 (C^5), 147.50 (C^1), 137.04 (C^3), 136.79 (C^7), 127.75 (C^9), 125.39 (C^2), 125.24 (C^{10}), 122.83 (C^{11}), 121.33 (C^4), 120.14 (C^{12}), 114.43 (C^8).

HRMS (ASAP+) *m/z* [M+H]$^+$ calc. for $C_{12}H_{10}N_3S$: 228.0595, found 228.0597.

2.4.3 Complex Syntheses with MCl$_3$ (M = Fe)

2.4.3.a [FeCl$_3$(pybtdaH$_{ox}$)(CH$_3$OH)]·CH$_3$OH (2.3a)

Solid ligand pybtdaH (0.023 g, 0.100 mmol) was added to a solution of $FeCl_3·6H_2O$ (0.027 g, 0.100 mmol) in CH_3OH (5 mL). The mixture was stirred for 30 min and a deep red solution obtained. The solution was filtered and dark red crystals were grown by layering with a mixture of diethyl ether/hexanes (1:1) within two weeks. Yield 0.012 g, 26%.

Elemental Analysis calc. for [$C_{14}H_{13}N_3FeSCl_3O_2$]: C, 37.41; H, 2.91; N, 9.35. Found: C, 35.39; H, 2.18; N, 10.21%.

IR (solid, cm^{-1}) $\widetilde{\nu}_{max}$ = 3230 (br), 1617 (m), 1543 (w), 1515 (m), 1471 (m), 1434 (m), 1362 (w), 1308 (w), 1256 (w), 1155 (w), 1059 (m), 1018 (m), 945 (m), 874 (w), 804 (m), 772 (s), 728 (m), 697 (m), 674 (m), 643 (m), 575 (m), 552 (m), 520 (w), 498 (m), 478 (m), 460 (m), 438 (m).

2.4.3.b Fe$_4$Cl$_4$(OCH$_3$)$_6$(pybtda$_{ox}$)$_2$ (2.3b)

Solid ligand pybtdaH (0.023 g, 0.100 mmol) was added to a solution of $FeCl_3·6H_2O$ (0.027 g, 0.100 mmol) in CH_3OH (10 mL). The mixture was stirred for 30 min and a deep red solution obtained. The solution was filtered and dark red crystals were grown by layering with a mixture of diethyl ether/hexanes (1:1) within five weeks. Yield 0.003 g, 3%.

2.4.4 Complex Syntheses with $M(OAc)_2$ (M = Co (2.4), Cu(2.5), Zn (2.6))

2.4.4.a $Co(pmbtda_{ox})_3$ (2.4)

Solid ligand pybtdaH (0.023 g, 0.100 mmol) was added to a solution of $Co(OAc)_2{\cdot}4H_2O$ (0.025 g, 0.100 mmol) in CH_3OH (10 mL). The mixture was stirred for 2.5 h and a deep red solution obtained. The solution was filtered and dark red crystals were grown by layering with a mixture of diethyl ether/hexanes (1:1) over six weeks. Yield 0.003 g, 4%.

Elemental Analysis calc. for $[C_{36}H_{24}N_9CoS_3O_3]{\cdot}5H_2O$: C, 49.37; H, 3.91; N, 14.39. Found: C, 49.33; H, 3.30; N, 14.24%.

IR (solid, cm^{-1}) $\tilde{\nu}_{max}$ = 1606 (w), 1594 (w), 1560 (m), 1524 (s), 1476 (m), 1458 (m), 1439 (m), 1330 (s), 1279 (m), 1259 (m), 1137 (m), 1119 (m), 1075 (m), 1033 (m), 935 (m), 864 (w), 822 (m), 790 (m), 759 (s), 737 (m), 698 (m), 670 (m), 561 (m), 547 (m), 508 (w), 475 (w), 458 (w), 438 (w), 417 (w).

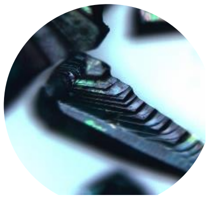

2.4.4.b $[Cu_2(OAc)_2(pybtda_{ox})_2(H_2O)_2]{\cdot}2H_2O$ (2.5)

Solid ligand pybtdaH (0.023 g, 0.100 mmol) was added to a solution of $Cu(OAc)_2{\cdot}2H_2O$ (0.020 g, 0.100 mmol) in CH_3OH (10 mL). The mixture was stirred for 1 h and a green solution obtained. The solution was filtered and green crystals were grown by layering with a mixture of diethyl ether/hexanes (1:1) over two days. Yield 0.006 g, 7%.

Elemental Analysis calc. for $[C_{28}H_{26}N_6CuS_2O_8]{\cdot}2H_2O$: C, 41.94; H, 3.77; N, 10.48. Found: C, 41.61; H, 3.63; N, 10.28%.

IR (solid, cm^{-1}) $\tilde{\nu}_{max}$ = 1580 (m), 1561 (m), 1522 (m), 1474 (m), 1427 (s), 1331 (m), 1275 (m), 1134 (m), 1075 (m), 1034 (s), 1025 (s), 935 (w), 866 (w), 830 (m), 775 (s), 750 (m), 677 (m), 653 (m), 620 (m), 565 (m), 532 (m), 508 (m), 482 (m), 460 (m), 445 (w), 422 (w).

2.4.4.c $Zn_2(OAc)_2(pybtda_{ox})_2$ (2.6)

Solid ligand pybtdaH (0.023 g, 0.100 mmol) was added to a solution of $Zn(OAc)_2{\cdot}2H_2O$ (0.022 g, 0.100 mmol) in CH_3OH (10 mL). The mixture was stirred for 1 h and an orange solution obtained. The solution was filtered and yellow crystals were grown by layering with a mixture of diethyl ether/hexanes (1:1) over two days. Yield 0.008 g, 10%.

Elemental Analysis calc. for $[C_{28}H_{28}N_6Zn_2S_2O_6]{\cdot}H_2O$: C, 44.76; H, 3.22; N, 11.18. Found: C, 45.17; H, 2.99; N, 11.15%.

IR (solid, cm^{-1}) $\tilde{\nu}_{max}$ = 1575 (m), 1563 (m), 1501 (m), 1462 (m), 1445 (m), 1418 (m), 1385 (m), 1335 (m), 1297 (m), 1262(m), 1240 (m), 1148 (w), 1049 (s), 1026 (s), 964 (m), 858 (m), 792 (m), 763 (m), 732 (m), 681 (s), 651 (m), 619 (m), 599 (m), 558 (m), 528 (m), 497 (w), 477 (m), 439 (m), 415 (m).

2.4.5 Complex Syntheses with $M(hfac)_2$ (M = Mn, Co, Ni, Cu, Zn)

2.4.5.a $Mn(hfac)_2(pybtdaH_{ox})$ (2.7)

Solid ligand pybtdaH (0.023 g, 0.100 mmol) was added to a solution of $Mn(hfac)_2{\cdot}3H_2O$ (0.026 g, 0.100 mmol) in $CHCl_3$ (15 mL). The mixture was stirred for 45 min in room temperature and for 15 min the solution was placed in a water bath of 35 °C. The light orange solution was filtered and yellow crystals were grown by slow evaporation the next day. Yield 0.017 g, 48%.

Elemental Analysis calc. for $[C_{22}H_{11}N_3MnSO_4F_{12}]$: C, 37.10; H, 1.56; N, 5.90. Found: C, 37.23; H, 1.48; N, 6.07%.

IR (solid, cm^{-1}) $\tilde{\nu}_{max}$ = 3010 (w), 1644 (m), 1616 (w), 1556 (w), 1517 (m), 1495 (m), 1467 (m), 1439 (w), 1253 (m), 1191 (m), 1136 (m), 1096 (s), 1082 (m), 1041 (m), 1016 (m), 943 (w), 797 (m), 751 (m), 683 (m), 663 (m), 638 (m), 581 (m), 552 (m), 527 (w), 515 (m), 474 (m), 457 (w), 441 (w).

2.4.5.b Co(hfac)$_2$(pybtdaH$_{ox}$) (2.8)

Solid ligand pybtdaH (0.023 g, 0.100 mmol) was added to a solution Co(hfac)$_2$ (0.047 g, 0.100 mmol) in $CHCl_3$ (15 mL). The mixture was stirred for 45 min and a deep red solution obtained. The solution was filtered and light orange crystals were grown by slow evaporation over five weeks. Yield 0.001 g, 1%.

IR (solid, cm^{-1}) $\tilde{\nu}_{max}$ = 3259 (br), 1622 (m), 1565 (m), 1526 (m), 1477 (s), 1462 (m), 1444 (m), 1303 (m), 1279 (m), 1156 (m), 1137 (m), 1076 (m), 943 (w), 826 (w), 759 (m), 698 (w), 665 (m), 613 (m), 560 (m), 558 (m), 545 (m), 535 (m), 508 (m), 498 (m), 469 (m), 458 (m), 422 (m), 412 (m).

2.4.5.c Zn(hfac)$_2$(pybtdaH$_{ox}$) (2.9)

Solid ligand pybtdaH (0.023 g, 0.100 mmol) was added to a solution Zn(hfac)$_2$ (0.052 g, 0.100 mmol) in CH_2Cl_2 (15 mL). The mixture was stirred for 30 min and a light orange solution obtained. The solution was filtered and colorless crystals were grown by slow evaporation over five weeks. Yield 0.003 g, 4%.

IR (solid, cm^{-1}) $\tilde{\nu}_{max}$ = 3200 (br), 1660 (m), 1616 (w), 1503 (m), 1474 (m), 1460 (m), 1385 (m), 1298 (w), 1257 (m), 1193 (m), 1138 (s), 1102 (m), 1052 (m), 1028 (m), 959 (m), 791 (m), 759 (m), 731 (m), 683 (m), 665 (m), 650 (m), 642 (m), 597 (m), 585 (m), 568 (m), 554 (m), 528 (m), 480 (m), 463 (m), 442 (m), 415 (m).

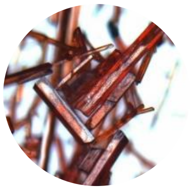

2.4.5.d Ni(hfac)$_2$(pybtdaH) (2.10)

Solid ligand pybtdaH (0.023 g, 0.100 mmol) was added to a solution of Ni(hfac)$_2$·xH$_2$O (0.047 g, 0.100 mmol) in CH$_2$Cl$_2$ (15 mL). The mixture was stirred for 30 min and an orange solution obtained. The solution was filtered and red crystals were grown by layering with hexanes over two days. Yield 0.042 g, 60%.

Elemental Analysis calc. for [$C_{22}H_{11}N_3NiSO_4F_{12}$]: C, 37.74; H, 1.58; N, 6.00. Found: C, 37.74; H, 1.51; N, 6.04%.

IR (solid, cm^{-1}) $\tilde{\upsilon}_{max}$ = 3368 (br), 1652 (m), 1638 (m), 1583 (m), 1554 (m), 1526 (m), 1466 (m), 1438 (m), 1348 (w), 1252 (m), 1191 (m), 1134 (s), 1099 (m), 1024 (m), 950 (w), 793 (m), 742 (m), 670 (m), 651 (m), 585 (m), 527 (w), 436 (w).

2.4.5.e [Ni$_3$(hfac)(pybtda$_{ox}$)$_5$(H$_2$O) (2.11)

Solid ligand pybtdaH (0.046 g, 0.100 mmol) was added to a solution of Ni(hfac)$_2$·xH$_2$O (0.047 g, 0.100 mmol) in CH$_2$Cl$_2$ (15 mL). Upon addition of Et$_3$N (0.05 mL, 0.400 mmol) the mixture was stirred for 1.5 h. The orange solution was filtered and was layering with hexanes. Red crystals formed over two days but after a prolong period of time green crystals appeared.

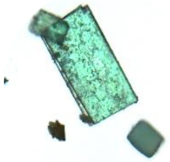

2.4.5.f [Cu(hfac)(pybtda$_{ox}$)]$_n$ (2.12)

Solid ligand pybtdaH (0.023 g, 0.100 mmol) was added to a solution of Cu(hfac)$_2$·xH$_2$O (0.049 g, 0.100 mmol) in CH$_3$OH (10 mL). The mixture was stirred for 30 min and a deep red solution obtained. The solution was filtered and green crystals were grown by slow evaporation over one week. Yield 0.005 g, 4%.

Elemental Analysis calc. for [$C_{24}H_{18}N_6Cu_2S_2O_6F_{12}$]: C, 39.13; H, 1.93; N, 8.05. Found: C, 39.09; H, 1.66; N, 7.77%.

IR (solid, cm^{-1}) $\tilde{\nu}_{max}$ = 1652 (m), 1609 (w), 1562 (m), 1552 (m), 1502 (m), 1475 (m), 1455 (m), 1383 (m), 1350 (m), 1298 (w), 1255 (m), 1191 (m), 1135 (s), 1102 (m), 1051 (m), 1032 (m), 974 (m), 940 (m), 854 (w), 811 (m), 789 (m), 756 (m), 731 (m), 670 (m), 654 (m), 584 (m), 558 (m), 529 (m), 483 (m), 441 (w), 414 (m).

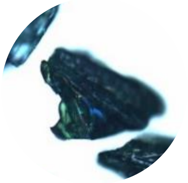

2.4.5.g [$Cu_4(OH)_4(pybtda_{ox})_4$]·$H_2O$ (2.13)

Solid ligand pybtdaH (0.023 g, 0.100 mmol) was added to a solution of Cu(hfac)$_2$·xH_2O (0.049 g, 0.100 mmol) in CH_3OH (10 mL). Upon addition of Et_3N (0.05 mL, 0.400 mmol) the mixture was stirred for 30 min in a water bath of 35 °C. The dark orange solution was filtered and dark brown crystals were grown by slow evaporation over six weeks. Yield 0.002 g, 1%.

IR (solid, cm^{-1}) $\tilde{\nu}_{max}$ = 3277 (br), 1673 (w), 1562 (m), 1523 (s), 1457 (m), 1333 (m), 1298 (w), 1277 (m), 1263 (m), 1135 (m), 1020 (s), 932 (m), 830 (m), 794 (m), 770 (m), 740 (m), 678 (m), 651 (m), 560 (m), 536 (m), 508 (m), 484 (m), 458 (m), 416 (m).

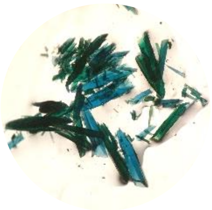

2.4.5.h [$Cu_{14}(OH)_{12}(CO_3)_2(pybtda_{ox})_{12}(H_2O)_2$]·14[$H_2O$]·[$CH_3OH$] (2.14)

Solid ligand pybtdaH (0.023 g, 0.100 mmol) was added to a solution of Cu(hfac)$_2$·xH_2O (0.049 g, 0.100 mmol) in CH_3OH (10 mL) and 2 μL H_2O. Et_3N (0.05 mL, 0.400 mmol) was added within 30 min. The mixture was stirred for another 50 min in a water bath of 42 °C. The dark olive solution was filtered and green crystals were grown by slow evaporation over three days. Yield 0.001 g, < 1%.

Elemental Analysis calc. for [$C_{147}H_{115}N_{36}Cu_{14}S_{12}O_{47}$]·5$H_2O$: C, 39.22; H, 3.80; N, 11.20. Found: C, 38.89; H, 2.55; N, 10.88%.

IR (solid, cm^{-1}) $\tilde{\nu}_{max}$ = 3441 (br), 1605 (w), 1560 (m), 1453 (m), 1384 (m), 1330 (m), 1273 (m), 1134 (w), 1017 (s), 985 (s), 827 (m), 791 (m), 748 (m), 678 (m), 641 (m), 597 (m), 560 (m), 530 (m), 479 (w), 442 (w).

2.4.6 Single-crystal X-ray crystallography

Crystals of the ligand and the complexes **2.2** − **2.13** were mounted on a cryoloop with paratone oil and examined on a Bruker APEX diffractometer equipped with CCD area detector and Oxford Cryostream cooler using graphite-monochromated Mo-*K*α radiation (λ = 0.71073 Å). Data were collected using the APEX-II software[32], integrated using SAINT[33] and corrected for absorption using a multi-scan approach (SADABS)[34]. Single crystals of complex **2.14** were mounted on a cryoloop with paratone oil and measured on a Bruker APEX-II diffractometer equipped with an Oxford Cryoflex low temperature device and an Incoatec Mo micro-source. Data were collected at 150(2) K using graphite-monochromated Mo-Kα radiation (λ = 0.71073 Å) using the APEX-II software.

Final cell constants were determined from full least squares refinement of all observed reflections. The structures were solved using Olex2[35], with the ShelXT structure solution program[36] using intrinsic phasing and refined within the ShelXL[37] refinement package using least-squares minimization on F^2. All hydrogen atoms were added at calculated positions and refined isotropically with a riding model.

PLATON/SQUEEZE[38] was used to treat the contents of the voids because the electron density was too diffuse to model on complexes **2.3b**, **2.4**, **2.6**, **2.7**, **2.11** and **2.13.**

Complex **2.5** exhibited disorder of the water molecule which was modelled over two sites in a 75:25 ratio with a common U_{iso}. Complex **2.7** exhibited rotational disorder on all four CF_3 groups in the asymmetric unit, which were modelled over two sites in a 1:1 ratio and refined anisotropically. TWINROTMAT within PLATON revealed a possible non-merohedral twin and a modest improvement in R_1 value. The data were re-examined using cell_now which confirmed the twin law and the data were re-integrated as a two component non-merohedral twin and an absorption correction applied using TWINABS. Complexes **2.8** and **2.10** exhibited rotational disorder on one of the four CF_3 groups in the asymmetric unit, which was modelled over two sites in a 1:1 ratio with a common U_{iso}. Complex **2.9** exhibited rotational disorder on two of the eight CF_3 groups in the asymmetric unit, which were modelled over two sites in a 1:1 ratio with a common U_{iso}. Complex **2.11** revealed substantial disorder of the one pyridyl ring which was modelled as two over two sites in a 70:30 ratio and also exhibited rotational disorder of both CF_3 groups in the asymmetric unit which were modelled over two sites in a 1:1 ratio with a common U_{iso}. A summary of key crystallographic data for the ligands and the complexes is presented in Appendix 1.

2.5. References

1 E. R. Clark, M. U. Anwar, B. J. Leontowicz, Y. Beldjoudi, J. J. Hayward, W. T. K. Chan, E. L. Gavey, M. Pilkington, E. Zysman-Colman and J. M. Rawson, *Dalton Trans.*, 2014, **43**, 12996.

2 E. R. Clark, J. J. Hayward, B. J. Leontowicz, M. U. Anwar, M. Pilkington and J. M. Rawson, *Dalton Trans.*, 2014, **44**, 2071.

3 A. K. Pal, D. B. Cordes, K. Pringouri, M. U. Anwar, A. M. Z. Slawin, J. M. Rawson and E. Zysman-Colman, *J. Coord. Chem.*, 2016, **69**, 1924.

4 N. Yutronkie, I. Kuehne, I. Korobkov, J. L. Brusso and M. Murugesu, *Chem. Commun.*, 2015, 677.

5 K. L. M. Harriman, I. A. Kühne, A. A. Leitch, I. Korobkov, R. Clérac, M. Murugesu and J. L. Brusso, *Inorg. Chem.*, 2016, **55**, 5375.

6 A. Trummal, L. Lipping, I. Kaljurand, I. A. Koppel and I. Leito, *J. Phys. Chem. A*, 2016, **120**, 3663.

7 N. J. Tro, *Chemistry: A molecular approach*, Pearson, New Jersey, 2nd Ed., 2011.

8 M. Ellinger, H. Duschner and K. Starke, *J. Inorg. Nucl. Chem.*, 1978, **40**, 1063.

9 Z. Chen, L. Quan, L. Liu, Y. Wang, H. Zou and F. Liang, *Eur. J. Inorg. Chem.*, 2015, **2015**, 1463.

10 E. E. Moushi, C. Lampropoulos, W. Wernsdorfer, V. Nastopoulos, G. Christou and A. J. Tasiopoulos, *J. Am. Chem. Soc.*, 2010, **132**, 16146.

11 J.-L. Jin, Y.-L. Shen, Y.-P. Xie and X. Lu, *CrystEngComm*, 2018, **20**, 2036.

12 H. Zhang, B. Li and E. V. Dikarev, *J. Clust. Sci.*, 2008, **19**, 311.

13 H. Zhang, B. Li, J. Sun, R. Clérac and E. V. Dikarev, *Inorg. Chem.*, 2008, **47**, 10046.

14 E. R. Clark, J. J. Hayward, B. J. Leontowicz, D. J. Eislera and J. M. Rawson, *CrystEngComm*, 2014, **16**, 1755.

15 J. Coates, *Encycl. Anal. Chem.*, 2006, 1.

16 J. G. Stark and H. G. Wallace, *Chemistry Data Book*, J. Murray. Publ., London, S. I. Edit., 1980.

17 N. N. Earnshaw and A. Greenwood, *Chemistry of the Elements*, Pergamon Press, Oxford, 1st edn., 1986.

18 P. Kaszynski and V. G. Young, *J. Org. Chem.*, 2004, **69**, 2551.

19 *AIST Integr. Spectr. Database Syst. Org. Compd. (Data were obtained from Natl. Inst. Adv. Ind. Sci. Technol. (Japan)), SciFinder search*.

20 *ACD-A Sigma-Aldrich (Spectral data were obtained from Adv. Chem. Dev. Inc.), SciFinder Search*.

21 N. N. Earnshaw and A. Greenwood, *Chemistry of the Elements*, Pergamon Press, Oxford, 1st edn., 1986.

22 A. W. Addison and T. N. Rao, *J. Chem. Soc., Dalton Trans.*, 1984, 1349.

23 M. Calligaris, *Coord. Chem. Rev.*, 2004, **248**, 351.

24 L. Yang, D. R. Powell and R. P. Houser, *Dalton Trans.*, 2007, 955.

25 R. M. Silverstein, G. C. Bassler and T. C. Morrill, *Spectroscopic Identification of Organic Compounds*, J. Wiley, 4th edn., 1981.

26 Y. Li, T. Thiemann, T. Sawada, S. Mataka and M. Tashiro, *J. Org. Chem.*, 1997, **62**, 7926.

27 PIP4WIN v.1.2, 2011, J.M. Rawson, University of Windsor, Windsor, ON.

28 A. D. Becke, *J. Chem. Phys.*, 1993, 5648.

29 C. Lee, W. Yang and R. G. Parr, *Phys. Rev. B Condens. Matter*, 1988, 785.

30 A. S. Miehlich, H. Stoll and H. Preuss, *Chem. Phys. Lett.*, 1989, 200.

31 A. D. Bochevarov, E. Harder, T. F. Hughes, J. R. Greenwood, D. A. Braden, D. M. Philipp, D. Rinaldo, M. D. Halls, J. Zhang and R. A. Friesner, *Int. J. Quantum Chem.*, 2013, **113**, 2110.

32 APEX-II, Bruker AXS, Inc., Madison, Wisconsin, USA.

33 SAINT, Bruker AXS Inc., Madison, Wisconsin, USA.

34 SADABS, Bruker AXS Inc., Madison, Wisconsin, USA.

35 O. V. Dolomanov, L. J. Bourhis, R. . Gildea, J. A. K. Howard and H. Puschmann, *J. Appl. Cryst.*, 2009, **42**, 339.

36 G. M. Sheldrick, *Acta Cryst.*, 2015, **A71**, 3.

37 G. M. Sheldrick, *Acta Cryst.*, 2015, **C71**, 3.

38 A. L. Spek, *Acta Crystallogr*, 2015, **C71**, 9.

CHAPTER 3.

Synthesis and characterization of pmbtdaH and its coordination chemistry

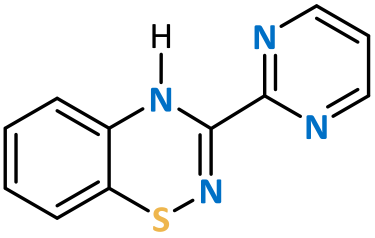

3.1. Introduction

The 3-(2′-pyridyl)-functionalized benzothiadiazine (pybtdaH) has been shown to form a series of chelate complexes to first row transition metal complexes of formula MCl$_x$(pybtdaH)$_y$.[1] More recently, it has been shown that the S^{II} system undergoes aerial oxidation to the S^{IV} system (Scheme 3.1) in the presence of a Lewis acidic metal and a base, such as Et$_3$N or K$_2$CO$_3$.[2] In this process, it seems likely that initial *N*-coordination activates the benzothiadiazine ring to *S*-oxidation and *N*-deprotonation, proceeding *via* a pybtda$_{ox}^{-}$ anion which has been isolated in the form of [Cu(pybtda$_{ox}$)$_2$]$_2$[2] and Ir(ppy)$_2$(pybtda$_{ox}$).[3] *S*-oxidation of some other thiazyl heterocycles at metal centres has also been described recently.[4,5]

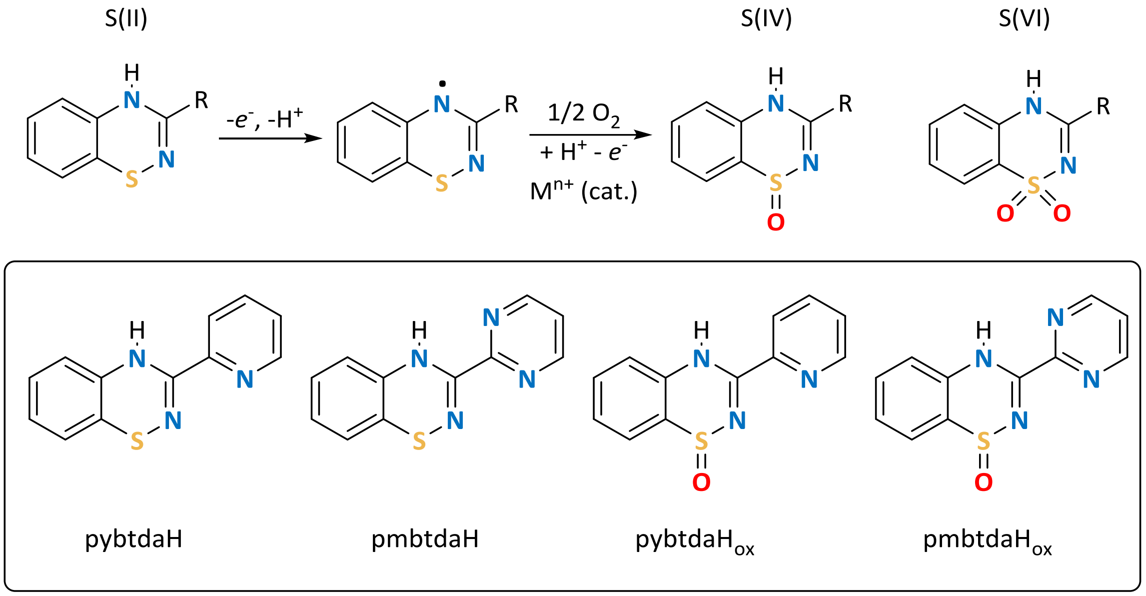

Scheme 3.1 (top) Formal S^{II}, S^{IV} and S^{VI} oxidation states of the benzothiadiazine framework; (bottom) S^{II} and S^{IV} variants of the 2-pyridyl and 2-pyrimidinyl benzothiadiazine heterocycles.

Although previous studies indicated that *S*-oxidation of pybtdaH and other benzothiadiazines only occurred in the presence of a metal ***and*** Et$_3$N[2], in Chapter 2 it was shown that the *S*-oxidation can also proceed in the presence of more basic auxiliary ligands, such as hfac^{-} and OAc^{-} groups, without the addition of any formal base. Specifically when using metal salts of strong acids such as MCl$_2$ the displaced anion (chloride) has no effect on pH since chloride is the conjugate base of a strong acid (pK_a (HCl) = -6.1 [6]) and has minimal base character. Conversely the hfac$^-$ anion is the conjugate base of a weak acid (pK_a (Hhfac) = 4.71 [7]) and generation of hfac$^-$ in solution appears sufficient to promote the oxidation of the coordinated pybtdaH ligand. Nevertheless the introduction of additional base (Et_3N) in the reaction scheme appears to assist the *S*-oxidation and the deprotonation of the pybtdaH ligand, resulting in higher nuclearity clusters.

In this chapter, we will present the synthesis and characterization of the 3-pyrimidinyl-benzothiadiazine (pmbtdaH, Scheme 3.1) as well as its coordination chemistry to selected first row transition metal centres. The choice of this ligand is based on its versatility of coordination modes to metal centres as shown in Figure 3.1. The pmbtdaH ligand offers one coordination pocket to a metal centre through *N*,*N*′-chelation but in its anionic (pmbtda$^-$) or radical form ($\text{pmbtda}^{\bullet}$) the ligand offers a second chelate pocket with the ability to bridge two metal centres (Figure 3.1, left). The *S*-oxidation of this ligand to S^{IV} offers a more versatile hard *O*-donor centre in addition to the favourable, softer, *N*,*N*′-chelate, leading to the potential for enhanced aggregation with the pmbtda_{ox}^- ligand capable of binding three metal ions (Figure 3.1, right).

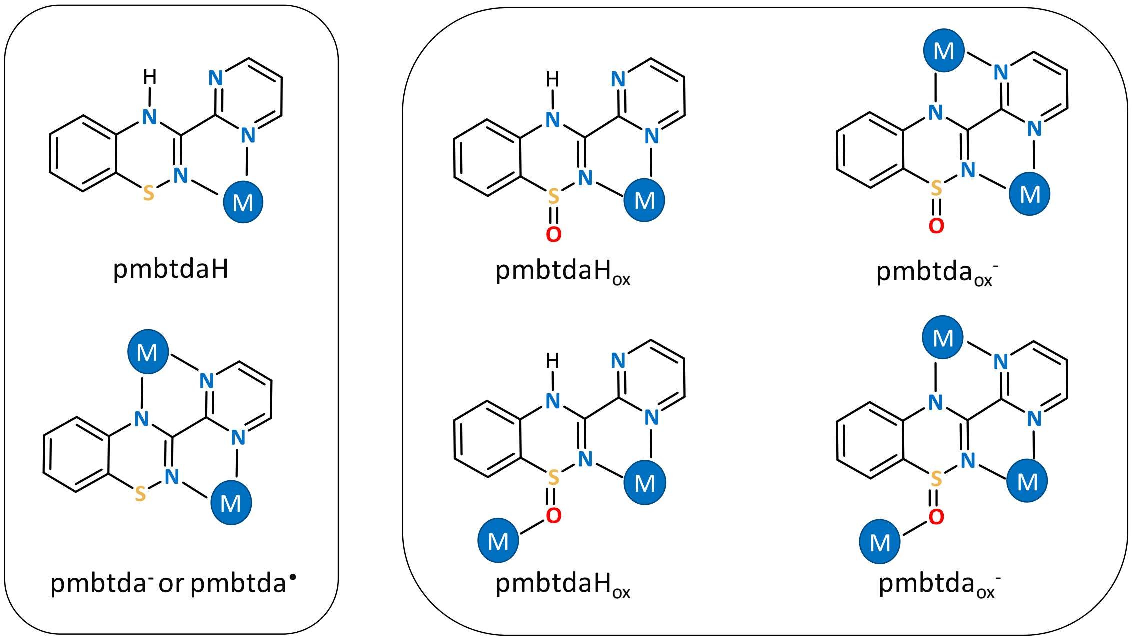

Figure 3.1 Coordination modes of neutral or anionic S^{II} (left) and the S^{IV} (right) benzothiadiazine ligand.

3.2. Results and Discussion

3.2.1 Synthesis and characterization of the ligand pmbtdaH

3.2.1.a Synthesis of pmbtdaH

The ligand pmbtdaH was synthesised according to the synthetic route shown in Scheme 3.2.[8]

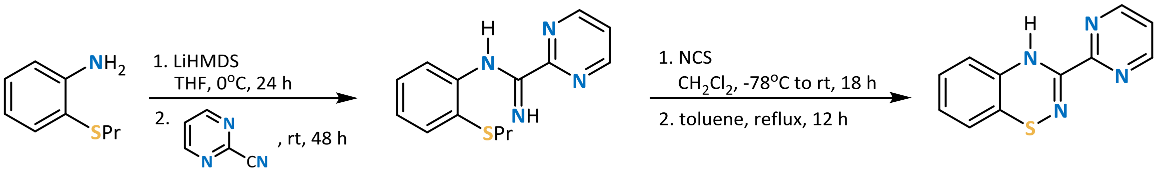

2.1 **3.1**, 59% **pmbtdaH**, 35%

Scheme 3.2 Synthetic route to ligand pmbtdaH.

Deprotonation of 2-(propylthio)phenylamine (**2.1**) with LiHMDS, under anaerobic, dry conditions followed by treatment with one equivalent of 2-pyrimidinecarbonitrile and work-up resulted in the intermediate product (**3.1**) as a brown oil. The oil was washed with hexanes to yield **3.1** in 59% yield as an off-white crystalline powder. Single-crystal X-ray diffraction revealed the product shown in Figure 3.2. The ^{1}H NMR proved problematic where a proton was absent from the spectrum and from the interpretation of 2D NMR spectra it was assigned as the proton on C(10). Further evidence from ^{13}C 135-DEPT NMR experiments identified all *sp*^{2} carbons of the compound present indicating the carbon

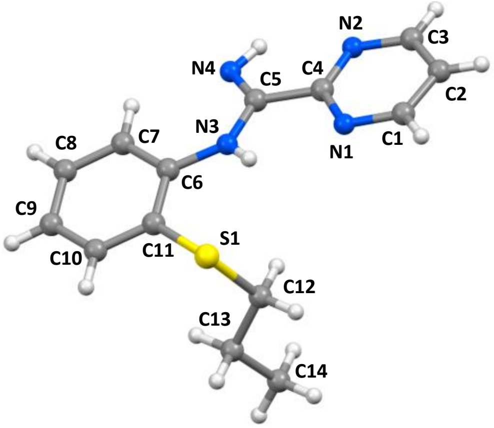

Figure 3.2 Molecular structure of 2-(propylthiophenyl)-picolinamidine (**3.1**).

C(10) has a hydrogen atom attached. In addition, the signal of the proton on C(10) is present in the NMR spectra of the ligand pmbtdaH.

The subsequent oxidative cyclization and pericyclic elimination of **3.1** in the presence of *N*-chlorosuccinimide (NCS) afforded the ligand pmbtdaH, which was isolated in 35% yield after purification by column chromatography using dichloromethane as eluent. The ^{1}H NMR spectrum of ligand pmbtdaH exhibits the expected proton environments in the aromatic region. The N-H vibration was observed at 3324 cm^{-1} and the imine C=N stretching vibration was observed at 1630 cm^{-1}, as expected.[9] Single crystals were grown by slow evaporation from dichloromethane.[10]

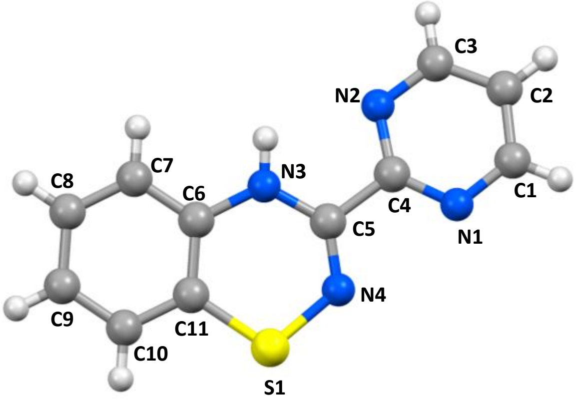

Figure 3.3 Molecular structure of pmbtdaH.

The molecular structure was further confirmed by single crystal X-ray studies. The compound crystallizes in the monoclinic space group $P2_1/c$ with one molecule in the asymmetric unit (Figure 3.3). The C(5)-N(4) distance is 1.282(3) Å, consistent with predominant double bond character (*cf* imine C=N at 1.279 Å)[11]. The bond length between C(5)-N(3) at 1.367(3) Å is more consistent with a conjugated C-N single bond (*cf* Ph-NH_2 at 1.355 Å).[11] The S-N bond length (1.691(2) Å) is comparable with other S-N single bonds (1.62 – 1.74 Å for isomers of $S_{8-x}(NH)_x$)[12] and 1.69 – 1.72 Å for other benzothiadiazine derivatives).[8] As with other benzothiadiazines, the ring is folded (by θ) about the trans-annular vector S(1)···N(3). The values for the majority of previously reported benzothiadiazines fall in the range 21° < θ < 42° [8] whereas θ is just 12.37° in pmbtdaH, presumably to optimize packing factors (*vide infra*). The folding of the ring is consistent with the formally 8π anti-aromatic nature of the thiadiazine framework. Two possible tautomers exist for the ligand, depending on whether N(3) or N(4) atom (Figure 3.3) is protonated. The shorter imine-like C(5)-N(4) and longer C(5)-N(3) bonds coupled with an N-H···N hydrogen bonding pattern along the crystallographic *c* axis ($d_{N\text{-}H\cdots N}$ = 2.826 Å, $\theta_{N\text{-}H\cdots N}$ = 145.10°, Figure 3.4) clearly point to protonation at N(3). This was additionally supported by DFT calculations (B3LYP-D3/6-311G^{*+}) which revealed the tautomer with the H atom bonded at N(3) was more stable by 30 kJ/mol.

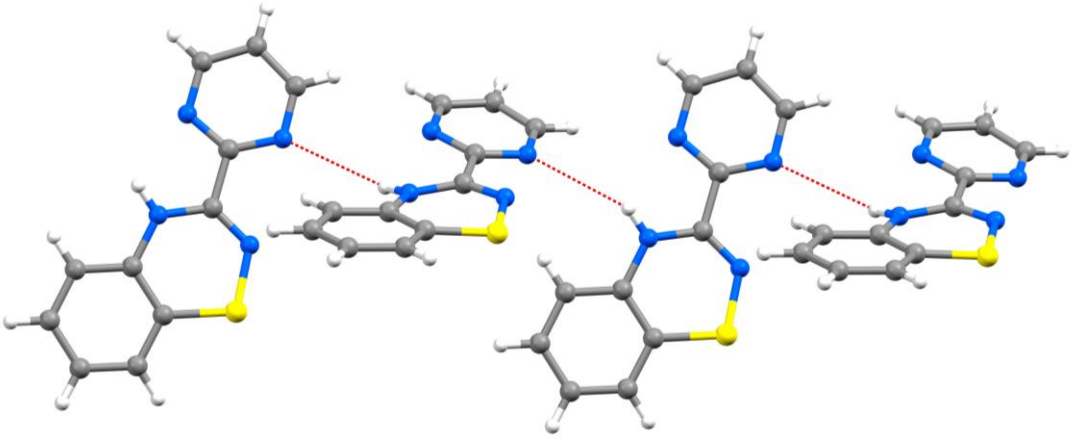

Figure 3.4 Crystal packing of pmbtdaH highlighting N-H···N hydrogen bonding along *c* axis.

Notably pmbtdaH was contaminated with slightly variable quantities (mostly < 10%) of Cl-pmbtdaH in which the benzo ring has been chlorinated *para* to the NH group. This was based on X-ray determination of the metal complexes, presented in Section 3.2.2 and 3.2.3, and it was the case only in some batches of the synthesis where the ligand was used without further purification. Chlorination appears to be driven by the presence of a slight molar excess of NCS during synthesis.

3.2.1.b Electrochemical studies on pmbtdaH

The redox state of pmbtdaH was monitored by cyclic voltammetry. The electrochemical studies of the ligand pmbtdaH ($C_0 = 8.72 \times 10^{-3}$ mol·L^{-1}) were performed using a deoxygenated solution of $^{n}Bu_4N(PF_6)$ (0.1 M) in dichloromethane with Pt workingand counter-electrodes and an Ag$^+$/AgCl/KCl reference electrode which was referenced to the ferrocene/ferrocenium redox couple ($E_{½}$(Fc$^+$/Fc) = 502 mV *vs* SCE) and values quoted are therefore calibrated to the saturated calomel electrode (SCE) scale. Two pseudo reversible oxidation peaks were observed at 1.01 V and 1.26 V (Figure 3.5). In contrast, the ligand pybtdaH revealed two non-reversible oxidation peaks at 0.75 and 1.25 V.[13]

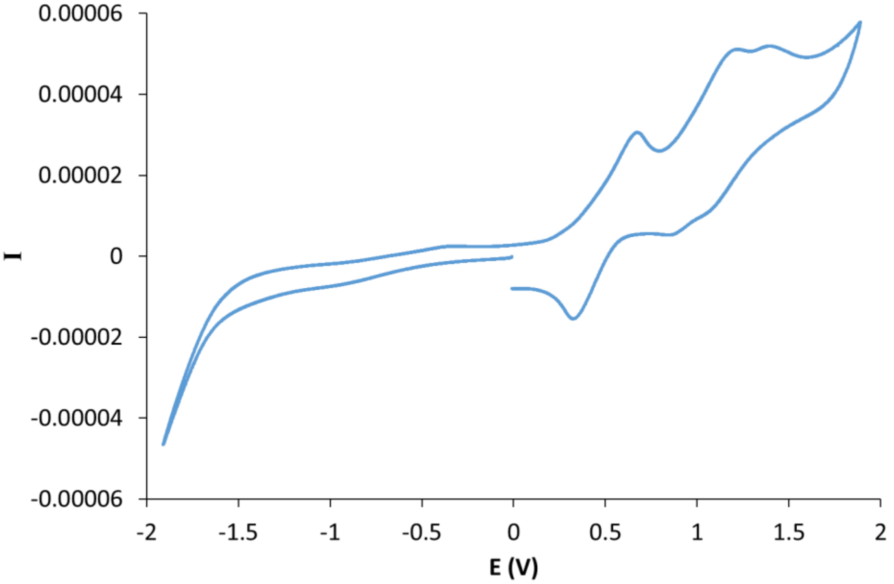

Figure 3.5 Cyclic voltammogram of ligand pmbtdaH (C_0 = 8.72 x 10^{-3} mol·L^{-1}) in a solution of ^{n}Bu$_4$N(PF$_6$) in dichloromethane (0.1 M) (Pt working- and counter-electrodes and an Ag$^+$/AgCl/KCl reference electrode which was referenced to the ferrocene/ferrocenium redox couple ($E_{½}$(Fc$^+$/Fc) = 502 mV *vs* SCE)) .

3.2.1.c *In situ* 1*e*⁻ oxidation of pmbtdaH: DFT and EPR studies

The *in situ* 1*e*⁻ oxidation of pmbtdaH with excess Ag$_2$O in dichloromethane at room temperature in an EPR tube afforded the radical pmbtda$^•$. This radical exhibited an apparent pentet spectrum consistent with coupling of the unpaired *e*⁻ to two near-equivalent ^{14}N nuclei and as expected for btda radicals.[14] The fine structure of the second derivative could only be replicated by taking into account coupling to an additional two ^{1}H nuclei. The best fit of the spectrum afforded g_{iso} = 2.0060, 1 x a_N = 5.66 G, 1 x a_N = 4.93 G, 1 x a_H = 2.11 G and 1 x a_H = 1.30 G (Figure 3.6, left). The EPR spectrum is consistent with the spin density distribution determined from DFT calculations which reveal spin delocalization around the benzothiadiazine ring but with significant (positive) spin density at just two of the four possible benzo C-H groups (Figure 3.6, right).

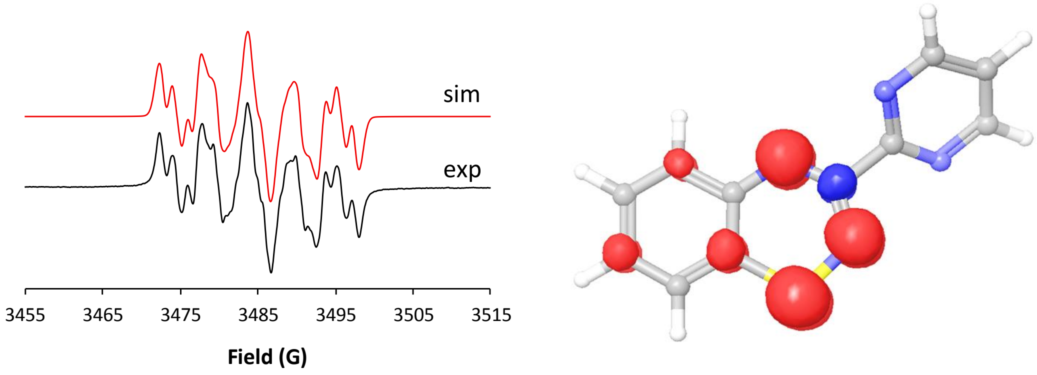

Figure 3.6 (left) Solution EPR spectrum and simulation of the radical pmbtda$^{\bullet}$; (right) computed spin density distribution (UB3LYP/6-311G*) with red indicating regions of positive spin density and blue reflecting regions of negative spin density.

3.2.2 Coordination chemistry of pmbtdaH with MCl_2 (M = Mn, Fe, Co, Ni, Zn)

3.2.2.a Syntheses and crystal structures of $[MCl_2(pmbtdaH)_2]\cdot 2CH_3OH$ (M = Mn (3.2), Fe (3.3), Co (3.4), Ni (3.5))

Reaction of pmbtdaH with the corresponding divalent metal chloride salt in CH_3OH in a 2:1 molar ratio at ambient temperature afforded the complexes $MCl_2(pmbtdaH)_2$ (M = Mn (**3.2**), Fe (**3.3**), Co (**3.4**), Ni (**3.5**)). Crystals suitable for X-ray diffraction were grown by storage of saturated solutions over periods between 1 and 5 days. The structures of $[MCl_2(pmbtdaH)_2]\cdot 2CH_3OH$ were found to be isomorphous, crystallising in the orthorhombic space group *Pbcn* with half a molecule of $MCl_2(pmbtdaH)_2$ and a methanol solvent molecule in the asymmetric unit. The formation of complexes **3.2** − **3.5** is summarized in Equation 3.1.

$$\mathrm{MCl_2 + 2\ pmbtdaH \longrightarrow MCl_2(pmbtdaH)_2}$$ Equation 3.1

In all cases, the metal centre is in oxidation state 2+ and adopts a pseudo-octahedral geometry with the two chloride ligands mutually *cis* and the N atoms located *trans* to the Cl atoms. The structure of complex **3.4** is shown in Figure 3.7 as representative of this series of structures (for complexes **3.2** − **3.5**) and selected bond lengths and angles are shown in Table 3.1. The general trend in metal-ligand bond lengths for complexes **3.2** − **3.5** are all consistent with a (high-spin) M^{II} centre with the decrease (M = Mn to Ni) associated with increasing effective nuclear charge on traversing the first transition metal series.

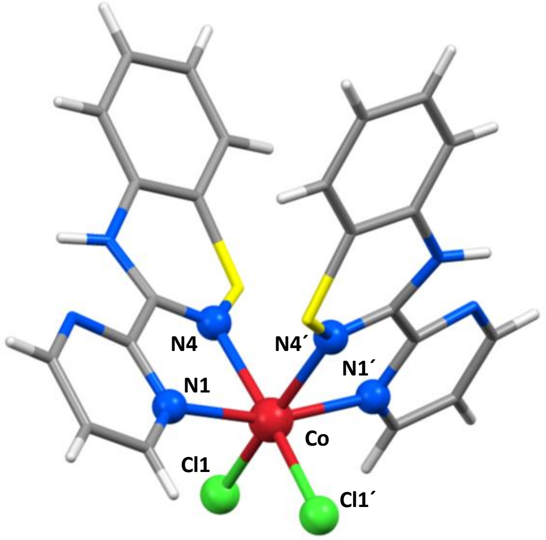

Figure 3.7 Molecular structure of $CoCl_2(pmbtdaH)_2$ (**3.4**, solvent molecules omitted for clarity).

The ligand adopts a simple *N*,*N*′-chelate mode to a single metal centre in which the pyrimidyl N(1) and the heterocyclic N(4) atoms are involved in metal binding. The chelate ligand pmbtdaH exhibits internal N_{pm}-M-N_{BTDA} angles in the range 70.93(7) – 77.28(7)°. The complexes have a partially occupied Cl atom on C(9) of the benzo ring of the pmbtdaH as a result of chlorination during the synthesis of the ligand (section 3.2.1.a) with site occupancy factors of 10 % based on fitting the residual electron density.

All the metal complexes of this series have two CH_3OH molecules in their lattice. The molecules are linked *via* a N-H···O hydrogen bonding interaction (for complex **3.4** $d_{N\text{-}H\cdots O}$ = 2.126 Å, $\theta_{N\text{-}H\cdots O}$ = 148.75°) from the heterocyclic N-H to one of the CH_3OH oxygen atoms. In addition, the molecules are linked *via* O-H···Cl hydrogen bonding from the CH_3OH oxygen atoms and the chlorides on the metal complex (for complex **3.4** $d_{O\text{-}H\cdots Cl}$ = 2.471 Å, $\theta_{O\text{-}H\cdots Cl}$ = 150.22°, Figure 3.8, top). The packing of **3.4** places the benzo rings of neighbouring molecules in close proximity having centroid···centroid distances of 3.751 Å with the closest C···C distance at 3.659 Å (*cf* interlayer separation in graphite at 3.354 Å[12]) (Figure 3.8, bottom).

Table 3.1 Selected bond lengths and angles for complexes **3.2** – **3.5**.

	M-N_{pm}/Å	M-N_{BTDA}/Å	M-Cl/Å	$N_{pm}MN_{BTDA}$/°^{a}	N_{pm}MCl/°	N_{BTDA}MCl/°	ClMCl/°
Mn (**3.2**)	2.2507(17)	2.3242(19)	2.4438(6)	70.93(7)	92.42(5)	87.54(5)	105.53(3)
				88.44(7)	104.17(5)	161.17(5)	
Fe (**3.3**)	2.1640(19)	2.237(2)	2.4002(7)	73.50(8)	92.69(6)	88.25(6)	101.61(6)
				89.54(8)	101.62(6)	164.37(6)	
Co (**3.4**)	2.132(2)	2.173(2)	2.3911(7)	75.29(8)	92.54(6)	87.45(6)	101.80(4)
				91.79(8)	98.46(5)	165.80(6)	
Ni (**3.5**)	2.0753(17)	2.1187(18)	2.3906(6)	77.28(7)	92.50(5)	87.41(5)	98.60(3)
				91.96(7)	97.21(5)	168.78(5)	

	N-H···O/Å	N-H···O/°	O-H···Cl/Å	O-H···Cl/°	C···C/Å^b	centroid-centroid/Å
Mn (**3.2**)	2.148	150.08	2.512	154.07	3.605	3.615
Fe (**3.3**)	2.127	150.29	2.500	149.45	3.625	3.635
Co (**3.4**)	2.126	148.75	2.471	150.22	3.659	3.751
Ni (**3.5**)	2.126	147.74	2.417	155.15	3.669	3.679

[a] top: Angle within the chelate ring; bottom: Angles between N atoms in different rings [b] Closest C···C distance

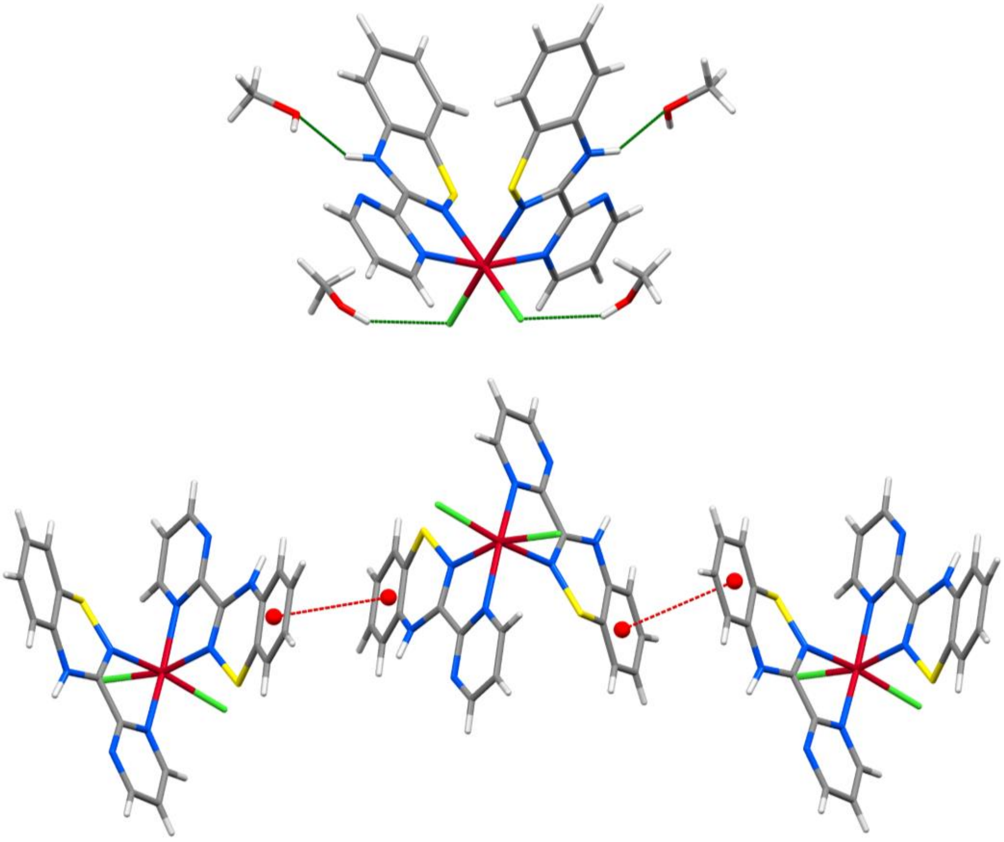

Figure 3.8 Molecular structure of **3.4** highlighting hydrogen bonding between the heterocyclic N-H and the O atoms of the solvent CH_3OH molecules, the O-H of the CH_3OH and the Cl of the complex (green); (bottom) π-π interactions between the benzo rings of the neighbouring molecules (red).

Complex **3.2** can also be isolated by the reaction in dichloromethane, where the methanol solvate molecules are replaced by two molecules of CH_2Cl_2 and the structure is crystallizing in the monoclinic space group $P2_1/c$ with one molecule and CH_2Cl_2 in the asymmetric unit). Complex **3.3**, in which Fe is in oxidation 2+, was produced from reaction of $FeCl_2$ with pmbtdaH but also formed unexpectedly from reaction of $FeCl_3$ with pmbtdaH. Notably the recovered yield was higher (23% as opposed to 15%) and the quality of the crystals proved better for single crystal X-ray diffraction. Generation of **3.3** from reaction of pmbtdaH with $FeCl_3$ can be considered to arise from stoichiometric $1e^-$ reduction of $FeCl_3$ by pmbtdaH which is known to oxidize to pmbtda$^\bullet$. The overall stoichiometric equation is shown in Equation 3.2.

$$FeCl_3 + 3\,\text{pmbtdaH} \longrightarrow FeCl_2(\text{pmbtdaH})_2 + \text{pmbtda}^{\bullet} + HCl \qquad \text{Equation 3.2}$$

Complex **3.4** (M = Co) can also be isolated by the 1:1 molar ratio of ligand to metal but with a lower yield, suggesting that the binding constant (β_2) for the second equivalent of pmbtdaH is greater than β_1 for Co which is in contrast to Zn (below).

3.2.2.b Synthesis and crystal structure of $Zn_2Cl_4(\text{pmbtdaH})_2$ (3.6)

Reaction of the ligand pmbtdaH with $ZnCl_2$ in CH_2Cl_2 in a 1:1 molar ratio at ambient temperature afforded a dark precipitate. Crystals of the red dinuclear complex $Zn_2Cl_4(\text{pmbtdaH})_2$ (**3.6**) were formed upon slow evaporation of a CH_3OH solution over one week. The structure of **3.6** was determined by X-ray diffraction (Figure 3.9) and crystallizes in the triclinic space group $P\overline{1}$ with half a molecule in the asymmetric unit and the complete molecule located about the crystallographic inversion centre. The formation of complex **3.6** is summarized in Equation 3.3.

$$2\,ZnCl_2 + 2\,\text{pmbtdaH} \longrightarrow Zn_2Cl_4(\text{pmbtdaH})_2 \qquad \text{Equation 3.3}$$

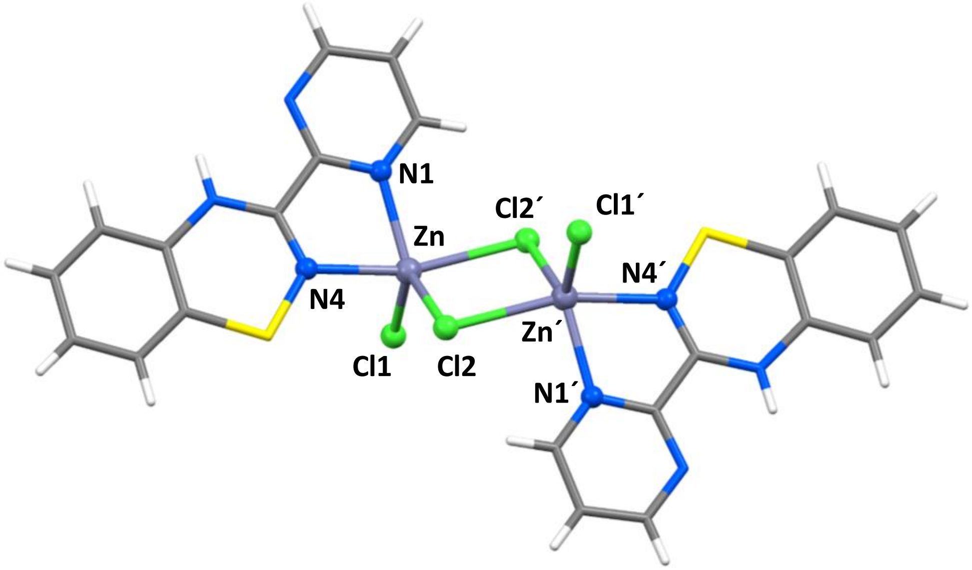

Figure 3.9 Molecular structure of $Zn_2Cl_4(\text{pmbtdaH})_2$ (**3.6**).

The crystallographically unique zinc ion adopts a 5-coordinate geometry with an N_2Cl_3 donor set. The Addison τ_5 value[15] (0.56) is consistent with a geometry intermediate between trigonal bipyramidal (τ = 1) and square pyramidal (τ = 0). Approximating the geometry to trigonal bipyramidal, the N(4)-Zn(1)-Cl(2′) angle (163.07(7)°) defines the axial orientation, with the remaining angles in the equatorial plane in the range 112.59(3) – 129.63(7)°. Notably, the two Cl anions adopt different coordination modes; Cl(1) adopts a terminal coordination mode whereas Cl(2) takes up a μ_2-bridging mode between two Zn^{II} centres. The Zn(1)-Cl(1) bond length (2.238(1) Å) for the terminal chlorine is comparable with other Zn-Cl bonds (2.125 – 2.760 Å).[16] The bond lengths for the two bridging chlorides (2.303(1) Å for Cl(2) and 2.5502(9) Å for Cl(2′)) are also comparable with other bridging Cl in the literature (2.253 – 2.708 Å).[17] The ligand adopts a simple *N*,*N*′-chelate mode to a single Zn(1) centre in which the pyrimidinyl N(1) and heterocyclic N(4) atoms are involved in metal binding, as discussed earlier. The packing of **3.6** places the benzo rings in close proximity with the pyrimidine rings of the neighbouring molecule having centroid···centroid distances of 3.762 Å with the closest C···centroid distance at 3.444 Å (*cf* interlayer separation in graphite at 3.354 Å[12]). In addition, the molecules are linked *via* N-H···Cl hydrogen bonding ($d_{N\cdots Cl}$ = 3.321(3) Å, $\theta_{N\text{-}H\cdots N}$ = 143.09°, Figure 3.10).

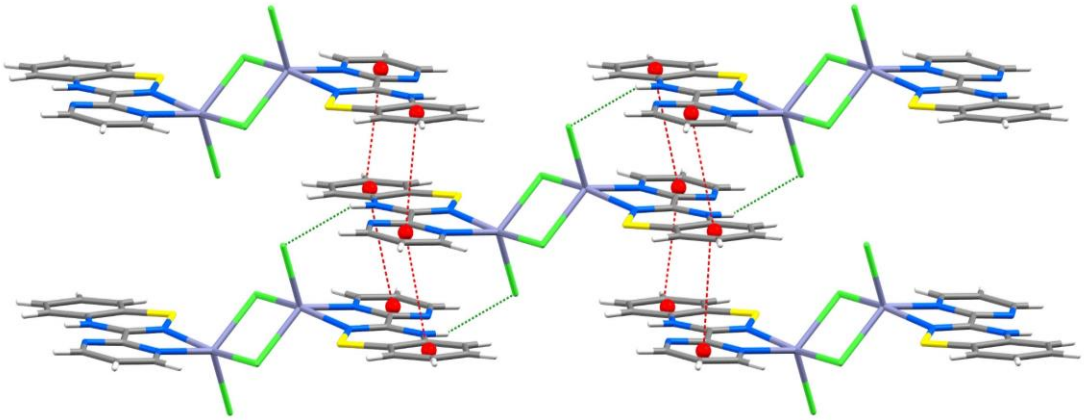

Figure 3.10 Crystal packing of **3.6** highlighting the π-π interactions (red) and the N-H···Cl hydrogen bonding between the heterocyclic N-H and the Cl atoms of the neighbouring molecule (green).

3.2.3 Coordination chemistry of pmbtdaH with M(hfac)$_2$ (M = Mn, Co, Ni, Cu, Zn)

3.2.3.a Syntheses and crystal structures of M(hfac)$_2$(pmbtdaH) (M = Mn (3.7a), Co (3.8a), Ni (3.9a), Cu (3.10a) and Zn (3.11a))

The metal salts [M(hfac)$_2$]·xH$_2$O, where M = Mn, Co, Ni, Cu, and Zn, were reacted with the ligand pmbtdaH in CH_2Cl_2 in a 1:1 molar ratio at ambient temperature and the solution was layered with hexanes. Red single crystals of the anticipated complexes M(hfac)$_2$(pmbtdaH) (M = Mn (**3.7a**), Co (**3.8a**), Ni (**3.9a**), Cu (**3.10a**) and Zn (**3.11a**)) which were suitable for X-ray diffraction formed over periods between two days and 3 weeks, reflecting the robust nature of these complexes with respect to ligand oxidation. Complex **3.7a** crystallizes in the triclinic space group $P\overline{1}$ with two molecules in the asymmetric unit, complexes **3.8a** and **3.9a** crystallize in the monoclinic $P2_1/c$ with one and two molecules in the asymmetric unit, respectively, whereas complexes **3.10a** and **3.11a** crystallize in the monoclinic space group $C2/c$ with one molecule in the asymmetric unit. The formation of complexes **3.7a** − **3.11a** is summarized in Equation 3.4.

$$\mathrm{M(hfac)_2} + \mathrm{pmbtdaH} \longrightarrow \mathrm{M(hfac)_2(pmbtdaH)} \qquad \text{Equation 3.4}$$

The structure of complex **3.11a** is shown in Figure 3.11 (left) as representative of the series of structures **3.7a** − **3.11a**. All the metal centres are divalent and have a distorted octahedral geometry with a N_2O_4 donor set. The heterocyclic ligand provides an *N*,*N*′-chelate pocket analogous to complex **3.4** through N(1) and N(4) atoms (Figure 3.7). The two hfac$^-$ groups also chelate the metal centre leading to an octahedral coordination geometry. Selected bond lengths and angles are shown in Table 3.2. The general trend in metal-ligand bond lengths for complexes **3.7a** – **3.11a** are consistent with a (high-spin) M^{II} centre with the initial decrease (M = Mn to Ni) associated with increasing effective nuclear charge on traversing the first transition metal series and subsequent increase (Cu and Zn) associated with the addition of extra electrons into the e_g* orbitals. In the case of Cu^{II} (**3.10a**), the complex exhibits a Jahn Teller elongation along the O(1)-Cu-O(4) axis with bond lengths at 2.3000(17) Å and 2.3209(17) Å.

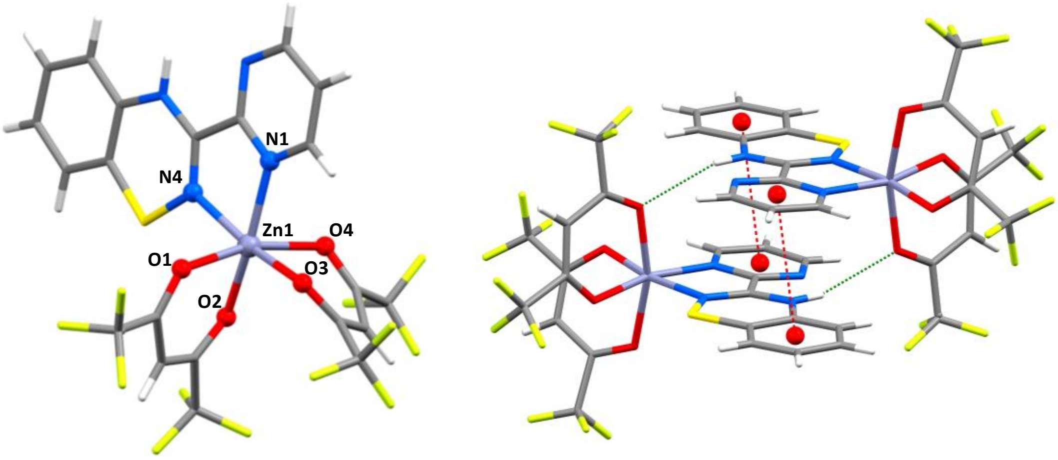

Figure 3.11 (left) Molecular structure of Zn(hfac)$_2$(pmbtdaH) (**3.11a**); (right) Crystal packing of **3.11a** highlighting the π-π interactions (red) and the N-H···O hydrogen bonding between the amino group and the O atoms of the neighbouring hfac$^-$ group (green).

Within the structure of **3.11a**, molecules are linked *via* a N-H···O hydrogen bonding interaction ($d_{\text{N-H}\cdots\text{O}}$ = 2.397 Å, $\theta_{\text{N-H}\cdots\text{O}}$ = 151.82°) from the heterocyclic N-H to one of the hfac$^-$ O atoms. Additional π-π stacking forms a centrosymmetric supramolecular dimer (centroid···centroid distance = 3.874 Å) (*cf* interlayer separation in graphite at 3.354 Å[12]) (Figure 3.11, right).

Table 3.2 Selected bond lengths and angles for complexes **3.7a** – **3.11a**.

	M-N_{pm}/Å	M-N_{BTDA}/Å	M-O/Å	N_{pm}-M-N_{BTDA}/°
Mn (**3.7a**)	2.269(11)(Mn1) 2.285(10)(Mn2)	2.287(11)(Mn1) 2.329(12)(Mn2)	2.146(11)(Mn1) 2.165(10)(Mn1) 2.183(10)(Mn1) 2.211(10)(Mn1) 2.161(8)(Mn2) 2.176(11)(Mn2) 2.178(9)(Mn2) 2.223(10)(Mn2)	72.9(4)(Mn1) 71.8(4)(Mn2)
Co (**3.8a**)	2.104(4)	2.106(4)	2.051(4) 2.054(3) 2.067(4) 2.077(3)	77.50(14)
Ni (**3.9a**)	2.102(5)(Ni1) 2.064(5)(Ni2)	2.113(5)(Ni1) 2.137(5)(Ni2)	2.015(4)(Ni1) 2.022(4)(Ni1) 2.029(4)(Ni1) 2.049(4)(Ni1) 2.001(4)(Ni2) 2.015(4)(Ni2) 2.017(4)(Ni2) 2.068(5)(Ni2)	76.91(18)(Ni1) 78.5(2)(Ni2)
Cu (**3.10a**)	2.004(2)	2.0183(19)	1.9447(18) 1.9696(17) 2.3000(17) 2.3209(17)	80.55(8)
Zn (**3.11a**)	2.123(4)	2.126(4)	2.02(3) 2.041(19) 2.092(18) 2.158(18)	77.42(15)

	N-H···O/Å	N-H···O/°	C···C/Å[a]	centroid-centroid/Å
Mn (**3.7a**)	2.252(Mn1) 2.270(Mn2)	153.92(Mn1) 150.17(Mn2)	3.840(Mn1) 3.510(Mn2)	4.093(Mn1) 3.652(Mn2)
Co (**3.8a**)	2.292	150.64	3.638	3.797
Ni (**3.9a**)	2.202(Ni1) 2.352(Ni2)	157.70(Ni1) 151.98(Ni2)	3.599(Ni1) 3.695(Ni2)	3.765(Ni1) 3.879(Ni2)
Cu (**3.10a**)	2.099	153.14	3.507	3.651
Zn (**3.11a**)	2.397	151.82	3.709	3.874

[a] Closest C···C distance

Such octahedral “triple-chelate” complexes can adopt Λ or Δ forms. In all these complexes both Λ and Δ forms exist in the crystal structure as a racemate. However this is manifested in different ways. In complex **3.11a** there is one molecule in the asymmetric unit with the two hfac$^-$ ligands exhibiting significant structural disorder such that it comprises a racemic mix of both optical isomers. For complex **3.9a** there is no structural disorder but both the Λ and Δ forms are present in the asymmetric unit. The Λ and Δ forms of complex **3.10a** are shown in Figure 3.12, and originate from X-ray collection data on two different crystals of the complex.

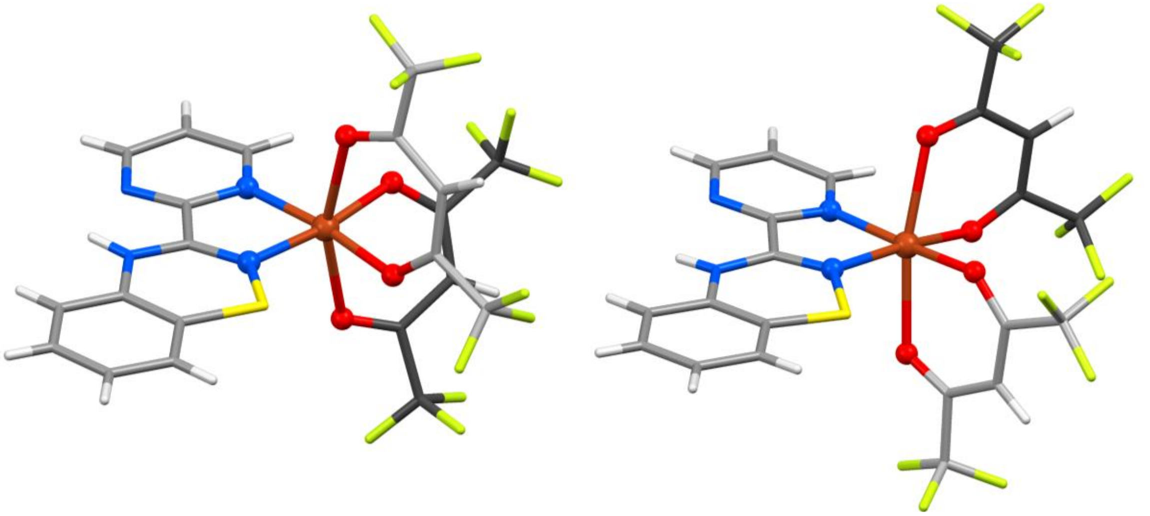

Figure 3.12 Molecular structure of complex **3.10a**, highlighting the two racemic forms the complex can adopt (lighter colour carbon in front of the plane, darker colour carbons behind the plane).

Complex **3.7a** (M = Mn) has a high R_{int} value (10.27%) and all attempts to improve the quality of the crystals, including different ratios, different solvents and crystallization methods, were unsuccessful. Nevertheless, the R_1 and wR_2 were satisfactory (6.97 and 21.37%, respectively) and the connectivity clearly identified.

3.2.3.b Synthesis and crystal structure of $[Mn_2(hfac)_2(tfa)_2(pmbtdaH_{ox})_2]\cdot 2CH_2Cl_2$ (3.7b)

The reaction of $[Mn(hfac)_2]\cdot 3H_2O$ with the ligand pmbtdaH in CH_2Cl_2 in a 1:1 molar ratio at ambient temperature afforded $Mn(hfac)_2(pmbtdaH)$ (**3.7a**) as red crystals (section 3.2.3.a). However, upon prolonged undisturbed storage, a number of lighter coloured crystals formed. The crystals were suitable for single X-ray crystallography which revealed the dinuclear complex $Mn_2(hfac)_2(tfa)_2(pmbtdaH_{ox})_2$ (**3.7b**). The tfa^- anion presumably arises from degradation of the $hfac^-$ anion and decomposition of $hfac^-$ to form tfa^- has been reported previously.[18,19] This is believed to occur through a retro-Claisen condensation reaction of β-diketones (to generate a ketone and a carboxylate) when strong bases are present (Equation 3.5).

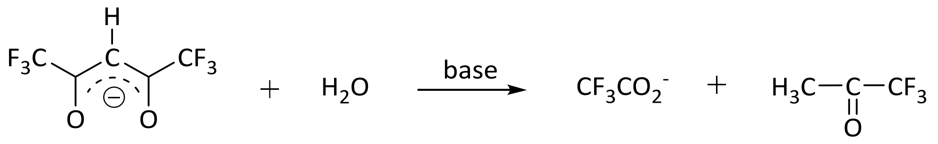

$hfac^-$ tfa^-

Equation 3.5

The decomposition of β-diketonate ligands in metal complexes with alkoxy ligands has also been observed previously[19] and was attributed to the presence of the trace amount of H_2O and the alkoxy ligand in the reaction medium. The pmbtdaH ligand itself could function as the base to promote the decomposition of the $hfac^-$ group. The formation of complex **3.7b** is summarized in Equation 3.6.

$$2Mn(hfac)_2 + 2pmbtdaH + 2H_2O + O_2 \longrightarrow Mn_2(hfac)_2(tfa)_2(pmbtdaH_{ox})_2 + 2CH_3COCF_3$$

Equation 3.6

Complex **3.7b** is the minor product of the reaction of $Mn(hfac)_2$ with pmbtdaH. Attempts to reproduce complex **3.7b** were made by the addition of base and/or H_2O to the reaction mixture but failed to produce **3.7b** without **3.7a** or in higher yields for full characterization.

The structure of complex **3.7b** is shown in Figure 3.13. Complex **3.7b** crystallizes in the triclinic space group $P\overline{1}$ with half a molecule in the asymmetric unit and one molecule of CH_2Cl_2. The two metal centres are in the +2 oxidation state and adopt a distorted octahedral geometry with an N_2O_4 donor set. The neutral ligand has been oxidized and provides an *N*,*N*′-chelate pocket analogous to complex **3.4** through N(1) and N(4) atoms (Figure 3.7) but in this case the oxygen of the sulfoxide does not act as an additional *S*-oxide donor. The chelate ligand pmbtdaH$_{ox}$ exhibits a N$_{pm}$-M-N$_{BTDA}$ bite angle of 72.57(19)° and the bond lengths of Mn-N are 2.257(5) Å for the pyrimidine N and 2.282(6) Å for the benzothiadiazine N. The two hfac⁻ groups chelate the metal centre providing two oxygen atoms to the metal center. The crystal structure also contains two trifluoroacetate (tfa) groups which each provide a μ_2-O bridge between the two metal centres, completing their coordination spheres. All Mn-O bond distances are in the range 2.143(5) – 2.229(4) Å.

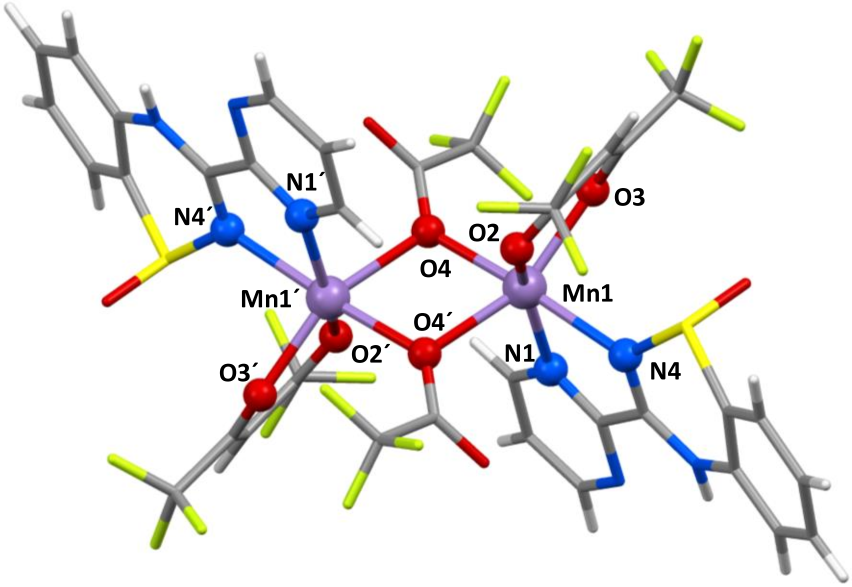

Figure 3.13 Molecular structure of $Mn_2(hfac)_2(tfa)_2(pmbtdaH_{ox})_2$ (**3.7b**, solvent molecules omitted for clarity).

The crystal packing of complex **3.7b** is shown in Figure 3.14. The dimers are linked *via* pairs of centrosymmetric N-H···O=S hydrogen bonding interactions ($d_{N\text{-}H\cdots O}$ = 3.086 Å, $\theta_{N\text{-}H\cdots O}$ = 150.39°) between the heterocyclic N-H group and the sulfoxide oxygen of a neighbouring dimer, forming a one dimensional chain structure parallel to the crystallographic *c*-axis. Formation of these dimers also places the benzo ring close to the pyrimidine ring with centroid···centroid distances of 4.019 Å (closest C···C distance at 3.561 Å). The oxygen atoms of the tfa⁻ group make hydrogen bonds with the C-H group of the benzo ring of another dimer ($d_{C\text{-}H\cdots Otfa}$ = 2.972 Å, $\theta_{C\text{-}H\cdots Otfa}$ = 167.80°) resulting a two dimensional network in the *ac* plane. The packing of **3.7b** places the benzo rings of neighbouring dimers in close proximity with centroid···centroid distances of 2.806 Å with the closest C···C distance at 3.991 Å (*cf* interlayer separation in graphite at 3.354 Å[12]) (Figure 3.14).

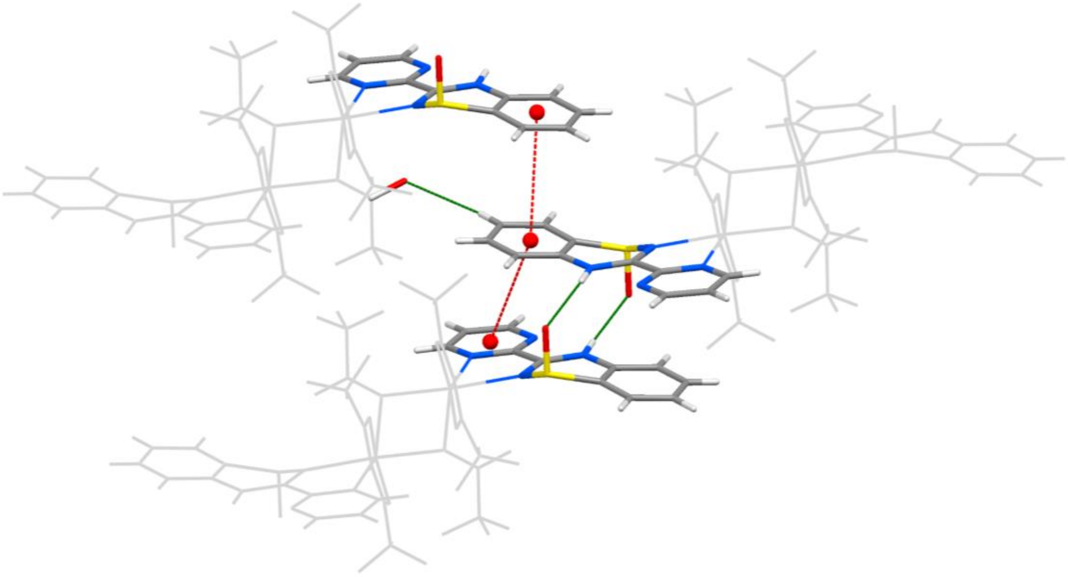

Figure 3.14 Crystal packing of **3.7b** highlighting the π-π (red) interactions and the N-H···O hydrogen bonding between the amino group and the O atoms of the neighbouring sulfoxide group (green) (solvent molecules omitted for clarity).

3.2.3.c Syntheses and crystal structures of M(hfac)$_2$(pmbtdaH$_{ox}$) (M= Co (3.8a), Ni (3.9a))

The reaction of [M(hfac)$_2$]·xH$_2$O, (M = Co, Ni) with the ligand pmbtdaH in CH$_2$Cl$_2$ in a 1:1 molar ratio at ambient temperature afforded the complexes M(hfac)$_2$(pmbtdaH) (M= Co (**3.8a**), Ni (**3.9a**)) as red crystals. The appearance of lighter colour crystals (orange for Co and green for Ni), after extended storage were consistent with ligand oxidation.

The crystals formed were suitable for X-ray diffraction and structural studies revealed mononuclear complexes of formula M(hfac)$_2$(pmbtdaH$_{ox}$) (M= Co (**3.8b**), Ni (**3.9b**·CH$_2$Cl$_2$)). The crystal structures of **3.8b** and **3.9b** are similar to complexes **3.8a** and **3.9a,** respectively, but in this case the ligand has been oxidised to the sulfoxide of the pmbtdaH to form the pmbtdaH$_{ox}$. The formation of complexes **3.8b** and **3.9b** is summarized in Equation 3.7.

$$\mathrm{M(hfac)_2 + pmbtdaH + \tfrac{1}{2}\,O_2 \longrightarrow M(hfac)_2(pmbtdaH_{ox})} \qquad \text{Equation 3.7}$$

Complexes **3.8b** and **3.9b** are the minor products of the reactions which primarily afford the complexes M(hfac)$_2$(pmbtdaH) (**3.8a** and **3.9a**) as the major products. Attempts to increase the yield of **3.8b** and **3.9b** through the introduction of base proved unsuccessful and the complexes could not be isolated in higher yields for full characterization beyond structure determination.

Complex **3.8b** crystallizes in the monoclinic $P2_1/n$ with one molecule in the asymmetric unit whereas complex **3.9b** crystallizes in the triclinic space group $P\overline{1}$ with one molecule and two dichloromethane molecules in the asymmetric unit. Crystals of **3.9b** had a high propensity for twinning and afforded high R_{int} value (13.43%). Nevertheless, the connectivity of the atoms can be clearly identified. The structure of complex **3.9b** is shown in Figure 3.15 (left), as representative of those two complexes (**3.8b** and **3.9b**) and selected bond lengths and angles are shown in Table 3.3.

The metal centres have a distorted octahedral geometry with a N$_2$O$_4$ donor set. The heterocyclic ligand provides an *N*,*N'*-chelate pocket analogous to complex **3.4** through N(1) and N(4) atoms with M-N distances in the range 2.074(11) – 2.122(5) Å and N$_{\text{pm}}$-M-N$_{\text{BTDA}}$ angles in the range 77.09(18) – 78.8(4)°. The two hfac$^-$ groups also chelate the metal centre leading to an octahedral coordination geometry with M-O distances in the range of 1.993(9) – 2.082(10) Å. A comparison with the M(hfac)$_2$(pmbtdaH) complexes (**3.8a** and **3.9a**) where the bond lengths of M-O are in the range of 2.015(4) – 2.077(3) indicates no significant effect on the distances in the metal sphere upon oxidation of the ligand. The M-N bonds show a slight decrease ranging from 2.074(11) – 2.115(5) Å upon oxidation in contrast with the not oxidised ligand pmbtdaH (2.102(5) – 2.137(5) Å).

While the packing of M(hfac)$_2$(pmbtdaH) features N-H···O contacts to hfac O atoms, this is replaced by N-H···O=S in M(hfac)$_2$(pmbtdaH$_{ox}$) indicating the pmbtdaH$_{ox}$ ligand is a good H-bond acceptor. The N-H···O hydrogen bond distances are in the range of $d_{N\text{-}H\cdots O}$ = 2.063 – 2.103 Å with angles in the range $\theta_{N\text{-}H\cdots O}$ = 150.96 – 155.80°. Additional π-π stacking forms a centrosymmetric supramolecular dimer (centroid···centroid distance = 3.816 – 3.817 Å) (Figure 3.15, right).

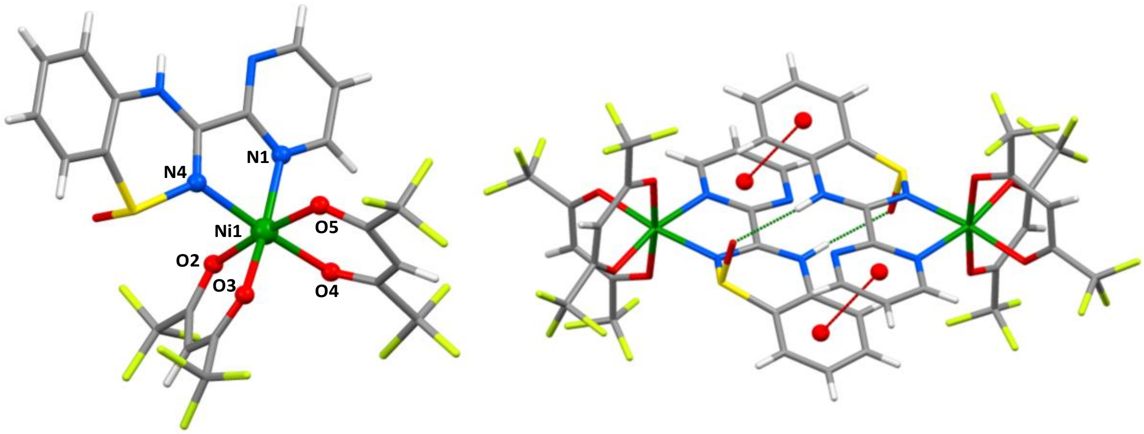

Figure 3.15 (left) Molecular structure of Ni(hfac)$_2$(pmbtdaH$_{ox}$) (**3.9b**); (right) Crystal packing of **3.9b** highlighting the π-π interactions (red) and the N-H···O hydrogen bonding between the amino group and the O atoms of the neighbouring sulfoxide (green) (solvent molecules have been omitted for clarity).

Table 3.3 Selected bond lengths and angles for complexes **3.8b** and **3.9b**.

	$M\text{-}N_{pm}$/Å	$M\text{-}N_{BTDA}$/Å	M-O/Å	$N_{pm}\text{-}M\text{-}N_{BTDA}$/°
Co (**3.8b**)	2.122(5)	2.111(5)	2.040(4) 2.041(4) 2.051(4) 2.058(4)	77.09(18)
Ni (**3.9b**)	2.077(11)	2.074(11)	1.993(9) 2.022(10) 2.045(10) 2.082(10)	78.8(4)
	N-H···O/Å	N-H···O/°	C···C/Å[a]	centroid-centroid/Å
Co (**3.8b**)	2.103	150.96	3.654	3.816
Ni (**3.9b**)	2.063	155.80	3.626	3.817

[a] Closest C···C distance

3.2.3.d Synthesis and crystal structure of $Cu_4(hfac)_4(tfa)_2(pmbtda_{ox})_2$ (3.10b)

The reaction of $[Cu(hfac)_2]\cdot xH_2O$ with the ligand pmbtdaH in CH_2Cl_2 in a 1:1 mole ratio at ambient temperature gave the complex $Cu(hfac)_2(pmbtdaH)$ (**3.10a**) as dark brown crystals. Again, extended storage of the reaction mixture led to the formation of a minor product. The disappearance of the dark coloration, diagnostic of the pmbtdaH ligand, and appearance of green coloured crystals were indicative of ligand oxidation. The crystals were suitable for single X-ray crystallography and revealed a tetranuclear complex of formula $Cu_4(hfac)_4(tfa)_2(pmbtda_{ox})_2$ (**3.10b**). As previously reported in section 2.2.4.b, the presence of tfa^- in the compound is the result of the decomposition of $hfac^-$ ligand (Equation 3.5). The formation of complex **3.11b** is summarized in Equation 3.8.

$$4\ Cu(hfac)_2 + 2\ pmbtdaH + 2\ H_2O + O_2 \longrightarrow Cu_4(hfac)_4(tfa)_2(pmbtda_{ox})_2 + 2\ CH_3COCF_3 + 2\ Hhfac$$

Equation 3.8

Complex **3.10b** (Figure 3.16) crystallizes in the triclinic space group $P\overline{1}$ with half a molecule in the asymmetric unit. In complex **3.10b** the pmbtdaH ligand has been (i) deprotonated and (ii) oxidized at S to form an *S*-oxide and adopts a distinctly different binding mode to complex **3.10a**. Deprotonation of the heterocyclic ring affords two *N*,*N*′-chelate pockets for metal binding through N(1)/N(4) and N(2)/N(3). In addition, oxidation of the ligand to the *S*-oxide offers an additional O-donor atom which is able to coordinate to a third metal. The S-O bond at 1.504(6) Å, is comparable with other literature reported sulfoxide bonds (1.500(4) Å).[20] The two crystallographically independent metal centres are in the +2 oxidation state and adopt 5-coordinate geometries with N_2O_3 donor sets. Cu(1) has one ligand, one hfac⁻ group and one tfa⁻ group attached, whereas Cu(2) has one ligand, one hfac⁻ group and an oxygen donor from the symmetry related oxidized ligand completing the coordination sphere. The Addison τ_5 value[15] for Cu(1) of 0.47 is consistent

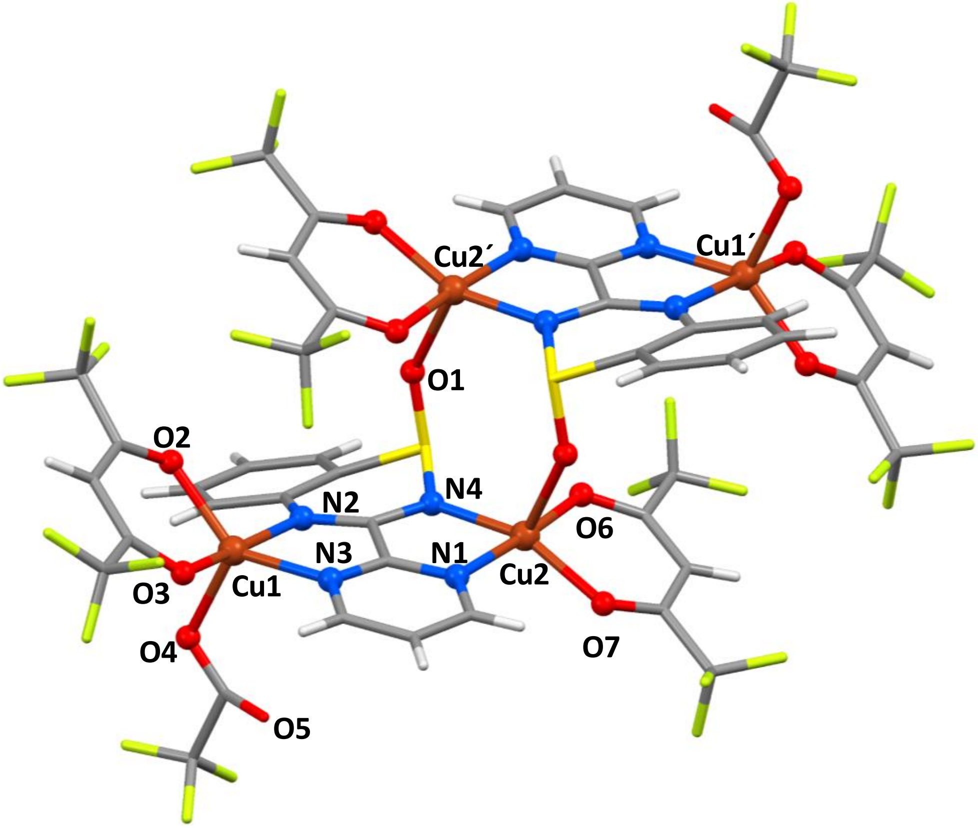

Figure 3.16 Molecular structure of $Cu_4(hfac)_4(tfa)_2(pmbtda_{ox})_2$ (**3.10b**).

with an intermediate geometry of trigonal bipyramidal and square pyramidal (τ = 1 for trigonal bipyramidal and 0 for square pyramidal) with N(3)-Cu(1)-O(3) = 167.0(2)° defining the axial orientation with the remaining angles in the equatorial plane in the range 109.2(2) – 139.1(3)°. For Cu(2) the Addison value is τ_5 = 0.27 consistent with a trigonal pyramidal geometry with the angles in the equatorial plane in the range 82.4(2) – 173.9(2)°. The $\text{pmbtda}_{\text{ox}}^{-}$ ligand bridges between a Cu(hfac) and a Cu(hfac)(tfa) unit to form $\text{Cu}_2(\text{hfac})_2(\text{tfa})(\text{pmbtda}_{\text{ox}})$. Two such $\text{Cu}_2(\text{hfac})_2(\text{tfa})(\text{pmbtda}_{\text{ox}})$ units dimerise through the *S*-oxide oxygen atoms to form a centrosymmetric tetranuclear $\text{Cu}_4(\text{hfac})_4(\text{tfa})_2(\text{pmbtda}_{\text{ox}})_2$ cluster. The chelate ligand $\text{pmbtda}_{\text{ox}}^{-}$ exhibits N_{pm}-Cu-N_{BTDA} angles of 81.4(2)° and 82.4(2)°. The Cu-N bond lengths are in the range 1.990(6) – 2.071(6) Å and the Cu-O are 1.929(5) – 2.217(5) Å. The four hfac^{-} groups chelate to the metal center and the two trifluoroacetate (tfa^{-}) groups are monodentate, providing two more atoms and completing the coordination sphere of the metal ions.

3.2.3.e Synthesis and crystal structure of $\text{Zn}_4(\text{hfac})_6(\text{pmbtda}_{\text{ox}})_2$ (3.11b)

Reaction of pmbtdaH with $\text{Zn}(\text{hfac})_2\cdot 2\text{H}_2\text{O}$ in CH_2Cl_2 in a 1:1 molar ratio, in an analogous fashion to **3.11a**, followed by leaving the solution undisturbed in a sealed vial for two weeks at ambient temperature afforded crystals of the colourless tetranuclear complex $\text{Zn}_4(\text{hfac})_6(\text{pmbtda}_{\text{ox}})_2$ (**3.11b**) (Figure 3.17). The structure of **3.11b** crystallizes in the monoclinic space group $P2_1/n$ with half a molecule in the asymmetric unit. In complex **3.11b** the ligand has been also deprotonated and oxidized at S to form an *S*-oxide and as in complex **3.10b** adopts a distinctly different binding mode to complex **3.11a**. The formation of complex **3.11b** is summarized in Equation 3.9.

$$4\,\text{Zn}(\text{hfac})_2 + 2\,\text{pmbtdaH} + \text{O}_2 \longrightarrow \text{Zn}_4(\text{hfac})_6(\text{pmbtda}_{\text{ox}})_2 + 2\,\text{hfacH}$$

Equation 3.9

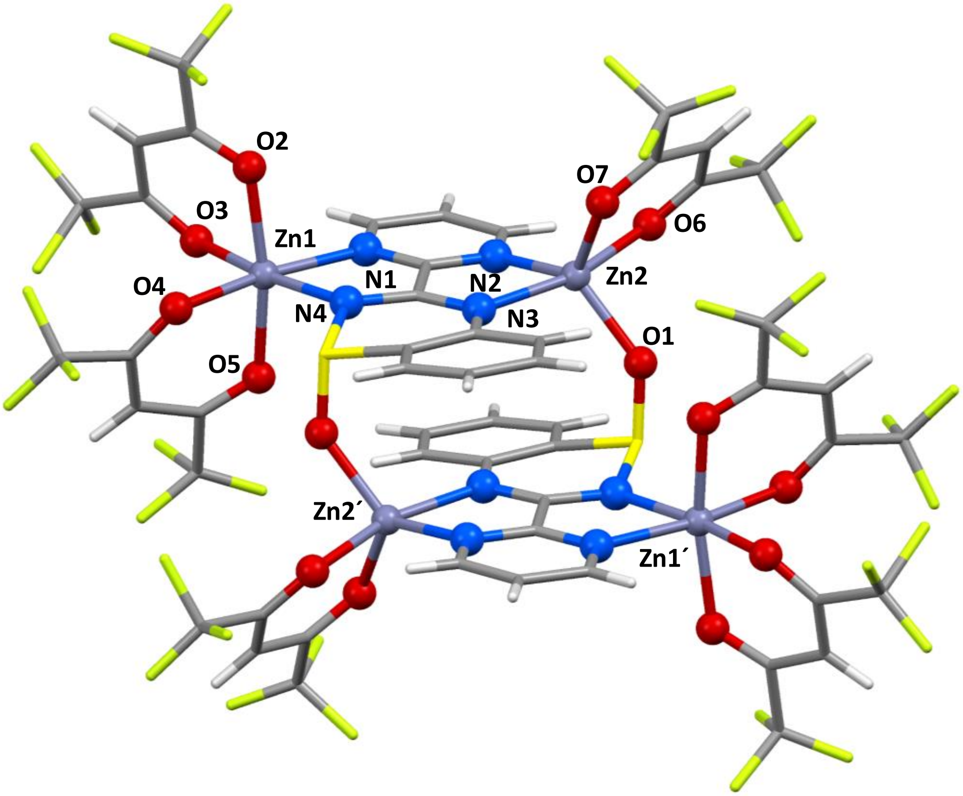

Figure 3.17 Molecular structure of $Zn_4(hfac)_6(pmbtda_{ox})_2$ (**3.11b**).

Deprotonation of the heterocyclic ring affords two *N*,*N*′-chelate pockets for metal binding through N(1)/N(4) and N(2)/N(3). In addition, oxidation of the ligand to the *S*-oxide offers an additional O-donor atom which is able to coordinate to a third metal. The S-O bond at 1.520(5) Å, is comparable with other literature reported sulfoxide bonds (1.500(4) Å[20]). The two crystallographically independent Zn^{II} centres adopt different coordination geometries. Zn(1) has a 6-coordinate geometry with a N_2O_4 donor set, having one ligand and two $hfac^-$ groups attached. On the other hand, Zn(2) is 5-coordinate with one chelate ligand, one chelate $hfac^-$ group and an oxygen donor from the symmetry related oxidized ligand completing the coordination sphere. The Addison τ_5 value[15] (0.67) is consistent with a geometry close to trigonal bipyramidal ($\tau = 1$ for trigonal bipyramidal and 0 for square pyramidal) with N(3)-Zn(2)-O(6) = 160.0(2)° defining the axial orientation with the remaining angles in the equatorial plane in the range 112.6(2) – 123.7(2)°.

The $\text{pmbtda}_{\text{ox}}^{-}$ ligand bridges between a $Zn(hfac)_2$ and a Zn(hfac) unit to form $Zn_2(hfac)_3(\text{pmbtda}_{\text{ox}})$. Two such $Zn_2(hfac)_3(\text{pmbtda}_{\text{ox}})$ units dimerise through the *S*-oxide oxygen atom to form a centrosymmetric tetranuclear $Zn_4(hfac)_6(\text{pmbtda}_{\text{ox}})_2$ cluster. The core structure of **3.11b** is analogous to **3.10b**, comprising a $M_2(\text{pmbtda}_{\text{ox}})_2(hfac)_2$ unit. In **3.10b** the remaining *N*,*N*′-chelate pocket binds a Cu(hfac)(tfa) unit but in **3.11b** it binds a $Zn(hfac)_2$ unit. The absence of heterocyclic N-H groups in the $\text{pmbtda}_{\text{ox}}^{-}$ ligand precludes a hydrogen bonded network and the molecular packing of **3.11b** appears driven by dispersion forces. Intermolecular π-π interactions form a chain parallel to the crystallographic *a* axis with centroid···centroid distances at 3.654 Å.

3.2.4 Spectroscopic studies of the metal complexes

The UV-Vis spectra of the complexes $MCl_2(pmbtdaH)_2$ (**3.2** − **3.6**) are dominated by a series of intense π-π* ligand-centered absorption bands between 230 and 300 nm (Figure 3.18). In particular, the visible region exhibits lower intensity absorption bands at 430 – 455 nm which are comparable to the free ligand, pmbtdaH (441 nm) and which give rise to the diagnostic red colour of the btda ligand[1] and its complexes (Figure 3.18, inset).

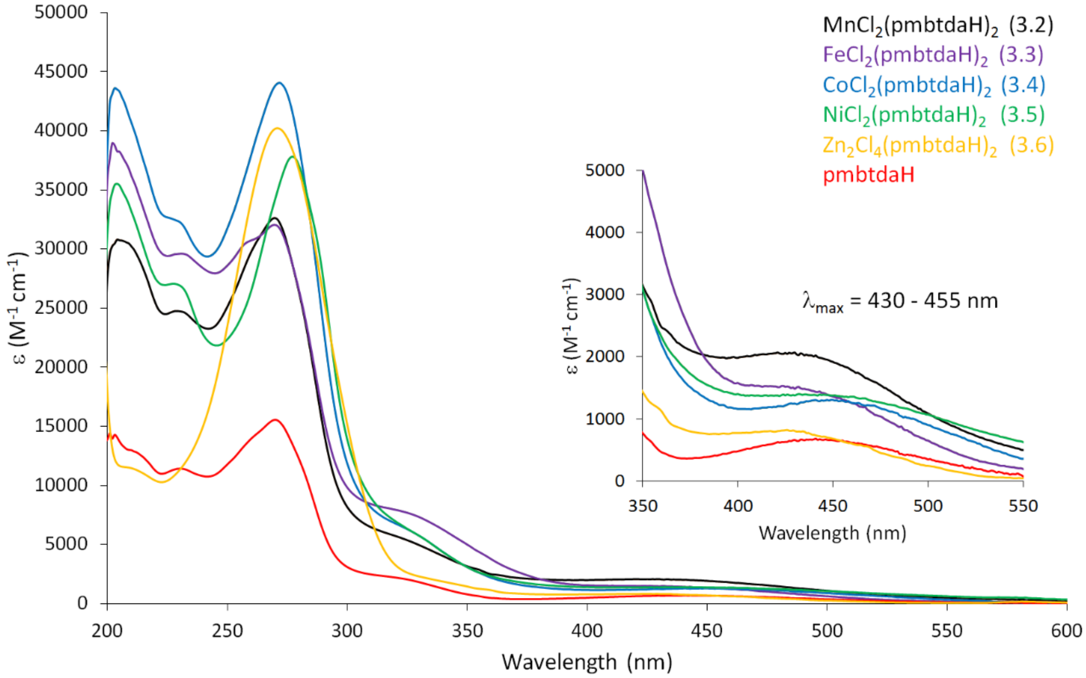

Figure 3.18 Solution UV-Vis spectra of complexes **3.2** − **3.5** with formula MCl$_2$(pmbtdaH)$_2$, complex Zn$_2$Cl$_4$(pmbtdaH)$_2$ (**3.6**) and the ligand pmbtdaH. Inset: expansion of the visible region highlighting the similar λ_{max} for complexes **3.2** − **3.6** and ligand pmbtdaH (CH_3OH or CH_3CN, rt, $C_{pmbtdaH} \approx 10^{-4}$ M; $C_{complexes} \approx 10^{-5}$ M).

The UV-Vis spectra of complexes M(hfac)$_2$(pmbtdaH) (**3.7a** − **3.11a**) are similar to complexes **3.2** − **3.6** and similarly dominated by a series of intense π-π* ligand-centered absorption bands between 250 and 350 nm (Figure 3.19). In particular, the visible region exhibits lower intensity absorption bands at 425 − 445 nm which are comparable to the free ligand, pmbtdaH (441 nm) and which give rise to the diagnostic red colour of the btda ligand[1] and its complexes (Figure 3.19, inset).

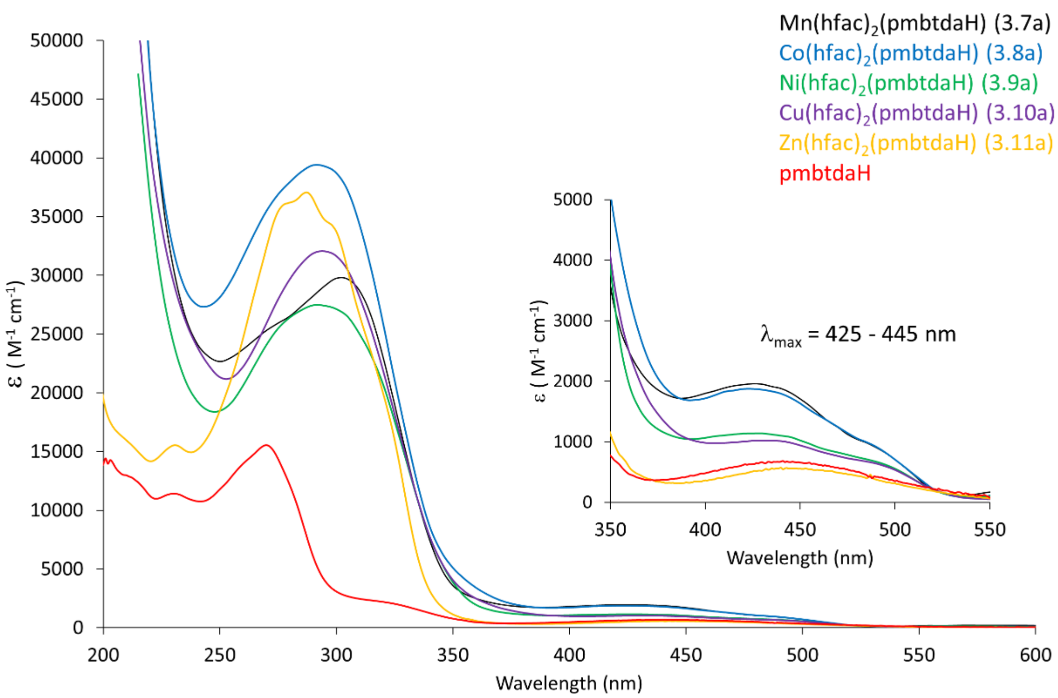

Figure 3.19 Solution UV-Vis spectra of M(hfac)$_2$(pmbtdaH) (**3.7a** – **3.11a**) and the ligand pmbtdaH. Inset: expansion of the visible region highlighting the similar λ_{max} for complexes **3.7a** – **3.11a** and ligand pmbtdaH (Solvent: CH_2Cl_2, CH_3OH or CH_3CN, rt, $C_{pmbtdaH} \approx 10^{-4}$ M; $C_{complexes} \approx 10^{-5}$ M).

Based on the solution UV-Vis spectra of **3.2** – **3.6** and **3.7a** – **3.11a** and pmbtdaH we can conclude that the absorption profiles are independent to the nature of the *d*-block metal ion and dominated by ligand-based transitions. This is particularly apparent for the high spin d^5 Mn^{II} and d^{10} Zn^{II} complexes (where *d-d* transitions are additionally spin forbidden as well as Laporte forbidden) and typically near colourless. Similar behaviour has been observed for the metal complexes of pybtdaH.[1]

The UV-Vis spectra of complexes **3.11a** (containing pmbtdaH) and **3.11b** (containing pmbtda$_{ox}^{-}$) exhibit distinct differences in the UV region of the spectrum associated with a series of intense π-π* ligand-centered absorption bands between 230 and 300 nm (Figure 3.20). The visible region exhibits lower intensity absorption bands at 461 nm for complex **3.11a** (*cf* pmbtdaH at 441 nm) whereas *S*-oxidation perturbs the conjugation within the btda ring and the 450±20 nm transition is suppressed and these S^{IV} derivatives appear colourless (Figure 3.20, inset).[2]

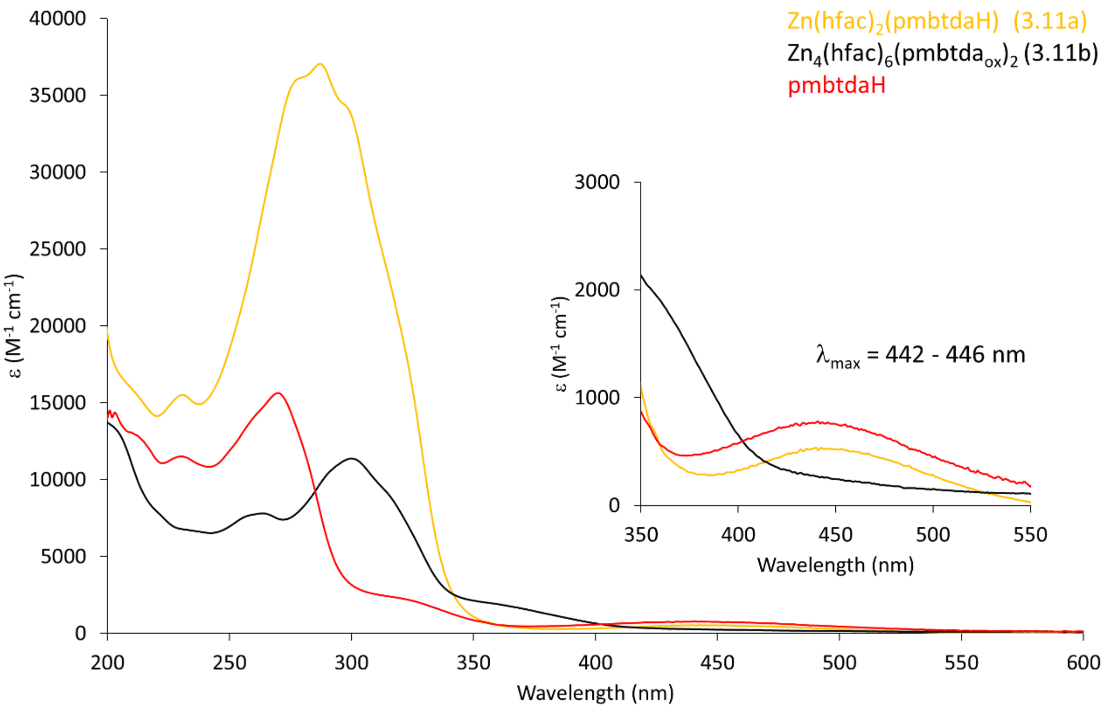

Figure 3.20 Solution UV-Vis spectra of complexes **3.11a**, **3.11b** and the ligand pmbtdaH. Inset: expansion of the visible region highlighting the similar λ_{max} for complexes **3.11a**, **3.11b** and ligand pmbtdaH (CH_3CN or CH_3OH, rt, $C_{pmbtdaH} \approx 10^{-4}$ M; $C_{complexes} \approx 10^{-5}$ M).

The IR spectra, incorporating the ligand pmbtdaH, exhibit a stretch at *ca.* 1640 cm^{-1} characteristic of the C=N imine bond for the complexes whereas in complex **3.11b** the stretch is at 1647 cm^{-1}.[9] The N-H stretch is present in all complexes where the ligand is not oxidised, in the range of 3221 – 3452 cm^{-1}, but is notably absent in complex **3.11b** as expected for the deprotonated state of the pmbtda$_{ox}^{-}$ ligand. Conversely, sulfoxides typically exhibit a strong $\nu_{S=O}$ in the IR (1070 – 1030 cm^{-1})[21] and the *S*-oxide complex **3.11b** exhibits a vibration at 1000 cm^{-1}, a feature notably absent in all other complexes. This vibration is consistent with the previously reported metal coordinated pybtda$_{ox}^{-}$ anion (985 cm^{-1}) and free *S*-oxide benzothiadiazines (*ca.* 1000 cm^{-1}).[2]

The diamagnetic nature of Zn^{II} ions permitted ^{1}H NMR studies to be undertaken for complex **3.11a**. Coordination of the pmbtdaH ligand to Zn(hfac)$_2$ leads to a diagnostic downfield shift of all ^{1}H peaks by less than 1 ppm (Figure 3.21). The appearance of a new signal at 6.04 ppm corresponds to the protons of the two hfac$^-$ groups of the complex. This C-H proton may be broadened due to equilibriation in solution between Λ and Δ forms of **3.11a** *via* a Bailar twist or Ray-Dutt mechanism.[22] Notably the structure of **3.11a** has O atoms either *cis* or *trans* to N leading to formally chemically inequivalent CF$_3$ groups, yet the observation of a singlet in the ^{19}F NMR is consistent with a dynamic process in solution.

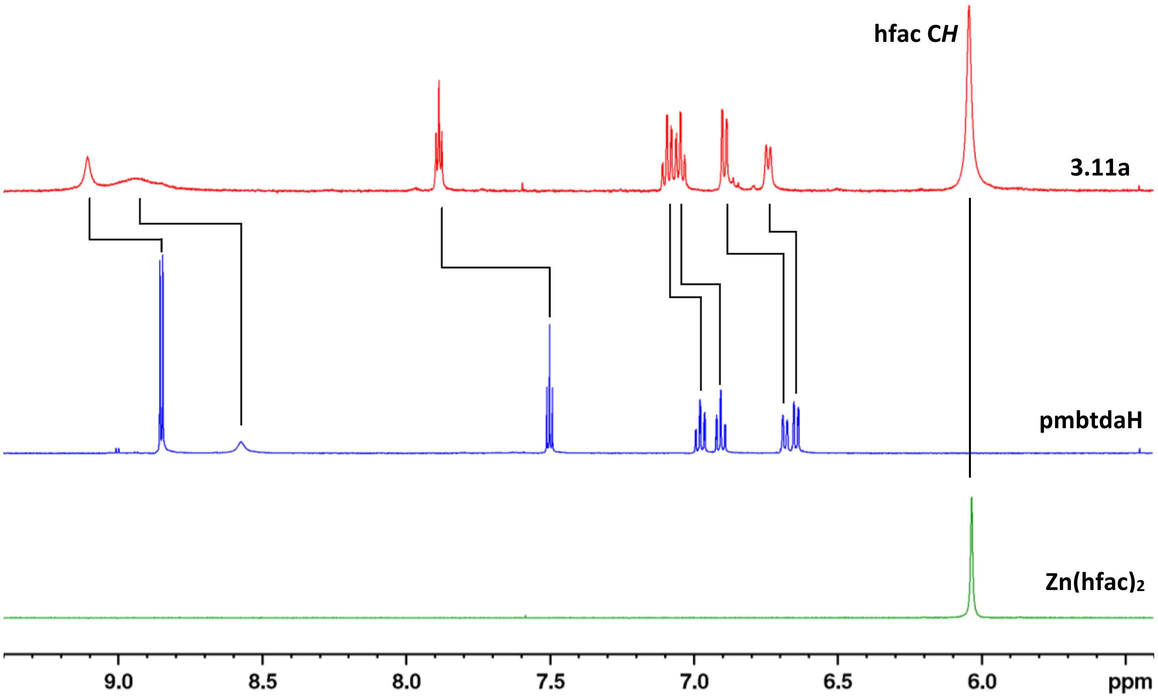

Figure 3.21 ^{1}H NMR of complex **3.11a** (red), pmbtdaH (blue) and Zn(hfac)$_2$ (green) (500 MHz, CD$_3$CN).

The solid state EPR of complex **3.10a** reveals a pseudo-axial spectrum with $g_x = 2.27$, $g_y = 2.25$, $g_z = 2.07$ ($<g>= 2.197$) consistent with a metal-based electron (Figure 3.22).

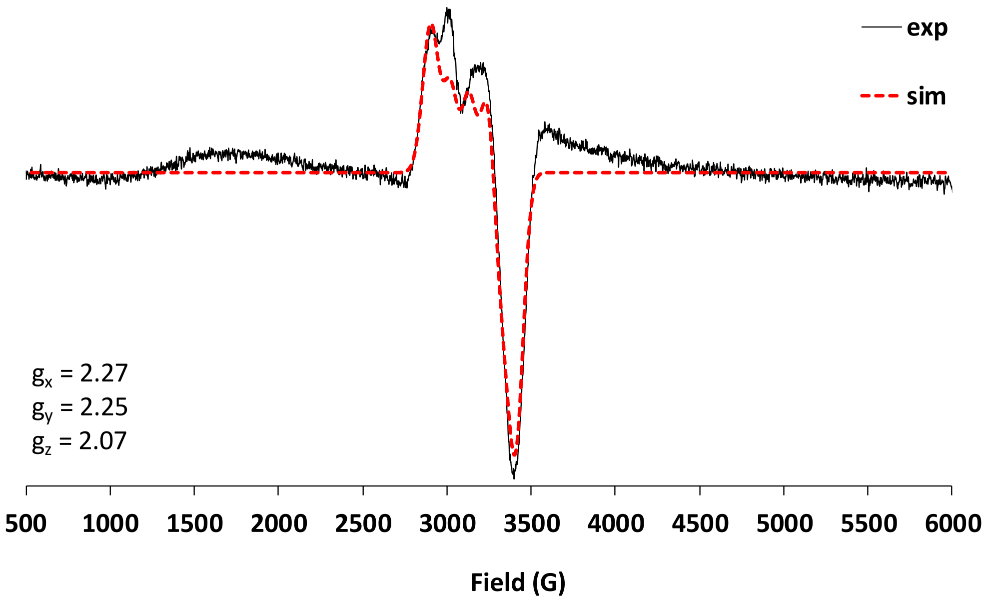

Figure 3.22 Solid state EPR of complex **3.10a** at room temperature (experimental-black, simulation-red); $g_x = 2.27$, $g_y = 2.25$, $g_z = 2.07$ ($\langle g \rangle = 2.197$), $a_x = a_y = 110$ G, $a_z = 0$ G.

3.2.5 Reactivity trends in the coordination chemistry of pmbtdaH

The ligand 3-(2′-pyridyl)benzothiadiazine (pybtdaH) can form a range of *N*,*N*′-chelate complexes with first row transition metals including $CuCl_2$(pybtdaH) and $CuCl_2(pybtdaH)_2$.[1] Previous studies indicated that *S*-oxidation of pybtdaH or related benzothiadiazines only occurred in the presence of a metal ***and*** Et_3N. For example, reaction of $CuCl_2$ with pybtdaH affords a stable red solution of $CuCl_2(pybtda)_2$ but which led to the isolation of the green dimetallic complex $[Cu(pybtda_{ox})_2]_2$ complex upon addition of Et_3N.[2] In Chapter 2, we showed that weakly basic counter ions (hfac$^-$ and OAc$^-$) could facilitate the oxidation of the ligand pybtdaH even without the introduction of base and afforded a series of polynuclear complexes containing the $pybtda_{ox}^-$ anion.

The isolation of the mononuclear complexes **3.2** − **3.5** with general formula $MCl_2(pmbtdaH)_2$ and the dimeric complex $Zn_2Cl_4(pmbtdaH)_2$ (**3.6**) on addition of pmbtdaH to MCl_2 was therefore unsurprising with the pmbtdaH ligand acting as a simple *N*,*N*′-chelate to transition metal ions in a similar fashion to the pybtdaH ligand.[1]

Replacement of Cl^- by the weakly basic OAc^- and $hfac^-$ anions revealed some differences in reactivity patterns between pybtdaH and pmbtdaH with pmbtdaH showing a stronger resilience to ligand oxidation. Thus reaction of pmbtdaH and $M(hfac)_2{\cdot}xH_2O$ afforded the mononuclear complexes $M(hfac)_2(pmbtdaH)$ (**3.7a** − **3.11a**) and the isolation of oxidized ligand complexes was only apparent after extended periods of storage. This led to a series of mononuclear complexes $M(hfac)_2(pmbtdaH_{ox})$ (M = Co (**3.8b**), Ni (**3.9b**)) and dinuclear $Mn_2(hfac)_2(tfa)_2(pmbtdaH_{ox})_2$ (**3.7b**) in which the $pmbtdaH_{ox}$ ligand is neutral and acts as an *N*,*N*′-chelate. In the tetranuclear complexes $Cu_4(hfac)_4(tfa)_2(pmbtda_{ox})_2$ (**3.10b**) and $Zn_4(hfac)_6(pmbtda_{ox})_2$ (**3.11b**) the ligand is deprotonated and offers two *N*,*N*′-chelate pockets as well as a bridging S=O unit. In most cases where the ligand is oxidised ($pmbtdaH_{ox}$ and $pmbtda_{ox}^-$), the metal complexes are only formed as the minor product with oxidation only occurring in the presence of (i) extended crystallization time coupled with (ii) the use of a more basic auxiliary ligand. To date, attempts to promote deprotonation (and oxidation) of the ligand by introducing a base in the reaction mixture with Cl^- or $hfac^-$ were not fruitful.

A comparison of the ligand coordination geometry with respect to the free ligand indicates, as expected, that the major changes in geometry of the coordinated ligand are associated with the N-bound heteroatom of the thiadiazine ring. The *N*-coordination leads to somewhat lengthening of both C-N and N-S bond lengths with C-N bond distances in the range 1.290 – 1.314 Å and N-S bond distances in the range 1.692 – 1.720 Å (*cf* free ligand at 1.282(3) and 1.691(2) Å, respectively). Upon oxidation of the ligand, the N-S bond lengths show no significant change (1.685 – 1.699 Å) whereas the C-N bonds (N *ortho* to S) show an increase of about 0.03 – 0.05 Å (1.308 – 1.327 Å) losing its double bond character. In contrast, the C-N bonds (N *para* to S) show a decrease of about 0.03 – 0.05 Å (1.316 – 1.343 Å) in comparison to the corresponding bond length in free ligand (1.367(3) Å). In the complexes where the ligand adopts the anionic form, $pmbtda_{ox}^-$, (**3.10b** and **3.11b**) the electronics of the heterocycle are altered, resulting to a lengthening of the C-N bonds (N *ortho* to S) of about 0.06 Å (1.341 – 1.343 Å) in comparison to the corresponding bond length in free ligand (1.282(3) Å). The C-N bonds (N *para* to S) show a decrease of 0.06 Å (1.312 – 1.316 Å) in comparison to the pmbtdaH (1.367(3) Å) indicative of double bond character. The S–O bonds are in the range of 1.483 – 1.504 Å and are comparable with the S-O bonds in Chapter 2 (1.488 – 1.499 Å) as well as other literature reported sulfoxide bonds (average 1.50 Å).[2,23] The only exception is on one of the two complexes with $\text{pmbtda}_{\text{ox}}^{-}$ (**3.11b**) in which the S-O is longer at 1.520 Å but also comparable with other coordinated oxygen atoms (Chapter 2, 1.506 – 1.548 Å).

3.3. Conclusions

The synthesis of the novel redox active ligand 3-(2',6'-pyrimidine)-benzo-1,2,4-thiadiazine (pmbtdaH) has been described. The radical pmbtda$^\bullet$ can be prepared by *in situ* 1e^- oxidation and its radical character is confirmed by EPR spectroscopy, along with DFT calculations of the spin density distribution.

Reaction of pmbtdaH with MCl_2 (M = Mn, Fe, Co, Ni) in a 2:1 mole ratio afforded the mononuclear complexes of general formula $MCl_2(pmbtdaH)_2$ (M = Mn (**3.2**), Fe (**3.3**), Co (**3.4**), Ni (**3.5**)) in which the ligand binds in a *N*,*N*′-chelate fashion *via* heterocyclic N(4) and the pyrimidinyl N(1) atom while the Cl^- ligands are located mutually *cis*. Reaction of pmbtdaH with $ZnCl_2{\cdot}2H_2O$ in a 1:1 mole ratio afforded the dinuclear complex $Zn_2Cl_4(pmbtdaH)_2$ (**3.6**) in which the two trigonal bipyramidal metal centres are linked *via* μ_2-bridging Cl^- ligands while the pmbtdaH ligand continues to bind in an *N*,*N*′-chelate fashion. Reaction of pmbtdaH with $M(hfac)_2$ (M = Mn, Co, Ni, Cu, Zn) in 1:1 mole ratio afforded the mononuclear complexes with general formula $M(hfac)_2(pmbtdaH)$ (M = Mn (**3.7a**), Co (**3.8a**), Ni (**3.9a**), Cu (**3.10a**), Zn (**3.11a**)). Here the ligand also binds in an *N*,*N*′-chelate fashion *via* heterocyclic N(4) and the pyrimidinyl N(1) atom. Only under extended storage does oxidation of the pmbtdaH ligand occur and appears to also require the presence of a weakly basic anion. The mononuclear complexes $M(hfac)_2(pmbtdaH_{ox})$ (M = Co (**3.8b**), Ni (**3.9b**)) provide the simplest examples of ligand oxidation. In other cases deprotonation of the ligand affords two *N*,*N*′-chelate pockets affording a bis-chelate bridge, exemplified by $Zn_4(hfac)_6(pmbtda_{ox})_2$ (**3.11b**). Under these reaction conditions hydrolysis of the $hfac^-$ ligand to generate tfa^- further complicates matters, exemplified by the dimer $Mn_2(hfac)_2(tfa)_2(pmbtdaH_{ox})_2$ (**3.7b**) and the tetranuclear complex $Cu_4(hfac)_4(tfa)_2(pmbtda_{ox})_2$ (**3.10b**). The different coordination modes isolated from reactivity studies with pmbtdaH are highlighted in Figure 3.23. Experimentally UV-Vis and IR studies prove useful diagnostic tools for discriminating between pmbtdaH (λ_{max} ~ 430 nm, $\nu_{N\text{-}H}$) and $pmbtda_{ox}^-$ ligands (absence of λ_{max} at 430 nm and IR $\nu_{S=O}$).

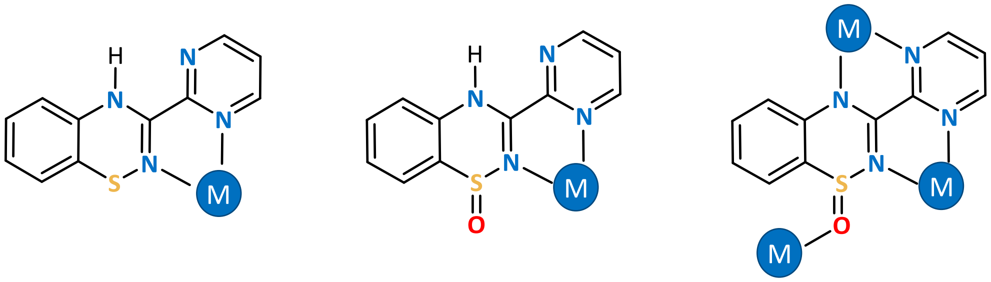

pmbtdaH pmbtdaH$_{ox}$ pmbtda$_{ox}^{-}$

Figure 3.23 Coordination modes of the ligand pmbtdaH observed in the metal complexes of Chapter 3.

3.4. Experimental

3.4.1 General considerations and physical measurements

Solvents, starting materials and metal salts were obtained from commercial suppliers and used without further purification. Manipulation of air-sensitive materials was carried out under an atmosphere of dry nitrogen using standard Schlenk techniques and a dry-nitrogen glove box (MBraun Labmaster). Melting points were determined using a Stanford Research Systems MPA120 EZ-Melt automated melting point apparatus. Elemental compositions were determined on a Perkin Elmer 2400 Series II CHNS/O Analyzer. UV-Vis spectra were measured on an Agilent 8453 Spectrophotometer using *ca.* 1×10^{-5} M solutions in methanol, acetonitrile or dichloromethane in the range 200 – 600 nm. IR spectra were obtained using a Bruker Alpha FT-IR spectrometer equipped with a Platinum single reflection diamond ATR module. NMR spectra were recorded on a Bruker 500 MHz spectrometer with a Broadband AX Probe using $CDCl_3$ (^1H δ = 7.26 ppm, s; ^{13}C δ = 77.16 ppm) or CD_3CN (^1H δ = 1.94 ppm, septet) as an internal reference point relative to Me_4Si (δ = 0 ppm). Mass spectra were recorded on a Waters XEVO G2-XS specifically using the atmospheric solids analysis probe in positive resolution mode. EPR spectra of pmbtda$^•$ and complex **3.10** were measured on a Bruker EMXplus X-band EPR spectrometer at room temperature. Simulation of the EPR spectrum of pmbtda$^•$ was made using WinSim software[24] and of the anisotropic EPR spectrum of complex **3.10** was made using the PIP4Win software. Density functional theory (DFT) calculations of pmbtdaH were undertaken using the dispersion-corrected B3LYP-D3 functional and 6-311G*+ basis set[25–27] functional within Jaguar[28] whereas spin density calculations on pmbtda$^•$ implemented the UB3LYP functional and 6-311G* basis set.

Cyclic voltammetry was performed at 25 °C, under argon, in anhydrous CH_2Cl_2 using $^nBu_4NPF_6$ (0.1 M) as supporting electrolyte. A Pine Research Compact voltammetry low volume cell equipped with a ceramic screen printed Pt electrode and a low profile $Ag^+/AgCl/KCl$ reference electrode was used to record data at 200 mV/s scan rates. Potentials were recalibrated *vs.* the Ferrocene/Ferrocenium couple (+502 mV *vs.*

$Ag^+/AgCl/KCl$ reference electrode in the above mentioned conditions). Concentrations of the electro-active species were around 10^{-3} M.

3.4.2 Ligand Synthesis

Ligand pmbtdaH was prepared according to a modification of the literature procedure for pybtdaH[8]:

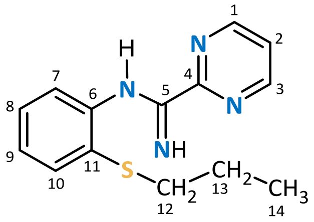

3.4.2.a N′-(2-propylthiophenyl)-picolinamidine (3.1)

2-Propylsulphanylphenylamine (**2.1**) (5.00 g, 30 mmol) was dissolved in THF (10 mL) and added dropwise to a stirred solution of lithium *bis*(trimethylsilyl)amide (6.02 g, 36 mmol) in THF (25 mL) at 0 °C under a nitrogen atmosphere. The dark reaction mixture was allowed to warm to room temperature and stirred for 24 h. A solution of 2-pyrimidinecarbonitrile (3.15 g, 30 mmol) in THF (10 mL) was added dropwise to the reaction mixture and stirred for a further 48 h. The solvent was removed *in vacuo* and the reaction mixture was extracted with CH_2Cl_2 and treated with 100 mL of $NaHCO_{3(aq.)}$. The organic phase was washed with $NaHCO_{3(aq.)}$ (1 × 50 mL) and brine (1 × 20 mL), dried over Na_2SO_4 and the solvent removed *in vacuo*. The resulting brown oil was washed with hexanes (3 × 10 mL) to yield the product as a white crystalline powder (4.82 g, 59%).

Melting point 80 °C.

Elemental Analysis calc. for $C_{14}H_{16}N_4S$: C, 61.74; H, 5.92; N, 20.57. Found: C, 61.73; H, 5.87; N, 20.46%.

IR (solid, cm^{-1}) $\tilde{\nu}_{max}$ = 3300 (m), 3278 (m), 3077 (w), 3062 (w), 2956 (w), 2932 (w), 2903 (w), 2870 (w), 1630 (m), 1563 (s), 1541 (s), 1455 (m), 1439 (m), 1405 (s), 1300 (m), 1239 (s), 864 (m), 811 (s), 757 (s), 710 (m), 651 (s), 636 (s), 588 (m).

^{1}H NMR (500 MHz, ppm, CDCl$_3$) δ_H = 8.89 (2H, d, *J* = 4.9 Hz, C^{1}*H,* C^{3}*H*), 8.27 (1H, bs, N*H*), 7.47 (1H, d, *J* = 7.5 Hz, C^{7}*H*), 7.40 (1H, t, *J* = 4.8 Hz, C^{2}*H*), 7.31 (1H, t, *J* = 7.6 Hz, C^{8}*H*), 6.98 (1H, td, *J* = 11.5, 1.2 Hz, C^{9}*H*), 2.80 (2H, t, *J* = 7.3 Hz, SC$^{12}H_2$), 1.61 (2H, sextet, *J* = 7.3 Hz, SCH$_2$C$^{13}H_2$), 0.97 (3H, t, *J* = 7.3 Hz, C$^{14}H_3$).

^{13}C NMR (125 MHz, ppm, CDCl$_3$) δ_C = 157.55 (C^{5}), 157.37 (C^{1,3}), 154.31 (C^{4}), 144.15 (C^{6}), 133.13 (C^{7}), 128.56 (C^{8}), 124.86 (C^{11}), 122.78 (C^{9}), 121.62 (C^{2}), 120.14 (C^{10}), 36.76 (C^{12}), 22.76 (C^{13}), 13.70 (C^{14}).

HRMS (ASAP+) *m/z* [M+H]$^+$ calc. for $C_{14}H_{17}N_4S$: 273.1174, found 273.1164.

3.4.2.b 3-(2',6'-pyrimidine)-benzo-1,2,4-thiadiazine (pmbtdaH)

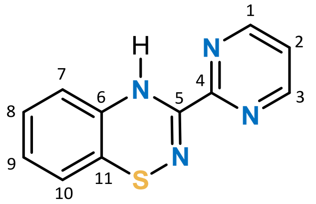

A solution of *N*-chlorosuccinimide (2.94 g, 22 mmol) in CH$_2$Cl$_2$ (40 mL) was added dropwise to a solution of **3.1** (5.00 g, 20 mmol) in CH$_2$Cl$_2$ (40 mL) at -78 °C, and the reaction mixture was allowed to warm to room temperature and stirred for 18 h. The reaction mixture was washed with water (2 × 20 mL), brine (1 × 20 mL) and then dried over Na$_2$SO$_4$. The solvent was removed *in vacuo* and the oily residue re-dissolved in toluene (30 mL) and brought to reflux for 12 h. The solvent was again removed *in vacuo* to yield a brown solid. The product was purified by column chromatography using a mixture of CH$_2$Cl$_2$/EtOH (4%) as eluent. The slow evaporation of the solvent resulted in red shiny crystals of ligand. Yield 1.60 g, 35%.

Melting point 114 °C.

Elemental Analysis calc. for $C_{11}H_8N_4S$: C, 57.88; H, 3.53; N, 24.54. Found: C, 57.78; H, 3.34; N, 24.45%.

UV-Vis (CH$_3$OH; λ_{max}, nm; ε, M^{-1}·cm^{-1}): 270 (15550), 320 (2200), 430 (662), 441 (683).

IR (solid, cm^{-1}) $\tilde{\nu}_{\max}$ = 3324 (m), 3045 (w), 2960 (w), 1630 (m), 1556 (s), 1513 (m), 1465 (s), 1437 (s), 1403 (s), 1319 (m), 1260 (m), 1123 (m), 1094 (m), 1015 (m), 931 (w), 859 (w), 813 (w), 744 (s), 709 (m), 631 (m).

^{1}H NMR (500 MHz, ppm, CDCl$_3$) δ_H = 8.81 (2H, d, *J* = 4.9 Hz, C^1*H,* C^3*H*), 8.22 (1H, bs, N*H*), 7.30 (1H, t, *J* = 4.9 Hz, C^2*H*), 6.89 (1H, td, *J* = 11.4, 1.5 Hz, C^9*H*), 6.84 (1H, td, *J* = 11.2, 1.3 Hz, C^8*H*), 6.60 (1H, d, *J* = 7.3 Hz, C^7*H*), 6.40 (1H, dd, *J* = 7.6, 1.2 Hz, C^{10}*H*).

^{13}C NMR (125 MHz, ppm, CDCl$_3$) δ_C = 157.25 (C^{1,3}), 155.72 (C^4), 152.17 (C^5), 136.43 (C^6), 127.86 (C^9), 125.68 (C^8), 122.64 (C^7), 121.78 (C^2), 119.97 (C^{11}), 114.31 (C^{10}).

HRMS (ASAP+) *m/z* [M+H]$^+$ calc. for $C_{11}H_9N_4S$: 229.0548, found 229.0553.

3.4.3 Reactivity of pmbtdaH with MCl$_2$ (M = Mn, Fe, Co, Ni, Zn)

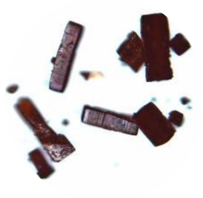

3.4.3.a [MnCl$_2$(pmbtdaH)$_2$]·2CH$_3$OH (3.2)

Ligand pmbtdaH (0.046 g, 0.200 mmol) was added to a solution of MnCl$_2$ (0.013 g, 0.100 mmol) in CH$_3$OH (10 mL). The mixture was stirred for 30 min and a deep red solution obtained. The solution was filtered and dark red crystals were grown by layering with a mixture of diethyl ether/hexanes (1:1) the next day. Yield 0.026 g, 45%.

Elemental Analysis calc. for [$C_{22}H_{16}N_8MnS_2Cl_2$]·0.5H_2O: C, 45.16; H, 3.03; N, 18.72. Found: C, 45.54; H, 2.89; N, 18.68%.

UV-Vis (CH$_3$OH; $\lambda_{\max}$, nm; ε, M^{-1} cm^{-1}): 205 (31010), 229 (25021), 270 (32888), 328 (5386), 421 (2340), 430 (2339).

IR (solid, cm^{-1}) $\tilde{\nu}_{\max}$ = 3452 (br), 1623 (w), 1579 (m), 1558 (m), 1516 (m), 1471 (s), 1440 (m), 1413 (s), 1261 (m), 1014 (s), 942 (m), 810 (m), 781 (m), 746 (s), 705 (m), 644 (s), 583 (w), 477 (w), 453 (w), 434 (w).

3.4.3.b [$FeCl_2(pmbtdaH)_2$]·$2CH_3OH$ (3.3)

Ligand pmbtdaH (0.023 g, 0.100 mmol) was added to a solution of $FeCl_3·6H_2O$ (0.027 g, 0.100 mmol) in CH_3OH (10 mL). The mixture was stirred for 30 min and a deep red solution obtained. The solution was filtered and dark brown crystals were grown by layering with a mixture of diethyl ether/hexanes (1:1) over five days. Yield 0.009 g, 15%.

Elemental Analysis calc. for [$C_{22}H_{16}N_8FeS_2Cl_2$]·$2H_2O$: C, 42.67; H, 3.25; N, 18.09. Found: C, 42.26; H, 2.51; N, 17.67%.

UV-Vis (CH_3OH; λ_{max}, nm; ε, M^{-1} cm^{-1}): 202 (38500), 231 (29177), 270 (31609), 340 (5831), 487 (608).

IR (solid, cm^{-1}) $\tilde{\nu}_{max}$ = 3411 (br), 1649 (w), 1609 (m), 1598 (m), 1555 (m), 1534 (m), 1474 (m), 1444 (m), 1413 (m), 1285 (w), 1176 (m), 1113 (w), 1084 (m), 1072 (m), 1012 (m), 945 (w), 827 (m), 762 (s), 709 (w), 669 (m), 646 (m), 584 (w), 552 (m), 516 (m), 455 (m), 430 (m), 424 (w), 410 (w).

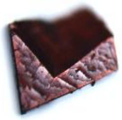

3.4.3.c [$CoCl_2(pmbtdaH)_2$]·$2CH_3OH$ (3.4)

Ligand pmbtdaH (0.046 g, 0.200 mmol) was added to a solution of anhydrous $CoCl_2$ (0.013 g, 0.100 mmol) in CH_3OH (10 mL). The mixture was stirred for 30 min and a deep red solution obtained. The solution was filtered and dark brown crystals were grown by layering with a mixture of diethyl ether/hexanes (1:1) the next day. Yield 0.023 g, 38%.

Elemental Analysis calc. for [$C_{22}H_{16}N_8CoS_2Cl_2$]·H_2O: C, 43.72; H, 3.00; N, 18.54. Found: C, 44.07; H, 2.55; N, 18.49%.

UV-Vis (CH_3OH; λ_{max}, nm; ε, M^{-1} cm^{-1}): 203 (44387), 230 (33090), 272 (44839), 330 (6514), 490 (1792).

IR (solid, cm^{-1}) $\tilde{\nu}_{max}$ = 3375 (br), 1633 (m), 1575 (m), 1557 (m), 1506 (m), 1477 (m), 1439 (m), 1404 (m), 1667 (w), 1197 (w), 1099 (w), 1016 (s), 940 (w), 812 (m), 781 (w), 742 (s), 705 (m), 644 (m), 525 (m), 488 (w), 454 (w).

3.4.3.d [$NiCl_2(pmbtdaH)_2$]·$2CH_3OH$ (3.5)

Ligand pmbtdaH (0.023 g, 0.100 mmol) was added to a solution of $NiCl_2·6H_2O$ (0.012 g, 0.050 mmol) in CH_3OH (10 mL). The mixture was stirred for 20 min and a deep red solution obtained. The solution was filtered and dark brown crystals were grown by layering with a mixture of diethyl ether/hexanes (1:1) over two days. Yield 0.013 g, 22%.

Elemental Analysis calc. for [$C_{22}H_{16}N_8NiS_2Cl_2$]·H_2O: C, 43.74; H, 3.00; N, 18.55. Found: C, 43.72; H, 2.53; N, 18.35%.

UV-Vis (CH_3OH; λ_{max}, nm; ε, M^{-1} cm^{-1}): 204 (35038), 227 (26579), 277 (37339), 330 (5250), 487 (832).

IR (solid, cm^{-1}) $\tilde{\nu}_{max}$ = 3376 (br), 1625 (m), 1580 (m), 1559 (m), 1520 (m), 1472 (s), 1444 (m), 1439 (m), 1408 (s), 1287 (w), 1261 (m), 1242 (w), 1204 (m), 1165 (w), 1127 (w), 1104 (w), 1072 (w), 1025 (s), 949 (m), 941 (m), 809(m), 794 (m), 647 (s), 559 (br), 527 (m), 477 (m), 455 (m), 435 (w), 422 (w).

3.4.3.e $Zn_2Cl_4(pmbtdaH)_2$ (3.6)

Ligand pmbtdaH (0.023 g, 0.100 mmol) was added to a solution of $ZnCl_2$ (0.013 g, 0.100 mmol) in CH_2Cl_2 (15 mL). The mixture was stirred for 1 h and a bright orange solution formed over a dark precipitate. The reaction mixture was filtered and re-dissolved in CH_3OH (6 mL). A small number of dark red crystals were grown by slow evaporation over a period of one week. Yield 0.003 g, 3%.

Elemental Analysis calc. for [$C_{22}H_{16}N_8Zn_2S_2Cl_4$]·3$CH_2Cl_2$: C, 30.52; H, 2.25; N, 11.39. Found: C, 30.86; H, 2.49; N, 11.33%.

UV-Vis (CH_3CN; λ_{max}, nm; ε, M^{-1}·cm^{-1}): 272 (39778), 357 (662), 432 (324).

IR (solid, cm^{-1}) $\tilde{\nu}_{max}$ = 3221 (br), 1634 (m), 1556 (m), 1517 (m), 1477 (s), 1440 (s), 1412 (s), 1262 (w), 1201 (w), 1158 (w), 1016 (w), 946 (w), 876 (w), 817 (w), 792 (w), 768 (s), 710 (w), 670 (w), 630 (s), 585 (m), 431 (w).

3.4.4 Reactivity of pmbtdaH with M(hfac)$_2$ (M = Mn, Co, Ni, Cu, Zn)

3.4.4.a Mn(hfac)$_2$(pmbtdaH) (3.7a)

Ligand pmbtdaH (0.023 g, 0.100 mmol) was added to a solution of Mn(hfac)$_2$·3H_2O (0.052 g, 0.100 mmol) in CH_2Cl_2 (15 mL). The mixture was stirred for 30 min and a deep red solution obtained. The solution was filtered and dark red crystals were grown by layering with hexanes over three weeks. Yield 0.014 g, 21%.

Elemental Analysis calc. for [$C_{21}H_{10}N_4MnSO_4F_{12}$]: C, 36.17; H, 1.45; N, 8.03. Found: C, 36.34; H, 1.41; N, 8.08%.

UV-Vis (CH_2Cl_2; λ_{max}, nm; ε, M^{-1} cm^{-1}): 274 (28963), 310 (35084), 440 (3953).

IR (solid, cm^{-1}) $\tilde{\nu}_{max}$ = 3306 (br), 1644 (m), 1581 (w), 1556 (m), 1484 (m), 1446 (m), 1416 (m), 1252 (m), 1192 (m), 1133 (br), 1094 (m), 1015 (w), 794 (m), 753 (m), 708 (w), 664 (w), 646 (m), 617 (w), 582 (m), 527 (w), 472 (w).

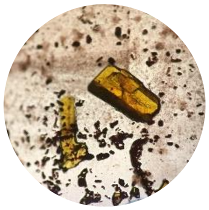

3.4.4.b [$Mn_2(hfac)_2(tfa)_2(pmbtdaH_{ox})_2$]$\cdot 2CH_2Cl_2$ (3.7b)

In the same reaction described in section 3.4.4.a, when the sealed vial was left for a longer period of time, a small number of yellow crystals formed in addition to the dark red crystals of complex **3.7a** which proved suitable for X-ray diffraction. No further analytical data were collected due to the very low yield of this product.

3.4.4.c $Co(hfac)_2(pmbtdaH)$ (3.8a)

Ligand pmbtdaH (0.023 g, 0.100 mmol) was added to a solution $Co(hfac)_2$ (0.047 g, 0.100 mmol) in CH_2Cl_2 (15 mL). The mixture was stirred for 15 min and a deep red solution obtained. The solution was filtered and dark brown crystals were grown by layering with hexanes over three weeks. Yield 0.033 g, 46%.

Elemental Analysis calc. for [$C_{21}H_{10}N_4CoSO_4F_{12}$]: C, 35.97; H, 1.44; N, 7.99. Found: C, 35.73; H, 1.88; N, 7.86%.

UV-Vis (CH_2Cl_2; λ_{max}, nm; ε, M^{-1} cm^{-1}): 280 (40892), 305 (43233), 425 (3865).

IR (solid, cm^{-1}) $\tilde{\nu}_{max}$ = 3307 (br), 1634 (m), 1583 (w), 1558 (m), 1524 (m), 1481 (m), 1446 (m), 1418 (m), 1251 (m), 1194 (m), 1136 (br), 1098 (m), 1019 (w), 949 (w), 797 (m), 748 (m), 666 (m), 648 (m), 581 (m), 527 (m), 432 (w), 424 (w).

3.4.4.d Co(hfac)$_2$(pmbtdaH$_{ox}$) (3.8b)

In the same reaction as in section 3.4.4.c, when the sealed vial was left for a longer period of time, orange plates formed in addition to the dark brown crystals of complex **3.8a** suitable for X-ray diffraction. No further analytical data were collected due to very low yield of this product.

3.4.4.e Ni(hfac)$_2$(pmbtdaH) (3.9a)

Ligand pmbtdaH (0.023 g, 0.100 mmol) was added to a solution of Ni(hfac)$_2$·xH$_2$O (0.047 g, 0.100 mmol) in CH$_2$Cl$_2$ (15 mL). The mixture was stirred for 20 min and a deep red solution obtained. The solution was filtered and dark brown crystals were grown by layering with hexanes over three weeks. Yield 0.026 g, 36%.

Elemental Analysis calc. for [$C_{21}H_{10}N_4NiSO_4F_{12}$]·0.25hexanes: C, 37.40; H, 1.88; N, 7.75. Found: C, 37.06; H, 1.50; N, 8.42%.

UV-Vis (CH$_2$Cl$_2$; λ_{max}, nm; ε, M^{-1} cm^{-1}): 280 (29875), 305 (29511), 435 (2558).

IR (solid, cm^{-1}) $\tilde{\nu}_{max}$ = 3295 (br), 1640 (m), 1583 (w), 1555 (m), 1477 (m), 1418 (m), 1348 (w), 1253 (m), 1193 (m), 1135 (br), 1096 (m), 1022 (m), 950 (w), 810 (m), 793 (m), 760 (m), 744 (m), 710 (w), 671 (m), 651 (m), 585 (m), 528 (m), 484 (w).

3.4.4.f [Ni(hfac)$_2$(pmbtdaH$_{ox}$)]·2CH$_2$Cl$_2$ (3.9b)

In the same reaction as in section 3.4.4.e, when the sealed vial was left for a longer period of time, green blocks formed in addition to the dark brown crystals of complex **3.9a** suitable for X-ray diffraction. No further analytical data were collected due to very low yield of this product.

3.4.4.g Cu(hfac)$_2$(pmbtdaH) (3.10a)

Ligand pmbtdaH (0.023 g, 0.100 mmol) was added to a solution of Cu(hfac)$_2$·xH$_2$O (0.049 g, 0.100 mmol) in CH$_2$Cl$_2$ (10 mL). The mixture was stirred for 30 min and a deep red solution obtained. The solution was filtered and dark brown crystals were grown by layering with hexanes over two days. Yield 0.009 g, 13%.

Elemental Analysis calc. for [$C_{21}H_{10}N_4CuSO_4F_{12}$]: C, 35.73; H, 1.43; N, 7.94. Found: C, 35.50; H, 1.12; N, 8.25%.

UV-Vis (CH$_2$Cl$_2$; λ_{max}, nm; ε, M^{-1} cm^{-1}): 290 (35355), 305 (33779), 440 (2960).

IR (solid, cm^{-1}) $\tilde{\nu}_{max}$ = 3242 (br), 1654 (m), 1585 (m), 1548 (m), 1527 (m), 1482 (m), 1454 (m), 1420 (m), 1340 (w), 1254 (m), 1190 (m), 1134 (br), 1087 (m), 1025 (m), 946 (m), 864 (w), 814 (m), 790 (m), 754 (m), 741 (m), 714 (m), 666 (m), 635 (m), 585 (m), 576 (m), 525 (m), 429 (w).

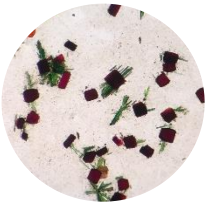

3.4.4.h Cu$_4$(hfac)$_4$(tfa)$_2$(pmbtda$_{ox}$)$_2$ (3.10b)

In the same reaction as in section 3.4.4.g, when the sealed vial was left for a longer period of time, green blocks formed in addition to the dark brown crystals of complex **3.10a** which proved suitable for X-ray diffraction. No further analytical data were collected due to very low yield of this product.

3.4.4.i Zn(hfac)$_2$(pmbtdaH) (3.11a)

Ligand pmbtdaH (0.023 g, 0.100 mmol) was added to a solution of Zn(hfac)$_2$·2H$_2$O (0.052 g, 0.100 mmol) in CH$_2$Cl$_2$ (15 mL). The mixture was stirred for 30 min and a deep red solution obtained. The solution was filtered and dark red crystals were grown over two days by layering with hexanes. Yield 0.055 g, 78%.

Elemental Analysis calc. for [$C_{21}H_{10}N_4ZnSO_4F_{12}$]: C, 35.64; H, 1.42; N, 7.92. Found: C, 35.36; H, 1.34; N, 7.80%.

UV-Vis (CH_3CN; λ_{max}, nm; ε, $M^{-1}\cdot cm^{-1}$): 234 (16844), 278 (38773), 287 (39012), 461 (1985).

IR (solid, cm^{-1}) $\tilde{\nu}_{max}$ = 3296 (br), 1640 (m), 1582 (w), 1557 (w), 1527 (w), 1481 (m), 1458 (w), 1447 (w), 1417 (m), 1250 (m), 1190 (m), 1134 (s), 1096 (s), 1020 (w), 949 (w), 795 (m), 752 (m), 711 (w), 665 (m), 648 (m), 618 (w), 581 (m), 526 (w).

^{1}H NMR (500 MHz, ppm, CD_3CN) δ_H = 9.06 (2H, bs, C^1*H,* C^3*H*), 8.94 (1H, bs, N*H*), 7.85 (1H, t, *J* = 5.2 Hz, C^2*H*), 7.06 (1H, td, *J* = 7.7, 1.4 Hz, C^9*H*), 7.02 (1H, td, *J* = 7.5, 1.3 Hz, C^8*H*), 6.87 (1H, d, *J* = 7.6 Hz, C^7*H*), 6.72 (1H, d, *J* = 7.9 Hz, C^{10}*H*), 6.04 (2H, bs, hfac-C*H*).

^{19}F NMR (470 MHz, ppm, CD_3CN) δ_F = -73.11 (bs).

3.4.4.j Zn$_4$(hfac)$_6$(pmbtda$_{ox}$)$_2$ (3.11b)

Ligand pmbtdaH (0.023 g, 0.100 mmol) was added to a solution of Zn(hfac)$_2$·2H$_2$O (0.052 g, 0.100 mmol) in CH$_2$Cl$_2$ (15 mL). The mixture was stirred for 30 min and a deep red solution obtained. The solution was filtered and left undisturbed in a sealed vial. White crystals were grown over two weeks. Yield 0.006 g, 3%.

Elemental Analysis calc. for [$C_{52}H_{20}N_8Zn_4S_2O_{14}F_{36}$]·4H$_2$O: C, 30.28; H, 1.37; N, 5.43. Found: C, 30.07; H, 1.25; N, 5.37%.

UV-Vis (CH_3CN; λ_{max}, nm; ε, $M^{-1}\cdot cm^{-1}$): 264 (7595), 300 (11163), 356 (16998).

IR (solid, cm^{-1}) $\tilde{\nu}_{max}$ = 1647 (m), 1570 (w), 1524 (w), 1494 (m), 1460 (m), 1375 (w), 1253 (m), 1194 (m), 1134 (s), 1000 (s), 969 (w), 837 (m), 824 (m), 804 (m), 770 (m), 743 (w), 665 (m), 582 (m), 559 (w), 527 (w), 485 (w).

3.4.5 Single-crystal X-ray crystallography

Crystals of the ligand and the complexes **3.1** − **3.10a** and **3.11** were mounted on a cryoloop with paratone oil and examined on a Bruker APEX diffractometer equipped with CCD area detector and Oxford Cryostream cooler using graphite-monochromated Mo-*K*α radiation (λ = 0.71073 Å). Data were collected using the APEX-II software[29], integrated using SAINT[30] and corrected for absorption using a multi-scan approach (SADABS)[31]. Single crystals of complex **3.10b** were mounted on a cryoloop with paratone oil and measured on a Bruker Kappa system APEX-II diffractometer equipped with an Oxford Cryoflex low temperature device. Data were collected at 150(2) K using graphite-monochromated Mo-Kα radiation (λ = 0.71073 Å) using the APEX-II software.

Final cell constants were determined from full least squares refinement of all observed reflections. The structures of pmbtdaH and complexes **3.10b** and **3.11a** were solved by direct methods (SHELXS within SHELXTL[32]) to reveal most non-H atoms. Remaining atom positions were located in subsequent difference maps and the structure refined with full least squares refinement on F^2 within the SHELXTL suite.[32] Structures **3.1** − **3.10a** and **3.11b** were solved using Olex2[33], with the ShelXT structure solution program[34] using intrinsic phasing and refined within the ShelXL[35] refinement package using least-squares minimization on F^2. All hydrogen atoms were added at calculated positions and refined isotropically with a riding model. In addition a residual electron density peak close to C(9) was identified as a partial occupancy Cl atom (10% occupancy) for complexes **3.2** − **3.5**, **3.7b** and **3.8b**. For complex **3.7a**, the occupancy of the Cl atoms was 40% and 60% and exhibited rotational disorder on two of the eight CF_3 groups in the asymmetric unit, which were modelled over two sites in a 1:1 ratio with a common U_{iso}. PLATON/SQUEEZE[36] was used to treat the contents of the voids because the electron density was too diffuse to model on complex **3.7a**. Complex **3.8a** exhibited rotational disorder of three of the four CF_3 groups in the asymmetric unit whereas complex **3.8b** exhibited rotational disorder of two of the four CF_3 groups in the asymmetric unit which were modelled over two sites in a 1:1 ratio with a common U_{iso}. Complex **3.9a** exhibited rotational disorder of three CF_3 groups in the asymmetric unit, which were modelled over two sites in a 1:1 ratio, and three CF_3 groups modelled over three sites with a common U_{iso}. A twin law was applied on complex **3.9b** and also exhibited rotational disorder of all four CF_3 groups in the asymmetric unit which were modelled over two sites in a 1:1 ratio with a common U_{iso}. Complex **3.10b** exhibited rotational disorder on the free O of the tfa^- group in the asymmetric unit which was modelled over two sites in a 60:40 ratio with a common U_{iso}. Complex **3.11a** revealed substantial disorder of the two $hfac^-$ ligands which were modelled as two orientations of the $hfac^-$ anion in a 50:50 ratio and exacerbated by additional rotational disorder of many of the CF_3 groups. Complex **3.11b** exhibited rotational disorder of four of the six CF_3 groups in the asymmetric unit which were modelled over two sites in a 1:1 ratio with a common U_{iso}. In addition a residual electron density peak close to C(9) was identified as a partially occupancy Cl atom (5% occupancy) and confirmed by a low abundance peak in the m/z data with appropriate isotopomer ratio. A summary of key crystallographic data for the ligands and complexes is presented in Appendix 2.

3.5. References

1 E. R. Clark, M. U. Anwar, B. J. Leontowicz, Y. Beldjoudi, J. J. Hayward, W. T. K. Chan, E. L. Gavey, M. Pilkington, E. Zysman-Colman and J. M. Rawson, *Dalton Trans.*, 2014, **43**, 12996.

2 E. R. Clark, J. J. Hayward, B. J. Leontowicz, M. U. Anwar, M. Pilkington and J. M. Rawson, *Dalton Trans.*, 2014, **44**, 2071.

3 A. K. Pal, D. B. Cordes, K. Pringouri, M. U. Anwar, A. M. Z. Slawin, J. M. Rawson and E. Zysman-Colman, *J. Coord. Chem.*, 2016, **69**, 1924.

4 N. Yutronkie, I. Kuehne, I. Korobkov, J. L. Brusso and M. Murugesu, *Chem. Commun.*, 2015, 677.

5 K. L. M. Harriman, I. A. Kühne, A. A. Leitch, I. Korobkov, R. Clérac, M. Murugesu and J. L. Brusso, *Inorg. Chem.*, 2016, **55**, 5375.

6 A. Trummal, L. Lipping, I. Kaljurand, I. A. Koppel and I. Leito, *J. Phys. Chem. A*, 2016, **120**, 3663.

7 M. Ellinger, H. Duschner and K. Starke, *J. Inorg. Nucl. Chem.*, 1978, **40**, 1063–1067.

8 E. R. Clark, J. J. Hayward, B. J. Leontowicz, D. J. Eislera and J. M. Rawson, *CrystEngComm*, 2014, **16**, 1755.

9 J. Coates, *Encycl. Anal. Chem.*, 2006, 1.

10 K. Pringouri, M. U. Anwar, B. J. Leontowicz and J. M. Rawson, *Polyhedron*, 2018, **150**, 110.

11 J. G. Stark and H. G. Wallace, *Chemistry Data Book*, J. Murray. Publ., London, S. I. Edit., 1980.

12 N. N. Earnshaw and A. Greenwood, *Chemistry of the Elements*, Pergamon Press, Oxford, 1st edn., 1986.

13 E. R. Clark, *Ph.D. Thesis,* 2008, Synthesis and chemistry of benzo-1,2,4thiadiazines.

14 J. Zienkiewicz, A. Fryszkowska, K. Zienkiewicz, F. Guo, P. Kaszynski, A. Januszko and D. Jones, *J. Org. Chem.*, 2007, **72**, 3510.

15 A. W. Addison and T. N. Rao, *J. Chem. Soc., Dalton Trans.*, 1984, 1349.

16 *CSD search Zn-Cl, mean Bond length all results*.

17 *CSD search Zn-Cl-Zn, mean Bond length all results*.

18 L. O. Occf, S. Wang, Z. Pang, K. D. L. Smith, C. Deslippe and M. J. Wagner, *Inorg. Chem.*, 1995, **4**, 908.

19 C. J. Milios, E. Kefalloniti, C. P. Raptopoulou, A. Terzis, A. Escuer, R. Vicente and S. P. Perlepes, *Polyhedron*, 2004, **23**, 83.

20 M. Calligaris, *Coord. Chem. Rev.*, 2004, **248**, 351.

21 R. M. Silverstein, G. C. Bassler and T. C. Morrill, *Spectroscopic Identification of Organic Compounds*, J. Wiley, 4th edn., 1981.

22 H. S. Rzepa and M. E. Cass, *Inorg. Chem.*, 2007, **46**, 8024.

23 Y. Li, T. Thiemann, T. Sawada, S. Mataka and M. Tashiro, *J. Org. Chem.*, 1997, **62**, 7926.

24 D.R. Duling, *J. Magn. Reson.*, 1994, **B104**, 105.

25 A. D. Becke, *J. Chem. Phys.*, 1993, 5648.

26 C. Lee, W. Yang and R. G. Parr, *Phys. Rev. B Condens. Matter*, 1988, 785.

27 A. S. Miehlich, H. Stoll and H. Preuss, *Chem. Phys. Lett.*, 1989, 200.

28 A. D. Bochevarov, E. Harder, T. F. Hughes, J. R. Greenwood, D. A. Braden, D. M. Philipp, D. Rinaldo, M. D. Halls, J. Zhang and R. A. Friesner, *Int. J. Quantum Chem.*, 2013, **113**, 2110.

29 APEX-II, Bruker AXS, Inc., Madison, Wisconsin, USA.

30 SAINT, Bruker AXS Inc., Madison, Wisconsin, USA.

31 SADABS, Bruker AXS Inc., Madison, Wisconsin, USA.

32 SHELXTL, *Bruker AXS Inc.,* Madison, Wisconsin, USA, 2015.

33 O. V. Dolomanov, L. J. Bourhis, R. . Gildea, J. A. K. Howard and H. Puschmann, *J. Appl. Cryst.*, 2009, **42**, 339.

34 G. M. Sheldrick, *Acta Cryst.*, 2015, **A71**, 3.

35 G. M. Sheldrick, *Acta Cryst.*, 2015, **C71**, 3.

36 A. L. Spek, *Acta Crystallogr*, 2015, **C71**, 9.

CHAPTER 4.

Synthesis and characterization of pybtdaSMe and its coordination chemistry

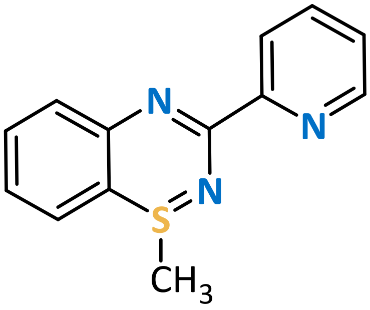

4.1. Introduction

The benzothiadiazine ligand pybtdaH has been reported to form a series of mononuclear complexes to first row transition metal complexes of formula $MCl_x(pybtdaH)_y$.[1] The S^{II} system undergoes aerial oxidation to the S^{IV} system (Scheme 4.1) in the presence of a Lewis acidic metal and a base.[2] The $pybtda_{ox}^{-}$ anion is formed which has been isolated in the form of $[Cu(pybtda_{ox})_2]_2$[2] and $Ir(ppy)_2(pybtda_{ox})$.[3] In Chapter 2, *S*-oxidation was shown to also proceed in the presence of more Lewis acidic metals (complexes **2.3a** and **2.3b**) or in the presence of more basic counterions, such as the hfac⁻ and OAc⁻ group. The introduction of additional base (Et_3N) assisted the *S*-oxidation and the deprotonation of the pybtdaH ligand, resulting in higher nuclearity clusters (complexes **2.11** – **2.14**). The *S*-oxidation of the benzothiadiazine ligands offers a more versatile, hard, *O*-donor centre in addition to the favourable, softer, *N*,*N*′-chelate, favouring aggregation and leading to polynuclear complexes such as those described in Chapters 2 and 3.

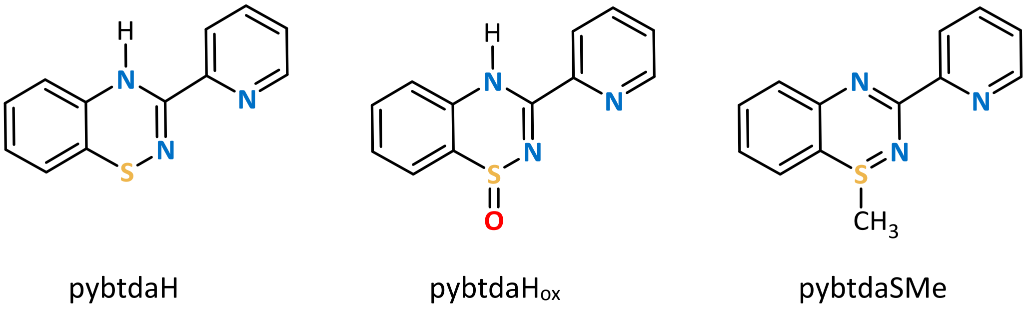

Scheme 4.1 Molecular structures of pybtdaH, pybtdaH$_{ox}$ and pybtdaSMe.

In the benzothiadiazine system, alkylation of the S or N is expected to alter the electronics of the heterocycle with respect to S^{II} pybtdaH ligand and the coordination behaviour of the *S*-methylated ligand pybtdaSMe (Scheme 4.1) is expected to differ significantly from pybtdaH and pybtdaH$_{ox}$. For example pybtdaH can undergo both $1e^{-}$ oxidation (loss of $H^{\bullet}$) and loss of H^{+} and pybtdaH$_{ox}$ can also lose H^{+}. For pybtdaSMe, the S atom is formally in the S(IV) oxidation state and there is no N-H group, potentially leading to more controlled reaction chemistry. In addition the methyl group can potentially hinder coordination at N(2) favouring the alternative *N*,*N*′ coordination pocket using N(4) (Figure 4.1).

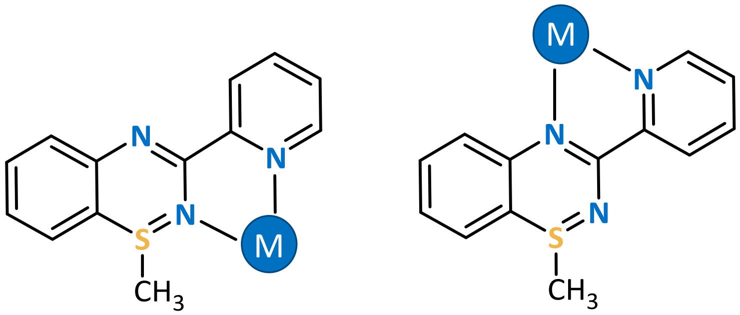

Figure 4.1 Coordination modes of ligand pybtdaSMe.

In this chapter, we present the synthesis and characterization of the 1-methyl-3-(pyridinyl)-1,2,4-benzothiadiazine (pybtdaSMe, Scheme 4.1) as well as examine its coordination chemistry to selected first row transition metal complexes.

4.2. Results and Discussion

4.2.1 Synthesis and characterization of the ligand pybtdaSMe

In order to prepare pybtdaSMe, we examined preparative routes to the alkylation of other S/N heterocycles. For example, Brusso has reported the preparation of a variety of *S*-alkyl-thiatriazines (TTA).[4,5] The synthesis involving the methyl and ethyl derivative of pyTTA is shown in Scheme 4.2.[4] The synthesis can proceed *via* two synthetic pathways which implement either cationic (Route A) or anionic (Route B) intermediates depending on the alkylating agent used. The synthetic route was of interest because of the functionalization of the *S* following the heterocycle ring formation.

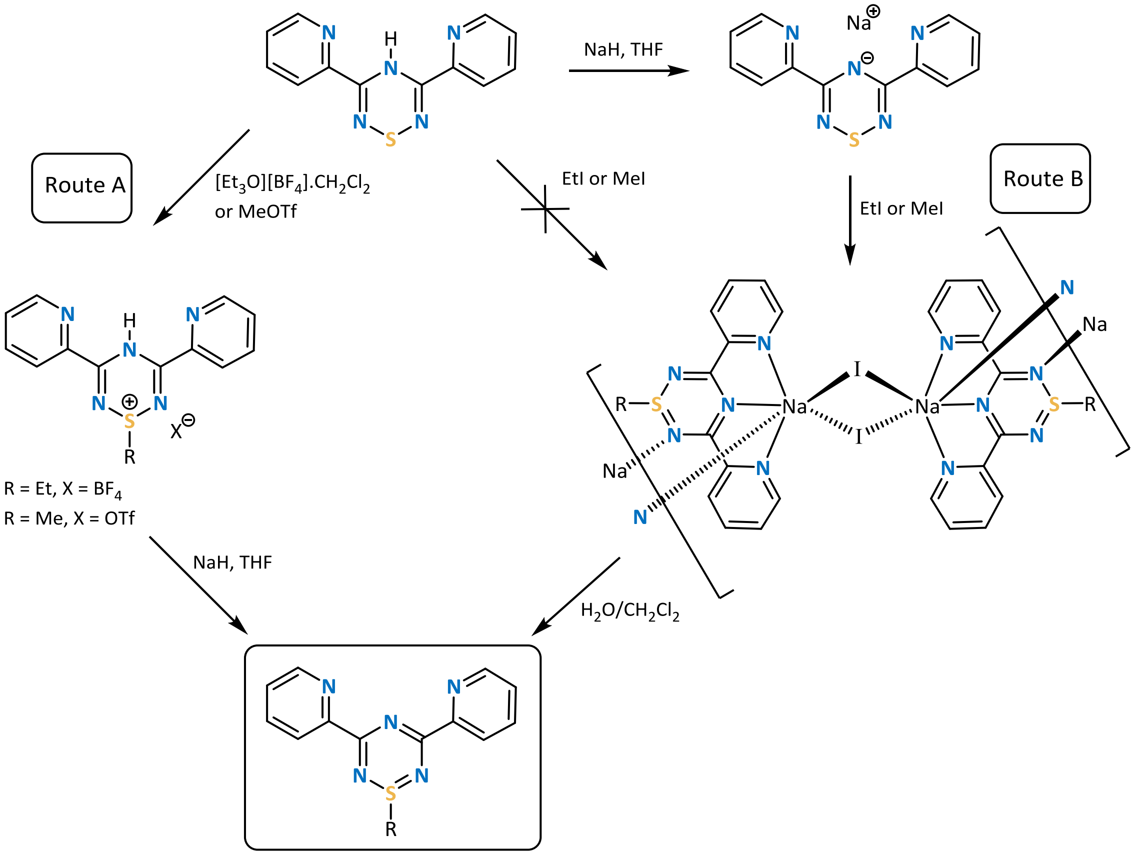

Scheme 4.2 Synthesis of *S*-alkyl-3,5-bis-(2-pyridyl)-1,2,4,6-thiatriazines (Scheme reproduced from publication[4]).

A similar synthetic way to Route B was used for the preparation of pybtdaSMe in the presence of a base and a alkylating agent shown in Scheme 4.3.

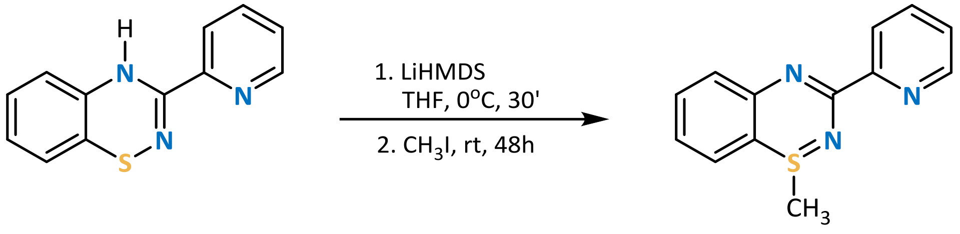

pybtdaH

pybtdaSMe, 89%

Scheme 4.3 Synthetic route to ligand pybtdaSMe.

The synthesis of the ligand pybtdaH is described in Chapter 2. Deprotonation of pybtdaH with LiHMDS, under anaerobic, dry conditions followed by treatment with one equivalent of iodomethane and work-up resulted in pybtdaSMe as a brown oil. Subsequent recrystallization from CH_2Cl_2 yielded the product as yellow crystals in 89% yield. The product showed some decomposition to red pybtdaH (detected by TLC) and therefore was stored in the freezer. Similar decomposition was reported previously for the phenyl derivative of the methylated benzothiadiazine.[6] The ^{1}H NMR spectrum of pybtdaSMe exhibits the expected proton environments in the aromatic region and a

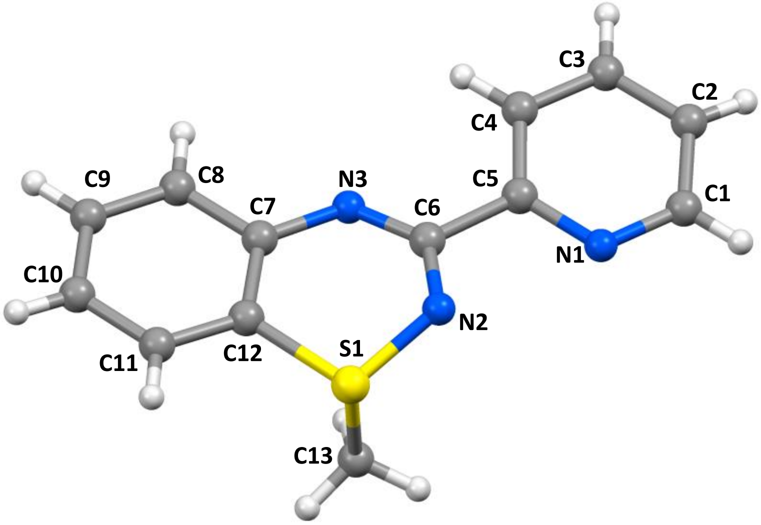

Figure 4.2 Molecular structure of pybtdaSMe.

singlet in the aliphatic region corresponding to the methyl group. The imine C=N stretching vibration was observed at 1585 cm^{-1}, as expected.[7]

The molecular structure was confirmed by single crystal X-ray diffraction studies and is shown in Figure 4.2. The compound crystallizes in the monoclinic space group $P2_1/c$ with one molecule in the asymmetric unit. The C(6)-N(3) distance is 1.312(4) Å, consistent with predominant double bond character (*cf* imine C=N at 1.279 Å)[8]. The bond length between C(6)-N(2) at 1.372(4) Å is more consistent with a conjugated C-N single bond (*cf* Ph-NH_2 at 1.355 Å)[8]. The S-N bond length (1.629(3) Å) is comparable with other S-N single bonds (1.62 – 1.74 Å for isomers of $S_{8-x}(NH)_x$)[9] and 1.69 – 1.72 Å for other benzothiadiazine derivatives)[10]. The bond lengths assess the best resonance structure as shown in Figure 4.3.

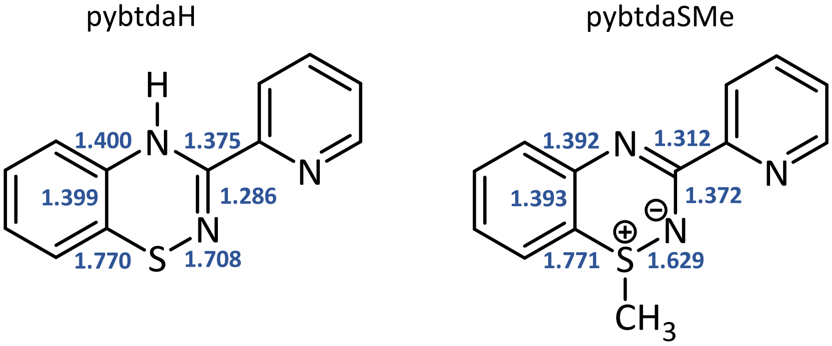

Figure 4.3 Comparison of the heterocycle bond lengths of pybtdaH and pybtdaSMe.

The preference for the crystallographically-determined isomer (orientation of the pyridyl ring) was confirmed by DFT calculations (B3LYP/6-311G*$^+$) on the two possible isomers which revealed the experimentally determined structure was only 6 kJ/mol more stable. Another notable feature in the benzothiadiazine ring is the folding (θ) of the molecule about the trans-annular vector S(1)···N(3). The values for the majority of previously reported benzothiadiazines fall in the range 21° < θ < 42° [10] consistent with formally 8π anti-aromatic structure. For pybtdaSMe, θ = 23.79°. Here alkylation at S breaks the π-delocalization such that there is conjugation around just the C_3N_2 part of the ring.

The crystal packing of pybtdaSMe is manifested by π-π interactions extending the network along the *bc* plane. The centroid···centroid distances are 3.573 Å with the closest C···C distance at 3.423 Å (*cf* interlayer separation in graphite at 3.354 Å[9]) (Figure 4.4).

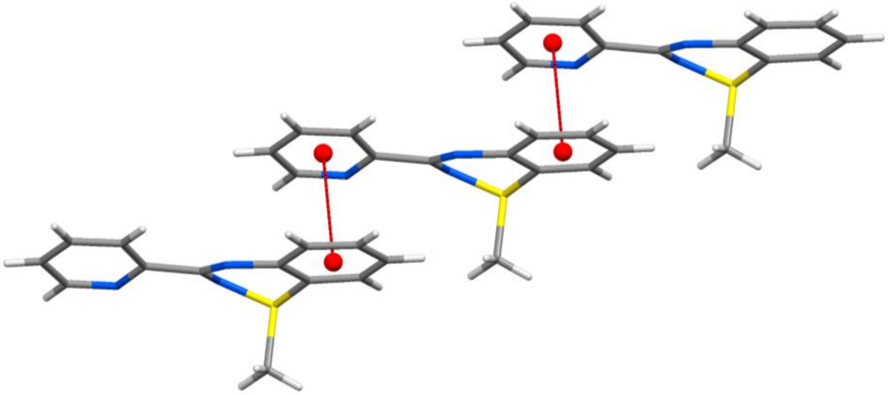

Figure 4.4 Crystal packing of pybtdaSMe highlighting π-π interactions along *bc* plane.

The ligand creates a two dimensional network through the π-π interactions and extended hydrogen bonding as shown in Figure 4.5 (left). The network is extended in the third dimension but only by another 2D plane creating a tube-like framework along *b* axis with the S-CH_3 in the periphery (Figure 4.5, right).

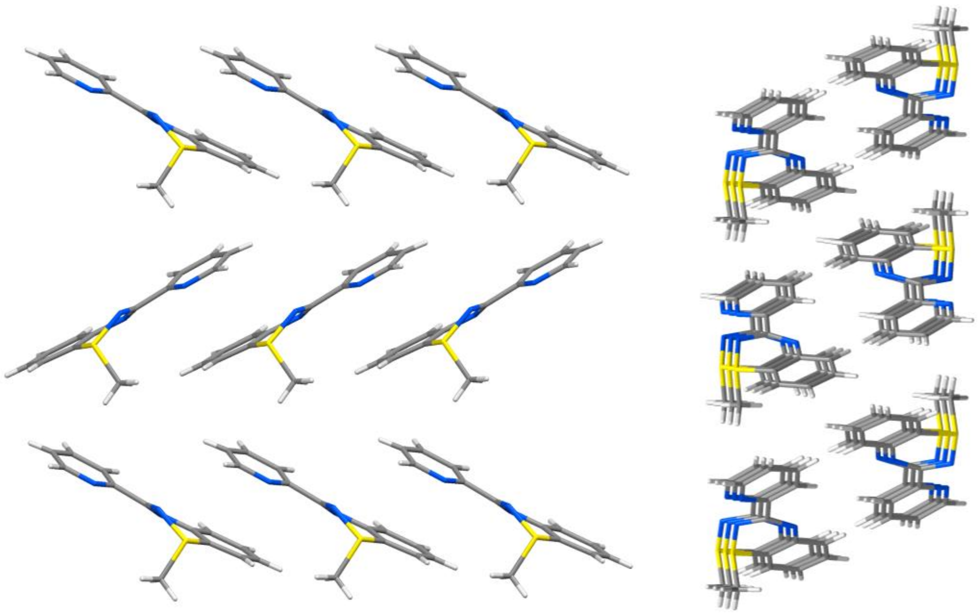

Figure 4.5 Crystal packing of pybtdaSMe illustrating the two dimensional network (left); three dimensional nature along *b* axis (right).

4.2.2 Reactivity of pybtdaSMe with MCl_2 (M = Mn, Ni, Cu, Zn)

4.2.2.a Syntheses and crystal structures of $MCl_2(pybtdaSMe)_2$ (M = Mn (4.1), Ni (4.2))

Reaction of pybtdaSMe with the metal chloride salt in CH_3OH in a 1:1 molar ratio at ambient temperature afforded the complexes $MCl_2(pybtdaSMe)_2$ (M = Mn (**4.1**), Ni (**4.2**)). Crystals suitable for X-ray diffraction were grown by layering with diethyl ether/pentane or diethyl ether/hexanes in 1:1 ratio over periods between 2 days to 2 weeks. The structures of $[MCl_2(pybtdaSMe)_2]$ were found to be isomorphous, crystallising in the triclinic space group $P\overline{1}$ with one molecule in the asymmetric unit. The formation of complexes **4.1** and **4.2** is summarized in Equation 4.1.

$$MCl_2 + 2\ pybtdaSMe \longrightarrow MCl_2(pybtdaSMe)_2 \qquad \text{Equation 4.1}$$

The structure of complex **4.2** is shown in Figure 4.6, as representative of complexes **4.1** and **4.2**, and selected bond lengths and angles are shown in Table 4.1. The metal centres adopt a pseudo-octahedral geometry with the two chloride ligands mutually *cis* and the pyridyl N atoms located *trans* to the Cl atoms. The ligand adopts a simple *N*,*N'*-chelate mode to the metal centre in which the pyridyl N(1) and the heterocyclic N(2) atoms are involved in metal binding. The chelate ligand pybtdaSMe exhibits internal N_{py}-M-N_{BTDA} angles in the range 71.17(11) – 77.57(8)°.

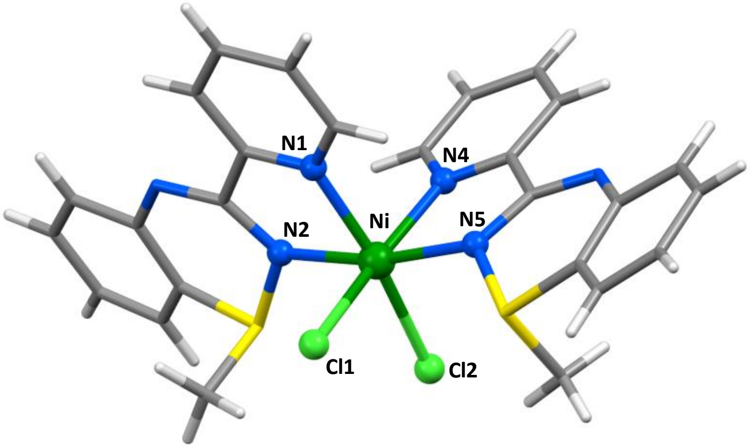

Figure 4.6 Molecular structure of $NiCl_2(pybtdaSMe)_2$ (**4.2**).

Table 4.1 Selected bond lengths and angles for complexes **4.1** and **4.2**.

	M-N_{py}/Å	M-N_{BTDA}/Å	M-Cl/Å	N_{py}-M-N_{BTDA}/°[a]	N_{py}-M-N_{BTDA}/°[b]
Mn (**4.1**)	2.267(3)	2.274(3)	2.4517(12)	71.18(11)	93.72(11)
	2.278(3)	2.283(3)	2.4580(11)	71.18(11)	93.69(11)
Ni (**4.2**)	2.093(2)	2.0925(19)	2.4060(9)	77.45(7)	93.79(8)
	2.097(2)	2.1047(19)	2.4148(9)	77.57(8)	94.92(8)
	N_{py}-M-Cl/°	N_{BTDA}-M-Cl/°	Cl-M-Cl/°	C···C/Å[c]	centroid-centroid/Å
Mn (**4.1**)	92.90(8)	91.61(6)	96.73(5)	3.722	3.828
	92.62(8)	92.51(6)		3.827	4.014
	100.41(8)	95.58(6)			
	101.18(9)	95.91(6)			
Ni (**4.2**)	87.88(6)	91.61(6)	93.12(3)	3.739	3.957
	91.35(6)	92.51(6)		3.837	4.039
	169.07(5)	95.58(6)			
	169.50(6)	95.91(6)			

[a] Angle within the chelate ring [b] Angles between N atoms in different rings [c] Closest C···C distance

The packing of **4.2** places the aromatic rings of neighbouring molecules in close proximity having π-π interactions which form an 1D chain along *ab* plane. The centroid···centroid distances are in the range 3.957 – 4.039 Å with the closest C···C distance at 3.739 Å (*cf* interlayer separation in graphite at 3.354 Å[9]) (Figure 4.7, top). The presence of C-H···Cl-M hydrogen bonds affords a three dimensional network (Figure 4.7, bottom).

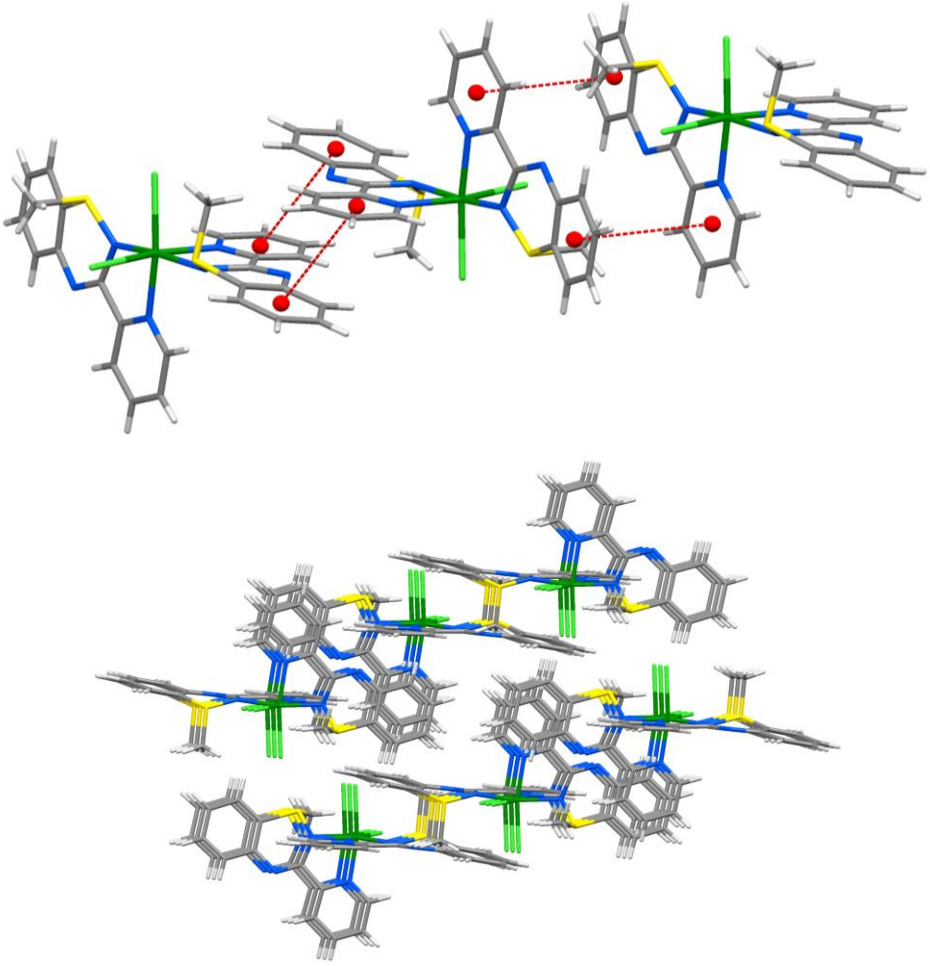

Figure 4.7 (top) Crystal packing of **4.2** highlighting the π-π interaction the aromatic rings of neighbouring ligand molecules; (bottom) in the *ab* plane revealing the three dimensional nature originated from the π-π interactions and hydrogen bonding.

4.2.2.b Synthesis and crystal structures of polymorphs $Cu_2Cl_4(pybtdaSMe)_2$ (4.3a) and $Cu_2Cl_4(pybtdaSMe)_2 \cdot 2(CuCl_2pybtdaSMe)$ (4.3b)

Reaction of the ligand pybtdaSMe with $CuCl_2$ in CH_3OH or CH_3CH_2OH in a 1:1 molar ratio at ambient temperature afforded a dark olive solution. Bright green crystals of the dinuclear complex $Cu_2Cl_4(pybtdaSMe)_2$ (**4.3a**) were formed by layering a CH_3CH_2OH solution with diethyl ether/hexanes (1:1 ratio) over two days. The formation of complex **4.3a** is summarized in Equation 4.2.

$$2\ CuCl_2 + 2\ pybtdaSMe \longrightarrow Cu_2Cl_4(pybtdaSMe)_2 \qquad \text{Equation 4.2}$$

Crystals of the second polymorph $Cu_2Cl_4(pybtdaSMe)_2 \cdot 2(CuCl_2pybtdaSMe)$ (**4.3b**) were formed by layering a CH_3OH solution with diethyl ether/hexanes (1:1 ratio) over 3 days and comprises a 1:2 mixture of dimers, $Cu_2Cl_4(pybtdaSMe)_2$, and monomers, $CuCl_2pybtdaSMe$.

The structure of **4.3a** was determined by X-ray diffraction at 170 K (Figure 4.8) and crystallizes in the triclinic space group $P\overline{1}$ with half a molecule in the asymmetric unit. The two Cu^{II} centres within **4.3a** are related *via* an inversion centre with each copper ion adopting a 5-coordinate geometry with a N_2Cl_3 donor set. The Addison τ_5 value[11] (0.16) is consistent with a square pyramidal geometry where for trigonal bipyramidal (τ = 1) and square pyramidal (τ = 0). The heterocyclic ligand provides an *N*,*N'*-chelate pocket analogous to complexes **4.1** and **4.2** through the pyridyl N(1) and the heterocyclic N(2) atoms with M-N distances at 2.008(3) Å and 2.030(2) Å and N_{py}-M-N_{BTDA} angle at 79.46(10)°. The two crystallographically independent Cl anions adopt different coordination modes; the first Cl atom is terminal, whereas the second Cl atom takes up a μ_2-bridging mode between two Cu^{II} centres. The Cu(1)-Cl(2) bond length (2.2650(10) Å) for the terminal chlorine is comparable with other Cu-Cl bonds (2.194 – 3.146 Å).[12] The Cu-Cl bond lengths for the bridging chlorides are 2.2595(9) Å for Cu(1)-Cl(1) and 2.7390(9) Å for Cu(1)-Cl(1′), comparable with other bridging Cl^- in the literature (2.214 – 3.167 Å).[13] The structure of **4.3a** is similar to the Zn complex, $Zn_2Cl_4(pmbtdaH)_2$[14] (**3.6**) which is discussed in Chapter 3.

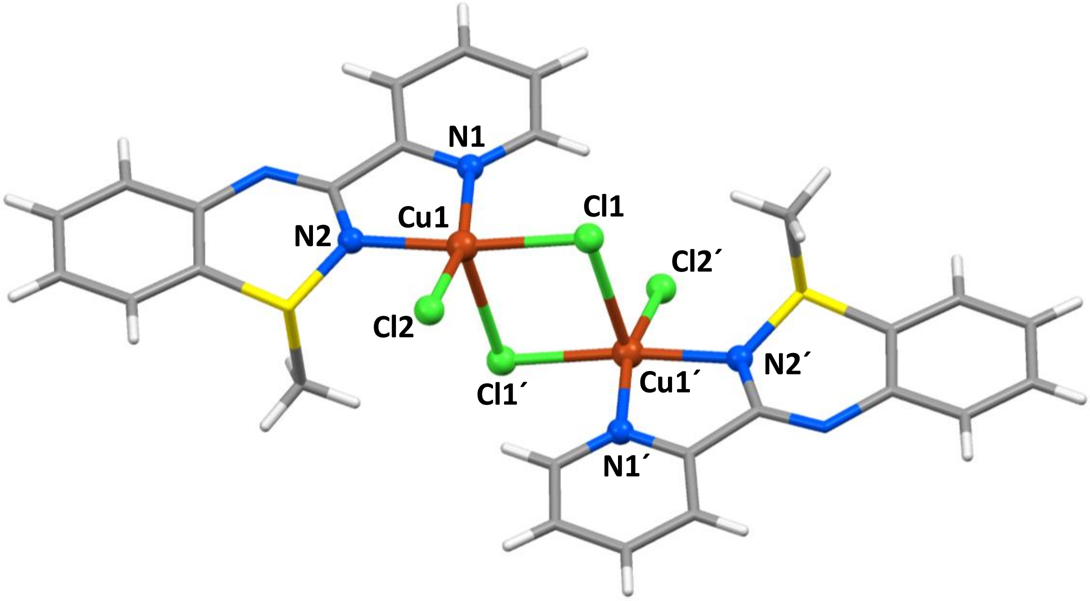

Figure 4.8 Molecular structure of $Cu_2Cl_4(pybtdaSMe)_2$ (**4.3a**).

The structure of polymorph **4.3b** was determined by X-ray diffraction (Figure 4.9) and adopts the formula $Cu_2Cl_4(pybtdaSMe)_2 \cdot 2CuCl_2(pybtdaSMe)$. It crystallizes in the triclinic space group $P\overline{1}$ with half a dimer and a whole monomer in the asymmetric unit. The dimer unit in **4.3b** has the same structure as **4.3a** based on a comparison of bond lengths and angles (Table 4.3) and structure overlay within Mercury.[15] The metal centre of the monomeric $CuCl_2$(pybtdaSMe) unit adopts a 4-coordinate geometry with a N_2Cl_2 donor set in which the ligand also adopts the same *N*,*N′*-chelate mode to the metal centre as **4.3a**. The geometry index $\tau_4 = 0.35$ is consistent with a distorted square planar geometry ($\tau = 1$ for tetrahedral geometry and $\tau = 0$ for square planar geometry).[16] The ligand pybtdaSMe exhibits a N_{py}-Cu-N_{BTDA} angle of 80.93° and the Cu-N bond lengths are 1.975(3) Å and 2.007(3) Å. The two Cl groups are acting as terminal ligands with distances at 2.2128(9) Å and 2.2192(10) Å.

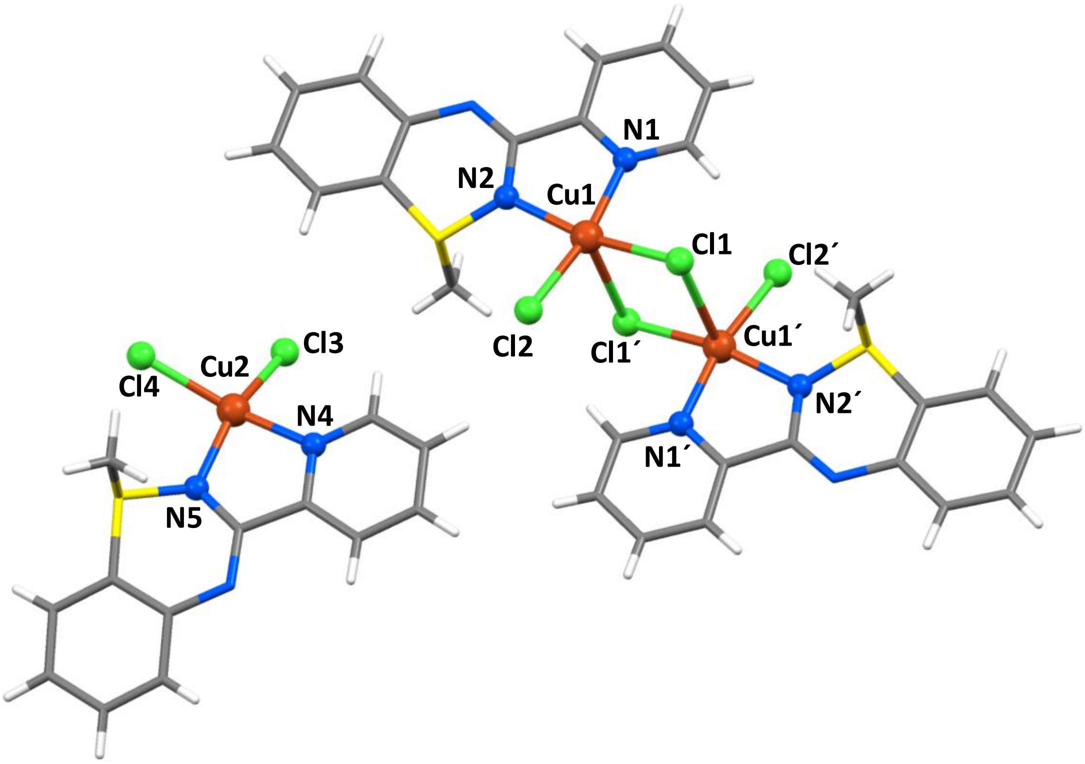

Figure 4.9 Molecular structure of $Cu_2Cl_4(pybtdaSMe)_2 \cdot 2CuCl_2(pybtdaSMe)$ (**4.3b**).

An additional crystallographic study was undertaken on **4.3b** at 280 K. The unit cell parameters were very close to those measured at 170 K (Table 4.2). An initial examination of the high temperature structure revealed breakdown of the dimer unit. Careful examination of the structure at 280 K showed Cu···Cl interactions at 2.961(2) Å, slightly larger than the sum of the van der Waals radii whereas the 170 K structure revealed a shorter Cu-Cl distance at 2.897(1) Å (Table 4.3) formally sufficiently close to be considered as a long bond corresponding to the molecular Jahn-Teller axis. An overlay of the structures collected at 170 and 280 K using Mercury[15] confirmed the similarity of these two structures (Figure 4.10).

Table 4.2 Unit cell parameters for complexes **4.3a** and **4.3b** in T = 170 K and 280 K.

	a/Å	b/Å	c/Å	α/°	β/°	γ/°	V/Å^3	Crystal system/ Space group
4.3a (170 K)	7.5688(14)	9.561(2)	9.935(2)	76.672(9)	86.204(9)	83.819(8)	694.8(2)	Triclinic $P\bar{1}$
4.3b (170 K)	9.6141(4)	11.5056(5)	14.2083(7)	68.672(2)	81.595(2)	78.836(2)	1431.38(11)	Triclinic $P\bar{1}$
4.3b (280 K)	9.6623(7)	11.5536(8)	14.3470(12)	68.94(4)	81.273(3)	78.873(3)	1460.6(2)	Triclinic $P\bar{1}$

Table 4.3 Selected bond lengths and angles for complexes **4.3a** and **4.3b** in T = 170 K and 280 K.

	dimer		monomer
	M-Cl$_{bridging}$/Å	M-Cl$_{terminal}$/Å	M-Cl$_{terminal}$/Å
4.3a (170K)	2.2595(9) 2.7390(9)	2.2650(10)	-
4.3b (170K)	2.2647(8) 2.897(1)	2.2492(8)	2.2128(9) 2.2192(10)
4.3b (280K)	2.2613(11) 2.961(2)	2.2483(11)	2.2155(13) 2.2154(12)

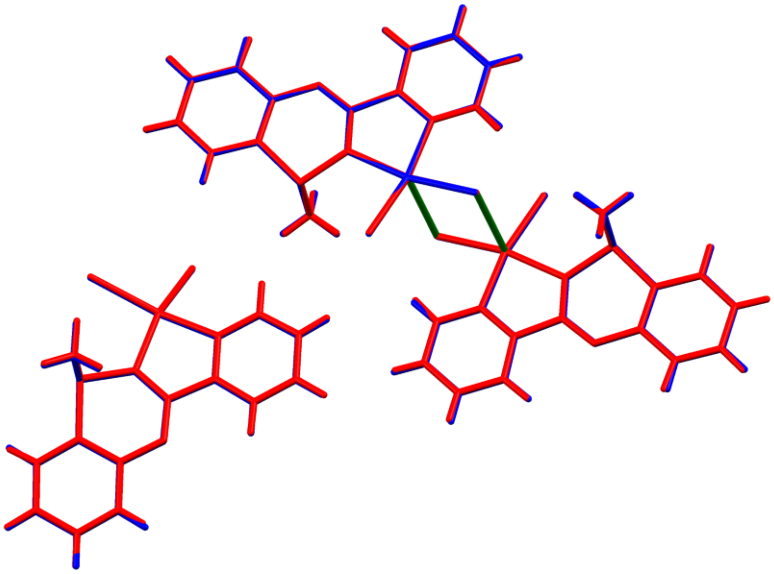

Figure 4.10 Structure overlay of complex **4.3b** at T = 170 K (red) and 280 K (blue); highlighting the bridging Cu-Cl bonds (green).

The similarity in the structures of **4.3b** determined at 170 and 280 K were confirmed through simulation and compared with the experimental room temperature PXRD pattern (Figure 4.11).

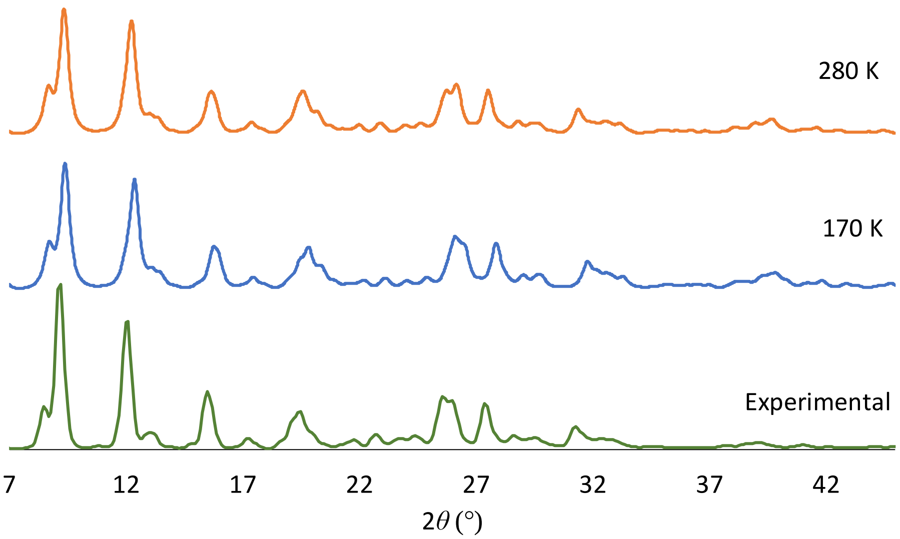

Figure 4.11 Powder X-ray diffraction patterns of the simulated data of the collection of complex **4.3b** at 170 K (blue) and 280 K (orange) and the experimental data for **4.3b** recorded at room temperature (green).

4.2.2.c Synthesis and crystal structure of ZnCl₂(pybtdaSMe) (4.4)

Reaction of the ligand pybtdaSMe with $ZnCl_2$ in CH_2Cl_2 in a 1:1 molar ratio at ambient temperature afforded the mononuclear complex $ZnCl_2$(pybtdaSMe) (**4.4**) (Figure 4.12). Crystals suitable for X-ray diffraction were grown by layering with diethyl ether/hexanes in a 1:1 ratio over 2 weeks. The complex crystallizes in the triclinic space group $P\bar{1}$ with one molecule in the asymmetric unit. The formation of complex **4.4** is summarized in Equation 4.3.

$$ZnCl_2 + \text{pybtdaSMe} \longrightarrow ZnCl_2(\text{pybtdaSMe}) \qquad \text{Equation 4.3}$$

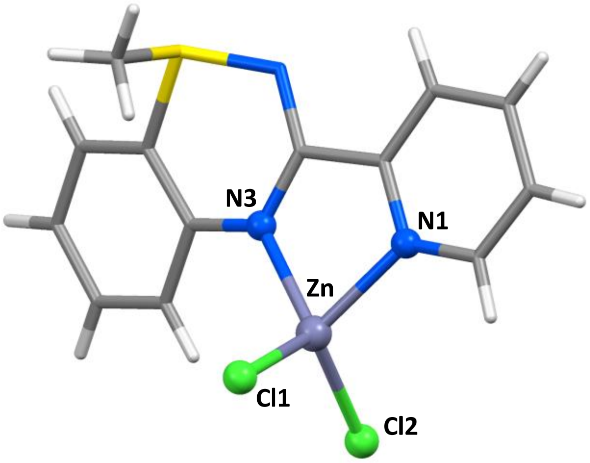

Figure 4.12 Molecular structure of $ZnCl_2$(pybtdaSMe) (**4.4**).

The metal centre adopts a 4-coordinate geometry with a N_2Cl_2 donor set. The geometry index has a value of $\tau_4 = 0.89$ consistent with a tetrahedral geometry ($\tau = 1$ for tetrahedral geometry and $\tau = 0$ for square planar geometry).[16] The ligand adopts a simple *N*,*N′*-chelate mode to the metal centre but in this case the ligand is coordinated through N(3) rather than N(2) which was previously observed for pybtdaSMe in complexes **4.1** – **4.3**. A similar rotation of the pyridyl ring has been previously reported on pybtdaH in a dimeric Cu complex, $[Cu(pybtda_{ox})_2]_2$.[2] This ligand conformation leaves the thiadiazine rings of neighbouring molecules 'exposed' leading to S···N interactions (3.192(2) Å) with a *trans*-oid configuration along *b* axis (Figure 4.13, cyan lines) as well as Cl···S type interactions at 3.3667(8) Å (Σ_{vdW} = 3.650 Å) with a Zn-Cl···S angle of 124.03(3)° (Figure 4.13, green lines).[17]

The packing of **4.4** places the aromatic rings of the neighbouring ligands in close proximity with centroid···centroid distances of 3.977 Å with the closest C···C distance at 3.690 Å (*cf* interlayer separation in graphite at 3.354 Å[9]) (Figure 4.13).

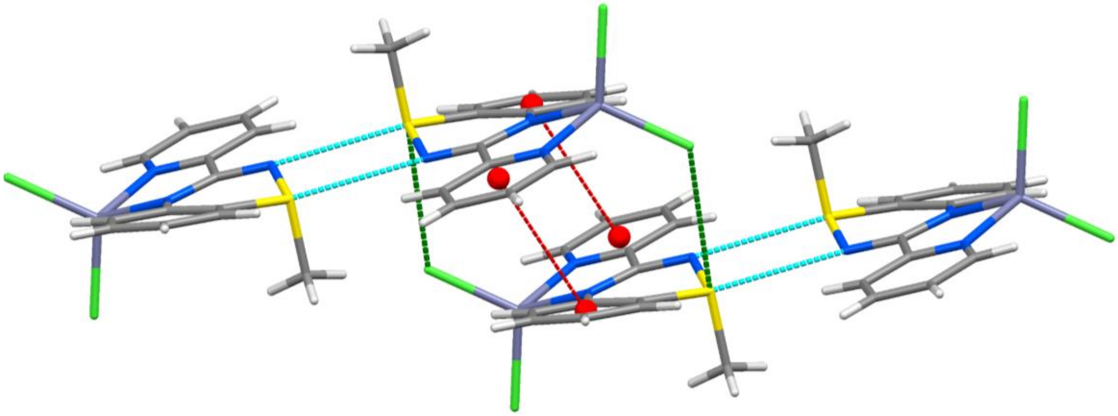

Figure 4.13 Crystal packing of **4.4** highlighting the π-π (red), the S···N (cyan) and the Cl···S interactions (green).

4.2.3 Reaction of pybtdaSMe with M(hfac)$_2$ (M = Co, Ni)

4.2.3.a Syntheses and crystal structures of M(hfac)$_2$(pybtdaSMe) (M = Co (4.5), Ni (4.6))

The metal salts M(hfac)$_2$·xH$_2$O, (M = Co, Ni) were reacted with pybtdaSMe in CH$_3$OH in a 1:1 molar ratio at ambient temperature and the solution was left for slow evaporation. Orange and green single crystals of the mononuclear complexes M(hfac)$_2$(pybtdaSMe) (M= Co (**4.5**), Ni (**4.6**) respectively) were grown over 2 weeks. The formation of complexes **4.5** and **4.6** is summarized in Equation 4.4.

$$\text{M(hfac)}_2 + \text{pybtdaSMe} \longrightarrow \text{M(hfac)}_2\text{(pybtdaSMe)} \qquad \text{Equation 4.4}$$

Complexes **4.5** and **4.6** crystallize in the orthorhombic *Pbca* with one molecule in the asymmetric unit. The structure of complex **4.5** is shown in Figure 4.14 (left), as representative of those two complexes (**4.5** and **4.6**) and selected bond lengths and angles are shown in Table 4.4.

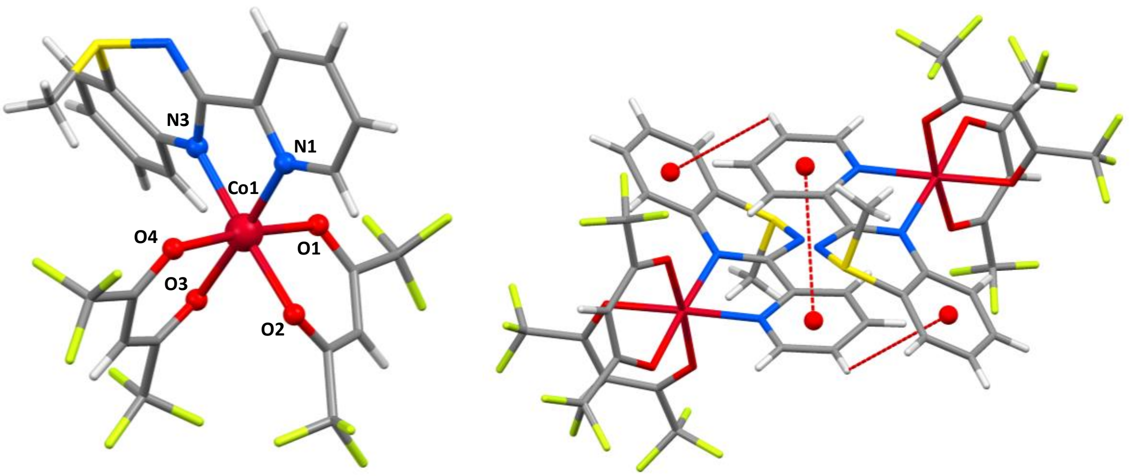

Figure 4.14 (left) Molecular structure of Co(hfac)$_2$(pybtdaSMe) (**4.5**); (right) Crystal packing of **4.5** highlighting the π-π and the C-H···centroid interactions highlighted in red.

Table 4.4 Selected bond lengths and angles for complexes **4.5** and **4.6**.

	M-N_{py}/Å	M-N_{BTDA}/Å	M-O/Å	$N_{py}MN_{BTDA}$/°
Co (**4.5**)	2.094(3)	2.101(3)	2.078(3) 2.074(3) 2.076(3) 2.093(3)	78.30(13)
Ni (**4.6**)	2.043(4)	2.071(5)	2.034(4) 2.053(4) 2.055(4) 2.069(4)	79.96(17)
	C-H···centroid/Å	C-H···centroid/°	centroid-centroid/Å	
Co (**4.5**)	3.687	118.36	4.038	
Ni (**4.6**)	3.689	117.66	4.048	

The metal centres have a distorted octahedral geometry with a N_2O_4 donor set. The heterocyclic ligand provides an *N*,*N*′-chelate pocket analogous to complex **4.4** through N(1) and N(3) atoms with M-N distances in the range 2.043(4) – 2.101(3) Å and N_{py}-M-N_{BTDA} angles at 78.30(17) – 79.69(17)°. The two hfac groups also chelate the metal centre leading to an octahedral complex with M-O distances in the range of 2.034(4) – 2.093(3) Å.

The molecules are linked *via* a C-H···centroid interaction ($d_{\text{C-H}\cdots\text{centroid}}$ = 3.687 – 3.689 Å, $\theta_{\text{N-H}\cdots\text{O}}$ = 117.66 – 118.36°) from the pyridyl C-H group to the centroid of the benzo ring at the neighbouring pybtdaSMe. Additional π-π stacking forms between the pyridyl rings with centroid···centroid distances at 4.038 Å for complex **4.5** and 4.048 Å for complex **4.6** (Figure 4.14, right). Intermolecular hydrogen bonds between C-H groups with oxygen and fluorine atoms of hfac forms a three dimensional network shown in Figure 4.15.

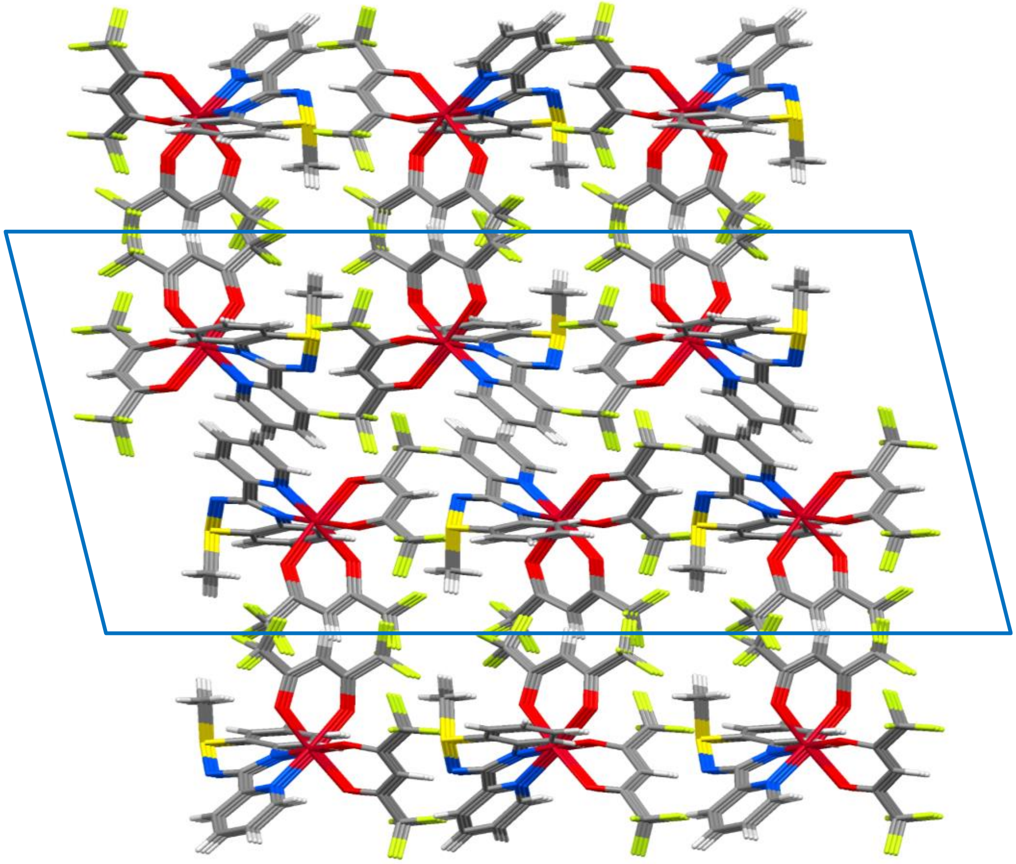

Figure 4.15 Crystal packing of **4.5** revealing the three dimensional nature originated from hydrogen bonding and π-π interactions highlighting the repeating unit (blue lines).

4.2.4 Spectroscopic studies of metal complexes 4.3a, 4.3b, 4.4 and 4.5

The solution UV-Vis spectra of the polymorphic complexes **4.3a** and **4.3b** are dominated by a series of intense π-π* ligand-centered absorption bands between 230 and 400 nm (Figure 4.16). The spectra of the two complexes are remarkably similar suggesting that the two polymorphs exhibit the same solution properties. Notably the visible region exhibits low intensity absorption bands around 420 nm which is absent to the free ligand, pybtdaSMe and which give rise to the diagnostic green colour of the Cu complexes and is likely attributable to a spin-forbidden '*d*-*d*' transition ($\varepsilon < 10^3$ M^{-1} cm^{-3}).

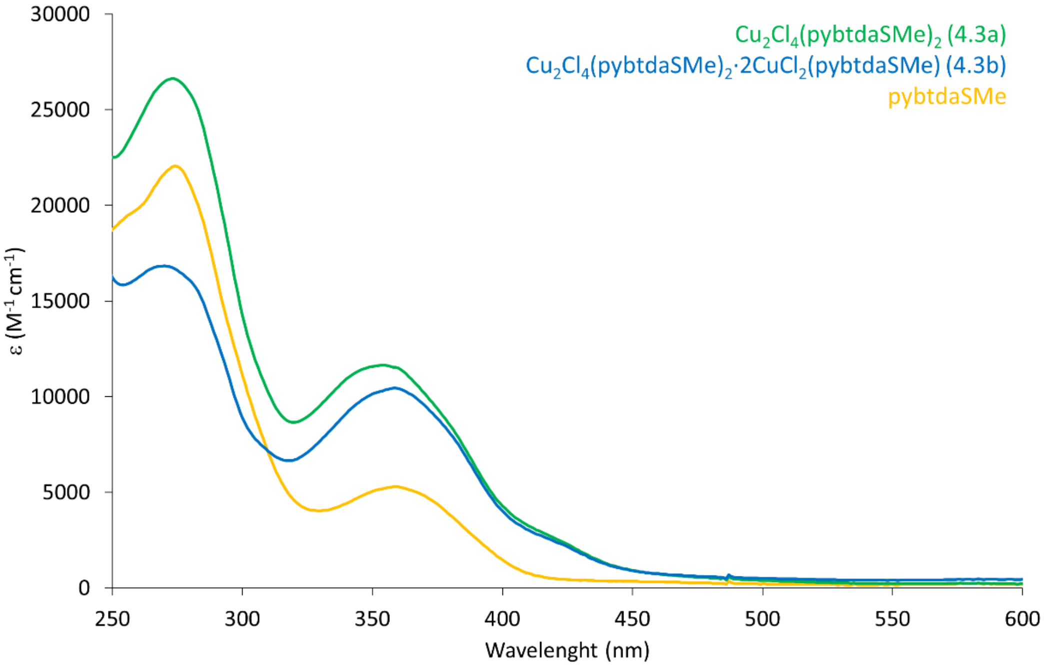

Figure 4.16 Solution UV-Vis spectra of complexes **4.3a** and **4.3b**, and the ligand pybtdaSMe (CH_2Cl_2, rt, $C \approx 10^{-5}$).

The UV-Vis spectra of complexes **4.5** and **4.6** are dominated by a series of π-π* ligand-centered absorption bands between 310 nm (Figure 4.17). In particular, near the visible region exhibits lower intensity absorption bands are observed around 370 nm. *S*-methylation perturbs the electronics of the btda ligand and appear almost colourless in a similar manner the *S*-oxidation does and the S^{IV} derivatives of the btda family appear colourless.[2,14]

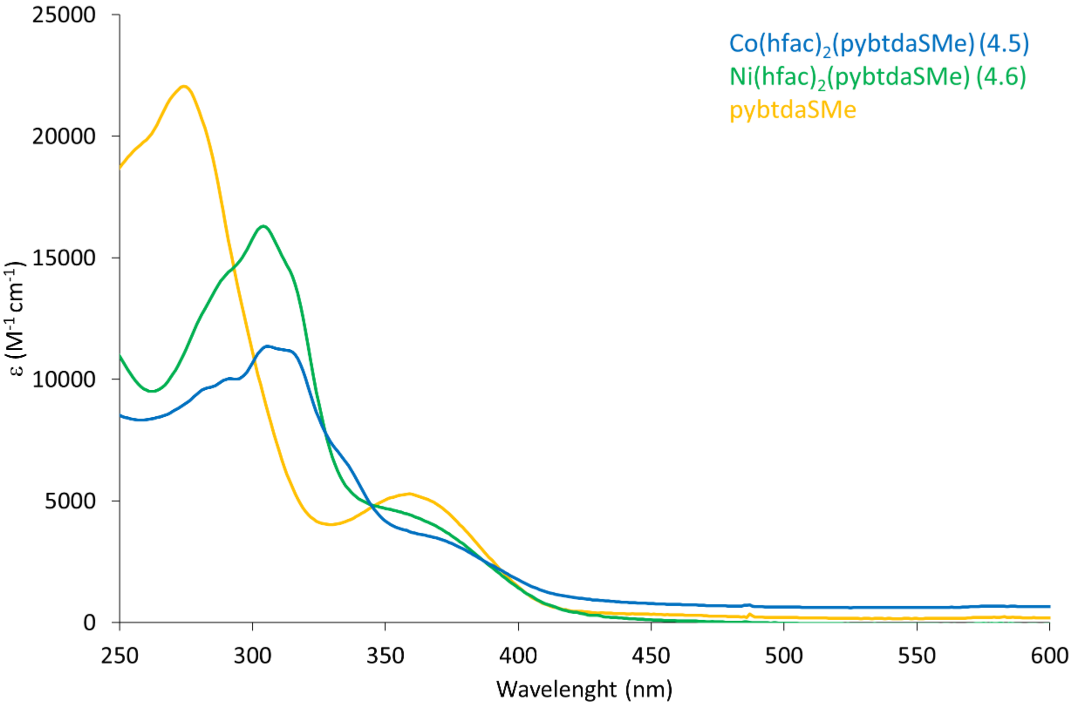

Figure 4.17 Solution UV-Vis spectra of complexes **4.5** and **4.6**, and the ligand pybtdaSMe (CH_2Cl_2 or CH_3CN, rt, C ≈ 10^{-5}).

The IR spectrum of the ligand pybtdaSMe exhibits a stretch at 1585 cm^{-1} characteristic of the C=N imine bond.[7] In the complexes, the stretch appears in the region of 1598 – 1642 cm^{-1} with an increase of 10 – 50 cm^{-1} upon complexation. The spectra of the ligand and the complexes exhibit stretches at *ca*. 2980, 2890 and 642 all related to the S-CH_3 group. The N-H stretch is absent for this ligand and in all complexes, as opposed to the S^{II} ligands, pybtdaH and pmbtdaH (Chapter 2 and 3).

4.2.5 Reactivity trends in the coordination chemistry of pybtdaSMe

The ligand 3-(2′-pyridyl)benzothiadiazine (pybtdaH) can form a range of *N*,*N*′-chelate complexes with first row transition metals with general formula $MCl_2(pybtdaH)_2$, including the 1:1 adduct $CuCl_2(pybtdaH)$.[1] In a similar fashion, the ligand pmbtdaH which could offer two binding pockets proved to also form a range of *N*,*N*′-chelate complexes with first row transition metals with general formula $MCl_2(pmbtdaH)_2$ as discussed in Chapter 3. Initial studies showed that *S*-oxidation of pybtdaH or related benzothiadiazines only occurred in the presence of a metal and Et_3N.[2] In Chapters 2 and 3, we presented the effect of the counter ions ($hfac^-$ and OAc^-) in the oxidation of the ligands pybtdaH and pmbtdaH even without the introduction of base in the reaction scheme where a series of polynuclear complexes have been isolated with $pybtda_{ox}^-$ and $pmbtda_{ox}^-$.[14]

Reaction of pybtdaSMe with MCl_2 (M = Mn, Ni) afforded the mononuclear octahedral complexes $MCl_2(pybtdaSMe)_2$ (M = Mn (**4.1**), Ni (**4.2**)) while reaction of pybtdaSMe with $ZnCl_2{\cdot}2H_2O$ afforded the mononuclear tetrahedral complex $ZnCl_2(pybtdaSMe)$ (**4.4**). In the case of the reaction of pybtdaSMe with $CuCl_2$ two polymorphs are found with **4.3b** containing both mononuclear $CuCl_2(pybtdaSMe)$ and dinuclear $Cu_2Cl_4(pybtdaSMe)_2$ units. While pybtdaH exhibits a tendency to oxidize in the presence of $M(hfac)_2$ and $M(OAc)_2$ salts, alkylation suppresses ligand oxidation affording the anticipated mononuclear complexes of formula $M(hfac)_2(pybtdaSMe)$ (M = Co (**4.5**), Ni (**4.6**)). The pybtdaSMe ligand adopts two coordination modes; through the heterocyclic N(3) and the pyridyl N(1) atom or through the heterocyclic N(2) and the pyridyl N(1) atom. As discussed in section 4.2.1 both conformations are very close energetically so the outcome depends mostly on intermolecular interactions and steric effects.

While the ligand pybtdaH is prone to oxidation resulting to the *S*-oxide of the ligand under basic conditions by introducing either Et_3N or more basic anions, such as $hfac^-$, the *S*-methylation is prohibiting such behaviour even in the presence of hfac. Although the possibility of further oxidation of sulphur cannot be excluded,[18,19] the detection would be more difficult given the loss of the red intense red colour of pybtdaH and pmbtdaH. Nevertheless, there was no indication of *S*-oxidation of pybtdaSMe in the experiments within the timeframe of this project.

4.3. Conclusions

The synthesis of the novel ligand 1-methyl-3-(pyridinyl)-1,2,4-benzothiadiazine (pybtdaSMe) is described. Reaction of pybtdaSMe with MCl_2 affords six-coordinate mononuclear complexes of general formula MCl_2(pybtdaSMe)$_2$ (M = Mn (**4.1**), Ni (**4.2**)) or four-coordinate mononuclear complexes MCl_2(pybtdaSMe) (M = Cu (**4.3b**), Zn (**4.4**)) or dimeric structures M_2Cl_4(pybtdaSMe)$_2$ (M = Cu, (**4.3a** and **4.3b**)). While all these structures comprise the pybtdaSMe ligand acting as an *N*,*N*′-chelate ligand, both N(2) or N(4) of the heterocyclic ring have the ability to act as an *N*-donor (Figure 4.1). Of these N(2) (adjacent to S) appears to act as the preferred btda *N*-donor group. Similarly reaction of pybtdaSMe with M(hfac)$_2$ (M = Co, Ni) in 1:1 mole ratio afforded the mononuclear complexes with general formula M(hfac)$_2$(pybtdaSMe) (M = Co (**4.5**), Ni (**4.6**)). In summary, pybtdaSMe has a more controlled reaction chemistry than pybtdaH, acting as an effective *N*,*N*′-chelate ligand. Notably the closely related structure pmbtdaSMe (Figure 4.18) should be well-suited for the development of extended systems through use of two *N*,*N*′-chelate pockets.

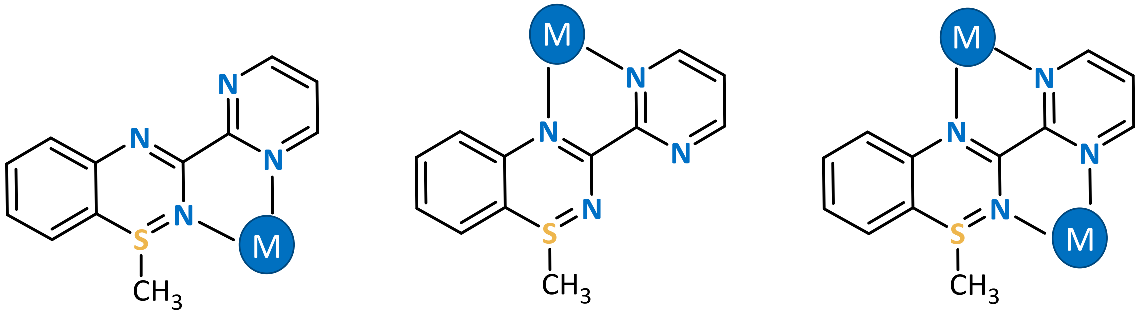

Figure 4.18 Potential bridging mode for ligand pmbtdaSMe.

4.4. Experimental

4.4.1 General considerations and physical measurements

Solvents, starting materials and metal salts were obtained from commercial suppliers and used without further purification. Manipulation of air-sensitive materials was carried out under an atmosphere of dry-nitrogen using standard Schlenk techniques and a dry-nitrogen glove box (MBraun Labmaster). Melting points were determined using a Stanford Research Systems MPA120 EZ-Melt automated melting point apparatus. Elemental compositions were determined on a Perkin Elmer 2400 Series II CHNS/O Analyzer. UV-Vis spectra were measured on an Agilent 8453 Spectrophotometer using *ca.* 1×10^{-5} M solutions in dichloromethane in the range 250-600 nm. IR spectra were obtained using a Bruker Alpha FT-IR spectrometer equipped with a Platinum single reflection diamond ATR module. NMR spectra were recorded on a Bruker 500 MHz spectrometer with a Broadband AX Probe using $CDCl_3$ (^1H $\delta = 7.26$ ppm, s; ^{13}C $\delta = 77.16$ ppm) as an internal reference point relative to Me_4Si ($\delta = 0$ ppm). Mass spectra were recorded on a Waters XEVO G2-XS specifically using the atmospheric solids analysis probe in positive resolution mode. Density functional theory (DFT) calculations of pybtdaSMe were undertaken using the B3LYP functional and 6-311G^{*+} basis set[20–22] functional within Jaguar[23].

4.4.2 Ligand Synthesis

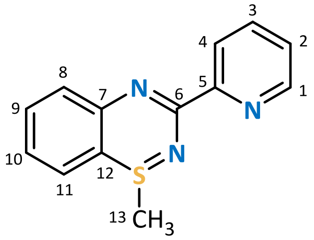

4.4.2.a 1-methyl-3-(pyridin-2-yl)-1λ^4,2,4-benzothiadiazine (pybtdaSMe)

3-(pyridin-2-yl)-4*H*-1,2,4-benzothiadiazine (0.5 g, 2.2 mmol) was dissolved in dry THF (10 mL) and added dropwise to a stirred solution of lithium *bis*(trimethylsilyl)amide (5.5 g, 3.3 mmol) in THF (25 mL) at 0 °C under a nitrogen atmosphere. The dark reaction mixture was allowed to warm to room temperature and stirred for 30 min. Iodomethane (0.18 mL, 2.8 mmol) was added dropwise to the solution and stirred for a further 48 h. The solvent was removed *in vacuo* and the reaction mixture was extracted with CH_2Cl_2. The organic phase was washed with H_2O (2 × 20 mL) and brine (1 × 20 mL), dried over Na_2SO_4 and the solvent was removed *in vacuo* to yield a dark brown viscous oil. The product was isolated as yellow crystals by slow evaporation of CH_2Cl_2. Yield 0.48 g, 89.6%.

Melting point 63 °C.

Elemental Analysis calc. for $[C_{13}H_{11}N_3S]\cdot 3H_2O$: C, 52.87; H, 5.80; N, 14.23. Found: C, 52.94 H, 5.45; N, 14.19%.

UV-Vis (CH_2Cl_2; λ_{max}, nm; ε, $M^{-1}\cdot cm^{-1}$): 274 (21560), 359 (4797).

IR (solid, cm^{-1}) $\tilde{\nu}_{max}$ = 3354 (br), 2970 (w), 2903 (w), 2872 (w), 1585 (w), 1560 (w), 1484 (m), 1448 (s), 1422 (m), 1330 (m), 1271 (m), 1247 (m), 1130 (m), 1112 (w), 1085 (w), 1045 (m), 993 (w), 964 (w), 917 (w), 851 (w), 819 (w), 762 (m), 686 (m), 662 (w), 621 (m), 576 (w), 547 (w), 473 (w), 452 (w).

^{1}H NMR (500 MHz, ppm, $CDCl_3$) δ_H = 8.61 (1H, dq, *J* = 4.75, 0.83 Hz, C^1H), 8.25 (1H, dt, *J* = 7.95, 0.93 Hz, C^4H), 7.63 (1H, td, *J* = 11.5, 1.75 Hz, C^3H), 7.37-7.43 (2H, m, C^9H, $C^{10}H$), 7.19 (1H, ddd, *J* = 7.45, 4.75, 1.15 Hz, C^2H), 7.12-7.14 (2H, m, C^8H, $C^{11}H$), 2.37 (3H, s, $C^{13}H_3$).

^{13}C NMR (125 MHz, ppm, $CDCl_3$) δ_C = 163.41 (C^6), 156.18 (C^5), 149.52 (C^1), 144.66 (C^7), 136.53 (C^3), 133.30 (C^9 or C^{10}), 127.22 (C^9 or C^{10}), 126.15 (C^8 or C^{11}), 124.76 (C^2), 124.63 (C^8 or C^{11}), 123.37 (C^4), 107.09 (C^{12}), 35.05 (C^{13}).

HRMS (ASAP) *m/z* $[M+H]^+$ calc. for $C_{13}H_{11}N_3S$: 242.0752, found 242.0750.

4.4.3 Complex Syntheses with MCl_2 (M = Mn, Ni, Cu, Zn)

4.4.3.a $MnCl_2(pybtdaSMe)_2$ (4.1)

$MnCl_2$ (0.006 g, 0.050 mmol) was added to a solution of pybtdaSMe (0.012 g, 0.050 mmol) in CH_3OH (5 mL). The mixture was stirred for 1 h and a yellow solution was obtained. The solution was filtered and yellow crystals were grown by layering with a mixture of diethyl ether/hexanes (1:1) in two days. Yield 0.007 g, 23%.

Elemental Analysis calc. for $[C_{26}H_{22}N_6MnS_2Cl_2]\cdot 0.1C_5H_{12}$: C, 51.70; H, 3.80; N, 13.65. Found: C, 51.60; H, 3.77; N, 12.87%.

IR (solid, cm^{-1}) $\tilde{\nu}_{max}$ = 2967 (w), 1598 (w), 1562 (w), 1509 (s), 1456 (m), 1439 (m), 1414 (m), 1320 (m), 1298 (m), 1268 (m), 1252 (w), 1151 (m), 1130 (m), 1112 (w), 1067 (m), 1044 (m), 1015 (m), 989 (m), 921 (m), 827 (m), 796 (m), 773 (s), 745 (m), 680 (m), 637 (m), 548 (w), 498 (m), 474 (m), 464 (m), 452 (m), 412 (m).

4.4.3.b $NiCl_2(pybtdaSMe)_2$ (4.2)

$NiCl_2\cdot 6H_2O$ (0.027 g, 0.050 mmol) was added to a solution of pybtdaSMe (0.012 g, 0.050 mmol) in CH_3OH (5 mL). The mixture was stirred for 30 min and a golden solution obtained. The solution was filtered and green crystals were grown by layering with a mixture of diethyl ether/hexanes (1:1) over two weeks. Yield 0.006 g, 19%.

Elemental Analysis calc. for $[C_{26}H_{22}N_6NiS_2Cl_2]\cdot CH_3OH$: C, 50.34; H, 4.07; N, 13.04. Found: C, 50.20; H, 4.14; N, 12.66%.

IR (solid, cm^{-1}) $\tilde{\nu}_{max}$ = 3043 (w), 2981 (w), 2885 (w) 1600 (w), 1587 (w), 1561 (w), 1511 (m), 1456 (m), 1412 (m), 1327 (m), 1295 (m), 1269 (m), 1255 (m), 1150 (w), 1132 (m), 1117 (m), 1067 (w), 1045 (m), 1020 (m), 988 (m), 954 (m), 924 (m), 860 (w), 834 (m), 797 (w), 773 (s), 747 (m), 676 (m), 642 (m), 550 (w), 510 (m), 452 (m), 417 (w).

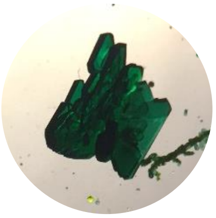

4.4.3.c Cu_2Cl_4(pybtdaSMe)$_2$ (4.3a)

Solid $CuCl_2$ (0.016 g, 0.100 mmol) was added to a solution of pybtdaSMe (0.024 g, 0.100 mmol) in EtOH (10 mL). The mixture was stirred for 30 min and a dark olive solution obtained. The solution was filtered and green crystals were grown by layering with a mixture of diethyl ether/hexanes (1:1) over two days. Yield 0.027 g, 36%.

Elemental Analysis calc. for $[C_{26}H_{22}N_6Cu_2S_2Cl_4]\cdot H_2O$: C, 40.58; H, 3.14; N, 10.92. Found: C, 40.82; H, 3.32; N, 10.75%.

UV-Vis (CH_2Cl_2; λ_{max}, nm; ε, M^{-1} cm^{-1}): 242 (39621), 273 (44919), 353 (19622).

IR (solid, cm^{-1}) $\tilde{\nu}_{max}$ = 2976 (w), 2898 (w), 1604 (m), 1590 (m), 1562 (m), 1533 (m), 1461 (m), 1408 (m), 1327 (m), 1293 (m), 1273 (m), 1259 (m), 1155 (m), 1129 (m), 1048 (m), 1024 (m), 971 (m), 952 (m), 928 (m), 892 (w), 870 (m), 843 (m), 790 (m), 765 (s), 745 (s), 702 (m), 688 (m), 667 (m), 646 (m), 547 (w), 521 (m), 450 (m), 417 (m).

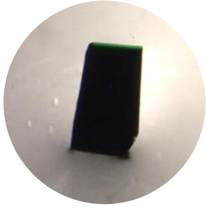

4.4.3.d Cu_2Cl_4(pybtdaSMe)$_2\cdot 2CuCl_2$(pybtdaSMe) (4.3b)

Solid $CuCl_2$ (0.008 g, 0.050 mmol) was added to a solution of pybtdaSMe (0.012 g, 0.050 mmol) in CH_3OH (5 mL). The mixture was stirred for 30 min and an olive solution obtained. The solution was filtered and dark green crystals were grown by layering with a mixture of diethyl ether/hexanes (1:1) over three days. Yield 0.003 g, 36%.

Elemental Analysis calc. for $[C_{13}H_{11}N_3CuSCl_2]$: C, 41.55; H, 2.95; N, 11.18. Found: C, 41.19; H, 2.73; N, 10.94%.

UV-Vis (CH_2Cl_2; λ_{max}, nm; ε, M^{-1} cm^{-1}): 237 (18006), 270 (16130), 359 (9755).

IR (solid, cm^{-1}) $\tilde{\nu}_{max}$ = 2993 (w), 1606 (w), 1565 (w), 1537 (m), 1464 (m), 1446 (m), 1410 (m), 1330 (m), 1297 (m), 1270 (m), 1261 (m), 1154 (w), 1132 (m), 1064 (w), 1045 (m), 1026 (m), 972 (m), 945 (m), 926 (m), 902 (w), 869 (m), 841 (m), 791 (m), 763 (s), 752 (s), 728 (m), 701 (w), 687 (m), 669 (m), 648 (m), 544 (w), 520 (m), 473 (m), 427 (w), 414 (w).

4.4.3.e ZnCl$_2$(pybtdaSMe) (4.4)

Solid ZnCl$_2$ (0.007 g, 0.050 mmol) was added to a solution of pybtdaSMe (0.012 g, 0.050 mmol) in CH$_2$Cl$_2$ (8 mL). The mixture was stirred for 2 h and a yellow solution obtained. The solution was filtered and light yellow crystals were grown by layering with a mixture of diethyl ether/hexanes (1:1) over two weeks. Yield 0.006 g, 34%.

Elemental Analysis calc. for [$C_{13}H_{11}N_3ZnSCl_2$]: C, 41.35; H, 2.94; N, 11.13. Found: C, 40.98; H, 2.80; N, 10.89%.

IR (solid, cm^{-1}) $\tilde{\nu}_{max}$ = 2981 (w), 2898 (w), 1604 (w), 1566 (w), 1494 (m), 1460 (m), 1431 (m), 1372 (m), 1294 (m), 1166 (w), 1137 (m), 1096 (w), 1049 (m), 1027 (m), 978 (m), 954 (m), 856 (w), 791 (m), 765 (s), 751 (s), 711 (m), 678 (m), 649 (m), 592 (m), 544 (w), 504 (m), 476 (m), 451 (m), 413 (m).

4.4.4 Complex Syntheses with M(hfac)$_2$ (M = Co, Ni)

4.4.4.a Co(hfac)$_2$(pybtdaSMe) (4.5)

Solid Co(hfac)$_2$ (0.039 g, 0.083 mmol) was added to a solution of pybtdaSMe (0.020 g, 0.083 mmol) in CH$_3$OH (10 mL). The mixture was stirred for 1 h and an orange solution obtained. The solution was filtered and orange crystals were grown by slow evaporation over two weeks. Yield 0.012 g, 21%.

Elemental Analysis calc. for [$C_{23}H_{13}N_3CoSO_4F_{12}$]: C, 38.76; H, 1.83; N, 5.88. Found: C, 38.89; H, 1.92; N, 5.88%.

UV-Vis (CH_3CN; λ_{max}, nm; ε, M^{-1} cm^{-1}): 240 (12102), 304 (16304), 366 (4128).

IR (solid, cm^{-1}) $\tilde{\nu}_{max}$ = 1639 (m), 1553 (w), 1524 (w), 1489 (m), 1456 (m), 1426 (w), 1375 (w), 1252 (m), 1205 (m), 1190 (m), 1135 (s), 1092 (m), 1050 (w), 1025 (w), 975 (w), 948 (w), 812 (w), 794 (m), 771 (w), 763 (w), 753 (w), 683 (w), 667 (m), 583 (m), 481 (w), 452 (w).

4.4.4.b Ni(hfac)$_2$(pybtdaSMe) (4.6)

Solid Ni(hfac)$_2$·xH_2O (0.039 g, 0.083 mmol) was added to a solution of pybtdaSMe (0.020 g, 0.083 mmol) in CH_3OH (10 mL). The mixture was stirred for 1 h and a yellow solution obtained. The solution was filtered and green crystals were grown by slow evaporation over two weeks. Yield 0.008 g, 13%.

Elemental Analysis calc. for [$C_{23}H_{13}N_3NiSO_4F_{12}$]: C, 38.69; H, 1.83; N, 5.88. Found: C, 38.29; H, 1.92; N, 5.88%.

UV-Vis (CH_3CN; λ_{max}, nm; ε, M^{-1} cm^{-1}): 295 (9336), 310 (10548), 374 (2602).

IR (solid, cm^{-1}) $\tilde{\nu}_{max}$ = 1642 (m), 1553 (w), 1524 (w), 1483 (m), 1421 (w), 1376 (m), 1252 (m), 1206 (m), 1190 (m), 1133 (s), 1093 (m), 1050 (m), 1028 (w), 949 (w), 935 (w), 813 (w), 792 (m), 771 (m), 762 (m), 753 (m), 682 (w), 669 (m), 584 (m), 528 (w), 481 (w), 453 (w).

4.4.5 Single-crystal X-ray crystallography

Crystals of the ligand and complexes **4.2** – **4.6** were mounted on a cryoloop with paratone oil and examined on a Bruker APEX diffractometer equipped with CCD area detector and Oxford Cryostream cooler using graphite-monochromated Mo-*K*α radiation (λ = 0.71073 Å). Single crystals of complex **4.1** were mounted on a cryoloop with paratone oil and measured on a Bruker Kappa system APEX-II diffractometer equipped with an Oxford Cryoflex low temperature device and an Incoatec Mo micro-source. Data were collected at 150(2) K using graphite-monochromated Mo-Kα radiation (λ = 0.71073 Å).

Data were collected using the APEX-II software[24], integrated using SAINT[25] and corrected for absorption using a multi-scan approach (SADABS)[26]. Final cell constants were determined from full least squares refinement of all observed reflections. The structures of pybtdaSMe and complexes **4.1** – **4.6** were solved using Olex2[27], with the ShelXT structure solution program[28] using intrinsic phasing and refined within the ShelXL[29] refinement package using least-squares minimization on F^2. Complex **4.1** was solved by direct methods (SHELXS within SHELXTL[30]) to reveal most non-H atoms. All hydrogen atoms were added at calculated positions and refined isotropically with a riding model.

Ligand pybtdaSMe exhibited some residual electron density and was treated with SQUEEZE.[31] Complex **4.1** had half a hexane solvent molecule in the asymmetric unit located about an inversion centre. There was some evidence for disorder in this solvent molecule but remaining residual electron density did not form a well-connected set. The half molecule of C_6H_{14} in the asymmetric unit was clearly defined and the poorly defined residual electron density in this region (likely a minor component of disorder) was left rather than treated with SQUEEZE. Complex **4.5** exhibited rotational disorder of two of the four CF_3 groups in the asymmetric unit which were modelled over two sites in a 1:1 ratio with a common U_{iso}. Complex **4.6** exhibited rotational disorder of three of the four CF_3 groups in the asymmetric unit which were modelled over two sites in a 1:1 ratio with a common U_{iso}. A summary of key crystallographic data for the ligands and complexes is presented in Appendix 3.

4.5. References

1 E. R. Clark, M. U. Anwar, B. J. Leontowicz, Y. Beldjoudi, J. J. Hayward, W. T. K. Chan, E. L. Gavey, M. Pilkington, E. Zysman-Colman and J. M. Rawson, *Dalton Trans.*, 2014, **43**, 12996.

2 E. R. Clark, J. J. Hayward, B. J. Leontowicz, M. U. Anwar, M. Pilkington and J. M. Rawson, *Dalton Trans.*, 2014, **44**, 2071.

3 A. K. Pal, D. B. Cordes, K. Pringouri, M. U. Anwar, A. M. Z. Slawin, J. M. Rawson and E. Zysman-Colman, *J. Coord. Chem.*, 2016, **69**, 1924.

4 E. Kleisath, N. J. Yutronkie, I. Korobkov, B. M. Gabidullin and J. L. Brusso, *New J. Chem.*, 2016, **40**, 4472.

5 N. J. Yutronkie, P. Tami, S. Singh, E. Kleisath, B. M. Gabidullin, R. Davis and J. L. Brusso, *New J. Chem.*, 2017, **41**, 2268.

6 T. L. Gilchrist, C. W. Rees and D. Vaughan, *J. Chem. Soc., Perkin Trans*, 1983, 55.

7 J. Coates, *Encycl. Anal. Chem.*, 2006, 1.

8 J. G. Stark and H. G. Wallace, *Chemistry Data Book*, J. Murray. Publ., London, S. I. Edit., 1980.

9 N. N. Earnshaw and A. Greenwood, *Chemistry of the Elements*, Pergamon Press, Oxford, 1st edn., 1986.

10 E. R. Clark, J. J. Hayward, B. J. Leontowicz, D. J. Eislera and J. M. Rawson, *CrystEngComm*, 2014, **16**, 1755.

11 A. W. Addison and T. N. Rao, *J. Chem. Soc., Dalton Trans.*, 1984, 1349.

12 *CSD search Cu-Cl, mean Bond length all results*.

13 *CSD search Cu-Cl-Cu, mean Bond length all results*.

14 K. Pringouri, M. U. Anwar, B. J. Leontowicz and J. M. Rawson, *Polyhedron*, 2018, **150**, 110.

15 C. F. Macrae, P. R. Edgington, P. McCabe, E. Pidcock, G. P. Shields, R. Taylor, M. Towler and J. Van De Streek, *J. Appl. Crystallogr.*, 2006, **39**, 453.

16 L. Yang, D. R. Powell and R. P. Houser, *Dalton Trans.*, 2007, 955.

17 G. Cavallo, P. Metrangolo, R. Milani, T. Pilati, A. Priimagi, G. Resnati and G. Terraneo, *Chem. Rev.*, 2016, **116**, 2478.

18 N. P. Kolesnik, A. B. Rozhenko, V. Kinzhybalo, T. Lis and Y. G. Shermolovich, *J. Fluor. Chem.*, 2014, **160**, 16.

19 J. Huang, Y. Huang, T. Wang, Q. Huang, Z. Wang and Z. Chen, *Org. Lett.*, 2017, **19**, 1128.

20 A. D. Becke, *J. Chem. Phys.*, 1993, 5648.

21 C. Lee, W. Yang and R. G. Parr, *Phys. Rev. B Condens. Matter*, 1988, 785.

22 A. S. Miehlich, H. Stoll and H. Preuss, *Chem. Phys. Lett.*, 1989, 200.

23 A. D. Bochevarov, E. Harder, T. F. Hughes, J. R. Greenwood, D. A. Braden, D. M. Philipp, D. Rinaldo, M. D. Halls, J. Zhang and R. A. Friesner, *Int. J. Quantum Chem.*, 2013, **113**, 2110.

24 APEX-II, Bruker AXS, Inc., Madison, Wisconsin, USA.

25 SAINT, Bruker AXS Inc., Madison, Wisconsin, USA.

26 SADABS, Bruker AXS Inc., Madison, Wisconsin, USA.

27 O. V. Dolomanov, L. J. Bourhis, R. . Gildea, J. A. K. Howard and H. Puschmann, *J. Appl. Cryst.*, 2009, **42**, 339.

28 G. M. Sheldrick, *Acta Cryst.*, 2015, **A71**, 3.

29 G. M. Sheldrick, *Acta Cryst.*, 2015, **C71**, 3.

30 SHELXTL, *Bruker AXS Inc.,* Madison, Wisconsin, USA, 2015.

31 A. L. Spek, *Acta Crystallogr*, 2015, **C71**, 9.

CHAPTER 5.

Synthesis and characterization of bisbtdaH$_2$ and its coordination chemistry

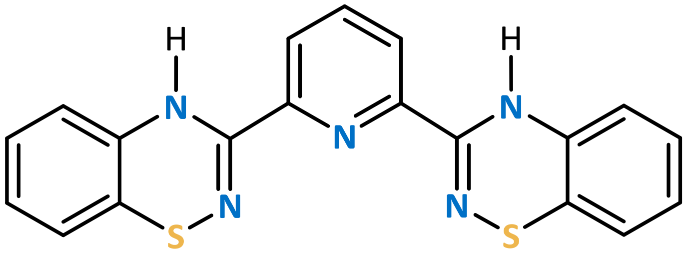

5.1. Introduction

Ligand design is a powerful tool to assemble desired supramolecular architectures through coordination chemistry. Such ligand-based approaches to the self-organization of coordination assemblies rely on the complementarity of ligand-based functional groups coupled with the conformational preference(s) of metal ions. In recent decades this has led to the emergence of elegant supramolecular structures such as molecular knots[1] and catenanes[2] as well as coordination polymers,[3,4] metal-organic frameworks[5,6] and recent extensions to reticular chemistry.[6–8] A key design element often involves placing the donor atoms within the ligand in such a way that five- or six-membered chelate rings are formed upon coordination.[9–11] Poly-pyridine ligands such as 2,2′-bipyridine and its terpyridine pincer analogue have a central position in coordination chemistry.[12–15] Among poly-pyridine ligands the terpyridine (terpy) pincer ligand (Scheme 5.1)[16,17] can bind to both low and high oxidation state metal ions almost always in a tridentate fashion. It has been extensively studied specifically for octahedral complexes with various transition metal ions such as Fe$^{II/III}$,[18–21] Co^{II},[22,23] Ru$^{II/III}$,[24] Zn^{II}.[25] Square planar complexes of Pt^{II},[26–29] Pd^{II},[30,31] and Au^{III} [32–35] with terpy are also well known. Its rich coordination chemistry and high binding affinity towards metal ions in conjunction with redox and photo-physical

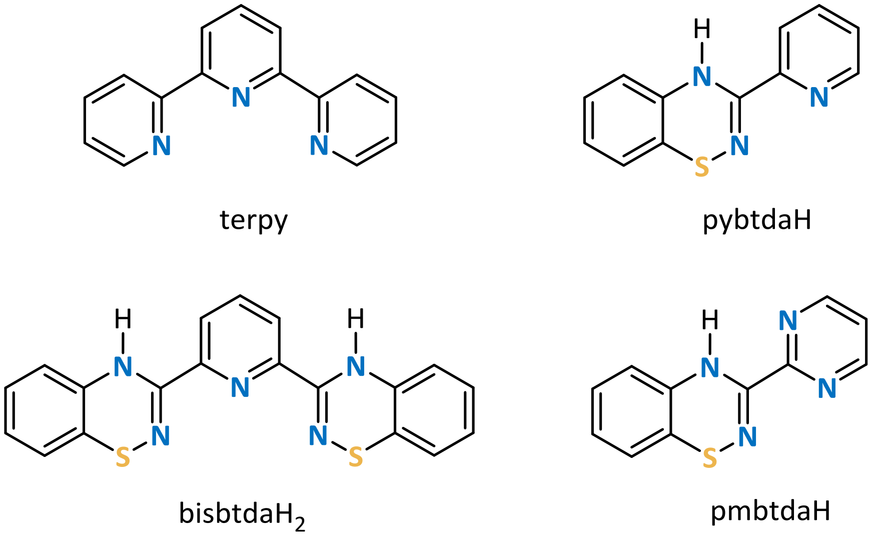
terpy

pybtdaH

bisbtdaH$_2$

pmbtdaH

Scheme 5.1 Molecular structures of terpy, bisbtdaH$_2$, pybtdaH and pmbtdaH.

properties have given rise to a variety of applications in material science, such as the development of solar cells,[36,37] light emitting electrochemical cells,[38–40] luminescent systems,[27,41] non-linear optical devices,[42] etc. In organic synthesis, terpy complexes have also been used as efficient catalysts for organic transformation such as C-C bond formation,[43] etherification,[44] oxidation of alcohols or ethers,[45,46] cyclopropanation,[47] cross coupling reactions,[44] hydrosilation,[48] controlled radical polymerization,[49] photocatalytic splitting of water[37] etc. They have also found applications in molecular magnetism since they offer a medium strength ligand field for first row transition metal complexes and exhibit spin crossover behaviour for systems in which the crystal field Δ is comparable with the magnitude of the inter-electron repulsion term (P_E) making the two possible electronic states near quasi-energetic. The Co^{II}(terpy)$_2$ complex ion was one of the first compounds to be shown to exhibit thermal spin crossover.[22,23,50,51] Terpyridine complexes have also found a wide range of potential application in pharmaceutical drug research e.g., Pt^{II} complexes of terpy were first reported to bind double-stranded DNA by intercalation.[52] Other biological activities such as antitumor, radiotherapy, antiprotozoal agents, and protein probes have been thoroughly documented.[53–57] Such a wide range of applications (*vide supra*) of terpy type complexes calls for high structural variability of this tridentate donor in terms of solubility, flexibility, redox chemistry etc. Recently, bis-azinyl analogues of terpyridine were reported with their 3*d* transition metal complexes exhibiting reversible redox properties, spin crossover, and superexchange coupling.[58]

In this chapter, we report the synthesis and characterization of a novel bis-btda pincer ligand bisbtdaH$_2$ (Scheme 5.1) designed to offer a tridentate *N,N′,N″ mer*-binding coordination geometry and describe its coordination chemistry with selected first row transition metal ions.

5.2. Results and Discussion

5.2.1 Synthesis and structural characterization of the ligand bisbtdaH₂

The ligand bisbtdaH₂ was synthesised according to the synthetic route shown in Scheme 5.2. The first step is the reaction of 2-aminothiophenol with *N*-propylbromide to form 2-(propylthio)aniline, as discussed in Chapter 2 (preparation of ligand **2.1**). Deprotonation of 2-(propylthio)aniline with LiHMDS, under anaerobic, dry conditions followed by treatment with half an equivalent of 2,6-dicyanopyridine[59] resulted in the intermediate carboximidamide in 80% yield. Subsequent cyclization and pericyclic elimination in the presence of *N*-chlorosuccinimide (NCS) afforded the ligand bisbtdaH₂ in 43% yield after purification by column chromatography using dichloromethane as eluent. Single crystals were grown by slow evaporation from dichloromethane.

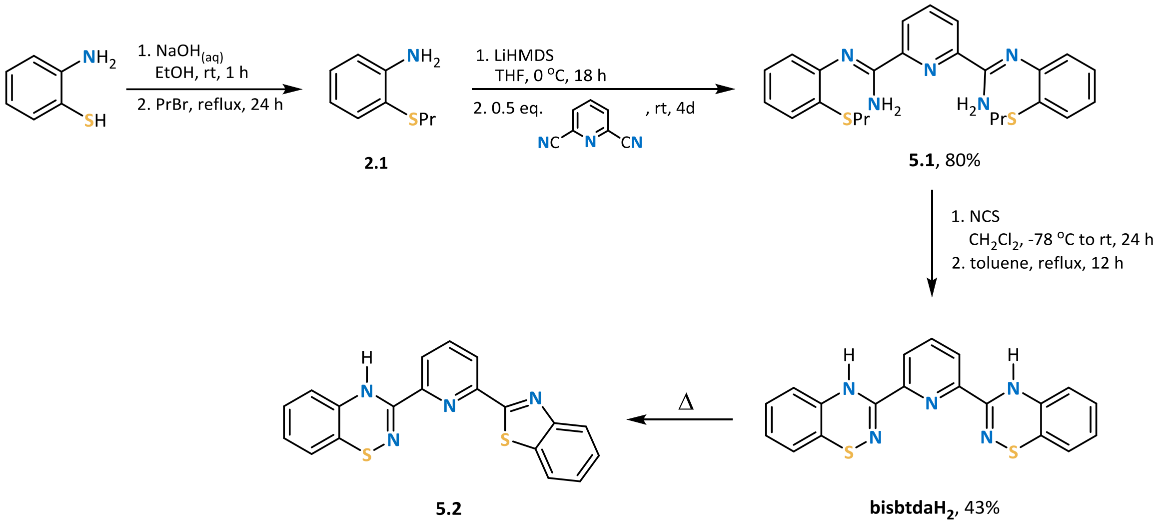

Scheme 5.2 Synthetic route to ligand bisbtdaH₂.

The ^1H NMR spectrum of ligand bisbtdaH₂ exhibits the expected proton environments in the aromatic region, consistent with a C_2 symmetric ligand geometry. The imine C=N stretching vibration was observed at 1615 cm^{-1}. The molecular structure was further confirmed by single crystal X-ray studies. The compound crystalizes in the triclinic space group $P\overline{1}$ with two molecules in the asymmetric unit (Figure 5.1).

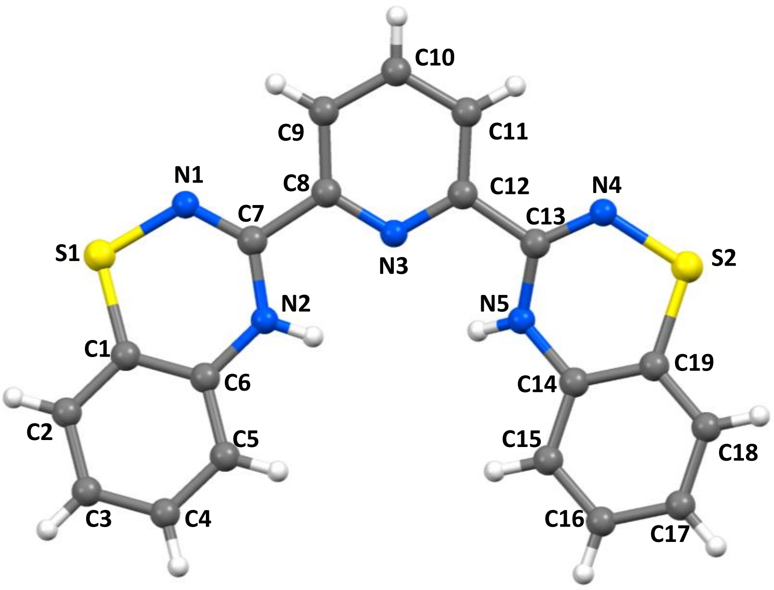

Figure 5.1 Molecular structure of bisbtdaH$_2$ in one of the two crystallographically independent molecules.

The C-N (C(7)-N(1) and C(13)-N(4)) distances are 1.285(3) Å and 1.281(3) Å respectively which are consistent with predominant double bond character (*cf* imine C=N at 1.279 Å).[60] The bond lengths between C(7)-N(2) and C(13)-N(5) are 1.358(3) Å and 1.362(3) Å respectively are more consistent with a conjugated C-N single bond (*cf* Ph-NH$_2$ at 1.355 Å).[60] The S-N bond lengths (1.705(2) and 1.696(2) Å) are comparable with other S-N single bonds (1.62 – 1.74 Å for isomers of $S_{8-x}(NH)_x$)[61] and 1.69 – 1.72 Å for other benzothiadiazine derivatives[62]). Another notable feature of the benzothiadiazine ring is the folding (θ) of molecule about the *trans*-annular vector S(1)···N(2) and S(2)···N(5) where θ values are 24.15 and 26.41 for the two rings, respectively, comparable with previous reported values (21° – 42°).[62] This folding of the ring is consistent with the formally 8π anti-aromatic nature of the thiadiazine framework.

In addition π-π stacking was manifested in the form of a one-dimensional chain motif along the crystallographic *b* axis dimer with centroid···centroid distances at 3.765 Å and 4.392 Å in which the shortest C-C distance is at 3.364 Å (Figure 5.2, top). The presence of hydrogen bonds between the molecules affords a three-dimensional hydrogen-bonded grid (Figure 5.2, bottom). The hydrogen bonding between the C-H and the N atom on the thiadiazine heterocycle extends the connectivity along *a* axis with distances at 2.633 Å ($\theta_{\text{C-H}\cdots\text{N}}$ = 140.84°) and 2.671 Å ($\theta_{\text{C-H}\cdots\text{N}}$ = 168.25°) and along *c* axis with distances at 2.641 Å ($\theta_{\text{C-H}\cdots\text{N}}$ = 144.39°).

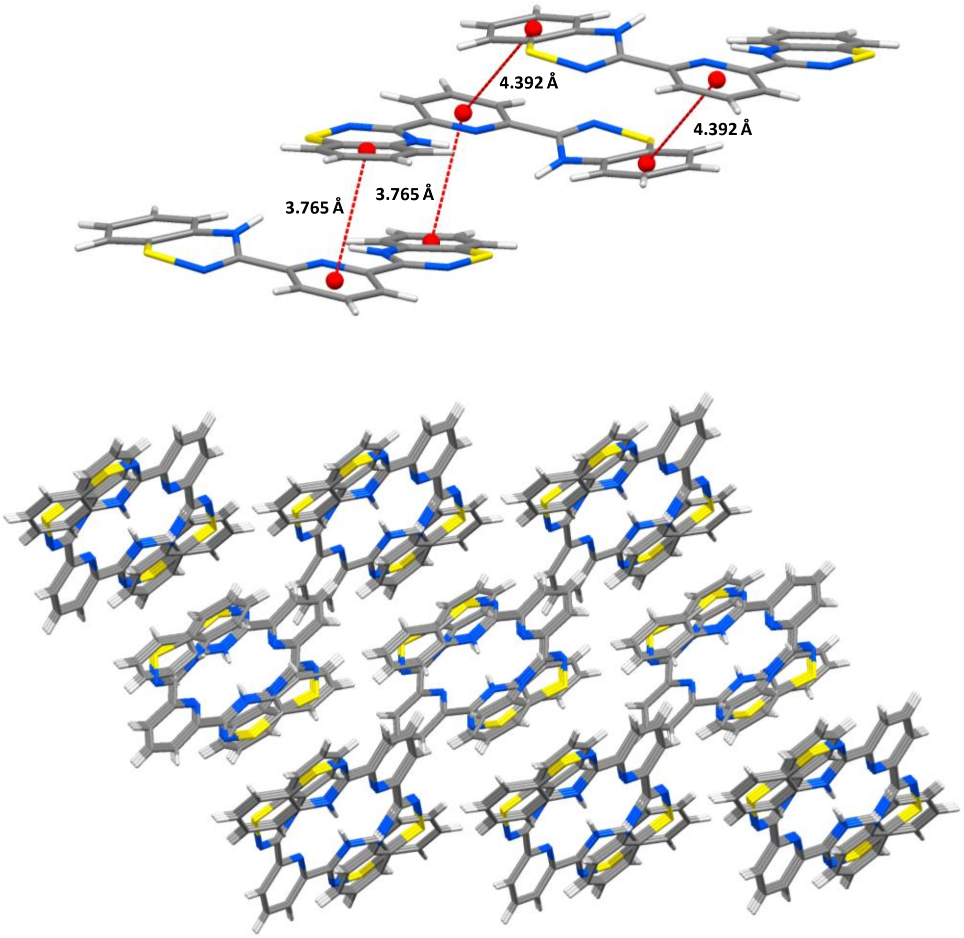

Figure 5.2 Crystal packing of bisbtdaH$_2$ highlighting π-π stacking along *b* axis (top) and the packing revealing the three dimensional nature of the hydrogen-bonded motif with a view down *b* axis (bottom).

The preference for the crystallographically-determined conformer was also confirmed by DFT calculations (B3LYP-D3/6-311G^{*+}) on the three possible conformers derived by rotating each heterocycle by 180^{o}; the crystallographically determined structure was computed to be more stable by 27 kJ/mol over the isomer where one btda ring is rotated by 180° and by 81 kJ/mol when both btda rings are rotated by 180° (Table 5.1).

Table 5.1 Density functional theory (DFT) calculations of the conformers of bisbtdaH$_2$ using the dispersion-corrected B3LYP-D3 functional and 6-311G^{*+}.

	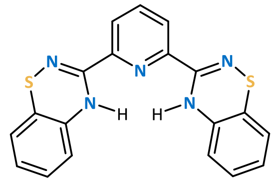	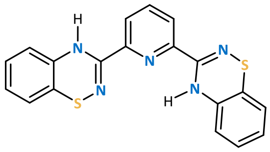	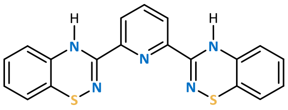
Energy/kJ/mol	0	27	81
Torsion angle/°	-7.3/3.65	2.95/-138.97	-128.84/136.59

Notably initial attempts to recrystallize bisbtdaH$_2$ from hexanes resulted in the formation of **5.2** which was characterized by X-ray crystallography (Figure 5.3). Such thermally-induced ring contractions of benzothiadiazines has previously been reported by Rees.[63] Subsequent ^{1}H NMR studies revealed bisbtdaH$_2$ was thermally unstable upon heating in hexanes and reflected in a lower symmetry structure with a peak for each chemically distinct different environment (Figure 5.4). The side product (**5.2**) also appears in the fragmentation pattern (calc. 361.0582, found 361.0578) of the ligand bisbtdaH$_2$.

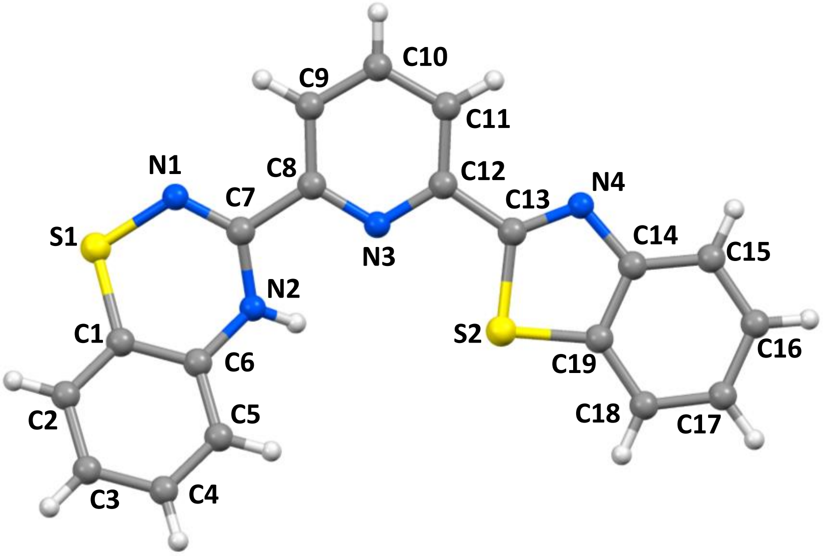

Figure 5.3 Molecular structure of the side product **5.2**.

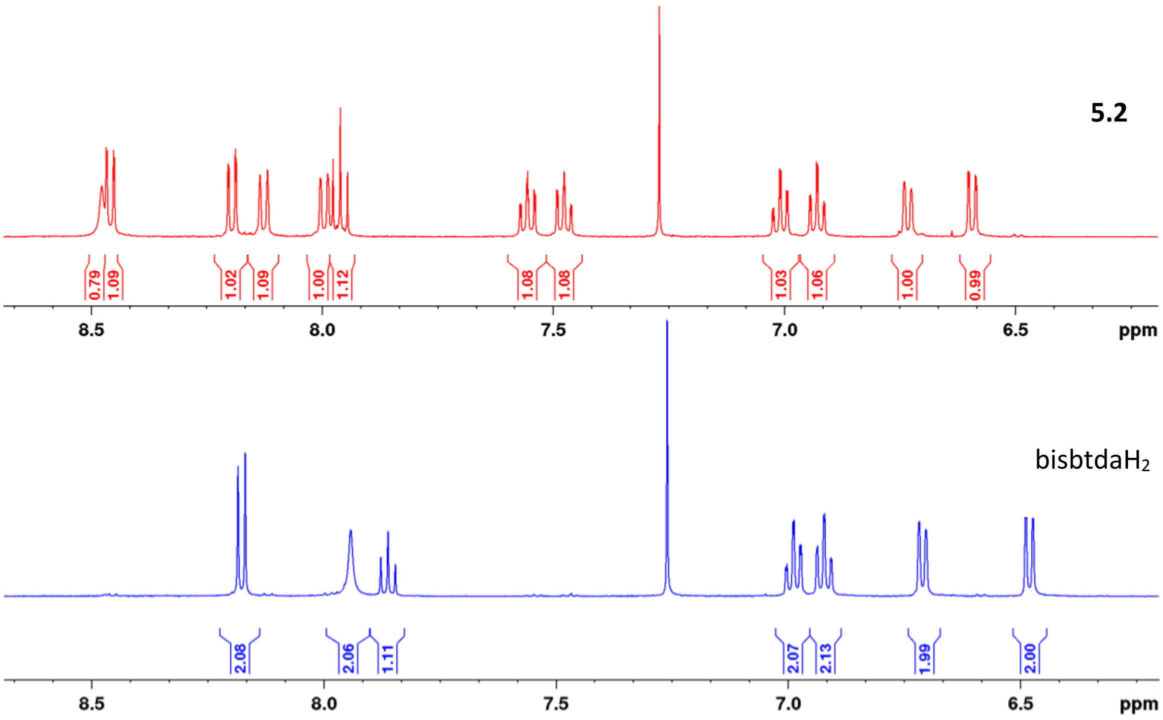

Figure 5.4 ^{1}H NMR of side product **5.2** (red) and bisbtdaH$_2$ (blue) for comparison (500 MHz, CDCl$_3$).

5.2.2 Redox studies on bisbtdaH$_2$

The ligand bisbtdaH$_2$ possesses two thiadiazine moieties which can be oxidized to generate the corresponding diradical ligand. However, the oxidation mechanism can be achieved through two sequential 1e^- transfer processes or *via* a single concomitant 2e^- transfer. Electrochemical studies on bisbtdaH$_2$ (C_0 = 5.96 x 10^{-3} mol·L^{-1}) were performed using a glassy carbon electrode (S = 1.57 mm^2) in a deoxygenated solution of ^{n}Bu$_4$N(PF$_6$) in dichloromethane (0.047 mol·L^{-1}). Initial cyclic voltammograms revealed a single reversible redox wave consistent with a 2e^- process with $E_{1/2}$ = +0.90 V *vs* Ag/AgCl (Figure 5.5a). The potential did not change as a function of the scan rate (Figure 5.5b) and the anodic current peaks were found to be linearly proportional to the square root of the scan rate (Figure 5.5c), consistent with a reversible process and the Nernstian system, in which electron transfer is faster than the diffusion rate.

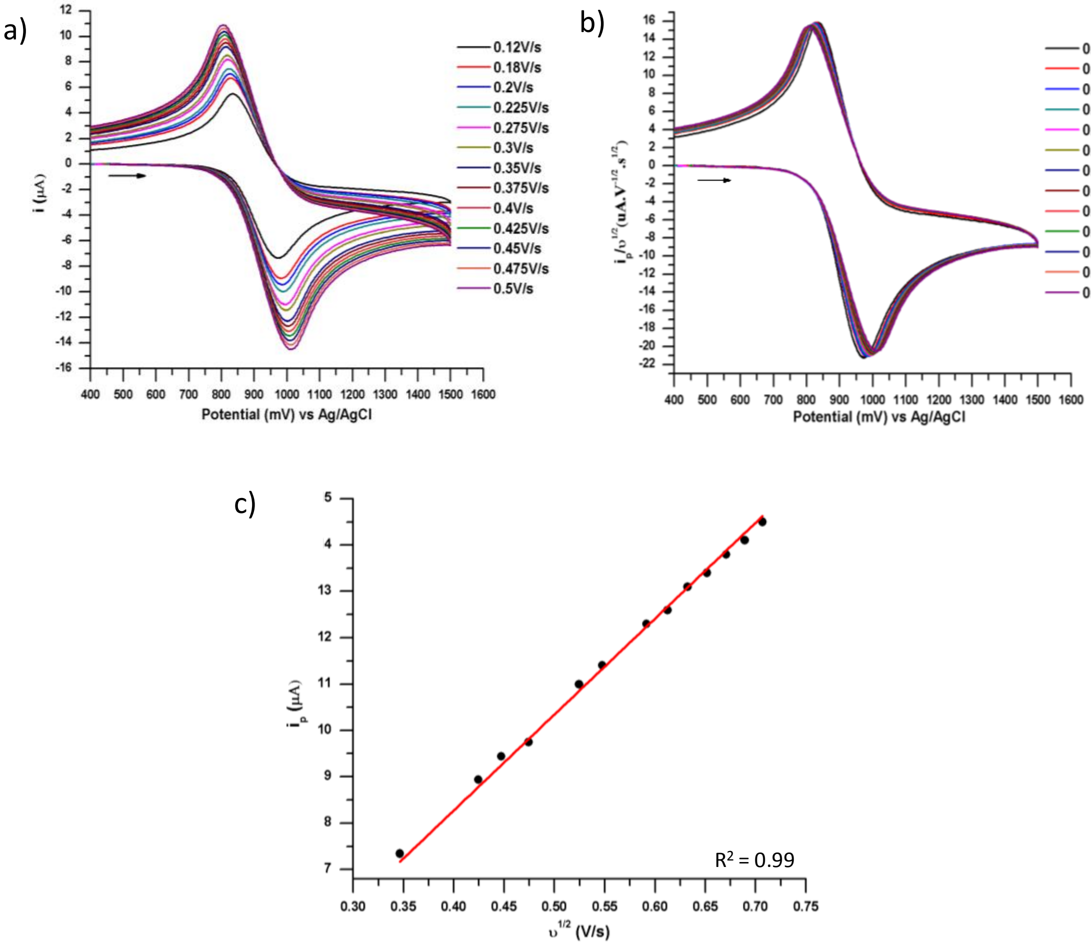

Figure 5.5 Cyclic voltammograms of ligand bisbtdaH$_2$ (C_0 = 5.96 mmol·L^{-1}) in a solution of ^{n}Bu$_4$N(PF$_6$) in dichloromethane (0.047 mol·L^{-1}). a) Cyclic voltammograms of the ligand bisbtdaH$_2$ obtained at different scan rates (from 0.12V/s to 0.5V/s); b) Normalized cyclic voltammograms of ligand; c) The intensity of the anodic current peaks as a function of the square root of the scan rate.

Within this framework, the Nernstian equation can be used to estimate the number of electrons transferred.[64] The difference between $E_{P/2}$ (the potential of the anodic peak at half-height) and E_p (the anodic peak potential) was found to be 56.5 mV, close to the value expected for a 2e^- transfer process (54.6 mV at 25 °C, Equation 5.1).

$$E_{p/2} - E_p = 2.20\frac{RT}{nF} = 54.6\text{ mV } (25\text{ °C, n = 2}) \qquad \text{Equation 5.1}$$

where R is the gas constant, T is the temperature, F is the faraday constant and n is the number of electron transferred.

Although the electrochemical studies in solution revealed a single 2e^- transfer, heterogeneous oxidation of bisbtdaH$_2$ with Ag$_2$O in dichloromethane appeared kinetically slow and we believe the evolution of the EPR spectra over time (*vide infra*) is consistent with initial formation of the mono-radical followed by generation of the diradical. The *in situ* room temperature EPR spectra of the ligand bisbtdaH$_2$, dissolved in dichloromethane and oxidized with an excess of Ag$_2$O, led firstly to the formation of pentet spectrum typical for btda radicals[65] consistent with two near-equivalent ^{14}N nuclei, expected for bisbtdaH$^{\bullet}$. The fine structure of the second derivative could only be replicated by taking into account coupling to two additional ^{1}H nuclei associated with the benzo-fused ring. The best fit of the spectrum afforded g_{iso} = 2.0058 and the hyperfine coupling constant of ^{14}N atoms, a$_N$ = 5.55 and 4.85 G, and ^{1}H atoms, a$_H$ = 2.00 and 1.27 G (Figure 5.6, left).

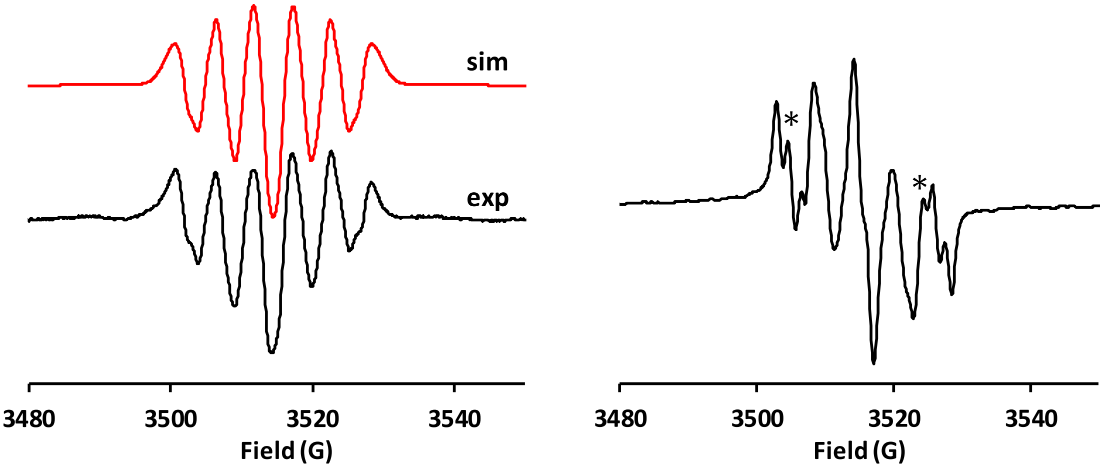

Figure 5.6 Solution EPR spectra of mono and di-radicals formed from oxidation of bisbtdaH$_2$; (left) Second derivative and simulation of the monoradical bisbtdaH$^{\bullet}$; (right) First derivative of diradical, bisbtda$^{\bullet\bullet}$ (stars indicating the additional features, right).

These parameters are similar to other btda radicals[65] and in accord with the computed spin density distribution (Figure 5.7, left) which delocalizes spin density to two positions on the benzo ring. After a few minutes, the shape of the spectrum changed and additional features emerged between the initial 5-line spectrum (Figure 5.6, right). The emergence of a second species which we tentatively assign to a diradical species in which the exchange coupling (*J*) is similar in energy to the hyperfine coupling constant suggesting the presence of weak intramolecular magnetic exchange between the two radicals.[66] The EPR spectra are consistent with the spin density distribution determined from DFT calculations which reveal that the nodal nature of the C(7) and C(13) positions of the btda rings leads to limited 'spin leakage' onto the pyridyl linker and only weak exchange coupling between these two radicals (Figure 5.7).

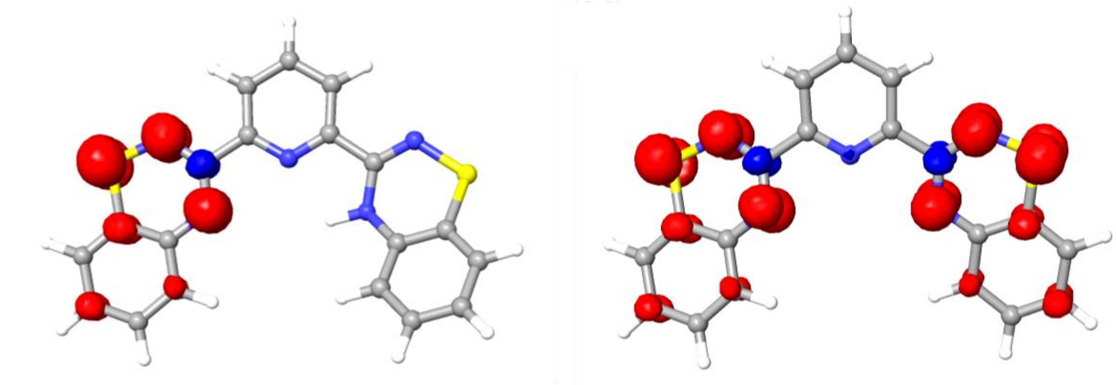

Figure 5.7 Spin density distribution (UB3LYP/6-311G*$^+$: (left) monoradical bisbtdaH$^\bullet$ and (right) the diradical triplet of bisbtda$^{\bullet\bullet}$.

5.2.3 Syntheses and characterization of metal complexes of bisbtdaH$_2$

5.2.3.a Syntheses and description of [M(bisbtdaH$_2$)$_2$][X]$_2$ (M = Mn, X = CF$_3$SO$_3$ (5.3); Fe, X = CF$_3$SO$_3$ (5.4); Fe, X = BF$_4$ (5.5); Co, X = Cl (5.6); Ni, X = Cl (5.7); Zn, X = CF$_3$SO$_3$ (5.8))

Reactions of ligand bisbtdaH$_2$ with a range of M^{II} salts in either CH$_3$OH or CH$_3$CN in a ratio of 2:1 at ambient temperatures afforded complexes with general formula

[M(bisbtdaH$_2$)$_2$][X]$_2$ (M = Mn, X = CF_3SO_3 (**5.3**); Fe, X =CF_3SO_3 (**5.4**); Fe, X = BF_4 (**5.5**); Co, X = Cl (**5.6**); Ni, X = Cl (**5.7**); Zn, X = CF_3SO_3 (**5.8**)). The crystals of complexes **5.3** – **5.8** proved slightly hygroscopic, absorbing small quantities of water upon standing in the open atmosphere but otherwise appeared air stable. All complexes were characterized by a variety of analytical techniques including X-ray crystallography, IR and elemental analysis.

Complex **5.3** crystallizes in the orthorhombic space group *Pccn* with half a cation and one OTf$^-$ anion in the asymmetric unit. Complex **5.4** crystallizes in the monoclinic space group *Pc* with one cation, two OTf$^-$ anions and two CH_3CN solvent molecules in the asymmetric unit. Complexes **5.5** crystallizes in the triclinic space group $P\overline{1}$ with one cation, two BF_4^- anions and two CH_3CN solvent molecules in the asymmetric unit. Complex **5.6** crystallizes in the monoclinic space group $P2_1/n$ with one cation and two Cl$^-$ in the asymmetric unit. Complex **5.7** crystallizes in the triclinic space group $P2_1/n$ with one cation, two Cl$^-$ anions and four CH_3OH solvent molecules in the asymmetric unit. Complex **5.8** crystallizes in the monoclinic space group $C2/c$ with two halves of two cations, two OTf$^-$ anions and one CH_3OH solvent molecules in the asymmetric unit. The formation of complexes **5.3** – **5.8** is summarized in Equation 5.2.

$$MX_2 + 2\ \text{bisbtdaH}_2 \longrightarrow [M(\text{bisbtdaH}_2)_2][X]_2 \quad X = Cl,\ CF_3SO_3,\ BF_4$$

Equation 5.2

Complexes **5.3** – **5.8** are mononuclear compounds of general formula [M(bisbtdaH$_2$)$_2$][X]$_2$ in which two bisbtdaH$_2$ ligands bind in a tridentate *N,N′,N″*-chelate fashion *via* two N_{BTDA} and N_{py} donor atoms, adopting a *mer* coordination geometry. Each metal adopts a six-coordinate MN_6 geometry. The structure of complex **5.4**, is shown in Figure 5.8 as representative of this series of structures (for complexes **5.3**, **5.5** – **5.8** see Appendix 4) and selected bond lengths and angles are shown in Table 5.2. The Fe^{II} has octahedral geometry with a N_6 donor set, with Fe-N distances in the range of 1.864(5) – 1.975(5) Å consistent with a low spin state.[67] The ligand bisbtdaH$_2$ exhibits internal N_{BTDA}-M-N_{py} angles in the range 79.9(2) – 80.1(2)°.

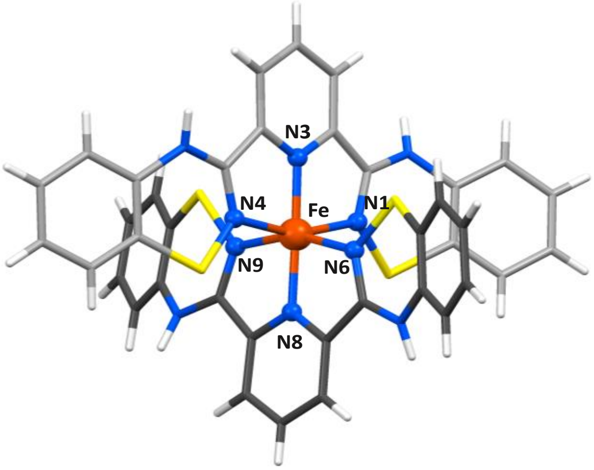

Figure 5.8 Molecular structure of **5.4** as representative of the series of complexes **5.3** − **5.8** (solvent molecules and counter-ions omitted for clarity).

Table 5.2 Selected bond lengths and angles for complexes **5.3** − **5.9**.

	M-N$_{py}$/Å	M-N$_{BTDA}$/Å	N$_{py}$MN$_{BTDA}$/°^{a}	N$_{py}$MN$_{BTDA}$/°^{b}	N$_{BTDA}$MN$_{BTDA}$/° ^{a}	N$_{BTDA}$MN$_{BTDA}$/° ^{b}	N$_{py}$MN$_{py}$/°
Mn (**5.3**)	2.276(2)	2.201(2)	71.00(8)	103.55(8)	142.96(8)	86.05(8)	171.23(12)
	2.297(2)		72.22(8)	113.50(8)		104.77(12)	
						106.62(12)	
Fe (**5.4**)	1.864(5)	1.969(5)	79.9(2)	98.7(2)	159.9(2)	91.2(2)	178.6(2)
	1.888(5)	1.969(5)	79.9(2)	99.3(2)	159.9(2)	91.6(2)	
		1.973(5)	80.0(2)	101.4(2)		91.7(2)	
		1.975(5)	80.1(2)	100.7(2)		92.4(2)	
Fe (**5.5**)	1.881(4)	1.962(5)	79.63(19)	98.20(17)	160.0(2)	89.48(19)	178.47(17)
		1.967(5)	79.80(18)	99.95(19)	160.09(19)	90.21(19)	
		1.970(4)	80.29(17)	100.04(19)		93.04(19)	
		1.976(4)	80.36(19)	101.71(17)		94.15(19)	
Co (**5.6**)	2.046(3)	2.128(3)	74.93(10)	93.94(10)	147.63(11)	90.38(11)	163.82(11)
	2.059(3)	2.139(3)	75.04(10)	94.45(10)	149.37(11)	92.28(11)	
		2.144(3)	75.51(11)	116.43(11)		93.94(11)	
		2.157(3)	75.61(10)	117.39(11)		99.90(11)	
Ni (**5.7**)	1.985(2)	2.080(2)	77.16(10)	93.16(10)	154.57(10)	91.85(10)	177.98(10)
	1.987(2)	2.081(2)	77.29(10)	93.32(9)	154.82(9)	92.66(9)	
		2.083(2)	77.41(9)	100.85(9)		93.16(10)	
		2.094(2)	77.53(9)	104.57(10)		93.32(9)	
Zn (**5.8**)	2.054(3)	2.165(3)	75.35(11)	73.63(11)	149.00(10)	78.85(11)	174.64(17)
	2.055(3)	2.266(3)	103.87(11)	73.98(11)	149.12(11)	80.69(11)	176.37(17)
		2.209(3)	75.39(11)	106.94(11)		105.11(16)	
		2.312(3)	103.17(11)	107.81(11)		109.38(15)	
						109.92(16)	
						110.12(16)	
Cu (**5.9**)^c	1.929(2)	2.041(2)	79.33(8)	-	157.77(8)	-	-
		2.051(2)	79.36(8)				

^{a} Angle within the chelate ring ^{b} Angles between N atoms in different rings ^{c} Cu-O/Å = 1.9298(16)-2.651(2), O-Cu-O/° = 53.95(7)-153.68(6), O-Cu-N/° = 86.83(7)-173.05(7)

A comparison of the *cis* N$_{BTDA}$-M-N$_{BTDA}$ bond angles at the metal centre reveal significant variation in conformation, ranging from 142.96(8) – 160.0(2)°. This variation is highlighted when comparing the angle formed between the two N$_3$ donor sets of the two coordinated bisbtdaH$_2$ ligands (Table 5.3, L$_1$-L$_2$ plane/°).

Table 5.3 Angles between planes for complexes **5.3** – **5.8** and the RMS deviation for each complex from idealised octahedral, trigonal prismatic or pentagonal bipyramid (with equatorial vacancy). For each complex the smallest deviation is underlined.

	Mn (**5.3**)	Fe (**5.4**)	Fe (**5.5**)	Co (**5.6**)	Ni (**5.7**)	Zn (**5.8**)
L$_1$ - L$_2$ plane/°	80.59	89.91	88.05	84.92	89.81	73.70 (Zn2) 75.83 (Zn1)
Octahedral	0.833	0.429	0.430	0.735	0.541	0.727 (Zn2) 0.751 (Zn1)
Trigonal prismatic	0.888	1.074	1.069	0.757	1.046	0.936 (Zn1) 0.955 (Zn2)
Pentagonal bipyramid with a vacancy (eq.)	0.828	1.575	0.742	0.690	0.752	0.841(Zn1) 0.844(Zn2)

For an idealized octahedral geometry this angle should be 90°. This is observed for Fe^{II} and Ni^{II} but deviates significantly for Mn^{II} and Zn^{II} and is highlighted in Figure 5.9. The effect of this distortion on the geometry of the metal centre was quantified using FindGeo.[68] In the cases of Fe and Ni, the RMS deviation clearly indicates an octahedral geometry but in all other cases, the calculated RMS deviation is comparable for octahedral, trigonal prismatic and pentagonal bipyramid geometries, as shown in Table 5.3.

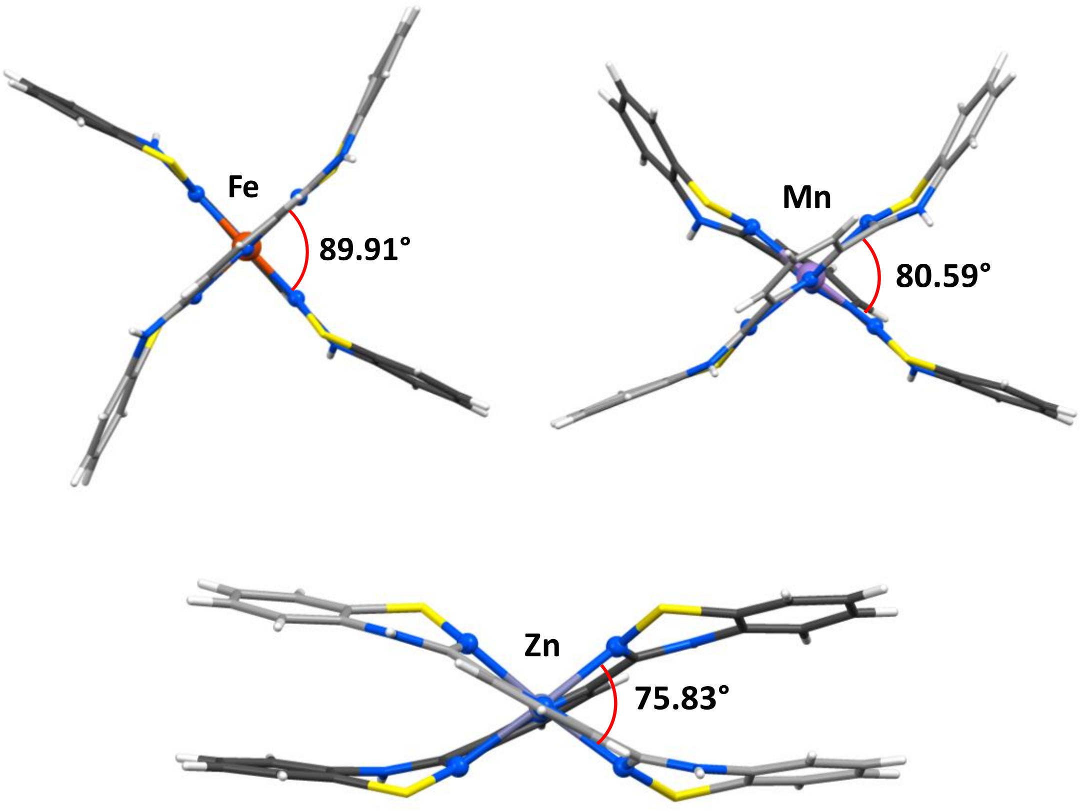

Figure 5.9 Side-view of complexes of Mn (**5.3**), Fe (**5.4**) and Zn (**5.8**) illustrating the different conformations the ligand adopts in each compound, along with the angle between the two planes of the ligand.

Notably, the distortion parameter is maximized for Mn^{II} and Zn^{II}, in which the high spin Mn^{II} (d^5) and the Zn^{II} (d^{10}) have no crystal field stabilization energy (CFSE) and so there is no electronic destabilization in distorting away from octahedral in these two cases. Conversely the distortion is minimal for low spin Fe^{II} ($-2.4\Delta_o$) and Ni^{II} ($-1.2\Delta_o$). These CFSE effects clearly provide some stabilizing influence for the octahedral coordination geometry over other 6-coordinate geometries, despite the contributions of other packing forces (cation-anion and/or cation-cation interactions) which may contribute to the overall lattice enthalpy. In addition, DFT calculations were performed on the conformation of the ligand found in the Mn (**5.3**), Fe (**5.4**) and Zn (**5.8**) complexes. The energy is lowest for the ligand conformation in Mn and Zn complexes, whereas the energy increased significantly for the conformer observed in the Fe complex (Table 5.4). These results further support the argument that the CFSE is the stabilizing parameter for the octahedral geometry of the Fe^{II} complex and that any destabilization of the ligand geometry is offset by the optimization of the CFSE.

Table 5.4 Density functional theory (DFT) single point energy calculations of the conformation of the ligand found in the metal complexes using the dispersion-corrected B3LYP-D3 functional and 6-311G**.

Complex	Mn (**5.3**)	Fe (**5.4**)	Zn (**5.8**)
	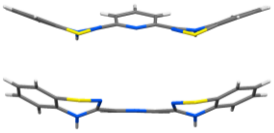		
Energy/ kJ/mol	0	46	18

The N-H groups of the bisbtdaH$_2$ ligands exhibit a propensity to be involved in hydrogen bonding. In complexes **5.2** and **5.3** the N-H groups form N-H···O$_{\text{OTf}}$ hydrogen bonds between the cationic complex and the triflate anion ($d_{\text{N-H}\cdots\text{O}}$ = 1.996 − 2.114 Å, $\theta_{\text{N-H}\cdots\text{O}}$ = 149.61 − 177.91° for **5.3** and $d_{\text{N-H}\cdots\text{O}}$ = 2.031 − 2.150 Å, $\theta_{\text{N-H}\cdots\text{O}}$ = 156.24 − 159.56° for **5.3**). The benzo rings in **5.3** and **5.4** are involved in π-π and C-H···π interactions (3.208 and 3.157 – 3.883 Å, $\theta_{\text{C-H}\cdots\text{C}}$ = 120.35 − 157.80° for **5.3** and 3.370 − 3.588 Å and 2.828 − 2.934 Å, $\theta_{\text{C-H}\cdots\text{C}}$ = 128.58 − 149.09° for **5.4**) (Figure 5.10).

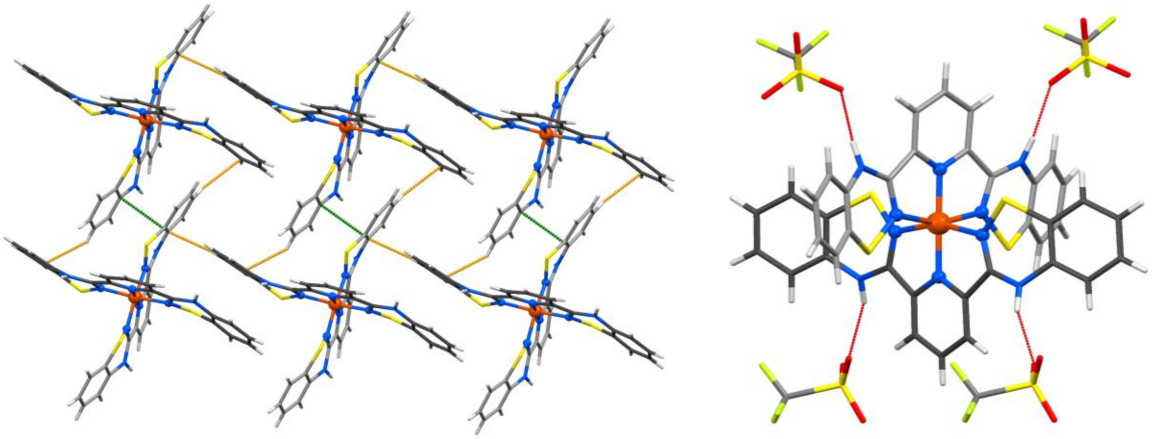

Figure 5.10 Crystal packing of **5.4** highlighting the π-π (green) and C-H···π (yellow) interactions (left) and the N-H···O hydrogen bonding between the amino group and the triflate counter ions (red lines, right).

In complex **5.5,** the N-H groups form N-H···Cl hydrogen bonds between the cationic complex and the Cl anions ($d_{N\text{-}H\cdots Cl}$ = 2.268 – 2.598 Å, $\theta_{N\text{-}H\cdots Cl}$ = 159.99 – 176.60°). In complex **5.6** the N-H groups form two N-H···Cl hydrogen bonds between the cationic complex and the Cl anions ($d_{N\text{-}H\cdots Cl}$ = 2.172 and 2.464 Å, $\theta_{N\text{-}H\cdots Cl}$ = 166.97 and 171.17°, respectively) and two hydrogen bonds with the CH_3OH solvent molecules ($d_{N\text{-}H\cdots O}$ = 1.896 and 1.898 Å, $\theta_{N\text{-}H\cdots O}$ = 170.23 and 173.19°, respectively).

The structure of zinc complex **5.8** exhibits the greatest distortion from octahedral geometry, placing two benzo rings in close proximity to exhibit an intramolecular π-π interaction with centroid···centroid distances of 3.784 Å (Figure 5.11). In this complex, the cationic complex of Zn(1) forms four N-H···O_{OTf} hydrogen bonds between the cationic complex and the triflate anions ($d_{N\text{-}H\cdots O}$ = 2.002 and 2.114 Å, $\theta_{N\text{-}H\cdots O}$ = 168.18 and 148.20° respectively); whereas Zn(2) forms two N-H···O_{OTf} hydrogen bonds between the cationic complex and the triflate anions ($d_{N\text{-}H\cdots O}$ = 2.495 Å, $\theta_{N\text{-}H\cdots O}$ = 128.74°) and two N-H···O_{CH3OH} between the cationic complex and the methanol solvent molecules ($d_{N\text{-}H\cdots O}$ = 2.113 Å, $\theta_{N\text{-}H\cdots O}$ = 138.19°).

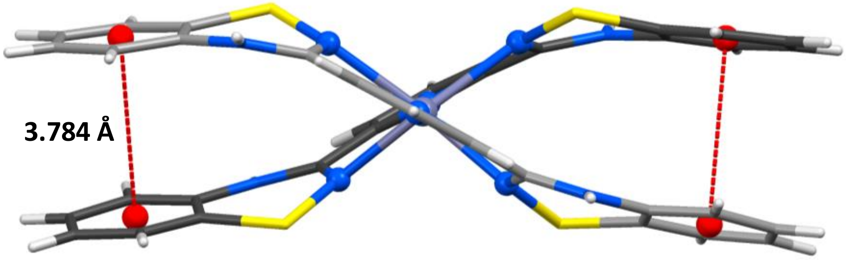

Figure 5.11 Crystal packing of **5.8** highlighting the π-π interactions between the benzo groups in one of the two complete cations in the crystal structure.

5.2.3.b Synthesis and characterization of complex [Cu(bisbtdaH$_2$)(NO$_3$)$_2$]·DMF (5.9)

Reaction of ligand bisbtdaH$_2$ with Cu(NO$_3$)$_2$ in CH$_3$OH in a ratio of 2:1 at ambient temperatures afforded the 1:1 adduct [Cu(bisbtdaH$_2$)(NO$_3$)$_2$] (**5.9**) with only one ligand per Cu atom (Figure 5.12). The reaction was performed in various ratios but the product was always found to exhibit a 1:1 ratio of Cu^{II} : bisbtdaH$_2$ and presumably arises out of the significant Jahn-Teller distortion of the d^9 Cu^{II} ion which destabilises octahedral coordination. This can be compared to our previous results using the chelate ligand pybtdaH which formed a series of 1:2 complexes, MCl$_2$(pybtdaH)$_2$ (M = Mn, Fe, Co, Ni, Cu

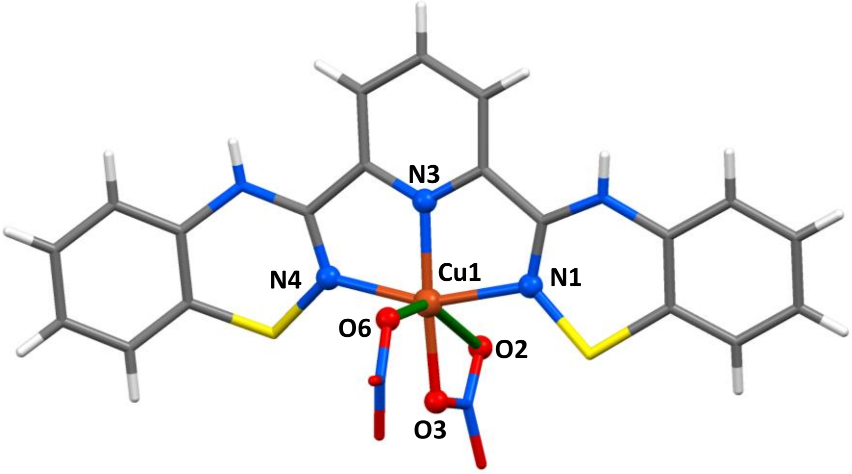

Figure 5.12 Crystal structure of [Cu(bisbtdaH$_2$)(NO$_3$)$_2$] (**5.9**) (Jahn-Teller axis is shown in green, methanol solvent omitted for clarity).

and Zn), whereas Cu^{II} is unique within this series in also forming a four coordinate complex with 1:1 ratio, MCl_2(pybtdaH).[69]

The 1:1 complex **5.9** crystallizes in the monoclinic space group $P2_1/c$. Unlike **5.3** – **5.8**, in which the coordination geometry is completed by two tridentate ligand bisbtdaH_2 donors and the counter-ions are not coordinated to the metal centre, the residual nitrate counter-ions of **5.9** are bound to the metal. One nitrate group acts as a chelate donor to Cu^{II} whereas the second nitrate ion is a monodentate donor leading to an overall distorted octahedral N_3O_3 geometry (Figure 5.12). The Cu-N distances are in range 1.9293(19) – 2.0506(19) Å while Cu-O distances are in range 1.9298(16) – 2.651(2) Å with a distinct Jahn-Teller elongation along the O(2)-Cu-O(6) axis. The N_{py}-M-N_{BTDA} angles are 79.34(8)° and 79.36(8)° and O-Cu-O angles are in the range 53.95(7) – 153.68(6)°. The formation of complex **5.9** is summarized in Equation 5.3.

$$Cu(NO_3)_2 + \text{bisbtdaH}_2 \longrightarrow Cu(\text{bisbtdaH}_2)(NO_3)_2 \qquad \text{Equation 5.3}$$

5.2.4 Spectroscopic studies of the metal complexes

5.2.4.a UV-Vis spectroscopy of complexes 5.3 – 5.8

The UV-Vis spectra of complexes **5.3** − **5.8** are dominated by a series of intense ($\varepsilon = 10^3 - 10^5\ M^{-1}\cdot cm^{-1}$) π-π* ligand-centered absorption bands at around 210, 230, 270 and 283 nm (Figure 5.13). There are additionally lower intensity absorption bands at 340 and 430 that are attributed to intra-ligand charge transfer transitions. These assignments are corroborated by the fact that the absorption profiles for the complexes match the absorption spectrum of the free ligand. The similar trend was observed previously with metal complexes of pybtdaH.[69]

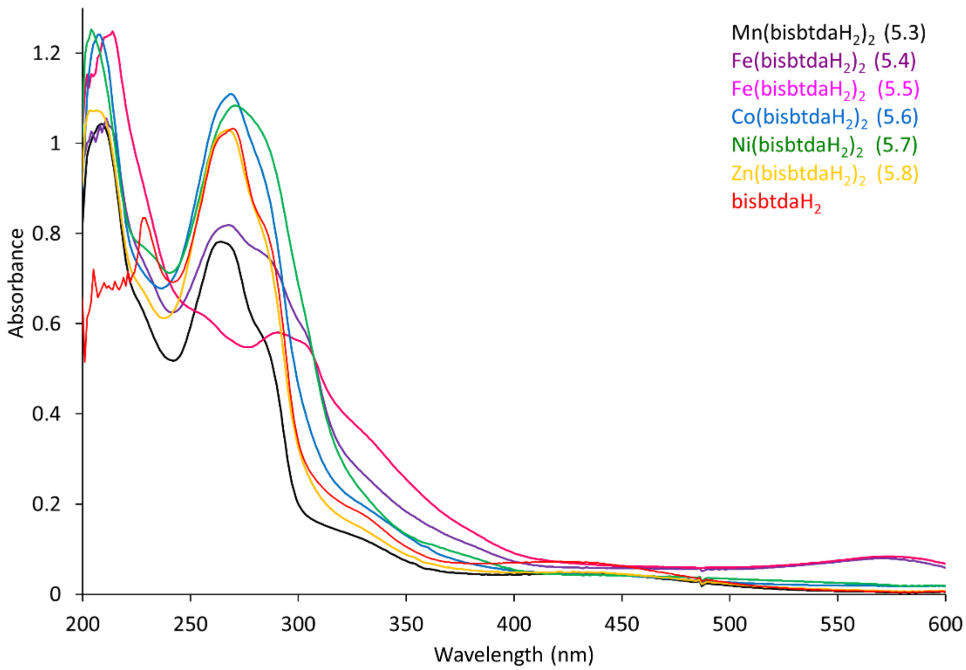

Figure 5.13 Solution UV-Vis spectra of complexes **5.3** – **5.8** as well as ligand bisbtdaH$_2$ to emphasize the ligand-based nature of the spectroscopic properties (Solvent: CH_3OH or CH_3CN, rt, $C_{bisbtdaH2} \approx 10^{-5}$ M; $C_{complexes} \approx 10^{-6}$ M).

5.2.4.b Electronic structure of complexes [Fe(bisbtdaH$_2$)$_2$]$^{2+}$ (5.4 and 5.5)

The Fe^{II} complexes **5.4** and **5.5** were found to be low-spin diamagnetic *d*^{6} based on structural parameters and ^{1}H NMR spectra which exhibit no paramagnetic shift or broadening. The ^{1}H NMR spectrum of **5.5** shows that the chemical shift range is in the 'normal' range expected consistent with low spin Fe^{II}. The peaks associated with the free ligand are fully replaced by the ^{1}H NMR signals for the coordinated ligand of complex **5.5** (Figure 5.14). Additional room temperature X-ray studies were performed on complex **5.5** but revealed no significant increase in bond length expected for a LS to HS phase transition.[67] These data are all consistent with a LS Fe^{II} centre.

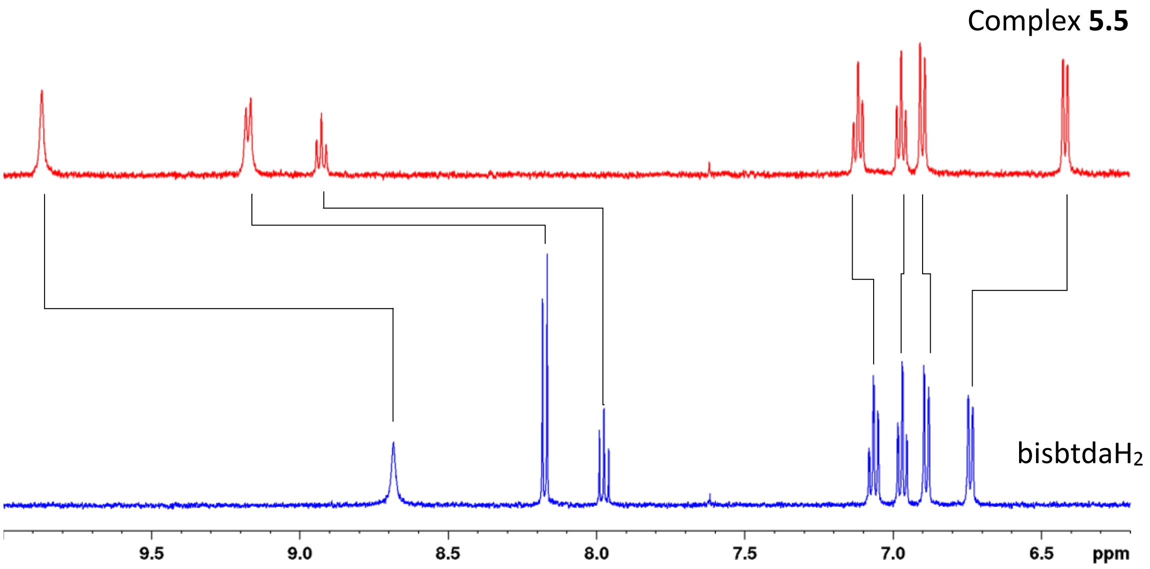

Figure 5.14 ^{1}H NMR of complex **5.5** (red) and bisbtdaH$_2$ (blue) (500 MHz, CD_3CN).

Attempts to model the binding affinity of bisbtdaH$_2$ to Fe^{II} by UV-Vis titration in MeCN proved ambiguous. While a marked absorption maximum was observed at 570 nm and increased on addition of bisbtdaH$_2$, a fit of the data to formation of both 1:1 and 2:1 complexes were similar (Figure 5.15).[70,71] Assuming formation of [Fe(bisbtdaH$_2$)$_2$]$^{2+}$, the formation constant (β) for the process:

$$Fe^{2+} + 2\ \text{bisbtdaH}_2 \longrightarrow [Fe(\text{bisbtdaH}_2)_2]^{2+} \qquad \text{Equation 5.4}$$

is $\beta = 4.6 \times 10^6$. For [Fe(terpy)]$^{2+}$ K_1 was found to be $10^{7.1}$ and $\beta = 10^{20.9}$ for formation of [Fe(terpy)$_2$]$^{2+}$.[72,60] These clearly suggest that bisbtdaH$_2$ is a significantly weaker coordinating ligand than terpy. This is perhaps unsurprising given the large computed reorientation energy for the ligand to adopt the tridentate *N,N´,N″* coordination geometry (80 kJ·mol^{-1}, *vide supra*).

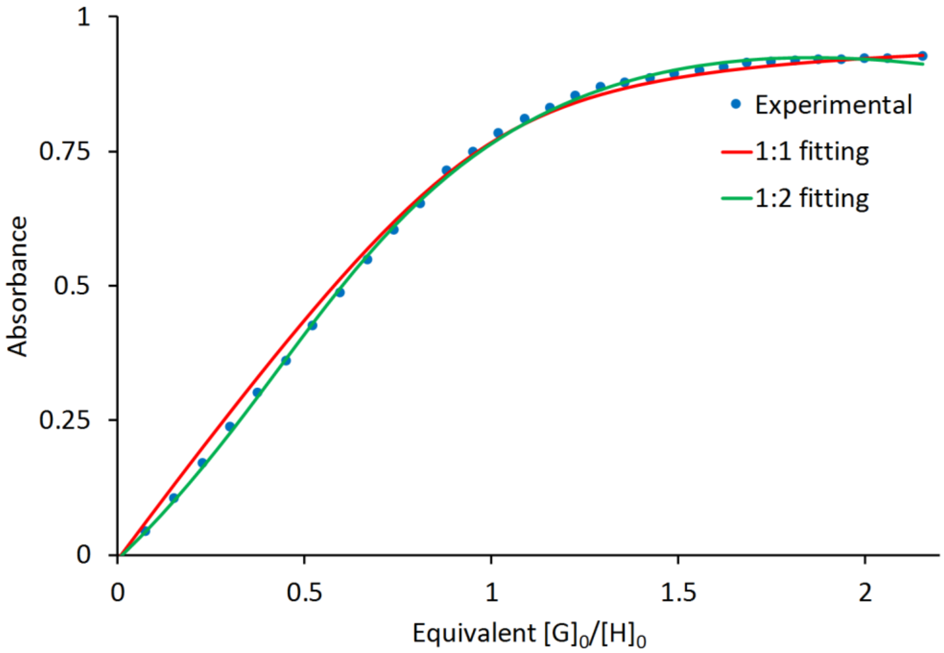

Figure 5.15 Titration profile at 570 nm. Changes in absorption spectra of Fe^{II} triflate (10^{-4} M) with an increasing amount of bisbtdaH$_2$ in CH_3CN (inset). Red line corresponds to the fit to formation of [Fe(bisbtdaH$_2$)]$^{2+}$ ($K_1 = 0.1 \times 10^6$) whereas the green line is the fit to formation of [Fe(bisbtdaH$_2$)$_2$]$^{2+}$ ($\beta = 4.6 \times 10^6$).

5.2.4.c Electrochemical studies on complex [Fe(bisbtdaH$_2$)$_2$]$^{2+}$ (5.4)

Electrochemical studies on **5.4** in dichloromethane using $^{n}Bu_4N(PF_6)$ as supporting electrolyte is shown in Figure 5.16 along with ligand bisbtdaH$_2$ for comparison. The electrochemical behaviour of bisbtdaH$_2$ appears completely reversible with $E_{1/2}$ = 0.90 V *vs* Ag/AgCl (*vide supra*). Although complex **5.4** shows one reversible oxidation wave (E_{ox} = 0.80 V) around the same potential as bisbtdaH$_2$ consistent with a ligand-based process. The corresponding reduction process shows two waves at 0.94 and 0.85 V, consistent with sequential reduction processes.

The structural variations in [M(bisbtdaH)$_2$]$^{2+}$ complexes reveal some variation in ligand geometry and we speculate that the difference in behaviour between oxidation and reduction waves may be associated with subtle geometric changes upon oxidation such that the first and second reduction waves appear at different potentials.

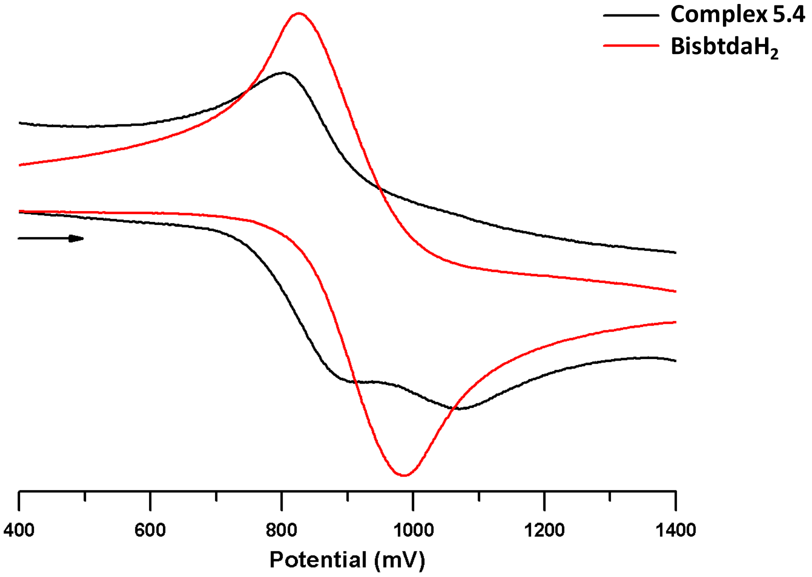

Figure 5.16 Cyclic voltammogram of **5.4** (black) and bisbtdaH$_2$ (red) in dichloromethane (0.047 mol·L^{-1}) with ^{n}Bu$_4$N(PF$_6$) supporting electrolyte at a scan rate of 0.2 V/s.

5.2.4.d Magnetic properties of complex [Co(bisbtdaH$_2$)$_2$][Cl]$_2$ (5.6)

The electronic structure of the Co^{II} complex (**5.6**) was probed through SQUID magnetometry (0.20 T, 5 – 300 K). Under O_h symmetry the Co^{II} ion has a ^{4}T ground term in which there is unquenched orbital angular momentum. In this case a change in gradient of the 1/χ *vs* T plot is often observed with the high temperature data fitting g ≈ 2 and S = 3/2 and a significant Weiss constant reflecting the single ion behaviour (Figure 5.17). In the low temperature range spin orbit coupling of the ^{4}T term affords a Kramers doublet ground state with the magnetic response behaving more like S_{eff} = ½ with g > 4 and often a negligible Weiss constant. Conversely if the structure is significantly distorted then the orbital contribution is effectively quenched and the system can be considered as an S = 3/2 ion with second order orbital angular momentum contributing to g > 2. In the case of **5.6**, the coordination geometry is clearly distorted from octahedral (Table 3) and it is perhaps unsurprising that **5.6** obeys Curie-Weiss behaviour across the temperature range 5 – 300 K with C = 2.465 emu·K·mol^{-1} consistent with S = 3/2 and g = 2.29. The small Weiss constant (θ = -0.48 K) is consistent with a largely quenched orbital angular momentum and negligible single ion or intermolecular dipolar exchange. The latter argument is supported by the nearest Co···Co contact in **5.6** at 7.437(1) Å.

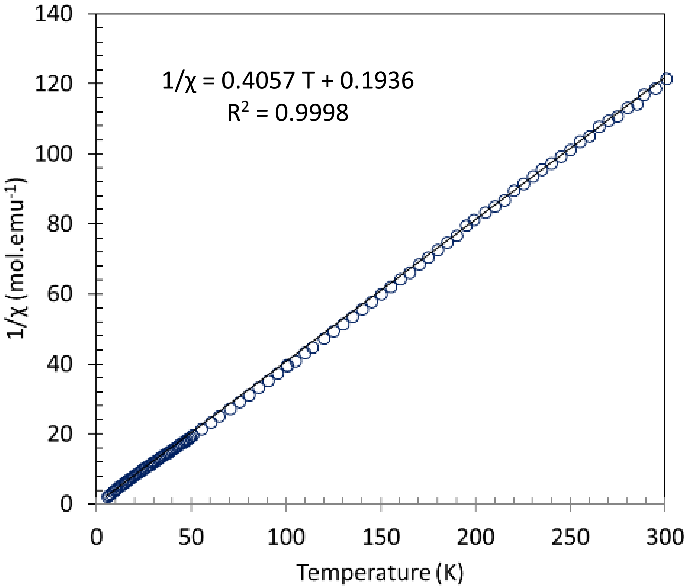

Figure 5.17 Temperature dependence of 1/χ for complex **5.6** with a fit to Curie-Weiss behaviour (C = 2.465 emu·K·mol^{-1}, θ = -0.48 K).

5.2.5 Reactivity trends in coordination chemistry of bisbtdaH₂

The ligand 2,2′:6′,2″-terpyridyl (terpy) can form a range of *N,N′,N″*-chelate complexes with first row transition metals as discussed in the introduction of this chapter.[18–21,22,23,25]

Therefore the isolation of mononuclear complexes with general formula [M(bisbtdaH$_2$)$_2$][X]$_2$ (**5.3** – **5.8**) and the 1:1 complex [Cu(bisbtdaH$_2$)(NO$_3$)$_2$] (**5.9**) in which the ligand bisbtdaH$_2$ is coordinated through the three N donor atoms was not unexpected. Although the formula and the binding mode of the ligand is identical in complexes **5.3** – **5.8** there is a significant distortion in the conformation of the ligands. A range of geometries between octahedral and trigonal prismatic is present with the greatest deviation from octahedral symmetry apparent for ions with no crystal field stabilisation energy, i.e. d^{10} Zn^{II} and high-spin d^5 Mn^{II} ions. The counter-ion has no effect in the cationic complex as confirmed from a comparison of the bond lengths of Fe complexes **5.4** and **5.5** (Table 5.2).

A CSD search[73] revealed that only 2% of the reported first row metal complexes of terpy analogues fall in the 70° – 80° range of which the majority is either non-symmetrical ligands[74] or the ligand is coordinating two metal centres resulting to a helix conformation.[75] In all cases, the distortion was due to the sterics of the terpy analogue and not a result of the electronic contribution.

A similar deviation in first fow transition metal complexes with the ligand 4′-methylthio-2,2′:6′,2″-terpyridyl has been reported by Turnbull.[76] In this work, the Mn complex has an angle of 78.6° between the two planes of the ligand, whereas the Fe and Ni complexes are close to 90°. The Co and Cu complexes were not characterized by X-ray crystallography for comparison, but they isolated a 1:1 adduct of Zn, in the metal center which is 5-coordinate.

5.3. Conclusions

The novel S/N based terpyridine type ligand bisbtdaH$_2$ has been synthesized and its coordination chemistry with first row transition metal complexes has been investigated. Electrochemical studies on the free ligand bisbtdaH$_2$ reveal a single well-defined 2e^- oxidation process with $E_{1/2}$ = +0.90 V. EPR studies of the *in situ* chemical oxidation on bisbtdaH$_2$ reveal the presence of both mono and diradical species. The anticipated six-coordinate metal complexes of general formula [M(bisbtdaH$_2$)$_2$][X]$_2$ (**5.3** − **5.8**) were isolated for M = Mn, Fe, Co, Ni and Zn whereas Cu generates an unexpected 1:1 adduct, [Cu(bisbtdaH$_2$)(NO$_3$)$_2$] (**5.9**). For the Co^{II} complex (**5.6**) SQUID measurements reflect the structure is high-spin across the temperature range whereas for Fe^{II} complexes (**5.4** and **5.5**) solution NMR data and crystallographic studies point to a low-spin configuration up to ambient temperature. Cyclic voltammetry of complex **5.4** reveals the oxidation process occurs *via* two single e^- oxidation waves. In all cases the bisbtdaH$_2$ ligand binds in a tridentate *N,N′,N″*-chelate fashion *via* benzothiadiazinyl N_{BTDA} and pyridyl N_{py} atoms. The geometries of the [M(bisbtdaH$_2$)$_2$]$^{2+}$ ions appear sensitive to the crystal field stabilisation energy; in the absence of a significant crystal field the geometry distorts significantly from octahedral and only provides systems with small distortion parameters when the CFSE can be maximized. This tendency to distort significantly from octahedral may contribute to the relatively low binding constant for bisbtdaH$_2$ towards M^{2+} ions, exemplified by Fe^{II}.

5.4. Experimental

5.4.1 General considerations and physical measurements

Solvents and other anhydrous or hydrated metal salts were obtained from commercial suppliers and used without further purification. 2,6-dicyanopyridine,[59] 2-(propylthio)-benzenamine,[77] Mn(CF_3SO_3)$_2$,[78] and Fe(CF_3SO_3)$_2$[79] were prepared according to reported methods. Zn(CF_3SO_3)$_2$ was prepared by a similar method reported in the literature.[78] Manipulation of air-sensitive materials was carried out under an atmosphere of dry nitrogen using standard Schlenk techniques and a dry-nitrogen glove box (MBraun Labmaster).

Melting points were determined using a Stanford Research Systems MPA120 EZ-Melt automated melting point apparatus. Elemental compositions were determined on a Perkin Elmer 2400 Series II CHNS/O Analyzer. UV-Vis spectra were measured on an Agilent 8453 Spectrophotometer using *ca.* 1×10^{-6} M solutions in methanol or acetonitrile in the ranger 200 – 600 nm. IR spectra were obtained using a Bruker Alpha FT-IR spectrometer equipped with a Platinum single reflection diamond ATR module. NMR spectra were recorded on a Bruker 500 MHz spectrometer with a Broadband AX Probe using $CDCl_3$ (^1H $\delta = 7.26$ ppm, s; ^{13}C $\delta = 77.16$ ppm), CD_2Cl_2 (^1H $\delta = 5.32$ ppm, t; ^{13}C $\delta = 53.84$ ppm) or CD_3CN (^1H $\delta = 1.94$ ppm, septet) as an internal reference point relative to Me_4Si ($\delta = 0$ ppm). Mass spectra were recorded on a Waters XEVO G2-XS specifically using the atmospheric solids analysis probe in positive resolution mode (ASAP+). EPR spectra of monoradical bisbtdaH$^{\bullet}$ and diradical bisbtda$^{\bullet\bullet}$ as well as complex **5.9** were measured on a Bruker EMXplus X-band EPR spectrometer at room temperature. Simulations of the EPR spectra were made using WinSim software[80] for the monoradical bisbtdaH$^{\bullet}$ and the PIP4Win software for the anisotropic spectrum of complex **5.9**.[81] Variable temperature magnetic data (2 – 300 K) on complex **5.6** were obtained using a Quantum Design MPMS SQUID magnetometer using a magnetic field strength of 0.1 T. Background corrections for the sample holder assembly and sample diamagnetism (Pascal's constants) were applied.

Density functional theory (DFT) calculations on bisbtdaH$_2$ were undertaken using the dispersion-corrected B3LYP-D3 functional and 6-311G** basis set[82–84] functional within

Jaguar[85] whereas spin density calculations on the mono and diradical of the ligand implemented the UB3LYP functional and 6-311G^{*+} and 6-311G* basis set, respectively.

UV-Vis titration experiments were performed on an Agilent 8453 Spectrophotometer, using quartz cuvettes (1 cm optical path length) at 25 °C. Solutions of Fe^{II} triflate in acetonitrile were titrated with standard solutions of bisbtdaH$_2$ in the same solvent mixture. Titrations were performed on 10 mL samples of known concentration (~10^{-4} M) of Fe^{II} triflate by adding known aliquots of titrant and recording an absorption spectrum after every addition. For the fitting of the data, the online site BindFit v0.5 was used.[70]

5.4.2 Ligand Synthesis

Ligand bisbtdaH$_2$ was prepared according to a modification of the literature procedure for pybtdaH[62]:

5.4.2.a (2Z,6Z)-*N'*^{2},*N'*^{6}-bis(2-(propylthio)phenyl)pyridine-2,6-bis(carboximidamide) (5.1)

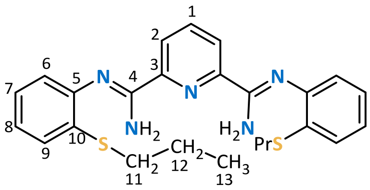

2-Propylsulphanylphenylamine (2.00 g, 11.95 mmol) was dissolved in dry THF (10 mL) and added dropwise to a stirred solution of lithium *bis*(trimethylsilyl)amide (2.50 g, 14.95 mmol) in THF (10 mL) at 0 °C under a nitrogen atmosphere. The dark reaction mixture was allowed to warm to room temperature and stirred for 18 h. A solution of 2,6-dicyanopyridine (0.70 g, 5.42 mmol) in THF (10 mL) was added dropwise to the above reaction mixture and the resultant dark brown solution was stirred for 2 days. The volume of solvent was reduced under vacuum to approximately 10 mL. To this solution a saturated aqueous solution of $NaHCO_3$ (50 mL) was added and extracted with CH_2Cl_2 (100 mL). The organic layer was then washed with $NaHCO_{3(aq.)}$ (1 x 50 mL) and brine (1 x 20 mL), dried over $MgSO_4$ and the solvent removed *in vacuo* to afford the crude product as a brown solid. The crude product was washed with excess hexane and dried *in vacuo* to yield the product as an off-white powder. Yield 2.00 g, 80%.

Melting point 114 °C.

Elemental Analysis calc. for $C_{25}H_{29}N_5S_2$: C, 64.76; H, 6.30; N, 15.10. Found: C, 64.42; H, 6.06; N, 15.10%.

IR (solid, cm^{-1}) $\tilde{\nu}_{max}$ = 3472 (w), 3324 (br), 2958 (w), 2926 (w), 1629 (s), 1574 (s), 1550 (s), 1458 (s), 1418 (m), 1396 (m), 1368 (w), 1263 (w), 1239 (w), 1225 (w), 1035 (w), 861 (w), 840 (w), 826 (m), 756 (m), 739 (m), 689 (w), 601 (br), 509 (w), 445 (w), 437 (w).

^{1}H NMR (500 MHz, ppm, CDCl$_3$) δ_H = 8.67 (2H, d, J = 7.9 Hz, C^2*H*), 8.01 (1H, t, J = 7.9 Hz, C^1*H*), 7.34 (2H, d, J = 7.9 Hz, C^9*H*), 7.19 (2H, t, J = 7.5 Hz, C^7*H*), 7.08 (2H, t, J = 7.4 Hz, C^8*H*), 6.96 (2H, d, J = 7.1 Hz, C^6*H*), 2.88 (4H, t, J = 7.3 Hz, C^{11}*H*), 1.71 (4H, sextet, J = 7.3 Hz, C^{12}*H*), 1.04 (6H, t, J = 7.3 Hz, C^{13}*H*).

^{13}C NMR (125 MHz, ppm, CDCl$_3$) δ_C = 151.72 (C^4), 150.07 (C^3), 147.64 (C^5), 138.07 (C^1), 129.88 (C^{10}), 127.74 (C^9), 126.23 (C^7), 124.05 (C^2), 123.93 (C^8), 120.88 (C^6), 33.92 (C^{11}), 22.48 (C^{12}), 13.87 (C^{13}).

HRMS (ASAP+) *m/z* [M+H]$^+$ calc. for $C_{25}H_{30}N_5S_2$: 464.1943. Found 464.1945.

5.4.2.b 3,3'-pyridine-2,6-diylbis(4H-1,2,4-benzothiadiazine) (bisbtdaH$_2$)

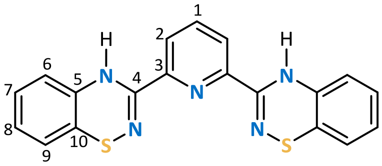

A solution of *N*-chlorosuccinimide (1.00 g, 7.49 mmol) in CH_2Cl_2 (10 mL) was added dropwise to a solution of bis(2-(propylthio)phenyl)pyridine-2,6-bis(carbox-imidamide) (2.0 g, 4.31 mmol) in CH_2Cl_2 (45 mL) at -78 °C, and the reaction mixture was allowed to warm to room temperature and stirred for 24 h. The reaction mixture was then washed with 0.1 M NaOH$_{(aq)}$, water, brine, and dried over MgSO$_4$. The solvent was removed *in vacuo* and the oily residue re-dissolved in toluene (30 mL), filtered, and brought to reflux for 12 h. The solvent was removed *in vacuo* and the crude product was purified by column chromatography using CH_2Cl_2 as eluent. The slow evaporation of CH_2Cl_2 resulted in red shiny crystals of ligand bisbtdaH$_2$**.** Yield 0.70 g, 43%.

Melting Point 208 ^{o}C (dec.)

Elemental Analysis calc. for $C_{19}H_{13}N_5S_2$: C, 60.78; H, 3.49; N, 18.65. Found: C, 60.90; H, 3.34; N, 18.24%.

UV-Vis (CH_3OH; λ_{max}, nm; ε, M^{-1} cm^{-1}): 203 (24761), 229 (33006), 270 (40828), 282 (33101), 335 (6332), 439 (2723).

IR (solid, cm^{-1}) $\tilde{\nu}_{max}$ = 3382 (w), 3357 (m), 1615 (m), 1564 (m), 1494 (m), 1425 (m), 1289 (m), 1240 (m), 1124 (m), 1068 (m), 995 (m), 920 (m), 822 (m), 747 (s), 643 (m), 610 (br), 466 (m), 429 (m).

^{1}H NMR (500 MHz, ppm, $CDCl_3$) δ_H = 8.18 (2H, d, *J* = 7.9 Hz, C^2H), 7.95 (2H, s, N*H*), 7.86 (1H, t, *J* = 7.9 Hz, C^1H), 6.99 (2H, t, *J* = 7.6 Hz, C^7H), 6.93 (2H, t, *J* = 7.5 Hz, C^8H), 6.71 (2H, d, *J* = 7.5 Hz, C^9H), 6.49 (2H, dd, *J* = 7.6, 0.9 Hz, C^6H).

^{13}C NMR (125 MHz, ppm, $CDCl_3$) δ_C = 153.26 (C^4), 146.83 (C^3), 138.20 (C^1), 136.26 (C^{10}), 127.96 (C^7), 125.82 (C^8), 123.47 (C^2), 123.09 (C^9), 120.26 (C^5), 114.48 (C^6).

HRMS (ASAP+) *m/z* $[M+H]^+$ calc. for $C_{19}H_{14}N_5S_2$: 376.0691. Found 376.0685.

5.4.2.c 3-[6-(1,3-benzothiazol-2-yl)pyridin-2-yl]-4H-1,2,4-benzothiadiazine (5.2)

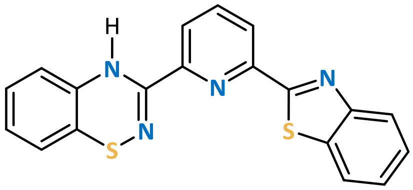

Formation upon heating in hexanes as orange crystals.

^{1}H NMR (500 MHz, ppm, $CDCl_3$) δ_H = 8.48 (1H, N*H*), 8.46 (1H, dd, *J* = 7.8, 1.0 Hz), 8.19 (1H, dd, *J* = 7.8, 1.0 Hz), 7.99 (1H, d, *J* = 8.0 Hz), 7.96 (1H, t, *J* = 7.8 Hz), 7.57-7.54 (1H, m), 7.49-7.46 (1H, m), 7.00 (1H, td, *J* = 11.4, 1.4 Hz), 6.92 (1H, td, *J* = 11.3, 1.2 Hz), 6.73 (1H, d, *J* = 7.5 Hz), 6.59 (1H, dd, *J* = 7.7, 1.1 Hz).

5.4.3 Complex Syntheses with MX$_2$ (M = Mn, Fe, Co, Ni, Cu, Zn, X = Cl, CF$_3$SO$_3$, NO$_3$)

5.4.3.a [Mn(bisbtdaH$_2$)$_2$][CF$_3$SO$_3$]$_2$ (5.3)

Solid ligand bisbtdaH$_2$ (0.020 g, 0.053 mmol) was added to a solution of Mn(CF$_3$SO$_3$)$_2$·CH$_3$CN (0.010 g, 0.025 mmol) in CH$_3$CN (10 mL). The mixture was stirred until a clear solution obtained. The solution was filtered and dark red crystals were grown by slow diffusion of diethyl ether into the mother liquor over several days. Yield 0.024 g, 79%.

Elemental Analysis calc. for [C$_{40}$H$_{26}$N$_{10}$MnS$_6$O$_6$F$_6$]·H$_2$O: C, 42.82; H, 2.52; N, 12.48. Found: C, 42.80; H, 2.51; N, 12.54%.

UV-Vis (CH$_3$OH; λ_{max}, nm; ε, M^{-1} cm^{-1}): 209 (107565), 230 (62412), 264 (80600), 286 (55908), 337 (10918), 440 (4670).

IR (solid, cm^{-1}) $\tilde{\nu}_{max}$ = 3249 (br), 1602 (w), 1583 (m), 1557 (m), 1526 (m), 1463 (s), 1434 (s), 1224 (br), 1150 (br), 1028 (s), 924 (m), 864 (w), 801(m), 758 (br), 666 (w), 631 (br), 569 (m), 513 (m), 468 (m), 470 (m).

5.4.3.b [Fe(bisbtdaH$_2$)$_2$][CF$_3$SO$_3$]$_2$·2CH$_3$CN (5.4)

Solid ligand bisbtdaH$_2$ (0.050 g, 0.133 mmol) was added to a solution of Fe(CF$_3$SO$_3$)$_2$·2CH$_3$CN (0.029 g, 0.067 mmol) in CH$_3$CN (10 mL). The mixture was stirred until a clear purple solution obtained. The solution was filtered and dark purple crystals were grown by slow diffusion of diethyl ether into the mother liquor over 3 days. Yield 0.020 g, 26%.

Elemental Analysis calc. for [C$_{40}$H$_{26}$N$_{10}$FeS$_6$O$_6$F$_6$]·3H$_2$O: C, 41.45; H, 2.78; N, 12.09. Found: C, 41.52; H, 2.51; N, 11.81%.

UV-Vis (CH$_3$CN; λ_{max}, nm; ε, M^{-1} cm^{-1}): 211 (122317), 231 (82067), 268 (94929), 289 (84308), 303 (67607), 334 (28875), 579 (8902).

IR (solid, cm^{-1}) $\tilde{\nu}_{max}$ = 3259 (br), 1606 (m), 1531 (s), 1471 (s), 1434 (s), 1398 (s), 1287 (br), 1219 (br), 1154 (br), 1024 (s), 931 (w), 873 (w), 805 (w), 742 (s), 689 (w), 678 (w), 631 (s), 571 (w), 613 (m), 513 (m), 437 (w).

5.4.3.c [Fe(bisbtdaH$_2$)$_2$][BF$_4$]$_2$·CH$_3$CN (5.5)

Solid ligand bisbtdaH$_2$ (0.020 g, 0.053 mmol) was added to a solution of Fe(BF$_4$)$_2$·6H$_2$O (0.010 g, 0.030 mmol) in CH$_3$CN (10 mL). The mixture was stirred for a few minutes to afford a dark purple solution which was filtered and left undisturbed. Dark purple crystals appeared in few days. Yield 0.010 g, 36%.

Elemental analysis calc. for [$C_{38}H_{26}N_{10}FeS_4B_2F_8$]·3H$_2$O: C, 44.12; H, 3.12; N, 13.54. Found: C, 44.44; H, 2.91; N, 13.15%.

UV-Vis (CH$_3$CN; λ_{max}, nm; ε, M^{-1} cm^{-1}): 214 (129161), 260 (62371), 290 (59994), 329 (37681), 580 (8563).

IR (solid, cm^{-1}) $\tilde{\nu}_{max}$ = 3300 (w), 1607 (s), 1521 (m), 1474 (m), 1433 (s), 1027 (w), 743 (s), 514 (w), 441 (s).

^{1}H NMR (500 MHz, ppm, CD$_3$CN) δ_H = 9.80 (2H, bs, N*H*), 9.07 (2H, d, *J* = 7.2 Hz, C^2*H*), 8.87 (1H, t, *J* = 8.2 Hz, C^1*H*), 7.08 (2H, t, *J* = 7.6 Hz, C^7*H*), 6.93 (2H, t, *J* = 7.4 Hz, C^8*H*), 6.87 (2H, d, *J* = 8.1 Hz, C^9*H*), 6.38 (2H, d, *J* = 7.5 Hz, C^6*H*).

5.4.3.d [Co(bisbtdaH$_2$)$_2$][Cl]$_2$ (5.6)

Solid ligand bisbtdaH$_2$ (0.020 g, 0.053 mmol) was added to a solution of anhydrous CoCl$_2$ (0.004 g, 0.031 mmol) in degassed CH$_3$OH (10 mL). The mixture was stirred for 15 min and the dark brown solution was filtered and left undisturbed. A few dark red crystals appeared over one week. Yield 0.002 g, 8%.

Elemental Analysis calc. for [$C_{38}H_{26}N_{10}CoS_4Cl_2$]·$CH_3OH$: C, 51.32; H, 3.31; N, 15.34. Found: C, 51.72; H, 3.00; N, 15.67%.

UV-Vis (CH_3OH; λ_{max}, nm; ε, M^{-1} cm^{-1}): 208 (283249), 269 (253317), 285 (207329), 338 (38933), 450 (9434).

IR (solid, cm^{-1}) $\tilde{\nu}_{max}$ = 2922 (w), 1605 (m), 1528 (m), 1466 (m), 1237 (w), 1023 (w), 922 (w), 870 (w), 809 (s), 778 (w), 636 (w), 527 (s), 470 (s), 434 (s).

5.4.3.e [Ni(bisbtdaH$_2$)$_2$][Cl]$_2$·4CH$_3$OH (5.7)

Solid ligand bisbtdaH$_2$ (0.010 g, 0.027 mmol) was added to a solution of $NiCl_2·6H_2O$ (0.010 g, 0.042 mmol) in CH_3OH (10 mL). The mixture was stirred for a few minutes and the dark red solution obtained was filtered. Dark red crystals were grown by slow diffusion with diethyl ether over one week. Yield 0.004 g, 21%.

Elemental Analysis calc. for [$C_{38}H_{26}N_{10}NiS_4Cl_2$]·$CH_3OH$: C, 51.33; H, 3.31; N, 15.35. Found: C, 50.88; H, 3.97; N, 15.77%.

UV-Vis (CH_3CN; λ_{max}, nm; ε, M^{-1} cm^{-1}): 204 (93664), 227 (57908), 271 (81012), 286 (74320), 370 (7268), 428 (3241).

IR (solid, cm^{-1}) $\tilde{\nu}_{max}$ = 2982 (br), 1608 (m), 1586 (m), 1531 (s), 1464 (s), 1432 (m), 1289 (m), 1283 (m), 1158 (w), 1108 (w), 1021 (m), 974 (w), 925 (w), 871 (w), 817 (s), 741 (s), 674 (w), 624 (br), 520 (w), 472 (w), 431 (m).

5.4.3.f [Zn(bisbtdaH$_2$)$_2$][CF$_3$SO$_3$]$_2$·CH$_3$OH (5.8)

Solid ligand bisbtdaH$_2$ (0.010 g, 0.027 mmol) was added to a solution of $Zn(CF_3SO_3)_2·2CH_3CN$ (0.010 g, 0.022 mmol) in CH_3OH (5 mL). The mixture was stirred for a few minutes and the dark red solution obtained was filtered and left undisturbed. Dark red crystals appeared over one week. Yield 0.008 g, 30%.

Elemental Analysis calc. for [$C_{40}H_{26}N_{10}ZnS_6O_6F_6$]·$H_2O$: C, 42.42; H, 2.49; N, 12.37. Found: C, 41.96; H, 2.52; N, 12.07%.

UV-Vis (CH_3CN; λ_{max}, nm; ε, M^{-1} cm^{-1}): 201 (360701), 264 (212953), 285 (149485), 323 (30927).

IR (solid, cm^{-1}) $\tilde{\upsilon}_{max}$ = 3468 (w), 1560 (w), 1531 (w), 1465(m), 1234 (w), 1171 (m), 1028 (s), 738 (s), 628 (m), 516 (m), 421 (s).

5.4.3.g [Cu(bisbtdaH$_2$)(NO_3)$_2$]·DMF (5.9)

Solid ligand bisbtdaH$_2$ (0.010 g, 0.027 mmol) was added to a solution of $Cu(NO_3)_2{\cdot}3H_2O$ (0.010 g, 0.041 mmol) in a mixture of CH_3OH (15 mL) and CH_2Cl_2 (5 mL). The mixture was stirred for an hour and the resultant dark precipitate was filtered, dried in air and re-dissolved in DMF. Slow diffusion of diethyl ether into the saturated DMF solution gave black crystals over 24 hours. Yield 0.009 g, 53%.

Elemental Analysis calc. for [$C_{19}H_{13}N_7CuS_2O_6$]·(C_3H_7NO): C, 41.54; H, 3.17; N, 17.61. Found: C, 41.50; H, 2.90; N, 17.29%.

IR (solid, cm^{-1}) $\tilde{\upsilon}_{max}$ = 3342 (w), 3080 (w), 1652 (w), 1608 (m), 1586 (m), 1539 (s), 1468 (s), 1439 (m), 1394 (br), 1315 (br), 1281(s), 1263 (m), 1237 (m), 1211 (w), 1165 (w), 1043 (m), 1020 (m), 978 (w), 929 (m), 863 (s), 760 (s), 675 (w), 622 (br), 525 (w), 493(w).

5.4.4 Single-crystal X-ray crystallography

Crystals of the ligand and the complexes were mounted on a cryoloop with paratone oil and examined on a Bruker D8 Venture diffractometer equipped with Photon 100 CCD area detector and Oxford Cryostream cooler using graphite-monochromated Mo-*K*α radiation (λ = 0.71073 Å). Data were collected using the APEX-II software[86], integrated using SAINT[87] and corrected for absorption using a multi-scan approach (SADABS).[88] Final cell constants were determined from full least squares refinement of all observed reflections. The structures **5.3**, **5.4**, **5.6** and **5.8** were solved by direct methods (SHELXS)[89] while structures bisbtdaH$_2$, **5.7** and **5.9** were solved using intrinsic phasing (SHELXT)[90]. All structures were refined with full least squares refinement on F^2 using either SHELXTL[91] or Olex^2 software[92]. All hydrogen atoms were added at calculated positions and refined isotropically with a riding model. Complex **5.3** exhibited rotational disorder of both the CF_3 and SO_3 groups of the triflate counterion which was modelled as two sites in a 1:1 ratio with common U_{iso}. Complex **5.4** was solved using direct methods to reveal all non-H atoms in cation and two triflate counterions. Two acetonitrile molecules were located, one of which was part occupancy. The *sof* of the partial occupancy was refined against the full-occupancy CH_3CN using a common U_{iso} for chemically equivalent atoms. Attempts to refine the CH_3CN anisotropically led to distorted ellipsoids indicating potential disorder in CH_3CN positions. The solvent was refined isotropically given the poor data: parameter ratio. Residual diffuse electron density appeared associated with a disordered solvent molecule which was modelled as an O atom (H_2O) over 5 sites until the residual electron density was less than $1e^-/A^3$. In the latter stages of refinement, a 2-component inversion twin was included to accommodate a slight twinning based on the Flack parameter (< 0.05). Complex **5.5** was solved by intrinsic phasing to reveal cationic complex and one BF_4^- anion. A second BF_4^- anion was located in subsequent difference maps along with several part occupancy CH_3CN solvent molecules and a water. Both BF_4^- anions showed some disorder. One BF_4^- *via* a rotation about two F atoms which are H-bonded to N-H groups and the second one *via* translational disorder reflected in U_{ij} for all five atoms elongated in the same direction. The former was modelled over two sites using common U_{iso} to identify *sof*'s and then *sof* and U_{ij} were fixed and refined anisotropically. The second BF_4^- was modelled isotropically over three sites with common U_{iso} and in a 0.25:0.25:0.50 ratio. Two CH_3CN molecules were identified and refined with 1,2- and 1,3-DFIX commands to maintain a linear geometry. One CH_3CN was disordered over two sites *via* a pivoting motion about the terminal N atom. Two part occupancy O atoms were located in the vicinity of a ligand N-H group - subsequent anisotropic refinement led to further splitting and in latter cycles of least squares the O was refined isotropically over 4 positions with common U_{iso}. Residual remaining electron density was treated with SQUEEZE. Although the final *R* values remained relatively high, the connectivity of the cationic complex and the two BF_4^- anions were clearly defined.

Complex **5.7** was solved using intrinsic phasing within APEX-II to reveal all non-H atoms. H atoms were added at calculated positions except N-H and H-bonded O-H groups of CH_3OH solvate which were located in the difference map and refined with a common U_{iso} and DFIX restraints. One of the four CH_3OH solvent molecules was not H-bonded and poorly defined within the structure. This was refined isotropically over three sites using common U_{iso} for C and O atoms to afford *sof*'s of 0.27, 0.37 and 0.37 respectively and led to residual electron density less than $1e^-$ in the vicinity of this solvent molecule. Complex **5.8** was solved using direct methods and has disorder in one triflate anion modelled over 2 sites in a 50:50 ratio with appropriate geometric constraints for CF_3 and SO_3 units. Complex **5.9** solved with intrinsic phasing within SHELXT to reveal all non-H atoms in main residue and (hydrogen bonded) DMF solvate molecule. All non-H atoms were refined anisotropically. Hydrogen atoms added at calculated positions except N-H protons which were located in difference map and refined freely with common U_{iso}. A summary of key crystallographic data for the ligand bisbtdaH_2, ligand **5.2** and complexes **5.3**-**5.9** is presented in Appendix 4.

5.5. References

1 D. A. Roberts, B. S. Pilgrim and J. R. Nitschke, *Chem. Soc. Rev.*, 2017, **47**, 626.

2 E. M. G. Jamieson, F. Modicom and S. M. Goldup, *Chem. Soc. Rev.*, 2018, 5266.

3 R. D. Mukhopadhyay, G. Das and A. Ajayaghosh, *Nat. Commun.*, 2018, **9**, 1987.

4 A. Y. Robin and K. M. Fromm, *Coord. Chem. Rev.*, 2006, **250**, 2127.

5 C. Avci, I. Imaz, A. Carné-Sánchez, J. A. Pariente, N. Tasios, J. Pérez-Carvajal, M. I. Alonso, A. Blanco, M. Dijkstra, C. López and D. Maspoch, *Nat. Chem.*, 2018, **10**, 78.

6 O. M. Yaghi and Q. Li, *MRS Bull.*, 2009, **34**, 682.

7 Y. Liu, M. O 'Keeffe, M. M. J. Treacy and O. M. Yaghi, *Chem. Soc. Rev.*, 2018, 4642.

8 C. S. Diercks, Y. Liu, K. E. Cordova and O. M. Yaghi, *Nat. Mater.*, 2018, **17**, 3017.

9 C. E. Housecroft, *Dalton Trans.*, 2014, **43**, 6594.

10 C. J. Elsevier, J. Reedijk, H. Walton and M. D. Ward, *Dalton Trans.*, 2003, 1869.

11 L. N. Dawe, K. V. Shuvaev and L. K. Thompson, *Chem. Soc. Rev.*, 2009, **38**, 2334.

12 J. A. G. Williams, *Chem. Soc. Rev.*, 2009, **38**, 1783.

13 H. Hofmeier and U. S. Schubert, *Chem. Soc. Rev.*, 2004, **33**, 373.

14 M. A. Halcrow, *Coord. Chem. Rev.*, 2005, **249**, 2880.

15 C. Bazzicalupi, A. Bencini, A. Bianchi, A. Danesi, E. Faggi, C. Giorgi, S. Santarelli and B. Valtancoli, *Coord. Chem. Rev.*, 2008, **252**, 1052.

16 E. C. Constable, *Chem. Soc. Rev.*, 2007, **36**, 246.

17 A. M. W. Cargill Thompson, *Coord. Chem. Rev.*, 1997, **160**, 1.

18 K. Naka, H. Sato, T. Fujita, N. Iyi and A. Yamagishi, *J. Phys. Chem. B*, 2003, **107**, 8469.

19 N. Anitha and M. Palaniandavar, *Dalton Trans.*, 2011, **40**, 1888.

20 T. Dhanalakshmi, M. Bhuvaneshwari and M. Palaniandavar, *J. Inorg. Biochem.*, 2006, **100**, 1527.

21 S. A. Cotton, V. Franckevicius and J. Fawcett, *Polyhedron*, 2002, **21**, 2055.

22 S. Hayami, Y. Komatsu, T. Shimizu, H. Kamihata and Y. H. Lee, *Coord. Chem. Rev.*, 2011, **255**, 1981.

23 C. A. Kilner and M. A. Halcrow, *Dalton Trans.*, 2010, **39**, 9008.

24 J. Delgado, Y. Zhang, B. Xu and I. R. Epstein, *J. Phys. Chem. A*, 2011, **115**, 2208.

25 G. Albano, V. Balzani, E. C. Constanble, M. Maestri and D. R. Smith, *Inorganica Chim. Acta*, 1998, 225.

26 R. McGuire, M. C. McGuire and D. R. McMillin, *Coord. Chem. Rev.*, 2010, **254**, 2574.

27 D. R. McMillin and J. J. Moore, *Coord. Chem. Rev.*, 2002, **229**, 113.

28 S. D. Cummings, *Coord. Chem. Rev.*, 2009, **253**, 449.

29 S. D. Cummings, *Coord. Chem. Rev.*, 2009, **253**, 1495.

30 S. Kern, P. Illner, S. Begel and R. Van Eldik, *Eur. J. Inorg. Chem.*, 2010, 4658.

31 Ž. D. Bugarčić, B. Petrović and E. Zangrando, *Inorganica Chim. Acta*, 2004, **357**, 2650.

32 V. Gomez, M. C. Hardwick and C. Hahn, *J. Chem. Crystallogr.*, 2012, **42**, 824.

33 A. Djeković, B. Petrović, Ž. D. Bugarčić, R. Puchta and R. van Eldik, *Dalton Trans.*, 2012, **41**, 3633.

34 Q. A. de Paula, J. B. Mangrum and N. P. Farrell, *J. Inorg. Biochem.*, 2009, **103**, 1347.

35 L. Messori, G. Marcon, A. Innocenti, E. Gallori, M. Franchi and P. Orioli, *Bioinorg. Chem. Appl.*, 2005, 239.

36 B. Bozic-Weber, E. C. Constable and C. E. Housecroft, *Coord. Chem. Rev.*, 2013, **257**, 3089.

37 K. J. Young, L. A. Martini, R. L. Milot, R. C. Snoeberger, V. S. Batista, C. A. Schmuttenmaer, R. H. Crabtree and G. W. Brudvig, *Coord. Chem. Rev.*, 2012, **256**, 2503.

38 B. Bozic-Weber, E. C. Constable, C. E. Housecroft, P. Kopecky, M. Neuburger and J. A. Zampese, *Dalton Trans.*, 2011, **40**, 12584.

39 H. Nishihara, K. Kanaizuka, Y. Nishimori and Y. Yamanoi, *Coord. Chem. Rev.*, 2007, **251**, 2674.

40 R. Sakamoto, S. Katagiri, H. Maeda and H. Nishihara, *Coord. Chem. Rev.*, 2013, **257**, 1493.

41 I. M. Dixon, E. Lebon, P. Sutra and A. Igau, *Chem. Soc. Rev.*, 2009, **38**, 1621.

42 M. Heller and U. S. Schubert, *Macromol. Rapid Commun.*, 2001, **22**, 1358.

43 P. Liu, C.-Y. Zhou, S. Xiang and C.-M. Che, *Chem. Commun.*, 2010, **46**, 2739.

44 D. Gnanamgari, C. H. Leung, N. D. Schley, S. T. Hilton and R. H. Crabtree, *Org. Biomol. Chem.*, 2008, **6**, 4442.

45 X. Chen, Q. Liu, H. B. Sun, X. Q. Yu and L. Pu, *Tetrahedron Lett.*, 2010, **51**, 2345.

46 M. K. Tse, S. Bhor, M. Klawonn, G. Anilkumar, H. Jiao, C. Döbler, A. Spannenberg, W. Mägerlein, H. Hugl and M. Beller, *Chem. - A Eur. J.*, 2006, **12**, 1855.

47 C. T. Yeung, W. S. Lee, C. S. Tsang, S. M. Yiu, W. T. Wong, W. Y. Wong and H. L. Kwong, *Polyhedron*, 2010, **29**, 1497.

48 T. Seckin, I. Özdemir, S. Köytepe and N. Gürbüz, *J. Inorg. Organomet. Polym. Mater.*, 2009, **19**, 143.

49 R. Hoogenboom and U. S. Schubert, *Chem. Soc. Rev.*, 2006, **35**, 622.

50 I. Krivokapic, M. Zerara, M. L. Daku, A. Vargas, C. Enachescu, C. Ambrus, P. Tregenna-Piggott, N. Amstutz, E. Krausz and A. Hauser, *Coord. Chem. Rev.*, 2007, **251**, 364.

51 S. Hayami, M. R. Karim and Y. H. Lee, *Eur. J. Inorg. Chem.*, 2013, 683.

52 A. Mccoubrey, H. C. Latham, P. R. Cook, A. Rodger and G. Lowe, *FEBS Lett.*, 1996, **380**, 73.

53 A. Anthonysamy, S. Balasubramanian, V. Shanmugaiah and N. Mathivanan, *Dalton Trans.*, 2008, **300**, 2136.

54 A. Hussain, K. Somyajit, B. Banik, S. Banerjee, G. Nagaraju and A. R. Chakravarty, *Dalton Trans.*, 2013, **42**, 182.

55 W. Zhou, X. Wang, M. Hu and Z. Guo, *J. Inorg. Biochem.*, 2013, **121**, 1140.

56 I. Eryazici, C. N. Moorefield and G. R. Newkome, *Chem. Rev.*, 2008, 1834.

57 G. Lowe, A. S. Droz, T. Vilaivan, G. W. Weaver, L. Tweedale, J. M. Pratt, P. Rock, V. Yardley and S. L. Croft, *J. Med. Chem.*, 1999, **42**, 999.

58 Y. Zhang, K. L. M. Harriman, G. Brunet, A. Pialat, B. Gabidullin and M. Murugesu, *Eur. J. Inorg. Chem.*, 2018, 1212.

59 A. M. Tondreau, J. M. Darmon, B. M. Wile, S. K. Floyd, E. Lobkovsky and P. J. Chirik, *Organometallics*, 2009, **28**, 3928.

60 J. G. Stark and H. G. Wallace, *Chemistry Data Book*, J. Murray. Publ., London, S. I. Edit., 1980.

61 N. N. Earnshaw and A. Greenwood, *Chemistry of the Elements*, Pergamon Press, Oxford, 1st edn., 1986.

62 E. R. Clark, J. J. Hayward, B. J. Leontowicz, D. J. Eislera and J. M. Rawson, *CrystEngComm*, 2014, **16**, 1755.

63 V. W. Bohnisch, T. L. Gilchrist and C. W. Rees, *J. Chem. Soc., Perkin Trans*, 1979, 2851.

64 A. Bard and L. R. Faulkner, *Electrochemical methods: Fundamentals and application*, Edit. 2nd., 2001.

65 J. Zienkiewicz, A. Fryszkowska, K. Zienkiewicz, F. Guo, P. Kaszynski, A. Januszko and D. Jones, *J. Org. Chem.*, 2007, **72**, 3510.

66 Y. Kanzaki, D. Shiomi, K. Sato and T. Takui, *J. Phys. Chem. B*, 2012, **116**, 1053.

67 H. Zheng, K. M. Langner, G. P. Shields, J. Hou, M. Kowiel, F. H. Allen, G. Murshudov and W. Minor, *Acta Crystallogr. Sect. D Struct. Biol.*, 2017, **73**, 316.

68 C. Andreini, G. Cavallaro and S. Lorenzini, *Bioinformatics*, 2012, **28**, 1658.

69 E. R. Clark, M. U. Anwar, B. J. Leontowicz, Y. Beldjoudi, J. J. Hayward, W. T. K. Chan, E. L. Gavey, M. Pilkington, E. Zysman-Colman and J. M. Rawson, *Dalton Trans.*, 2014, **43**, 12996.

70 P. Thordarson, *Chem. Soc. Rev.*, 2011, **40**, 1305.

71 *BindFit*, http://supramolecular.org.

72 R. H. Holyer, C. D. Hubbard, S. F. A. Kettle and R. G. Wilkins, *Inorg. Chem.*, 1966, **5**, 622.

73 *CSD search [M(terpy)2], mean angle between planes 3 nitrogen atoms each ligand*.

74 D. B. Dell' Amico, F. Calderazzo, M. Curiardi, L. Labella and F. Marchetti, *Inorg. Chem.*, 2004, **43**, 5459.

75 E. C. Constable, G. Baum, E. Bill, R. Dyson, R. van Eldik, D. Fenske, S. Kaderli, D. Morris, A. Neubrand, M. Neuburger, D. R. Smith, K. Wieghardt, M. Zehnder and A. D. Zuberbühler, *Chem. - A Eur. J.*, 1999, **5**, 498.

76 J. R. Jeitler, M. M. Turnbull and J. L. Wikaira, *Inorganica Chim. Acta*, 2003, **351**, 331.

77 M. Uchida, K. Otsubo, J. Matsubara, T. Ohtani, S. Morita and K. Yamasaki, *Chem. Pharm. Bull. (Tokyo).*, 1995, **43**, 693.

78 P. S. Bryan and J. C. Dabrowiak, *Inorg. Chem.*, 1975, **14**, 296.

79 K. S. Hagen, *Inorg. Chem.*, 2000, **39**, 5867.

80 D.R. Duling, *J. Magn. Reson.*, 1994, **B104**, 105.

81 PIP4WIN v.1.2, 2011, J.M. Rawson, University of Windsor, Windsor, ON.

82 A. D. Becke, *J. Chem. Phys.*, 1993, 5648.

83 C. Lee, W. Yang and R. G. Parr, *Phys. Rev. B Condens. Matter*, 1988, 785.

84 A. S. Miehlich, H. Stoll and H. Preuss, *Chem. Phys. Lett.*, 1989, 200.

85 A. D. Bochevarov, E. Harder, T. F. Hughes, J. R. Greenwood, D. A. Braden, D. M. Philipp, D. Rinaldo, M. D. Halls, J. Zhang and R. A. Friesner, *Int. J. Quantum Chem.*, 2013, **113**, 2110.

86 APEX-II, Bruker AXS, Inc., Madison, Wisconsin, USA.

87 SAINT, Bruker AXS Inc., Madison, Wisconsin, USA.

88 SADABS, Bruker AXS Inc., Madison, Wisconsin, USA.

89 G. G. M. Sheldrick, SHELXS-97, A Program for Automatic Solution of Crystal Structures, University of Göttingen, 1997.

90 G. M. Sheldrick, *Acta Cryst.*, 2015, **A71**, 3.

91 SHELXTL, *Bruker AXS Inc.,* Madison, Wisconsin, USA, 2015.

92 O. V. Dolomanov, L. J. Bourhis, R. Gildea, J. A. K. Howard and H. Puschmann, *J. Appl. Cryst.*, 2009, **42**, 339.

CHAPTER 6.

Conclusions and Future Work

6.1. Conclusions

Initial studies of the coordination chemistry of the pybtdaH ligand has been previously explored with MCl_2 forming a range of *N*,*N′*-chelate complexes with first row transition metals with general formula $MCl_2(pybtdaH)_2$.[1] Previous studies indicated that *S*-oxidation of pybtdaH or related benzothiadiazines only occurred in the presence of a metal and Et_3N.[2] The isolation of the $pybtda_{ox}^-$ in the dimetallic complex $[Cu(pybtda_{ox})_2]_2$ showed the greater versatility of the oxidized ligand to adopt a bridging mode through the oxygen atom of the sulfoxide group.[2]

Further investigation of the coordination chemistry of pybtdaH with more acidic metal ions (Fe^{III}) and the employment of more basic co-ligands ($hfac^-$ and OAc^-) was described in Chapter 2. These studies revealed that the pybtdaH ligand is prone to oxidation to form the $pybtda_{ox}^-$ upon reaction with first row metal ions (except for Ni^{II}, complex **2.10**) in the presence of Lewis acidic metals and weak basic anions (complexes **2.3** – **2.9** and **2.12**). The bridging ability of the acetate groups, as discussed in the introduction of this dissertation, also affect the nuclearity of the final product, by bridging two metal centres, resulting in the dimetallic Cu complex, **2.5**. Increasing the basic conditions of the reaction scheme, by introducing Et_3N, afforded the polymetallic complexes **2.11**, **2.13** and **2.14** with nuclearities of 3, 4 and 14, respectively. The S^{II} pybtdaH and the S^{IV} $pybtdaH_{ox}$ ligands adopt a simple *N*,*N′*-chelate coordination modes through the pyridyl and the heterocyclic nitrogen atoms. The deprotonated S^{IV} $pybtda_{ox}^-$ adopts a bridging/chelate mode coordinating through the *N*,*N′*-pocket and the oxygen of the sulfoxide leading to aggregation and the isolation of polymetallic complexes.

The pyrimidine analogue of 1,2,4-benzothiadiazine, pmbtdaH was synthesised and its reactivity to first row transition metals is discussed in Chapter 3. The coordination of pmbtdaH is promising upon deprotonation as it provides two *N*,*N′*-chelate pockets and upon deprotonation/oxidation has the potential to implement both *N*,*N′*-chelate pockets and an additional *S*-oxide donor. A series of mononuclear complexes of general formula $MCl_2(pmbtdaH)_2$ (complexes **3.2** – **3.5**) were formed from the reaction of pmbtdaH with MCl_2 (M = Mn, Fe, Co, Ni) and the dimer $Zn_2Cl_4(pmbtdaH)_2$ (**3.6**) was isolated from the reaction with $ZnCl_2$. The ligand acts as a simple *N*,*N*′-chelate as anticipated given the neutral conditions of the reaction mixture (pK_a (HCl) = -6.1).[3] While both OAc^- and $hfac^-$ counterions appeared to promote oxidation of pybtdaH (Chapter 2), the introduction of these more basic co-ligands did not prove sufficient to promote rapid oxidation/deprotonation of the corresponding pmbtdaH ligand. Instead, the mononuclear complexes $M(hfac)_2(pmbtdaH)_2$ (M = Mn, Co, Ni, Cu, Zn, complexes **3.7a** – **3.11a**) were isolated as the major product. However, upon prolonged storage, oxidation of pmbtdaH was observed to occur and a manganese dimer (**3.7b**) and two mononuclear complexes (M = Co (**3.8b**), Ni(**3.9b**)) were formed where the ligand has its oxidised protonated form, $pmbtdaH_{ox}$. The neutral oxidised $pmbtdaH_{ox}$ ligand acts as a simple *N*,*N*′-chelate to transition metal ions. In the cases of $Cu(hfac)_2$ and $Zn(hfac)_2$, two tetranuclear complexes with formulas $Cu_4(hfac)_4(tfa)_2(pmbtda_{ox})_2$ (**3.10b**) and $Zn_4(hfac)_6(pmbtda_{ox})_2$ (**3.11b**) were isolated with the ligand being deprotonated and oxidised. In both cases the $pmbtda_{ox}^-$ ligand bridges three metal ions, through both *N*,*N*′-chelate pockets and the sulfoxide oxygen atom, favouring formation of polynuclear metal complexes. All complexes containing the oxidised ligand, except **3.11b**, were the minor products of the reactions making reproducibility and full characterization more problematic.

In Chapters 2 and 3, we presented the coordination chemistry of the ligands pybtdaH and pmbtdaH. Both ligands formed the S^{IV} systems upon metal-assisted aerial oxidation. Although the oxidation/deprotonation of the pybtdaH and pmbtdaH ligands showed the potential to bridge two and three metal centres, respectively, the propensity was quite different. The ligand pmbtdaH showed a much slower oxidation to $pmbtdaH_{ox}$ than the corresponding pybtdaH to $pybtdaH_{ox}$, reflected in the isolation of $pmbtda_{ox}^-$ complexes as minor products. Since the sterics of pybtdaH and pmbtdaH are similar, it would appear that the electronics of the substituent at C(3) (py or pm) would appear to alter the reactivity of the thiadiazine ring. Hammett parameters are a convenient approach to assess the electronic factors of a diverse range of substituents.[4] These indicate that the more electron-withdrawing pyridyl ring in the meta position of the heterocycle (σ_m = 0.33) activates the heterocycle and the $S^{\delta+}$ character making it more susceptible to oxidation than the pyrimidyl ring ($\sigma_m = 0.23$). This is in qualitative agreement with the experimental observations. It is also noteworthy that the addition of the external base, such as Et_3N, resulted to complexes mostly (**2.11**) or completely (**2.13** and **2.14**) free of the auxiliary ligands (hfac$^-$), despite the strongly chelate nature of the hfac$^-$ ligand. The complexes isolated in the presence of Et_3N have the highest nuclearities (3, 4 and 14) observed for pybtdaH, in which the ligand is in its oxidised and deprotonated form. The metal centres of the complexes are linked mainly by pybtda$_{ox}^-$ and/or OH^- groups.

A common characteristic of many complexes incorporating neutral ligands, either oxidized or not, is the hydrogen bond network they form through the N-H group. The pmbtdaH ligand forms a one dimensional chain through N-H···N interactions between the N-H group and one nitrogen atom of the pyrimidine ring. In the mononuclear complexes of pmbtdaH with formula MCl_2(pmbtdaH) the N-H group is hydrogen bonded to methanol solvate molecules via N-H···O hydrogen bonds or, in the absence of lattice methanol, N-H···Cl hydrogen bonds are formed between neighbouring molecules.[1] For complexes of formula $M(hfac)_2$(pmbtdaH), a centrosymmetric supramolecular dimer is generated via N-H···O contacts to the hfac$^-$ group in a neighbouring molecule. Upon oxidation the pybtdaH$_{ox}$ and pmbtdaH$_{ox}$ ligands offer an S=O group which can also act as an H-bond acceptor of the form N-H···O=S. In their deprotonated forms pybtda$_{ox}^-$ and pmbtda$_{ox}^-$ offer both N atoms and O atoms which can act as hydrogen bond acceptors. The combination of H-bond donors and acceptors could be used to construct supramolecular framework structures.

Recently, Brusso has reported the metal coordination of pyTTAH chemistry to iron salts in which the ligand binds through the *N*,*N'*,*N"*-pocket. The metal complexes were affected from the nature of the halide employed; the use of $FeCl_3$ and $FeBr_3$ resulted in mononuclear 5-coordinate iron complexes ($FeX_2(py_2TTA)$, X = Cl, Br, Scheme 6.1).[5] In addition, the reaction of $FeCl_2$ with the radical pyTTA$^\bullet$ gave the same product as the use of $FeCl_3$.[6] In contrast, the fluoro- derivative resulted in oxidation of the ligand and the formation of an one dimensional coordination polymer held together through a bridging fluoride ion whereas the oxygen of the S=O is not coordinating to a metal center ($[FeF_2(py_2TTA_{ox})]_n$, Scheme 6.1).[5] The reaction of $FeCl_3$ with pybtdaH lead to the oxidation of the ligand (complexes **2.3a** and **2.3b**) whereas the use of either $FeCl_2$ or $FeCl_3$ with pmbtdaH lead to the mononuclear complex with Fe^{II} (**3.3**) and a neutral S^{II} ligand. The ligand pmbtdaH shows more robust behaviour towards oxidation than the reported pyTTA complexes. The oxidation of pyTTAH to the *S*-oxide has been also observed upon reaction with lanthanides resulting in the dimer $Ln_2(py_2TTA_{ox})_2(NO_3)_4(H_2O)_2$ bridged by the O atom (Scheme 6.1).[7]

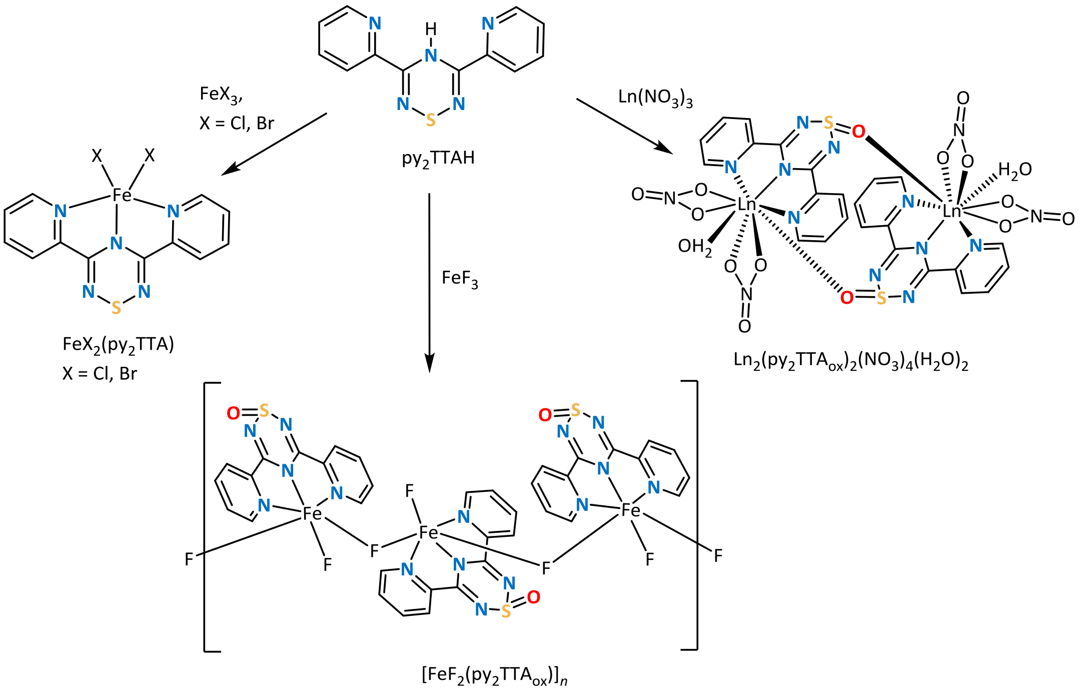

Scheme 6.1 Synthetic routes of coordination chemistry of py_2TTAH.

Similarly to pmbtdaH, the 2-pyrimidyl-dithiadiazolyl (pymDTDA) ligand was designed to act as a paramagnetic analogue of 2,2'-bipyrimidine with the ability to bridge two metal centres *via* the two chelate pockets (Scheme 6.2). A series of dinuclear complexes were isolated from which the Co^{II} and Ni^{II} showed ferromagnetic coupling.[8,9]

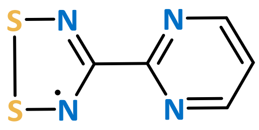

Scheme 6.2 Molecular structure 2-pyrimidyl-dithiadiazolyl (pymDTDA).

Although the pendant *O*-donor atom upon oxidation favours the aggregation leading to polynuclear complexes, it was interesting to investigate a S^{IV} system and the effect on the coordination without offering additional donor atoms. In this context, the *S*-methylated derivative of pybtdaH, pybtdaSMe, was selected as there was no potential for deprotonation and the oxidation state of the S is already formally S^{IV} and so pybtdaSMe offers more controlled reactivity pathways. Its preparation and coordination to first row transition metals was presented in Chapter 4. These studies, as anticipated, revealed more predictable reactivity with pydtdaSMe acting as an *N*,*N*′-chelate ligand in all cases. Thus the reaction of pybtdaSMe with MCl_2 (M = Mn, Ni) afforded the mononuclear complexes with general formula $MCl_2(pybtdaSMe)_2$ (M = Mn (**4.1**), Ni (**4.2**)) whereas the reaction with $ZnCl_2$ gave the mononuclear 4-coordinate Zn complex, $ZnCl_2(pybtdaSMe)$ (**4.4**). In the case of pybtdaSMe with $CuCl_2$, the reaction resulted in two polymorphs depending on the reaction solvent; either the dinuclear complex $Cu_2Cl_4(pybtdaSMe)_2$ (**4.3a**) or the co-crystal polymorph $Cu_2Cl_4(pybtdaSMe)_2\cdot 2CuCl_2(pybtdaSMe)$ (**4.3b**). The reaction of pybtdaSMe with $M(hfac)_2$ ((M = Co, Ni) afforded the mononuclear complexes with general formula $M(hfac)_2(pybtdaSMe)$ (M = Co (**4.5**), Ni (**4.6**)). In all these cases, the pybtdaSMe ligand binds in an *N*,*N*′-chelate fashion through one of the two heterocyclic N atoms and the pyridyl nitrogen atom. The modest steric bulk of the *S*-methyl group does not seem to greatly influence the coordination ability of the *ortho*-nitrogen. Preliminary results using more basic counterions showed no signs of ligand oxidation to date. It is noteworthy that a series of alkyl-functionalized pyTTAH derivatives (Scheme 6.3) have been isolated[10,11] but the coordination chemistry of these alkylated derivatives has yet to be reported.

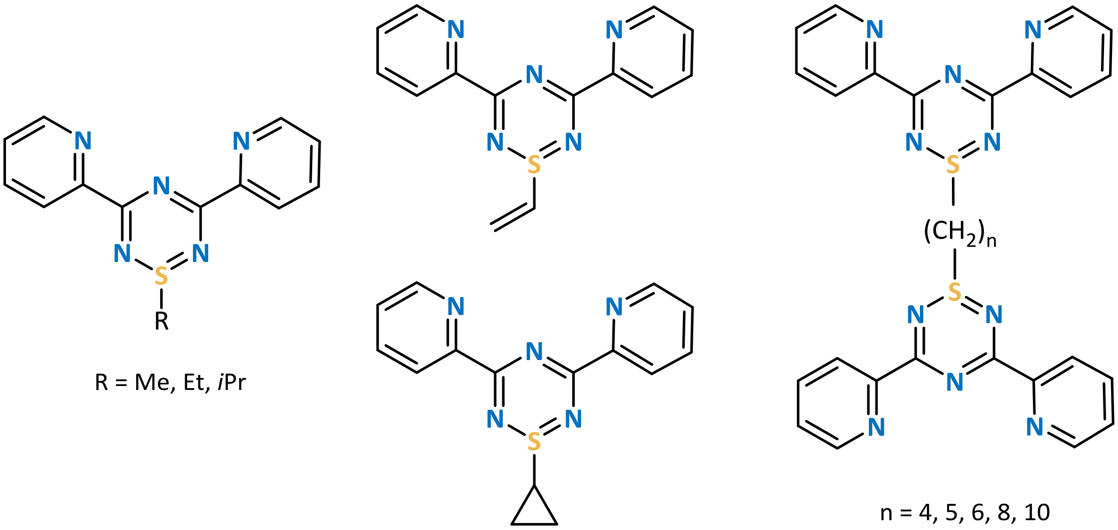

Scheme 6.3 Molecular structure of *S*-alkylated 3,5-bis(2-pyridyl)-1,2,4,6-thiatriazines.

In Chapter 5, the synthesis of the novel S/N based terpyridine type ligand, bisbtdaH$_2$, was described and a series of mononuclear complexes of general formula [M(bisbtdaH$_2$)$_2$][X]$_2$ (M = Mn, Fe, Co, Ni, Zn, **5.3** – **5.8**) were isolated as well as the 1:1 adduct, [Cu(bisbtdaH$_2$)(NO$_3$)$_2$] (**5.9**). In all cases the bisbtdaH$_2$ ligand binds in a tridentate *N*,*N*′,*N″*-chelate fashion *via* benzothiadiazinyl N$_{BTDA}$ and pyridyl N$_{py}$ atoms. The geometries of the [M(bisbtdaH$_2$)$_2$]$^{2+}$ ions appear sensitive to the crystal field stabilisation energy; in the absence of a significant crystal field, the geometry distorts significantly from octahedral and only provides systems with small distortion parameters when the CFSE is maximized.

In conclusion, the coordination ability of the btda ligands to first row transition metals is affected by the conditions of the reaction mixture. Under neutral conditions the ligands pybtdaH, pmbtdaH and pybtdaSMe bind in a *N*,*N*′-chelate fashion, whereas bisbtdaH$_2$ offers a tridentate *N*,*N*′,*N″*-chelate pocket to metal ions. The coordination modes of those ligands reported are shown in Figure 6.1.

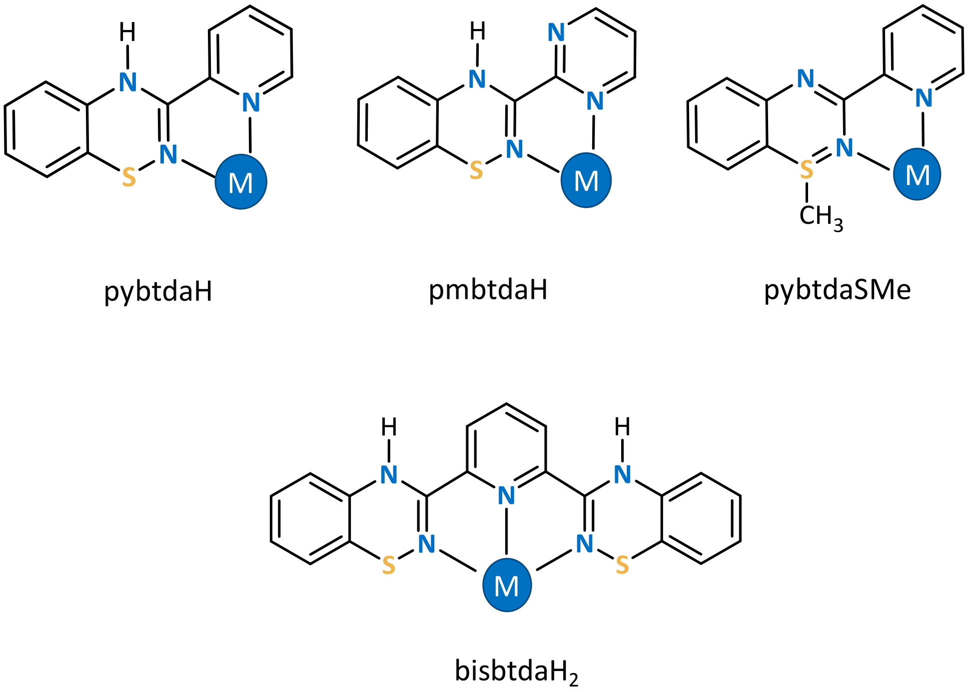

pybtdaH pmbtdaH pybtdaSMe

bisbtdaH$_2$

Figure 6.1 Coordination modes of the ligands pybtdaH, pmbtdaH, pybtdaSMe and bisbtdaH$_2$ under neutral conditions.

Under basic conditions, by introducing weak auxiliary co-ligands (OAc$^-$ and hfac$^-$), the oxidation of the ligand to S^{IV} is promorted. The ligand pybtdaH$_{ox}$ binds to one metal ion through the *N*,*N*′-chelate whereas pybtda$_{ox}^-$ has observed to adopt two coordination modes; as terminal ligand through the *N*,*N*′-chelate and as bridging through the O of the S=O. The ligand pmbtdaH$_{ox}$ acts as a *N*,*N*′-chelate ligand whereas the deprotonated form pmbtda$_{ox}^-$ is bridging three metal centres; offering two *N*,*N*′ binding sites for bridging two metal centres as well as a pendant *O*-donor. The *S*-functionalization on pybtdaSMe did not lead to further oxidation of sulphur and the ligand binds in a simple *N*,*N*′-chelate fashion. The coordination modes of the ligands under basic conditions are shown in Figure 6.2.

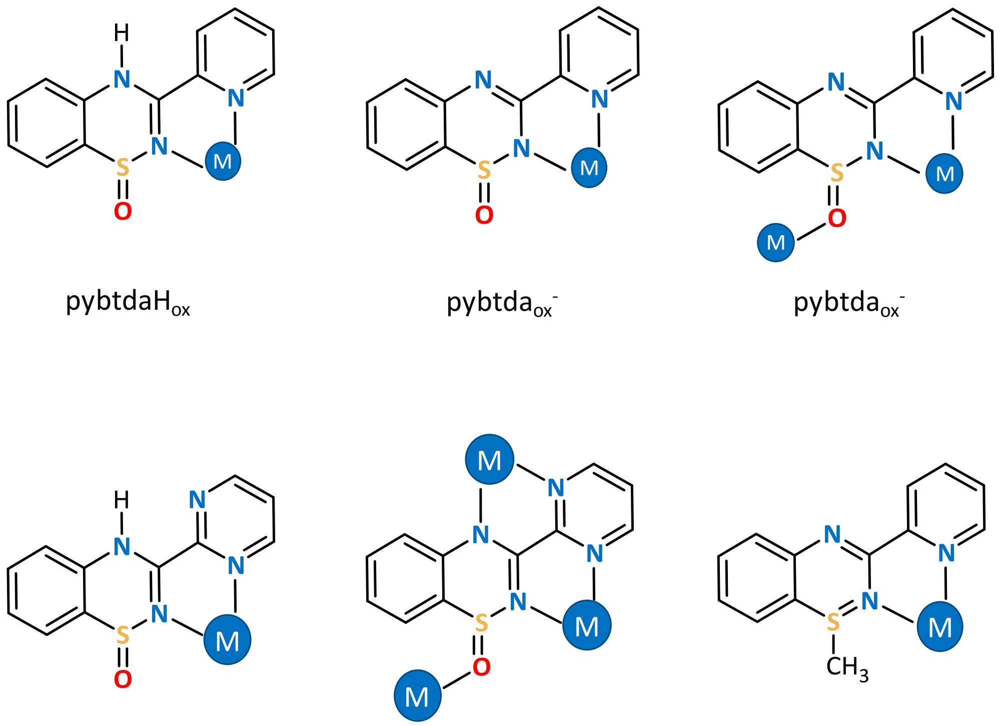

pybtdaH$_{ox}$

pybtda$_{ox}^-$

pybtda$_{ox}^-$

pmbtdaH$_{ox}$

pmbtda$_{ox}^-$

pybtdaSMe

Figure 6.2 Coordination modes of the ligands pybtdaH, pmbtdaH and pybtdaSMe under basic conditions.

6.2. Future Work

A large number of metal complexes synthesized in this dissertation incorporate the S^{IV} system of the pyridyl and pyrimidine derivatives of the 1,2,4-benzothiadiazines. The metal-assisted oxidation was found to be relatively slow for the pmbtdaH ligand resulting in lower yields and, in some cases, irreproducible results. The isolation of the *S*-oxide ligand prior to coordination would therefore offer a possible solution. The conversion of the S^{II} system to S^{IV} is conventionally achieved by the use of stoichiometric quantities of strong oxidants such as peracids, high oxidation state metals (such as MnO_2 and CrO_3) or oxidizing non-metal species (such as IO_4^- or PhIO).[12] Rawson structurally characterized the first *S*-oxides of the thiadiazine family through a metal-assisted oxidation, in which the substituent on C(3) was the non-coordinating phenyl and 2-thienyl rings.[13] Preliminary results, using the same synthetic way afforded the pyridyl derivative of the benzothiadiazine *S*-oxide (pybtdaH$_{ox}$, Figure 6.3). More experiments are underway to optimize the synthetic route with final goal to employ the ligand in coordination chemistry with first row transition metals. However, treatment with organic mild oxidants such as Me_3NO might also prove to be a direct process to generate pybtdaH$_{ox}$ directly. With this parent ligand in hand it will permit comparative studies with pybtdaH and potentially a more directed route to some of the less easily accessed compounds isolated during the course of this dissertation. In particular, structural studies on pmbtda$_{ox}^-$ complexes have so far been scarce due to the apparently much longer incubation time required for aerial

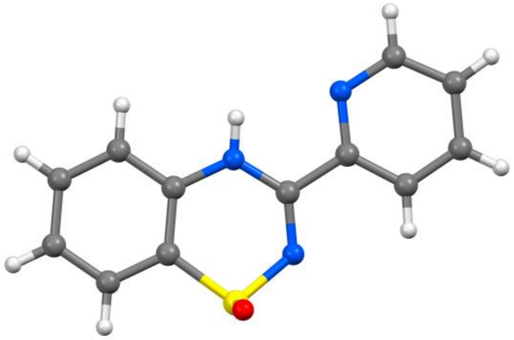

Figure 6.3 Crystal structure of the S-oxide of the pyridyl derivative of benzothiadiazines (pybtdaH$_{ox}$).

oxidation. This ligand has the potential to develop a large family of polynuclear complexes whose magnetic properties might be of interest.

Given the propensity of the *S*-oxide ligand to also become involved in bonding, the *S,S*- dioxide derivative could potentially offer two binding sites *via* the SO_2 unit in addition to the *N*,*N*′-chelate pocket. A dioxide derivative of 1,10-phenanthroline, [1,2,5]thiadiadiazolo[3,4-*f*][1,10]phenanthroline 1,1-dioxide (tdapO_2), was introduced by Awaga, in which the dioxide acts as a chelate pocket in addition to the *N*,*N*′-chelation *via* phenanthroline bridging two potassium ions (Scheme 6.4).[14]

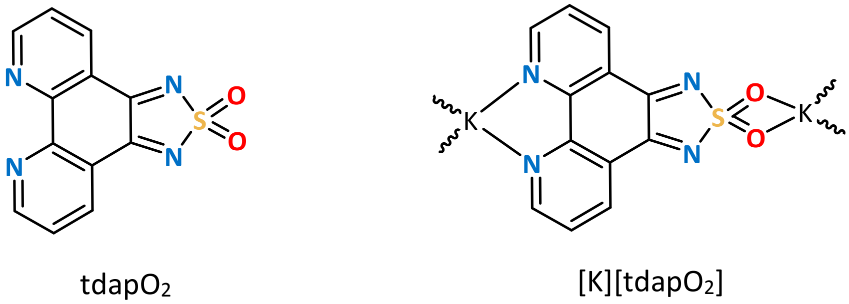

Scheme 6.4 Molecular structure of tdapO_2 and the potassium salt of its radical anion demonstrating the chelating ability of the ligand.

Oxidation of S^{IV} to the dioxide S^{VI} system is typically achieved under quite harsh conditions (35% H_2O_2 at 100 °C in glacial acetic acid) in moderate yields.[15] A series of 1,2,4-benzothiadiazine dioxides have previously been synthesized by condensation of sulfonamide with heterocyclic methyl carbimidates[16] but no crystallographic characterization was reported. We were able to isolate the dioxide derivative of the pyridyl benzothiadiazine by reaction of the S^{II} pybtdaH treated with NaOCl (Figure 6.4). The coordination chemistry of the dioxide would be interesting and it could potentially lead to polynuclear complexes and/or polymers.

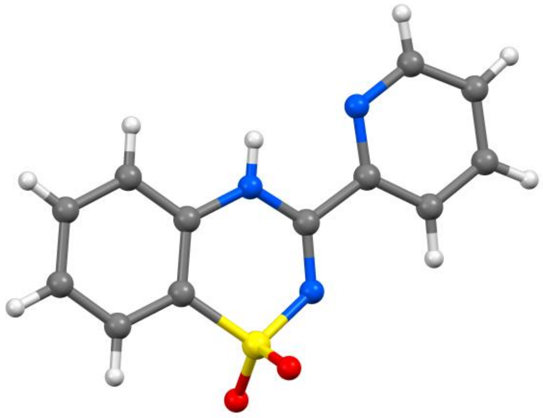

Figure 6.4 Crystal structure of the *S,S*-dioxide of the pyridyl derivative of benzothiadiazines (pybtdaH$_{diox}$).

Studies of the biological properties of the S^{II} ligands and their precursors are underway. The pmbtdaH showed promising results with 78% urease inhibition and will be tested for anticancer and antidiabetic properties. The metal complexes of these ligands will be tested as well. Initial biological studies on the *S*-oxides proved more challenging due to their low solubility in aqueous media and methanol.

In Chapter 4, the methylated derivative of the pybtdaH was synthesized and its coordination chemistry was discussed. The ligand is not protonated and therefore the nitrogen at the heterocyclic 4-position is more prone to coordination to the metal centres. The coordination site of the complexes isolated was mostly dictated by steric hindrance rather than the availability of the unpaired electrons. The pyrimidine derivative of the methylated benzothiadiazine (pmbtdaSMe, Figure 6.5) would be an ideal candidate as an *N*-donor ligand offering two *N*,*N*′-chelate pockets for metal coordination. The

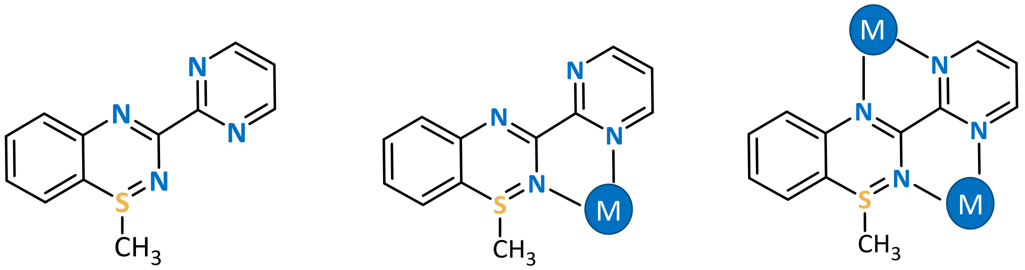

Figure 6.5 The methylated derivative of pyrimidine analogue of 1,2,4-benzothiadiazine (pmbtdaSMe) and its potential chelation modes.

pmbtdaSMe ligand would offer similar binding sites as 2,2-bipyrimidine, the employment of has led to the isolation of polynuclear complexes and metal-organic polymers.[17–20]

A future avenue of direction in the coordination chemistry explored here is the ability to further tune the crystal field at the metal ion. For both Co^{II} (d^7) and Fe^{II} (d^6) complexes there is the potential to adopt either high-spin or low-spin electronic configurations depending on the magnitude of the crystal field (Δ) in relation to the pairing energy P_E. Clearly the *N*-donor system offered by these btda ligands is of the right order of magnitude to drive spin crossover (SCO) behaviour since $Fe(pybtdaH)_2Cl_2$ is high-spin but $[Fe(bisbtdaH_2)_2][X]_2$ is low-spin. Replacement of the chloride ligand by a moderate field ligand may lead to such SCO phenomenon. Preliminary studies by Mr. Nathan Doupnik in this group has shown that metathesis of high-spin $Fe(pmbtdaH)_2Cl_2$ with NCS^- generates $Fe(NCS)_2(pmbtdaH_{ox})_2$ (Figure 6.6) which still appears high-spin across the temperature range 150 – 300 K. Further studies with yet stronger field ligands should permit some tunability to a SCO regime. Notably cooperativity in SCO phenomena have been linked to the existence of intermolecular interactions between the SCO complexes and either counterions or lattice solvent.[21,22] Ligands such as pmbtdaH which show a strong propensity for hydrogen bonding are therefore well-suited to potentially exhibit cooperative SCO behaviour.

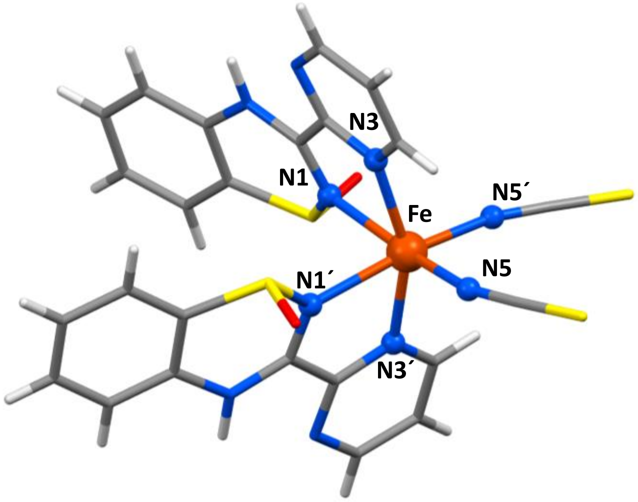

Figure 6.6 Molecular structure of $Fe(NCS)_2(pmbtdaH_{ox})_2$.

Overall there is considerable potential for the study of btda derivatives and their complexes for their biological and materials properties and the fundamental studies of ligand reactivity described here will help guide future studies in this area.

6.3. References

1 E. R. Clark, M. U. Anwar, B. J. Leontowicz, Y. Beldjoudi, J. J. Hayward, W. T. K. Chan, E. L. Gavey, M. Pilkington, E. Zysman-Colman and J. M. Rawson, *Dalton Trans.*, 2014, **43**, 12996.

2 E. R. Clark, J. J. Hayward, B. J. Leontowicz, M. U. Anwar, M. Pilkington and J. M. Rawson, *Dalton Trans.*, 2014, **44**, 2071.

3 A. Trummal, L. Lipping, I. Kaljurand, I. A. Koppel and I. Leito, *J. Phys. Chem. A*, 2016, **120**, 3663.

4 C. Hansch, A. Leo and R. W. Taft, *Chem. Rev.*, 1991, **91**, 165.

5 K. L. M. Harriman, I. A. Kühne, A. A. Leitch, I. Korobkov, R. Clérac, M. Murugesu and J. L. Brusso, *Inorg. Chem.*, 2016, **55**, 5375.

6 K. L. M. Harriman, A. A. Leitch, S. A. Stoian, F. Habib, J. L. Kneebone, S. I. Gorelsky, I. Korobkov, S. Desgreniers, M. L. Neidig, S. Hill, M. Murugesu and J. L. Brusso, *Dalton Trans.*, 2015, **44**, 10516.

7 N. Yutronkie, I. Kuehne, I. Korobkov, J. L. Brusso and M. Murugesu, *Chem. Commun.*, 2015, 677.

8 M. Jennings, K. E. Preuss and J. Wu, *Chem. Commun.*, 2006, 341.

9 J. Wu, D. J. MacDonald, R. Clérac, I. R. Jeon, M. Jennings, A. J. Lough, J. Britten, C. Robertson, P. A. Dube and K. E. Preuss, *Inorg. Chem.*, 2012, **51**, 3827.

10 E. Kleisath, N. J. Yutronkie, I. Korobkov, B. M. Gabidullin and J. L. Brusso, *New J. Chem.*, 2016, **40**, 4472.

11 N. J. Yutronkie, P. Tami, S. Singh, E. Kleisath, B. M. Gabidullin, R. Davis and J. L. Brusso, *New J. Chem.*, 2017, **41**, 2268.

12 K. Kaczorowska, Z. Kolarska, K. Mitka and P. Kowalski, *Tetrahedron*, 2005, **61**, 8315.

13 E. R. Clark, J. J. Hayward, B. J. Leontowicz, M. U. Anwar, M. Pilkington and J. M. Rawson, *Dalton Trans.*, 2014, **44**, 2071.

14 Y. Shuku, R. Suizu and K. Awaga, *Inorg. Chem.*, 2011, **50**, 11859.

15 G. Kresze, C. Seyfried and A. Trede, *Liebigs Ann. Chem.*, 1968, **715**, 223.

16 K. Gobis, H. Foks, J. Sławiński, E. Augustynowicz-Kopeć and A. Napiórkowska, *Monatshefte für Chemie - Chem. Mon.*, 2013, **144**, 1197.

17 P. Alborés and E. Rentschler, *Inorg. Chem.*, 2010, **49**, 8953.

18 P. O. Adelani, N. D. Cook and P. C. Burns, *Cryst. Growth Des.*, 2014, **14**, 5692.

19 I. F. Díaz-Ortega, J. M. Herrera, D. Aravena, E. Ruiz, T. Gupta, G. Rajaraman, H. Nojiri and E. Colacio, *Inorg. Chem.*, 2018, **57**, 6362.

20 P. Alborés and E. Rentschler, *Dalton Trans.*, 2013, **42**, 9621.

21 G. Dupouy, M. Marchivie, S. Triki, J. Sala-Pala, J. Y. Salaün, C. J. Gómez-García and P. Guionneau, *Inorg. Chem.*, 2008, **47**, 8921.

22 J. A. Thomas, *Dalton Trans.*, 2011, **40**, 12005.

APPENDIX 1: Crystal Data and Structure Refinement for Compounds of Chapter 2

2.2 *N′*-(2-propylthiophenyl)-picolinamidine

Table 1 Crystal data and structure refinement for mo_KP_ND30_0m_a.

Identification code	mo_KP_ND30_0m_a
Empirical formula	$C_{15}H_{17}N_3S$
Formula weight	271.38
Temperature/K	170.0
Crystal system	monoclinic
Space group	C2/c
a/Å	24.0886(12)
b/Å	8.1080(4)
c/Å	14.3429(7)
α/°	90
β/°	100.188(2)
γ/°	90
Volume/Å^3	2757.1(2)
Z	8
ρ_{calc}g/cm^3	1.308
μ/mm^{-1}	0.225
F(000)	1152.0
Crystal size/mm^3	0.54 × 0.46 × 0.24
Radiation	MoKα (λ = 0.71073)
2Θ range for data collection/°	5.772 to 51.5
Index ranges	$-29 \leq h \leq 28$, $-9 \leq k \leq 9$, $-17 \leq l \leq 17$
Reflections collected	14310
Independent reflections	2639 [$R_{int} = 0.0267$, $R_{sigma} = 0.0180$]
Data/restraints/parameters	2639/0/240
Goodness-of-fit on F^2	1.121
Final R indexes [I>=2σ (I)]	$R_1 = 0.0327$, $wR_2 = 0.0809$
Final R indexes [all data]	$R_1 = 0.0376$, $wR_2 = 0.0855$
Largest diff. peak/hole / e Å^{-3}	0.18/-0.35

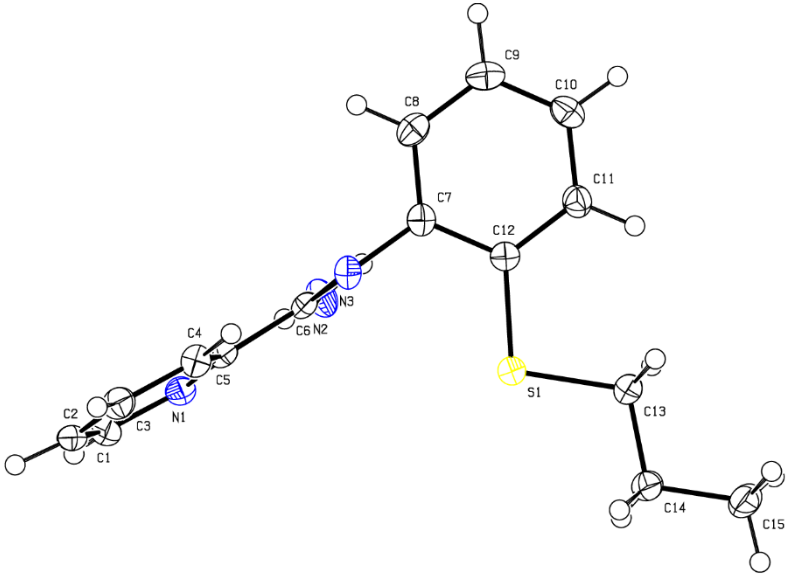

pybtdaH

Table 1 Crystal data and structure refinement for pyH.

Identification code	pyH
Empirical formula	$C_{12}H_9N_3S$
Formula weight	227.28
Temperature/K	180(2)
Crystal system	triclinic
Space group	P-1
a/Å	6.2054(2)
b/Å	11.0782(4)
c/Å	15.7022(4)
α/°	79.2620(18)
β/°	81.6799(18)
γ/°	81.0105(10)
Volume/Å^3	1040.06(6)
Z	4
ρ_{calc}g/cm^3	1.452
μ/mm^{-1}	0.282
F(000)	472.0
Crystal size/mm^3	0.28 × 0.21 × 0.14
Radiation	MoKα (λ = 0.71073)
2Θ range for data collection/°	7.2 to 54.9
Index ranges	$-7 \leq h \leq 8$, $-14 \leq k \leq 14$, $-20 \leq l \leq 20$
Reflections collected	9857
Independent reflections	4640 [R_{int} = 0.0331, R_{sigma} = 0.0365]
Data/restraints/parameters	4640/0/361
Goodness-of-fit on F^2	1.041
Final R indexes [I>=2σ (I)]	R_1 = 0.0382, wR_2 = 0.0991
Final R indexes [all data]	R_1 = 0.0439, wR_2 = 0.1047
Largest diff. peak/hole / e Å^{-3}	0.34/-0.32

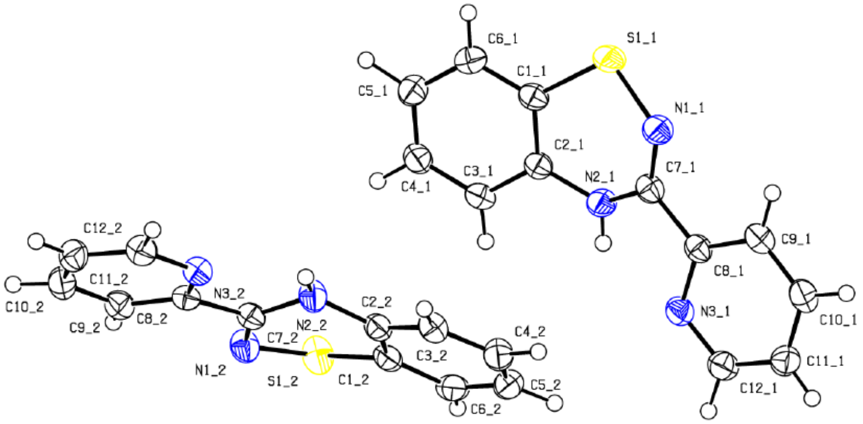

2.3a $FeCl_3(pybtdaH_{ox})(CH_3OH)]\cdot CH_3OH$

Table 1 Crystal data and structure refinement for kp68_2_a.

Identification code	kp68_2_a
Empirical formula	$C_{14}H_{17}Cl_3FeN_3O_3S$
Formula weight	469.57
Temperature/K	273(2)
Crystal system	triclinic
Space group	P-1
a/Å	8.436(2)
b/Å	14.802(3)
c/Å	15.019(3)
α/°	89.24(3)
β/°	89.87(3)
γ/°	79.62(3)
Volume/Å^3	1844.6(7)
Z	4
ρ_{calc}g/cm^3	1.691
μ/mm^{-1}	1.384
F(000)	956.0
Crystal size/mm^3	0.135 × 0.035 × 0.020
Radiation	MoKα (λ = 0.71073)
2Θ range for data collection/°	5.61 to 60.94
Index ranges	$-10 \le h \le 10$, $-18 \le k \le 18$, $-18 \le l \le 18$
Reflections collected	39591
Independent reflections	7684 [R_{int} = 0.0645, R_{sigma} = 0.0359]
Data/restraints/parameters	7684/10/471
Goodness-of-fit on F^2	1.171
Final R indexes [I>=2σ (I)]	R_1 = 0.0656, wR_2 = 0.1321
Final R indexes [all data]	R_1 = 0.0923, wR_2 = 0.1556
Largest diff. peak/hole / e Å^{-3}	1.35/-1.08

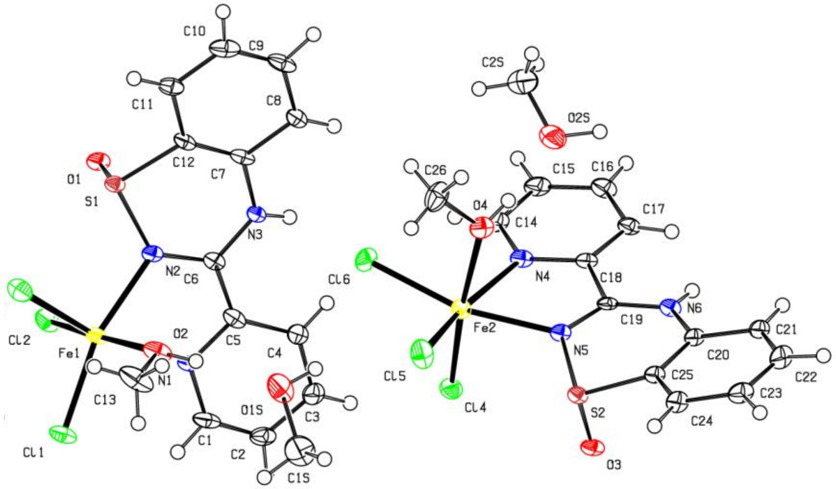

2.3b $Fe_4Cl_4(OCH_3)_6(pybtda_{ox})_2$

Table 1 Crystal data and structure refinement for mo_kp66_2_0m_a_sq.

Identification code	mo_kp66_2_0m_a_sq
Empirical formula	$C_{30}H_{34}Cl_4Fe_4N_6O_8S_2$
Formula weight	1035.95
Temperature/K	170.01
Crystal system	triclinic
Space group	P-1
a/Å	8.7648(13)
b/Å	9.5451(15)
c/Å	13.732(2)
α/°	94.962(8)
β/°	93.331(7)
γ/°	111.366(7)
Volume/Å^3	1060.8(3)
Z	1
ρ_{calc}g/cm^3	1.622
μ/mm^{-1}	1.742
F(000)	524.0
Crystal size/mm^3	0.277 × 0.13 × 0.082
Radiation	MoKα (λ = 0.71073)
2Θ range for data collection/°	5.782 to 52.984
Index ranges	$-10 \le h \le 10$, $-11 \le k \le 11$, $-17 \le l \le 17$
Reflections collected	22652
Independent reflections	4345 [$R_{int} = 0.0690$, $R_{sigma} = 0.0480$]
Data/restraints/parameters	4345/1/247
Goodness-of-fit on F^2	1.069
Final R indexes [I>=2σ (I)]	$R_1 = 0.0494$, $wR_2 = 0.1136$
Final R indexes [all data]	$R_1 = 0.0863$, $wR_2 = 0.1399$
Largest diff. peak/hole / e Å^{-3}	2.07/-1.53

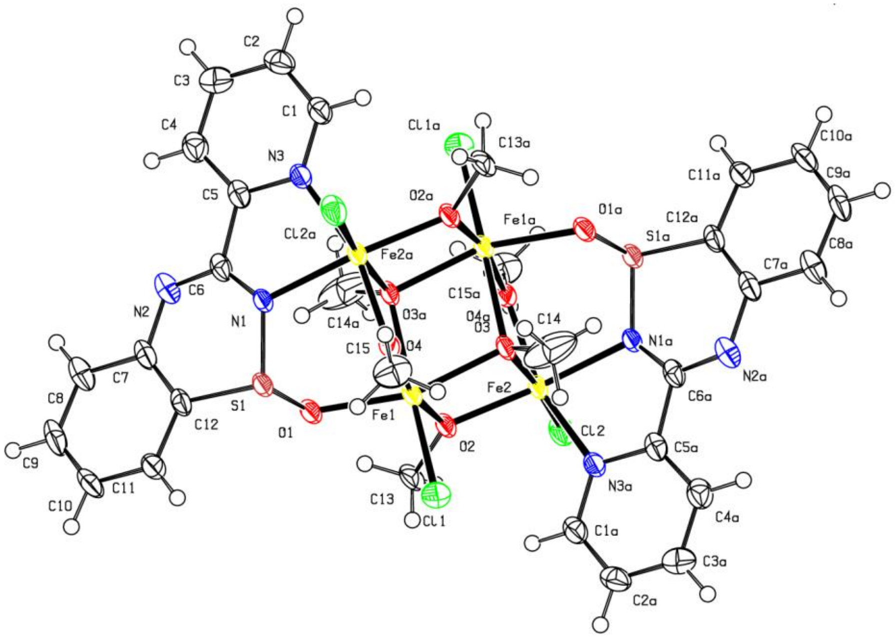

2.4 Co(pybtda$_{ox}$)$_3$

Table 1 Crystal data and structure refinement for mo_kp125b_0m_a_sq.

Identification code	mo_kp125b_0m_a_sq
Empirical formula	$C_{36}H_{24}CoN_9O_3S_3$
Formula weight	785.75
Temperature/K	170.0
Crystal system	monoclinic
Space group	$P2_1/n$
a/Å	10.7258(4)
b/Å	23.5148(10)
c/Å	15.4790(6)
α/°	90
β/°	94.831(2)
γ/°	90
Volume/Å^3	3890.2(3)
Z	4
ρ_{calc}g/cm^3	1.342
μ/mm^{-1}	0.649
F(000)	1608.0
Crystal size/mm^3	0.35 × 0.29 × 0.17
Radiation	MoKα (λ = 0.71073)
2Θ range for data collection/°	5.64 to 51.528
Index ranges	$-13 \leq h \leq 13$, $-28 \leq k \leq 28$, $-18 \leq l \leq 18$
Reflections collected	66273
Independent reflections	7428 [R_{int} = 0.0485, R_{sigma} = 0.0234]
Data/restraints/parameters	7428/0/470
Goodness-of-fit on F^2	1.092
Final R indexes [I>=2σ (I)]	R_1 = 0.0380, wR_2 = 0.0850
Final R indexes [all data]	R_1 = 0.0509, wR_2 = 0.0919
Largest diff. peak/hole / e Å^{-3}	0.32/-0.36

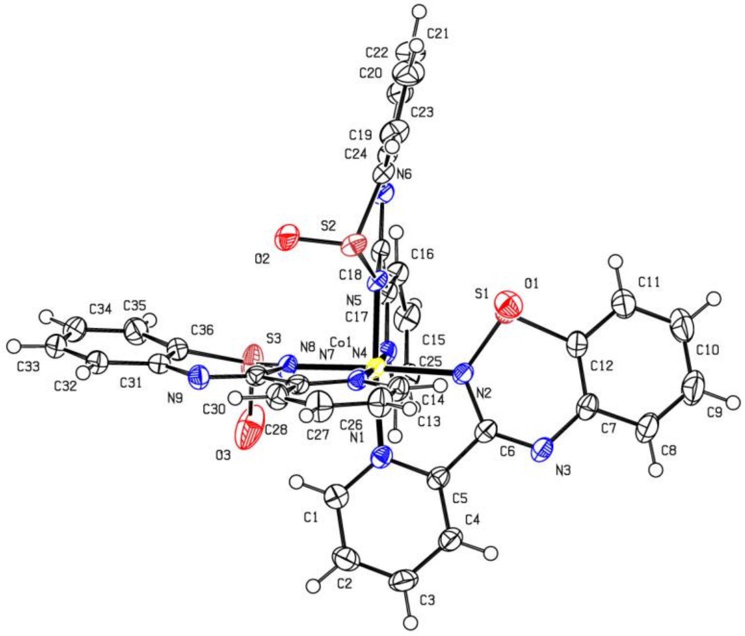

2.5 $[Cu_2(OAc)_2(pybtda_{ox})_2(H_2O)_2]\cdot 2H_2O$

Table 1 Crystal data and structure refinement for mo_KP55B_a.

Identification code	mo_KP55B_a
Empirical formula	$C_{28}H_{30}N_6O_{10}S_2Cu_2$
Formula weight	801.78
Temperature/K	129.98
Crystal system	monoclinic
Space group	C2/c
a/Å	22.002(10)
b/Å	11.974(5)
c/Å	13.429(6)
α/°	90
β/°	118.433(14)
γ/°	90
Volume/Å^3	3111(2)
Z	4
ρ_{calc}g/cm^3	1.712
μ/mm^{-1}	1.570
F(000)	1640.0
Crystal size/mm^3	0.45 × 0.22 × 0.17
Radiation	MoKα (λ = 0.71073)
2Θ range for data collection/°	5.902 to 56.84
Index ranges	$-29 \leq h \leq 29$, $-16 \leq k \leq 15$, $-17 \leq l \leq 17$
Reflections collected	23705
Independent reflections	3896 [R_{int} = 0.0354, R_{sigma} = 0.0233]
Data/restraints/parameters	3896/12/239
Goodness-of-fit on F^2	1.090
Final R indexes [I>=2σ (I)]	R_1 = 0.0450, wR_2 = 0.0976
Final R indexes [all data]	R_1 = 0.0602, wR_2 = 0.1083
Largest diff. peak/hole / e Å^{-3}	1.18/-0.75

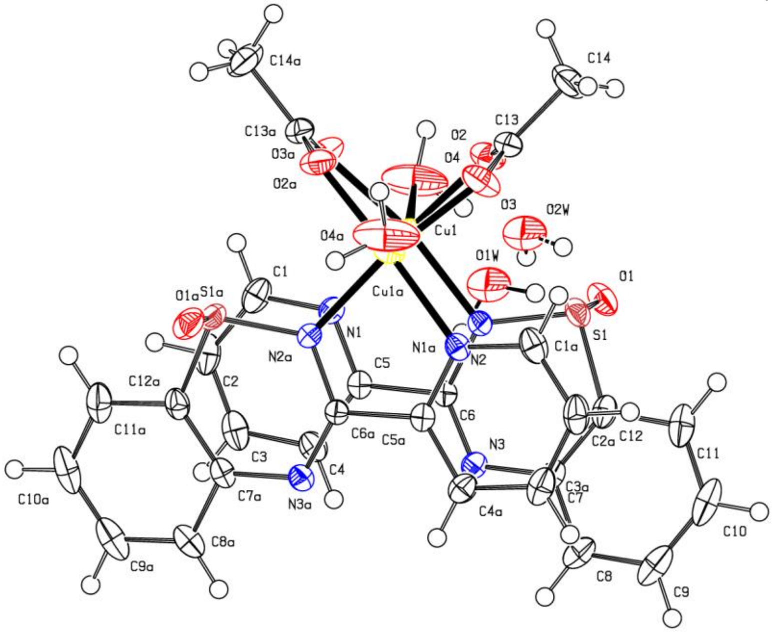

2.6 $Zn_2(OAc)_2(pybtda_{ox})_2$

Table 1 Crystal data and structure refinement for mo_KP57_0m_a.

Identification code	mo_KP57_0m_a
Empirical formula	$C_{28}H_{22}N_6O_6S_2Zn_2$
Formula weight	366.69
Temperature/K	110.01
Crystal system	triclinic
Space group	P-1
a/Å	7.4145(4)
b/Å	11.1175(6)
c/Å	17.6763(9)
α/°	81.178(2)
β/°	86.950(2)
γ/°	83.267(2)
Volume/Å^3	1428.98(13)
Z	2
ρ_{calc}g/cm^3	1.704
μ/mm^{-1}	1.880
F(000)	744.0
Crystal size/mm^3	0.194 × 0.072 × 0.072
Radiation	MoKα (λ = 0.71073)
2Θ range for data collection/°	5.93 to 61.2
Index ranges	$-10 \le h \le 10$, $-15 \le k \le 15$, $-25 \le l \le 25$
Reflections collected	77029
Independent reflections	8768 [R_{int} = 0.0720, R_{sigma} = 0.0452]
Data/restraints/parameters	8768/0/399
Goodness-of-fit on F^2	1.017
Final R indexes [I>=2σ (I)]	R_1 = 0.0358, wR_2 = 0.0603
Final R indexes [all data]	R_1 = 0.0639, wR_2 = 0.0677
Largest diff. peak/hole / e Å^{-3}	0.53/-0.47

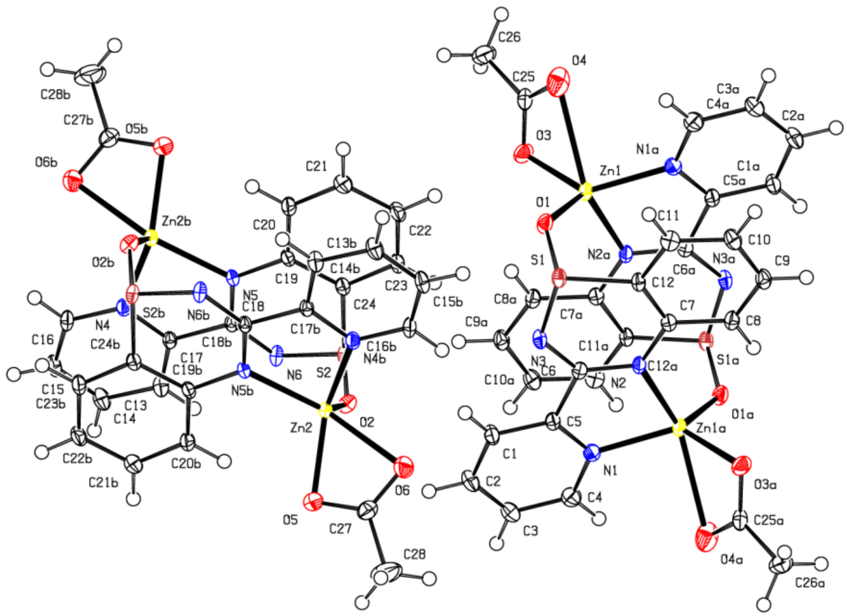

2.7 Mn(hfac)$_2$(pybtdaH$_{ox}$)

Table 1 Crystal data and structure refinement for kp37agtwin4_sq.

Identification code	kp37agtwin4_sq
Empirical formula	$C_{22}H_{11}F_{12}MnN_3O_5S$
Formula weight	712.34
Temperature/K	170(2)
Crystal system	triclinic
Space group	P-1
a/Å	9.6268(7)
b/Å	10.6691(9)
c/Å	17.8830(14)
α/°	73.780(4)
β/°	88.391(3)
γ/°	80.084(4)
Volume/Å^3	1736.9(2)
Z	2
ρ_{calc}g/cm^3	1.362
μ/mm^{-1}	0.536
F(000)	706.0
Crystal size/mm^3	0.20 × 0.18 × 0.03
Radiation	MoKα (λ = 0.71073)
2Θ range for data collection/°	6.336 to 51.418
Index ranges	$? \le h \le 11$, $? \le k \le 13$, $? \le l \le 21$
Reflections collected	6424
Independent reflections	6424 [$R_{int} = 0.0515$, $R_{sigma} = 0.0456$]
Data/restraints/parameters	6424/220/389
Goodness-of-fit on F^2	1.080
Final R indexes [I>=2σ (I)]	$R_1 = 0.0941$, $wR_2 = 0.2399$
Final R indexes [all data]	$R_1 = 0.1358$, $wR_2 = 0.2633$
Largest diff. peak/hole / e Å^{-3}	0.96/-1.47

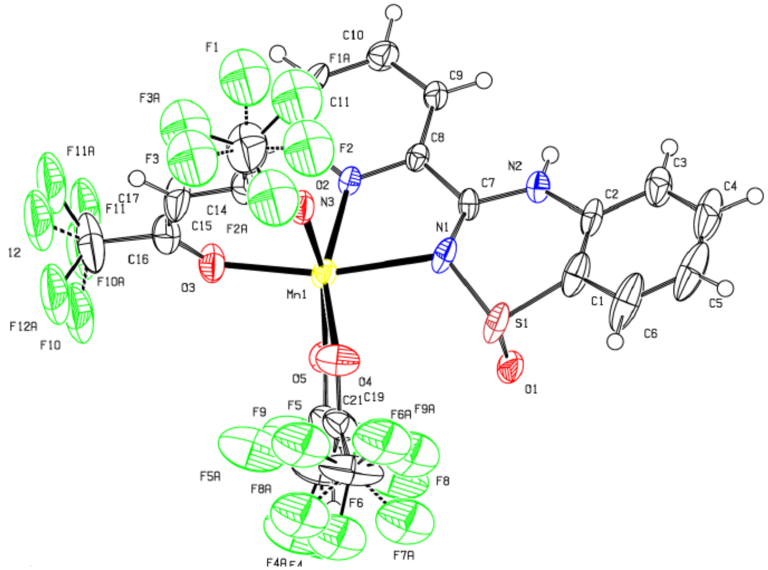

2.8 Co(hfac)$_2$(pybtdaH$_{ox}$)

Table 1 Crystal data and structure refinement for mo_kp89D_0m_a.

Identification code	mo_kp89D_0m_a
Empirical formula	$C_{22}H_{11}CoF_{12}N_3O_5S$
Formula weight	716.33
Temperature/K	170.0
Crystal system	triclinic
Space group	P-1
a/Å	8.346(4)
b/Å	12.286(5)
c/Å	13.072(5)
α/°	89.753(11)
β/°	75.015(10)
γ/°	82.185(11)
Volume/Å^3	1282.1(9)
Z	2
ρ_{calc}g/cm^3	1.855
μ/mm^{-1}	0.880
F(000)	710.0
Crystal size/mm^3	0.32 × 0.13 × 0.04
Radiation	MoKα (λ = 0.71073)
2Θ range for data collection/°	5.918 to 49.614
Index ranges	$-9 \leq h \leq 9$, $-14 \leq k \leq 14$, $-15 \leq l \leq 15$
Reflections collected	17175
Independent reflections	4369 [R_{int} = 0.1453, R_{sigma} = 0.1231]
Data/restraints/parameters	4369/12/389
Goodness-of-fit on F^2	1.032
Final R indexes [I>=2σ (I)]	R_1 = 0.0714, wR_2 = 0.1434
Final R indexes [all data]	R_1 = 0.1409, wR_2 = 0.1732
Largest diff. peak/hole / e Å^{-3}	1.75/-0.81

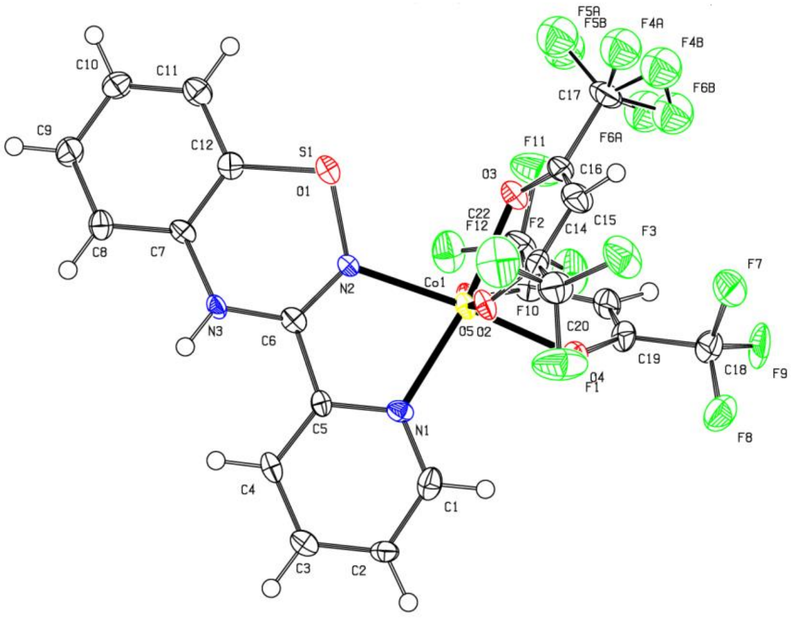

2.9 Zn(hfac)$_2$(pybtdaH$_{ox}$)

Table 1 Crystal data and structure refinement for mo_KP84_a.

Identification code	mo_KP84_a
Empirical formula	$C_{22}H_{11}F_{12}N_3O_5SZn$
Formula weight	722.77
Temperature/K	293(2)
Crystal system	triclinic
Space group	P-1
a/Å	13.628(12)
b/Å	13.989(10)
c/Å	15.653(12)
α/°	112.07(5)
β/°	103.90(4)
γ/°	99.20(6)
Volume/Å^3	2578(4)
Z	4
ρ_{calc}g/cm^3	1.862
μ/mm^{-1}	1.162
F(000)	1432.0
Crystal size/mm^3	0.8 × 0.2 × 0.15
Radiation	MoKα (λ = 0.71073)
2Θ range for data collection/°	5.73 to 52.894
Index ranges	$-17 \leq h \leq 17$, $-17 \leq k \leq 17$, $-19 \leq l \leq 19$
Reflections collected	55314
Independent reflections	10547 [R_{int} = 0.0411, R_{sigma} = 0.0294]
Data/restraints/parameters	10547/24/796
Goodness-of-fit on F^2	1.045
Final R indexes [I>=2σ (I)]	R_1 = 0.0525, wR_2 = 0.1096
Final R indexes [all data]	R_1 = 0.1014, wR_2 = 0.1458
Largest diff. peak/hole / e Å^{-3}	1.48/-1.02

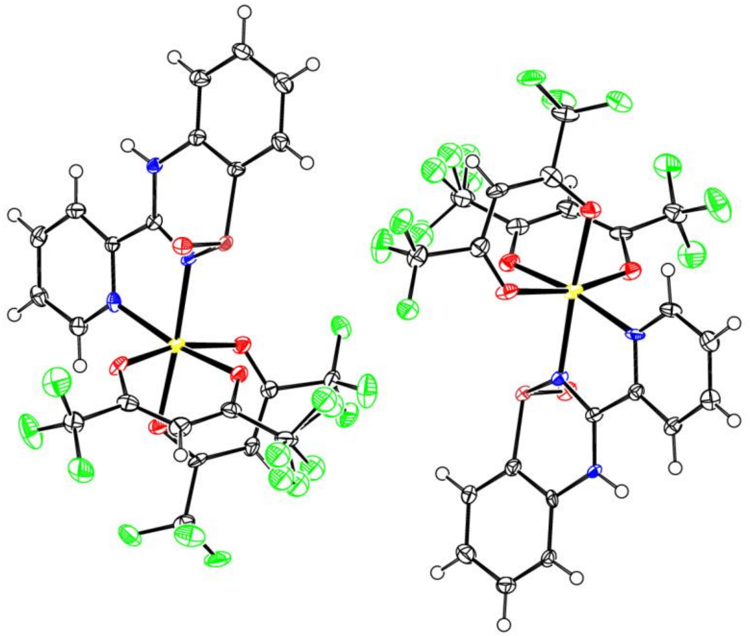

2.10 Ni(hfac)$_2$(pybtdaH)

Table 1 Crystal data and structure refinement for kp16.

Identification code	kp16
Empirical formula	$C_{22}H_{11}F_{12}N_3NiO_4S$
Formula weight	700.11
Temperature/K	293(2)
Crystal system	triclinic
Space group	P-1
a/Å	8.8925(7)
b/Å	10.7163(8)
c/Å	14.1361(12)
α/°	92.328(5)
β/°	108.306(3)
γ/°	93.315(4)
Volume/Å^3	1274.32(18)
Z	2
ρ_{calc}g/cm^3	1.825
μ/mm^{-1}	0.968
F(000)	696.0
Crystal size/mm^3	0.26 × 0.11 × 0.09
Radiation	MoKα (λ = 0.71073)
2Θ range for data collection/°	6.048 to 66.434
Index ranges	$-13 \le h \le 13$, $-16 \le k \le 16$, $-21 \le l \le 21$
Reflections collected	52725
Independent reflections	9702 [R_{int} = 0.0691, R_{sigma} = 0.0677]
Data/restraints/parameters	9702/12/380
Goodness-of-fit on F^2	1.056
Final R indexes [I>=2σ (I)]	R_1 = 0.0684, wR_2 = 0.1645
Final R indexes [all data]	R_1 = 0.1193, wR_2 = 0.1918
Largest diff. peak/hole / e Å^{-3}	1.50/-1.20

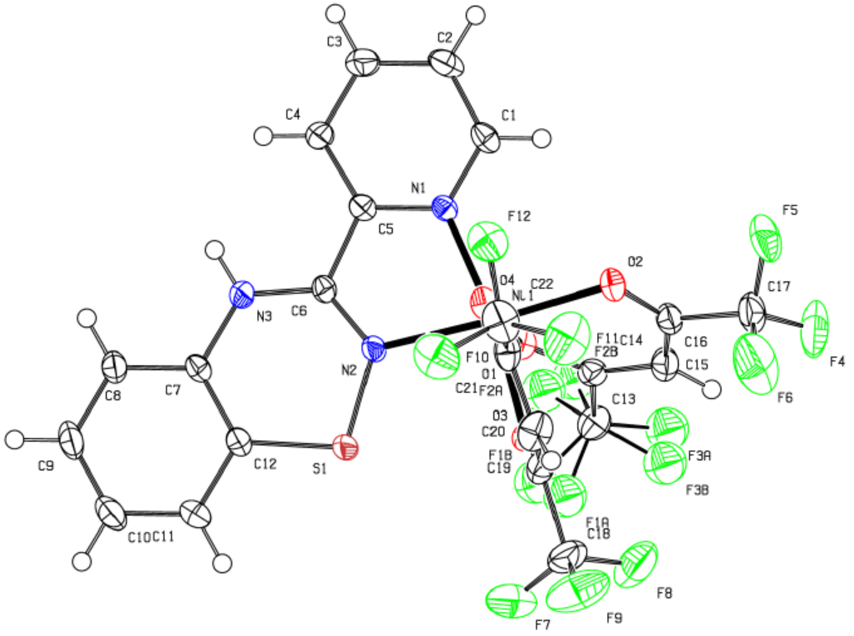

2.11 $Ni_3(hfac)(pybtda_{ox})_5(H_2O)$

Table 1 Crystal data and structure refinement for kp121c_a_sq.

Identification code	kp121c_a_sq
Empirical formula	$C_{65}H_{43}F_6N_{15}Ni_3O_8S_5$
Formula weight	1612.57
Temperature/K	170(2)
Crystal system	monoclinic
Space group	$P2_1/c$
a/Å	17.496(3)
b/Å	25.153(5)
c/Å	17.657(3)
α/°	90
β/°	102.521(4)
γ/°	90
Volume/Å^3	7585(2)
Z	4
ρ_{calc}g/cm^3	1.412
μ/mm^{-1}	0.950
F(000)	3280.0
Crystal size/mm^3	0.165 × 0.100 × 0.100
Radiation	MoKα (λ = 0.71073)
2Θ range for data collection/°	5.696 to 49.482
Index ranges	$-19 \le h \le 20$, $-29 \le k \le 29$, $-20 \le l \le 20$
Reflections collected	269041
Independent reflections	12928 [$R_{int} = 0.1059$, $R_{sigma} = 0.0300$]
Data/restraints/parameters	12928/93/906
Goodness-of-fit on F^2	1.087
Final R indexes [I>=2σ (I)]	$R_1 = 0.0487$, $wR_2 = 0.1098$
Final R indexes [all data]	$R_1 = 0.0785$, $wR_2 = 0.1315$
Largest diff. peak/hole / e Å^{-3}	0.89/-0.88

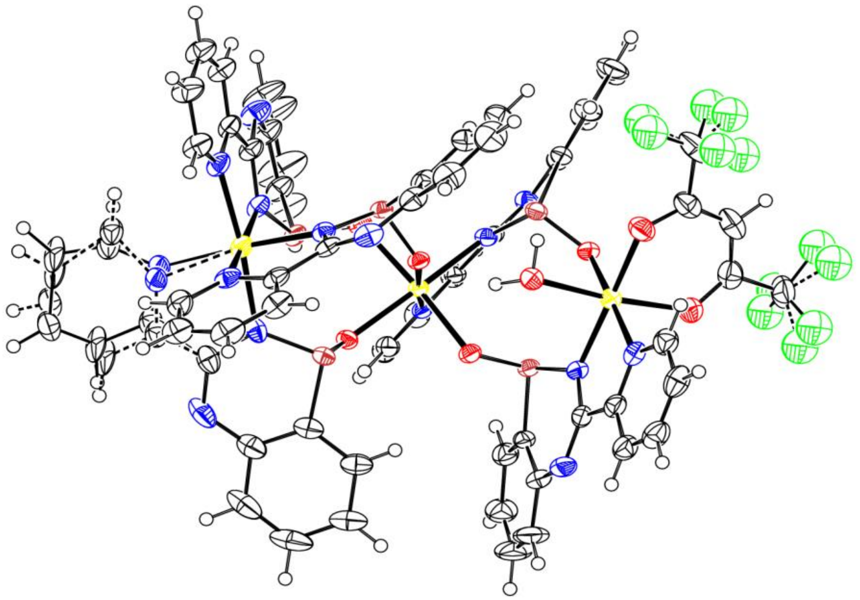

2.12 [Cu(hfac)(pybtda$_{ox}$)]$_n$

Table 1 Crystal data and structure refinement for mo_kp38_1_a.

Identification code	mo_kp38_1_a
Empirical formula	$C_{17}H_9N_3O_3F_6SCu$
Formula weight	512.87
Temperature/K	104.99
Crystal system	monoclinic
Space group	$P2_1$
a/Å	9.792(6)
b/Å	15.151(9)
c/Å	13.079(8)
α/°	90
β/°	99.68(2)
γ/°	90
Volume/Å^3	1913(2)
Z	4
ρ_{calc}g/cm^3	1.781
μ/mm^{-1}	1.334
F(000)	1020.0
Crystal size/mm^3	0.385 × 0.18 × 0.05
Radiation	MoKα (λ = 0.71073)
2Θ range for data collection/°	5.682 to 52.96
Index ranges	$-12 \le h \le 12$, $-18 \le k \le 18$, $-16 \le l \le 16$
Reflections collected	26562
Independent reflections	7833 [R_{int} = 0.0331, R_{sigma} = 0.0319]
Data/restraints/parameters	7833/1/560
Goodness-of-fit on F^2	1.065
Final R indexes [I>=2σ (I)]	R_1 = 0.0387, wR_2 = 0.1010
Final R indexes [all data]	R_1 = 0.0451, wR_2 = 0.1061
Largest diff. peak/hole / e Å^{-3}	2.45/-0.45
Flack parameter	0.372(16)

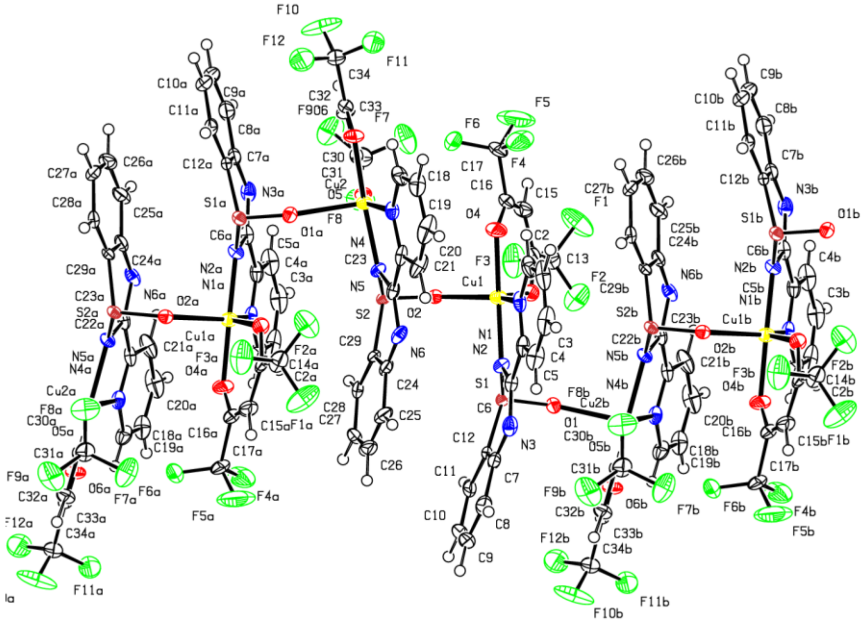

2.13 $[Cu_4(OH)_4(pybtda_{ox})_4]\cdot H_2O$

Table 1 Crystal data and structure refinement for mo_kp39dt_0m_a_sq.

Identification code	mo_kp39dt_0m_a_sq
Empirical formula	$C_{48}H_{40}N_{12}O_{10}S_4Cu_4$
Formula weight	1327.32
Temperature/K	109.99
Crystal system	triclinic
Space group	P-1
a/Å	7.8104(6)
b/Å	14.3349(10)
c/Å	14.4460(8)
α/°	63.301(3)
β/°	76.242(3)
γ/°	87.034(4)
Volume/Å^3	1400.66(17)
Z	1
ρ_{calc}g/cm^3	1.574
μ/mm^{-1}	1.712
F(000)	672.0
Crystal size/mm^3	0.2 × 0.09 × 0.02
Radiation	MoKα (λ = 0.71073)
2Θ range for data collection/°	5.704 to 52.852
Index ranges	$-9 \leq h \leq 9$, $-17 \leq k \leq 17$, $-18 \leq l \leq 18$
Reflections collected	25685
Independent reflections	5726 [R_{int} = 0.0752, R_{sigma} = 0.0602]
Data/restraints/parameters	5726/75/358
Goodness-of-fit on F^2	1.044
Final R indexes [I>=2σ (I)]	R_1 = 0.0665, wR_2 = 0.1833
Final R indexes [all data]	R_1 = 0.1012, wR_2 = 0.2108
Largest diff. peak/hole / e Å^{-3}	4.99/-0.73

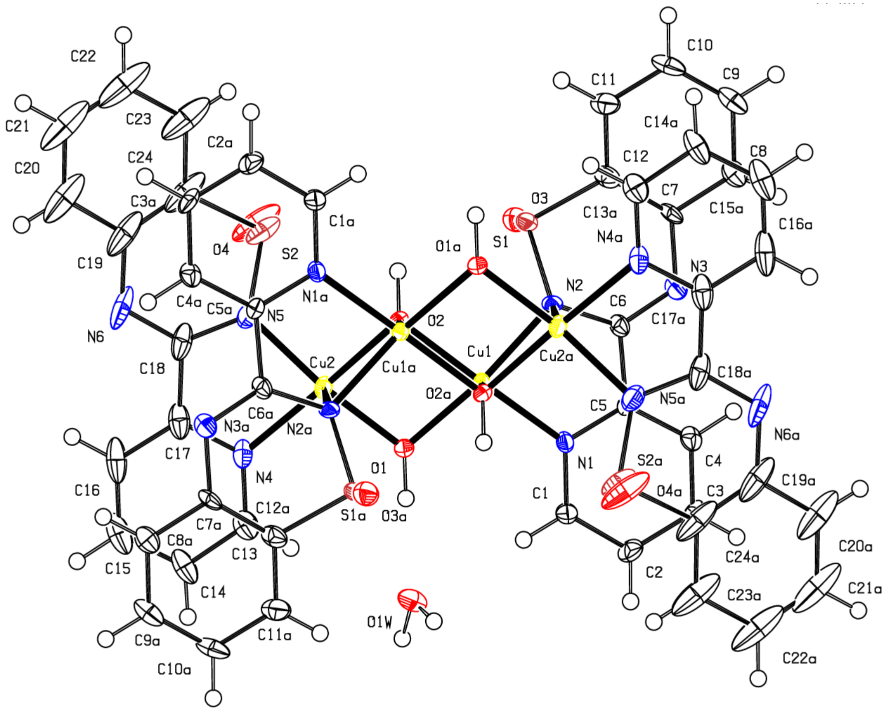

2.14 $[Cu_{14}(OH)_{12}(CO_3)_2(pybtda_{ox})_{12}(H_2O)_2]\cdot 14[H_2O]\cdot[CH_3OH]$

Table 1 Crystal data and structure refinement for jmrcu14_5runs_a_sq.

Identification code	jmrcu14_5runs_a_sq
Empirical formula	$C_{147}H_{115}Cu_{14}N_{36}O_{47}S_{12}$
Formula weight	4412.02
Temperature/K	150(2)
Crystal system	monoclinic
Space group	$P2_1/n$
a/Å	20.8348(19)
b/Å	31.629(3)
c/Å	30.349(3)
α/°	90
β/°	102.966(4)
γ/°	90
Volume/Å^3	19490(3)
Z	4
ρ_{calc}g/cm^3	1.504
μ/mm^{-1}	1.701
F(000)	8892.0
Crystal size/mm^3	0.13 × 0.04 × 0.03
Radiation	MoKα (λ = 0.71073)
2Θ range for data collection/°	1.886 to 46.948
Index ranges	$-23 \le h \le 17$, $-35 \le k \le 35$, $-33 \le l \le 33$
Reflections collected	166366
Independent reflections	27236 [R_{int} = 0.0852, R_{sigma} = 0.0755]
Data/restraints/parameters	27236/828/2230
Goodness-of-fit on F^2	1.035
Final R indexes [I>=2σ (I)]	R_1 = 0.0901, wR_2 = 0.2230
Final R indexes [all data]	R_1 = 0.1354, wR_2 = 0.2593
Largest diff. peak/hole / e Å^{-3}	2.30/-0.98

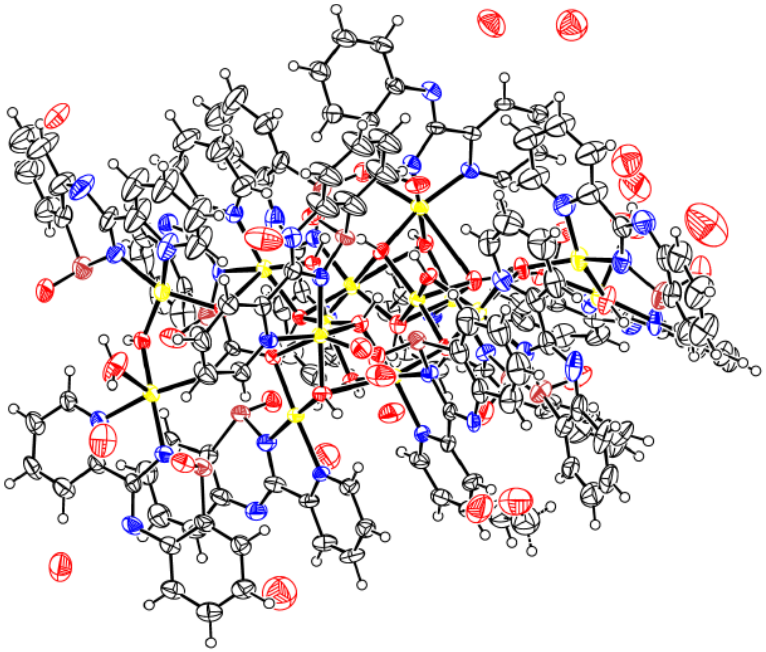

APPENDIX 2: Crystal Data and Structure Refinement for Compounds of Chapter 3

3.1 *N′*-(2-propylthiophenyl)-picolinamidine

Table 1 Crystal data and structure refinement for mo_KPstep2_0m_a.

Identification code	mo_KPstep2_0m_a
Empirical formula	$C_{14}H_{16}N_4S$
Formula weight	272.37
Temperature/K	173.2
Crystal system	monoclinic
Space group	$P2_1/c$
a/Å	7.5170(3)
b/Å	23.1295(9)
c/Å	8.0964(3)
α/°	90
β/°	103.220(2)
γ/°	90
Volume/Å^3	1370.37(9)
Z	4
ρ_{calc}g/cm^3	1.320
μ/mm^{-1}	0.228
F(000)	576.0
Crystal size/mm^3	0.277 × 0.133 × 0.05
Radiation	MoKα (λ = 0.71073)
2Θ range for data collection/°	5.566 to 51.416
Index ranges	$-9 \leq h \leq 9$, $-28 \leq k \leq 28$, $-9 \leq l \leq 9$
Reflections collected	16406
Independent reflections	2597 [R_{int} = 0.0559, R_{sigma} = 0.0327]
Data/restraints/parameters	2597/0/176
Goodness-of-fit on F^2	1.063
Final R indexes [I>=2σ (I)]	R_1 = 0.0364, wR_2 = 0.0801
Final R indexes [all data]	R_1 = 0.0540, wR_2 = 0.0869
Largest diff. peak/hole / e Å^{-3}	0.19/-0.29

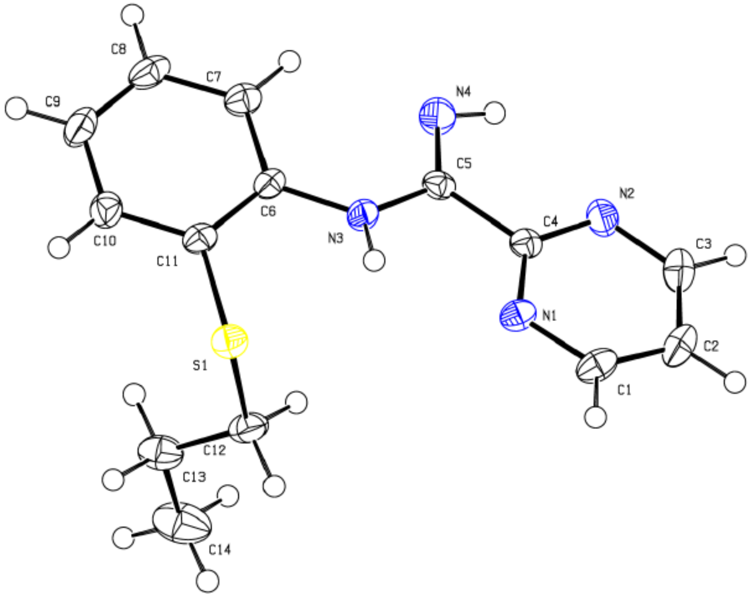

pmbtdaH

Table 1 Crystal data and structure refinement for BL06d_0m.

Identification code	BL06d_0m
Empirical formula	$C_{11}H_8N_4S$
Formula weight	228.27
Temperature/K	150(2)
Crystal system	monoclinic
Space group	$P2_1/c$
a/Å	11.7228(10)
b/Å	7.5007(7)
c/Å	11.9325(11)
α/°	90
β/°	103.078(4)
γ/°	90
Volume/Å^3	1022.00(16)
Z	4
ρ_{calc}g/cm^3	1.484
μ/mm^{-1}	0.290
F(000)	472.0
Crystal size/mm^3	0.300 × 0.300 × 0.030
Radiation	MoKα (λ = 0.71073)
2Θ range for data collection/°	6.464 to 49.99
Index ranges	$-13 \leq h \leq 13$, $-8 \leq k \leq 8$, $-14 \leq l \leq 14$
Reflections collected	21906
Independent reflections	1797 [R_{int} = 0.0308, R_{sigma} = 0.0134]
Data/restraints/parameters	1797/0/145
Goodness-of-fit on F^2	1.216
Final R indexes [I>=2σ (I)]	R_1 = 0.0514, wR_2 = 0.1157
Final R indexes [all data]	R_1 = 0.0525, wR_2 = 0.1163
Largest diff. peak/hole / e Å^{-3}	0.51/-0.26

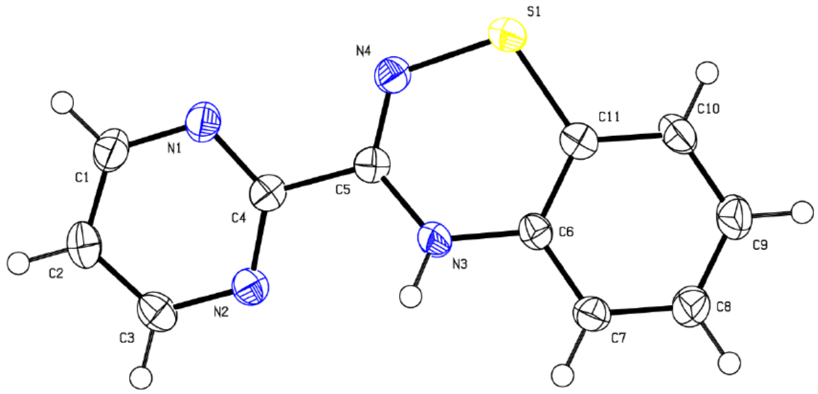

3.2 [$MnCl_2(pmbtdaH)_2$]·$2CH_3OH$

Table 1 Crystal data and structure refinement for kp17.

Identification code	kp17
Empirical formula	$C_{24}H_{23.86}Cl_{2.15}MnN_8O_2S_2$
Formula weight	651.38
Temperature/K	150.01
Crystal system	orthorhombic
Space group	Pbcn
a/Å	12.6583(4)
b/Å	10.8572(4)
c/Å	20.1472(8)
α/°	90
β/°	90
γ/°	90
Volume/Å^3	2768.90(17)
Z	4
ρ_{calc}g/cm^3	1.563
μ/mm^{-1}	0.874
F(000)	1333.0
Crystal size/mm^3	0.485 × 0.321 × 0.128
Radiation	MoKα (λ = 0.71073)
2Θ range for data collection/°	6.388 to 56.608
Index ranges	$-16 \le h \le 16$, $-14 \le k \le 14$, $-26 \le l \le 26$
Reflections collected	40425
Independent reflections	3445 [R_{int} = 0.0391, R_{sigma} = 0.0179]
Data/restraints/parameters	3445/0/197
Goodness-of-fit on F^2	1.081
Final R indexes [I>=2σ (I)]	R_1 = 0.0432, wR_2 = 0.1056
Final R indexes [all data]	R_1 = 0.0500, wR_2 = 0.1126
Largest diff. peak/hole / e Å^{-3}	0.58/-0.49

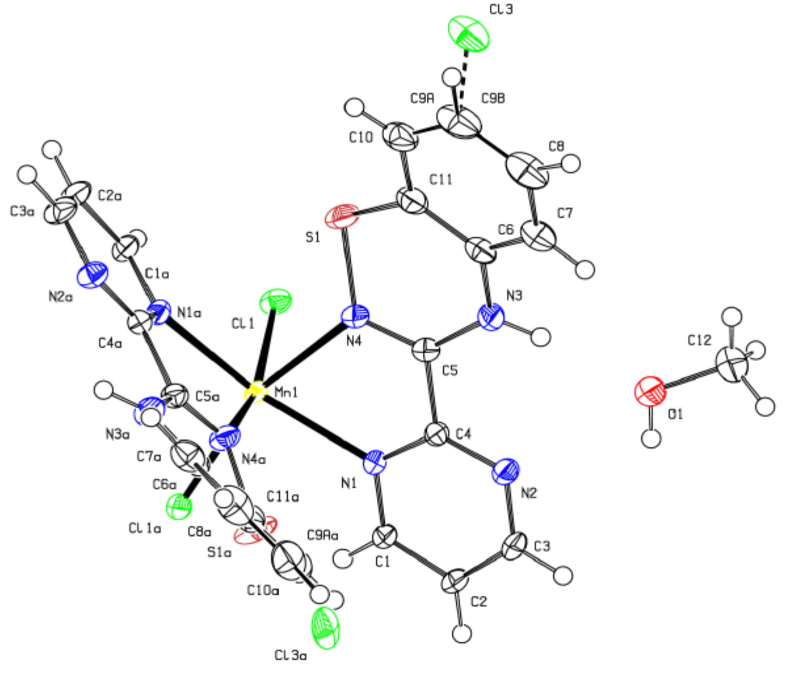

3.3 [FeCl$_2$(pmbtdaH)$_2$]·2CH$_3$OH

Table 1 Crystal data and structure refinement for KP52B_a.

Identification code	KP52B_a
Empirical formula	$C_{12}H_{12}ClFe_{0.5}N_4OS$
Formula weight	323.69
Temperature/K	173(2)
Crystal system	orthorhombic
Space group	Pbcn
a/Å	12.6352(4)
b/Å	10.6862(3)
c/Å	20.3415(7)
α/°	90
β/°	90
γ/°	90
Volume/Å^3	2746.56(15)
Z	8
ρ_{calc}g/cm^3	1.566
μ/mm^{-1}	0.935
F(000)	1328.0
Crystal size/mm^3	75.000 × 0.453 × 0.310
Radiation	MoKα (λ = 0.71073)
2Θ range for data collection/°	6.402 to 56.636
Index ranges	$-16 \le h \le 16$, $-13 \le k \le 14$, $-27 \le l \le 27$
Reflections collected	38979
Independent reflections	3408 [$R_{int} = 0.0601$, $R_{sigma} = 0.0242$]
Data/restraints/parameters	3408/0/179
Goodness-of-fit on F^2	1.089
Final R indexes [I>=2σ (I)]	$R_1 = 0.0565$, $wR_2 = 0.1450$
Final R indexes [all data]	$R_1 = 0.0751$, $wR_2 = 0.1586$
Largest diff. peak/hole / e Å^{-3}	2.77/-0.34

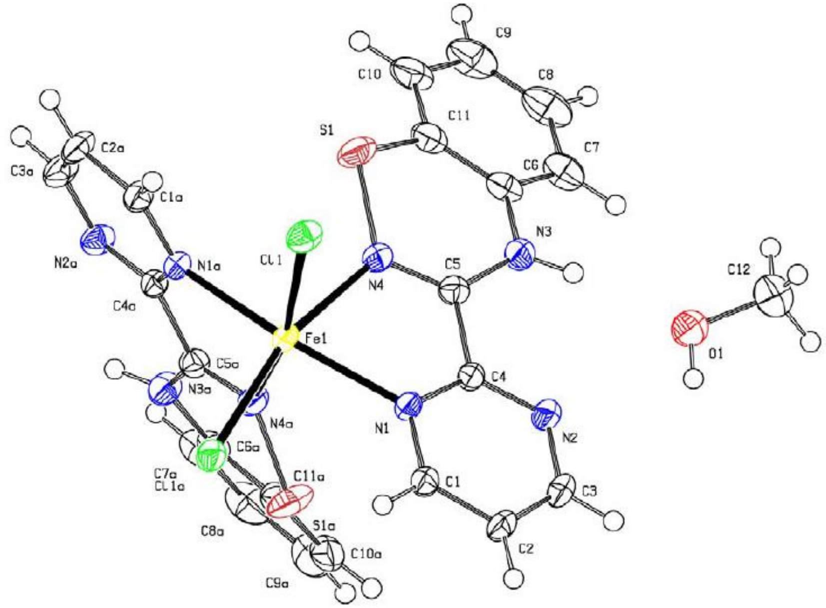

3.4 $[CoCl_2(pmbtdaH)_2]\cdot 2CH_3OH$

Table 1 Crystal data and structure refinement for kp19A_a.

Identification code	kp19A_a
Empirical formula	$C_{24.26}H_{24}Cl_{2.26}CoN_8O_2S_2$
Formula weight	662.80
Temperature/K	173.2
Crystal system	orthorhombic
Space group	Pbcn
a/Å	12.5844(4)
b/Å	10.5219(3)
c/Å	20.6171(7)
α/°	90
β/°	90
γ/°	90
Volume/Å^3	2729.95(15)
Z	4
ρ_{calc}g/cm^3	1.613
μ/mm^{-1}	1.044
F(000)	1356.0
Crystal size/mm^3	0.247 × 0.185 × 0.064
Radiation	MoKα (λ = 0.71073)
2Θ range for data collection/°	6.41 to 56.626
Index ranges	$-16 \leq h \leq 16$, $-13 \leq k \leq 14$, $-27 \leq l \leq 27$
Reflections collected	38781
Independent reflections	3392 [R_{int} = 0.0550, R_{sigma} = 0.0221]
Data/restraints/parameters	3392/0/197
Goodness-of-fit on F^2	1.128
Final R indexes [I>=2σ (I)]	R_1 = 0.0429, wR_2 = 0.0976
Final R indexes [all data]	R_1 = 0.0599, wR_2 = 0.1076
Largest diff. peak/hole / e Å^{-3}	0.81/-0.44

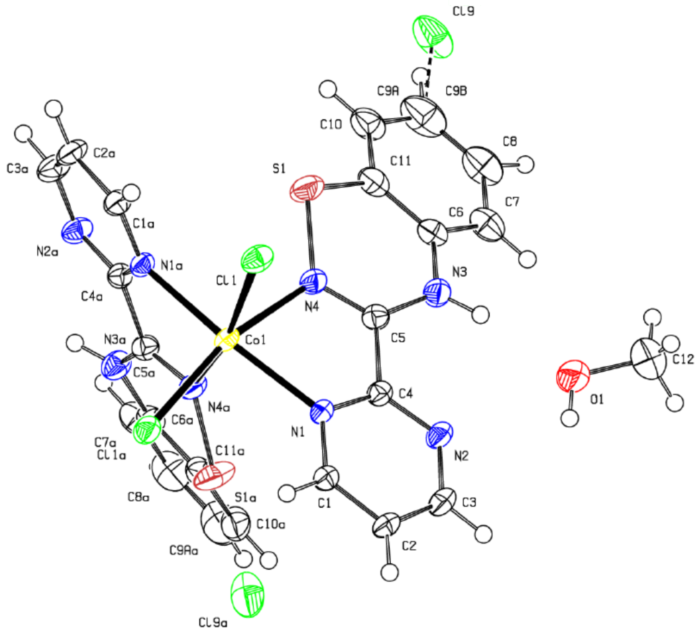

3.5 [$NiCl_2(pmbtdaH)_2$]·$2CH_3OH$

Table 1 Crystal data and structure refinement for kp48_a.

Identification code	kp48_a
Empirical formula	$C_{12}H_{11.89}Cl_{1.11}N_4Ni_{0.5}OS$
Formula weight	328.87
Temperature/K	173(2)
Crystal system	orthorhombic
Space group	Pbcn
a/Å	12.5332(4)
b/Å	10.4404(3)
c/Å	20.6518(7)
α/°	90
β/°	90
γ/°	90
Volume/Å^3	2702.32(15)
Z	8
ρ_{calc}g/cm^3	1.617
μ/mm^{-1}	1.132
F(000)	1350.0
Crystal size/mm^3	0.189 × 0.162 × 0.054
Radiation	MoKα (λ = 0.71073)
2Θ range for data collection/°	6.432 to 61.068
Index ranges	$-17 \le h \le 17$, $-14 \le k \le 11$, $-29 \le l \le 29$
Reflections collected	40312
Independent reflections	4114 [R_{int} = 0.0678, R_{sigma} = 0.0373]
Data/restraints/parameters	4114/0/189
Goodness-of-fit on F^2	1.073
Final R indexes [I>=2σ (I)]	R_1 = 0.0430, wR_2 = 0.0858
Final R indexes [all data]	R_1 = 0.0733, wR_2 = 0.0971
Largest diff. peak/hole / e Å^{-3}	0.72/-0.41

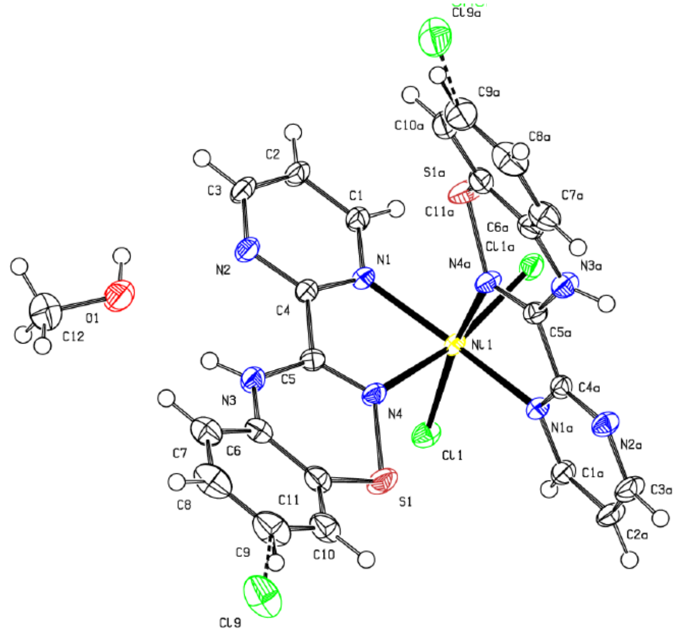

3.6 $Zn_2Cl_4(pmbtdaH)_2$

Table 1 Crystal data and structure refinement for mo_kp113G_0m_a.

Identification code	mo_kp113G_0m_a
Empirical formula	$C_{22}H_{16}Cl_4N_8S_2Zn_2$
Formula weight	729.09
Temperature/K	170.2
Crystal system	triclinic
Space group	P-1
a/Å	7.4817(16)
b/Å	9.0407(17)
c/Å	10.477(2)
α/°	100.104(11)
β/°	103.533(11)
γ/°	109.771(11)
Volume/Å^3	622.8(2)
Z	1
ρ_{calc}g/cm^3	1.944
μ/mm^{-1}	2.556
F(000)	364.0
Crystal size/mm^3	0.445 × 0.132 × 0.08
Radiation	MoKα (λ = 0.71073)
2Θ range for data collection/°	6.1 to 51.45
Index ranges	$-9 \le h \le 9, -11 \le k \le 11, -12 \le l \le 12$
Reflections collected	11636
Independent reflections	2362 [$R_{int} = 0.0397, R_{sigma} = 0.0290$]
Data/restraints/parameters	2362/0/172
Goodness-of-fit on F^2	1.038
Final R indexes [I>=2σ (I)]	$R_1 = 0.0270, wR_2 = 0.0642$
Final R indexes [all data]	$R_1 = 0.0411, wR_2 = 0.0707$
Largest diff. peak/hole / e Å^{-3}	0.92/-0.33

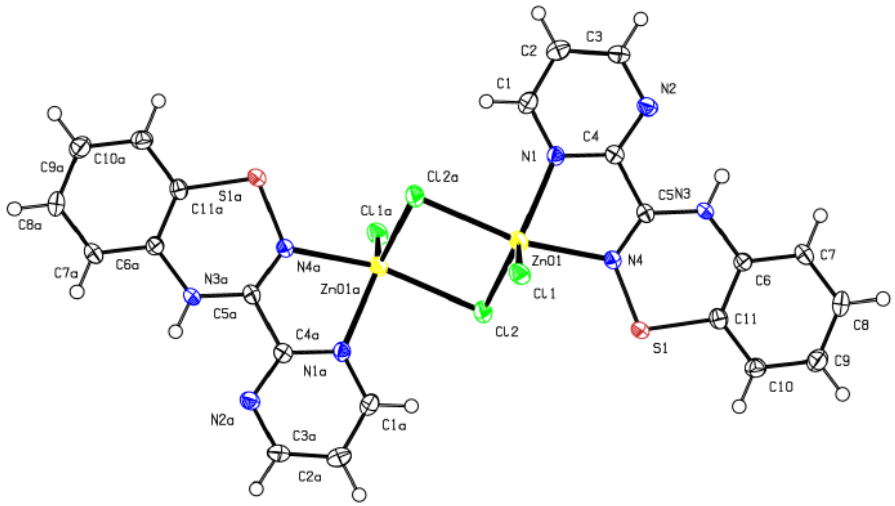

3.7a Mn(hfac)$_2$(pmbtdaH)

Table 1 Crystal data and structure refinement for mo_kp_42_2_Mo_0m_a.

Identification code	mo_kp_42_2_Mo_0m_a
Empirical formula	$C_{21}H_{9.5}Cl_{0.5}F_{12}MnN_4O_4S$
Formula weight	714.55
Temperature/K	105.01
Crystal system	triclinic
Space group	P-1
a/Å	14.67(7)
b/Å	15.31(6)
c/Å	15.98(7)
α/°	65.3(3)
β/°	70.39(15)
γ/°	87.7(3)
Volume/Å^3	3052(24)
Z	4
ρ_{calc}g/cm^3	1.555
μ/mm^{-1}	0.651
F(000)	1412.0
Crystal size/mm^3	0.718 × 0.081 × 0.02
Radiation	MoKα (λ = 0.71073)
2Θ range for data collection/°	5.676 to 50.72
Index ranges	$-17 \le h \le 17$, $-18 \le k \le 18$, $-19 \le l \le 19$
Reflections collected	48983
Independent reflections	10963 [R_{int} = 0.1027, R_{sigma} = 0.0829]
Data/restraints/parameters	10963/24/783
Goodness-of-fit on F^2	1.049
Final R indexes [I>=2σ (I)]	R_1 = 0.0697, wR_2 = 0.1603
Final R indexes [all data]	R_1 = 0.1310, wR_2 = 0.2137
Largest diff. peak/hole / e Å^{-3}	1.88/-0.94

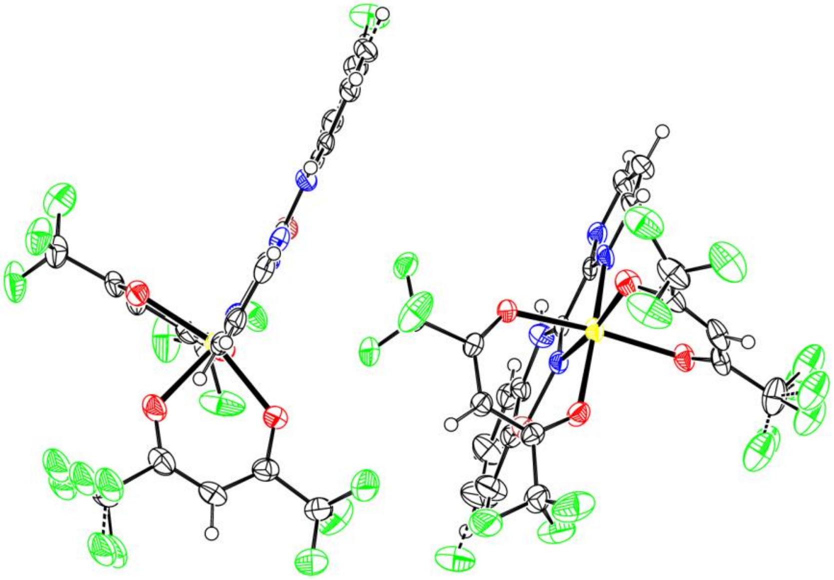

3.7b $[Mn_2(hfac)_2(tfa)_2(pmbtdaH_{ox})_2]\cdot 2CH_2Cl_2$

Table 1 Crystal data and structure refinement for mo_kp42_yellow_0m_a.

Identification code	mo_kp42_yellow_0m_a
Empirical formula	$C_{19}H_{10.92}Cl_{2.08}F_9MnN_4O_5S$
Formula weight	706.97
Temperature/K	130.01
Crystal system	triclinic
Space group	P-1
a/Å	9.414(17)
b/Å	10.676(16)
c/Å	12.98(3)
α/°	80.61(9)
β/°	80.50(7)
γ/°	81.05(6)
Volume/Å^3	1258(4)
Z	2
ρ_{calc}g/cm^3	1.866
μ/mm^{-1}	0.937
F(000)	701.0
Crystal size/mm^3	0.2 × 0.19 × 0.1
Radiation	MoKα (λ = 0.71073)
2Θ range for data collection/°	5.742 to 52.842
Index ranges	$-11 \le h \le 11$, $-13 \le k \le 13$, $-16 \le l \le 16$
Reflections collected	22287
Independent reflections	5127 [$R_{int} = 0.0750$, $R_{sigma} = 0.0479$]
Data/restraints/parameters	5127/0/379
Goodness-of-fit on F^2	1.122
Final R indexes [I>=2σ (I)]	$R_1 = 0.0683$, $wR_2 = 0.1643$
Final R indexes [all data]	$R_1 = 0.1011$, $wR_2 = 0.1935$
Largest diff. peak/hole / e Å^{-3}	2.50/-1.26

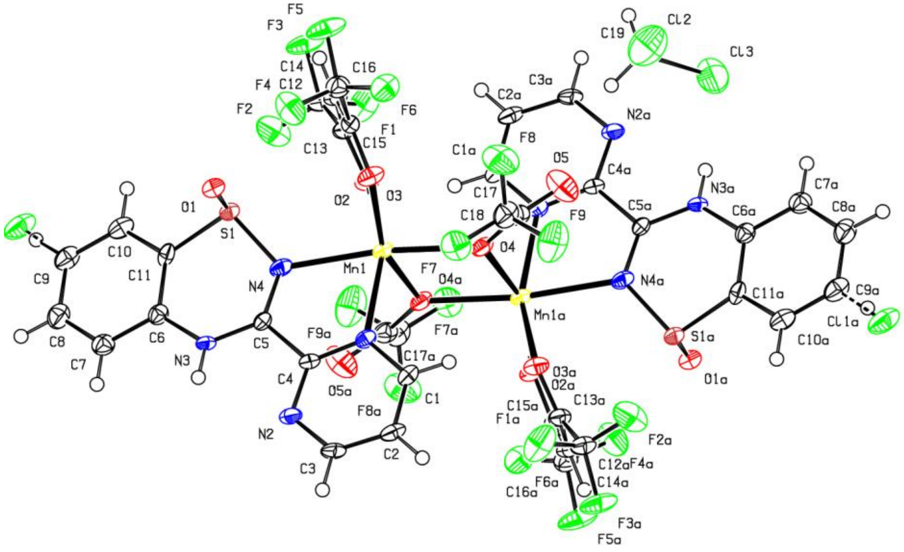

3.8a Co(hfac)$_2$(pmbtdaH)

Table 1 Crystal data and structure refinement for KP046a.

Identification code	KP046a
Empirical formula	$C_{21}H_{9.85}Cl_{0.15}CoF_{12}N_4O_4S$
Formula weight	706.49
Temperature/K	293(2)
Crystal system	monoclinic
Space group	$P2_1/c$
a/Å	8.9523(18)
b/Å	17.308(3)
c/Å	17.160(3)
α/°	90
β/°	93.45(3)
γ/°	90
Volume/Å^3	2654.1(8)
Z	4
ρ_{calc}g/cm^3	1.768
μ/mm^{-1}	0.862
F(000)	1398.0
Crystal size/mm^3	0.517 × 0.24 × 0.18
Radiation	MoKα (λ = 0.71073)
2Θ range for data collection/°	5.77 to 54.994
Index ranges	$-11 \le h \le 11$, $-22 \le k \le 22$, $-22 \le l \le 22$
Reflections collected	77441
Independent reflections	6093 [R_{int} = 0.0288, R_{sigma} = 0.0116]
Data/restraints/parameters	6093/60/413
Goodness-of-fit on F^2	1.047
Final R indexes [I>=2σ (I)]	R_1 = 0.0815, wR_2 = 0.2040
Final R indexes [all data]	R_1 = 0.0933, wR_2 = 0.2179
Largest diff. peak/hole / e Å^{-3}	1.12/-0.99

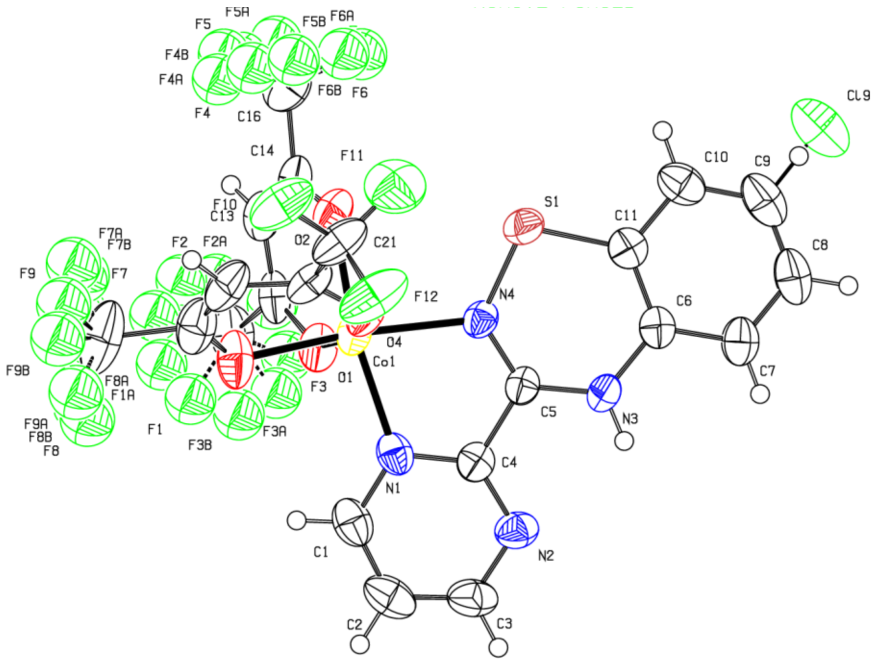

3.8b Co(hfac)$_2$(pmbtdaH$_{ox}$)

Table 1 Crystal data and structure refinement for mo_KP46_orange_a.

Identification code	mo_KP46_orange_a
Empirical formula	$C_{84}H_{40}N_{16}O_{20}F_{48}Co_4S_4$
Formula weight	2869.28
Temperature/K	132.49
Crystal system	monoclinic
Space group	$P2_1/n$
a/Å	9.670(10)
b/Å	14.631(14)
c/Å	18.475(19)
α/°	90
β/°	98.90(3)
γ/°	90
Volume/Å^3	2583(4)
Z	1
ρ_{calc}g/cm^3	1.845
μ/mm^{-1}	0.875
F(000)	1420.0
Crystal size/mm^3	0.25 × 0.08 × 0.06
Radiation	MoKα (λ = 0.71073)
2Θ range for data collection/°	5.568 to 53.276
Index ranges	$-12 \le h \le 12$, $-18 \le k \le 18$, $-23 \le l \le 23$
Reflections collected	35582
Independent reflections	5376 [R_{int} = 0.0921, R_{sigma} = 0.0516]
Data/restraints/parameters	5376/24/380
Goodness-of-fit on F^2	1.032
Final R indexes [I>=2σ (I)]	R_1 = 0.0790, wR_2 = 0.1806
Final R indexes [all data]	R_1 = 0.1112, wR_2 = 0.2034
Largest diff. peak/hole / e Å^{-3}	1.70/-1.90

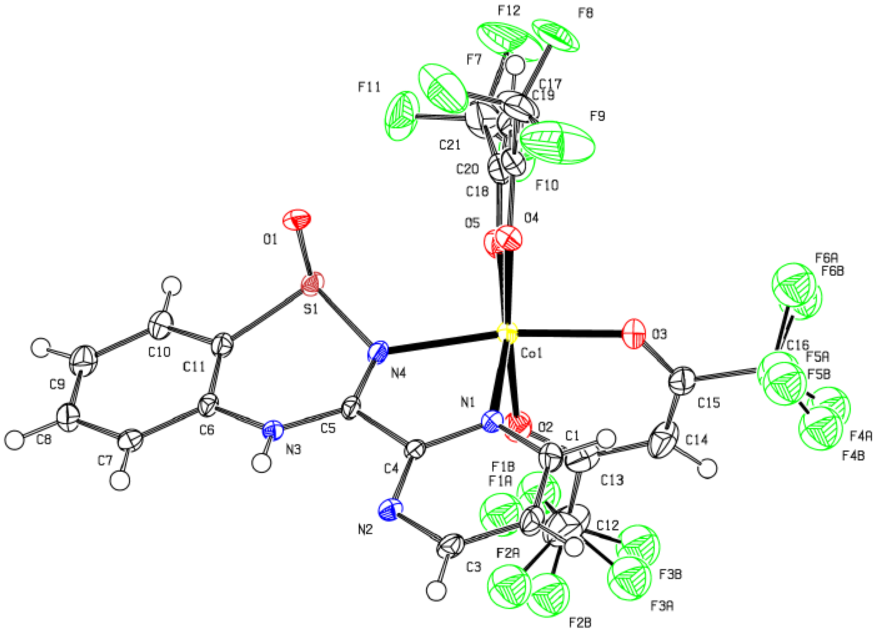

3.9a Ni(hfac)$_2$(pmbtdaH)

Table 1 Crystal data and structure refinement for mo_kp49_01a_a_sq.

Identification code	mo_kp49_01a_a_sq
Empirical formula	$C_{21}H_{10}F_{12}N_4NiO_4S$
Formula weight	701.10
Temperature/K	173.21
Crystal system	monoclinic
Space group	$P2_1/c$
a/Å	16.2797(9)
b/Å	22.1233(12)
c/Å	16.7396(10)
α/°	90
β/°	100.344(2)
γ/°	90
Volume/Å^3	5931.0(6)
Z	8
ρ_{calc}g/cm^3	1.570
μ/mm^{-1}	0.833
F(000)	2784.0
Crystal size/mm^3	0.303 × 0.101 × 0.08
Radiation	MoKα (λ = 0.71073)
2Θ range for data collection/°	5.33 to 51.996
Index ranges	$-20 \leq h \leq 20$, $-27 \leq k \leq 27$, $-20 \leq l \leq 20$
Reflections collected	79983
Independent reflections	11641 [R_{int} = 0.0703, R_{sigma} = 0.0351]
Data/restraints/parameters	11641/90/754
Goodness-of-fit on F^2	1.085
Final R indexes [I>=2σ (I)]	R_1 = 0.0763, wR_2 = 0.1796
Final R indexes [all data]	R_1 = 0.1143, wR_2 = 0.2266
Largest diff. peak/hole / e Å^{-3}	1.11/-0.92

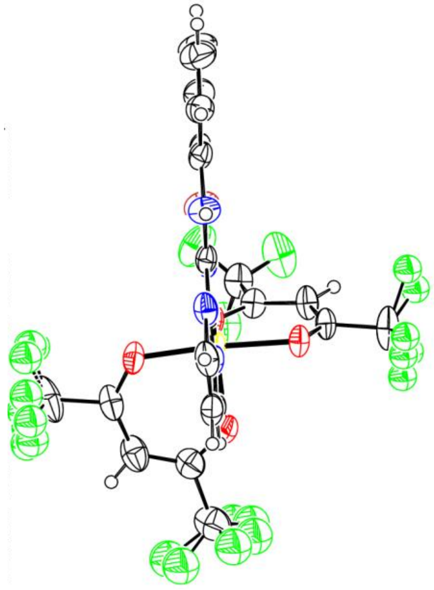

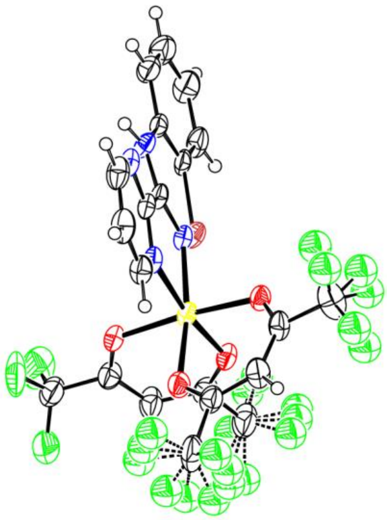

3.9b $[Ni(hfac)_2(pmbtdaH_{ox})]\cdot 2CH_2Cl_2$

Table 1 Crystal data and structure refinement for mo_kp49_2_0m_a.

Identification code	mo_kp49_2_0m_a
Empirical formula	$C_{23}H_{14}Cl_4F_{12}N_4NiO_5S$
Formula weight	886.95
Temperature/K	104.99
Crystal system	triclinic
Space group	P-1
a/Å	9.269
b/Å	10.361
c/Å	17.436
α/°	75.36
β/°	87.36
γ/°	80.20
Volume/Å^3	1596.5
Z	2
ρ_{calc}g/cm^3	1.845
μ/mm^{-1}	1.121
F(000)	880.0
Crystal size/mm^3	0.35 × 0.15 × 0.12
Radiation	MoKα (λ = 0.71073)
2Θ range for data collection/°	6.458 to 53.572
Index ranges	$-11 \leq h \leq 11$, $-13 \leq k \leq 13$, $-21 \leq l \leq 22$
Reflections collected	28328
Independent reflections	6692 [$R_{int} = 0.1343$, $R_{sigma} = 0.0786$]
Data/restraints/parameters	6692/55/408
Goodness-of-fit on F^2	2.620
Final R indexes [I>=2σ (I)]	$R_1 = 0.2341$, $wR_2 = 0.5553$
Final R indexes [all data]	$R_1 = 0.2678$, $wR_2 = 0.5933$
Largest diff. peak/hole / e Å^{-3}	3.93/-2.40

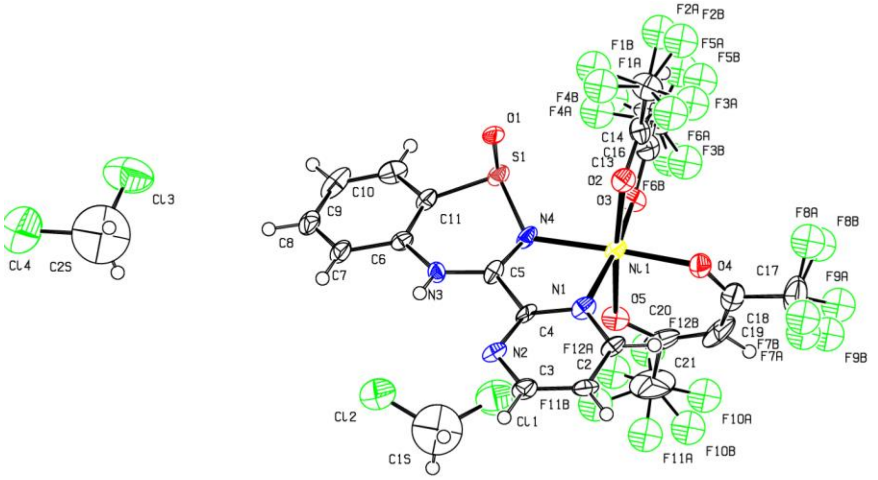

3.10a Cu(hfac)$_2$(pmbtdaH)

Table 1 Crystal data and structure refinement for mo_KP128B_1_0m_a.

Identification code	mo_KP128B_1_0m_a
Empirical formula	$C_{21}H_{10}CuF_{12}N_4O_4S$
Formula weight	705.93
Temperature/K	170.01
Crystal system	monoclinic
Space group	$P2_1/n$
a/Å	9.2070(4)
b/Å	18.5714(7)
c/Å	15.0514(6)
α/°	90
β/°	93.8750(10)
γ/°	90
Volume/Å^3	2567.71(18)
Z	4
ρ_{calc}g/cm^3	1.826
μ/mm^{-1}	1.057
F(000)	1396.0
Crystal size/mm^3	0.35 × 0.18 × 0.08
Radiation	MoKα (λ = 0.71073)
2Θ range for data collection/°	5.496 to 56.634
Index ranges	$-12 \leq h \leq 12$, $-24 \leq k \leq 24$, $-20 \leq l \leq 20$
Reflections collected	41543
Independent reflections	6356 [R_{int} = 0.0637, R_{sigma} = 0.0386]
Data/restraints/parameters	6356/0/388
Goodness-of-fit on F^2	1.032
Final R indexes [I>=2σ (I)]	R_1 = 0.0392, wR_2 = 0.0820
Final R indexes [all data]	R_1 = 0.0705, wR_2 = 0.0954
Largest diff. peak/hole / e Å^{-3}	0.55/-0.48

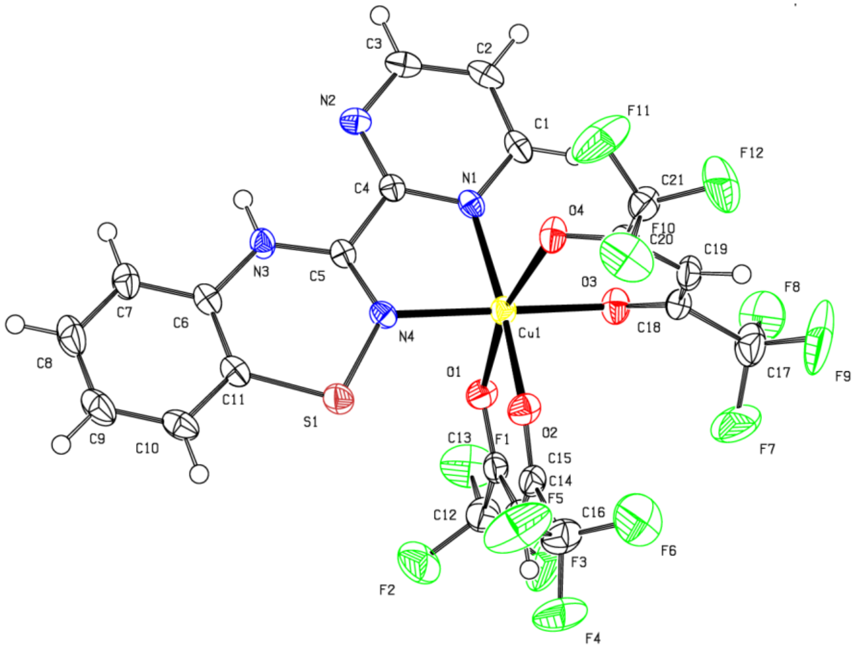

3.10b $Cu_4(hfac)_4(tfa)_2(pmbtda_{ox})_2$

Table 1 Crystal data and structure refinement for kp128c_0m_a.

Identification code	kp128c_0m_a
Empirical formula	$C_{46}H_{18}N_8O_{14}S_2Cu_4F_{30}$
Formula weight	1794.96
Temperature/K	149.99
Crystal system	triclinic
Space group	P-1
a/Å	8.9912(10)
b/Å	13.0115(14)
c/Å	13.8258(15)
α/°	79.955(5)
β/°	71.563(5)
γ/°	73.593(4)
Volume/Å^3	1465.5(3)
Z	1
ρ_{calc}g/cm^3	2.034
μ/mm^{-1}	1.670
F(000)	880.0
Crystal size/mm^3	0.025 × 0.02 × 0.01
Radiation	MoKα (λ = 0.71073)
2Θ range for data collection/°	4.308 to 56.84
Index ranges	$-11 \leq h \leq 12$, $-17 \leq k \leq 17$, $-18 \leq l \leq 18$
Reflections collected	39812
Independent reflections	7285 [R_{int} = 0.0836, R_{sigma} = 0.0716]
Data/restraints/parameters	7285/224/466
Goodness-of-fit on F^2	1.113
Final R indexes [I>=2σ (I)]	R_1 = 0.0972, wR_2 = 0.2077
Final R indexes [all data]	R_1 = 0.1389, wR_2 = 0.2317
Largest diff. peak/hole / e Å^{-3}	1.34/-1.06

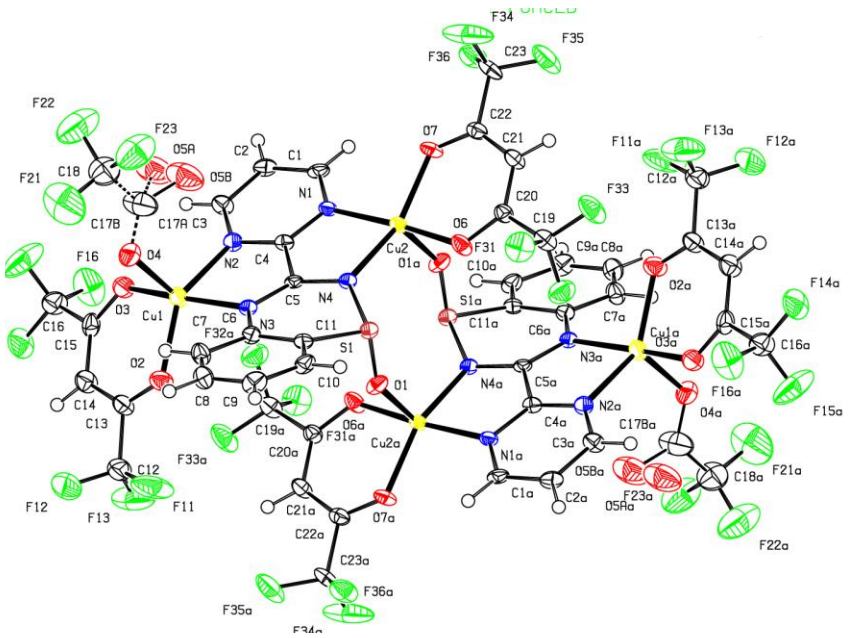

3.11a Zn(hfac)$_2$(pmbtdaH)

Table 1 Crystal data and structure refinement for mo_kp180_1D_red_0m_a.

Identification code	mo_kp180_1D_red_0m_a
Empirical formula	$C_{21}H_{10}F_{12}N_4O_4SZn$
Formula weight	707.76
Temperature/K	170(2)
Crystal system	monoclinic
Space group	C2/c
a/Å	26.1975(10)
b/Å	8.8979(4)
c/Å	22.6728(11)
α/°	90
β/°	92.139(2)
γ/°	90
Volume/Å^3	5281.4(4)
Z	8
ρ_{calc}g/cm^3	1.780
μ/mm^{-1}	1.131
F(000)	2800.0
Crystal size/mm^3	0.590 × 0.500 × 0.100
Radiation	MoKα (λ = 0.71073)
2Θ range for data collection/°	5.992 to 53.004
Index ranges	$-32 \leq h \leq 32$, $-11 \leq k \leq 11$, $-28 \leq l \leq 28$
Reflections collected	28205
Independent reflections	5460 [R_{int} = 0.0492, R_{sigma} = 0.0334]
Data/restraints/parameters	5460/423/547
Goodness-of-fit on F^2	1.023
Final R indexes [I>=2σ (I)]	R_1 = 0.0690, wR_2 = 0.1738
Final R indexes [all data]	R_1 = 0.0903, wR_2 = 0.1913
Largest diff. peak/hole / e Å^{-3}	0.99/-1.10

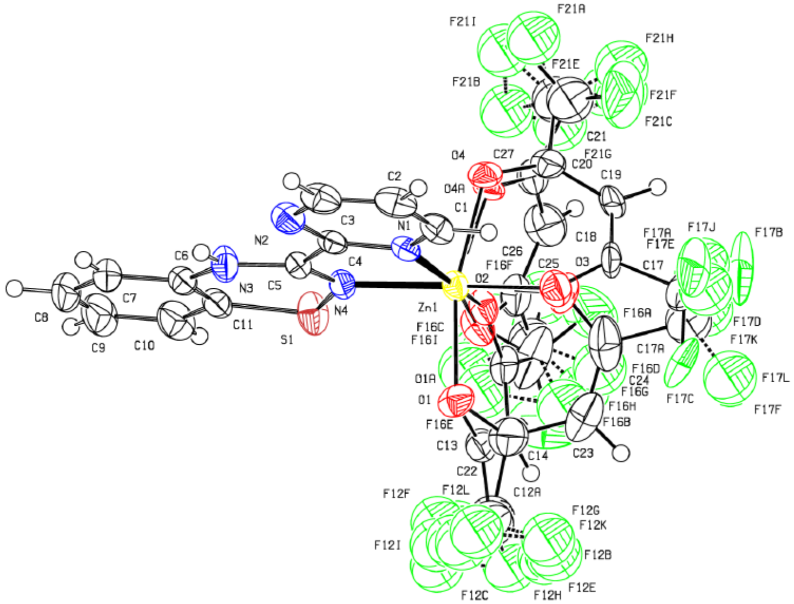

3.11b $Zn_4(hfac)_6(pmbtda_{ox})_2$

Table 1 Crystal data and structure refinement for kp85_res082_a.

Identification code	kp85_res082_a
Empirical formula	$C_{52}H_{19.91}Cl_{0.1}F_{36}N_8O_{14}S_2Zn_4$
Formula weight	1993.63
Temperature/K	104.99
Crystal system	monoclinic
Space group	$P2_1/n$
a/Å	8.4243(4)
b/Å	15.2522(7)
c/Å	25.8141(10)
α/°	90
β/°	93.153(2)
γ/°	90
Volume/Å^3	3311.8(3)
Z	2
ρ_{calc}g/cm^3	1.999
μ/mm^{-1}	1.669
F(000)	1955.0
Crystal size/mm^3	0.24 × 0.14 × 0.02
Radiation	MoKα (λ = 0.71073)
2Θ range for data collection/°	5.678 to 51.452
Index ranges	$-10 \leq h \leq 10$, $-18 \leq k \leq 18$, $-31 \leq l \leq 30$
Reflections collected	56755
Independent reflections	6314 [$R_{int} = 0.0524$, $R_{sigma} = 0.0241$]
Data/restraints/parameters	6314/42/486
Goodness-of-fit on F^2	1.079
Final R indexes [I>=2σ (I)]	$R_1 = 0.0791$, $wR_2 = 0.1747$
Final R indexes [all data]	$R_1 = 0.0888$, $wR_2 = 0.1808$
Largest diff. peak/hole / e Å^{-3}	1.94/-1.98

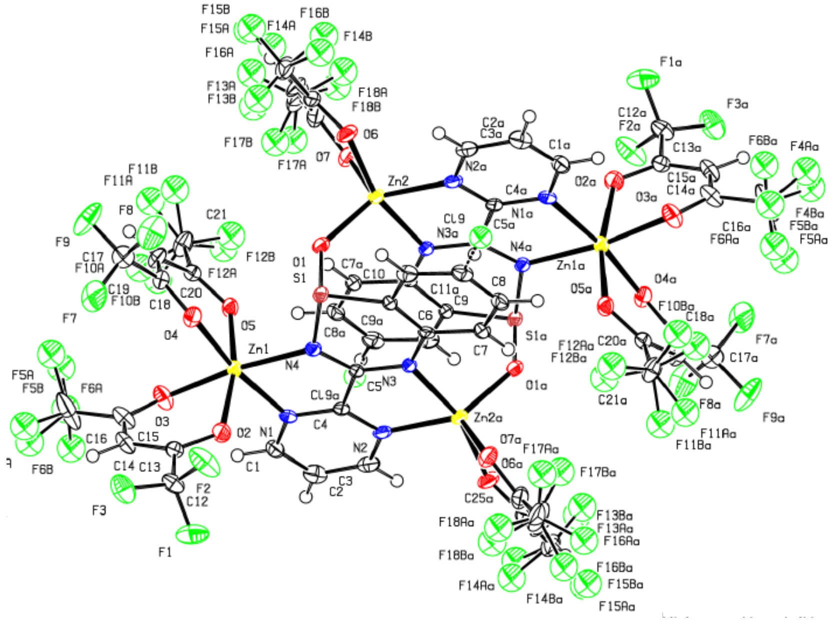

APPENDIX 3: Crystal Data and Structure Refinement for Compounds of Chapter 4

pybtdaSMe

Table 1 Crystal data and structure refinement for unsorted_0m_a.

Identification code	unsorted_0m_a
Empirical formula	$C_{13}H_{11}N_3S$
Formula weight	241.31
Temperature/K	279.96
Crystal system	monoclinic
Space group	$P2_1/c$
a/Å	13.767(14)
b/Å	6.820(6)
c/Å	15.306(15)
α/°	90
β/°	90.71(5)
γ/°	90
Volume/Å^3	1437(2)
Z	4
ρ_{calc}g/cm^3	1.115
μ/mm^{-1}	0.208
F(000)	504.0
Crystal size/mm^3	0.33 × 0.267 × 0.2
Radiation	MoKα (λ = 0.71073)
2Θ range for data collection/°	6.124 to 53
Index ranges	$-17 \le h \le 17$, $-8 \le k \le 8$, $-19 \le l \le 19$
Reflections collected	13994
Independent reflections	2958 [R_{int} = 0.0796, R_{sigma} = 0.0576]
Data/restraints/parameters	2958/0/187
Goodness-of-fit on F^2	1.017
Final R indexes [I>=2σ (I)]	$R_1 = 0.0526$, $wR_2 = 0.1345$
Final R indexes [all data]	$R_1 = 0.0916$, $wR_2 = 0.1541$
Largest diff. peak/hole / e Å^{-3}	0.27/-0.25

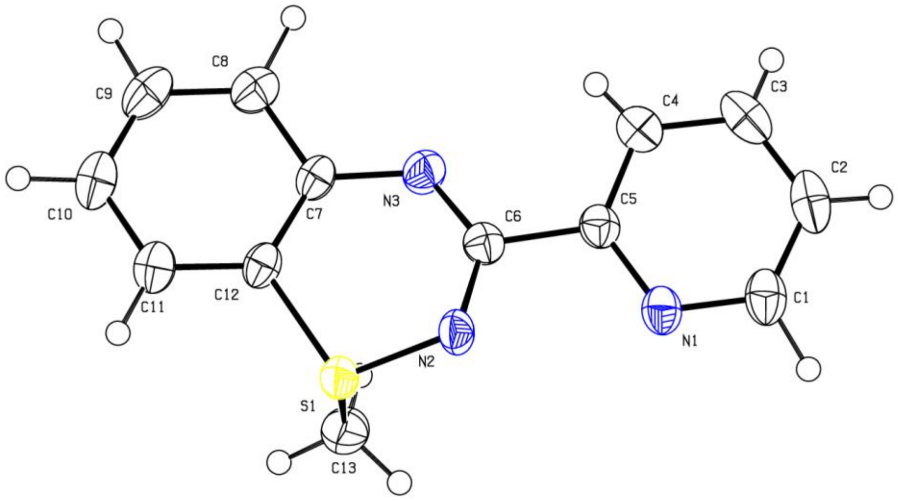

4.1 $MnCl_2(pybtdaSMe)_2$

Table 1 Crystal data and structure refinement for KP139b_0m_a.

Identification code	KP139b_0m_a
Empirical formula	$C_{29}H_{29}N_6S_2Cl_2Mn$
Formula weight	651.54
Temperature/K	150.01
Crystal system	triclinic
Space group	P-1
a/Å	10.6391(5)
b/Å	11.1889(6)
c/Å	12.0721(6)
α/°	92.105(3)
β/°	99.116(3)
γ/°	95.124(3)
Volume/Å^3	1411.35(12)
Z	2
ρ_{calc}g/cm^3	1.533
μ/mm^{-1}	0.837
F(000)	672.0
Crystal size/mm^3	0.14 × 0.02 × 0.01
Radiation	MoKα (λ = 0.71073)
2Θ range for data collection/°	3.422 to 56.87
Index ranges	$-14 \le h \le 14$, $-14 \le k \le 14$, $-16 \le l \le 16$
Reflections collected	42199
Independent reflections	7054 [R_{int} = 0.0532, R_{sigma} = 0.0441]
Data/restraints/parameters	7054/4/349
Goodness-of-fit on F^2	1.127
Final R indexes [I>=2σ (I)]	R_1 = 0.0722, wR_2 = 0.1439
Final R indexes [all data]	R_1 = 0.0868, wR_2 = 0.1504
Largest diff. peak/hole / e Å^{-3}	1.78/-0.99

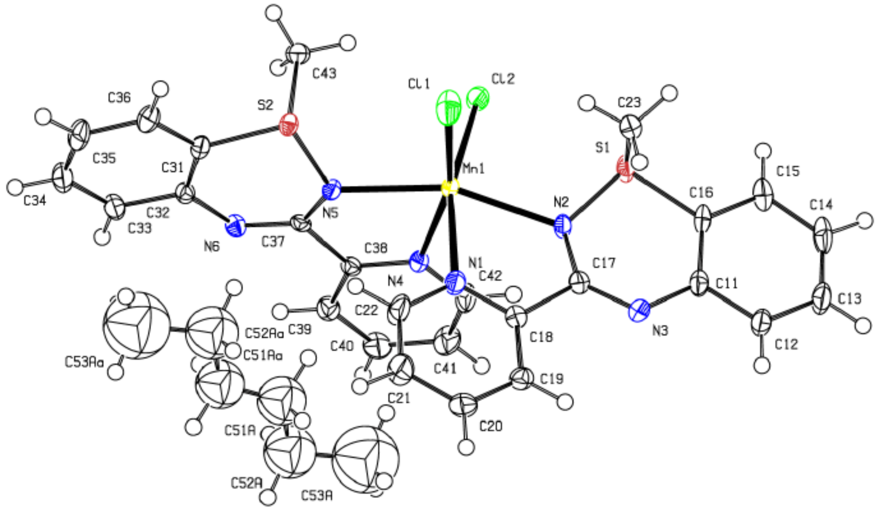

4.2 $NiCl_2(pybtdaSMe)_2$

Table 1 Crystal data and structure refinement for mo_kp137B_0m_a.

Identification code	mo_kp137B_0m_a
Empirical formula	$C_{26}H_{22}Cl_4Cu_2N_6S_2$
Formula weight	751.49
Temperature/K	170.0
Crystal system	triclinic
Space group	P-1
a/Å	7.5688(14)
b/Å	9.561(2)
c/Å	9.935(2)
α/°	76.672(9)
β/°	86.204(9)
γ/°	83.819(8)
Volume/Å^3	694.8(2)
Z	1
ρ_{calc}g/cm^3	1.796
μ/mm^{-1}	2.096
F(000)	378.0
Crystal size/mm^3	0.23 × 0.135 × 0.04
Radiation	MoKα (λ = 0.71073)
2Θ range for data collection/°	6.648 to 52.848
Index ranges	$-9 \le h \le 9$, $-11 \le k \le 11$, $-12 \le l \le 12$
Reflections collected	14903
Independent reflections	2849 [R_{int} = 0.0369, R_{sigma} = 0.0257]
Data/restraints/parameters	2849/0/182
Goodness-of-fit on F^2	1.094
Final R indexes [I>=2σ (I)]	R_1 = 0.0351, wR_2 = 0.0908
Final R indexes [all data]	R_1 = 0.0429, wR_2 = 0.0965
Largest diff. peak/hole / e Å^{-3}	1.36/-0.52

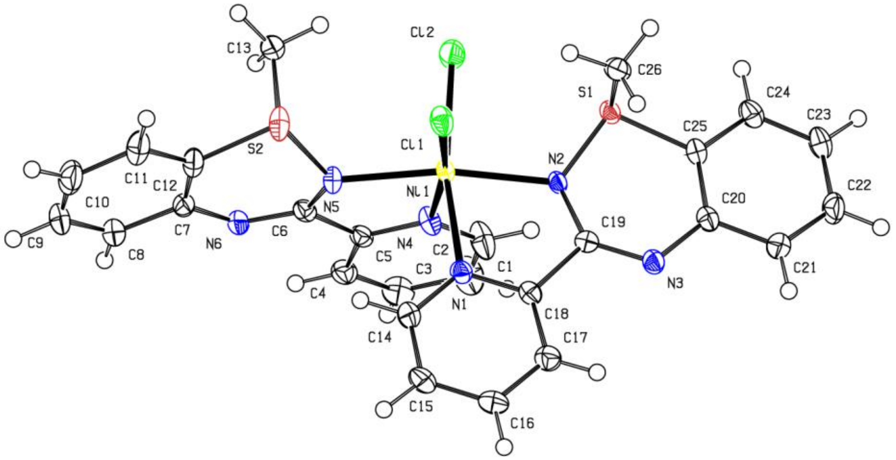

4.3a $Cu_2Cl_4(pybtdaSMe)_2$

Table 1 Crystal data and structure refinement for mo_kp155B_repeat_0m_a.

Identification code	mo_kp155B_repeat_0m_a
Empirical formula	$C_{26}H_{22}Cl_2N_6NiS_2$
Formula weight	612.22
Temperature/K	170.01
Crystal system	triclinic
Space group	P-1
a/Å	10.573(3)
b/Å	11.030(3)
c/Å	11.927(3)
α/°	90.395(14)
β/°	100.445(13)
γ/°	96.452(14)
Volume/Å^3	1358.6(7)
Z	2
ρ_{calc}g/cm^3	1.497
μ/mm^{-1}	1.092
F(000)	628.0
Crystal size/mm^3	0.43 × 0.16 × 0.04
Radiation	MoKα (λ = 0.71073)
2Θ range for data collection/°	5.714 to 56.924
Index ranges	$-14 \le h \le 14$, $-14 \le k \le 14$, $-15 \le l \le 15$
Reflections collected	45834
Independent reflections	6766 [R_{int} = 0.0905, R_{sigma} = 0.0559]
Data/restraints/parameters	6766/0/336
Goodness-of-fit on F^2	1.021
Final R indexes [I>=2σ (I)]	$R_1 = 0.0383$, $wR_2 = 0.0772$
Final R indexes [all data]	$R_1 = 0.0680$, $wR_2 = 0.0870$
Largest diff. peak/hole / e Å^{-3}	0.76/-0.42

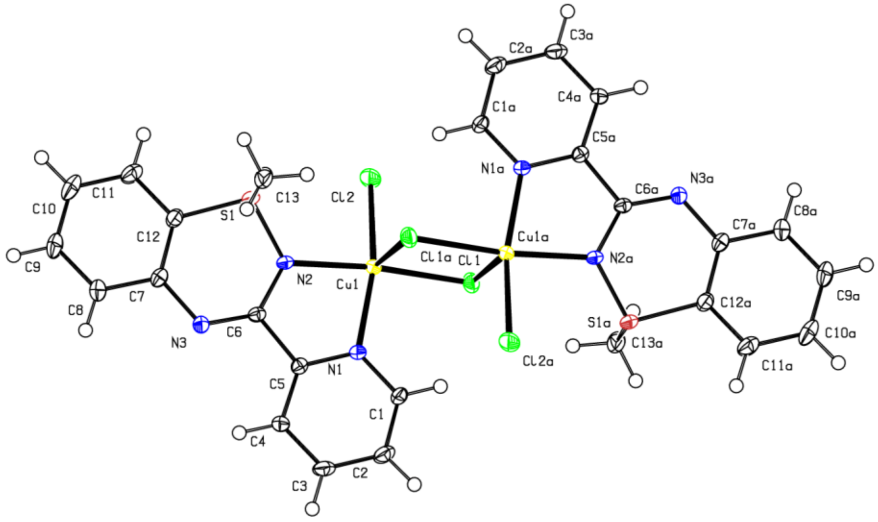

4.3b $Cu_2Cl_4(pybtdaSMe)_2 \cdot 2CuCl_2(pybtdaSMe)$

Table 1 Crystal data and structure refinement for mo_KP137B_6_0m_a.

Identification code	mo_KP137B_6_0m_a
Empirical formula	$C_{13}H_{11}Cl_2CuN_3S$
Formula weight	375.75
Temperature/K	170.2
Crystal system	triclinic
Space group	P-1
a/Å	9.6141(4)
b/Å	11.5056(5)
c/Å	14.2083(7)
α/°	68.672(2)
β/°	81.595(2)
γ/°	78.836(2)
Volume/Å^3	1431.38(11)
Z	4
ρ_{calc}g/cm^3	1.744
μ/mm^{-1}	2.035
F(000)	756.0
Crystal size/mm^3	0.5 × 0.4 × 0.2
Radiation	MoKα (λ = 0.71073)
2Θ range for data collection/°	5.704 to 52.886
Index ranges	$-12 \leq h \leq 12$, $-14 \leq k \leq 14$, $-17 \leq l \leq 17$
Reflections collected	31311
Independent reflections	5877 [R_{int} = 0.0605, R_{sigma} = 0.0408]
Data/restraints/parameters	5877/0/430
Goodness-of-fit on F^2	1.060
Final R indexes [I>=2σ (I)]	R_1 = 0.0347, wR_2 = 0.0807
Final R indexes [all data]	R_1 = 0.0506, wR_2 = 0.0904
Largest diff. peak/hole / e Å^{-3}	1.32/-0.55

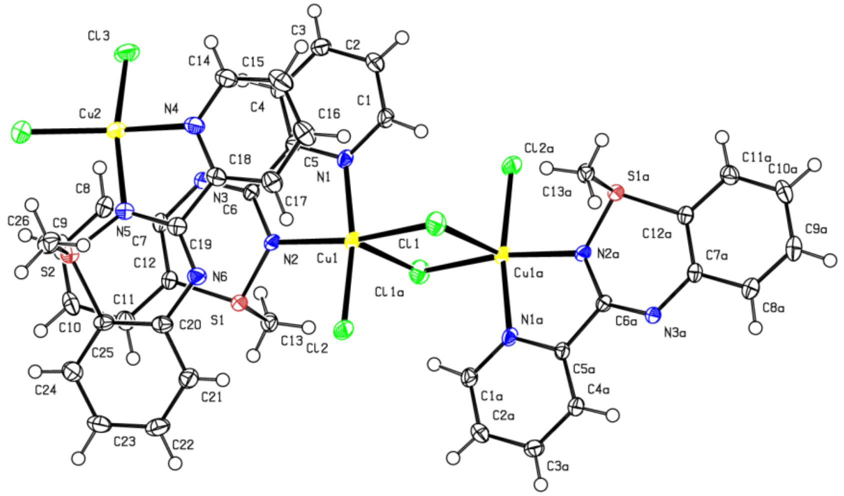

4.4 ZnCl$_2$(pybtdaSMe)

Table 1 Crystal data and structure refinement for mo_kp183A_0m_a.

Identification code	mo_kp183A_0m_a
Empirical formula	$C_{26}H_{22}Cl_4N_6S_2Zn_2$
Formula weight	755.15
Temperature/K	170.0
Crystal system	triclinic
Space group	P-1
a/Å	9.0804(5)
b/Å	9.4757(6)
c/Å	10.2690(7)
α/°	70.623(2)
β/°	74.274(2)
γ/°	64.885(2)
Volume/Å^3	745.90(8)
Z	1
ρ_{calc}g/cm^3	1.681
μ/mm^{-1}	2.135
F(000)	380.0
Crystal size/mm^3	0.336 × 0.269 × 0.05
Radiation	MoKα (λ = 0.71073)
2Θ range for data collection/°	5.682 to 56.736
Index ranges	$-12 \le h \le 12$, $-12 \le k \le 12$, $-13 \le l \le 13$
Reflections collected	29648
Independent reflections	3724 [R_{int} = 0.0363, R_{sigma} = 0.0194]
Data/restraints/parameters	3724/0/210
Goodness-of-fit on F^2	1.068
Final R indexes [I>=2σ (I)]	R_1 = 0.0295, wR_2 = 0.0685
Final R indexes [all data]	R_1 = 0.0415, wR_2 = 0.0762
Largest diff. peak/hole / e Å^{-3}	1.04/-0.47

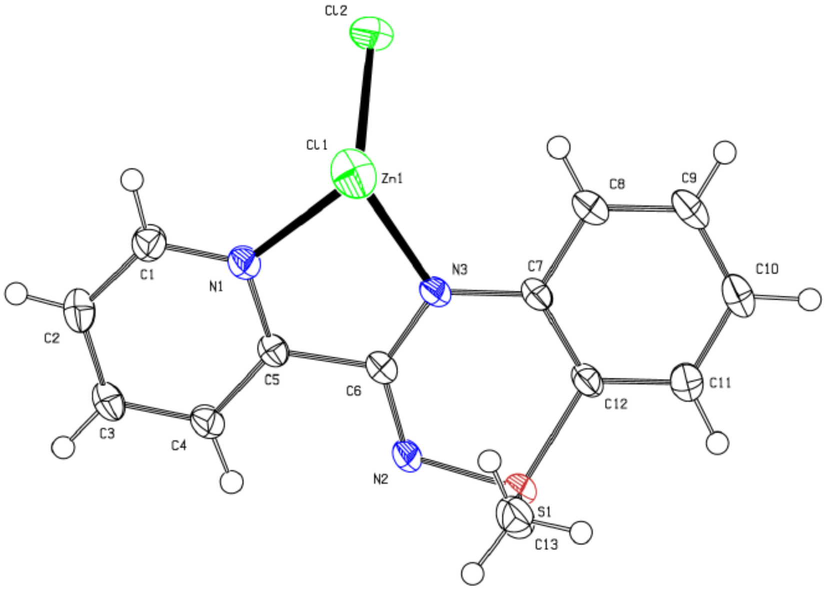

4.5 Co(hfac)$_2$(pybtdaSMe)

Table 1 Crystal data and structure refinement for mo_KP246_0m_a.

Identification code	mo_KP246_0m_a
Empirical formula	$C_{23}H_{13}CoF_{11.94}N_3O_4S$
Formula weight	713.26
Temperature/K	169.81
Crystal system	orthorhombic
Space group	Pbca
a/Å	10.1245(4)
b/Å	17.8990(7)
c/Å	29.6465(12)
α/°	90
β/°	90
γ/°	90
Volume/Å^3	5372.5(4)
Z	8
ρ_{calc}g/cm^3	1.764
μ/mm^{-1}	0.837
F(000)	2836.0
Crystal size/mm^3	0.68 × 0.55 × 0.05
Radiation	MoKα (λ = 0.71073)
2Θ range for data collection/°	6.142 to 50.726
Index ranges	$-10 \le h \le 12$, $-21 \le k \le 21$, $-35 \le l \le 35$
Reflections collected	54562
Independent reflections	4915 [$R_{int} = 0.0969$, $R_{sigma} = 0.0424$]
Data/restraints/parameters	4915/24/395
Goodness-of-fit on F^2	1.069
Final R indexes [I>=2σ (I)]	$R_1 = 0.0570$, $wR_2 = 0.1346$
Final R indexes [all data]	$R_1 = 0.0822$, $wR_2 = 0.1527$
Largest diff. peak/hole / e Å^{-3}	0.94/-0.56

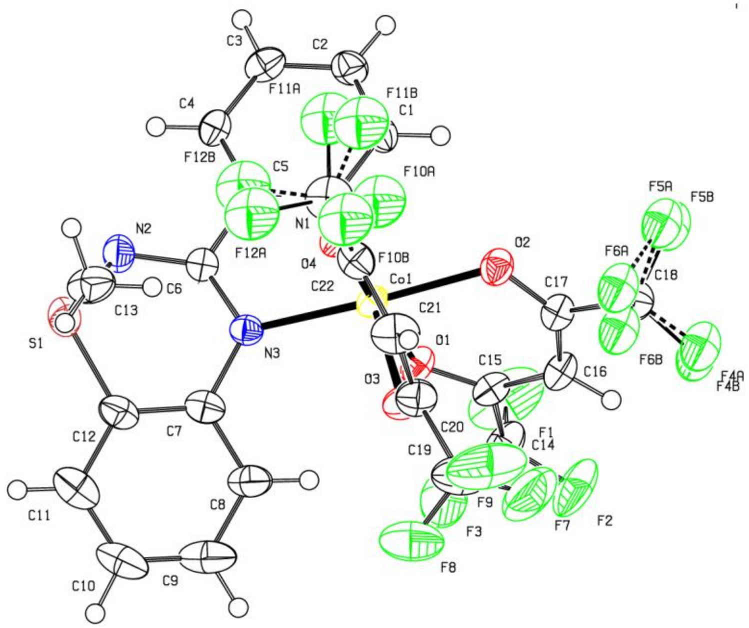

4.6 Ni(hfac)$_2$(pybtdaSMe)

Table 1 Crystal data and structure refinement for mo_KP247A_0m_a.

Identification code	mo_KP247A_0m_a
Empirical formula	$C_{23}H_{13}F_{12}N_3NiO_4S$
Formula weight	714.13
Temperature/K	169.8
Crystal system	orthorhombic
Space group	Pbca
a/Å	10.1226(3)
b/Å	17.8921(6)
c/Å	29.5312(8)
α/°	90
β/°	90
γ/°	90
Volume/Å^3	5348.5(3)
Z	8
ρ_{calc}g/cm^3	1.774
μ/mm^{-1}	0.925
F(000)	2848.0
Crystal size/mm^3	0.02 × 0.3 × 0.2
Radiation	MoKα (λ = 0.71073)
2Θ range for data collection/°	6.154 to 51.438
Index ranges	$-12 \le h \le 12$, $-21 \le k \le 21$, $-36 \le l \le 31$
Reflections collected	118508
Independent reflections	5076 [$R_{int} = 0.1089$, $R_{sigma} = 0.0301$]
Data/restraints/parameters	5076/36/383
Goodness-of-fit on F^2	1.089
Final R indexes [I>=2σ (I)]	$R_1 = 0.0753$, $wR_2 = 0.1577$
Final R indexes [all data]	$R_1 = 0.1023$, $wR_2 = 0.1752$
Largest diff. peak/hole / e Å^{-3}	1.18/-0.82

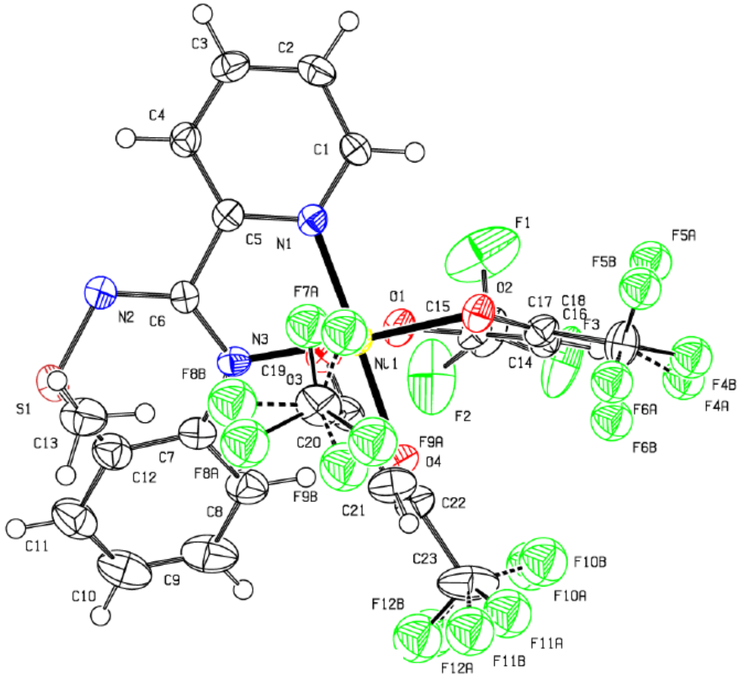

APPENDIX 4: Crystal Data and Structure Refinement for Compounds of Chapter 5

5.2 3-[6-(1,3-benzothiazol-2-yl)pyridin-2-yl]-4*H*-1,2,4-benzothiadiazine

Table 1 Crystal data and structure refinement for muabis.

Identification code	muabis
Empirical formula	$C_{19}H_{12}N_4S_2$
Formula weight	360.45
Temperature/K	173.15
Crystal system	orthorhombic
Space group	$Pna2_1$
a/Å	22.486(7)
b/Å	6.0358(18)
c/Å	11.857(4)
α/°	90
β/°	90
γ/°	90
Volume/Å^3	1609.3(8)
Z	4
ρ_{calc}g/cm^3	1.488
μ/mm^{-1}	0.340
F(000)	744.0
Crystal size/mm^3	0.3 × 0.1 × 0.1
Radiation	MoKα (λ = 0.71073)
2Θ range for data collection/°	6.872 to 55.524
Index ranges	$-25 \leq h \leq 29$, $-7 \leq k \leq 7$, $-15 \leq l \leq 11$
Reflections collected	6296
Independent reflections	3201 [$R_{int} = 0.0387$, $R_{sigma} = 0.0611$]
Data/restraints/parameters	3201/1/226
Goodness-of-fit on F^2	1.055
Final R indexes [I>=2σ (I)]	$R_1 = 0.0459$, $wR_2 = 0.0956$
Final R indexes [all data]	$R_1 = 0.0612$, $wR_2 = 0.1063$
Largest diff. peak/hole / e Å^{-3}	0.30/-0.28
Flack parameter	0.12(8)

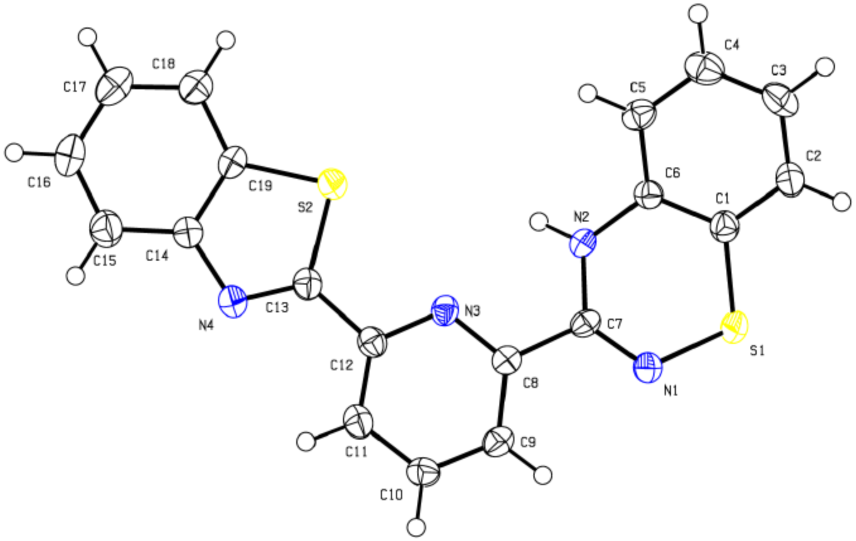

bisbtdaH$_2$

Table 1 Crystal data and structure refinement for mo_KP244_0m.

Identification code	mo_KP244_0m
Empirical formula	$C_{19}H_{13}N_5S_2$
Formula weight	375.46
Temperature/K	293.15
Crystal system	triclinic
Space group	P-1
a/Å	11.185(4)
b/Å	12.015(5)
c/Å	13.609(8)
α/°	102.372(19)
β/°	94.93(2)
γ/°	107.958(17)
Volume/Å^3	1676.4(14)
Z	4
ρ_{calc}g/cm^3	1.488
μ/mm^{-1}	0.331
F(000)	776.0
Crystal size/mm^3	0.7 × 0.4 × 0.12
Radiation	MoKα (λ = 0.71073)
2Θ range for data collection/°	6.176 to 52.96
Index ranges	$-13 \leq h \leq 13, -15 \leq k \leq 15, -17 \leq l \leq 17$
Reflections collected	62120
Independent reflections	6843 [$R_{int} = 0.0363, R_{sigma} = 0.0176$]
Data/restraints/parameters	6843/0/469
Goodness-of-fit on F^2	1.132
Final R indexes [I>=2σ (I)]	$R_1 = 0.0496, wR_2 = 0.1016$
Final R indexes [all data]	$R_1 = 0.0699, wR_2 = 0.1205$
Largest diff. peak/hole / e Å^{-3}	0.61/-0.51

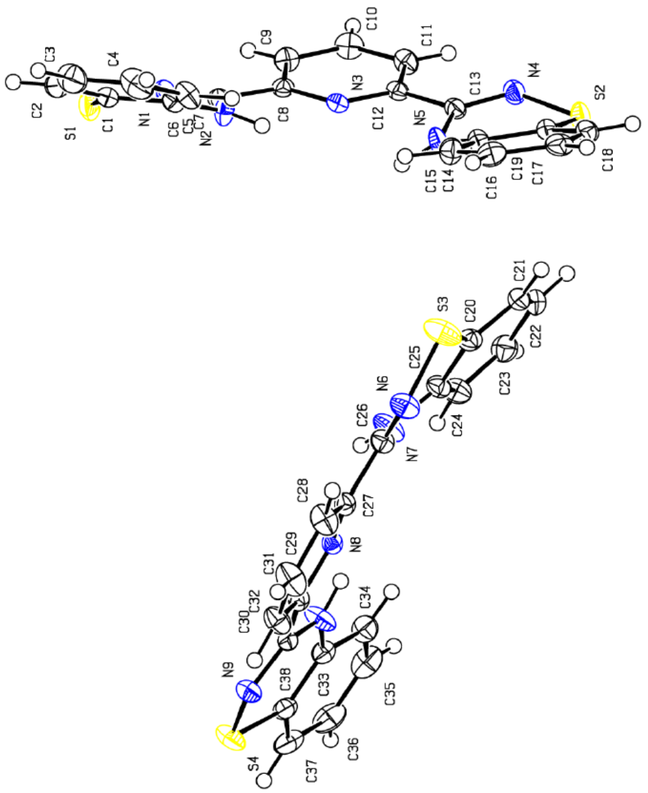

5.3 [Mn(bisbtdaH$_2$)$_2$][CF$_3$SO$_3$]$_2$

Table 1 Crystal data and structure refinement for kp_mua261_a.

Identification code	kp_mua261_a
Empirical formula	$C_{40}H_{26}F_6MnN_{10}O_6S_6$
Formula weight	1104.01
Temperature/K	170.0
Crystal system	orthorhombic
Space group	Pccn
a/Å	15.7882(7)
b/Å	19.1313(9)
c/Å	14.6344(8)
α/°	90
β/°	90
γ/°	90
Volume/Å^3	4420.3(4)
Z	4
ρ_{calc}g/cm^3	1.659
μ/mm^{-1}	0.669
F(000)	2236.0
Crystal size/mm^3	0.3 × 0.225 × 0.08
Radiation	MoKα (λ = 0.71073)
2Θ range for data collection/°	5.704 to 52.844
Index ranges	$-17 \leq h \leq 19$, $-23 \leq k \leq 23$, $-18 \leq l \leq 18$
Reflections collected	65724
Independent reflections	4530 [R_{int} = 0.0756, R_{sigma} = 0.0250]
Data/restraints/parameters	4530/429/332
Goodness-of-fit on F^2	1.042
Final R indexes [I>=2σ (I)]	R_1 = 0.0412, wR_2 = 0.0933
Final R indexes [all data]	R_1 = 0.0619, wR_2 = 0.1060
Largest diff. peak/hole / e Å^{-3}	0.74/-0.74

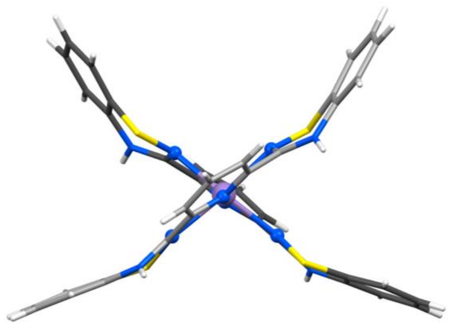

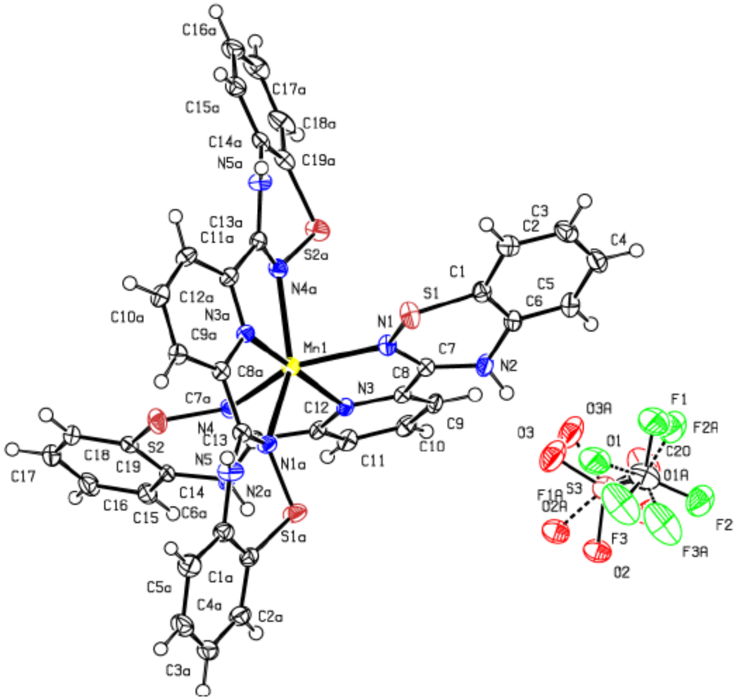

5.4 [Fe(bisbtdaH$_2$)$_2$][CF$_3$SO$_3$]$_2$·2CH$_3$CN

Table 1 Crystal data and structure refinement for MUA2yb_2.

Identification code	MUA2yb_2
Empirical formula	$C_{43.2}H_{30.8}F_6FeN_{11.6}O_7S_6$
Formula weight	1186.60
Temperature/K	150.0
Crystal system	monoclinic
Space group	Pc
a/Å	10.9579(4)
b/Å	11.0245(4)
c/Å	22.8045(8)
α/°	90
β/°	103.5220(12)
γ/°	90
Volume/Å^3	2678.54(17)
Z	2
ρ_{calc}g/cm^3	1.471
μ/mm^{-1}	0.594
F(000)	1206.0
Crystal size/mm^3	0.24 × 0.16 × 0.07
Radiation	MoKα (λ = 0.71073)
2Θ range for data collection/°	5.91 to 49.894
Index ranges	$-12 \le h \le 12$, $-13 \le k \le 13$, $-26 \le l \le 26$
Reflections collected	53922
Independent reflections	9207 [$R_{int} = 0.0403$, $R_{sigma} = 0.0282$]
Data/restraints/parameters	9207/3/667
Goodness-of-fit on F^2	1.086
Final R indexes [I>=2σ (I)]	$R_1 = 0.0433$, $wR_2 = 0.1180$
Final R indexes [all data]	$R_1 = 0.0465$, $wR_2 = 0.1200$
Largest diff. peak/hole / e Å^{-3}	1.02/-0.46
Flack parameter	0.03(2)

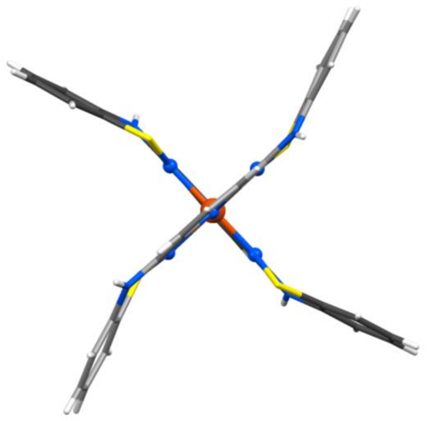

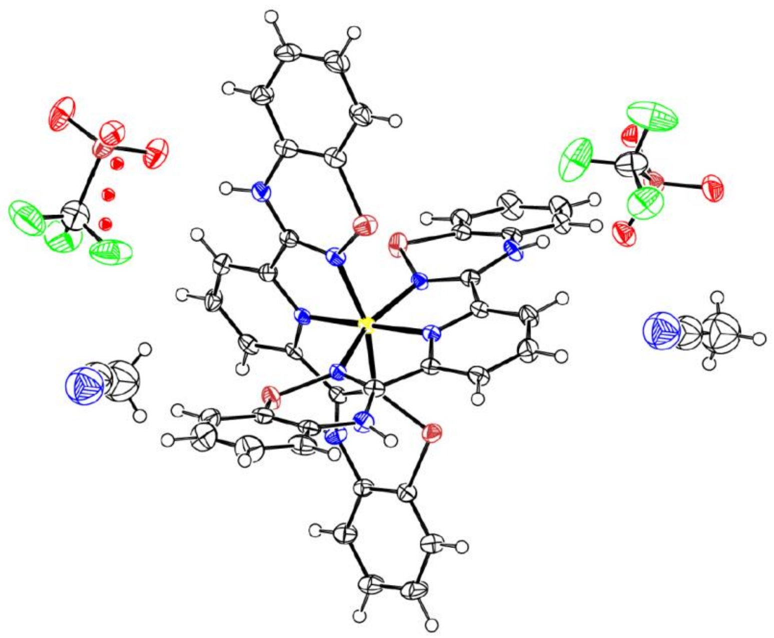

5.5 $[Fe(bisbtdaH_2)_2][BF_4]_2\cdot CH_3CN$

Table 1 Crystal data and structure refinement for mo_kp220_1_0m_a_sq.

Identification code	mo_kp220_1_0m_a_sq
Empirical formula	$C_{41}H_{32.5}FeN_{11.5}S_4B_2F_8O$
Formula weight	1057.98
Temperature/K	170(2)
Crystal system	triclinic
Space group	P-1
a/Å	10.4736(7)
b/Å	11.5949(7)
c/Å	20.9064(15)
α/°	95.960(3)
β/°	95.697(3)
γ/°	94.746(3)
Volume/Å^3	2501.6(3)
Z	2
ρ_{calc}g/cm^3	1.405
μ/mm^{-1}	0.543
F(000)	1074.0
Crystal size/mm^3	0.465 × 0.270 × 0.030
Radiation	MoKα (λ = 0.71073)
2Θ range for data collection/°	5.858 to 52.892
Index ranges	$-13 \leq h \leq 13$, $-14 \leq k \leq 14$, $-26 \leq l \leq 26$
Reflections collected	58676
Independent reflections	10232 [R_{int} = 0.0435, R_{sigma} = 0.0290]
Data/restraints/parameters	10232/74/660
Goodness-of-fit on F^2	1.078
Final R indexes [I>=2σ (I)]	R_1 = 0.0924, wR_2 = 0.2449
Final R indexes [all data]	R_1 = 0.1145, wR_2 = 0.2643
Largest diff. peak/hole / e Å^{-3}	1.46/-0.97

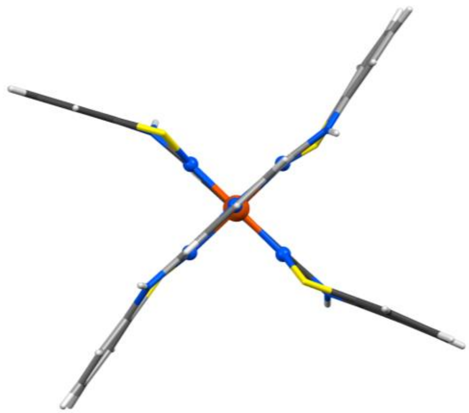

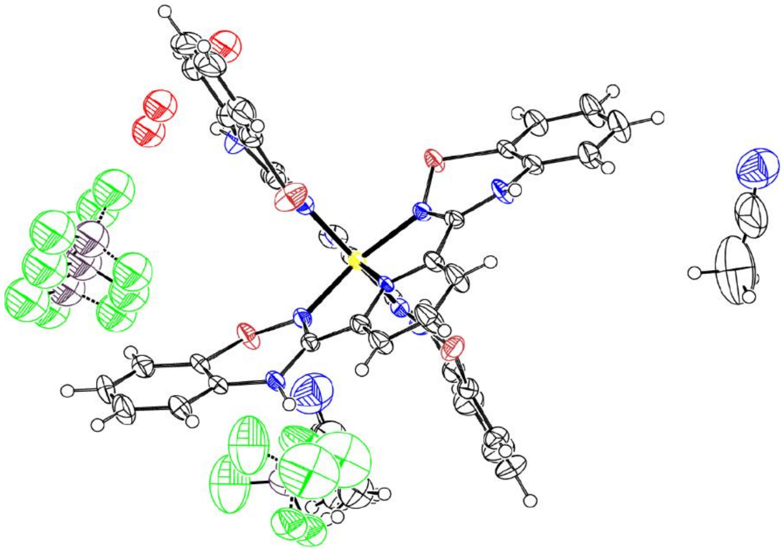

5.6 [Co(bisbtdaH$_2$)$_2$][Cl]$_2$

Table 1 Crystal data and structure refinement for MUAL4.

Identification code	MUAL4
Empirical formula	$C_{38}H_{26}N_{10}S_4Cl_2Co$
Formula weight	880.76
Temperature/K	170.0
Crystal system	monoclinic
Space group	$P2_1/n$
a/Å	17.532(4)
b/Å	11.793(3)
c/Å	18.170(4)
α/°	90
β/°	91.443(8)
γ/°	90
Volume/Å^3	3755.5(14)
Z	4
ρ_{calc}g/cm^3	1.558
μ/mm^{-1}	0.867
F(000)	1796.0
Crystal size/mm^3	0.15 × 0.1 × 0.03
Radiation	MoKα (λ = 0.71073)
2Θ range for data collection/°	5.792 to 49.988
Index ranges	$-20 \le h \le 20$, $-14 \le k \le 14$, $-21 \le l \le 21$
Reflections collected	78969
Independent reflections	6593 [R_{int} = 0.0410, R_{sigma} = 0.0167]
Data/restraints/parameters	6593/0/508
Goodness-of-fit on F^2	1.126
Final R indexes [I>=2σ (I)]	R_1 = 0.0425, wR_2 = 0.0898
Final R indexes [all data]	R_1 = 0.0562, wR_2 = 0.1059
Largest diff. peak/hole / e Å^{-3}	0.69/-0.38

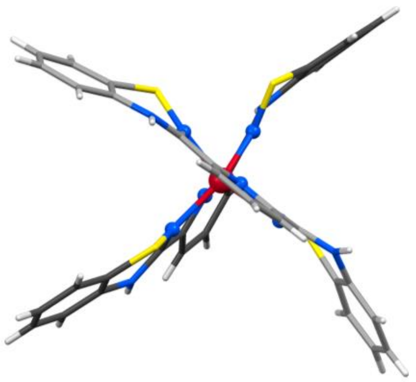

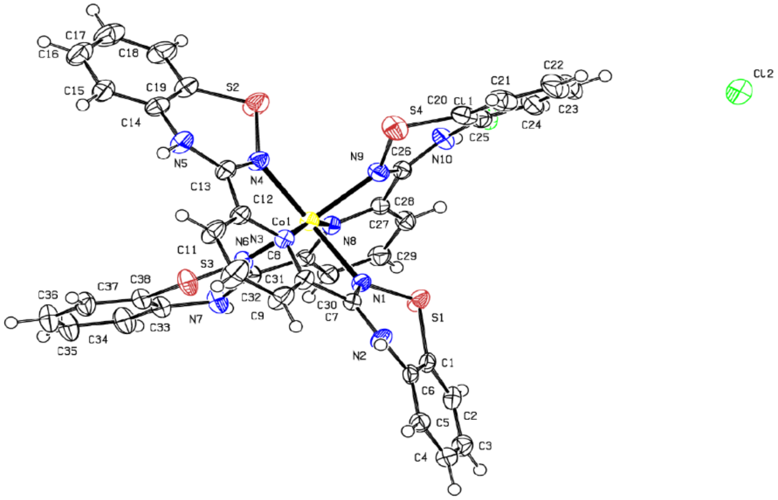

5.7 [Ni(bisbtdaH$_2$)$_2$][Cl]$_2$·2CH$_3$OH

Table 1 Crystal data and structure refinement for MUA307.

Identification code	MUA307
Empirical formula	$C_{42}H_{42}N_{10}S_4Cl_2NiO_4$
Formula weight	1008.70
Temperature/K	172.98
Crystal system	triclinic
Space group	P-1
a/Å	11.1570(8)
b/Å	11.2770(9)
c/Å	18.8943(13)
α/°	75.071(3)
β/°	82.746(3)
γ/°	89.138(3)
Volume/Å^3	2278.2(3)
Z	2
ρ_{calc}g/cm^3	1.470
μ/mm^{-1}	0.780
F(000)	1044.0
Crystal size/mm^3	0.22 × 0.21 × 0.16
Radiation	MoKα (λ = 0.71073)
2Θ range for data collection/°	5.86 to 54.378
Index ranges	$-14 \le h \le 14$, $-14 \le k \le 14$, $-24 \le l \le 24$
Reflections collected	83596
Independent reflections	10113 [R_{int} = 0.0522, R_{sigma} = 0.0263]
Data/restraints/parameters	10113/10/602
Goodness-of-fit on F^2	1.128
Final R indexes [I>=2σ (I)]	R_1 = 0.0506, wR_2 = 0.1100
Final R indexes [all data]	R_1 = 0.0640, wR_2 = 0.1200
Largest diff. peak/hole / e Å^{-3}	0.66/-0.61

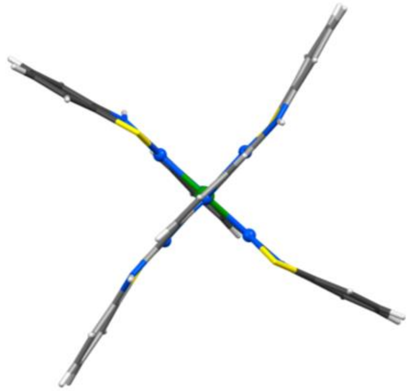

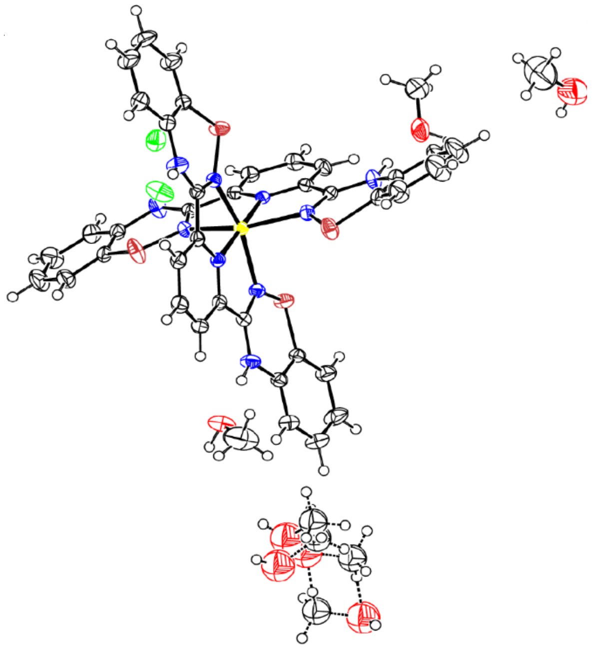

5.8 $[Zn(bisbtdaH_2)_2][CF_3SO_3]_2\cdot 2CH_3OH$

Table 1 Crystal data and structure refinement for mo_LM10B_0m.

Identification code	mo_LM10B_0m
Empirical formula	$C_{41}H_{30}N_{10}O_7F_6S_6Zn$
Formula weight	1146.48
Temperature/K	173.19
Crystal system	monoclinic
Space group	C2/c
a/Å	27.6103(9)
b/Å	11.4305(4)
c/Å	29.8443(8)
α/°	90
β/°	103.9985(10)
γ/°	90
Volume/Å^3	9139.1(5)
Z	8
ρ_{calc}g/cm^3	1.666
μ/mm^{-1}	0.899
F(000)	4656.0
Crystal size/mm^3	0.23 × 0.11 × 0.06
Radiation	MoKα (λ = 0.71073)
2Θ range for data collection/°	5.692 to 52.806
Index ranges	$-34 \le h \le 34$, $-14 \le k \le 14$, $-37 \le l \le 36$
Reflections collected	110527
Independent reflections	9368 [R_{int} = 0.0526, R_{sigma} = 0.0228]
Data/restraints/parameters	9368/66/687
Goodness-of-fit on F^2	1.159
Final R indexes [I>=2σ (I)]	R_1 = 0.0541, wR_2 = 0.1127
Final R indexes [all data]	R_1 = 0.0672, wR_2 = 0.1182
Largest diff. peak/hole / e Å^{-3}	1.57/-1.27

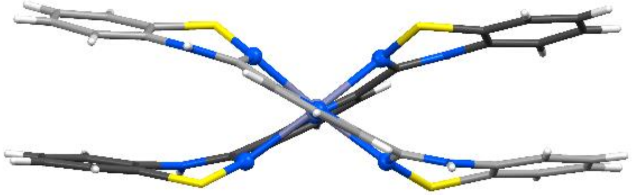

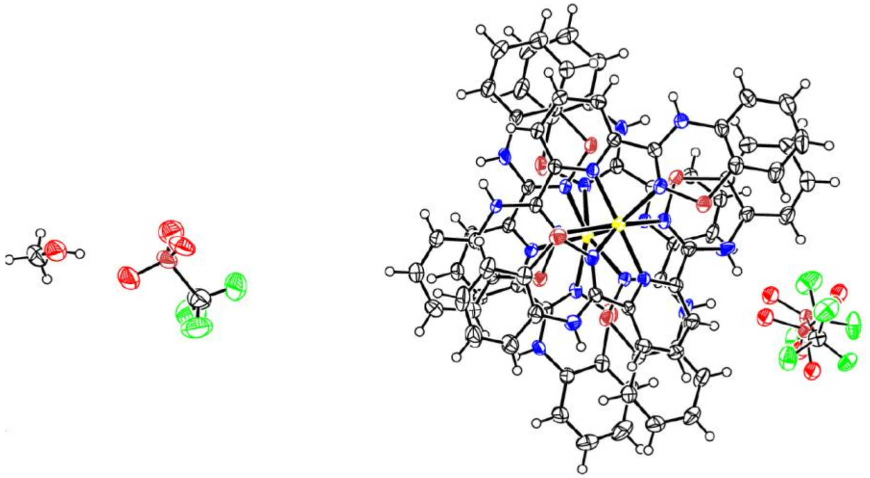

5.9 [Cu(bisbtdaH$_2$)(NO$_3$)$_2$]·DMF

Table 1 Crystal data and structure refinement for MUA300_a.

Identification code	MUA300_a
Empirical formula	$C_{22}H_{20}N_8O_7S_2Cu$
Formula weight	636.12
Temperature/K	172.82
Crystal system	monoclinic
Space group	$P2_1/c$
a/Å	9.3785(4)
b/Å	18.3497(9)
c/Å	14.9570(7)
α/°	90
β/°	92.4220(16)
γ/°	90
Volume/Å^3	2571.7(2)
Z	4
ρ_{calc}g/cm^3	1.643
μ/mm^{-1}	1.072
F(000)	1300.0
Crystal size/mm^3	0.6 × 0.38 × 0.38
Radiation	MoKα (λ = 0.71073)
2Θ range for data collection/°	5.888 to 52.742
Index ranges	$-11 \leq h \leq 11$, $-22 \leq k \leq 22$, $-18 \leq l \leq 18$
Reflections collected	82285
Independent reflections	5254 [$R_{int} = 0.0470$, $R_{sigma} = 0.0168$]
Data/restraints/parameters	5254/0/370
Goodness-of-fit on F^2	1.179
Final R indexes [I>=2σ (I)]	$R_1 = 0.0355$, $wR_2 = 0.0796$
Final R indexes [all data]	$R_1 = 0.0425$, $wR_2 = 0.0872$
Largest diff. peak/hole / e Å^{-3}	0.40/-0.40

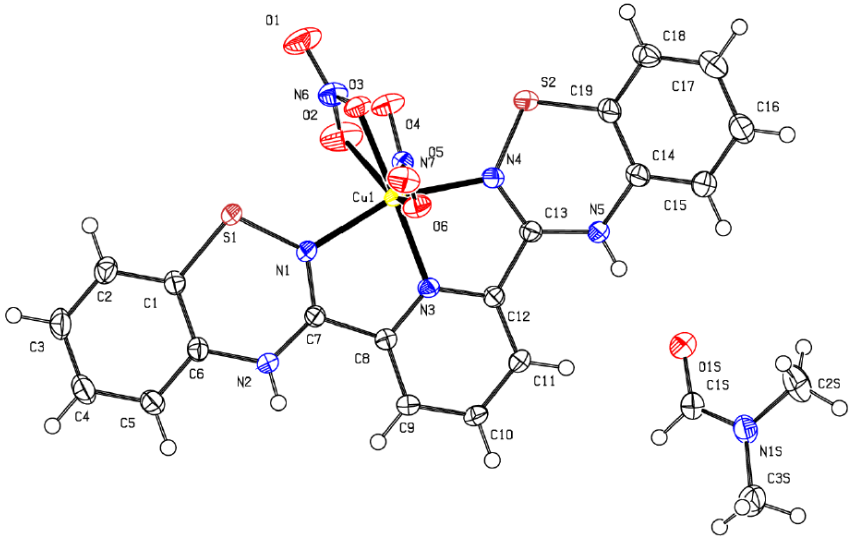

VITA AUCTORIS

NAME: Konstantina Pringouri
PLACE OF BIRTH: Amaroussio, Attikis, GREECE
EDUCATION: **Ph.D. Chemistry**
Department of Chemistry and Biochemistry
University of Windsor
Windsor, ON, CANADA 2018
M.Sc. Chemistry
Department of Chemistry
University of Florida
Gainesville, FL, U.S.A. 2008
B.Sc. Chemistry
Department of Chemistry
University of Patras
Patras, GREECE 2006

AWARDS

- Ontario Trillium Scholarship (2014, $40,000 annually)
- Travel Award for ACA Summer Course in Chemical Crystallography (2017, $300)

PUBLICATIONS

1. Amlan K. Pal, David B. Cordes, **Konstantina Pringouri**, Muhammad U. Anwar, Alexandra M. Z. Slawin, Jeremy M. Rawson, and Eli Zysman-Colman,
   "Synthesis and characterization of green-to-yellow emissive Ir(III) complexes of pyridylbenzothiadiazine ligand"
   Journal of Coordination Chemistry, 2016, **11-13**, 1924-1937

2. **Konstantina Pringouri**, Muhammad U. Anwar, Bryce J. Leontowicz, and Jeremy M. Rawson,
   "Zinc complexes of 3-pyrimidinyl-benzo-1,2,4-thiadiazine"
   Polyhedron, 2018, **150**, 110-117

3. **Konstantina Pringouri**, Muhammad U. Anwar, Liz Mansour, Nathan Doupnik, Yassine Beldjoudi, Emma L. Gavey, Melanie Pilkington, and Jeremy M. Rawson,
   "A novel bis-1,2,4-benzothiadiazine pincer ligand: Synthesis, characterization and its first row transition metal complexes"
   Dalton Trans., *Under revision*

PRESENTATIONS

1. **Konstantina Pringouri**, Muhammad U. Anwar, and Jeremy M. Rawson,

   "Exploring New Derivatives of 1,2,4-Benzothiadiazines and their Coordination Chemistry"

   98th CSC, June 13-17, 2015, Ottawa, Ontario, Canada, Poster Presentation

2. **Konstantina Pringouri**, Muhammad U. Anwar, and Jeremy M. Rawson,

   "Exploring New Derivatives of 1,2,4-Benzothiadiazines and their Coordination Chemistry"

   3rd CEMWOQ, May 14-15, 2016, University of Windsor, Windsor, Ontario, Canada, Poster Presentation

3. **Konstantina Pringouri**, Muhammad U. Anwar, and Jeremy M. Rawson,

   "Exploring New Derivatives of 1,2,4-Benzothiadiazines and their Coordination Chemistry"

   99th CSC, June 5-9, 2016, Halifax, Nova Scotia, Canada, Poster Presentation

4. **Konstantina Pringouri**, Muhammad U. Anwar, and Jeremy M. Rawson,

   "New Derivatives of 1,2,4-Benzothiadiazines and their Coordination Chemistry"

   49th IDW, November 11-13, 2016, Hamilton, Ontario, Canada, Oral Presentation

5. **Konstantina Pringouri**, Muhammad U. Anwar, and Jeremy M. Rawson,

   "New Derivatives of 1,2,4-Benzothiadiazines and their Coordination Chemistry"

   4th CEMWOQ, May 26 - 28, 2017, Wilfrid Laurier University, Waterloo, Ontario, Canada, Poster Presentation

6. **Konstantina Pringouri**, Muhammad U. Anwar, and Jeremy M. Rawson,

   "New Derivatives of 1,2,4-Benzothiadiazines and their Coordination Chemistry"

   100th CSC, May 28 - June 1, 2017, Toronto, Ontario, Canada, Poster Presentation

7. **Konstantina Pringouri**, Muhammad U. Anwar, and Jeremy M. Rawson,

   "A Novel Bis-1,2,4-benzothiadiazine Pincer Ligand: Synthesis, Characterization and Coordination Chemistry"

   50th IDW, November 3-5, 2017, Ryerson University, Toronto, Ontario, Canada, Oral Presentation